

VIBRATIONS IN PHYSICAL SYSTEMS

Volume XXVI

Editors

**Czesław CEMPEL, Marian W. DOBRY,
Tomasz STREK**

Poznan 2014



VIBRATIONS IN PHYSICAL SYSTEMS
Vol. 26, 2014

ISSN 0860-6897

EDITORIAL OFFICE

Poznan University of Technology
Institute of Applied Mechanics
ul. Jana Pawła II 24, 61-139 Poznań, Poland
tel. +48 61 665 23 87, fax: +48 61 665 23 07
e-mail: office_am@put.poznan.pl
www.vibsys.put.poznan.pl

EDITORIAL BOARD

Editor: Czesław CEMPEL

Co-editor: Marian W. DOBRY

Co-editor: Tomasz STRĘK

Secretary: Małgorzata WOJSZNIS

ADVISORY BOARD

Vladimir I. ALSHITS, Jan AWREJCEWICZ, Romuald BĘDZIŃSKI, Roman BOGACZ,
Tadeusz BURCZYŃSKI, Enzo CIANCIO, Yevhen CHAPLYA, Marian DOBRY,
Antoni GAJEWSKI, Joseph GRIMA, Jan HOLNICKI-SZULC, Stefan JONIAK, David JOU,
Jerzy KALETA, Jan KOŁODZIEJ, Tomasz ŁODYGOWSKI, Krzysztof MAGNUCKI,
Krzysztof MARCHELEK, Bogdan MARUSZEWSKI, Stanisław MATYSIAK,
Gerard A. MAUGIN, Wolfgang MUSCHIK, Józef NIZIOŁ, Andrzej RADOWICZ,
Liliana RESTUCCIA, Tomasz SZOLC, Franciszek TOMASZEWSKI, Andrzej TYLIKOWSKI,
Tadeusz UHL, Aleksandr YAVLENSKY, Józef WOJNAROWSKI, Czesław WOŹNIAK

Typeset: Paweł JASION

Cover design: Piotr GOŁĘBNIAK

PUBLISHED AND PRINTED

Agencja Reklamowa COMPRINT

ul. H. Rzepeckiej 26 A, 60-465 Poznań, Poland

Tel. +48 602 26 64 26, e-mail: comprint@data.pl, www.comprint.com.pl

© Copyright by Poznań University of Technology, Poznań, Poland 2014

Edition based on ready-to-publish materials submitted by authors.

No part of this work may be reproduced, stored in a retrieval system, or transmitted in any form
or by any means, electronic, mechanical, photocopying, microfilming, recording or otherwise,
without written permission from the copyright owner.

**The volume was published in the cooperation of the Institute of Applied Mechanics at Poznań
University of Technology and Polish Society of Theoretical and Applied Mechanics.
This journal has been indexed in the list of Ministry of Science and Higher Education (4 points).**

**POZNAN UNIVERSITY OF TECHNOLOGY
MECHANICAL ENGINEERING
AND MANAGEMENT FACULTY
INSTITUTE OF APPLIED MECHANICS
POLISH SOCIETY OF THEORETICAL
AND APPLIED MECHANICS**

**XXVI SYMPOSIUM
VIBRATIONS
IN PHYSICAL SYSTEMS**

2014

XXVI SYMPOSIUM VIBRATIONS IN PHYSICAL SYSTEMS

Bedlewo (near Poznan), May 4-8, 2014

Present edition of Symposium Vibrations in Physical Systems is under auspices of

President of Poznan University of Technology

Tomasz ŁODYGOWSKI

Dean of Mechanical Engineering and Management Faculty

Olaf CISZAK

SCIENTIFIC COMMITTEE

Czesław CEMPEL – president, Andrzej TYLIKOWSKI – vice-president,
Vladimir I. ALSHTIS, Jan AWREJCEWICZ, Romuald BĘDZIŃSKI, Roman BOGACZ,
Tadeusz BURCZYŃSKI, Enzo CIANCIO, Yevhen CHAPLYA, Marian DOBRY,
Antoni GAJEWSKI, Joseph GRIMA, Jan HOLNICKI-SZULC, Stefan JONIAK, David JOU,
Jerzy KALETA, Jan KOŁODZIEJ, Tomasz ŁODYGOWSKI, Krzysztof MAGNUCKI,
Krzysztof MARCHELEK, Bogdan MARUSZEWSKI, Stanisław MATYSIAK,
Gerard A. MAUGIN, Wolfgang MUSCHIK, Józef NIZIOŁ, Andrzej RADOWICZ,
Liliana RESTUCCIA, Tomasz SZOLC, Franciszek TOMASZEWSKI, Tadeusz UHL,
Alexandr YAVLENSKY, Józef WOJNAROWSKI, Czesław WOŹNIAK

REVIEWERS OF PAPERS

Jan AWREJCEWICZ, Roman BARCZEWSKI, Romuald BĘDZIŃSKI, Roman BOGACZ,
Tadeusz BURCZYŃSKI, Jacek BUŚKIEWICZ, Czesław CEMPEL, Yevhen CHAPLYA,
Michał CIAŁKOWSKI, Marian W. DOBRY, Paweł FRITZKOWSKI, Adam GLEMA,
Zdzisław GOLEC, Jan HOLNICKI-SZULC, Stefan JONIAK, Hubert JOPEK,
Henryk KAŽMIERCZAK, Jan KOŁODZIEJ, Roman LEWANDOWSKI, Wojciech ŁAPKA,
Krzysztof MAGNUCKI, Bogdan MARUSZEWSKI, Józef NIZIOŁ, Marian OSTWALD,
Tomasz STRĘK, Tomasz SZOLC, Maciej TABASZEWSKI, Franciszek TOMASZEWSKI

ORGANIZING COMMITTEE

Bogdan T. MARUSZEWSKI – chairman, Roman STAROSTA – co-chairman,
Paweł FRITZKOWSKI – secretary, Czesław CEMPEL, Marian DOBRY, Paulina FOPP,
Magdalena GRYGOROWICZ, Paweł JASION, Hubert JOPEK, Tomasz MACHNICKI,
Tomasz STRĘK, Maciej TABASZEWSKI, Tomasz WALCZAK

FINANCIAL SUPPORT

Ministry of Science and Higher Education
Mechanical Engineering and Management Faculty

SPONSORS

- EC Test Systems Sp. z o.o. • Brüel & Kjaer Polska Sp. z o.o.
 - Klimatest Trzymadłowski i Wspólnicy Sp. j. • ENVIBRA Sp. z o.o.
 - Gambit Centrum Oprogramowania i Szkoleń Sp. z o.o. • VOL Sp. z o.o. Sp. k.
-

Introduction to the Volume XXVI Collection of Papers of the Conference Vibrations in Physical Systems -2014

The phenomena of vibrations, oscillations and waves as physical phenomena are omni-present around us. They are the sign of life, the sign of the operation of machines and devices and they accompany any production processes. Their effects may be harmful, useful and they may also be a source of information on the technical condition of the supervised machines and devices. Volume XXVI of Vibrations in Physical Systems published every second year deals with these widespread phenomena. It comprises the papers presented by specialists from our country but also from abroad at many sessions of XXVI Symposium of Vibrations in Physical Systems organized also every second year. The symposium has been organized since 1960 in Poznan by a local branch of the **Polish Society of Theoretical and Applied Mechanics** and the **Institute of Applied Mechanics at Poznan University of Technology**.

This conference is unusual one; we are present in a scientific space 26th times since 1960. This means the subjects we are dealing are still important and still brings the attention of scientific community and co working practitioners. Of course, year by year our outlook is evolving; and the scope of current conference has been widened from the previous one, and is currently as follows:

- Mathematical Modeling in Sound and Vibration Analysis
- Experimental Techniques in Sound and Vibration Engineering
- Wave Problems in Solid Mechanics
- Analysis of the Non-Linear Deterministic / Stochastic Vibrations Phenomena
- Computational Methods in Vibration Problems
- Modeling and Identification of Dynamical Systems
- Signal Processing and Analysis
- Active Vibration Control
- Energy Methods in Vibration Engineering
- Vibration and Energy Problems Related to Biomechanics
- Dynamics of Machinery and Rotating Systems
- Vibroacoustics of Machinery, Diagnostics
- Vibrations and Noise of Transport Systems, Vehicles, Roads
- Structural Dynamics, Vibrations of Composite Materials Structures
- Vibration Problems in Environmental Engineering, Vibration of Granular Materials
- Vibrations and Dynamic Stability of Structural Elements, Beams, Plates, Shells
- Flow-induced vibrations, Fluid-structure interaction, Aeroelasticity
- Dynamic behavior of Vibration Isolation Elements and Systems.

As it is seen the topics of the publications relate to a wide range of issues connected with modelling and identification of mechanical systems, their stability and dynamics of mechanical systems as well as physical phenomena such as propagation of acoustic waves and vibrations in all aspects of science and engineering, beginning from the theory and modelling up to the applicational subjects in machines, environment and the human body

The monograph comprises also numerously presented publications relating to the issues of dynamics in biological as well as biological and mechanical systems. They mainly concern mechanical properties of a human body and its organs or parts. Other publications describe the dynamic interaction of power between man and machine (*Human – Hand-held Powered Tool*) or distribution of power and the energy flow in Human-Machine Systems.

Many of the publications present the results of research carried out through simulation with the application of modern digital technologies worked out for the needs of solving linear and non-linear issues of the dynamics of solid bodies or physical phenomena such as propagation of acoustic waves or dynamics and stability of complicated structures. The publications comprise the results that are analysed from the point of view of the applied methodology or the validity of the obtained data.

There are also some publications devoted to methods of passive, active and semi-active reduction of vibrations and noise and to modelling of vibrations damping with viscous damper. The publications concerning dynamic issues also analysed the stability of the tested mechanical systems.

Other significant publications concern the monitoring of technical facilities with the use of the propagation of elastic waves that allow us to detect cracks in the composite structure under the test and to specify their location. They also describe methods of modelling the propagation of sound waves in public rooms, like churches, where the acoustic quality of sound is of prime interest.

All the papers comprised in this volume have been reviewed by members of the Scientific Committee, and in some cases by specialists outside the Committee, should the issues concern problems outside the scope of knowledge of the Committee members. We would like to thank all those persons who help us review papers in this published monograph and improve their quality.

Co-editors of the 26th Volume

Czesław CEMPEL
Marian W. DOBRY

CONTENTS

INVITED PAPERS

1. Vladimir ALSHITS, Dmitrii BESSONOV, Vasilii LYUBIMOV, Andrzej RADOWICZ	13
CONVERSION EXCITATION OF INTENSE SOUND FIELDS IN CRYSTALS	
2. Wojciech BATKO	21
UNCERTAINTY IN VIBROACOUSTIC INVESTIGATIONS – RESEARCH CHALLENGES	
3. Jeremiah RUSHCHITSKY	33
NONLINEAR SURFACE ELASTIC WAVES IN MATERIALS	

PAPERS

4. Andrzej CHUDZIKIEWICZ, Andrzej MYŚLIŃSKI	41
THERMOELASTIC WHEEL-RAIL CONTACT PROBLEM FOR A MULTI-LAYER STRUCTURE	
5. Marian Witalis DOBRY, Tomasz HERMANN	49
A COMPARISON OF HUMAN PHYSICAL MODELS USED IN THE ISO 10068:2012 STANDARD BASED ON POWER DISTRIBUTION PART 1	
6. Marian Witalis DOBRY, Tomasz HERMANN	57
A COMPARISON OF HUMAN PHYSICAL MODELS USED IN THE ISO 10068:2012 STANDARD BASED ON POWER DISTRIBUTION PART 2	
7. Marian DOLIPSKI, Piotr CHELUSZKA, Piotr SOBOTA	65
NUMERICAL TESTS OF ROADHEADER'S BOOM VIBRATIONS	
8. Łukasz DOMAGALSKI, Jarosław JĘDRYSIAK	73
NONLINEAR VIBRATIONS OF PERIODIC BEAMS	
9. Jakub Krzysztof GRABSKI, Sylwia KAZIMIERCZUK, Tomasz WALCZAK	79
ANALYSIS OF THE ELECTROMYOGRAPHIC SIGNAL DURING REHABILITATION EXERCISES OF THE KNEE JOINT	

10. Rafal HEIN.....	87
THE MODELLING METHOD OF DISCRETE-CONTINUOUS SYSTEMS	
11. Jarosław JĘDRYSIAK, Ewelina PAZERA.....	93
FREE VIBRATIONS OF THIN MICROSTRUCTURED PLATES	
12. Magda KAŽMIERCZAK-SOBIŃSKA, Jarosław JĘDRYSIAK....	99
VIBRATIONS OF THIN FUNCTIONALLY GRADED PLATES	
WITH TOLERANCE-PERIODIC MICROSTRUCTURE	
13. Lidiya KHARCHENKO, Yevhen KHARCHENKO	105
FLUCTUATIONS OF MULTI-SECTION ABOVEGROUND PIPELINE	
REGION UNDER THE INFLUENCE OF MOVING	
DIAGNOSTIC PISTON	
14. Artur KROWIAK.....	113
FREE VIBRATION OF STRUCTURES BY RADIAL BASIS	
FUNCTION – PSEUDOSPECTRAL METHOD	
15. Wojciech ŁAPKA	121
TRANSMISSION LOSS AND PRESSURE DROP OF SELECTED	
RANGE OF HELICOIDAL RESONATORS METHOD	
16. Magdalena ŁASECKA-PLURA, Roman LEWANDOWSKI	129
DESIGN SENSITIVITY ANALYSIS OF FREQUENCY RESPONSE	
FUNCTIONS AND STEADY-STATE RESPONSE FOR STRUCTURES	
WITH VISCOELASTIC DAMPERS	
17. Waldemar ŁATAS.....	137
DISTRIBUTED DYNAMIC VIBRATION ABSORBER IN BEAM	
18. Waldemar ŁATAS.....	145
MULTIPLE TUNED TUNABLE TRANSLATIONAL-ROTATIONAL	
VIBRATION ABSORBERS IN BEAM	
19. Mykhailo MARCHUK, Taras GORIACHKO,	
Vira PAKOSH.....	153
GEOMETRICALLY NONLINEAR FREE TRANSVERSAL	
VIBRATIONS OF THIN-WALLED ELONGATED PANELS	
WITH ARBITRARY GENERATRIX	
20. Jakub MARCZAK, Jarosław JĘDRYSIAK	161
ANALYSIS OF VIBRATIONS OF PLATE STRIP	
WITH CONCENTRATED MASSES USING TOLERANCE AVERAGING	
TECHNIQUE	

21. Jędrzej MĄCZAK	169
MODEL BASED LOCAL FAULT DETECTION IN HELICAL GEARS	
22. Waldemar MORZUCH.....	177
DYNAMICS OF CELLULAR ROTOR OF ASYNCHRONOUS MOTOR WITH DEFORMABLE STATOR	
23. Waldemar MORZUCH.....	183
INFLUENCE OF THE DAMPING IN THE SANDWICH BAR ON THE DYNAMIC STABILITY	
24. Marek MORZYŃSKI, Michał NOWAK, Witold STANKIEWICZ	189
NOVEL METHOD OF PHYSICAL MODES GENERATION FOR REDUCED ORDER FLOW CONTROL-ORIENTED MODELS	
25. Michał NIEŁACZNY, Juliusz GRABSKI Jarosław STRZAŁKO	195
3D DYNAMIC MODEL OF THE UNICYCLE – UNICYCLIST SYSTEM	
26. Maria NIENARTOWICZ, Tomasz STREK	203
FINITE ELEMENT ANALYSIS OF DYNAMIC PROPERTIES OF THERMALLY OPTIMAL TWO-PHASE COMPOSITE STRUCTURE	
27. Stanisław NOGA.....	211
TRANSVERSE VIBRATION ANALYSIS OF A COMPOUND PLATE WITH USING CYCLIC SYMMETRY MODELING	
28. Stanisław NOGA, Tadeusz MARKOWSKI	217
VIBRATION ANALYSIS OF A THICK RING INTERACTING WITH THE DISK TREATED AS AN ELASTIC FOUNDATION	
29. Michał NOWAK, Witold STANKIEWICZ, Marek MORZYŃSKI.....	223
MODAL ANALYSIS OF VISCOUS FLOW AND REDUCED ORDER MODELS	
30. Oleksii PAVLOVSKYI, Nadiia BOURAOU	229
ON-BOARD VIBRATION DIAGNOSTICS OF SHAFT DAMAGE OF THE AVIATION ENGINE	
31. Stanisław RADKOWSKI, Adam GAŁĘZIA	235
SIGNALS REPRESENTATION ON ENERGETIC PLANE BASED ON TEAGER-KAISER ENERGY OPERATOR	

32. Igor SELEZOV	243
EXTENDED MODELS OF SEDIMENTATION IN COASTAL ZONE	
33. Wojciech SOCHACKI, Marta BOLD	251
DAMPED VIBRATION OF A NON-PRISMATIC BEAM WITH A ROTATIONAL SPRING	
34. Wojciech SOCHACKI, Piotr ROSIKOŃ, Sandra TOPCZEWSKA	257
THE INFLUENCE OF INTERNAL AND CONSTRUCTIONAL SUPPORTS DAMPING ON THE Γ-TYPE FRAME VIBRATIONS	
35. Roman STAROSTA, Grażyna SYPNIEWSKA-KAMIŃSKA	265
NONLINEAR VIBRATIONS OF ROTATING SYSTEM NEAR RESONANCE	
36. Stanisław STRZELECKI, Zdzisław SOCHA, Zygmunt TOWAREK, Sergiusz ZAKRZEWSKI	273
EFFECT OF PAD OFFSET ON THE STABILITY OF JEFFCOTT ROTOR OPERATING IN TILTING 4-PAD JOURNAL BEARINGS	
37. Anna SYGULSKA	281
ACOUSTIC INVESTIGATIONS OF THE CONTEMPORARY CHURCHES IN POZNAŃ	
38. Janusz SZMIDLA, Ilona CIEŚLIŃSKA-GĄSIOR	289
IMPACT OF PRE-STRESS ON STABILITY AND VIBRATION OF GEOMETRIC NONLINEAR COLUMN AT A LOAD FORCE DIRECTED TO THE POSITIVE POLE	
39. Janusz SZMIDLA, Justyna WIKTOROWICZ	297
THE VIBRATIONS AND THE STABILITY OF A FLAT FRAME TYPE Γ REALIZING THE EULER'S LOAD TAKING INTO ACCOUNT THE VULNERABILITY OF THE STRUCTURAL NODE CONNECTING THE POLE AND THE BOLT OF THE SYSTEM	
40. Tomasz SZOLC, Zbigniew L. KOWALEWSKI	305
AN APPLICATION OF LONGITUDINAL ELASTIC WAVES FOR INVESTIGATION OF MATERIALS UNDER HIGH STRAIN RATES USING THE HOPKINSON BAR	
41. Sebastian UZNY	311
FREE VIBRATIONS OF COLUMN BUILT OUT PIPE AND ROD WITH TWO-PARAMETRIC ELASTIC CONNECTOR	

42. Sebastian UZNY, Krzysztof SOKÓŁ.....	319
FREE VIBRATIONS OF COLUMN SUBJECTED TO EULER'S LOAD	
WITH CONSIDERATION OF TIMOSHENKO'S THEORY	
43. Małgorzata WOJSZNIS, Jacek SZULCZYK	327
INFRASOUND AND LOW FREQUENCY NOISE OF A WIND TURBINE	
44. Aleksandr E. ZAKRZHEVSKY	335
DEPLOYMENT OF LONG-MEASURED FLEXIBLE STRUCTURE	
IN ORBIT	
45. Roman ZINKO	342
RESEARCH OF WORK OF A ROTOR CRUSH MACHINE ON ELASTIC	
FOUNDATION WITH THE USE OF GRAPHS	

Conversion Excitation of Intense Sound Fields in Crystals

Vladimir ALSHITS

A.V. Shubnikov Institute of Crystallography, Russian Academy of Sciences

Leninskii pr. 59, 119333 Moscow, Russia

Polish-Japanese Institute of Information Technology

Koszykowa 86, 02-008 Warsaw, Poland

alshits@ns.crys.ras.ru

Dmitrii BESSONOV

A.V. Shubnikov Institute of Crystallography, Russian Academy of Sciences

Leninskii pr. 59, 119333 Moscow, Russia

dabessonov@gmail.com

Vasilii LYUBIMOV

A.V. Shubnikov Institute of Crystallography, Russian Academy of Sciences

Leninskii pr. 59, 119333 Moscow, Russia

lyubvn36@mail.ru

Andrzej RADOWICZ

Kielce University of Technology

Al. Tysiaclecia P.P. 7, 25-314 Kielce, Poland

radowicz@tu.kielce.pl

Abstract

The resonant excitation of an intense elastic wave in a crystal is described through a special nonspecular reflection close to a conversion when almost all the energy from the incident pump wave falls into the near-surface narrow high-intensity reflected beam. The resonance arises when the excited reflected wave is close to the bulk eigenmode satisfying the condition of free boundary. It is shown that the choice of the crystal surface parallel to a symmetry plane allows simultaneous optimization of reflection geometry when the intensity maximum for the excited wave is accompanied by the intensity minimum for the other (parasite) reflected wave. And the conversion criterion of vanishing of the above minimum is determined by one definite condition on elastic moduli. On this basis the series of real monoclinic, orthorhombic and hexagonal crystals were chosen where the resonant reflection in non-symmetric sagittal planes proves to be very close to conversion.

Keywords: Elastic wave, resonance reflection, conversion, pump wave, anisotropy, diffraction divergence

1. Introduction

Modern acoustics of crystals create new principles of functioning of various instruments and devices based on the use of ultra- and hypersonic waves [1, 2]. Intense ultrasonic beams are widely used in engineering, medicine, scientific instrument technique, etc. The reflection and refraction of such beams at the interfaces between layered isotropic structures are commonly used for their transformation. Crystals open new possibilities of beams transformation. Many acoustic effects arise only due to medium anisotropy [2-4]. For instance, piezoelectricity exists only in crystals and is widely used in acoustic devic-

es. Another spectacular example of a nontrivial role of anisotropy is phonon focusing; the concentration of energy in a crystal along special directions for which the acoustic beam in Poynting vectors is much narrower than that in wave vectors. Here, we will consider another principle of energy concentration in acoustic waves that is also entirely attributable to crystal anisotropy.

In [5, 6] the idea was proposed of resonant energy concentrating in narrow acoustic beams through a nonspecular reflection in the geometry close to a scheme of the total internal reflection (Figure 1). One of the two reflected beams propagates at a small angle β_r to the surface and therefore narrows greatly to width d_r upon the reflection of an incident beam with width D_i . Then the intensity of the narrow reflected beam can exceed considerably the intensity of the pump wave. The beam amplification factor K_2 is estimated by the ratio $\eta D_i/d_r = \eta \sin\alpha_i / \sin\beta_r \gg 1$, where η is the fraction of energy falling into the compressed beam from the incident one.

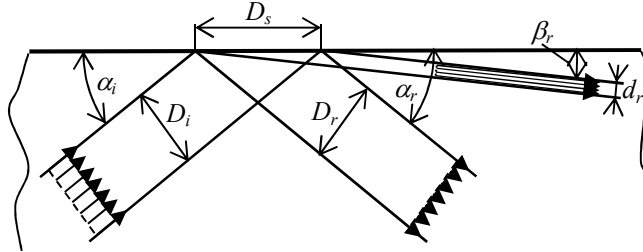


Figure 1. Scheme of resonant excitation of intense acoustic beam; arrows indicate Poynting vectors in the incident and reflected beams

It is essential that we deal here with a purely anisotropic effect. In isotropic media an analogous beam compression for the incidence angles close to the angle of total internal reflection does not result in any amplification. In this case, the fraction η of energy in the reflected beam approaches zero as its width decreases. The same would occur in a crystal as well if the geometry of reflection is not chosen in a specific way. The choice of the plane and angle of incidence is dictated by the requirement that the excited reflected wave be close to the bulk eigenmode with its energy flow along a free boundary.

The fraction η of the pump energy transferred to the excited beam depends on the specific relations between the elastic moduli for specially chosen crystals. The maximum effectiveness ($\eta = 1$) of the considered amplification effect is realized when the conversion reflection occurs, i.e. when the amplitude of the parasite quasi-specular reflected wave vanishes. As shown in [5], for unrestricted anisotropy the two basic characteristics of the resonance, K_2 and η , attain their maximums in different geometries of reflection. That is why in [5, 6] we considered more symmetric crystals and reflection geometries related to surfaces and sagittal planes close to symmetry planes. In these cases the extremal conditions for K_2 and η are attained simultaneously for the same reflection geometries. And the maximum effectiveness $\eta = 1$ determined by only one condition on elastic moduli may be approximately realized in a series of crystals.

In this paper we shall demonstrate that the minimum symmetry requirement providing a realizable high effectiveness of the resonance is more modest. Namely, for a coincidence of the maximums of K_2 and η it is sufficient to orient the surface of a crystal to be parallel to a symmetry plane. And the condition for a conversion, $\eta = 1$, is again reduced to only one relation between elastic moduli. This means that even for monoclinic system there is a good chance to find crystals providing the resonances of reflection close to conversion. Below we shall choose several monoclinic, orthorhombic and hexagonal crystals where the computations predict the effectiveness close to 100% for geometries related to surfaces parallel to symmetry planes whereas the propagation planes are non-symmetric and even are not close to symmetry planes.

2. Statement of the Problem

Consider an arbitrary half-infinite elastic medium of unrestricted anisotropy with the free surface. Let \mathbf{n} be the internal unit normal to it. We suppose that on this surface there is such direction \mathbf{m}_0 along which an exceptional one-partial bulk eigenwave belonging to the intermediate sheet of the slowness surface may propagate with Poynting vector along the boundary and zero traction at it. There is the existence theorem [7] which guarantees such eigen-solutions occupying the whole lines on the sphere of propagation direction for any anisotropic media. In this sagittal plane $\{\mathbf{m}_0, \mathbf{n}\}$, apart from the exceptional wave, a tree-partial special reflection must also exist [5] for the same tracing velocity v of stationary wave motion along the surface. It includes the incident and reflected waves from the outer sheet of the slowness surface and the localized partial component from the innermost sheet. In the case of a weak perturbation of the initial geometry in which the surface does not change and the exceptional direction \mathbf{m}_0 is rotated $\mathbf{m}_0 \rightarrow \mathbf{m}$ around the normal \mathbf{n} through a small angle $\varphi = \angle(\mathbf{m}, \mathbf{m}_0)$, none of the two wave solutions can be retained. In this case, instead of two disappeared solutions, their superposition should appear. The former exceptional bulk wave will enter this superposition as a new reflected component in which the energy flow makes a small angle with the surface. Clearly, a small perturbation of the initial geometry will violate relatively weakly the satisfaction of the boundary condition for a free surface by this near-surface component. This violation is compensated for by the remaining partial components. Therefore, the new near-surface reflected wave should have amplitude exceeding considerably the amplitudes of other partial waves, including the incident one. This process may be considered as the resonant excitation of an intense bulk wave by a weak pump wave incident on the crystal surface at an appropriate angle.

The combined displacement wave field of the perturbed four-partial reflection can be expressed in the form

$$\mathbf{u}(\mathbf{r}, t) = \sum_{\alpha=1}^4 C_\alpha \mathbf{A}_\alpha \exp\{ik[(\mathbf{m} + p_\alpha \mathbf{n}) \cdot \mathbf{r} - vt]\} \quad (1)$$

where C_α and \mathbf{A}_α are the scalar amplitudes and normalized polarization vectors of the partial waves, respectively, k is the common projection of all wave vectors onto the surface: $k = \mathbf{k}_\alpha \cdot \mathbf{m} = k_x$, $p_\alpha = \mathbf{k}_\alpha \cdot \mathbf{n}/k = k_{\alpha\theta}/k$ and $v = \omega/k$ is the tracing velocity. Each

partial wave $\mathbf{u}_\alpha(\mathbf{r}, t)$ in (1) must satisfy the equation of the dynamical theory of elasticity [3]. And the sum of their tractions at the surface ($y = 0$)

$$\hat{\sigma}_\alpha \mathbf{n} \Big|_{y=0} \equiv -ikC_\alpha \mathbf{L}_\alpha \exp[ik(x - vt)] \quad (2)$$

must vanish in accordance with the boundary condition of a free surface. Thus, we obtain

$$\sum_{\alpha=1}^4 C_\alpha \mathbf{L}_\alpha = 0. \quad (3)$$

In further considerations we shall choose the numeration so that $\alpha = 4$ would correspond to the incident wave ($C_4 \rightarrow C_i$), $\alpha = 1$ to the parasite reflected wave of the same branch as the incident wave ($C_1 \rightarrow C_{r1}$), $\alpha = 2$ to the excited reflected wave being the perturbed exceptional wave ($C_2 \rightarrow C_{r2}$), and $\alpha = 3$ to the localized partial mode ($C_3 \rightarrow C_l$). In these notations equation (3) leads to the following reflection coefficients [5]

$$R_1 = \frac{C_{r1}}{C_i} = -\frac{[\mathbf{L}_4 \mathbf{L}_2 \mathbf{L}_3]}{[\mathbf{L}_1 \mathbf{L}_2 \mathbf{L}_3]}, \quad R_2 = \frac{C_{r2}}{C_i} = -\frac{[\mathbf{L}_4 \mathbf{L}_1 \mathbf{L}_3]}{[\mathbf{L}_1 \mathbf{L}_2 \mathbf{L}_3]} \quad (4)$$

where $[\mathbf{abc}]$ means the mixed product of the vectors \mathbf{a} , \mathbf{b} and \mathbf{c} .

3. The Case of Surface Parallel to a Symmetry Plane

In the case when the surface is parallel to a symmetry plane of the crystal the expressions in (4) acquire a more simple structure. Indeed, in this case the vectors \mathbf{L}_α and $\mathbf{L}_{\alpha+3}$ must be symmetric with respect to this plane. This relates both to the real vectors

$$\mathbf{L}_1 = \mathbf{L}_1^s + \mathbf{L}_1^n, \quad \mathbf{L}_4 = \mathbf{L}_1^s - \mathbf{L}_1^n, \quad (5)$$

and to the only complex conjugate pair

$$\mathbf{L}_3 = \mathbf{L}_3^s + i\mathbf{L}_3^n, \quad \mathbf{L}_6 = \mathbf{L}_3^s - i\mathbf{L}_3^n. \quad (6)$$

Here the superscripts s and n indicate the in-plane ($\mathbf{L}_\alpha^s \perp \mathbf{n}$) and out-plane ($\mathbf{L}_\alpha^n \parallel \mathbf{n}$) orthogonal components of the vector \mathbf{L}_α .

With (5), (6), the equations in (4) acquire the structure

$$R_1 = -\frac{\phi - \lambda' + i\lambda''}{\phi + \lambda' + i\lambda''}, \quad R_2 = -\frac{\mu}{\phi + \lambda' + i\lambda''}, \quad (7)$$

where

$$\phi = [\mathbf{L}_1^s \mathbf{L}_2^s \mathbf{L}_3^s], \quad \lambda' = [\mathbf{L}_1^n \mathbf{L}_2^s \mathbf{L}_3^s], \quad \lambda'' = [\mathbf{L}_1^s \mathbf{L}_2^n \mathbf{L}_3^s], \quad \mu = 2[\mathbf{L}_1^s \mathbf{L}_3^s \mathbf{L}_1^n]. \quad (8)$$

One should keep in mind that the vectors $\mathbf{L}_\alpha^{s,n}$ in (8) are determined by the perturbed reflection geometry, i.e. by the orientation of the sagittal plane, $\varphi = \angle(\mathbf{m}, \mathbf{m}_0)$, and by the incidence angle $\delta\alpha$ counted from the angle α_{0i} related to the total internal reflection.

The angle $\delta\alpha$ is directly connected with the shift Δv of the tracing velocity and with the perturbation δp of the parameter $p_2 = k_{2y}/k$ which vanishes at $\delta\alpha = 0$ (Figure 2).

The first equation in (7) transforms the conversion condition $R_1 = 0$ into the following two relations

$$\lambda' = \phi, \quad \lambda'' = 0. \quad (9)$$

Here the first equation establishes the relation between the angles φ and $\delta\alpha$ (or δp) for arbitrary crystal moduli. And the second equation determines the condition for those moduli. In fact, this equation is reduced to a requirement of the vanishing component:

$$L_3^n = 0. \quad (10)$$

Thus, for a medium with the surface parallel to a symmetry plane we have got the simple general criterion for a choice of crystals with the high effectiveness of the resonance.

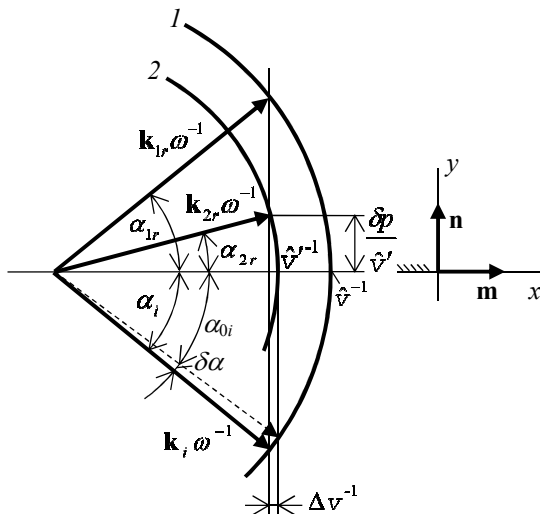


Figure 2. Fragments of external sheets 1 and 2 of the slowness surface in its cut by the sagittal plane and schematic diagram of the reflection

4. Approximate Analytical and Exact Computer Results

Let us give more rigorous definitions to the earlier introduced two basic characteristics of the resonance, the amplification factor K_2 and the effectiveness of excitation η :

$$K_2 = |R_2|^2 s_2 / s_4, \quad \eta = 1 - |R_1|^2 \quad (11)$$

where $s_{2,4}$ are the group speeds of the excited and incident waves. After the substitution here the relations from (7) with parameters (8) found in the main order in φ and δp [5],

$$\phi \approx \kappa\varphi^2, \quad \lambda' \approx \kappa\lambda'_0\delta p, \quad \lambda'' \approx \kappa\lambda''_0\delta p, \quad \mu \approx \kappa\mu_0\varphi, \quad (12)$$

one obtains the approximate expressions for the functions $K_2(\varphi, \delta p)$ and $\eta(\varphi, \delta p)$:

$$K_2 = \frac{|\mu_0|^2 (s_2/s_4)\varphi^2}{(\varphi^2 + \lambda'_0\delta p)^2 + (\lambda''_0\delta p)^2}, \quad \eta = \frac{4\lambda'_0\delta p\varphi^2}{(\varphi^2 + \lambda'_0\delta p)^2 + (\lambda''_0\delta p)^2}. \quad (13)$$

It is easily seen that the both functions in (13) have maximums under the same condition

$$\varphi^2 = \lambda'_0\delta p, \quad (14)$$

which represents an approximate concretization of the first equation in (9). And the second equation in (9) is transformed with the same accuracy to the condition $\lambda''_0 = 0$ which is just the criterion for a choice of crystals close to conversion ($\eta \approx 1$).

The computer analysis was based on the exact formulae (7) and the data [8] for elastic moduli of large number of crystals of various symmetry systems. We were interested in monoclinic, orthorhombic and hexagonal crystals admitting the propagation of exceptional waves in non-symmetric sagittal planes along surfaces parallel to symmetry planes. Many crystals were found where the fraction η of energy in the excited intensive wave exceeded 90% of energy in the incident wave. In some cases the magnitude of η proves to be close to 100% (Table 1).

Table 1. The effectiveness η of the resonance in some crystals for $K_2 = 5$, φ_0 is the azimuth of the exceptional wave normal \mathbf{m}_0 in the crystallographic coordinates

Crystals	φ_0 , rad	$\delta\alpha$, rad	η
<i>Monoclinic system</i>			
Stilbene	1.5562	0.14	0.996
Tolan C ₁₄ H ₁₀	1.0332	0.063	0.968
Triglycine sulphate (TGS)	1.4709	0.084	0.94
Tartaric acid C ₄ H ₆ O ₆	-1.4282	0.02	0.966
<i>Orthorhombic system</i>			
Rochelle salt	0.48	0.015	0.999
Boron-epoxy composite	0.2	0.014	0.9999
<i>Hexagonal system</i>			
AgI	0.1457	0.012	0.993
CeF ₃	0.2918	0.011	0.99

Figure 3 demonstrates the dependencies $K_2(\varphi, \delta\alpha)$ and $\eta(\varphi, \delta\alpha)$ for the three crystals of monoclinic (a), orthorhombic (b) and hexagonal (c) systems for similar (monoclinic) symmetry of reflection geometry: the surface was parallel to a symmetry plane while the sagittal plane had non-symmetric orientation. As is seen from the Figure, the sensitivity of the resonance to changes $\delta\alpha$ in the angle of incidence is much sharper than to rotations of the sagittal plane. This manifests itself in different scales of the angles plotted along

two axes. The ranges of angles in Figure 3 were chosen so that the amplitude of the amplification factor K_2 remained within the practically acceptable values.

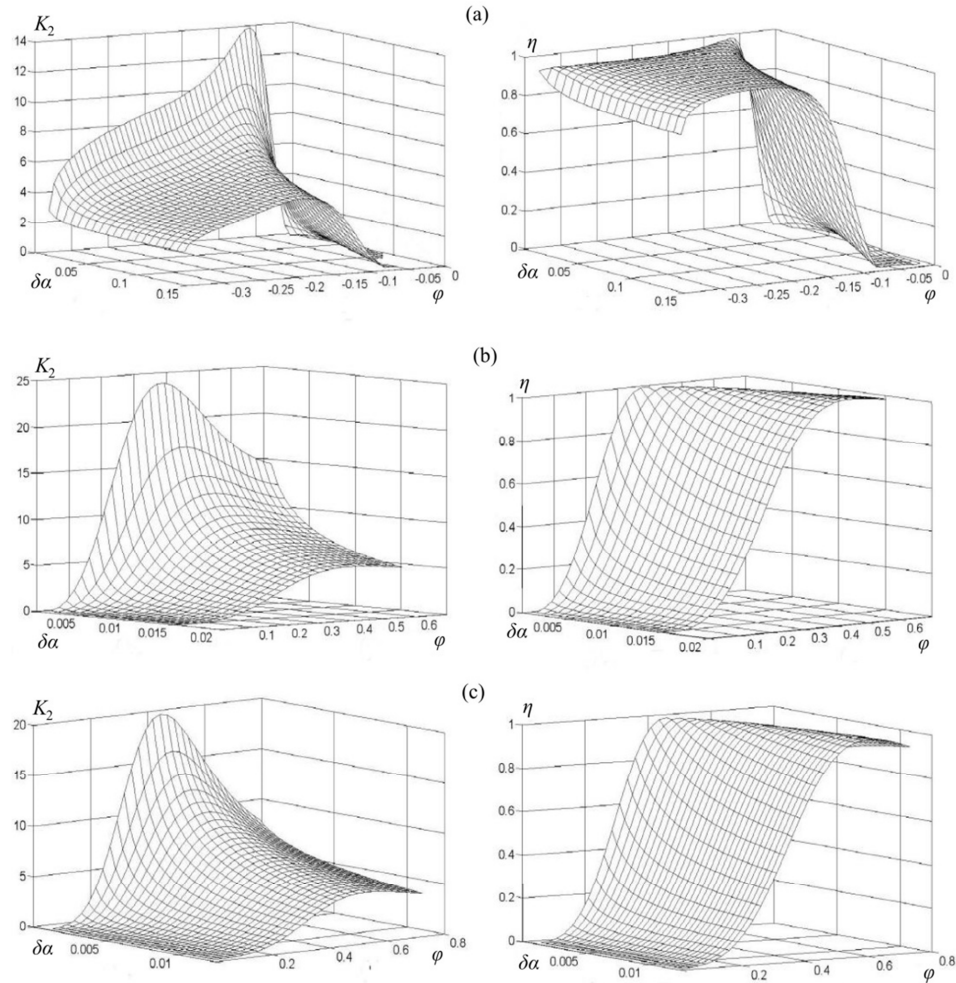


Figure 3. Amplification factor K_2 and fraction of energy in the excited beam η versus angle of incidence $\delta\alpha$ and the deviation angle φ of the sagittal plane in the stilbene (a), Rochelle salt (b) and AgI (c) crystals

We note that the factor K_2 in (13) fast increases with a decrease in perturbation parameters φ , $\delta\varphi$ and $\delta\alpha$. However, the higher is the resonance peak, the narrower it becomes. Certainly, it is senseless to make the width of the peak in the angles $\delta\alpha$ less than the angle of diffraction divergence of the incident beam. And the divergence of the excited beam is even more limiting with respect to the increase in K_2 . Indeed, this critical

parameter $\delta\psi_r$, together with K_2 , grows inversely proportionally to the width d_r of this beam (Figure 1). Still, according to [5], one can obtain $\delta\psi_r \sim 10^{-2}$ rad keeping $K_2 \sim 5-10$.

3. Conclusions

As is shown in the above analysis, the discussed effect of resonant reflection in crystals, where a wide incident acoustic beam converts almost all of its energy into a narrow high intensity reflected beam, appears to be quite realizable. By special choice of crystals with a definite relation between elastic moduli the resonance may be optimized up to the effectiveness $\eta \sim 100\%$. Since the resonance region is narrow in angles of incidence, stringent requirements for a weak divergence of the incident beam, $\delta\psi_i \sim 10^{-3}$ rad arise, which can be realized only at sufficiently high ultrasonic frequencies ~ 100 MHz. For the same reason, the amplitude of the excitation coefficient is also limited to $K_2 \approx 5-10$. However, in the case of retransformation of the emergent beam through its narrowing in the perpendicular dimension as well, the intensification factor increases many fold, to $\sim 10^2$. In the hypersonic frequency range, the amplification amplitudes can be increased significantly. In this case, however, one might expect additional restrictions due to an increase in the absorption of acoustic waves.

References

1. K.S. Aleksandrov, B.P. Sorokin, S.I. Burkov, *Effective piezoelectric crystals for acoustoelectronics, piezotechnics and sensors*, Nauka, Novosibirsk 2007.
2. D. Royer, E. Dieulesaint, *Elastic waves in solids, I, II*, Springer, Berlin 2000.
3. F.I. Fedorov, *Theory of elastic waves in crystal*, Plenum, New York 1968.
4. V.I. Alshits, in: *Surface waves in anisotropic and laminated bodies and defects detection*, Eds. R.V. Goldstein, G.A. Maugin, Kluwer Academic, Dordrecht 2004.
5. V.I. Alshits, D.A. Bessonov, V.N. Lyubimov, *Resonant excitation of intense acoustic waves in crystals*, J. Exp. Theor. Phys., **116**, No. 6 (2013) 928–944.
6. V. I. Alshits, D.A. Bessonov, V.N. Lyubimov, *Excitation of intense acoustic waves in hexagonal crystals*, Crystallography Reports, **58**, No. 6 (2013) 867–876.
7. V.I. Alshits, J. Lothe, *Elastic waves in triclinic crystals. III. Existence problem and some general properties of exceptional surface waves*, Krystallografiya, **24**, No. 6 (1979) 1122–1130 [translation: Sov. Phys. Crystallogr., **24**, No. 6 (1979) 644–648].
8. H.H. Landolt, R. Börnstein, *Zahlenwerte und funktionen aus naturwissenschaften und technik: neue serie*, Vol. III/11, Ed. K.-H. Hellwege, Springer, Berlin 1979.

Uncertainty in Vibroacoustic Investigations – Research Challenges

Wojciech BATKO

*AGH University of Science and Technology
Faculty of Mechanical Engineering and Robotics
Department of Mechanics and Vibroacoustics
Al. Mickiewicza 30, 30-059 Kraków, Poland
batko@uci.agh.edu.pl*

Abstract

The paper formulates the need of the modification of currently applied solutions of uncertainty assessments in vibroacoustic investigations, including the ones which use the convention rules developed by 7 international metrological organisations and described in the ‘Guide to the Uncertainty’. Reservations versus currently used solutions are given in the hereby paper. It directs attention toward assumptions limiting the likelihood assessment of uncertainties of the obtained acoustic results.

It draws the possible ways of the problem solutions and related to them methods. It presents the need of connecting belonging to them algorithms with not classic statistical methods, allowing taking into account departures from generally used assumptions in presently applied solutions of uncertainty estimations of acoustic investigations results. The paper presents new research trends related to the uncertainty assessment of the environment acoustic hazards control.

The presented results and their conclusions can constitute the base for wider verification of the correctness of the currently applied procedures of acoustic measurements assessment and related to them estimations of errors levels of the uncertainty estimation of acoustic investigations results.

1. Introduction

The basic task of vibroacoustic measurements is obtaining reliable information on the vibroacoustic effect being investigated, since only likelihood results enable taking proper decisions. The problem of the uncertainty assessment of effects identified in vibroacoustic experiments is inseparably related to the uncertainty of measurements. It requires the validation of measurement procedures, the analysis of sources of possible random errors and the way of their working out in dependence of the probability distribution of their occurrence. The attention is focused on the determination methods of the standard uncertainty at direct and indirect measurements, on the uncertainty budget analysis and on determining conditions of selecting the expansion factor k , which is necessary in the expanded uncertainty assessment.

The unification of principles of calculations and uncertainty expressing was developed by the Joint Committee for Guides in Metrology (JCGM); under the aegis of the International Office of Measures (BIPM). These principles are contained in the ‘Guide to the Expression of Uncertainty in Measurement (**GUM**) [2]. This Guide determines the methods of: drawing up measured data, principles of expressing uncertainty of measurements, and also defines the basic terminology. They are contained in nine documents under the common title: ‘*Evaluation of measurement data*’ [1]. The document is accepted and recognised by the European co-operation for Accreditation as the basic pattern for the uncertainty determination in the certified research labora-

tories EA in every field of their activity, it means also in units dealing with vibroacoustic investigations. Whenever possible it is required, that the certified laboratories act according to the GUM when determining uncertainties related to quantitative results. The recommendations are also contained in legal acts and standards determining principles of the estimation of environment acoustic hazards.

The basic principle applied in uncertainty calculations, according to this document, is the uncertainty division into type A and type B. The type A uncertainty is determined on the basis of statistical conclusions, related to the analysis of the random measurement sample. The type B uncertainty is determined on the basis of the expert knowledge related to available information on possible systematic errors, e.g. errors resulting from Certificates of Standardisation of the equipment applied in the experimental process.

Both information on the possible errors of the type A and B should be treated equally, when estimating the uncertainty. This fact generates several methodological problems related to the compilation of the type A random error with the type B error being the determined variable.

The basis assumption of the GUM convention - in the type A uncertainty estimation process - is building the model of the measurement result, as the random variable Y described by the density probability function $g(y)$, for which two basic parameters i.e.: expected value $\mu(y)$ and standard deviation $\sigma(y)$ are determined. According to the idea contained in these guidelines, the uncertainty is understood as the numerical measure of the measurement inaccuracy, described in probabilistic categories and interpreted in the interval way. This interval is formed around the average value considered equitable with the expected value with the discussed parameter. It is given by the following relation:

$$P = P \{y \in (y - U; y + U)\} \quad (1)$$

determining with the required probability, equal the confidence level α , the fact that inside this interval the unknown, but real, measured value is present. This interval – determining the error of the measurement result U – is called the expanded uncertainty. It is estimated at assuming the known distribution $g(y)$ of the discussed parameter of the analysed vibroacoustic effect, using the condition:

$$\int_U^{+U} g(y)dy = \alpha = np. \cong 95 \% \quad (2)$$

The expanded uncertainty: $U = k u$, is the product of standard uncertainty u and the expansion factor k , which is the quantile of the probability distribution of the measurement error, for the required confidence level α .

The standard way of working out the results given by the measuring series y_i ; $i=1, 2, \dots, n$, is based on calculating: average

$$\bar{y} = \frac{1}{n} \sum_{i=1}^n y_i \quad (3)$$

from control results and related to them standard deviation $s(y_i)$ during observations:

$$s(y_i) = \sqrt{\frac{1}{n-1} \sum_{i=1}^n (y_i - \bar{y})^2} \quad (4)$$

and the standard deviation of the average distribution observation y_i :

$$s(\bar{y}) = \frac{s(y_i)}{\sqrt{n}} = u_A(\bar{y}) \quad (5)$$

equated with the average uncertainty called the standard type A uncertainty $u_A(\bar{y})$.

In the common application of this approach it is assumed that the distribution of the measured value is - in approximation - the normal distribution, which at assuming the confidence level being 95% leads to the expansion factor 2. In this case the measurement result is hedged with the uncertainty interval:

$$y = \bar{y} \pm 2 u_A(\bar{y}) \quad (6)$$

The value of the discussed parameter Y can be inaccessible directly in measurements. This value can be a function of several measured values X_i , being random variables described by affiliated to them density probability functions $g_i(x_i)$, with expected values $\mu_i(x_i)$ and standard deviations $\sigma_i(x_i)$. It is usually assumed, in such investigation procedure, that the function of this parameter $y=f(x_1, x_2, \dots, x_n)$ is selected in such way as to have input quantities not correlated and random values X_i independent.

At such assumption concerning the discussed value Y , its expected value $\mu(y)$ and standard deviation $\sigma_i(x_i)$ are expressed as follows:

$$\mu(y) = \sum_{i=1}^N c_i \mu_i(x_i); \quad \sigma(y) = \sqrt{\sum_{i=1}^N c_i^2 \sigma_i^2(x_i)} \quad (7)$$

where: $c_i = \frac{\partial f}{\partial x_i}$, and between functions of density probability distribution the convolution occurs:

$$g(y) = \lim_{\infty} g_1(x_1) * g_2(x_2) \dots \dots g_N(x_1) = g_i(x_i) * g_{i+1}(x_{i+1}) = \int_{-\infty}^{\infty} g_i(x_i) * g_{i+1}(x - x_{i+1}) dx_i = \int_{-\infty}^{\infty} g_i(x - x_i) * g_{i+1}(x_{i+1}) dx_i \quad (8)$$

The problem of selecting the probability distribution for the estimated measurement results is the most difficult for the uncertainty estimation in such case. The determination of the convolution of the density probability of measured variables requires performing complex calculations not providing solution in a closed form. Generally the distribution form is either determined by numerical operations or approximated by the „Monte Carlo” method.

2. Methodological problems in applications of classic solutions of the uncertainty estimation determined by the gum convention

The problem of the uncertainty type A estimation in acoustic investigations is related to the determined statistical drawing up process. On the basis of the random measurement test the acoustic parameters of the considered effects are determined and equated with

these effects. The correctness of such conclusion drawing is relevant to the correctness of applying the proper statistical methods. Their improper application leads to significant errors, which was broadly described in papers [4,5].

The lack of the probabilistic properties of the identified effect in relation to assumptions of the applied method of the statistical conclusions drawing should be recognised as the most often made methodological errors. Especially the attention should be directed to: randomness of the measurement test, verification of the assumptions correctness of the applied method of the statistical conclusions drawing, selection of the appropriately numerous measurement tests, and also to the selection of the proper estimators for the assessment of position statistics of the investigated acoustic effects, which determine uncertainties of considered identifications.

Thus, the correct application of the recommended in the '*Guide to the uncertainty*' [1] procedures of uncertainty estimations, requires fulfilling the determined class of assumptions, which acceptability should be analysed in-depth and which is often, unfortunately a marginalised activity. Especially, the uncertainty assessment of the result of the environment acoustic hazards control is related to the assumption, which takes the normal distribution form as the representative of the mathematical observation model for the sound level measurement results L_{Ai} ; $i=1, 2, \dots, n$. The condition of the lack of the correlation of results in measurement series is essential. It seems obvious, that in case of inaccuracy of these assumptions, the average sound level value (representing the control assessment) or another noise indicator from the test measurement and their standard deviation (also from the test), cannot be the best estimation of the measurement result and thereby the best assessment of its standard uncertainty type A.

The majority of scientists intuitively assume the normality of the sound measurement results distribution of the tested population (*from which the random test for the estimation of the controlled noise indicators is taken*). They are relating it to the results of the central limited theorem of Lindeberg-Levy, determining the convergent form of the random events distribution with the normal distribution. They do not consider the mechanism, which generates the sound level measurements results.

Taking into account this mechanism leads to distributions significantly differing from the normal distribution, as it was shown in papers [22,23]. This fact was also confirmed in works [8-11], in which the likelihood of this assumption was verified.

The condition that the results of sound level measurements in processes of controlling acoustic hazards must not be correlated can also be not fulfilled. A high level of noise disturbances can essentially influence successive calculations of the equivalent sound level constituting the investigated random test. Also measured tests of the equivalent sound level, necessary for calculating the controlled noise indicators, estimated in not distant time intervals can be correlated by external factors generating noises. This is documented by the results presented in paper [31], in which the effects related to this fact are also shown. They cause essential increasing of the standard uncertainty of the controlled noise indicator results.

Doubts related to a small likelihood of two out of three basic assumptions of the applied methodology of noise indicators estimation - according to the convention GUM presented in the '*Guide to the Uncertainty*' [2]; generate the need of the development of

new model formalisms for the realisation of such tasks. Their realisation ideas will be presented in the next item.

3. New concepts and their model formalisms dedicated to the uncertainty assessments in environment acoustic investigations

The described above limitations of generally applied estimation methods of the uncertainty of the acoustic investigations results with restricted assumptions, generated approaches of looking for the new model. In works of Department of Mechanics and Vibroacoustics AGH an attention was directed towards model formalisms allowing analysing statistic measurement data in which departures from classic assumptions, mainly from the assumption of normality of distribution of the controlled noise indicator results and of not correlated random sample results, are possible. The attention was directed towards the currently developed methodology of statistical investigations of effects, which have the same specificity of conditions, colloquially called 'not classic statistical methods' [15,20].

To the solutions of statistical conclusions drawing, related to these methods, enabling the estimation of the expected values of the investigated populations and assessment of their variance (i.e. allowing to create confidence intervals for the realised estimations) belong the methods based on the model formalism of:

- time series [16,26],
- kernel estimators [16],
- bootstrap analysis [13,19,20],
- Bayes' analysis [21],
- propagation of distributions [22-25].

The analysis of the application possibility of these solutions and their adaptation for the needs of the estimation of long-term noise indicators and building of assigned to them confidence intervals was the subject of numerous scientific works in the Department of Mechanics and Vibroacoustics and related to them Ph.D. Thesis, either finished or in the realisation stage . Their results were presented in several publications [15,-17,19-21, 22-25].

It is assumed, in the process of assigning to results of control measurements $\{x_1, x_2, \dots, x_n\}$ the representative in the form of **time series** [26]; (*being a sequence of random values of variable X describing the state of the analyzed acoustic effect*); that its probabilistic structure can be shaped by the mechanism:

$$X_t = \mu_t + \varphi_t + \xi_t; \quad t = 1,2, \dots, n \quad (9)$$

It has the following components: trend μ_t related to a constant tendency forcing the level of changed values of the analyzed acoustic parameters, cyclic component φ_t - representing cyclic changes related to recurrent characteristic excitations, and the residual component representing random disturbances (or inaccuracy of the model description) ξ_t of the normal distribution $N(0, \sigma_\xi^2)$.

In contrast to the classic model of the random control test (which assumes that random observations are of a normal distribution), the proposed approach assumes the pres-

ence of a certain mechanism forcing changes of control results values, which can be represented with the accuracy characteristic to Gaussian disturbances of the expected value being zero and variance σ_ξ^2 .

The estimation problem, of the expected value and variance of the analyzed acoustic parameters in such approach, is reduced to the identification of the time series structure. It requires determining the proper approximation $\widehat{\mu}_t$, $\widehat{\varphi}_t$ for components μ_t and φ_t , which should provide the correct variability description of successively observed results of control tests (with a random Gaussian error ε_t , of the expected value being zero and variance σ_ε^2).

The correct selection of the approximation for the observed series of changes of the acoustic parameters values being controlled, requires the identification of its variability properties. Helpful in this process are generally applied solutions allowing to resolve problems concerning:

- stationary of the analysed time series;
- presence of the cyclic component (in this time series);
- homogeneity of the observation set and properties, including the random component variance.

The results of such identifications are helpful in selecting the correct modelling of time series formed from the control results values.

The realised examples of such analyses, in relation to the estimation of noise indicators determining the acoustic climate and assessments of their uncertainties, are given in the Ph.D. thesis of R. Bal [16]. They were referred to the results of the continuous noise monitoring, recorded at one of the main arteries in Krakow. They provided recommendations for the proper model selection for the estimation of the long-term sound indicators, describing the acoustic climate in the analysed areas and for the assessment of their uncertainty.

The application of kernel estimators allowing the likelihood estimation of the density probability distribution function of the analysed acoustic parameters and related to them uncertainty assessments can become the helpful solution [18]. The unknown function of the density probability $f(x)$ of n -dimensional random variable X , is – according to this procedure – calculated on the basis of experimentally determined values of m -element test: x_1, x_2, \dots, x_m of the analysed random variable from the following dependence:

$$\hat{f}(x) = \frac{1}{mh^n} \sum_{i=1}^m K\left(\frac{x-x_i}{h}\right) \quad (10)$$

in which the function $K(x)$ meets the condition:

$$\int_{-\infty}^{\infty} K(x) dx = 1 \quad (11)$$

It is called the nucleus, while the positive index h is called the smoothing parameter. It is possible to apply various nuclear functions, presented in paper [18], in the estimation process. The selection is related to the condition of the proper adapting of estimator $\hat{f}(x)$ to the real density function $f(x)$, characterised by the effectiveness factor, defined as:

$$Ef(K) = \frac{3}{5\sqrt{5}} \left[\int_{-\infty}^{\infty} t^2 K(t) dt \right]^{\frac{1}{2}} \left[\int_{-\infty}^{\infty} K(t) dt^2 \right]^{-1} \quad (12)$$

The adaptation of this solution for the needs of the acoustic environment control, together with its effectiveness assessment was the subject of the Ph.D. Thesis of B. Stępień [20] and analyses given in papers [19,20]. They illustrate conditions of the effective estimation of the long-term noise indicators expected values and assessments of their uncertainties.

Similar analyses were performed in relation to the **bootstrap method** [13] recommended for the uncertainty assessment in acoustic investigations. Its solution leads to the distribution function determination for the expected value and variance of the analyzed acoustic parameters, on the grounds of the results of the individual random sample $\{x_1, x_2, \dots, x_n\}$. It does not require the determined assumptions concerning the measuring test probability distribution. It provides the way of creating research statistics. Bootstrap copies constitute its data base. Their data are generated in such way that from the set of measurement results $\{x_i\}$ the test of the determined size is drawn $\{x_i^*\}$ and the drawn numbers are not removed from the test. In such way not one but several copies, allowing to calculate the statistical characteristic of the analyzed acoustic parameters, are formed. Functional properties of the bootstrap method (*based on copied data*) analyzed in the estimation process of controlled noise indicators and assessments of their uncertainty, were published in several papers [19,20]. The proposed solution occurred to be the efficient tool in the estimation of the expected value and variances of the controlled noise indicators.

The successive estimation method of the controlled noise indicators [] and assessments of their uncertainties (*recommended for using in environment control*), currently being developed in KMiWA AGH, is the solution based on the **Bayes' method**. The estimated parameter, is a random variable, for which the *a priori* distribution is assumed on the grounds of logical premises and analyses as well as on other information originated from outside of the control test. From the formal point of view the proposed Bayes' mathematical formalism is reduced to treating the estimated acoustic parameters and assessments of their uncertainties (*being random variables, not known a priori*) in relation with the classic reasoning, based on the probability mathematics. Especially two probabilistic principles are applied: *determinations* versus the value of the observed measurement test (i.e. statistic control data) and the *determination of boundary distributions 'a posteriori'*, for the variable being under investigations (i.e. possible future values of the controlled acoustic parameter).

Bayes' reasoning answers directly (intuitively) the question concerning the probability of the hypothesis, in relation to the obtained measurements results. Thus, it should be expected that this solution can have *a good, wider application perspective* in practical control of acoustic investigations. In favour of this approach application will act more and more general access to computational tools (e.g. *allowing multidimensional numerical integration*), inseparably related to the Bayes' analysis. The studies performed within this scope in the Department of Mechanics and Vibroacoustics [21] are reminding its realisation grounds and showing its practical potential from the perspective of the already realized long-term noise indicators and assessments of their uncertainties.

An important direction of works, concerning uncertainty assessments in the estimation of the environment acoustic state, is looking for the density probability distribution $p[x(\sum_{i=1}^n q_i)]$, being the summary result of all measured variables q_i , contributing to the final assessment of the controlled acoustic parameter.

To this aim it is possible to look for the solution by the **method of propagation of partial distributions** related to transformations of measuring results q_i , in the analyzed control assessment. As the example of such task can serve the problem of the logarithmic mean estimation $L_{sr} = 10 \log(1/n \sum_{i=1}^n 10^{0.1L_i})$, being the sum of independent sound level random results L_i , $i = 1, 2, \dots, n$. The analytical solution of this problem is difficult, due to the necessity of performing complex transformations leading to the determination of the looked for probability distribution:

$$p[x(\sum_{i=1}^n q_i)] = p[x(q_1)] * p[x(q_2)] * \dots * p[x(q_n)] \quad (13)$$

which is the convolution of the partial variables distributions. On its grounds, it is possible to estimate the expected value of the controlled noise indicator and the expansion factor $k(\infty)$, allowing to determine confidence intervals for the controlled variable.

This problem was applied for the task of the estimation – of the mentioned above – average sound level $L_{sr} = 10 \log(1/n \sum_{i=1}^n 10^{0.1L_i})$, determined by the sum of independent random results L_i , $i = 1, 2, \dots, n$ of sound level measurement [6, 7]. The possibility of obtaining – by this method – the recurrent algorithm for the expected value and variance (of this variable) estimation at the assumed form of the probability distribution of controlled results, was indicated.

The new document of the Joint Committee for Guides in Metrology (JCGM 102:2008) [28] Guide to Uncertainty [2] (edited by the International Standardisation Organisation) corresponds with the studies in KMiWA, the estimation approach to controlled variables, based on the distributions propagation method. The ISO document propagates new standard in the scope of uncertainty calculations of the control result by distributions propagation method. The probability distribution of the controlled variable – according to the recommendations contained in this document – should be calculated by means of the Monte Carlo simulation by the mathematical model of input values, contrary to the analytical approached being developed in Department of Mechanics and Vibroacoustics AGH.

4. Research challenges

The analysis of the realisation basis of uncertainty assessments in identifications of acoustic investigations indicates that its correctness is fully attributed to the correctness of the statistic inferences with respect to the performed acoustic measurements. Analyses of assumptions related to inferences are indispensable as well as looking for the proper interpretation for the mechanism of generating measurements random test results. Fulfilling these conditions is necessary for the correct statistic inferences, which are aimed at the determination of the confidence interval containing – with the determined probability – the hypothetic, true value of the acoustic variable being under control.

Applications of estimated uncertainty solutions, based on not fully random techniques of obtaining control data and also not having properties of random test, required

for the correct uncertainty assessment, is quite common in investigation practice of the identification of the determined acoustic effects parameters (*including numerous control procedures of the environment acoustic hazards*).

It especially concerns the problems listed below:

- The lack of investigation specifications related to the analyzed acoustic effect and – connected with it – randomness requirement and representativeness of the random test (taking the measurement test for inferences from not properly defined, or not defined at all, investigation population).
- None reflections on the correctness of assumptions of the estimated uncertainty solutions, including: the normality of the measurement results distribution and the lack of the correlation of the random test results.
- Not taking into consideration the requirement of the proper testing sample size versus the realised assessments of the measurement results uncertainty.
- Not proper verification of the hypotheses - being assumptions of the assumed estimative solutions of uncertainties.
- Using the same data base in processes of formulating and of testing of the assumed investigation hypothesis - in relation to the identified acoustic effects.

Inferences concerning acoustic investigations uncertainties – according to the GUM convention – i.e. on the bases of the measurements results distribution creating random measurement series, are burdened by numerous faults and limitations in acoustic tests. The impossibility to assure properly numerous measurements series (in the majority of realised acoustic investigations) belongs to these limitations. This is usually related to a large size of the investigation task, its costs and labour-consumption. Assumptions contained in them are difficult to be accepted (*as can be noticed in several references*), and their correctness is questioned by several environmental noise tests.

There is also a serious mathematical problem in selecting the model formalism, which would allow to join the type A uncertainty with type B, it means the uncertainty estimated by statistic methods with information on possible error ranges given by the a priori expertise.

In case when information – on the possible error of the acoustic measurement – are not sufficient or of a small reliability the characteristics of the identified effect could be restricted only to the statistic description and not to the statistic inferring in relation to the uncertainty assessment of the obtained results. The observed correctness in the test should be treated as the test representative, however without attributing to it the error size with the determined probability of its correctness. The statistic inferring application, recommended by the GUM convention in uncertainty assessments, seems unjustified.

The proposed in papers [30,31] formalisation based on interval algebra seems to be the worthy recommendation method of solving the problem. In this case the metrological interpretation for both ways of defining the measurement result uncertainty, i.e. described in papers [30,31] and guidelines of the GUM, can be quite similar. However, within the range of the mathematical formalisation of both ways essential differences can be seen. In case, when the uncertainty is defined as the interval of possible values of measurement variables, successive steps towards obtaining the interval result of

the control measurement can be consistently realised from the measuring process description. It does not require meeting – difficult for the measuring practice – assumptions of the GUM convention.

This behaviour differs from the solutions recommended in the Guide, which applications can be really limited to laboratories, since only in laboratories the numerous, homogeneous and not correlated measurement series can be achieved. Such requirement is difficult to be accepted in the control of the acoustic environment state. Essential variances of measuring conditions, in which the results reproducibility is disturbed, occur in acoustic environment measurements. This type of limitations create uncomfortable situations in which legally recognised way of uncertainty determining has a limited application and which in effect causes – very often – ignoring the needs of the verification of assumptions applied in the uncertainty assessment method, by persons performing measurements.

The fact that for the solutions determined by the GUM convention it is difficult to find the mathematical justification in physical interpretations of the measurements of analysed acoustic effects, to assumed statistical models used for assessments of uncertainties of their identification, is the essential argument for the possible marginalising of these solutions.

The approach based on the Bayes' method can be interesting for the application [20,21]. Admittedly, in such case a priori knowledge of probabilistic error characteristics is needed, but the modern technique provides several useful tools, and thus this will not constitute an essential limitation.

Summarising, it can be stated that current analyses of the uncertainty in acoustic investigations based on the GUM convention (*in basic assumptions and formal ways of their model solutions*) are weakly justified. There is a noticeable gap between their assumptions and constraints supplied so far by investigation experiences from the environment acoustic monitoring.

Limitations in the currently binding assessments of the uncertainty of acoustic investigations results, sketched in the hereby paper, can become a source of inspiration for searching and development of better formal bases for the calculation procedures of their uncertainty.

Thus, broader investigations concerning the model formalisms, indicated in the paper, based on '*not classic statistics methods*' (free from limitations of the current methods of the uncertainty assessment) should be undertaken. This would allow to verify the divergence level in uncertainty assessments of the controlled acoustic effects.

References

1. EA-04/16 rev00 December 2003 *EA guidelines on the expression of uncertainty in quantitative testing*.
2. *GUM - Guide to the Expression of Uncertainty in Measurements*. BIPM, IEC, IFCC, ISO, IUPAC, IUPAP, OIML. International Organization for Standardization, Switzerland 1993, 1995.

3. EN ISO 4871: *Acoustics – Declaration and verification of noise emission values of machinery and equipment.*
4. P.I. Good, J.W. Hardin, *Common Errors in Statistics (and How to Avoid Them)*, John Wiley & Sons, 2003.
5. D. Huffa, *How To Lie With Statistics*, W.W. Norton & Company, 1954, 1982, 1993.
6. DIN 45 641 *Mittelung von Schallpegeln*, Juni 1990.
7. VDI 3723: *Anwendung Statistische Methoden bei der Kennzeichnung schwankender Gerauschimmisionen (Application of statistical methods for the description of variating ambient noise levels)*, VDI-Handbuch Lärmminderung, 1993.
8. T. Wszolek, M. Kłaczyński, *Effect of traffic noise statistical distribution on $L_{Aeq,T}$ measurement uncertainty*, Archives of Acoustics, **31** (2006) 311–318 (supplement).
9. M. Gałuszka, *Statistical distribution levels and energy road noise*, Proc. I International Conference Environment Monitoring, AGH, Kraków 2010.
10. W. Batko, B. Stępień, *Analysis of the Probability Distribution of traffic Noises*, Conference Proc. XXXV-th Winter School of Vibroacoustic Hazards Control 5- 16, Gliwice-Ustroń 2007 (in Polish).
11. W. Batko, R. Bal, *Verification of the calculation assumptions applied to solutions of the acoustic measurements uncertainty*, Proc. 16th International Conference on Noise Control'13, 26-29 May, Ryn-Poland, 2013.
12. C. Domaniński C., K. Pruska, *Nieklasyczne metody statystyczne*, PWE, Warszawa 2000.
13. B. Efron, R. Tibshirani, *An Introduction to the Bootstrap*, Chapman & Hall, New York 1993.
14. S. Martinez, *Geraeuschkennungen und Immissionsprognosen: Ermittlung von Mess- und Prognoseunsicherheiten, Anwendung der Bootstrap- und der Gaußschen Methode*, Laermbekaempfung BD, **3**, 1 (2008) 16–25.
15. W. Batko, R. Bal, *Analysis of usefulness of R.G. Brown model for estimation process of long term noise ratio*, Archives of Acoustics, **33** (2008).
16. R. Bal, *Analysis of estimation conditions of the long-term noise indicators*, Ph.D. Thesis, AGH, 2010 (in Polish).
17. W. Batko, R. Bal, *Modeling of Estimation Tasks of the Year Long Noise Indicators*, Mechanics and Mechanical Engineering, Technical University of Lodz, **15** (2011) 11–20.
18. P. Kulczycki, *Estymatory jądrowe w analizie systemowej*, WNT, Warszawa 2005.
19. W. Batko, B. Stępień, *Application of the bootstrap estimator for uncertainty analysis of the long-term noise indicators*, Acta Physica Polonica A, **118** (2010) 11–16.
20. B. Stępień, *Estimation of uncertainties of the environment noise hazard indicators*, Ph. D. Thesis, AGH, 2011 (in Polish).

-
21. W. Batko, B. Stępień, *Application of the Bayesian inference for estimation of the long-term noise indicators and their uncertainty*, Acta Physica Polonica A, **119** (2011) 916–920.
 22. W. Batko, B. Przysucha, *Determination of the Probability Distribution of the Mean Sound Level*, Archives of Acoustics, **35** (2010) 543–550.
 23. W. Batko, B. Przysucha, *Random Distribution of Long - Term Indicators of Variable Emission Conditions*, Acta Physica Polonica A, **119-6-A** (2011) 1086–1090.
 24. W. Batko, B. Przysucha, *Determination of the distribution form for sound level measurements results* (sent for publication in Archives od Acoustics).
 25. W. Batko, B. Przysucha, *Cascade method of the determination of the sound level probability distribution function* (sent for publication in Archives od Acoustics).
 26. G.E.P Box, G.M. Jenkins, *Analysis of time series: forecasting and control*, PWN, 1983 (in Polish).
 27. L. Robert, R.L. Launer, G.N. Wilkinson, *Robustness in Statistics*, Academic Press, New York 1979.
 28. *Evaluation of measurement data – Supplement 1 to the Guide to the expression of uncertainty in measurement – Propagation of distributions using a Monte Carlo method* (GUM), BIPM, JCGM 101:2008.
 29. W. Batko, P. Pawlik, *Uncertainty Evaluation in Modelling of Acoustic Phenomena with Uncertain Parameters Using Interval Arithmetic*, Acta Physica Polonica A, **121** (2012) A-152-155.
 30. W. Batko, P. Pawlik, *New approach to uncertainty assessment of acoustic effects in the environment*, Archives of Acoustics, **37** (2012) 57–61.
 31. W. Batko, R. Bal, *Analiza skorelowania wyników pomiarowych w ocenach stanu zagrożeń hałasowych środowiska*, Rozdz. w monografii „Systemy wspomagania w inżynierii produkcji: środowisko i bezpieczeństwo w inżynierii produkcji. Red. W. Biały, A. Kuboszek, pp. 67–74, Wydawnictwo PA NOVA S.A., Gliwice 2013.

Nonlinear Surface Elastic Waves in Materials

Jeremiah RUSHCHITSKY

S.P.Timoshenko Institute of Mechanics, Nesterov str.3, Kiev, 03680, Ukraine
rushch@inmech.kiev.ua

Abstract

This paper is devoted to analysis of the surface nonlinear elastic harmonic waves of four types (Rayleigh and Stoneley harmonic waves within the framework of plane strain state; Love and Mozhaev harmonic wave within the framework of anti-plane strain state). The nonlinear model is based on introducing the Murnaghan elastic potential, which includes both geometrical and physical nonlinearities. Each type of surface waves is discussed in four steps: statement of the problem, nonlinear wave equations, approximate solution (first two approximations), so-me conclusions. A nonlinear analysis of waves required many novelties: new variants of the Murnaghan potential, new nonlinear wave equations and new nonlinear boundary conditions. The nonlinear wave equations were solved by the method of successive approximations. A new approach to analyze the boundary conditions is offered. Some new nonlinear wave effects are observed theoretically: a wave picture is reached by the 2nd harmonic and becomes changing in time of propagation, the wave numbers become depending on the initial amplitude.

Keywords: surface nonlinear elastic harmonic waves, Rayleigh wave, Love wave, Stoneley wave, Mozhaev wave

1. Introduction

The theory of elastic harmonic waves forms the big fragment both linear and nonlinear theory of elasticity. Chronologically, the free waves were first studied. Their main characteristics is that they propagate in the space without boundaries. The plane harmonic waves have to be referred just to this type of waves [7]. Further, the waves with curvilinear fronts (cylindrical, spherical and so on) were studied, where the curvilinear boundary is presented, on which the waves are generating and then passing to infinity. The surface waves present the next, third, group in complexity of theoretical analysis [8]. A necessary here allowance for the influence of interface and a condition of quick attenuation of the wave amplitudes while being gone from the boundary, form a more complicate wave picture.

An intrinsic logics of development of the theory of elastic waves was dictated, at least, three lines of the subsequent study of elastic waves. The 1st line consists in complication of the model of elastic deformation (for example, transition from the structural model of the 1st order to the models of the 2nd order - micropolar, elastic mixture, micro-morphic and so forth. The 2nd line includes allowance for the initial stresses what is impossible in the framework of the linear theory and has many applications. The 3rd line is associated with the full allowance for a nonlinearity of deformation and can be divided on different sub-lines, part of each is pure theoretical, whereas other one is more applied. Among the theoretical sublines, the Moscow, Tallinn, Nizhnii Novgorod, and Kyiv ones can be outlined. The shown in this paper analysis is related to the 4th subline. It is based on introduction in-to the model a nonlinearity, described by the Murnaghan elastic potential. Here, some results from analysis of the Rayleigh, Love, Stoneley, and Mozhaev waves are shown. The Rayleigh and Stoneley waves are related to the surface waves and can be analyzed in the 3D approach. The 2D analysis (a statement in the framework of

the plane strain approach) seems the only more convenient for the pilot consideration. The Love and Mozhaev waves are related to the surface wave and are analyzed in the 2D approach (a statement in the framework of the anti-plane strain approach).

2. Nonlinear elastic surface Rayleigh wave

2.1. Statement of the problem

The case is considered, when an interface is the plane. Then the Cartesian coordinates are chosen in the way that interface is described by equation $x_3 = 0$ and an elastic material occupies the upper half-space. Let the material is isotropic and the wave propagates along the axis Ox_1 . In this case, the motion becomes not depending on the coordinate x_2 . The mechanical state becomes plane strain state. Consider now the problem of nonlinear Rayleigh waves within an approach based on the Murnaghan model of description of nonlinearity of elastic deformation. The starting point is then the variant of Murnaghan potential [5,7] is chosen

$$\begin{aligned} W = & (1/2)\lambda(u_{1,1} + u_{3,3})^2 + \mu\left\{(u_{1,1})^2 + (u_{3,3})^2 + (1/2)(u_{1,3} + u_{3,1})^2\right\} + \dots \\ & \dots + (1/3)A\left[(u_{1,1})^3 + (u_{3,3})^3 + (3/4)(u_{1,3} + u_{3,1})(u_{1,1} + u_{3,3})\right] + \\ & + B(u_{1,1} + u_{3,3})\left[(u_{1,1})^2 + (u_{3,3})^2 + (u_{1,3} + u_{3,1})^2\right] + (1/3)C(u_{1,1} + u_{3,3})^3. \end{aligned} \quad (1)$$

The next basic formulas represent the components of the Kirchhoff stress tensor, that are evaluated from (1) using the rule $t_{nm} = (\partial W / \partial u_{m,n})$.

2.2. Nonlinear wave equations

Substitution of these components into the motion equations $t_{11,1} + t_{31,3} = \rho\ddot{u}_1$; $t_{13,1} + t_{33,3} = \rho\ddot{u}_3$ gives two nonlinear equations of Lame type

$$\begin{aligned} \rho\ddot{u}_1 - (\lambda + 2\mu)u_{1,11} - (\lambda + \mu)u_{3,13} - \mu u_{1,33} = & [3(\lambda + 2\mu) + 2(A + 3B + C)]u_{1,1}u_{1,11} + \quad (2) \\ & + [\mu + ((A/2) + B)](u_{1,1}u_{1,33} + u_{1,3}u_{3,11} + u_{1,3}u_{3,33} + u_{3,3}u_{1,33}) + \\ & + [2(\lambda + \mu) + \left(\frac{A}{2} + 3B + 2C\right)](u_{1,1}u_{3,13} + u_{3,3}u_{3,13}) + [(\lambda + 3\mu) + A + 2B](u_{1,3}u_{1,33} + u_{3,1}u_{1,13}) + \\ & + [(\lambda + 2\mu) + (A/2) + B](u_{3,1}u_{3,11} + u_{3,1}u_{3,33}) + [\lambda + 2(B + C)]u_{3,3}u_{1,11}. \end{aligned}$$

The second equation can be obtained from the first one by a change of indexes $1 \leftrightarrow 3$.

Each equation involves 12 nonlinear summands. The total number of distinguishing summands is 24. A similar increase of nonlinear summands is typical for cylindrical waves [8].

2.3. Approximate solutions (first two approximations)

The linear analysis is based on introduction of two new functions (potentials), which can be determined as solutions of the mutually independent linear wave equations. In the nonlinear case, the wave equations are nonlinear and coupled ones. To analyze the nonlinear case, let us introduce two potentials by the classical scheme [5,8]

$$u_1(x_1, x_3, t) = [\varphi(x_1, x_3, t)]_1 + [\psi(x_1, x_3, t)]_3; u_3(x_1, x_3, t) = [\varphi(x_1, x_3, t)]_3 - [\psi(x_1, x_3, t)]_1. \quad (3)$$

In the first approximation, these potentials have the form corresponding to harmonic wave with frequency ω , wave number k_{Rlin} and decaying by the exponential law, when being moved away from the plane $x_1 = 0$ [4]

$$\begin{aligned} \varphi^{(1)}(x_1, x_3, t) &= A_\varphi E E_L, \quad \psi^{(1)}(x_1, x_3, t) = A_\psi E E_T, \\ E &= e^{i(k_{Rlin}x_1 - \omega t)}, \quad E_L = e^{-k_\varphi x_3} = e^{-\sqrt{k_{Rlin}^2 - k_L^2}}, \quad E_T = e^{-k_\psi x_3} = e^{-\sqrt{k_{Rlin}^2 - k_T^2}}. \end{aligned} \quad (4)$$

The final expressions for the second approximation solution are as follows (below only one potential is shown)

$$\begin{aligned} \varphi^{(2)}(x_1, x_3, t) &= \frac{\rho}{4(\lambda + 2\mu)} x_1 x_3 (A_\varphi)^2 e^{2i(k_{Rlin}x_1 - \omega t)} \left\{ -\frac{1}{4k_L^2} \frac{\sqrt{k_{Rlin}^2 - k_L^2} x_1 + ik_{Rlin} x_3}{\left(\sqrt{k_{Rlin}^2 - k_L^2} x_1\right)^2 + (k_{Rlin} x_3)^2} \times \right. \\ &\quad \times M_\varphi^L e^{-2\sqrt{k_{Rlin}^2 - k_L^2} x_3} - \frac{1}{4k_T^2} \frac{\sqrt{k_{Rlin}^2 - k_T^2} x_1 + ik_{Rlin} x_3}{\left(\sqrt{k_{Rlin}^2 - k_T^2} x_1\right)^2 + (k_{Rlin} x_3)^2} M_\varphi^T e^{-2\sqrt{k_{Rlin}^2 - k_T^2} x_3} + \\ &\quad \left. \frac{1}{\sqrt{(k_{Rlin}^2 - k_L^2)(k_{Rlin}^2 - k_T^2)} - k_{Rlin}^2} \frac{2x_1 \left(\sqrt{k_{Rlin}^2 - k_L^2} + \sqrt{k_{Rlin}^2 - k_T^2}\right) + 4ik_{Rlin} x_3}{4x_1^2 \left(\sqrt{k_{Rlin}^2 - k_L^2} + \sqrt{k_{Rlin}^2 - k_T^2}\right)^2 + 16(k_{Rlin} x_3)^2} M_{\varphi\psi}^{LT} e^{-\sqrt{(k_{Rlin}^2 - k_L^2)(k_{Rlin}^2 - k_T^2)} x_3} \right\}, \end{aligned} \quad (5)$$

2.4. Some conclusions

Conclusion 1. The 2nd approximation includes the 2nd harmonic, that is, it includes the 2nd harmonic relative to the harmonic wave propagating in direction of the horizontal coordinate and to the exponential decay of the wave along the vertical coordinate. New harmonics have amplitudes, which depend nonlinearly on coordinates and then increase with increasing the time of Rayleigh wave propagation. As a result, the 1st harmonic distorts.

Conclusion 2. The dependence of amplitude of the 2nd harmonic on the squared corresponding amplitude of the 1st harmonic is standard for the used method within an approach that the nonlinearity is weak. It has some consequence relative to the 2nd harmonic distortion.

Conclusion 3. For the pure surface wave ($x_3 = 0$) the 2nd approximation is at beginning the zeroth, but for the near-the-surface wave this approximation can introduce the essential contribution into the wave picture.

3. Nonlinear elastic surface Stoneley wave

3.1. Statement of the problem

Consider the case, when two nonlinear elastic half-spaces with different densities and mechanical properties are separated by a plane and are joined according to the condition of full mechanical contact. Choose also the Cartesian coordinates $Ox_1 x_2 x_3$ and assume that an interface is the coordinate plane and is described by equation $x_3 = 0$ [9]. Suppose further that the mechanical state does not depend on coordinate x_2 and the transverse

horizontal displacement u_2 is absent. Then the problem is reduced to analysis of two half-planes (upper and lower) with the straight interface. This exhausts the geometrical part of statement of the problem on Stoneley wave. The mechanical part consists in using the equations of motion for the present case of absence of the transverse horizontal displacements.

This approach is based on introduction of nonlinearity of deformations of both half-planes by use of the Cauchy-Green nonlinear strain tensor and the Murnaghan potential

$$\begin{aligned} W^{U(L)} = & \frac{1}{2} \lambda_{U(L)} (u_{1,1}^{U(L)} + u_{3,3}^{U(L)})^2 + \mu_{U(L)} \left\{ (u_{1,1}^{U(L)})^2 + (u_{3,3}^{U(L)})^2 + \frac{1}{2} (u_{1,3}^{U(L)} + u_{3,1}^{U(L)})^2 \right\} + \dots \quad (6) \\ & \dots + B_{U(L)} (u_{1,1}^{U(L)} + u_{3,3}^{U(L)}) \left[(u_{1,1}^{U(L)})^2 + (u_{3,3}^{U(L)})^2 + (u_{1,3}^{U(L)} + u_{3,1}^{U(L)})^2 \right] + \frac{1}{3} C_{U(L)} (u_{1,1}^{U(L)} + u_{3,3}^{U(L)})^3, \end{aligned}$$

where the superscript U (upper) is used for the upper half-plane and the superscript L (lower) is used for the lower half-plane.

3.2 Nonlinear equations of motion

These equations are written through the nonsymmetric Kirchhoff stress tensor $t_{nm}^{U(L)}$

$$t_{11,1}^{U(L)} + t_{31,3}^{U(L)} = \rho_{U(L)} \ddot{u}_1^{U(L)}; \quad t_{13,1}^{U(L)} + t_{33,3}^{U(L)} = \rho_{U(L)} \ddot{u}_3^{U(L)}, \quad (7)$$

The Kirchhoff tensors are determined by the formula $t_{nm}^{U(L)} = (\partial W^{U(L)} / \partial u_{m,n}^{U(L)})$.

Let us introduce the potentials like the case (3)

$$\begin{aligned} u_1^{U(L)}(x_1, x_3, t) &= [\varphi^{U(L)}(x_1, x_3, t)]_1 + [\psi^{U(L)}(x_1, x_3, t)]_3; \\ u_3^{U(L)}(x_1, x_3, t) &= [\varphi^{U(L)}(x_1, x_3, t)]_3 - [\psi^{U(L)}(x_1, x_3, t)]_1. \end{aligned} \quad (8)$$

Substitute representations (8) into (7) and obtain a system of two geometrically nonlinear equations relative to potentials

$$\begin{aligned} & \left[\rho_{B(H)} \ddot{\varphi}^{B(H)} - (\lambda_{B(H)} + 2\mu_{B(H)}) \Delta \varphi^{B(H)} \right]_1 + \left[\rho_{B(H)} \ddot{\psi}^{B(H)} - \mu_{B(H)} \Delta \psi^{B(H)} \right]_3 = \\ & = (\lambda_{B(H)} + 2\mu_{B(H)}) (3\varphi_{,11}^{B(H)} \varphi_{,111}^{B(H)} - \psi_{,11}^{B(H)} \psi_{,133}^{B(H)} - \psi_{,33}^{B(H)} \psi_{,111}^{B(H)}) + \dots \\ & \dots + \lambda_{B(H)} \varphi_{,33}^{B(H)} \varphi_{,111}^{B(H)} + \mu_{B(H)} (\psi_{,11} \psi_{,111} + \psi_{,33} \psi_{,133}); \\ & \left[\rho_{B(H)} \ddot{\varphi}^{B(H)} - (\lambda_{B(H)} + 2\mu_{B(H)}) \Delta \varphi^{B(H)} \right]_3 - \left[\rho_{B(H)} \ddot{\psi}^{B(H)} - \mu_{B(H)} \Delta \psi^{B(H)} \right]_1 = \quad (9) \\ & = \dots + (\lambda_{B(H)} + 3\mu_{B(H)}) (3\varphi_{,13} \varphi_{,133} + 2\psi_{,13} \psi_{,133} + \varphi_{,13} \varphi_{,111}) + \dots \\ & \dots + \lambda_{B(H)} \varphi_{,11} \varphi_{,333} + \mu_{B(H)} (\psi_{,33} \psi_{,333} + \psi_{,11} \psi_{,113}). \end{aligned}$$

3.3. Approximate solutions (first two approximations)

Apply now the method of successive approximations and choose the 1st approximation solution in the form of the classical linear representation of the Stoneley wave. Thus, the four potentials have the form of harmonic wave with frequency ω and wave number

k . These waves attenuate by the exponential law, when they move away from the plane $x_1 = 0$ (different for the upper and lower half-planes)

$$(10) \quad \begin{aligned} \varphi^{(1)B}(x_1, x_3, t) &= \tilde{A}_\varphi^B e^{-\sqrt{(k_s)^2 - (k_T^B)^2} x_3} e^{i(k_s x_1 - \omega t)} \equiv \tilde{A}_\varphi^B e^{-\beta_L^B x_3} e^{i(k_s x_1 - \omega t)}, \dots \\ \dots \psi^{(1)H}(x_1, x_3, t) &= \tilde{A}_\psi^H e^{+\sqrt{(k_s)^2 - (k_T^H)^2} x_3} e^{i(k_s x_1 - \omega t)} \equiv \tilde{A}_\psi^H e^{+\beta_T^H x_3} e^{i(k_s x_1 - \omega t)}. \end{aligned}$$

The amplitudes $A_\varphi^{B(H)}(x_3)$, $A_\psi^{B(H)}(x_3)$ have to fulfill the condition of attenuation with increasing the distance x_3 and the wave number $k_s = (\omega/v_s)$ has to be determined from the additional considerations.

The second approximation is as follows (only one potential is shown)

$$(11) \quad \begin{aligned} \varphi^{B(H)(2)}(x_1, x_3, t) &= \frac{1}{4} x_1 x_3 \left(A_\varphi^{B(H)(1)} \right)^2 E^2 \frac{\rho_{B(H)}}{\lambda_{B(H)} + 2\mu_{B(H)}} \times \\ &\times \left\{ -\frac{1}{4(k_L^{B(H)})^2} \frac{k_\varphi^{B(H)} x_1 + i k_{lin}^{B(H)} x_3}{(k_\varphi^{B(H)} x_1)^2 + (k_{lin}^{B(H)} x_3)^2} M_\varphi^{B(H)L} (E_L^{B(H)})^2 - \right. \\ &- \frac{1}{4(k_T^{B(H)})^2} \frac{k_\psi^{B(H)} x_1 + i k_{lin}^{B(H)} x_3}{(k_\psi^{B(H)} x_1)^2 + (k_{lin}^{B(H)} x_3)^2} M_\varphi^{B(H)T} (E_T^{B(H)})^2 + \\ &+ \frac{1}{k_\varphi^{B(H)} k_\psi^{B(H)} - (k_{lin}^{B(H)})^2} \left[\frac{2x_1 (k_\varphi + k_\psi) + 4ik_{lin} x_3}{[2x_1 (k_\varphi^{B(H)} + k_\psi^{B(H)})]^2 + 16(k_{lin}^{B(H)} x_3)^2} M_{\varphi\psi}^{B(H)LT} E_L^{B(H)} E_T^{B(H)} \right] \left. \right\}. \end{aligned}$$

3.4. Some conclusions

Conclusion 1. The 2nd approximation solutions include the 2nd harmonic relative the 1st (linear) approximation, that is, it includes the 2nd harmonic relative to harmonic waves propagating in direction of the horizontal coordinate and to the exponential decay of the wave along the vertical coordinate. New harmonics have amplitudes, which depend non-linearly on coordinates and then increase with increasing the Stoneley wave propagation time. As a result, the 1st harmonic distorts.

Conclusion 2. The characteristic feature of non-linearity is dependence of the 2nd approximation on squared amplitudes and coordinates. This means that the 2nd harmonic can dominate with time.

4. Nonlinear elastic surface Love wave

4.1. Statement of the problem

Consider the problem on the Love elastic wave in the classical statement under additional assumption on nonlinearity of deformation process. From the geometrical point of view, the nonlinear problem statement coincides in many parts with the linear one and

consists in that the system is considered: the layer of constant thickness defined by condition $-h \leq x_1 \leq 0$ and the upper half-space $x_1 \geq 0$ are described by Cartesian coordinates $Ox_1x_2x_3$ (the abscissa axis is directed deep into the half-space, the ordinate axis is directed along the interface) [1].

From point of view of mechanics, the problem includes some initial assumptions: (1) It is supposed that the half-space and the layer are filled by nonlinearly elastic materials with distinguishing properties (further, the quantities describing the layer and half-space are assigned the indexes L and H , respectively). (2) Materials are deformed by the Murnaghan model and, therefore, the properties include density $\rho_{L(H)}$ and five elastic constants $\lambda_{L(H)}$, $\mu_{L(H)}$, $A_{L(H)}$, $B_{L(H)}$, $C_{L(H)}$. (3) It is supposed also that the half-space and the layer are in conditions of full mechanical contact (equality of displacements and stresses at the interface) and the layer lower plane $x_1 = -h$ is free of stresses.

The possibility of propagation of the harmonic plane vertically polarized transverse wave is studied under the condition of absence of displacements u_1 , u_2 in longitudinal and horizontal directions, respectively.

The form of Murnaghan potential corresponding to the stated problem is as follows

$$\begin{aligned} W = & \frac{1}{4} \lambda \left[(u_{3,1})^2 + (u_{3,2})^2 \right]^2 + \mu \left[\frac{1}{2} (u_{3,1})^2 + \frac{1}{2} (u_{3,2})^2 + \frac{1}{4} (u_{3,1})^4 + \frac{1}{4} (u_{3,2})^4 + \frac{1}{4} (u_{3,1} u_{3,2})^2 \right] + \dots \\ & + \frac{1}{8} B \left[2(u_{3,1})^2 + 2(u_{3,2})^2 + (u_{3,1})^4 + (u_{3,2})^4 + (u_{3,1} u_{3,2})^2 \right] \left[(u_{3,1})^2 + (u_{3,2})^2 \right] + \dots \end{aligned} \quad (12)$$

The main feature of representation (12) is only occurrence even degrees of nonzero components $u_{3,1}$, $u_{3,2}$: the 2nd degrees (corresponding to the linear approach), the 4th degrees (corresponding to the cubically nonlinear approach), and the 6th degrees (corresponding to nonlinearity of the 5th order) are presented in (12).

4.2. Nonlinear wave equation

The stress tensor is determined by the classical formula $t_{ik} = (\partial W / \partial u_{k,i})$. Only two t_{13} , t_{23} of nine components of the stress tensor are nonzero.

Note the goal is stated to analyze the possibility of propagation in direction Ox_1 (at the neighborhood of interface) of the wave with unknown amplitude $\hat{u}_3^{L(H)}(x_1)$ and wave number k . Then the wave can be represented in the form $u_3^{L(H)} = \hat{u}_3^{L(H)}(x_1) e^{i(kx_2 - \omega t)}$.

If the requirement is formulated that the wave is localized near the interface, that is, it has the maximal amplitude at the interface and the amplitude decays essentially with increase of the absolute values of x_1 , then the statement in the framework of linear theory of elasticity corresponds to the nonlinear statement of the problem on Love wave. Two of three equations of motion are degenerated into identities in this problem, whereas the third one has a form $t_{13,1} + t_{23,2} = \rho \ddot{u}_3$, which can be transformed into the next nonlinear wave equation

$$\rho \ddot{u}_3 - \mu (u_{3,11} + u_{3,22}) = T_1 (u_{3,1})^2 u_{3,11} + T_2 (u_{3,2})^2 u_{3,11} + T_1 (u_{3,2})^2 u_{3,22} +$$

$$\begin{aligned}
& +T_2(u_{3,1})^2 u_{3,22} + 4T_2 u_{3,1} u_{3,2} u_{3,12} + F_1(u_{3,1})^4 u_{3,11} + F_1(u_{3,2})^4 u_{3,22} + \\
& + F_2(u_{3,2})^4 u_{3,11} + F_2(u_{3,1})^4 u_{3,22} + F_3(u_{3,1})^3 u_{3,2} u_{3,12} + F_3 u_{3,1}(u_{3,2})^3 u_{3,12} + \\
& + F_4(u_{3,1})^2 (u_{3,2})^2 u_{3,11} + F_4(u_{3,2})^2 (u_{3,1})^2 u_{3,22},
\end{aligned} \tag{13}$$

$$\begin{aligned}
T_1 &= 3[(\lambda+\mu) + (1/4)A + (1/2)B], \quad T_2 = (1/2)[(\lambda+\mu) + A + B], \quad F_1 = (5/4)(A + B + C), \\
F_2 &= A + (1/4)B + (1/4)C, \quad F_3 = 2A + (3/2)B + 2C, \quad F_4 = (3/4)(2A + B + 2C).
\end{aligned}$$

The equation (13) contains the nonlinear summands of the 3rd (five summands) and the 5th (eight summands) orders. This feature of absence of even order summands is the consequence of the problem statement. A similar situation was arisen in the study of plane transverse wave in the 3rd approximation [7].

Let us save in (13) only the cubic nonlinearity and search the solution by the method of successive approximations.

4.3. Approximate solutions (first two approximations)

The solution in the framework of first two approximations is as follows

$$\text{for } x_2 \in (-\infty, \infty), x_1 \in [0; \infty) : \quad u_3^H(x_1, x_2, t) = u_3^{H(1)} + u_3^{H(2)} = \tag{14}$$

$$= L_H e^{-\sqrt{1-(v/v_T^H)^2} kx_1} e^{i(kx_2 - \omega t)} + \frac{x_1 x_2 \left[\sqrt{1-(v/v_T^H)^2} x_2 + i x_1 \right]}{\left[1-(v/v_T^H)^2 \right] (x_2)^2 + (x_1)^2} K_H^{(2)} e^{-3\beta_H kx_1} e^{i3(kx_2 - \omega t)};$$

$$\text{for } x_2 \in (-\infty, \infty), x_1 \in [-h; 0] : \quad u_3^L(x_1, x_2, t) = u_3^{L(1)} + u_3^{L(2)} = \tag{15}$$

$$\begin{aligned}
& = \left\{ \left[-L_H \frac{\mu_\Pi}{\mu_C} \frac{\sqrt{1-(v/v_T^H)^2}}{\sqrt{(v/v_T^L)^2 - 1}} + x_1 x_2 \frac{(L_H)^3 k^3}{24} K_{1s} \right] \sin \sqrt{[(v/v_T^L)^2 - 1]} kx_1 + \right. \\
& \quad \left. + \left[L_\Pi + x_1 x_2 \frac{(L_H)^3 k^3}{24} K_{1c} \right] \cos \sqrt{[(v/v_T^L)^2 - 1]} kx_1 \right\} e^{i(kx_2 - \omega t)} + \\
& \quad + K_{3s} \sin 3\sqrt{[(v/v_T^L)^2 - 1]} kx_1 + K_{3c} \cos 3\sqrt{[(v/v_T^L)^2 - 1]} kx_1 \left. \right\} e^{3i(kx_2 - \omega t)}.
\end{aligned}$$

The solutions (14) and (15) contain the unknown parameters: amplitude L_H and wave number k . If the amplitude can be assumed to be arbitrary according to the fact that the Love wave is the running surface wave, then the wave number should be determined from the boundary conditions. But for the nonlinear statement these conditions are already nonlinear what enables allowance for effect of nonlinearity on the wave number.

4.4. Some conclusions

Conclusion 1. The wave is dispersive one, because analysis of boundary conditions testifies the nonlinear dependence of phase velocity v on wave number k : (1) For zero value of wave number (for infinite wave length), the velocity is equal to the phase velocity of plane transverse waves in the half-space v_T^H . (2) With increasing the wave number, the velocity decreases.

Conclusion 2. The 2nd approximation includes the 3rd harmonic relative the 1st (linear) approximation, that is, it includes the 3rd harmonic relative to the harmonic wave propagating along the horizontal coordinate and to the exponential decay of the wave along the vertical coordinate. These new harmonics have amplitudes, which depend nonlinearly on coordinates and then increase with increasing the time of Love wave propagation. As a result, the 1st harmonic distorts.

Conclusion 3. The dependence of amplitudes of the 2nd harmonic on the cubed corresponding amplitudes of the 1st harmonic is standard for the used method within an approach that the nonlinearity is weak [7].

5. Nonlinear elastic surface Mozhaev wave

Analysis of the nonlinear elastic surface wave propagating within the condition of anti-plane strain state in the half-plane (in contrast to the case of Love wave, where presence of layer is predicted) is proposed in [3]. In [2], such a virtual wave was called the Mozhaev wave. Unfortunately, the presented in this lecture four cases of harmonic and solitary waves do not certificate existence of such a wave.

References

1. A.E.H. Love, *Some problems of geodynamics*, Cambridge University Press, Cambridge 1911.
2. G.A. Maugin, Y. Chevalier, M. Louzar, *Interfacial waves in the presence of areas of slip*, Geophys. J. Int. **118** (1994) 305-316.
3. V.G. Mozhaev, *A new type of surface waves in solids due to nonlinear elasticity*, Physics Letters A, **139**(7) (1989) 333-336.
4. J.W. Rayleigh, *On waves propagated along the plane surface of an elastic body*, Proc. Math. Soc. London, **17** (1885) 4-11.
5. J.J. Rushchitsky, *Certain Class of Nonlinear Hyperelastic Waves: Classical and Novel Models, Wave Equations, Wave Effects*, Int. J. Appl. Math. and Mech. **9**(1) (2013) 400-443.
6. J.J. Rushchitsky, *Theory of waves in materials*, Ventus Publishing ApS, Copenhagen 2011 (free text-book in BookBooN.com)
7. J.J. Rushchitsky, *Nonlinear Elastic Waves in Materials*, Springer, Heidelberg 2014.
8. J.J. Rushchitsky, *Quadratically nonlinear cylindrical hyperelastic waves: Derivation of wave equations for axisymmetric and other states*, Int. Appl. Mech., **41**(6) (2005) 646-656.
9. R. Stoneley, *Elastic waves at the surface of separation of two solids*, Proc. R. Soc. London A, **106** (1924) 416-428.

Thermoelastic Wheel-Rail Contact Problem for a Multi-Layer Structure

Andrzej CHUDZIKIEWICZ

Institute of Transport, Warsaw University of Technology

ul. Koszykowa 75, 00 - 662 Warsaw

ach@it.pw.edu.pl

Andrzej MYŚLIŃSKI

Systems Research Institute, ul. Newelska 6, 01 - 447 Warsaw

Faculty of Manufacturing Engineering, Warsaw University of Technology

ul. Narbutta 85, 02-524 Warsaw

myslinsk@ibspan.waw.pl

Abstract

Wheel-rail thermoelastic contact problem is analysed and numerically solved in the paper. The surface of the rail is assumed to consist from layers having distinct constant material parameters and a functionally graded material layer between. Thermal and mechanical properties of the graded layer are dependent on its depth rather than constant as it is considered in the literature. Numerous laboratory experiments indicate that graded materials layers or coatings covering the conventional steel body can reduce the magnitude of contact and/or thermal stresses as well as the noise and the rolling contact fatigue. The contact phenomenon includes friction as well as frictional heat generation and wear. Quasistatic numerical approach is used to solve numerically this contact problem. Numerical results are provided and discussed.

Keywords: thermoelastic rolling contact problem, functionally graded materials, quasistatic method

1. Introduction

Two-dimensional rolling contact problems including friction, frictional heat generation and wear are solved numerically in this paper. The unilateral contact of a rigid wheel with an elastic rail lying on a rigid foundation is considered. The friction between the bodies is described by Coulomb law [1,2,3]. The coefficient of friction is assumed constant. Due to the heat conduction, the frictional heat flow is directed into the coated medium [4]. We employ Archard's law of wear [5]. In the model the wear is identified as an increase in the gap between bodies.

The thermoelastic contact or rolling contact problems were considered by many authors (see references in [1,3,6,7,8,9,10,11,12]). Numerous laboratory experiments indicate [2,8] that the use of a coating material attached to the conventional steel body reduce the magnitude of residual or thermal stresses. It leads to the reduction of the rolling contact fatigue and noise. However in a conventional coating structure homogeneous materials are used. The abrupt change in the mechanical properties of the materials at the surface coating-substrate interface results in stress concentration or degraded bonding strength [9]. Thermoelastic rolling contact problem with two layer surface model with the material properties governed by the power law are considered in [12].

In this paper, following [13], we assume that between the homogeneous coating layer and the homogeneous substrate there exists the graded interlayer which properties depend on its depth according to the exponential law. We consider also thermoelastic contact phenomenon with the frictional heat flow rather than elastic contact model as in [13].

In the paper we take special features of this rolling contact problem and use so-called quasistatic approach [14] to solve it numerically. In this approach the inertial terms in elastic and heat equations are replaced by the stationary terms reflecting the dynamics of the body and heat transfer rather than completely neglect them as in the classical quasistatic formulation. Therefore, after brief introduction of the thermoelastic model of the rolling contact problem with friction and wear in the framework of two-dimensional linear elasticity theory the general coupled time dependent system describing this physical phenomenon is formulated. This system is transformed into equivalent stationary system in so-called quasistatic formulation. To solve numerically this stationary system we will decouple it into mechanical and thermal parts. Finite element method is used as a discretization method. The numerical results including the distribution of temperature field in the contact zone are provided and discussed.

2. Problem formulation

Consider deformations of an elastic strip lying on a rigid foundation (see Figure 1). The strip has constant height h and occupies domain $\Omega \subset \mathbb{R}^2$ with the boundary Γ .

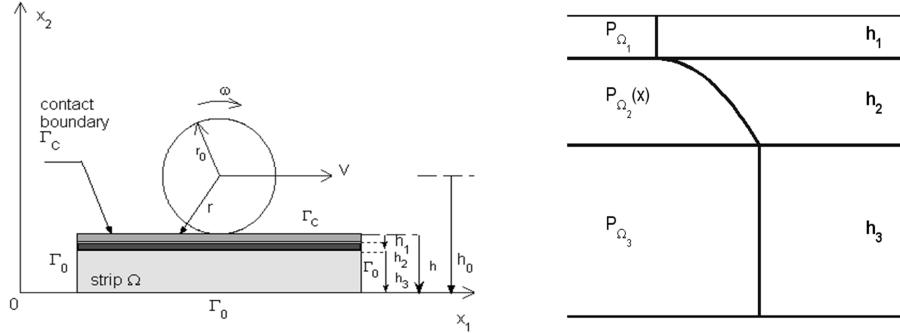


Figure 1. Wheel rolling over the strip

Figure 2. Three-layers model

A wheel rolls along the upper surface Γ_C of the strip. The wheel has radius r_0 , rotating speed ω and linear velocity V . The axis of the wheel is moving along a straight line at a constant altitude h_0 where $h_0 < h + r_0$, i.e., the wheel is pressed in the elastic strip. It is assumed, that the head and tail ends of the strip are clamped, i.e., we assume that the length of the strip is much bigger than the radius of the wheel. Moreover it is assumed, that there is no mass forces in the strip. The body is clamped along a portion Γ_0 of the boundary Γ of the domain Ω . The contact conditions are prescribed on a portion Γ_C of the boundary Γ . Moreover, $\overline{\Gamma}_0 \cap \overline{\Gamma}_C = \emptyset$. $\overline{\Gamma} = \overline{\Gamma}_0 \cup \overline{\Gamma}_C$.

We denote by $u=(u_1, u_2)$, $u = u(x, t)$, depending on the spatial variables $x=(x_1, x_2) \in \Omega$, and time variable $t \in [0, T]$, $T > 0$, a displacement of the strip and by θ the absolute temperature of the strip. Assume $\Omega = \Omega_1 \cup \Omega_2 \cup \Omega_3$ where Ω_1 , Ω_2 and Ω_3 denote the homogeneous coating layer, graded interlayer, and substrate layer, respectively. The heights of these layers are h_1 , h_2 , h_3 , respectively. In the middle layer Ω_2 material parameters depend on the height of the layer according to the exponential law. The displacement u of the strip satisfies the evolution equation [9] in the cylinder $\Omega \times (0, T)$:

$$\rho \frac{\partial^2 u}{\partial t^2} = A^* D A u - \alpha(3\lambda + 2\gamma) \nabla \theta, \quad (1)$$

The temperature θ of the strip satisfies the parabolic equation in the cylinder $\Omega \times (0, T)$:

$$\rho c_p \frac{\partial \theta}{\partial t} = \bar{\kappa} \Delta \theta \quad (2)$$

The following initial and boundary conditions are imposed:

$$u(0) = u_{0i}, \quad u'(0) = u_{1i}, \quad i=1, 2, \quad \theta(0) = \theta_0 \text{ in } \Omega, \quad (3)$$

$$u = 0 \text{ on } \Gamma_0 \times (0, T) \text{ and } B^* D A u = F \text{ on } \Gamma_C \times (0, T), \quad (4)$$

$$\frac{\partial \theta}{\partial n} = q(t) \text{ on } \Gamma \quad (5)$$

where $u(0) = u(x, 0)$, $u' = du/dt$, u_{0i} and u_{1i} , θ_0 , $q(t)$ are given functions, ρ is a mass density of the strip material, α is a coefficient of thermal expansion, $\bar{\kappa}$ is a thermal conductivity coefficient, c_p is a heat capacity coefficient, $\Gamma_0 = \Gamma \setminus \Gamma_C$. The operators A , B and D are defined as follows [10]

$$A = \begin{pmatrix} \frac{\partial}{\partial x_1} & 0 & \frac{\partial}{\partial x_2} \\ 0 & \frac{\partial}{\partial x_2} & \frac{\partial}{\partial x_1} \end{pmatrix}^*, \quad B = \begin{pmatrix} n_1 & 0 & n_2 \\ 0 & n_2 & n_1 \end{pmatrix}^*, \quad D = \begin{pmatrix} \lambda + 2\gamma & \lambda & 0 \\ \lambda & \lambda + 2\gamma & 0 \\ 0 & 0 & 2\gamma \end{pmatrix}, \quad (6)$$

where $n = (n_1, n_2)$ is the outward normal vector to the boundary Γ of the domain Ω , λ and γ are Lame coefficients, A^* denotes a transpose of A . In Ω_2 operator D is assumed to depend on the depth of the graded interlayer according to the exponential law. By $\sigma = (\sigma_{11}, \sigma_{22}, \sigma_{12})$ and F we denote the stress tensor in domain Ω and surface traction vector on the boundary Γ , respectively. The surface traction vector $F = (F_1, F_2)$ on the boundary Γ_C is a priori unknown and is given by conditions of contact and friction. Under the assumptions that the strip displacement is small the contact conditions on the boundary $\Gamma_C \times (0, T)$ take a form:

$$u_2 + g_r + w \leq 0, \quad F_2 \leq 0, \quad (u_2 + g_r + w)F_2 = 0, \quad g_r = h - h_0 + \sqrt{r_0^2 - (u_1 + x_1)^2}, \quad (7)$$

$$|F_1| \leq \mu |F_2|, F_1 \frac{du_1}{dt} \leq 0, (|F_1| - \mu |F_2|) \frac{du_1}{dt} = 0, \quad (8)$$

where μ is a friction coefficient. Conditions (5)-(6) describe the non-penetration condition as well as Coulomb law of friction, respectively [1,6]. Assuming that the dimensional wear coefficient $k > 0$ is given the wear $w=w(x,t)$ is governed by the equation [4]:

$$\frac{dw}{dt} = k V F_2. \quad (9)$$

Remark, in (7) the wear w increases the gap between the contacting surfaces.

2.1 Material properties of functionally graded materials

In subdomains Ω_1 and Ω_3 the operator D characterizing the properties of the material occupying strip Ω or the conductivity coefficient take different constant values, respectively (see Figure 2). In the subdomain Ω_2 the operator D or the conductivity coefficient are assumed to depend on the depth of the layer. This dependence is governed by the exponential law [8,9]:

$$P(x_2) = P_{\Omega_1} \exp(n \frac{x_2 + h_1}{h_2}), \quad x_2 \in [-h_2 - h_1, -h_1], \quad (10)$$

where $n = \log(P_{\Omega_1}/P_{\Omega_3})$, h_1, h_2 are given parameters, x_2 denotes the spatial variable and $P(x_2)$, P_{Ω_1} , P_{Ω_3} denote the height dependent material property (material density, conductivity coefficient or Young modulus) of layer Ω_2 as well as the material properties of layers Ω_1 and Ω_3 , respectively. The continuity of the displacements, temperatures and the stresses along the interfaces $\partial\Omega_1 \cap \partial\Omega_2$ and $\partial\Omega_2 \cap \partial\Omega_3$ are assumed.

3. Quasistatic formulation

Taking into account the special features of the contact problem (1)-(9) one can reformulate it in the framework of the quasistatic approach. This approach is based on the assumption that for the observer moving with a wheel its displacement does not depend on time [14].

Consider an observer moving with the wheel with the constant linear velocity V . We introduce the new Cartesian coordinate system $O'x'_1 x'_2$ hooked in the middle of the wheel. The systems $O'x'_1 x'_2$ and $Ox_1 x_2$ are related by: $x'_1 = x_1 - Vt$ and $x'_2 = x_2$. Therefore the displacement $u(x'_1, x'_2)$ does not depend on time [14] and we obtain:

$$\frac{du}{dt} = (x'_1, x'_2) = \frac{du}{dt} (x_1 - Vt, x_2) = 0. \quad (11)$$

It implies:

$$\frac{du}{dt} = -V \frac{du}{dx_1} \text{ and } \frac{d^2 u}{dt^2} = V^2 \frac{d^2 u}{dx_1^2}. \quad (12)$$

Using the same arguments for the temperature field we obtain

$$\frac{\partial \theta}{\partial t} = -V \frac{\partial \theta}{\partial x_1} \quad \text{and} \quad \frac{\partial w}{\partial t} = -V \frac{\partial w}{\partial x_1}. \quad (13)$$

Using (12)-(13) the inertial terms in equations (1)-(2) are replaced by the stationary terms depending on the wheel velocity and spatial derivatives of displacement or temperature fields and reflecting the dynamics of the moving body rather than completely neglected it as in the classical quasistatic formulation [1]. Taking into account (12)-(13), quasistatic approximation of the contact problem (1)-(10) takes the form: find displacement u and temperature θ satisfying:

$$A^*D(x)Au - \rho V^2 u_{1,1} - \alpha(3\lambda + 2\gamma) \nabla \theta = 0 \quad \text{in } \Omega, \quad (14)$$

$$-V \frac{\partial \theta}{\partial x_1} = \bar{\kappa} \frac{\partial^2 \theta}{\partial x_2^2}, \quad (15)$$

as well as the boundary conditions

$$u = 0 \quad \text{on } \Gamma_0, \quad B^*D(x) Au = F \quad \text{on } \Gamma_C, \quad (16)$$

$$u_2 + g_r + w \leq 0, \quad F_2 \leq 0, \quad (u_2 + g_r + w)F_2 = 0, \quad \text{on } \Gamma_C, \quad (17)$$

$$|F_1| \leq \mu |F_2|, \quad F_1 u_{1,1} \leq 0, \quad (|F_1| - \mu |F_2|) u_{1,1} = 0, \quad \text{on } \Gamma_C, \quad (18)$$

$$-\kappa \frac{\partial \theta}{\partial x_2} = \bar{\alpha} \left[\frac{\theta}{r} F_2 + (1 - \frac{k\rho c \theta}{\mu}) \mu V F_2 \right] \quad \text{on } \Gamma_C, \quad (19)$$

$$\frac{dw}{dx_1} = -k F_2, \quad \text{on } \Gamma_C, \quad (20)$$

where $u_{i,j} = \frac{\partial u_i}{\partial x_j}$, $u_{i,j,k} = \frac{\partial^2 u_i}{\partial x_i \partial x_k}$, $i,j,k=1,2$ and r denotes thermal resistant constant.

Moreover, $u_{0i} = u_{1i} = 0$ is set in (2).

3.1 Friction Regularization

In order to ensure the existence of solutions to the problem (14)-(20) we have to regularize it, i.e., we will consider it as the problem with the prescribed friction. Let $\varepsilon > 0$ be a regularization parameter. We use the following formula relating tangential and normal tractions on the contact boundary Γ_C [14]:

$$F_1 = F_1(\varepsilon, F_2, u_1) = -\mu |F_2| \arctan \frac{V u_{1,1}}{\varepsilon}. \quad (21)$$

4. Numerical methods and results

Finite element method is used to approximate thermoelastic contact problem (14)-(21) as the approximation method. Problem (14)-(21) is a coupled thermoelastic problem. Remark, the contact traction depends on the thermal distortion of the bodies and wear pro-

cess. On the other hand, the amount of heat generated due to friction depends on the contact traction. The main solution strategies for coupled problems are global solution algorithms where the differential systems for the different variables are solved together or operator splitting methods. In this paper we employ operator split algorithm. The numerical algorithm consists first in calculating for a given temperature field and wear the corresponding displacement and stress fields, i.e., in solving the mechanical subproblem. Next for the calculated displacement and stress fields we solve the thermal part of the system and calculate wear. The algorithm is terminated when the calculated temperature becomes steady, i.e., the temperature changes from iteration to iteration are less than the prescribed tolerance. The convergence of the operator split algorithm is shown using Fixed Point Theorem (see references in [12]). For details of the method see [14].

The obtained distributions of normal and tangential temperature distributions in the contact zone for different values of parameter $n=0.28, 0, -0.28$ are displayed in Figures 3 and 4, respectively. These distributions are strongly dependent on parameter η . The temperature is rapidly decreasing inside the strip and in front of the wheel. Behind the wheel the decrease of temperature is mild.

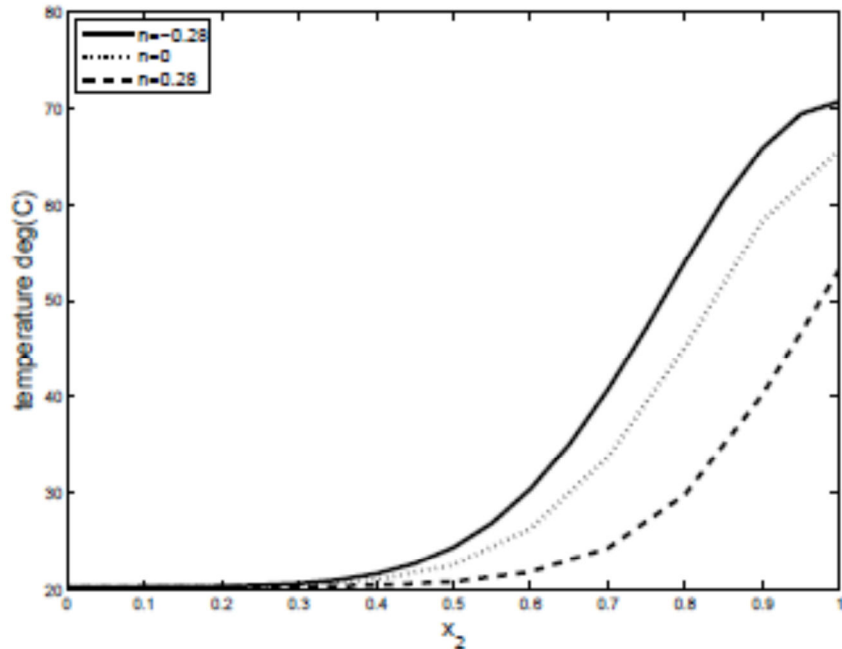
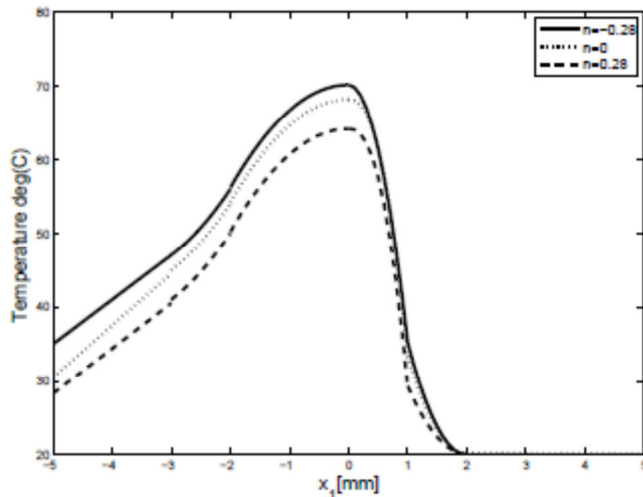


Figure 3. Rail temperature distribution along x_2 direction

Figure 4. Rail temperature distribution along x_1 direction

5. Conclusions

The thermoelastic rolling contact problem where the properties of the elastic layer between the homogeneous surface coating and the substrate of the rail are dependent on its depth is solved numerically using the quasistatic approach. The material properties of the graded layer are assumed to be governed by the exponential law. The applied exponential model of the graded material allows to control the normal contact pressure, temperature and the size of the contact area comparing to the pure homogeneous case. The dependence of the obtained stress distributions on the parameter n is stronger than on the nonhomogeneity index in power law (see [12]). The decrease in the nonhomogeneity index n reduces the maximum normal contact pressure and temperature at a cost of the widening of the contact area. The relationship between the applied normal load and the size of the contact zone is nonlinear. Remark also, that using the quasistatic approach we can observe dynamic phenomena of the rolling wheel.

References

1. W. Han, M. Sofonea, *Quasistatic contact problems in viscoelasticity and viscoplasticity*, AMS and IP, 2002.
2. M. Hiensch et al., *Two-material rail development field test results regarding rolling contact fatigue and squeal noise behavior*, Wear, **258** (2005) 964-972.
3. M. Shillor, M. Sofonea, J.J Telega, *Models and analysis of quasistatic contact: variational methods*, Springer, Berlin, 2004.
4. H.J. Choi, G.H. Paulino, *Thermoelastic contact mechanics for a flat punch sliding over a graded coating/substrate system with frictional heat generation*, Journal of the Mechanics and Physics of Solids, **56**(2008) 1673-1692.

5. H.C. Meng, K.C. Ludema, *Wear models and predictive equations: their form and content*, Wear, **181-183** (1995) 443-457.
6. W. Sextro, *Dynamical contact problems with friction*, Springer, Berlin, 2007.
7. P. Wriggers, *Computational contact mechanics*, Second Edition, Springer, Berlin, 2006.
8. S. Suresh, *Graded materials for resistance to contact deformation and damage*, Science, **292** (2001) 2447-2451.
9. J. Yang, L.L. Ke, *Two-dimensional contact problem for a coating-graded layer - substrate structure under a rigid cylindrical punch*, International Journal of Mechanical Sciences, **50** (2008) 985-994.
10. P. Chen, S. Chen, *Thermo-mechanical contact behavior of a finite graded layer under a sliding punch with heat generation*, International Journal of Solids and Structures, **50** (2013) 1108-1119.
11. S.P. Barik, M. Kanoria, P.K. Chaudhuri, *Steady state thermoelastic problem in an infinite functionally graded solid with a crack*, Int. J. of Appl. Math. And Mech. **6** (2010) 44-66.
12. A. Chudzikiewicz, A. Myśliński, *Thermoelastic Wheel-Rail Contact Problem with Elastic Graded Materials*, Wear, **271** (2011) 417 - 425.
13. A. Chudzikiewicz, A. Myśliński, *Rolling contact problems with nonhomogeneous materials*, Vibrations in Physical Systems, Eds. C. Cempel and M. Dobry, **25** (2012) 103-108.
14. A. Chudzikiewicz, A. Żochowski, A. Myśliński, *Quasistatic versus Kalker approach for Solving Rolling Contact Problems*, The Archive of Transport, **4** (1992) 103-120.

A Comparison of Human Physical Models Used in the ISO 10068:2012 Standard Based on Power Distribution PART 1

Marian Witalis DOBRY

*Poznan University of Technology, Institute of Applied Mechanics
24 Jana Pawła II Street, 60-965 Poznań
marijan.dobry@put.poznan.pl*

Tomasz HERMANN

*Poznan University of Technology, Institute of Applied Mechanics
24 Jana Pawła II Street, 60-965 Poznań
tomasz.hermann@put.poznan.pl*

Abstract

The study analyses differences in the flow of energy for two human physical models specified in the ISO 10068:2012 standard. For this purpose, two mathematical models of the Human–Tool system in question were developed using the Lagrange equation of the second kind. Corresponding energy models were then created for each mathematical model and tested by means of digital simulation in the MATLAB/simulink environment. The study revealed a discrepancy between the models in terms of different types of power and in the total power.

Keywords: biomechanical system, local vibrations, power distribution

1. Introduction

Biomechanical models of the hand and the hand-arm system are effectively used to represent the human response to mechanical vibrations. At present, the impact of vibrations can be studied based on any of the existing models, which differ in the number of degrees of freedom, the number of component parts of the dynamic structure and the manner in which they are connected (Fig. 1).

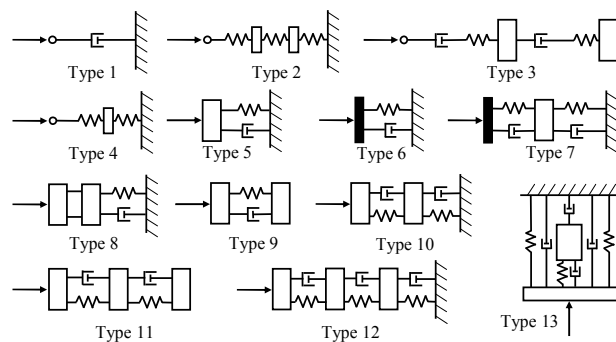


Figure 1. Biomechanical models of the hand and the hand-arm system [6]

One area that requires further research is the composition and verification of new models which are being developed to replace previous models and better represent the human response to mechanical vibrations. This kind of research is being conducted all over the world, including influential contributions from Griffin [5], Reynolds [8] and Meltzer [7].

To date, many studies into the impact of vibrations on the human body have relied on the “Type 12” model (Fig. 1), whose dynamic parameters are specified in the ISO 10068:1998 standard [9]. The fact that this long-favoured solution is being abandoned confirms that choosing the right model to assess the impact of vibrations on the human body is not an easy task. This study is an attempt at comparing power distribution in two biomechanical models of the human body, which are specified in the ISO 10068:2012 standard [10] – models 1 and 2 (Annexes B and C). The criterion for assessing model validity was the equality of energy phenomena occurring the dynamic structure during operation.

2. The First Principle of Power Distribution in a Mechanical System

The First Principle of Power Distribution in a Mechanical System can be expressed in the following way [1 – 4]:

„The net input power introduced into the mechanical system (after subtracting power loss) is equal to reflected power (accumulated or stored) in the system and output power from the system.”

A graphical interpretation of the First Principle of Power Distribution in a Mechanical System (FPoPDiMS) is shown in Figure 2.

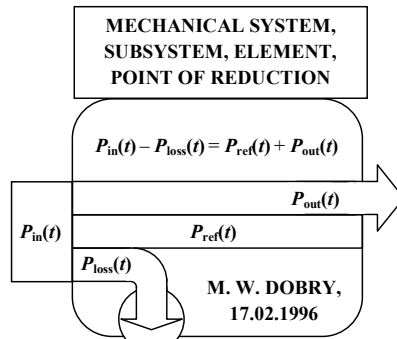


Figure 2. Graphical interpretation of the First Principle of Power Distribution [1-4]

This rule has the following mathematical form [1-4]:

$$P_{in}(t) - P_{loss}(t) = P_{ref}(t) + P_{out}(t) \quad (1)$$

where:

$$P_{in}(t) = \vec{W}_{in}(t) \cdot \vec{v}_{in}(t)$$

– the power of the resultant force – the drive input power introduced to the mechanical system,

- $P_{\text{loss}}(t) = P_{\text{int loss}}(t) + \vec{R}(t) \cdot \vec{v}_R(t)$ – power loss equal to the sum of the internal losses in the system and the power of the forces of resistance present during the operation of the system,
- $P_{\text{ref}}(t) = \vec{B}(t) \cdot \vec{v}_B(t) + \vec{S}(t) \cdot \vec{v}_S(t)$ – reflected power in the mechanical system, equal to the sum of inertial forces and the power of the forces of elasticity,
- $P_{\text{out}}(t) = \vec{O}(t) \cdot \vec{v}_{\text{out}}(t)$ – output power equal to the power output of a mechanical system.

3. The methodology of solving the problem – composition of energy models

To conduct a comparative assessment of the two models it was necessary to create physical models of the Human–Tool system. These models are the result of combining the human physical models specified in the ISO 10068:2012 standard [10] with the tool model – Fig. 3.

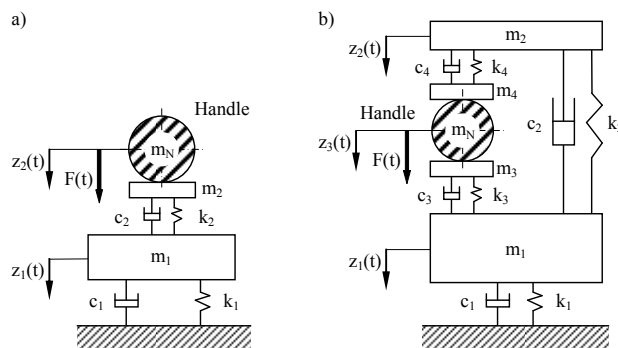


Figure 3. A synthesis of the ISO 10068:2012-based human physical models and the tool model: a) model 1 – Annex B; b) model 2 – Annex C [10]

The models in question are discrete in the sense that certain reduction points are connected by means of spring and damping systems. Tables 1 and 2 present dynamic parameters for the models, as indicated in the ISO 10068:2012 standard [10]. In the dynamic analysis only one vibration direction was considered – the z direction, which is the most significant in tool testing

The next step involved expressing the mathematical models of the dynamic structures using the Lagrange equation of the second kind in the following form:

$$\frac{d}{dt} \left(\frac{\partial E}{\partial \dot{q}_j} \right) - \frac{\partial E}{\partial q_j} = Q_j + Q_{jp} + Q_{jr} \quad j = 1, 2, \dots, s \quad (2)$$

where: E – kinetic energy of the system, q_j – generalized coordinates, \dot{q}_j – generalized velocities, Q_j – external active forces, Q_{jp} – potential forces, Q_{jr} – dissipation forces, s – number of degrees of freedom.

Table 1. Values of dynamic parameters for model 1 – Annex B [10]

Parameter	Unit	Vibration direction		
		x	y	z
m_1	kg	0.5479	0.5374	1.2458
m_2	kg	0.0391	0.0100	0.0742
k_1	N/m	400	400	1000
k_2	N/m	0	17648	50000
c_1	N·s/m	22.5	38.3	108.1
c_2	N·s/m	202.6	75.5	142.4

Table 2. Values of dynamic parameters for model 2 – Annex C [10]

Parameter	Unit	Vibration direction		
		x	y	z
m_1	kg	0.4129	0.7600	1.1252
m_2	kg	0.0736	0.0521	0.0769
m_3	kg	0.0163	0.0060	0.0200
m_4	kg	0.0100	0.0028	0.0100
k_1	N/m	400	500	1000
k_2	N/m	200	100	12000
k_3	N/m	4000	4907	43635
k_4	N/m	8000	17943	174542
c_1	N·s/m	20.0	28.1	111.5
c_2	N·s/m	100	39.7	39.3
c_3	N·s/m	144.6	50.7	86.8
c_4	N·s/m	79.9	14.3	121.0

For an unequivocal description generalized coordinates were adopted. For model 1 from the ISO 10068:2012 standard [10], the following generalized coordinates were used (Fig. 3a):

$$\begin{aligned} j=1 &\Rightarrow q_1 = z_1(t) \quad -\text{displacement of mass } m_1, \\ j=2 &\Rightarrow q_2 = z_2(t) \quad -\text{displacement of mass } m_2 \text{ and } m_N. \end{aligned}$$

In the case of model 2 from the ISO 10068:2012 standard [10] combined with the tool model (Fig. 3b), the following generalized coordinates were used:

$$\begin{aligned} j=1 &\Rightarrow q_1 = z_1(t) \quad -\text{displacement of mass } m_1, \\ j=2 &\Rightarrow q_2 = z_2(t) \quad -\text{displacement of mass } m_2, \\ j=3 &\Rightarrow q_3 = z_3(t) \quad -\text{displacement of mass } m_3, m_4 \text{ and } m_N. \end{aligned}$$

On adopting generalized coordinates, it was possible to formulate mathematical models of the Human–Tool system. For the Human–Tool system (ISO 10068:2012 combined with model 1 [10]) the mathematical model can be expressed as – Fig. 3a:

$$\begin{aligned} j=1, \quad &m_1 \ddot{z}_1 + (c_1 + c_2) \dot{z}_1 + (k_1 + k_2) z_1 - c_2 \dot{z}_2 - k_2 z_2 = 0; \\ j=2, \quad &(m_2 + m_N) \ddot{z}_2 + c_2 \dot{z}_2 + k_2 z_2 - c_2 \dot{z}_1 - k_2 z_1 = F(t). \end{aligned} \quad (3)$$

The mathematical model of the synthesis of the ISO 10068:2012-based model 2 [10] with the tool model – Fig. 3b, can be written as:

$$\begin{aligned} j = 1, \quad & m_1 \ddot{z}_1 + (c_1 + c_2 + c_3) \dot{z}_1 + (k_1 + k_2 + k_3) z_1 - c_3 \dot{z}_3 - c_3 z_3 - c_2 \dot{z}_2 - k_2 z_2 = 0; \\ j = 2, \quad & m_2 \ddot{z}_2 + (c_2 + c_4) \dot{z}_2 + (k_2 + k_4) z_2 - c_2 \dot{z}_1 - k_2 z_1 - c_4 \dot{z}_3 - k_4 z_3 = 0; \\ j = 3, \quad & (m_3 + m_4 + m_N) \ddot{z}_3 + (c_3 + c_4) \dot{z}_3 + (k_3 + k_4) z_3 - c_4 \dot{z}_2 - k_4 z_2 - c_3 \dot{z}_1 - k_3 z_1 = F(t). \end{aligned} \quad (4)$$

Based on differential equations of motion (3) and (4), corresponding energy models were created for the systems in question. By applying the First Principle of Power Distribution in a Mechanical System (1) one can move from a conventional dynamic analysis based on amplitudes of kinematic quantities to an energetic analysis of power distribution.

The energy model for the Human–Tool system, based on the model with two reduction points from the ISO 10068:2012 standard has the form:

$$\begin{aligned} j = 1, \quad & m_1 \ddot{z}_1 \dot{z}_1 + (c_1 + c_2) \dot{z}_1^2 + (k_1 + k_2) z_1 \dot{z}_1 - c_2 \dot{z}_2 \dot{z}_1 - k_2 z_2 \dot{z}_1 = 0; \\ j = 2, \quad & (m_2 + m_N) \ddot{z}_2 \dot{z}_2 + c_2 \dot{z}_2^2 + k_2 z_2 \dot{z}_2 - c_2 \dot{z}_1 \dot{z}_2 - k_2 z_1 \dot{z}_2 = F(t) \dot{z}_2. \end{aligned} \quad (5)$$

The energy model for the other Human–Tool system – Fig. 3b can be formulated as:

$$\begin{aligned} j = 1, \quad & m_1 \ddot{z}_1 \dot{z}_1 + (c_1 + c_2 + c_3) \dot{z}_1^2 + (k_1 + k_2 + k_3) z_1 \dot{z}_1 - \\ & - c_3 \dot{z}_3 \dot{z}_1 - k_3 z_3 \dot{z}_1 - c_2 \dot{z}_2 \dot{z}_1 - k_2 z_2 \dot{z}_1 = 0; \\ j = 2, \quad & m_2 \ddot{z}_2 \dot{z}_2 + (c_2 + c_4) \dot{z}_2^2 + (k_2 + k_4) z_2 \dot{z}_2 - \\ & - c_2 \dot{z}_1 \dot{z}_2 - k_2 z_1 \dot{z}_2 - c_4 \dot{z}_3 \dot{z}_2 - k_4 z_3 \dot{z}_2 = 0; \\ j = 3, \quad & (m_3 + m_4 + m_N) \ddot{z}_3 \dot{z}_3 + (c_3 + c_4) \dot{z}_3^2 + (k_3 + k_4) z_3 \dot{z}_3 - \\ & - c_4 \dot{z}_2 \dot{z}_3 - k_4 z_2 \dot{z}_3 - c_3 \dot{z}_1 \dot{z}_3 - k_3 z_1 \dot{z}_3 = F(t) \dot{z}_3. \end{aligned} \quad (6)$$

Energy models for the Human–Tool systems were implemented in MATLAB/simulink software to calculate timelines of power of inertia, dissipation and elasticity. The resulting data was used to compare models in terms of power distribution.

4. An energy-based comparison of biomechanical Human–Tool systems

The biomechanical systems were subjected to a sinusoidal driving force $F(t)$ with the amplitude of 200 N. The analysis was conducted at following frequencies: 16Hz, 30Hz, 60Hz and 90Hz, assuming the mass of the tool m_N to be 6kg. Simulations were conducted for operation time t equal to 300 seconds, owing to the average deviation of the power value – below 1%. Simulations in the MATLAB/simulink software were implemented using integration time steps ranging from a maximum of 0.0001 to a minimum of 0.00001 second. The integration procedure ode113 (Adams) with a tolerance of 0.001 was used.

Figure 4 shows the impact of the frequency of driving impulses f on the percentage increase in the corresponding types of forces in for the model with three reduction points compared to values obtained for the model with two reduction points. The increase between the models is given by the following formula:

$$I_p = \frac{P_{3X(RMS),f}}{P_{2X(RMS),f}} \cdot 100\% \quad (7)$$

where:

$P_{3X(RMS),f}$ – RMS power of inertia, dissipation and elasticity for the Human–Tool system with three reduction points – power (RMS) in [W]:

- power of inertia expressed in [W]:

$$P_{3\text{INE},f} = \sqrt{\frac{1}{t} \int_0^t [m_1 \ddot{z}_1 \dot{z}_1]^2 dt} + \sqrt{\frac{1}{t} \int_0^t [m_2 \ddot{z}_2 \dot{z}_2]^2 dt} + \sqrt{\frac{1}{t} \int_0^t [(m_3 + m_4 + m_N) \ddot{z}_3 \dot{z}_3]^2 dt};$$

- power of dissipation expressed in [W]:

$$P_{3\text{LOS},f} = \sqrt{\frac{1}{t} \int_0^t [(c_1 + c_2 + c_3) \dot{z}_1^2]^2 dt} + \sqrt{\frac{1}{t} \int_0^t [(c_2 + c_4) \dot{z}_2^2]^2 dt} + \sqrt{\frac{1}{t} \int_0^t [(c_3 + c_4) \dot{z}_3^2]^2 dt};$$

- power of elasticity expressed in [W]:

$$P_{3\text{ELA},f} = \sqrt{\frac{1}{t} \int_0^t [(k_1 + k_2 + k_3) z_1 \dot{z}_1]^2 dt} + \sqrt{\frac{1}{t} \int_0^t [(k_2 + k_4) z_2 \dot{z}_2]^2 dt} + \sqrt{\frac{1}{t} \int_0^t [(k_3 + k_4) z_3 \dot{z}_3]^2 dt};$$

$P_{2X(RMS),f}$ – RMS power of inertia, dissipation and elasticity for the Human–Tool system with two reduction points – power (RMS) in [W]:

- power of inertia expressed in [W]:

$$P_{2\text{INE},f} = \sqrt{\frac{1}{t} \int_0^t [m_1 \ddot{z}_1 \dot{z}_1]^2 dt} + \sqrt{\frac{1}{t} \int_0^t [(m_2 + m_N) \ddot{z}_2 \dot{z}_2]^2 dt};$$

- power of dissipation expressed in [W]:

$$P_{2\text{LOS},f} = \sqrt{\frac{1}{t} \int_0^t [(c_1 + c_2) \dot{z}_1^2]^2 dt} + \sqrt{\frac{1}{t} \int_0^t [c_2 \dot{z}_2^2]^2 dt};$$

- power of elasticity expressed in [W]:

$$P_{2\text{ELA},f} = \sqrt{\frac{1}{t} \int_0^t [(k_1 + k_2) z_1 \dot{z}_1]^2 dt} + \sqrt{\frac{1}{t} \int_0^t [k_2 z_2 \dot{z}_2]^2 dt}.$$

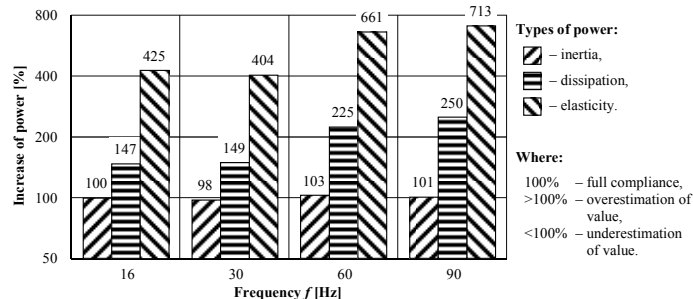


Figure 4. Impact of the frequency of driving impulses f on the increase in different types of powers

The comparison revealed that the contribution of the power of inertia in the human models from the ISO 10068:2012 standard is similar. Depending on the frequency of driving impulses, the maximum difference between the two models did not exceed 3%. Further analysis, however, showed much higher differences. The difference in the power of dissipation ranged from 47% to 150%. In the case of the power of elasticity, differences were much higher and ranged from 304% to as much as 613%. It should be noted that the difference between the models in terms of the power of dissipation and elasticity grows with increasing frequency. Assuming the maximum relative error of 30%, one cannot conclude that the results generated by the models are similar, except for the power of inertia.

Figure 5 depicts the influence of the frequency of driving impulses f on the percentage increase in the total power, which is the sum of the three kinds of power for the model with three reduction points in comparison with values obtained for the model with two reduction points, both from the ISO 10068:2012 standard. The percentage difference is given by the formula:

$$I_G = \frac{P_{3INE,f} + P_{3LOS,f} + P_{3ELA,f}}{P_{2INE,f} + P_{2LOS,f} + P_{2ELA,f}} \cdot 100\% \quad (8)$$

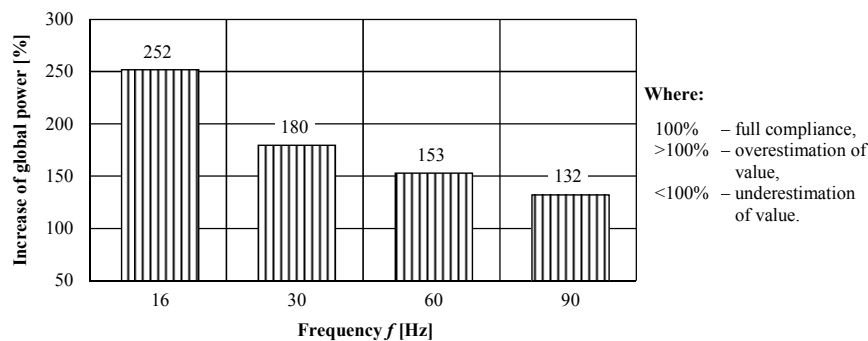


Figure 5. Influence of the frequency of driving impulses f on the increase in the total power

The results shown in Figure 5 indicate that the model with three reduction points always predicts higher total power compared to the reference model. What is more, the compatibility between the models increases significantly with increasing frequency f . An almost five-fold increase in accuracy can be observed for frequencies of 16 and 90 Hz, since the discrepancy between the models decreases from 152% to 32%. It is worth noting that even assuming the maximum relative error of 30% between the models, the corresponding results for each operating frequency of the Human–Tool system are never similar.

5. Summary

The comparison of human physical models specified in the ISO 10068:2012 standard revealed evident differences between them. The study showed a discrepancy between

the models considering the criterion of model similarity: the equality of different types of power. More importantly, the results indicated the biggest degree of similarity in the case of power of inertia, with a difference of no more than 3%. The results were much worse when it comes to the power of dissipation and elasticity, with difference ranging from 47% to 150% and from 304% to 613% respectively. The resulting differences obviously contributed to the degree of discrepancy in the total power, as shown in Fig. 5.

Moreover, the ISO 10068:2012-based model with three reduction points, shown in Fig. 3b, will undoubtedly provide a better protection for the operator of hand tools. This can be expected on account of a better power distribution predicted in the model, which is likely to increase the requirements for such tools. A more reliable verification of the models, would require energy measurements in a laboratory setting. For the time being it can only be concluded that the models we analysed are significantly different in their power distribution.

References

1. M.W. Dobry, *Optymalizacja przepływu energii w systemie Człowiek - Narzędzie - Podłożoże (CNP)*, Rozprawa habilitacyjna, Seria „Rozprawy” nr 330, ISSN 0551-6528, Wydawnictwo Politechniki Poznańskiej, Poznań, 1998.
2. M.W. Dobry, *Energy diagnostics and assessment of dynamics of mechanical and biomechatronics systems*, Machine Dynamics Problems, **25**(3/4) (2001), Warsaw University of Technology, Warsaw, 35-54.
3. M.W. Dobry, *Diagnostyka energetyczna systemów technicznych*, Inżynieria Diagnostyki Maszyn, Polskie Towarzystwo Diagnostyki Technicznej, Instytut Technologii Eksplotacji, Warszawa, Bydgoszcz, Radom, 2004, 314-339.
4. M.W. Dobry, *Podstawy diagnostyki energetycznej systemów mechanicznych i biomechanicznych*, Wydawnictwo Naukowe Instytutu Technologii Eksplotacji – PIB, Poznań-Radom 2012.
5. M.J. Griffin, *Handbook of Human Vibration*, Academic Press, London 1990.
6. A.M. Książek, *Analiza istniejących modeli biodynamicznych układu ręka – ramię pod kątem wibroizolacji człowieka – operatora od drgań emitowanych przez narzędzia ręczne*, Czasopismo Techniczne 2M/1996, Wydawnictwo Politechniki Krakowskiej, 87-114.
7. G. Meltzer, *A Vibration Model for the Human Hand-Arm-System*, Studies in Environmental Science, **13** (1981) 210-221.
8. D.D. Reynolds, W. Soedel, *Dynamic response of the hand-arm system to a sinusoidal input*. Journal of Sound and Vibration, **21**(3) (1972) 339-353.
9. ISO 10068:1998, Mechanical vibration and shock - Free, mechanical impedance of the human hand-arm system at the driving point.
10. ISO 10068:2012, Mechanical vibration and shock - Mechanical impedance of the human hand-arm system at the driving point.

A Comparison of Human Physical Models Used in the ISO 10068:2012 Standard Based on Power Distribution PART 2

Marian Witalis DOBRY

*Poznan University of Technology, Institute of Applied Mechanics
24 Jana Pawła II Street, 60-965 Poznań, Poland
marijan.dobry@put.poznan.pl*

Tomasz HERMANN

*Poznan University of Technology, Institute of Applied Mechanics
24 Jana Pawła II Street, 60-965 Poznań, Poland
tomasz.hermann@put.poznan.pl*

Abstract

This article is a continuation of the article entitled „A comparison of human physical models used in the ISO 10068:2012 standard based on power distribution – Part 1” [5], which presented a method of energy-based assessment of two human physical models. The first article revealed a discrepancy between the models in terms of three types of power and the total power. The focus of the present study was to determine the order of energy inputs in the dynamic structure and link different types of power to potential threats they pose to human health. Additionally, differences between the models were discussed.

Keywords: biomechanical system, energy flow, energy method, hand-arm vibrations

1. Introduction

Mechanical vibrations generated by vibrating systems of power tools or transport vehicles can have a negative impact on the human body. Long-term exposure to vibrations can cause many disorders in the operator's body, leading to permanent damage. The multitude of clinical symptoms is referred to as the hand-arm vibration syndrome [8]. In many countries, including Poland, HAVS has been classified as an occupational disease [1,7]. In Poland HAVS was added to the list of occupational diseases in 1968 [13], and was ranked 6th most commonly diagnosed ailment in the period 1985–1994 [10].

It is worth noting that lists of occupational disease have been revised to reflect the development of knowledge in the area of occupational health and safety and new ways of protecting people against the harmful effects of occupational hazards. Nowadays, according to the ordinance of the Council of Ministers of 30 June 2009 [14], HAVS is listed as a 22nd occupational disease. Additionally, because of its varied symptomatology, the list mentions different forms of the syndrome:

- vascular-nervous disorders,
- musculoskeletal disorders,
- mixed disorders: vascular-nervous and musculoskeletal.

Health hazards can be connected with a concentrated energy flow through the human body. This explanation is confirmed by physiological research in this area [8, 9, 11].

2. The influence of power distribution – changes in biological-mechanical systems

In the case of Human–Tool systems it is possible to determine the level of health hazard that a human operator is exposed to [2-4]. In the Table 1 has been shown the distribution of total power and different types of power in the two systems under investigation. [12]. Data analysis reveals that maximum power distribution for both models can be observed at low frequencies of operation, with the power distribution decreasing as frequency f increases. This observation indicates an interesting relationship that characterises Human–Tool systems, which can be used as a preventive measure: to protect tool operators from exposure to negative effects of vibrations only tools with a higher operating frequency, e.g. 60 Hz, should be used.

Table 1. Three types of power and total power for the two models specified in ISO 10068:2012 [12] in watts and percentages

ANALYZED MODEL ISO 10068:2012		Model 1 (Annex B) 2 points of reduction		Model 2 (Annex C) 3 points of reduction	
		W	%	W	%
Frequency f		16 Hz			
Average Power (RMS)	Inertia	21.27	28.28	21.27	11.24
	Dissipation	22.15	29.45	32.66	17.26
	Elasticity	31.80	42.28	135.3	71.51
Total Power		75.22	100	189.2	100
Frequency f		30 Hz			
Average Power (RMS)	Inertia	13.61	49.44	13.35	27.01
	Dissipation	7.93	28.80	11.84	23.96
	Elasticity	6.00	21.78	24.23	49.03
Total Power		27.53	100	49.42	100
Frequency f		60 Hz			
Average Power (RMS)	Inertia	6.82	81.78	7.00	54.89
	Dissipation	0.97	11.65	2.18	17.08
	Elasticity	0.54	6.49	3.57	27.99
Total Power		8.34	100	12.76	100
Frequency f		90 Hz			
Average Power (RMS)	Inertia	4.30	89.58	4.34	68.65
	Dissipation	0.34	7.08	0.85	13.39
	Elasticity	0.16	3.36	1.14	17.97
Total Power		4.80	100	6.33	100

The energy-based comparison of the two models produces a power distribution, which can be used to identify those elements of the biological structure that are exposed

to the highest energy input. In this way, different types of power can be linked to specific effects in the human body [2-4].

The two models exhibit a high degree of similarity only at operational frequency $f = 16$ Hz. Simulation data show an almost identical order of energy input experienced by the biological structure. At this frequency, it is the spring elements that are exposed to the highest energy input levels. This can lead to upper limb dysfunction and result in tendon, muscle and joint damage. Under these circumstances one can observe a rise in temperature due to the dissipation of energy over time – the power of dissipation, and blood circulation disorders resulting from increased accelerations – the power of inertia. It is worth pointing out that for the model with two points of reduction (model 1) values of the three types of powers are similar. This means that the resulting changes in the body will be nearly equally manifested in all the elements of the biological structure. In contrast, the model with three points of reduction (model 2) exhibits a different intensity of changes. While the order of energy input into the biological structure remains largely identical, the contribution of the power of elasticity is much higher than that of the other two types. It can therefore be concluded that it is the elastic elements of the human body that will be exposed to the highest levels of energy input and most likely to be affected first. Only later will changes be manifested in the other two systems: nervous and vascular.

Energy input levels experienced by the dynamic structure at frequency of 30 Hz are quite different. In the case of the model with three points of reduction the energy analysis revealed the highest energy input levels for spring elements, as evidenced by the power of elasticity, followed by mass elements, as measured by the power of inertia, with dissipation elements being least under energy input, as indicated by the loss power. An entirely different order of harmfulness of vibration could be observed in the case of the model with two points of reduction, with the biggest contribution of the power of inertia, followed by power of dissipation and elasticity.

Further differences can be observed in the order of energy input levels for the remaining frequencies. The energy comparison of the two models revealed high levels of energy input applied to mass elements, as measured by the power of inertia. There is also a discrepancy between the order of energy input levels in the dynamic structure in terms of the two other types of power.

The energy analysis shows partial similarity between the models in terms of the energy input experienced by the human biological structure. Nonetheless, the study provides the basis for a comparative evaluation of different construction variants of tools used – in this case estimating the impact of vibration on the human body depending on the operational frequency of the tool.

3. The impact of mechanical vibrations on the human body – differences between the models

Mechanical stimuli (vibrations) affect receptors, whose sensitivity varies depending on their location: on the skin, tendons, periosteum and internal organs. The intensity and the degree to which vibrations are transmitted depends on other factors, the most im-

portant ones being intensity and frequency of vibrations and the place, time and rate of their propagation. Another significant factor is the damping capacity of body tissues which are in contact with the vibrating source. The influence of vibration at a certain frequency can induce resonant vibration in individual tissues or whole organs, which is a very destructive phenomenon [8]. Resonant frequency values for different parts of the human body have been determined statistically based on detailed studies. However, these frequencies are only an approximation, since they depend on an individual's physical characteristics [6]. The model of the human body developed by R. R. Coerman and shown in Figure 1 specifies resonant frequency values for different body parts.

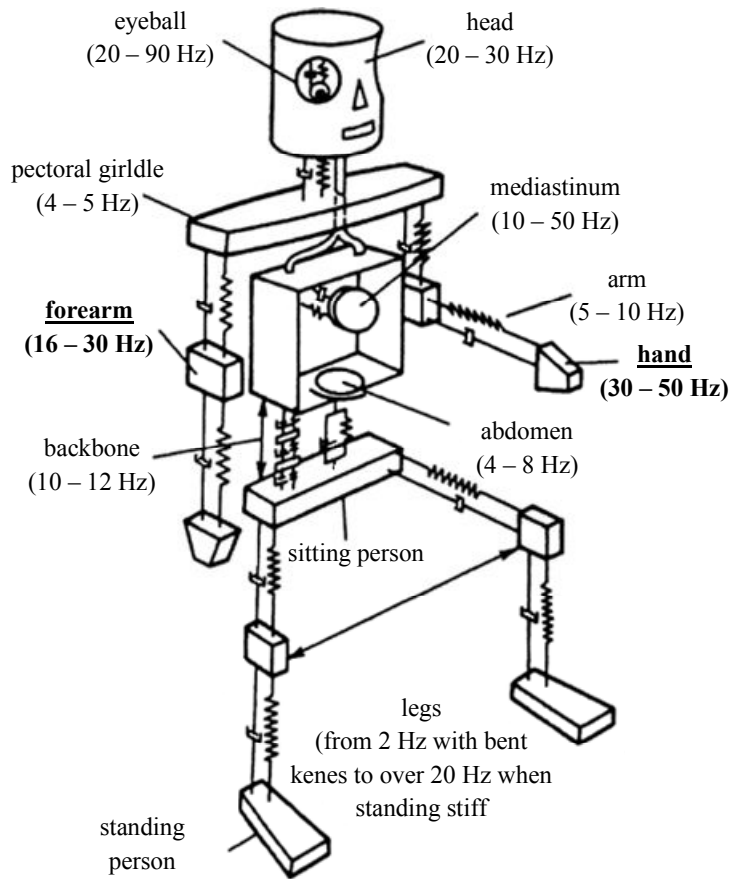
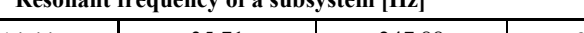


Figure 1. A model of the human body according to R. R. Coerman [6]

The model suggests that frequency is a critical factor considering the energy input into the dynamic structure of a mechanical-biological system. Human–Tool systems can differ with respect to frequencies of their subsystems – which are represented by mathematical models (3) and (4) in this study [5]. Our analysis also addresses this question.

Table 2 presents resonant frequency values for the human physical models at particular points of reduction.

Table 2. Resonant frequencies for the human physical models from the ISO 10068:2012 standard at different points of reduction

human physical model from ISO 10068:2012				
Model 1 (Annex B)		Model 2 (Annex C)		
2 points of reduction		3 points of reduction		
j = 1	j = 2	j = 1	j = 2	j = 3
Resonant frequency of a subsystem [Hz]				
31,28	14,44	35,71	247,88	30,27
 frequencies depending on the tool mass m_N				

As can be seen in Figure 1, in the case of the Human–Tool system based on model 1 – Annex B from the ISO 10068:2012 standard [12], resonant frequencies are similar to the resonant frequencies of the hand and forearm. For model 2 – Annex C, the corresponding values are also similar to the reference values for the upper limb. Additionally, this model exhibits another frequency of almost 248 Hz, which represents resonant vibrations of the whole upper limbs [6]. Studies have also shown the possibility of deformations occurring in other internal organs, since local effects of vibrations can cause systemic disturbances [8]. In such cases, resonant vibrations can be induced in other parts of the body, such as the upper torso and backbone at 10÷14 Hz, the chest at 7÷11 Hz, the head at 20÷30 Hz, muscles at 13÷20 Hz, eyeballs at 20÷90 Hz, etc.

Different values of resonant frequencies for the models are due to dynamic parameters specified in the ISO 10068:2012 standard [12] – tables 1 and 2 in [5]. This relationship is especially visible in the case of resonant frequencies obtained for the model with three points of reduction. The differences result from the third point of reduction added to the system, in particular, the way it is attached to the rest of the model by spring and damping systems – Fig. 3 in [5]. In this case large values of spring parameters k_3 and k_4 , which significantly contribute to one of the resonant frequencies for this model. It should be noted that not all computed values are constant. Resonant frequencies computed for both Human–Tool systems depend on the tool mass m_N – frequencies dependent on the tool mass m_N are indicated 2. This situation results from the impact of mass on the dynamic characteristics of one point of reduction in each system and the dynamic reaction of the whole Human–Tool system.

Energy analysis is a synchronic method of analysis, in which results of conventional dynamic analysis {mathematical models (3) and (4) in [5]} of amplitudes of kinematic quantities are used for energy analysis {energy models (5) and (6) in [5]} – of energy flows. This implies that an analysis conducted in a new domain, i.e. power distribution, is very sensitive to the adequacy of the model used to describe the system's dynamic

structure. Undoubtedly, the development of the HAVS syndrome depends mostly on the intensity of vibrations and the amount of vibration energy introduced into the human body. For this reason, it is necessary to determine amplitude values, since the models in question can differ in this respect. Amplitude values of kinematic quantities for the models in question at specific points of reduction are shown in Table 3.

Table 3. Maximum amplitude values of kinematic quantities at specific points of reduction from the ISO 10068:2012 standard

Point of reduction	kinematic quantity (maximum)	Operational frequency f [Hz] of the tool							
		16		30		60		90	
		the model from ISO 10068:2012 standard							
$j=1$	a [m/s ²]	31,79	31,73	36,20	38,26	15,77	18,31	8,45	9,24
	v [m/s]	0,316	0,316	0,192	0,203	0,042	0,049	0,015	0,016
	z [m]	3,15 $\cdot 10^{-3}$	3,14 $\cdot 10^{-3}$	1,02 $\cdot 10^{-3}$	1,08 $\cdot 10^{-3}$	1,11 $\cdot 10^{-4}$	1,29 $\cdot 10^{-4}$	2,66 $\cdot 10^{-5}$	2,90 $\cdot 10^{-5}$
$j=2$	a [m/s ²]	28,08	28,76	30,42	30,95	33,86	33,97	33,44	34,34
	v [m/s]	0,279	0,286	0,161	0,164	0,090	0,090	0,059	0,061
	z [m]	2,78 $\cdot 10^{-3}$	2,85 $\cdot 10^{-3}$	8,56 $\cdot 10^{-4}$	8,71 $\cdot 10^{-4}$	2,38 $\cdot 10^{-4}$	2,39 $\cdot 10^{-4}$	1,05 $\cdot 10^{-4}$	1,08 $\cdot 10^{-4}$
$j=3$	a [m/s ²]	—	28,36	—	29,92	—	34,08	—	33,48
	v [m/s]	—	0,282	—	0,159	—	0,090	—	0,059
	z [m]	—	2,81 $\cdot 10^{-3}$	—	8,42 $\cdot 10^{-4}$	—	2,40 $\cdot 10^{-4}$	—	1,05 $\cdot 10^{-4}$

Based on the maximum amplitude values of kinematic quantities shown in table 3, it can be concluded that the results generated by the models are very similar. Moreover, amplitude values of kinematic quantities for the model with three points of reduction are almost identical at the second ($j = 2$) and third ($j = 3$) point of reduction. A very similar level of energy input at these two points of reduction raises an interesting question of whether this model actually needs to be so complex.

Finally, an important conclusion should be drawn from the study. The comparative analysis suggests that health hazards for the tool operator predicted on the basis of the dynamic analysis can be completely different from those indicated by the energy

analysis. The examples presented in the study lead to a more general conclusion that the similarity of models in terms of their dynamics by no means implies their energy identity.

4. Conclusions

The study demonstrated a partial compatibility between energy levels observed in two models of the human biological structure. The method of energy analysis enabled a comparative evaluation of different structural variants of tools – in this particular case, the impact of different operational frequencies. Moreover, with the method of energy analysis it was possible to assess the health hazard for the tool operator depending on the characteristics of the source of vibration. The order of energy inputs based on types of powers can also be determined when operating an impulse tool, e.g. a demolition hammer.

In addition, the study analysed the relationship between resonant frequencies of subsystems and those of the human bodies. It was possible to determine those points of the biological structure, where resonant vibrations can be induced, above all, the hands and forearms. Finally, amplitude values of kinematic quantities for both models were presented and found to be similar. It can therefore be concluded that the human physical models specified in the ISO 10068:2012 standard exhibit both similarities and discrepancies.

Acknowledgments

The investigations were made possible owing to partial funding by the Ministry of Science and Higher Education in research project: The flow of energy in mechanical and biomechanical systems 21-431/2013 DS-MK.

References

1. D. Augustyńska, M. Pośniak: *Czynniki szkodliwe w środowisku pracy - wartości dopuszczalne*, Centralny Instytut Ochrony Pracy – Państwowy Instytut Badawczy, Warszawa 2010.
2. M.W. Dobry: *Diagnostyka energetyczna systemów technicznych, Inżynieria Diagnostyki Maszyn*, Polskie Towarzystwo Diagnostyki Technicznej, Instytut Technologii Eksplotacji PIB Radom, Warszawa, Bydgoszcz, Radom 2004, 314-339.
3. M.W. Dobry: *Energetyczna metoda diagnostyki technicznych i inteligentnych biologiczno-technicznych systemów oraz jej zastosowania*, 3rd International Congress of Technical Diagnostics „DIAGNOSTICS' 2004”, September 6-9, 2004, Poznań, Poland, Diagnostyka, vol. 30, tom 1, 2004, pp. 137-146.
4. M.W. Dobry, *Podstawy diagnostyki energetycznej systemów mechanicznych i biomechanicznych*, Wydawnictwo Naukowe Instytutu Technologii Eksplotacji – PIB, Poznań-Radom 2012.

-
5. M.W. Dobry, T. Hermann: *A comparison of human physical models used in ISO 10068:2012 based on the distribution of power – Part 1*, Vibrations in Physical Systems, Vol. 26, Poznan University of Technology, Poznan 2014.
 6. Z. Engel, W. M. Zawieska: *Halas i drgania w procesach pracy – źródła, ocena, zagrożenia*, Centralny Instytut Ochrony Pracy – Państwowy Instytut Badawczy, Warszawa 2010.
 7. L. Kochański, S. Lach: *Zbiór przepisów ochrony pracy*, Instytut Wydawniczy CRZZ, Warszawa 1976.
 8. K. Marek: *Choroby zawodowe*, Wydawnictwo Lekarskie PZWL, Warszawa 2009.
 9. L. Markiewicz: *Fizjologia i higiena pracy. Vibracja*, Instytut Wydawniczy CRZZ, Warszawa 1980.
 10. I. Mulicka, M. Gajek: *Ocena zagrożenia zdrowia pracowników warunkami pracy w latach 1985-1994*, Dolegliwości zdrowotne a warunki pracy, Oficyna Wydawnicza Uniwersytetu Zielonogórskiego, Zielona Góra 2008.
 11. W. Taylor, P. L. Pelmear: *Vibration White Finger in Industry*, Academic Press, London – New York – San Francisco, 1973.
 12. ISO 10068:2012, Mechanical vibration and shock - Mechanical impedance of the human hand-arm system at the driving point.
 13. *Wykaz chorób zawodowych uprawniających do świadczeń w razie inwalidztwa lub śmierci pracownika* – Rozporządzenie Rady Ministrów z dnia 18 czerwca 1968 r. (Dziennik Ustaw 1968, Nr 22, poz. 147).
 14. *Wykaz chorób zawodowych* – Rozporządzenie Rady Ministrów z dnia 30 czerwca 2009 r. (Dziennik Ustaw 2009, Nr 105, poz. 869).

Numerical Tests of Roadheader's Boom Vibrations

Marian DOLIPSKI

*Institute of Mining Mechanisation, Faculty of Mining and Geology
Silesian University of Technology, Akademicka 2, 44–100 Gliwice*

Piotr CHELUSZKA

*Institute of Mining Mechanisation, Faculty of Mining and Geology
Silesian University of Technology, Akademicka 2, 44–100 Gliwice*

Piotr SOBOTA

*Institute of Mining Mechanisation, Faculty of Mining and Geology
Silesian University of Technology, Akademicka 2, 44–100 Gliwice*

Abstract

The work presents a dynamic model of a telescopic boom of a roadheader. The boom represents a load-carrying structure of cutting heads and of their drive system. Together with the cutting heads' drive, it represents a cutting system of a roadheader performing the roadheader's basic function, that is cutting the heading face. A physical model with a discrete structure was created for the purpose of analysing the vibrations accompanying the operation of a roadheader. Due to the design of the telescopic boom, three vibrating masses are distinguished in this model concentrated in the centre of gravity of rigid bodies representing: the fixed part of the boom, the extendable part (telescope) and a reduction gear (with transverse cutting heads mounted in the output shaft journals) fitted to the extendable part of the boom. It is a spatial model with 18 degrees of freedom. The mathematical model established was used in simulation tests the aim of which was to identify the value and sources of vibrations in the selected structural nodes of the boom during the performance of a working process. The excitation of vibrations is an effect of a computer simulation of the rock cutting process with transverse heads with the set stereometry. The article presents selected results of numerical tests using the established dynamic model.

Keywords: roadheader, boom, dynamic model, dynamic loads, vibrations

1. Introduction

Roadheaders are the fundamental cutting machines used in mechanised technologies for tunnelling in underground mines and civil engineering. The key process carried out by such type of machine is the cutting of rock deposited in the cross section of the drilled headings. In case of boom-type roadheaders commonly used in hard coal mines, cutting is accomplished with picks mounted to cutting heads. The heads are mounted at the end of a boom which is inclined in the line parallel and perpendicular to the floor, hence they can be advanced along the face surface of the drilled heading along any trajectory. A roadheader boom represents a load-carrying structure for cutting heads and their drive system. It ensures the required range of cutting determining the maximum size and shape of the drilled tunnel.

The drive of cutting heads, their carrying structure (boom) and other roadheader sub-assemblies functionally related to the cutting system (including boom swinging mechanisms) are subject to the strong excitations of vibrations accompanying the working process carried out. The process of rock cutting is indeed a source of high dynamic

loads, especially when cutting rocks with poor workability. The excitation of vibrations is of a stochastic nature and similarly, as in the case of, e.g. machines for earthworks (excavators, bulldozers, etc.), it results to a large degree from the properties of the worked medium [1]. For the purpose of a dynamic state analysis of cutting machines, they are considered, however, as determined (polyharmonic), provided the cutting process conditions remain unchanged [2]. An excessive dynamic load and overloads resulting from cutting process performance may lead to a boom's failure conditions caused by immediate or fatigue damages to its parts. An analysis of dynamic states of a roadheader cutting system (cutting heads' drive and their load-carrying structure – boom) is indispensable for assessing the design correctness of the roadheaders currently produced and sets a starting point for developing new design solutions.

2. Dynamic model of roadheader boom

A dynamic model of a roadheader boom consists of a physical model and a mathematical model. Three rigid bodies connected with each other with weightless viscoelastic elements are distinguished in the structure of the physical model (Fig. 1) [3]. The bodies represent the key parts of a roadheader boom, i.e.: fixed part (1), extendable part (2) and a reduction gear (3) in the cutting head (6) drive attached to extendable part. The fixed part of the boom is mounted to the movable part of the turntable by means of two slide bearings and is supported with two hydraulic lifting cylinders (4) – a right one (SPR) and a left one (SPL). The extendable part of the boom (2) is seated as sliding in the fixed part of the boom (1), and its extended by means of a telescopic mechanism's cylinders (5) – a right one (STR) and a left one (STL). The length of the boom may change within the range of L_1 to $L_1 + \Delta L_1$.

The fixed part of the boom has the form of a rigid body with the mass m_{WS} , concentrated in its centre of gravity O_{WS} , and with moments of inertia I_{WSX} , I_{WSY} and I_{WSZ} , determined in relation to the parallel axes to the axis of the system of coordinates $X_WY_WZ_W$, passing through the point O_{WS} . The mounting of the fixed part of the boom to the turntable is modelled as three viscoelastic constraints with specific rigidity marked, respectively, as: k_{WSX} , k_{WSI} and k_{WS2} and with the damping coefficients: c_{WSX} , c_{WSI} and c_{WS2} . The boom lifting actuators are modelled as viscoelastic elements with substitute specific rigidity k_{SPR} (an actuator on the right side of the boom) and k_{SPL} (an actuator on the left side of the boom) and the damping coefficient: c_{SPR} and c_{SPL} . The elastic properties of the working fluid in the cylinder were considered in the model of the hydraulic cylinders, along with piston rod flexibility and deformability of the cylinder walls [4]. The substitute values of the parameters mentioned are determined as for a serial connection of flexible parts.

The coupling of the fixed part of the boom with the extendable part was modelled as 16 viscoelastic constraints with the specific rigidity k_{Ti} and the damping coefficient c_{Ti} (for $i=1, 2, \dots, 16$). The constraints are arranged in the same point of application of resultant reactive forces in the fulcrums of the extendable part relative to the fixed part of the boom. Eight of the reactions are parallel to the plane Y_WZ_W (points 1 – 8), while others are parallel to the plane X_WY_W . The elements which are modelling a connection of the extendable part with the fixed part of the boom carry compressive loads only.

The possible occurrence of clearances in this connection is predicted. The temporary location of a body modelling the fixed part of the boom is described by means of six coordinates: three translation coordinates – x_{WS} , y_{WS} and z_{WS} and three rotation coordinates – φ_{WSX} , φ_{WSY} , and φ_{WSZ} (six degrees of freedom).

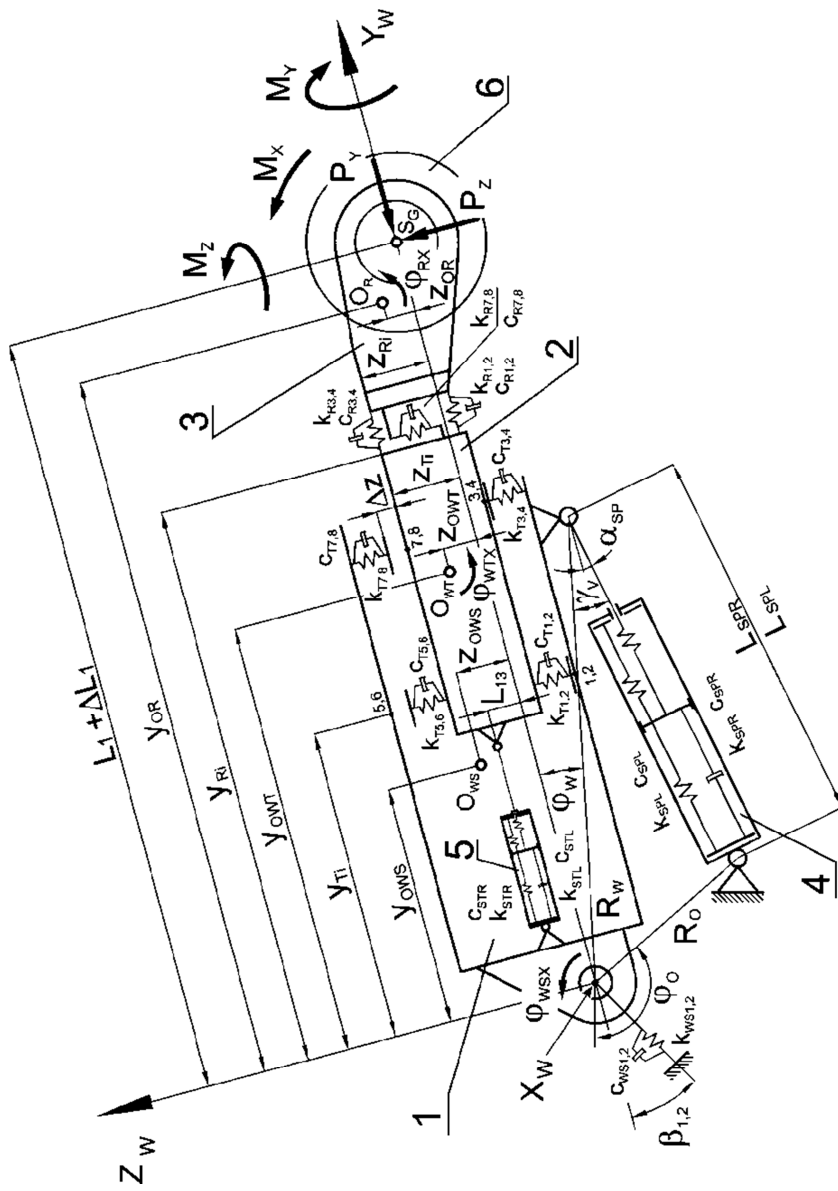


Figure 1. Physical model of a roadheader telescopic boom [3]
 1 – fixed part, 2 – extendable part (telescope), 3 – reduction gear in the drive of transverse cutting heads,
 4 – hydraulic lifting cylinders, 5 – hydraulic cylinders of telescopic mechanism, 6 – cutting heads

The extendable part of the boom is modelled as a rigid body with the mass m_{WT} concentrated in its centre of gravity O_{WT} and with the moments of inertia: I_{WTX} , I_{WTY} and I_{WTZ} . The location of this part relative to the fixed part of the boom is determined by the length of telescopic mechanism cylinders: L_{STP} and L_{STL} . Similar, as in the case of boom lifting cylinders, the dynamic properties of boom extension are characterised with substitute rigidities k_{STR} and k_{STL} and damping coefficients c_{STR} and c_{STL} . The extendable part of the boom also has six degrees of freedom. The temporary location of this mass is hence described with the six coordinates: x_{WT} , y_{WT} , z_{WT} , φ_{WTX} , φ_{WTY} , φ_{WTZ} .

The third element of a physical model of the telescopic boom is a reduction gear together with transverse cutting heads mounted in the output shaft journals. It is modelled as a rigid body with the mass m_R concentrated in its centre of gravity O_R and the moments of inertia I_{RX} , I_{RY} and I_{RZ} . The reduction gear is coupled with the extendable part of the boom by means of eight weightless viscoelastic elements with the specific rigidity k_{Ri} and the damping coefficient c_{Ri} ($i=1, 2, \dots, 8$). The temporary location of the considered body is defined here with the following coordinates: x_R , y_R and z_R as well as φ_{RX} , φ_{RY} , and φ_{RZ} .

A spatial discreet model of the telescopic boom is subject to the activity of vibration excitations from the external load which are the result of working process performance (cutting the heading face). This load was reduced to the intersection point of the boom longitudinal axis with an axis of rotation of cutting heads and was described with six components – the concentrated forces applied in the point S_G (P_X , P_Y and P_Z) and the moments of forces (M_X , M_Y and M_Z).

The equations of motion in the physical model were written using the Lagrange second order equation. A system of 18 ordinary nonlinear second-order differential equations were obtained this way. For example, the equations of motion for the extendable part of the boom (telescope) assume the following form:

$$m_{WT} \cdot \ddot{x}_{WT} - \sum_{i=9}^{16} \{H[A_{Ti}] \cdot (k_{Ti} \cdot A_{Ti} + c_{Ti} \cdot B_{Ti})\} + \sum_{i=5}^6 (k_{Ri} \cdot A_{Ri} + c_{Ri} \cdot B_{Ri}) + Q_{WTXW} + W_X \cdot \text{Sign}(\dot{x}_{WT} - \dot{x}_{WS}) = 0 \quad (1)$$

$$m_{WT} \cdot \ddot{y}_{WT} - k_{STP} \cdot A_{ST} - c_{STP} \cdot B_{ST} - k_{STL} \cdot A_{ST} - c_{STL} \cdot B_{ST} + \sum_{i=1}^4 (k_{Ri} \cdot A_{Ri} + c_{Ri} \cdot B_{Ri}) + Q_{WTYW} + W_Y \cdot \text{Sign}(\dot{y}_{WT} - \dot{y}_{WS}) = 0 \quad (2)$$

$$m_{WT} \cdot \ddot{z}_{WT} - \sum_{i=1}^8 \{H[A_{Ti}] \cdot (k_{Ti} \cdot A_{Ti} + c_{Ti} \cdot B_{Ti})\} + \sum_{i=7}^8 (k_{Ri} \cdot A_{Ri} + c_{Ri} \cdot B_{Ri}) + Q_{WTZW} + W_Z \cdot \text{Sign}(\dot{z}_{WT} - \dot{z}_{WS}) = 0 \quad (3)$$

$$\begin{aligned} I_{WTX} \cdot \ddot{\varphi}_{WTX} - k_{STP} \cdot A_{ST} \cdot (z_{OWT} - L_{13}) - c_{STP} \cdot B_{ST} \cdot (z_{OWT} - L_{13}) + \\ - k_{STL} \cdot A_{ST} \cdot (z_{OWT} - L_{13}) - c_{STL} \cdot B_{ST} \cdot (z_{OWT} - L_{13}) + \\ + \sum_{i=1}^8 \{H[A_{Ti}] \cdot (k_{Ti} \cdot A_{Ti} + c_{Ti} \cdot B_{Ti}) \cdot (y_{OWT} - y_{Ti})\} + \sum_{i=1}^2 [(k_{Ri} \cdot A_{Ri} + c_{Ri} \cdot B_{Ri}) \cdot (z_{OWT} + z_{Ri})] + \\ + \sum_{i=3}^4 [(k_{Ri} \cdot A_{Ri} + c_{Ri} \cdot B_{Ri}) \cdot (z_{OWT} - z_{Ri})] - \sum_{i=7}^8 [(k_{Ri} \cdot A_{Ri} + c_{Ri} \cdot B_{Ri}) \cdot (y_{OWT} - y_{Ri})] + W_{TX} = 0 \end{aligned} \quad (4)$$

$$\begin{aligned}
I_{WTY} \cdot \ddot{\varphi}_{WTY} + \sum_{i=1}^4 \{H[A_{Ti}] \cdot (k_{T(2i-1)} \cdot A_{T(2i-1)} + c_{T(2i-1)} \cdot B_{T(2i-1)}) \cdot x_{T(2i-1)}\} + \\
- \sum_{i=1}^4 \{H[A_{Ti}] \cdot (k_{T(2i)} \cdot A_{T(2i)} + c_{T(2i)} \cdot B_{T(2i)}) \cdot x_{T(2i)}\} + \\
- \sum_{i=5}^8 \{H[A_{Ti}] \cdot (k_{T(2i-1)} \cdot A_{T(2i-1)} + c_{T(2i-1)} \cdot B_{T(2i-1)}) \cdot (z_{T(2i-1)} - z_{OWT})\} + \\
+ \sum_{i=5}^8 \{H[A_{Ti}] \cdot (k_{T(2i)} \cdot A_{T(2i)} + c_{T(2i)} \cdot B_{T(2i)}) \cdot (z_{T(2i)} + z_{OWT})\} + \\
- \sum_{i=5}^6 (k_{Ri} \cdot A_{Ri} + c_{Ri} \cdot B_{Ri}) \cdot (z_{OWT} - z_{Ri}) + \\
- (k_{R7} \cdot A_{R7} + c_{R7} \cdot B_{R7}) \cdot x_{R7} + (k_{R8} \cdot A_{R8} + c_{R8} \cdot B_{R8}) \cdot x_{R8} = 0
\end{aligned} \tag{5}$$

$$\begin{aligned}
I_{WTZ} \cdot \ddot{\varphi}_{WTZ} - \sum_{i=9}^{16} \{H[A_{Ti}] \cdot (k_{Ti} \cdot A_{Ti} + c_{Ti} \cdot B_{Ti}) \cdot (y_{OWT} - y_{Ti})\} + \\
+ \sum_{i=1}^2 [(k_{R(2i-1)} \cdot A_{R(2i-1)} + c_{R(2i-1)} \cdot B_{R(2i-1)}) \cdot x_{R(2i-1)}] + \\
- \sum_{i=1}^2 [(k_{R(2i)} \cdot A_{R(2i)} + c_{R(2i)} \cdot B_{R(2i)}) \cdot x_{R(2i)}] + \\
+ \sum_{i=5}^6 [(k_{Ri} \cdot A_{Ri} + c_{Ri} \cdot B_{Ri}) \cdot (y_{OWT} - y_{Ri})] + W_{TZ} = 0
\end{aligned} \tag{6}$$

where:

A_{Ti} , B_{Ti} , A_{Ri} , B_{Ri} – auxiliary values connecting the coordinates of individual vibrating masses and their speeds;

A_{ST} , B_{ST} – auxiliary values describing displacement and speed of piston rods of telescopic mechanism cylinders;

$H[A_{Ti}]$ – the Heaviside function modelling a possibility of conveying compressive loads only by the nodes situated in the fulcrums of the extendable part relative to the fixed part;

Q_{WTXW} , Q_{WTYW} , Q_{WTZW} – components of the gravity force of the boom extendable part in the direction of the axis of the reference system $X_W Y_W Z_W$;

W_X , W_Y , W_Z , W_{TX} , W_{TY} , W_{TZ} – components of friction forces in the fulcrums of the extendable part relative to the boom fixed part and moments of friction forces relative to axes parallel to the axis of the system of coordinates $X_W Y_W Z_W$.

The excitation curve of boom vibrations (components of an external load) is determined during a simulation of the process of cutting the heading face surface with cutting heads. The values of load components of the picks taking part in the cutting process are determined starting with the projections of cuts made by individual cutting head picks based on the values of cut parameters determined on the basis thereof. Next, by simulating the rotary motion of a cutting head, the curves of the following forces are

determined numerically: P_x , P_y , P_z , M_x , M_y and M_z being an external load of the roadheader boom in the dynamic model created.

3. Analysis of dynamic state of telescopic boom

The cutting of rock was simulated for the purpose of determining dynamic loads and vibrations in constructional nodes of the telescopic boom with the rock compressive strength of $R_c=120$ MPa with transverse heads fitted with 80 picks. The cutting of a rock layer with the height of $h=0.45$ m and with the web of $z=0.2$ m in the working motion was accompanied by boom deflection in a plane parallel to the floor with the angular velocity of $\omega_{ow}=0.022$ rad/s. A rotary motion of the cutting head was simulated here with the angular velocity of $\omega_G=4.4$ rad/s. It was also assumed that the telescope is completely extended, so that boom length is $L_I+\Delta L_I=4$ m.

Figure 2 shows fragments of vibration curves in the intersection points of the boom's longitudinal axis with the axis of rotation of cutting heads (point S_G). The vibrations are the response of the examined system to an excitation from cutting. The load generated with the cutting process is exciting the boom to vibrations in all the considered directions, with the largest displacement of the point S_G along the axis Z_w (Fig. 2a – dotted thick line). As far as the maximum displacement of this point in the direction of the axis X_w and Y_w is, respectively: 10^{-2} and $-6 \cdot 10^{-3}$ m, then in the direction of the axis Z_w it reaches $4 \cdot 10^{-2}$ m (the symbol “–” means displacement in the direction opposite to the assumed turn of the axis of the system $X_wY_wZ_w$). A much higher level of vibrations in the direction of the axis Z_w results from the fact that the investigated system is highly flexible in the lifting plane (Y_wZ_w), which is a result of supporting the boom with hydraulic cylinders. Due to relatively low rigidity of the cylinders as compared to other elastic constraints, the boom is performing high-amplitude rotational vibrations around the axis X_w . A manner of loading the external boom is also important. The forces exciting the vibrations, coming from cutting resistance, reduced to the point S_G , are acting on a large arm (equivalent to the boom length). The boom is, therefore, subject to the activity of a large torque in the plane Y_wZ_w .

The velocity of vibrations in the point S_G of the boom, in the direction of the axis X_w , ranges between ± 0.13 m/s (Fig. 2b – thin continuous line), while acceleration varies within the range of -17 to $+8$ m/s 2 (Fig. 2c – thin continuous line). The effective values of velocity and acceleration of vibrations in this case are: 0.05 m/s and ~ 3 m/s 2 . The maximum values, according to a relative value, of velocity and acceleration of vibrations in the direction of the axis Y_w are, respectively: 0.3 m/s and 70 m/s 2 (thick continuous line), with the effective values of such values of: 0.11 m/s and 17 m/s 2 . On the other hand, the maximum values of the analysed boom vibration parameters in the direction of the axis Z_w equal to: 0.6 m/s and 75 m/s 2 (thick dotted line), while the effective vibration speed and acceleration values in this direction are, respectively: 0.2 m/s and 18 m/s 2 . Boom vibrations in the direction of the axis X_w are weakest. It is because the effective values of the parameters characterising the vibration motion in this direction are 4 times (velocity) and 6 times (acceleration) smaller as compared to the effective values determined for vibrations in the direction of the axis Z_w . At the same

time, the effective values of vibration velocity and acceleration in the direction of the axis Y_w are only by 45% and 6% smaller compared to the effective values of such parameters for vibrations in the direction of the axis Z_w . The highest intensity have, therefore, the vibrations in the boom lifting plane perpendicular to the displacement direction of cutting heads in the working motion.

A spectral analysis of the studied curves has revealed that a number of characteristic vibration components exists (Fig. 3). The share of such components varies for relevant vibration directions. For example, vibrations with the frequency of 35 rad/s (Fig. 3a) dominate in the vibration acceleration spectrum in the direction of the axis X_w . Components are also evident with the frequency of: 53; 87; 139 and 244 rad/s. Meanwhile, three components with the frequency of: 35; 209 and 297 rad/s dominate in the vibration acceleration spectrum in the direction of the axis Z_w (Fig. 3b). The following vibrations: 35; 87 and 139 rad/s are the first three own frequencies of the studied system. Vibrations with the frequency of 53 rad/s result from the fact that picks are positioned along the helixes with a small twisting angle (helix frequency), and vibrations with the frequency of 209 rad/s are the result of the next picks advancing to the cutting zone (pick frequency). The other identified vibration components are higher harmonics of vibration excitations.

4. Conclusions

The created dynamic model allowed to perform comprehensive simulation tests in order to determine dynamic loads in the constructional nodes of a roadheader telescopic boom and analyse its vibrations. The numerical tests carried out allowed to identify the basic sources of boom vibrations and – for the set cutting process performance conditions – to determine the values of the parameters characterising telescopic boom vibrations with the defined constructional form. Conclusions from simulation tests were used for formulating requirements for dynamic properties of a telescopic boom for a newly designed roadheader in terms of reduction in dynamic loads and vibrations.

The presented dynamic model of a roadheader's telescopic boom has been created for the design of roadheader's telescopic boom. The usefulness of this model and the reliability of the results will be soon verified based on the results of experimental studies of roadheader after manufacture developed telescopic boom.

References

1. W. Borkowski, S Konopka, L. Prochowski, *Dynamika maszyn roboczych* WNT, Warszawa 1996
2. M. Dolipski, P.Cheluszka, *Dynamika układu urabiania kombajnu chodnikowego*, Wydawnictwo Politechniki Śląskiej, Gliwice 2002
3. M. Dolipski, P. Cheluszka, P. Sobota, *Ermittlung der dynamischen Beanspruchungen eines Teleskopauslegers bei einer Streckenvortriebsmaschine*, Glückauf **146**(12) (2010) 599-607
4. B. Podsiadła (red.), *Modelowanie i badania zjawisk dynamicznych wysięgników teleskopowych i żurawi samojezdnych*, WNT, Warszawa 2000

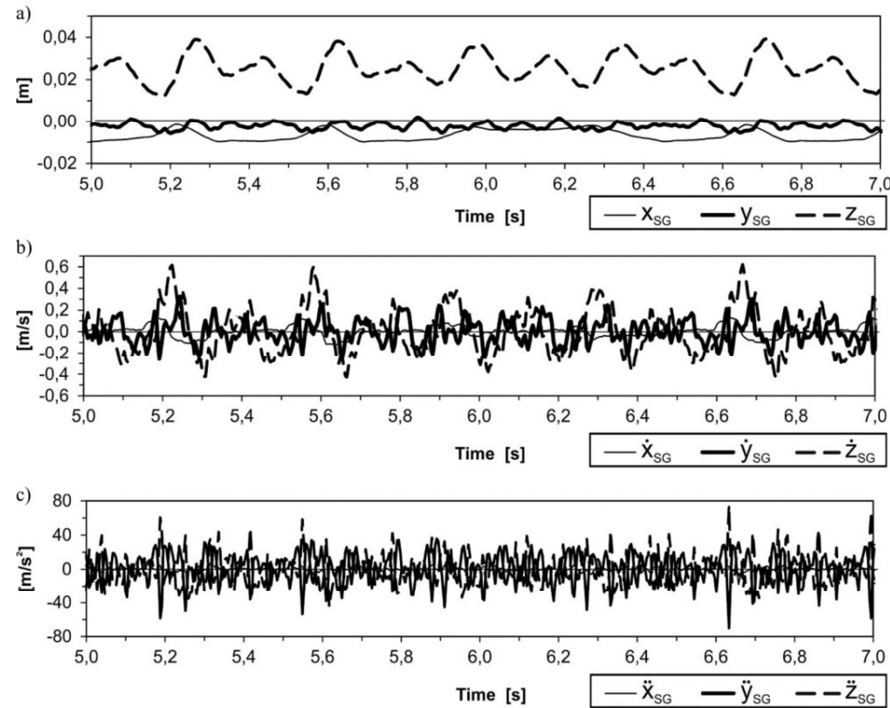


Figure 2. Boom vibration components in the intersection point of the boom longitudinal axis with the axis of rotation of cutting heads: a) displacement, b) speed, c) acceleration

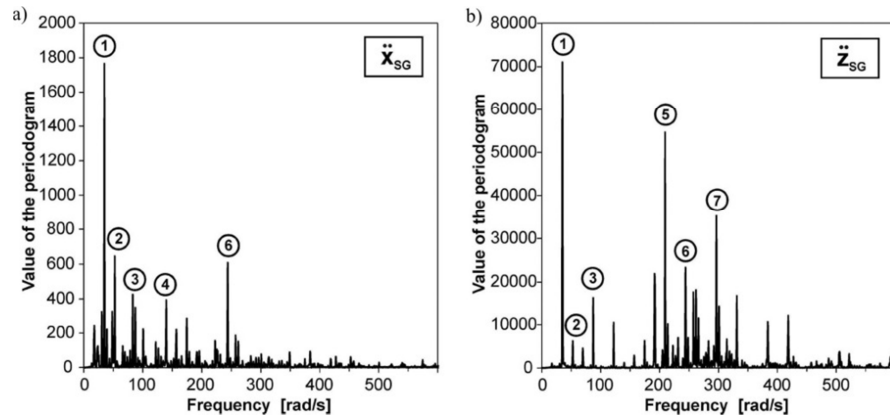


Figure 3. Spectrum of vibration acceleration in the direction of the axis: a) X_w , b) Z_w
 (1)–35 rad/s (2)–53 rad/s (3)–87 rad/s (4)–139 rad/s (5)–209 rad/s (6)–244 rad/s (7)–297 rad/s

Nonlinear Vibrations of Periodic Beams

Łukasz DOMAGALSKI

Department of Structural Mechanics, Łódź University of Technology
al. Politechniki 6, 90-924 Łódź, Poland
lukasz.domagalski@p.lodz.pl

Jarosław JĘDRYSIAK

Department of Structural Mechanics, Łódź University of Technology
al. Politechniki 6, 90-924 Łódź, Poland
jarek@p.lodz.pl

Abstract

Geometrically nonlinear vibrations of beams with properties periodically varying along the axis are investigated. The tolerance method of averaging differential operators with highly oscillating coefficients is applied to obtain the governing equations with constant coefficients. The proposed model describes the dynamics of the beam with the effect of the microstructure size.

Keywords: nonlinear vibrations, periodic beams, tolerance modelling

1. Introduction

The note concerns with geometrically nonlinear vibrations of beams with periodically varying mass, geometric and material properties along the beam axis. Moreover, this beam can interact with periodically nonhomogeneous viscoelastic subsoil. A fragment of such beam is shown in Fig. 1. Equations of motion of such structures have usually non-continuous, highly oscillating, periodic coefficients. Since, various averaging methods which lead to approximate models, determined by equations with constant coefficients, are applied. Among them methods based on the asymptotic homogenization can be mentioned, cf. [3].

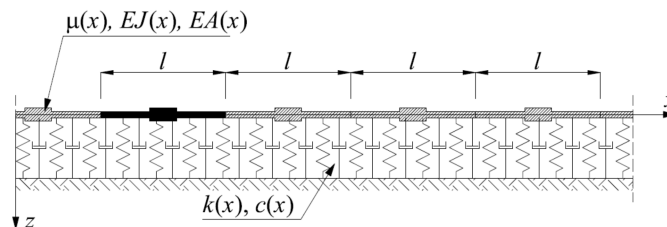


Figure 1. A fragment of a periodic beam

In this contribution, in order to replace the differential equations with highly oscillating coefficients by equations with constant coefficients, the tolerance modelling is applied. This approach was introduced for the purpose of analysis of various thermomechanical problems of periodic elastic composites, e.g. it was used to analyse vibrations of beams within the linear theory, cf. [5], where equations and their generalization by in-

cluding influence of the axial force, an elastic subsoil and viscous damping have been derived in this way.

The main aim of this note is to derive the tolerance model equations with constant coefficients, which describe geometrically nonlinear vibrations of periodic beams resting on a periodic viscoelastic foundation, with taking into account the effect of the microstructure size.

2. Formulation of the problem

The object under consideration is a linearly elastic prismatic beam, bilaterally interacting with a periodic viscoelastic foundation. Let $Oxyz$ be an orthogonal Cartesian coordinate system, the Ox axis coincides with the axis of the beam, the cross section of the beam be symmetric with respect to the plane of the load Oxz , the load acts in the direction of the axis Oz . The problem can be treated as one-dimensional.

The beam is assumed to be made of many repetitive small elements, called *periodicity cells*, each of which is defined as $\Delta=[-l/2, l/2]$, where $l \ll L$ is the length of the cell and named the *microstructure parameter*.

Our considerations are based on the Euler-Bernoulli theory of beams. Additionally large transverse deflection but small deformations are assumed, cf. [4]. The effects of axial and rotational inertia are neglected in further considerations. Let $\partial^k = \partial^k / \partial x^k$ be the k -th derivative of a function with respect to the x coordinate. Let the transverse deflection, the longitudinal displacement, tensile and flexural stiffness, the elastic coefficient of the foundation, the damping coefficient of the foundation, density of beam material per unit length, transverse load and dissipative force by $w = w(x, t)$, $u_0 = u_0(x, t)$, $EA = EA(x)$, $EJ = EJ(x)$, $k = k(x)$, $c = c(x)$, $\mu = \mu(x)$, $q = q(x, t)$, $p = p(x, t)$, the system of nonlinear coupled differential equations for the longitudinal displacements u_0 and the transverse deflection w can be written as:

$$\begin{aligned} \partial[EA(\partial u_0 + \frac{1}{2}(\partial w)^2)] &= 0, \\ \partial^2(EJ\partial^2 w) - EA[\partial u_0 + \frac{1}{2}(\partial w)^2]\partial^2 w + cw + \mu\ddot{w} &= q. \end{aligned} \quad (1)$$

The coefficients EA , EJ , k , μ , c , and in some cases the load q , are highly oscillating, often non-continuous functions of the x coordinate.

3. Introductory concepts and basic assumptions of the tolerance modelling

The averaged equations of periodic beams with large deflections are derived using the tolerance averaging technique, cf. [7, 8].

Let $\Delta(x)=x+\Delta$, $\Omega_\Delta = \{x \in \Omega : \Delta(x) \subset \Omega\}$ be a cell with center at $x \in \Omega_\Delta$. The averaging operator for an arbitrary integrable function f is defined by:

$$\langle f \rangle(x) = \frac{1}{l} \int_{\Delta(x)} f(y) dy, \quad x \in \Omega_\Delta, \quad y \in \Delta(x). \quad (2)$$

It can be shown that for periodic function f of x , its averaged value (2) is constant.

The first of the basic assumptions is *the micro-macro decomposition* of the unknown functions:

- for the transverse deflection:

$$w(x,t) = W(x,t) + h^A(x)V^A(x,t), \quad A=1,\dots,N, \quad (3)$$

- and for the axial displacement x :

$$u_0(x,t) = U(x,t) + g^K(x)T^K(x,t), \quad K=1,\dots,M, \quad (4)$$

where the functions $W(\cdot), V^A(\cdot) \in SV_d^2(\Omega, \Delta)$, $U(\cdot), T^K \in SV_d^1(\Pi, \Delta)$ are new basic unknowns, being slowly-varying functions in x ; the fluctuation shape functions $h^A(\cdot) \in FS_d^2(\Omega, \Delta)$, $g^K(\cdot) \in FS_d^1(\Omega, \Delta)$ are postulated *a priori* in every problem under consideration. The new basic kinematic unknowns $W(\cdot)$ and $U(\cdot)$ are called *the macrodeflection* and *the in-plane macrodisplacements*, respectively; $V^A(\cdot)$ and $T^K(\cdot)$ are additional kinematic unknowns, called the fluctuation amplitudes.

4. The governing equations of proposed models

4.1. The governing equations of the tolerance model

After substitution the micro-macro decompositions (3) and (4) into equations (1), the next step of modelling is averaging (2) over an arbitrary periodicity cell. In case of symmetric or antisymmetric cell, some of the averaged coefficients yield zero automatically.

After some manipulations we arrive at the following system of equations:

$$\begin{aligned} & \partial[\langle EA \rangle (\partial U + \frac{1}{2} \partial W \partial W) + \langle EA \partial g^K \rangle T^K + \\ & \quad + \frac{1}{2} \langle EA \partial h^A \partial h^B \rangle V^A V^B] = 0, \\ & \langle EJ \rangle \partial^4 W + \langle EJ \partial^2 h^A \rangle \partial^2 V^A + \langle \mu \rangle \ddot{W} + \langle k \rangle W + \underline{\langle kh^A \rangle} V^A + \\ & \quad + \langle c \rangle \dot{W} + \underline{\langle ch^A \rangle} \dot{V}^A - \langle q \rangle + \partial(\langle EA \partial h^A \partial h^B \rangle V^A V^B \partial W) + \\ & \quad + [\langle EA \rangle (\partial U + \frac{1}{2} \partial W \partial W) + \langle EA \partial g^K \rangle T^K + \\ & \quad + \frac{1}{2} \langle EA \partial h^A \partial h^B \rangle V^A V^B] \partial^2 W = 0, \quad (5) \\ & \langle EJ \partial^2 h^A \rangle \partial^2 W + \langle \partial^2 h^A EJ \partial^2 h^B \rangle V^B + \underline{\langle \mu h^A h^B \rangle} \ddot{V}^B + \underline{\langle ch^A \rangle} \dot{W} + \\ & \quad + \underline{\langle ch^A h^B \rangle} \dot{V}^B + \underline{\langle kh^A \rangle} W + \underline{\langle kh^A h^B \rangle} V^B - \underline{\langle qh^A \rangle} + \\ & \quad + \underline{\langle EA \partial h^A \partial h^B \rangle} (\partial U + \frac{1}{2} \partial W \partial W) V^B + \underline{\langle EA \partial h^A \partial h^B \rangle} V^B \partial W \partial W + \\ & \quad + \frac{1}{2} \underline{\langle EA \partial h^A \partial h^B \partial h^C \partial h^D \rangle} V^B V^C V^D + \underline{\langle EA \partial g^L \partial h^A \partial h^B \rangle} V^B T^L = 0, \\ & \langle EA \partial g^K \rangle (\partial U + \frac{1}{2} \partial W \partial W) + \langle EA \partial g^K \partial g^L \rangle T^L + \\ & \quad + \frac{1}{2} \underline{\langle EA \partial g^K \partial h^A \partial h^B \rangle} V^A V^B = 0. \end{aligned}$$

It is a system of $2+N+M$ differential equations for the macrodisplacements $U(\cdot)$, $W(\cdot)$ and for the fluctuation amplitudes of the deflection $V^A(\cdot)$ and of the axial displacement $T^K(\cdot)$. The coefficients of these equations are constant, some of them (the underlined ones) depend on the size l of the periodicity cell. Hence, the tolerance model describes the effect of the microstructure size on vibrations of the beams under consideration. For instance, free vibration frequencies of higher order vibrations can be analysed, which are related to the microstructure of these beams.

4.2. The governing equations of the simplified tolerance model

In order to formulate a simplified model it can be assumed that the deflection fluctuation impact on the relative elongation of the beam middle axis is negligible. Therefore, the nonlinear components of the strain that involve the fluctuation amplitudes can be omitted.

Introducing the following denotations:

$$\begin{aligned} B &\equiv \langle EA \rangle, \quad B^K \equiv \langle EA \partial g^K \rangle, \quad B^{KL} \equiv \langle EA \partial g^K \partial g^L \rangle, \quad Q \equiv \langle q \rangle, \\ D &\equiv \langle EJ \rangle, \quad D^A \equiv \langle EJ \partial^2 h^A \rangle, \quad D^{AB} \equiv \langle \partial^2 h^A EJ \partial^2 h^B \rangle, \quad Q^A \equiv l^{-2} \langle q h^A \rangle, \\ K &\equiv \langle k \rangle, \quad K^A \equiv l^{-2} \langle kh^A \rangle, \quad K^{AB} \equiv l^{-4} \langle kh^A h^B \rangle, \quad M \equiv \langle \mu \rangle, \\ C &\equiv \langle c \rangle, \quad C^A \equiv l^{-2} \langle ch^A \rangle, \quad C^{AB} \equiv l^{-4} \langle ch^A h^B \rangle, \quad M^{AB} \equiv l^{-4} \langle \mu h^A h^B \rangle, \end{aligned} \tag{6}$$

governing equations of the simplified tolerance model take the form:

$$\begin{aligned} \partial[B(\partial U + \frac{1}{2}\partial W \partial W) + B^K T^K] &= 0, \\ D \partial^4 W + D^A \partial^2 V^A + M \ddot{W} + K W + l^2 K^A V^A + C \dot{W} + l^2 C^A \dot{V}^A - Q + \\ + [B(\partial U + \frac{1}{2}\partial W \partial W) + B^K T^K] \partial^2 W &= 0, \\ D^A \partial^2 W + D^{AB} V^B + l^4 M^{AB} \ddot{V}^B + l^2 C^A \dot{W} + l^4 C^{AB} \dot{V}^B + l^2 K^A W + \\ + l^4 K^{AB} V^B - l^2 Q^A &= 0, \\ B^K (\partial U + \frac{1}{2}\partial W \partial W) + B^{KL} T^L &= 0. \end{aligned} \tag{7}$$

Because the matrix B^{KL} in equation (7)₄ is nonsingular there exists a matrix $(B^{KL})^{-1}$ and this equation can be written as:

$$T^K = -(B^{LK})^{-1} B^L (\partial U + \frac{1}{2}\partial W \partial W). \tag{8}$$

Introducing the effective tensile stiffness of the beam:

$$B_0 \equiv B - B^K (B^{LK})^{-1} B^L, \tag{9}$$

denoting:

$$\bar{N} = B_0(\partial U + \frac{1}{2}\partial W\partial W), \quad (10)$$

and after substituting the right-hand side of (8) into (7), we have, instead of (7), the following equations:

$$\begin{aligned} \partial \bar{N} &= 0, \\ D\partial^4 W + D^A\partial^2 V^A + M\ddot{W} + KW + l^2 K^A V^A + C\dot{W} + l^2 C^A \dot{V}^A - \\ - Q + \bar{N}\partial^2 W &= 0, \\ D^A\partial^2 W + D^{AB}V^B + l^4 M^{AB}\ddot{V}^B + l^2 C^A \dot{W} + l^4 C^{AB}\dot{V}^B + l^2 K^A W + \\ + l^4 K^{AB}V^B - l^2 Q^A &= 0, \\ T^K &= -(B^{LK})^{-1} B^L (\partial U + \frac{1}{2}\partial W\partial W). \end{aligned} \quad (11)$$

Equations (11) stand the system of differential-algebraic equations. Similarly to equations (7) the above equations have the terms dependent of the microstructure parameter l . Hence, the simplified tolerance model makes it possible also to investigate the effect of the microstructure size on vibrations of these beams.

4.3. The governing equations of the asymptotic model

Neglecting in equations (7) or (11) the terms with the microstructure parameter l and introducing the effective stiffness of bending of beam:

$$D_0 \equiv D - D^A(D^{AB})^{-1}D^B, \quad (12)$$

we arrive at the equations in the form:

$$\begin{aligned} \partial \bar{N} &= 0, \quad \bar{N} = B_0(\partial U + \frac{1}{2}\partial W\partial W), \\ D_0\partial^4 W + M\ddot{W} + KW + C\dot{W} - Q + \bar{N}\partial^2 W &= 0, \\ V^A &= -(D^{AB})^{-1}D^B\partial^2 W, \\ T^K &= -(B^{LK})^{-1} B^L (\partial U + \frac{1}{2}\partial W\partial W). \end{aligned} \quad (13)$$

The above equations do not describe the effect of the microstructure size on the behaviour of the periodic beams under consideration. Hence, the asymptotic model makes it possible to analyse vibrations on the macrolevel only.

5. Remarks

In this contribution the mathematical model, called *the tolerance model*, is shown, which describes dynamics of a periodically nonhomogeneous beam. The governing equations

of this model are obtained by using the tolerance method, cf. [9, 8, 7]. Hence, the fundamental equations with highly oscillating, periodic, noncontinuous functional coefficients are replaced by the equations with constant coefficients.

The following general remarks can be formulated.

1. It can be observed that only *the tolerance model* and *the simplified tolerance model* make it possible to investigate *the effect of the microstructure size* on dynamic problems of periodic beams under consideration, e.g. the “higher order” vibrations related to the beam microstructure.
2. The governing equations of both *the tolerance models* have a physical sense for unknowns $W, U, V^A, A=1, \dots, N, T^K, K=1, \dots, M$, being slowly-varying functions.
3. *The asymptotic model* of periodic beams makes it possible to investigate only lower order (fundamental) vibrations.

References

1. J. Awrejcewicz, *Matematyczne Metody Mechaniki*, Wydawnictwo Politechniki Łódzkiej, Łódź 1995.
2. G.L. Baker, J.P. Gollub, *Wstęp do dynamiki układów chaotycznych*, PWN, Warszawa 1998.
3. A. Bensoussan, J.L. Lions, G. Papanicolaou, *Asymptotic analysis for periodic structures*, North-Holland, Amsterdam 1978.
4. A. Kacner, *Pręty i płyty o zmiennej sztywności*, PWN, Warszawa 1969.
5. K. Mazur-Śniady, *Macro-dynamics of micro-periodic elastic beams*, J. Theor. Appl. Mech. **31** (1993) 781-793.
6. J.J. Stoker, *Nonlinear Vibrations*, Interscience, New York 1950.
7. Cz. Woźniak et al. (eds.), *Mathematical modeling and analysis in continuum mechanics of microstructured media*, Wydawnictwo Politechniki Śląskiej, Gliwice 2010.
8. Cz. Woźniak, B. Michalak, J. Jędrysiak (eds.), *Thermomechanics of microheterogeneous solids and structures. Tolerance averaging approach*, Wydawnictwo Politechniki Łódzkiej, Łódź 2008.
9. Cz. Woźniak, E. Wierzbicki, *Averaging techniques in thermomechanics of composite solids*, Wydawnictwo Politechniki Częstochowskiej, Częstochowa 2000.

Analysis of the Electromyographic Signal During Rehabilitation Exercises of the Knee Joint

Jakub Krzysztof GRABSKI

*Institute of Applied Mechanics, Poznan University of Technology
ul. Jana Pawła II 24, 60-965 Poznań
jakubgrabski@poczta.onet.pl*

Sylwia KAZIMIERCZUK

*Institute of Applied Mechanics, Poznan University of Technology
ul. Jana Pawła II 24, 60-965 Poznań*

Tomasz WALCZAK

*Institute of Applied Mechanics, Poznan University of Technology
ul. Jana Pawła II 24, 60-965 Poznań
tomasz.walczak@put.poznan.pl*

Abstract

The system of human locomotion is very complex. Generally we can divide it into the skeletal and muscle systems. The muscle system (muscles) enable to move the body which is formed by the skeletal system (bones). Electromyography is a technique of measurement the electrical activity of muscles which is related with shortening or lengthening of muscle fibers (muscle contraction). In the paper analysis of the electromyographic signal (EMG) recorded during knee rehabilitation exercises was conducted. The records of EMG from person after knee injury were compared with records of EMG from healthy person.

Keywords: electromyography, knee rehabilitation, rehabilitative exercises

1. Introduction

The human movement is possible by interaction between three systems: the nervous system, the muscle system and the skeletal system. Each of the aforementioned systems has specified functions for human movement performing. The skeletal system maintains the shape of human body. The joints which are part of the skeletal system enable movement of the body. The movements of the body in the joints are performed by contraction of muscles which are connected to the bones by the tendons. Decisions about human movement are taken in the brain which is part of the nervous system.

The nerves which directly innervate the muscle fibers are located in the vertebrae and they are called alpha motor neuron. The alpha motor neuron, muscle fibers which are innervated by single alpha motor neuron and axons constitute the motor unit. One alpha motor neuron can innervate from several to several thousand muscle fibers. The muscle fibers are grouped together in the muscle fibers bundles (which contain from 10 to 100 muscle fibers).

A single signal which is received by the group of muscle fibers is called motor unit action potential. The disorder propagates along the muscle fibers. Electromyographic signal is a sum of the disorders at the time and the place of electrodes application. There-

fore electromyographic signal depends on many factors (internal and external) which are detailed described in [1].

Electromyography plays more and more important role in medicine, kinesiology rehabilitation, biomechanics, sport and ergonomics [2,5,6]. Many interesting articles on analysis and applications of electromiographic signal can be find in Journal of Electromyography & Kinesiology. Recommendable publication on electromyographic signal, its recording and processing was written by Merletti and Parker [4].

In the paper the results of electromiographic signal recording results during knee rehabilitation exercises with pillow were presented. The main purpose of the paper is to show the relationship between muscle activity and assessing progress of rehabilitation.

2. Description of the knee rehabilitation exercises

Causes of motor organs injury can be divided into internal and external factors. The main internal factors are: anatomical abnormalities, friction forces in the motor system and extensive stretching of tendons. The external factors are associated with training errors (extensive training volume and training intensity, errors in technique of performing exercises).

The main aim of knee rehabilitation exercises is to learn maintaining of the equilibrium state and appropriate technique of the performed exercises [3]. Bad habits in the technique of rehabilitation exercises can result in deepening the disease state. The knee rehabilitation exercises are static exercises with load. There were three knee rehabilitation exercises taking into account in our research: partial squat on the pillow (Fig. 1), one leg partial squat (Fig. 2) and one leg partial squat on the pillow with performing of the semicircle (Fig. 3).

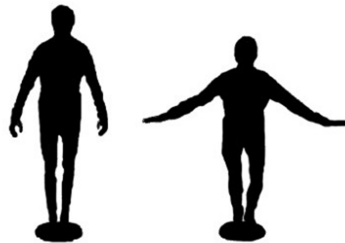


Figure 1. Partial squat on the pillow



Figure 2. One leg partial squat on the pillow



Figure 3. One leg partial squat on the pillow with performing of the semicircle

3. Method of measurements

The measurements were performed using NORAXON electromyographic system and were collected from four muscles on each leg (together eight muscles): the rectus femoris muscle, the vastus medialis muscle, the semitendinosus muscle and the biceps femoris muscle, which were depicted in Fig. 4.

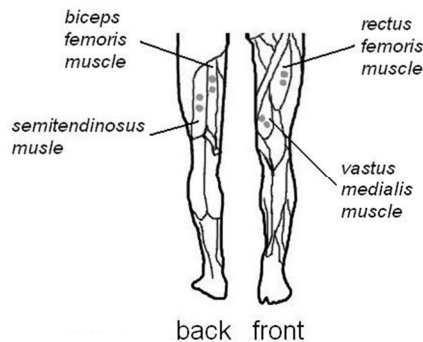


Figure 4. Arrangement of the electrodes on the leg muscles

The EMG signal was recorded for muscles presented in Fig. 4, during described exercises. The raw electromiographic signal is difficult to analyse and therefore various algorithms for its processing are applied. In the paper the RMS algorithm with 100 ms frame was used.

4. Results

The first tested person was a woman who as a result of wrong settings of mechanical axis of the left leg, has a diagnosed injury in her left knee. In this case is extremely important to develop the rectus femoris muscle which is responsible for keeping the kneecap in the correct position. In all considered cases each of experiences performed at least ten times.

In Fig. 5 one can observe big differences between left and right rectus femoris muscle and biceps femoris muscle in the first month of the rehabilitation. The activity partial squat on the pillow in the first month of the rehabilitation of these muscles show that

the left leg is significant weaker than right one. In order to observe the rehabilitation progress similar measurements were done after second month of the rehabilitation (Fig. 6).

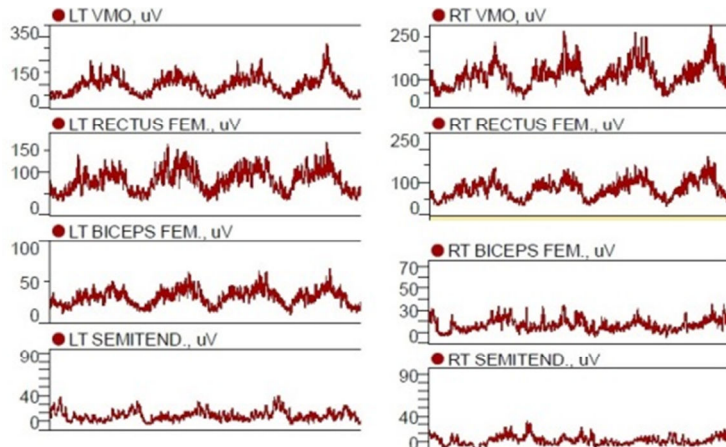


Figure 5. Comparison of the RMS signal for selected muscles of left and right leg during

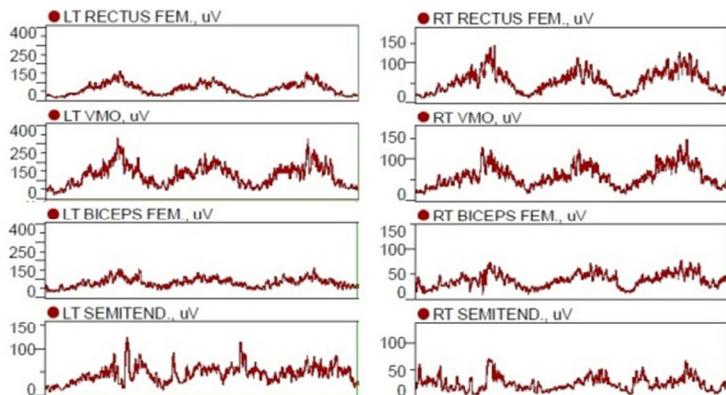


Figure 6. Comparison of the RMS signal for selected muscles of left and right leg during partial squat on the pillow in the second month of the rehabilitation

After two months of the rehabilitation improvement of the left leg could be observed. Significant increase of recorded EMG signal is noticed in the case of the vastus medialis muscle. The difference between left and right muscles activity smaller than the difference in the first month of rehabilitation.

During the one leg squat exercise average activity of muscles is much higher than in the first exercise (Fig. 7). One can conclude that it is difficult to observe find the difference between the healthy leg and the leg with injury. The progress of the rehabilitation in

all considered muscles could be observed analysing graphs presented in Fig. 8. That fact shows efficiency of the used rehabilitation.

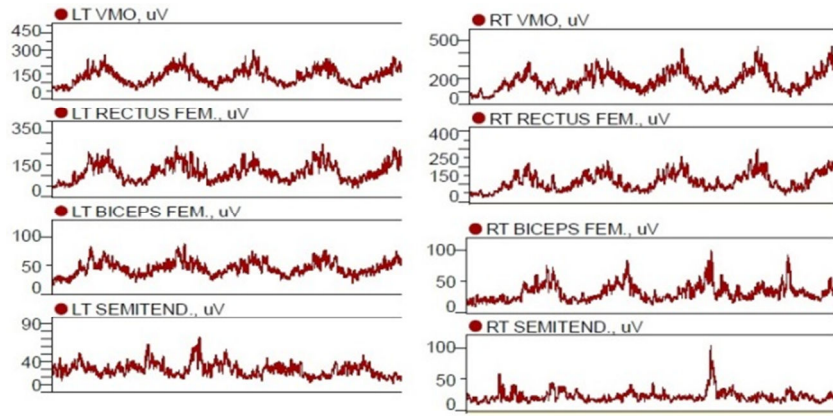


Figure 7. Comparison of the RMS signal for selected muscles of left and right leg during one leg squat on the pillow in the first month of the rehabilitation

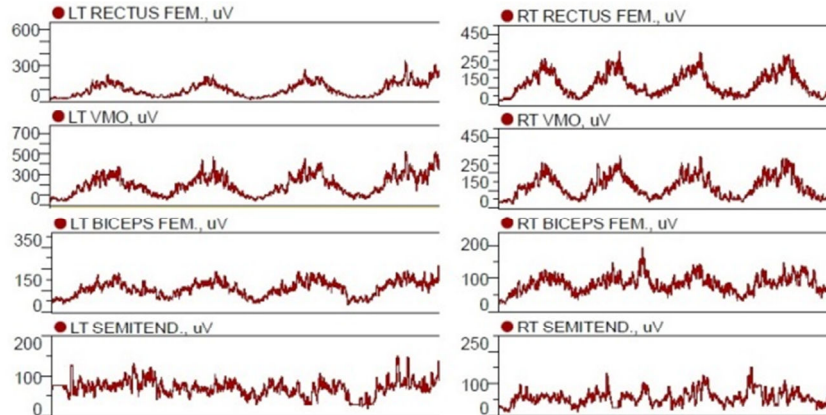


Figure 8. Comparison of the RMS signal for selected muscles of left and right leg during one leg squat on the pillow in the first month of the rehabilitation

The last considered exercise (Fig. 8) is very good indicator which shows whether the muscles are proper protection (stabilization of the knee). In this case one can see disproportion between left and right leg. Shapes of signals from leg with injury are less regular than from healthy one. The vastus medialis muscle, the rectus femoris muscle and the biceps femoris muscle in the left leg have similar activity graph. On the other hand the biceps femoris muscle in the right leg has completely different characteristic. It could be caused by necessity of participating the left biceps femoris in stabilization of the injured knee in that kind of motion.

Records of electromyographic signal for the same exercise but after two months of the rehabilitation was presented in Fig. 10. The average activity of muscles in the left and the right legs is very similar.

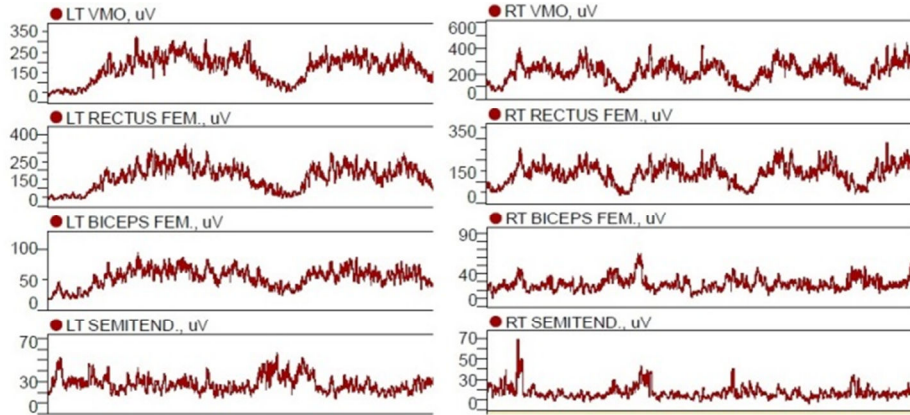


Figure 9. Comparison of the RMS signal for selected muscles of left and right leg during partial one leg squat on the pillow with performing of the semicircle in the first month of the rehabilitation

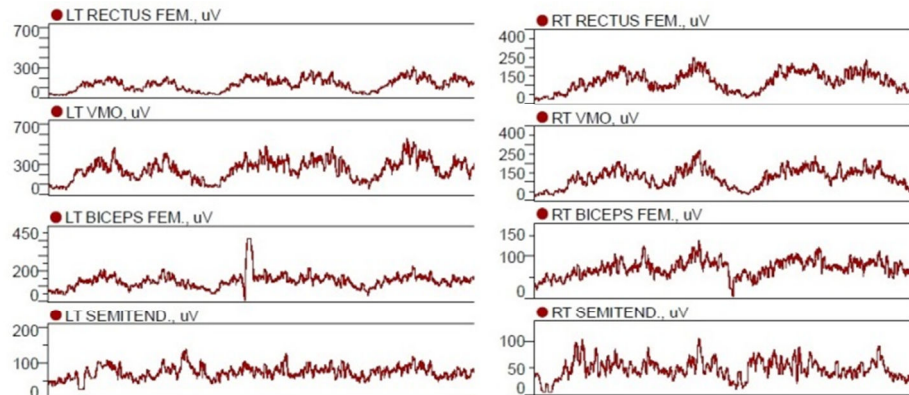


Figure 10. Comparison of the RMS signal for selected muscles of left and right leg during partial one leg squat on the pillow with performing of the semicircle in the second month of the rehabilitation

In Fig. 11-13 records of EMG signal for healthy person were presented. One can observed that in all cases of considered exercises the muscles activity measured for both legs is alike. Work of the considered muscles for left and right leg respectively is much more symmetric than in case of injured person. That kind of signal analysis can be useful for injury prediction.

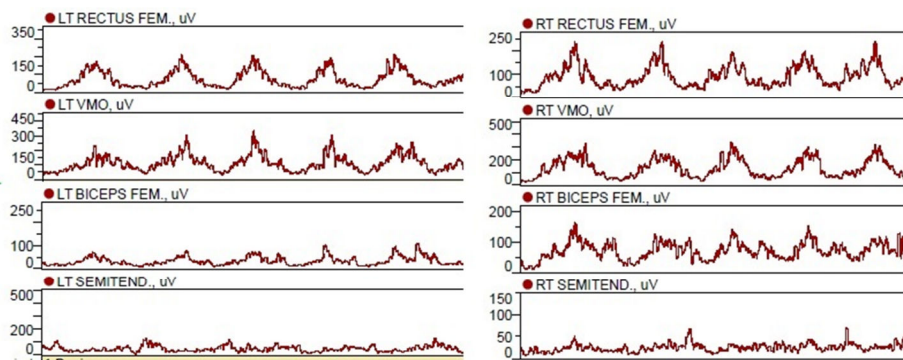


Figure 11. Comparison of the RMS signal for selected muscles of left and right leg during partial squat on the pillow – healthy person

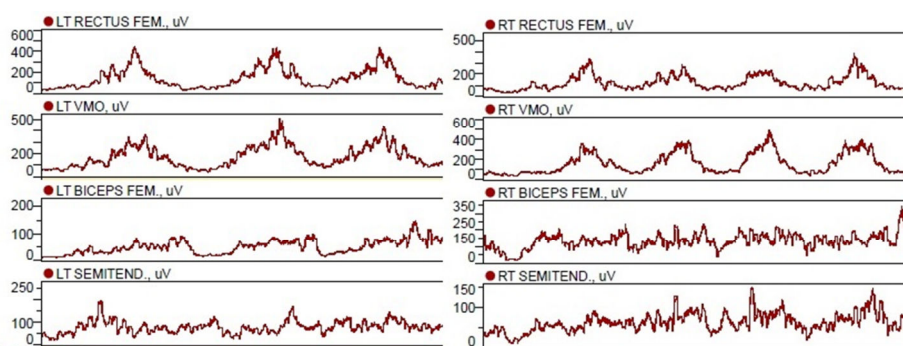


Figure 12. Comparison of the RMS signal for selected muscles of left and right leg during one leg squat on the pillow – healthy person

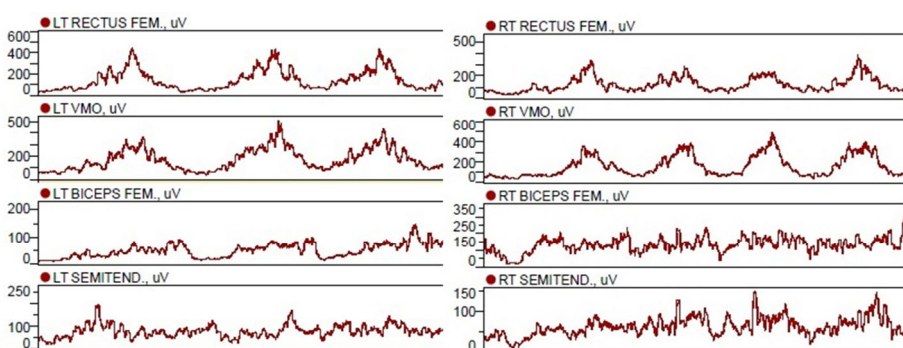


Figure 13. Comparison of the RMS signal for selected muscles of left and right leg during partial one leg squat on the pillow with performing of the semicircle – healthy person

5. Conclusions

The paper presents the electromyographic signal as valuable source of information in the rehabilitation of the knee joint. Injuries of the knee can be manifested by increased activity of some muscle groups which can be seen in electromyographic signal records. Presented results of the research show that progress of the rehabilitation could be in the easily way observed. The difference between muscles activity in healthy and injured leg is well visible. Therefore the electromyographic signal can be a good source of information about progress of the rehabilitation process and potential joints injuries.

References

1. C.J. De Luca, *The use of surface electromyography in biomechanics*, J. Appl. Biomech., **13** (1997), 135- 163.
2. A. Główacka, E. Świtoński, R. Michnik, *Wyznaczanie sił mięśniowych podczas chodu dzieci zdrowych* (in Polish), Aktualne Problemy Biomechaniki, **6** (2012), 31-36.
3. S.M. Gryzlo, R.M. Patek, M. Pink, J. Perry, *Electromyographic analysis of knee rehabilitation exercises*, J. Orthop. Sports Phys. Ther., **20** (1994), 36- 43.
4. R. Merletti, P.A. Parker, *Electromyography. Physiology, Engineering and Noninvasive Applications*, A John Wiley & Sons, Inc., Publication, New Jersey 2004.
5. K. Najarian, R. Splinter, *Biomedical signal and image processing*, second edition, CRC Press, Boca Raton 2012.
6. E. Świtoński, R. Michnik, A. Główacka, *Zastosowanie modelowania matematycznego i pomiarów EMG do oceny chodu dzieci z zaburzeniami neurologicznymi* (in Polish), Modelowanie inżynierskie, **47** (2013) 190- 196.

The Modelling Method of Discrete-Continuous Systems

Rafał HEIN

Gdańsk University of Technology, Department of Mechanical Engineering
G. Narutowicza 11/12, 80-233 Gdańsk

Abstract

The paper introduces a method of discrete-continuous systems modelling. In the proposed method a three-dimensional system is divided into finite elements in only two directions, with the third direction remaining continuous. The thus obtained discrete-continuous model is described by a set of partial differential equations. General difference equations of discrete system are obtained using the rigid finite element method. The limit of these equations leads to partial differential equations. The derived equations, expressed in matrix form, allow for the creation of a global matrix for the whole system. The equations are solved using the distributed transfer function method. Proposed approach is illustrated with the example of a simple beam fixed at both ends.

Keywords: modelling, model reduction, modal analysis, mechanical system, dynamic systems, vibration.

1. Introduction

Many different methods for modelling dynamic systems are known [1,2,5]. However, there is no universal approach which is both accurate and applicable to the wide range of dynamic systems. One of the most commonly used approaches is the finite element method, which is particularly useful in providing approximate models of the real systems. Its accuracy depends on the number of finite elements. The greater their number, the more accurate the model. However, there is an optimal division density, above which rounding errors start to seriously affect numerical calculation. The use of finite element methods for slender elements or structures is inefficient and basically ineffective, as maintaining appropriate proportions would require a very fine mesh, leading to the said rounding errors in numerical calculations. A very large number of finite elements also means creating a high-order model. Such models are not suitable for designing control systems. Additionally, the exact analytical solutions for a slender elements, such as strings, bars and beams, are already known and therefore more suitable for continuous models.

This paper proposes a hybrid method of modelling that combines the advantages of spatial discretization methods with the advantages of continuous systems modelling method. In the classical finite element method, the body is divided into all three spatial directions (Fig. 1a, 1c). In the proposed method, the same body is divided into one (Fig. 1b) or two (Fig. 1d) spatial directions, with one direction remaining continuous. Such a division results in finite elements with parameters distributed along one of the axes. Two-dimensional elements are called strips (Fig. 1b) and three-dimensional elements are called prisms (Fig. 1d). Both these elements are one-dimensional distributed systems and are therefore described by second order partial differential equations. However, these equations also have terms related to interactions between elements. Hence, the given system is described by coupled second order partial differential equations.

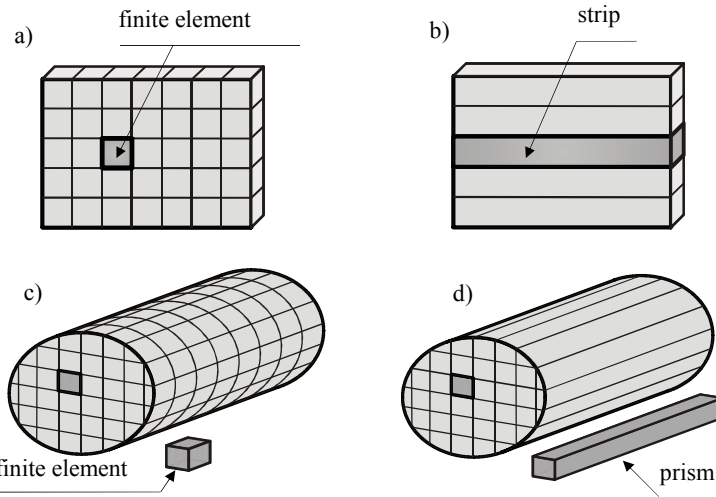


Figure 1. Spatial discretization of 2D and 3D body: a), c) conventional finite element method, b), d) proposed hybrid method

2. General model of discrete-continuous system

In order to derive a general model of the discrete-continuous system, let us consider two prisms, r and p , connected together by a layer of spring-damping elements, k , with distributed parameters (Fig. 2a). Such a discrete model is shown in Fig. 2b. Each element has 6 degrees of freedom. By applying the rigid finite element method to this discrete model, one obtains an appropriate system of ordinary differential equations for prism r . Such an FEM model may be transformed into a continuous model by letting $dx \rightarrow 0$. In this way small differences, divided by dx , become derivatives. After these transformations, the following six differential equations of the r -th prism are obtained:

$$\begin{aligned} f_{r,1}\Delta y\Delta z = & \rho\Delta y\Delta z\ddot{q}_{r,1} - E\Delta y\Delta zq''_{r,1} + \\ & + c_{xk,1}(q_{r,1} - q_{p,1}) + c_{xk,1}(s_{r,k,3}q_{i,j,5} - s_{p,k,3}q_{p,5}) - c_{xk,1}(s_{r,k,2}q_{r,6} - s_{p,k,2}q_{p,6}) \end{aligned} \quad (1)$$

$$\begin{aligned} f_{r,2}\Delta y\Delta z = & \rho\Delta y\Delta z\ddot{q}_{r,2} - \kappa G\Delta y\Delta zq''_{r,2} + \kappa G\Delta y\Delta zq'_{r,6} \\ & + c_{xk,2}(q_{r,2} - q_{p,2}) - c_{xk,2}(s_{r,k,3}q_{r,4} - s_{p,k,3}q_{p,4}) \end{aligned} \quad (2)$$

$$\begin{aligned} f_{r,3}\Delta y\Delta z = & \rho\Delta y\Delta z\ddot{q}_{r,3} - \kappa G\Delta y\Delta zq''_{r,3} - \kappa G\Delta y\Delta zq'_{r,5} \\ & + c_{xk,3}(q_{r,3} - q_{p,3}) + c_{xk,3}(s_{r,k,2}q_{r,4} - s_{p,k,2}q_{p,4}) \end{aligned} \quad (3)$$

$$\begin{aligned}
f_{r,4}\Delta y \Delta z = & \rho I_{0x} \ddot{q}_{r,4} - GI_{0x} q''_{r,4} + \\
& c_{xk,4}(q_{r,4} - q_{p,4}) + c_{xk,3}(s_{r,k,2}q_{r,3} - s_{r,k,2}q_{p,3}) + c_{xk,3}(s_{r,k,2}^2 q_{r,4} - s_{r,k,2}s_{p,k,2}q_{p,4}) + \quad (4) \\
& + c_{xk,2}(s_{r,k,2}^2 q_{r,4} - s_{r,k,3}s_{p,k,3}q_{p,4}) + c_{xk,2}(s_{r,k,3}q_{p,2} - s_{r,k,3}q_{r,2})
\end{aligned}$$

$$\begin{aligned}
f_{r,5}\Delta y \Delta z = & \rho I_{yx} \ddot{q}_{r,5} - EI_{yx} q''_{r,5} + \kappa G \Delta y \Delta z q'_{r,3} + \kappa G \Delta y \Delta z q_{r,5} \\
& c_{xk,5}(q_{r,5} - q_{p,5}) + c_{xk,1}s_{r,k,3}(q_{r,1} - q_{p,1}) + c_{xk,1}(s_{r,k,3}^2 q_{r,5} - s_{r,k,3}s_{p,k,3}q_{p,5}) + \quad (5) \\
& - c_{xk,1}(s_{r,k,2}s_{r,k,3}q_{r,6} - s_{r,k,3}s_{p,k,2}q_{p,6})
\end{aligned}$$

$$\begin{aligned}
f_{r,6}\Delta y \Delta z = & \rho I_{zx} \ddot{q}_{r,6} - EI_{zx} q''_{r,6} - \kappa G \Delta y \Delta z q'_{r,2} + \kappa G \Delta y \Delta z q_{r,6} \\
& - c_{xk,1}s_{r,k,2}(q_{r,1} - q_{p,1}) - c_{xk,1}(s_{r,k,2}s_{r,k,3}q_{r,5} - s_{r,k,2}s_{p,k,3}q_{p,5}) \quad (6) \\
& + c_{xk,1}(s_{r,k,2}^2 q_{r,6} - s_{r,k,2}s_{p,k,2}q_{p,6})
\end{aligned}$$

where: E – Young's modulus, G – shear modulus, $I_{\alpha\beta}$ – geometric moment of inertia of cross section area perpendicular to the β axis about α axis, Δy , Δz – elementary dimensions of finite element (Fig. 2b), κ – numerical shape factor of cross section, ρ – mass per unit volume, q_i – transverse displacements in i direction, $f_{r,i}$ – distributed general force applied at r -th element (excitation) in i direction, $i=1,2,\dots,6$, $s_{\alpha,\beta,\gamma}$ – distance between body α and distributed spring-damping element β in γ direction, $c_{x\alpha\beta}$ – distributed stiffness coefficient of spring element α in β direction.

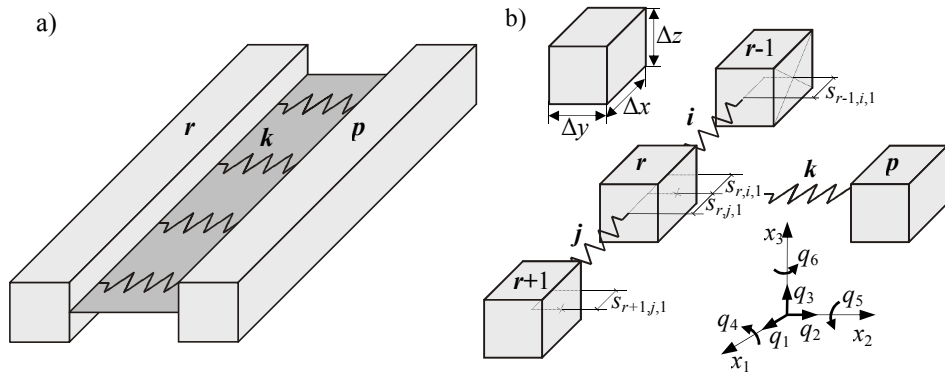


Figure 2. General model of considered system: a) discrete-continuous, b) discrete

In the same way equations for the p element can be determined. These p element equations can also be obtained from equations (1÷6) by replacing r indices with p indices and p indices with r indices. Equations (1÷6) for the r element and the corresponding equations for the p element may be written in matrix form:

$$\mathbf{A}_{02}\ddot{\mathbf{q}}(x,t) + \mathbf{A}_{20}\mathbf{q}''(x,t) + \mathbf{A}_{10}\mathbf{q}'(x,t) + \mathbf{A}_{00}\mathbf{q}(x,t) = \mathbf{f}(x,t) \quad (7)$$

with boundary conditions

$$\left(\mathbf{M}_{01} + \mathbf{M}_{11}\frac{\partial}{\partial x}\right)\mathbf{q}(0,t) = \gamma_1(t), \quad \left(\mathbf{N}_{02} + \mathbf{N}_{12}\frac{\partial}{\partial x}\right)\mathbf{q}(l,t) = \gamma_2(t),$$

where:

$$\begin{aligned} \mathbf{A}_{02} &= \text{diag}(\mathbf{A}_{02r}, \mathbf{A}_{02p}), \quad \mathbf{A}_{02r} = \text{diag}(\rho\Delta y\Delta z, \rho\Delta y\Delta z, \rho\Delta y\Delta z, \rho I_{0x}, \rho I_{yx}, \rho I_{zx}), \\ \mathbf{A}_{02p} &= \text{diag}(\rho\Delta y\Delta z, \rho\Delta y\Delta z, \rho\Delta y\Delta z, \rho I_{0x}, \rho I_{yx}, \rho I_{zx}), \\ \mathbf{A}_{20} &= \text{diag}(\mathbf{A}_{20r}, \mathbf{A}_{20p}), \quad \mathbf{A}_{20r} = \text{diag}(-E\Delta y\Delta z, -\kappa G\Delta y\Delta z, -\kappa G\Delta y\Delta z, -GI_{0x}, -EI_{yx}, -EI_{zx}), \\ \mathbf{A}_{20p} &= \text{diag}(-E\Delta y\Delta z, -\kappa G\Delta y\Delta z, -\kappa G\Delta y\Delta z, -GI_{0x}, -EI_{yx}, -EI_{zx}), \quad \mathbf{A}_{10} = \text{diag}(\mathbf{A}_{10r}, \mathbf{A}_{10p}), \end{aligned}$$

$$\begin{aligned} \mathbf{A}_{10r} &= \begin{bmatrix} 0 & 0 & 0 & 0 & 0 & 0 \\ 0 & 0 & 0 & 0 & 0 & \kappa G\Delta y\Delta z \\ 0 & 0 & 0 & 0 & -\kappa G\Delta y\Delta z & 0 \\ 0 & 0 & 0 & 0 & 0 & 0 \\ 0 & 0 & \kappa G\Delta y\Delta z & 0 & 0 & 0 \\ 0 & -\kappa G\Delta y\Delta z & 0 & 0 & 0 & 0 \end{bmatrix}, \quad \mathbf{A}_{00} = \begin{bmatrix} \mathbf{K}_{rrk} & | & \mathbf{K}_{rpk} \\ \hline \mathbf{K}_{prk} & | & \mathbf{K}_{ppk} \end{bmatrix}, \\ \mathbf{K}_{rrk} &= \begin{bmatrix} c_{xk1} & 0 & 0 & 0 & c_{xk1}s_{rk3} & -c_{xk1}s_{rk2} \\ 0 & c_{xk2} & 0 & -c_{xk2}s_{rk3} & 0 & 0 \\ 0 & 0 & c_{xk3} & c_{xk3}s_{rk2} & 0 & 0 \\ 0 & -c_{xk2}s_{rk3} & c_{xk3}s_{rk2} & c_{xk4} + c_{xk2}s_{rk3}^2 + c_{xk3}s_{rk2}^2 & 0 & 0 \\ c_{xk1}s_{rk3} & 0 & 0 & 0 & c_{xk5} + c_{xk1}s_{rk3}^2 & -c_{xk1}s_{rk2}s_{rk3} \\ -c_{xk1}s_{rk2} & 0 & 0 & 0 & -c_{xk1}s_{rk2}s_{rk3} & c_{xk6} + c_{xk1}s_{rk2}^2 \end{bmatrix}, \\ \mathbf{K}_{rpk} &= \begin{bmatrix} -c_{xk1} & 0 & 0 & 0 & -c_{xk1}s_{pk3} & c_{xk1}s_{pk2} \\ 0 & -c_{xk2} & 0 & c_{xk2}s_{pk3} & 0 & 0 \\ 0 & 0 & -c_{xk3} & -c_{xk3}s_{pk2} & 0 & 0 \\ 0 & c_{xk2}s_{rk3} & -c_{xk3}s_{rk2} & -c_{xk4} - c_{xk2}s_{rk3}s_{pk3} - c_{xk3}s_{rk2}s_{pk2} & 0 & 0 \\ -c_{xk1}s_{rk3} & 0 & 0 & 0 & -c_{xk5} - c_{xk1}s_{rk3}s_{pk3} & c_{xk1}s_{rk3}s_{pk2} \\ c_{xk1}s_{rk2} & 0 & 0 & 0 & c_{xk1}s_{rk2}s_{pk3} & -c_{xk6} - c_{xk1}s_{rk2}s_{pk2} \end{bmatrix} \end{aligned}$$

$\mathbf{K}_{prk} = \mathbf{K}_{rpk}^T$, matrices \mathbf{K}_{ppk} and \mathbf{A}_{10p} are obtained from \mathbf{K}_{rrk} and \mathbf{A}_{10r} by replacing indices r with p .

A global model for the whole system is built the same way as the FEM model. Global matrices \mathbf{A}_{02} , \mathbf{A}_{20} , \mathbf{A}_{10} include sub-matrices of each prism element, located on their main diagonal. Matrix \mathbf{A}_{00} is formed by summing the stiffness matrices of each prism element in the global system.

The solution of these equations with appropriate boundary conditions gives semi-analytical results for the tree-dimensional structure. To solve partial differential equation (7), the distributed transfer function method was used [2,4].

The proposed approach may be applied in modelling 1D, 2D and 3D continuous systems. In the case of a 1D system, there are of course no interactions between prisms.

3. Example of method application

As a simple example, let us consider a beam fixed at both ends (Fig. 3) with the following parameters: $E = 2 \cdot 10^{11}$ [Pa], $G = 8 \cdot 10^{10}$ [Pa], $\rho = 8000$ [kg/m³], $\Delta y = 0.15$ [m], $\Delta z = 0.15$ [m], $l = 1$ [m], $\kappa = 1.2$.

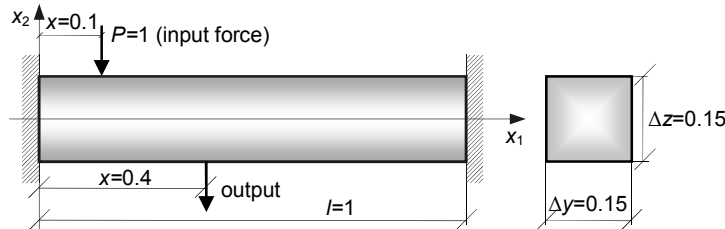


Figure 3. Fixed beam

The beam is divided into four prisms (Fig. 4) and four distributed spring elements. Each prism has three degrees of freedom – displacement along x_1 and x_2 axes and rotation angle around x_3 axis.

For this example the frequency responses of the proposed model are compared with those of Euler and Timoshenko beam models (Fig. 5).

The beam frequency responses (Fig. 5) are obtained for the unit step force input signal acting at beam point $x=0.1$ [m] (Fig. 3) and the displacement output signal is observed at the $x=0.4$ [m] point.

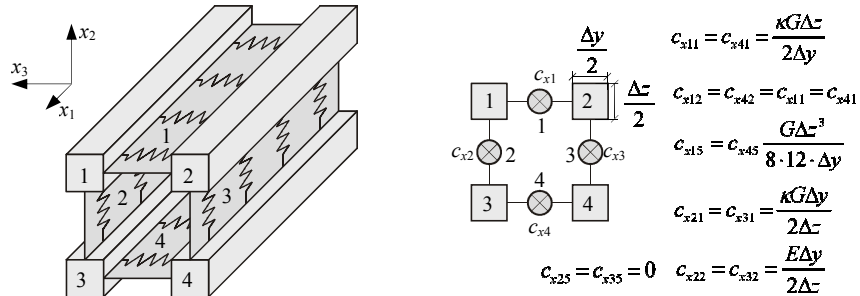


Figure 4. Discrete model of beam: a) general scheme, b) equivalent scheme

The characteristic in Fig. 5 shows that the first two frequencies of the proposed model and that of the Timoshenko beam model are very similar. This proves that the proposed model is correct. The later trend shows that the frequencies in the proposed model are even more to the left than in Timoshenko's model. The characteristic of the Euler beam model differs significantly from the other two. This is because the Euler beam

model does not take into account the effect of shear deformation and is therefore less accurate. Timoshenko included shear deformation to produce a more accurate model than Euler, with a frequency trend more to the left. The beam model proposed in this paper is closer to Timoshenko's model but the subsequent frequency trend is even more to the left. In the future, these results will be verified and compared with a corresponding FEM model.

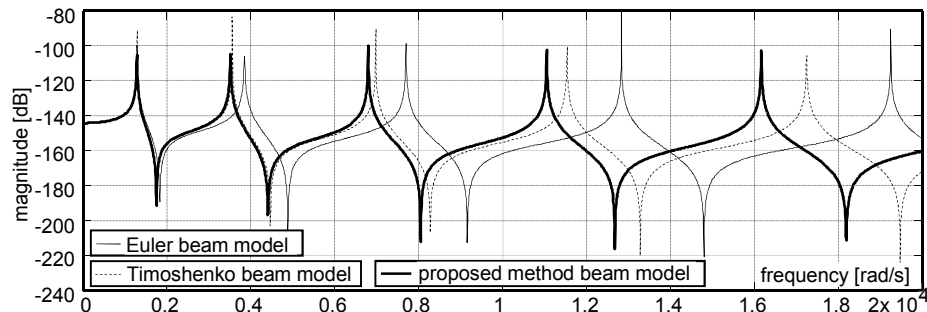


Figure 5. Frequency characteristics

4. Conclusions

This paper has presented a discrete-continuous modelling method. For the proposed method, general partial differential equations were derived. These equations were next written in a formalized matrix form that is very easily applied in computer algorithms. A beam fixed at both ends was used to illustrate the general concept. The obtained numerical calculation results show that the proposed method is efficient and applicable to discrete-continuous dynamic system modelling.

Acknowledgments

The research is supported from the science budget resources in 2011-2014 as the research project (N N501 120240).

References

1. R. Hein, C. Orlikowski: *Hybrid reduced model of rotor*, The archive of mechanical engineering, LX(3) (2013) 319-333
2. R. Hein, C. Orlikowski: Hybrid reduced model of continuous system, *Vibrations in physical systems*, Vol. XXIV, pp. 143-149, Poznan 2010, Poland
3. R. Hein, C. Orlikowski: *Reduced order model of 2D system*, Selected problems of modal analysis of mechanical systems, Editor T. Uhl, AGH, Kraków 2009, Poland,
4. Yang B., Tan C.A.: *Transfer Function of One-Dimentional Distributed Parameter Systems*, ASME Journal of Applied Mechanics, **59** (1992) 1009-1014.
5. J. Kruszewski, and others: *Rigid finite element method*, Arkady, Warsaw 1975.

Free Vibrations of Thin Microstructured Plates

Jarosław JĘDRYSIAK

Department of Structural Mechanics, Łódź University of Technology

al. Politechniki 6, 90-924 Łódź, Poland

jarek@p.lodz.pl

Ewelina PAZERA

Department of Structural Mechanics, Łódź University of Technology

al. Politechniki 6, 90-924 Łódź, Poland

ewelinapazera@interia.pl

Abstract

In this paper it is presented a problem of free vibrations of thin microstructured plates, which can be treated as made of functionally graded material on the macrolevel. The size of the microstructure of the plates is of an order of the plate thickness. In order to obtain averaged governing equations of these plates the tolerance modelling technique is applied, cf. [14, 15, 7]. The derived tolerance model equations have the terms dependent of the microstructure size. Hence, the tolerance model describes the effect of the microstructure size. In order to evaluate results, the asymptotic model is introduced. Obtained results can be compared to those calculated by using the finite element method.

Keywords: thin functionally graded plates, microstructure, tolerance modelling

1. Introduction

The objects under consideration are thin functionally graded plates with microstructure in planes parallel to the plate midplane along one, i.e. the x_1 -axis direction. All plate properties along the perpendicular direction are assumed to be constant. Moreover, let the size of the microstructure be of an order of the plate thickness. An example of these plates is shown in Figure 1.

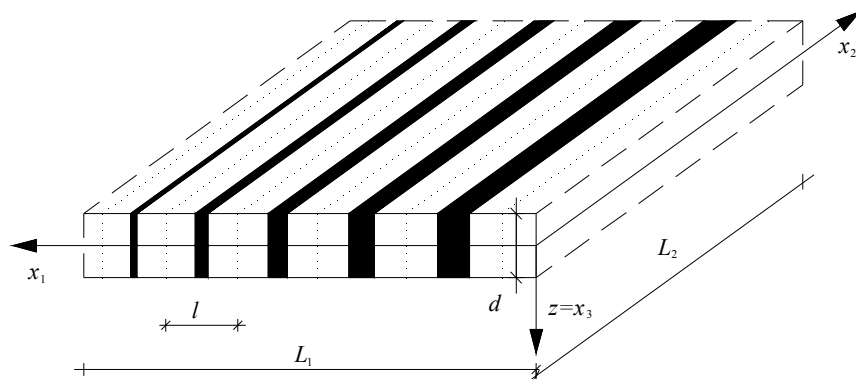


Figure 1. Fragment of a functionally graded plate with the microstructure

Plates of this kind are consisted of many small elements along the x_1 -axis, called the cells, which have a span equal l , cf. Figure 2, ($x=x_1$). This length l is called the microstructure parameter and describes the size of the microstructure.

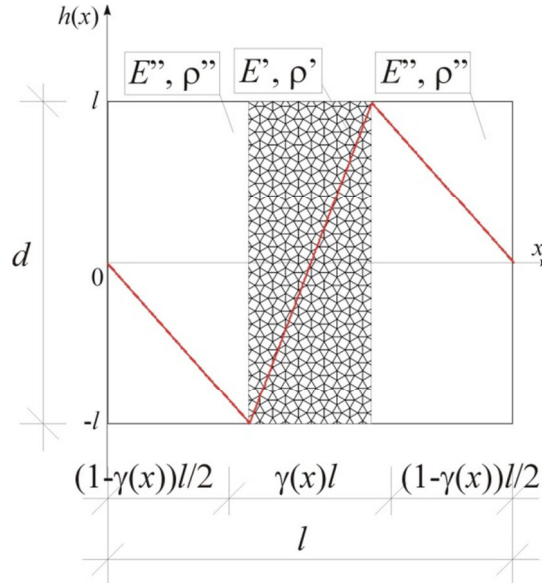


Figure 2. Element of a functionally graded plate with an example of the fluctuation shape function

A description of various thermomechanical problems of functionally graded structures or composites is often made using averaging approaches for macroscopically homogeneous structures, cf. Jędrysiak [6]. Between them it has to be mentioned models for periodic plates, cf. Kohn and Vogelius [11], based on the asymptotic homogenization method. Other method, used to describe various problems of thermoelasticity for beams, plates and shells are shown in a lot of papers, cf. [4, 13, 1, 2]. Unfortunately, model equations, obtained in this way, do not take into account the effect of the microstructure size.

However, in order to describe this effect the tolerance averaging technique can be used, cf. [14, 15, 6]. This method is applied to model various periodic structures in a series of papers, [5, 3]. Moreover, the tolerance method is also adopted to functionally graded structures like transversally tolerance-periodic plates, cf. [6, 7, 8, 9, 10] and for longitudinally functionally graded structures [12].

2. Modelling foundations

Let $Ox_1x_2x_3$ stand orthogonal Cartesian coordinate system and t be the time coordinate. Denote: $\mathbf{x}=(x_1, x_2)$, $z=x_3$ and the region of the undeformed plate by $\Omega \equiv \{(\mathbf{x}, z) : -d/2 \leq z \leq d/2, \mathbf{x} \in \Pi\}$, with the midplane Π and the plate thickness d . Let $\Delta \equiv [-$

$l/2, l/2]$ be the “basic cell” in the interval $\Lambda = (-L_1/2, L_1/2)$ on the x_1 -axis, and l be the length of cell Δ , called *the microstructure parameter*. It is assumed that this parameter l satisfies the conditions $d \sim l \ll L_1$.

Let us introduce tolerance-periodic functions in x : a mass density μ , a rotational inertia ϑ and bending stiffnesses $d_{\alpha\beta\gamma\delta}$ given by:

$$\begin{aligned}\mu(x) &\equiv \int_{-d/2}^{d/2} \rho(x, z) dz, & \vartheta(x) &\equiv \int_{-d/2}^{d/2} \rho(x, z) z^2 dz, \\ d_{\alpha\beta\gamma\delta}(x) &\equiv \int_{-d/2}^{d/2} c_{\alpha\beta\gamma\delta}(x, z) z^2 dz\end{aligned}\quad (1)$$

Using the Kirchhoff-type plates theory assumptions we can write the equation for deflection $w(x, t)$ of functionally graded plates under consideration in the following form:

$$\partial_{\alpha\beta}(d_{\alpha\beta\gamma\delta}\partial_{\gamma\delta}w) + \mu\ddot{w} - \partial_\alpha(\vartheta\partial_\beta\dot{w})\delta_{\alpha\beta} = 0, \quad (2)$$

which describes free vibrations of these plates.

The above equation has highly oscillating, tolerance-periodic, non-continuous coefficients being functions in x .

3. Modelling concepts

Averaged equations for functionally graded plates will be obtained using the tolerance averaging technique. The basic concepts of the modelling procedure are defined in books, cf. [14, 15, 6].

Let $\Delta(x) \equiv x + \Delta$, $\Lambda_\Delta = \{x \in \Lambda : \Delta(x) \subset \Lambda\}$, be a cell at $x \in \Lambda_\Delta$. The averaging operator for an arbitrary integrable function f is defined by

$$\langle f \rangle(x, x_2) = \frac{1}{l} \int_{\Delta(x)} f(y, x_2) dy, \quad x \in \Lambda_\Delta. \quad (3)$$

If a function f is tolerance-periodic in x , then averaged value by (3) is a slowly-varying function in x .

Following the aforementioned books let us denote a set of tolerance-periodic functions by $TP_\delta^\alpha(\Lambda, \Delta)$, a set of slowly-varying functions by $SV_\delta^\alpha(\Lambda, \Delta)$, a set of highly oscillating functions by $HO_\delta^\alpha(\Lambda, \Delta)$, where $\alpha \geq 0$, δ is a tolerance parameter. Denote by $h(\cdot)$ a continuous highly oscillating function, $h \in FS_\delta^1(\Lambda, \Delta)$, having a piecewise continuous and bounded gradient $\partial^1 h$. Function $h(\cdot)$ is called *the fluctuation shape function* of the 1-st kind, if it depend on l as a parameter and satisfies conditions: $\partial^k h \in O(l^{a-k})$ for $k=0, 1, \dots, a$, $\partial^k h \equiv h$, and $\langle \mu h \rangle(x) \approx 0$ for every $x \in \Lambda_\Delta$, $\mu > 0$, $\mu \in TP_\delta^1(\Lambda, \Delta)$.

4. Fundamental assumptions of the tolerance modelling

The tolerance modelling is based on two fundamental modelling assumptions, cf. the book edited by Woźniak et al. [14, 15] and for thin functionally graded plates by [6, 7].

The first assumption of this procedure is *the micro-macro decomposition*, where the plate displacements are decomposed as:

$$\begin{aligned} u_3(\mathbf{x}, z, t) &= w(\mathbf{x}, t), \\ u_\alpha(\mathbf{x}, z, t) &= -z[\partial_\alpha w(\mathbf{x}, t) + h(x)v_\alpha(\mathbf{x}, t)], \quad \alpha = 1, 2. \end{aligned} \tag{4}$$

Functions $w(\cdot, x_2, t) \in SV_\delta^2(\Lambda, \Delta)$, $v_\alpha(\cdot, x_2, t) \in SV_\delta^1(\Lambda, \Delta)$ are basic kinematic unknowns, called *the macrodeflection* and *the fluctuation amplitudes*, respectively; $h(\cdot)$ is the known *fluctuation shape function*, cf. Figure 2.

The second assumption is *the tolerance averaging approximation*, i.e. terms of an order of $O(\delta)$ are treated as negligibly small, cf. [14, 15, 7], e.g. for $f \in TP_\delta^2(\Lambda, \Delta)$, $h \in FS_\delta^1(\Lambda, \Delta)$, $F \in SV_\delta^a(\Lambda, \Delta)$, $a = 1, 2$, in: $\langle f \rangle(x) = \langle \bar{f} \rangle(x) + O(\delta)$, $\langle fF \rangle(x_1) = \langle f \rangle(x_1)F(x_1) + O(\delta)$, $\langle f\partial_\alpha(hF) \rangle(x) = \langle f\partial_\alpha h \rangle(x)F(x) + O(\delta)$.

5. The outline of the tolerance modelling procedure

The tolerance modelling procedure is shown in the books [14, 15, 7]. Here, there is presented only an outline of this method.

In the tolerance modelling two basic steps can be introduced. In the first step micro-macro decomposition (4) is applied. In the second step averaging operator (3) is used to the resulting formula. Hence, the tolerance averaged lagrangean $\langle \Lambda_h \rangle$ is obtained:

$$\begin{aligned} \langle \Lambda_h \rangle &= \frac{1}{2}(\langle \mu \rangle \dot{w}\dot{w} + \langle \vartheta \rangle \partial_\alpha \dot{w} \partial_\beta \dot{w} \delta_{\alpha\beta} + \langle \vartheta h h \rangle \dot{v}_\alpha \dot{v}_\beta \delta_{\alpha\beta}) - \\ &\quad - \frac{1}{2}(\langle b_{\alpha\beta\gamma\delta} \rangle \partial_{\alpha\beta} w \partial_{\gamma\delta} w + 2 \langle b_{\alpha\beta\delta} \partial_\alpha h \rangle \partial_{\alpha\beta} w v_\delta + \\ &\quad + \langle b_{\beta\delta} \partial_1 h \partial_1 h \rangle v_\beta v_\delta + \langle b_{2\beta2\delta} h h \rangle \partial_2 v_\beta \partial_2 v_\delta). \end{aligned} \tag{5}$$

From the principle of stationary applied to (5) the Euler-Lagrange equations for $w(\cdot, x_2, t)$ and $v_\alpha(\cdot, x_2, t)$ can be derived:

$$\begin{aligned} \frac{\partial}{\partial t} \frac{\partial \langle \Lambda_h \rangle}{\partial \dot{w}} - \frac{\partial}{\partial t} \partial_\alpha \frac{\partial \langle \Lambda_h \rangle}{\partial \partial_\alpha \dot{w}} - \partial_{\alpha\beta} \frac{\partial \langle \Lambda_h \rangle}{\partial \partial_{\alpha\beta} w} - \frac{\partial \langle \Lambda_h \rangle}{\partial w} &= 0, \\ \frac{\partial}{\partial t} \frac{\partial \langle \Lambda_h \rangle}{\partial \dot{v}_\alpha} + \partial_2 \frac{\partial \langle \Lambda_h \rangle}{\partial \partial_2 v_\alpha} - \frac{\partial \langle \Lambda_h \rangle}{\partial v_\alpha} &= 0. \end{aligned} \tag{6}$$

6. Governing equations of presented models

In this section equations of two models are presented: *the tolerance model*, *the asymptotic model*.

Substituting $\langle \Lambda_h \rangle$, (5), to the Euler-Lagrange equations (6), after some manipulations we arrive at the following system of equations for $w(\cdot, x_2, t)$ and $v_\alpha(\cdot, x_2, t)$:

$$\begin{aligned} \partial_{\alpha\beta}(\langle b_{\alpha\beta\gamma\delta} \rangle \partial_{\gamma\delta} w + \langle b_{\alpha\beta\gamma\delta} \partial_1 h \rangle v_\gamma) + \langle \mu \rangle \ddot{w} - \langle \vartheta \rangle \partial_{\alpha\beta} \ddot{w} \delta_{\alpha\beta} &= 0, \\ \langle b_{\alpha\beta\gamma\delta} \partial_1 h \rangle \partial_{\gamma\delta} w + \langle b_{\alpha\beta\gamma\delta} \partial_1 h \rangle v_\gamma - \underbrace{\langle b_{\alpha\beta\gamma\delta} h h \rangle \partial_{22} v_\gamma}_{\varphi_\gamma} + \underbrace{\langle \vartheta h h \rangle \ddot{v}_\alpha}_{=0} &= 0, \end{aligned} \tag{7}$$

where all coefficients are slowly-varying functions in x . Equations (7) together with micro-macro decomposition (4) stand *the tolerance model of thin functionally graded*

plates with the microstructure size of an order of the plate thickness. These equations describe free vibrations of these plates. There are the underlined terms, which depend on the microstructure parameter l , in these equations. Hence, the effect of the microstructure size on dynamic problems of these plates is taken into account. All coefficients of equations (7) are slowly-varying functions in $x=x_1$ in contrast to equation (2), in which there are non-continuous, highly oscillating and tolerance-periodic coefficients. The basic unknowns $w, v_\alpha, \alpha=1,2$, are slowly-varying functions in $x=x_1$. It can be observed that boundary conditions have to be formulated for the *macrodeflection* w on all edges, and for the *fluctuation amplitudes* v_α only for edges normal to the x_2 -axis.

The asymptotic modelling procedure is shown in [15, 6, 7]. However, in order to obtain equations of an approximate model, which does not take into account the effect of the microstructure size, the underlined terms in equations (7) can be neglected. Hence, we arrive at the following equations of the *asymptotic model*:

$$\begin{aligned} \partial_{\alpha\beta}(< b_{\alpha\beta\gamma\delta} > \partial_{\gamma\delta} w + < b_{\alpha\beta\gamma} \partial_\gamma h > v_\gamma) + < \mu > \ddot{w} - < \mathfrak{g} > \partial_{\alpha\beta} \ddot{w} \delta_{\alpha\beta} = 0, \\ < b_{\alpha\gamma\delta} \partial_\gamma h > \partial_{\gamma\delta} w + < b_{\alpha\gamma} \partial_\gamma h \partial_\delta h > v_\gamma = 0. \end{aligned} \quad (8)$$

These equations have smooth, slowly-varying coefficients in the contrast to equation (2). The asymptotic model equations describe free vibrations of thin plates under consideration on the macrolevel only.

7. Final remarks

Two modelling procedures are applied to the known differential equation of Kirchhoff-type plates with functionally graded macrostructure and the microstructure size of an order of the plate thickness in this note. Using these procedures the governing equation with non-continuous, tolerance-periodic functional coefficients of x_1 can be replaced by the systems of differential equations with slowly-varying, continuous coefficients of x_1 for each model.

Using the tolerance model, where the effect of the microstructure size is taken into account, not only macrovibrations can be investigated, but also microvibrations, which are related to the microstructure of the functionally graded plates.

The *tolerance model* equations have a physical sense for unknowns w, v_α , which are slowly-varying functions in x_1 . However, these conditions can be treated as a certain *a posteriori* criterion of physical reliability for the model.

The second presented model, the asymptotic model, with the governing equations neglecting the aforementioned effect, can describe only macrovibrations of these plates under consideration.

References

1. A.H. Akbarzadeha, M. Abbasib, M.R. Eslami, *Coupled thermoelasticity of functionally graded plates based on the third-order shear deformation theory*, Thin-Walled Struct., **53** (2012) 141-155.

-
2. T.Q. Bui, A. Khosravifard, Ch. Zhang, M.R. Hematiyan, M.V. Golm, *Dynamic analysis of sandwich beams with functionally graded core using a truly meshfree radial point interpolation method*, Engng. Struct., **47** (2013) 90-104.
 3. Ł. Domagalski, J. Jędrysiak, *On the elastostatics of thin periodic plates with large deflections*, Meccanica, **47** (2012) 1659-1671.
 4. A.J.M. Ferreira, R.C. Batra, C.M.C. Roque, L.F. Qian, R.M.N. Jorge, *Natural frequencies of functionally graded plates by a meshless method*, Composite Struct., **75** (2006) 593-600.
 5. J. Jędrysiak, *Higher order vibrations of thin periodic plates*, Thin-Walled Struct., **47** (2009) 890-901.
 6. J. Jędrysiak, *Thermomechanics of laminates, plates and shells with functionally graded structure*, Lodz, Publishing House of Lodz University of Technology 2010 [in Polish].
 7. J. Jędrysiak, *Modelling of dynamic behaviour of microstructured thin functionally graded plates*, Thin-Walled Struct., **71** (2013) 102-107.
 8. J. Jędrysiak, B. Michalak, *On the modelling of stability problems for thin plates with functionally graded structure*, Thin-Walled Struct., **49** (2011) 627-635.
 9. M. Kaźmierczak, J. Jędrysiak, *Tolerance modeling of vibrations of thin functionally graded plates*, Thin-Walled Struct., **49** (2011) 1295-1303.
 10. M. Kaźmierczak, J. Jędrysiak, *A new combined asymptotic-tolerance model of vibrations of thin transversally graded plates*, Engng. Struct., **46** (2013) 322-331.
 11. R.V. Kohn, M. Vogelius, *A new model for thin plates with rapidly varying thickness*, Int. J. Solids Struct., **20** (1984) 333-350.
 12. B. Michalak, *Thermomechanics of solids with a certain inhomogeneous microstructure*, Lodz, Publishing House of Lodz University of Technology 2011 [in Polish].
 13. F. Tornabene, E. Viola, *Free vibration analysis of functionally graded panels and shells of revolution*, Meccanica, **44** (2009) 255-281.
 14. Cz. Woźniak, B. Michalak, J. Jędrysiak, *Thermomechanics of heterogeneous solids and structures*, Lodz, Publishing House of Lodz University of Technology 2008.
 15. Cz. Woźniak, et al. (eds.), *Mathematical modeling and analysis in continuum mechanics of microstructured media*, Gliwice, Publishing House of Silesian University of Technology 2010.

Vibrations of Thin Functionally Graded Plates with Tolerance-Periodic Microstructure

Magda KAŽMIERCZAK-SOBIŃSKA

*Department of Structural Mechanics, Lodz University of Technology
al. Politechniki 6, 90-924 Łódź, Poland
magda.kazmierczak@p.lodz.pl*

Jarosław JĘDRYSIAK

*Department of Structural Mechanics, Lodz University of Technology
al. Politechniki 6, 90-924 Łódź, Poland
jarek@p.lodz.pl*

Abstract

This paper presents a problem of vibrations of thin functionally graded plates. To describe this kind of plates three averaged models are proposed: a tolerance model, an asymptotic model and a combined asymptotic-tolerance model, cf. [10]. Calculational results obtained for a functionally graded plate band using the proposed models are compared to each other.

Keywords: thin functionally graded plates, tolerance-periodic microstructure, tolerance modelling

1. Introduction

There are considered thin plates with functionally graded macrostructure in planes parallel to the plate midplane. However, the microstructure is tolerance-periodic, cf. Figure 1.

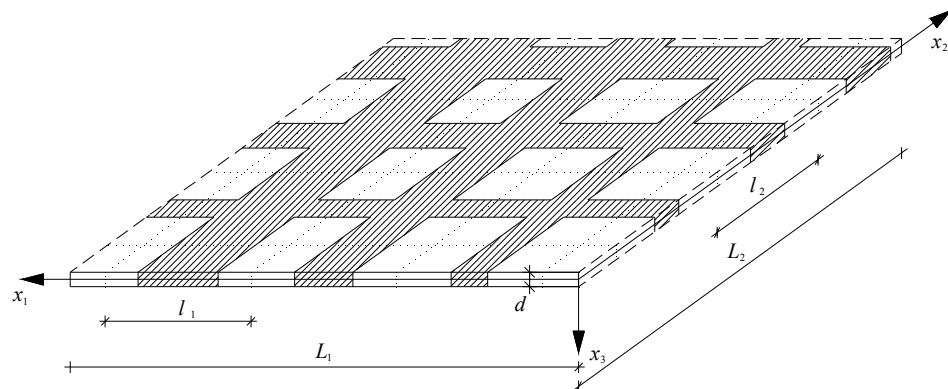


Figure 1. Fragment of a functionally graded plate

Plates of this kind consist of many small elements, where adjacent elements are nearly identical but the distant ones may be variable. Every element is treated as a thin plate with spans l_1 and l_2 along the x_1 - and x_2 -axis, respectively, cf. Figure 2.

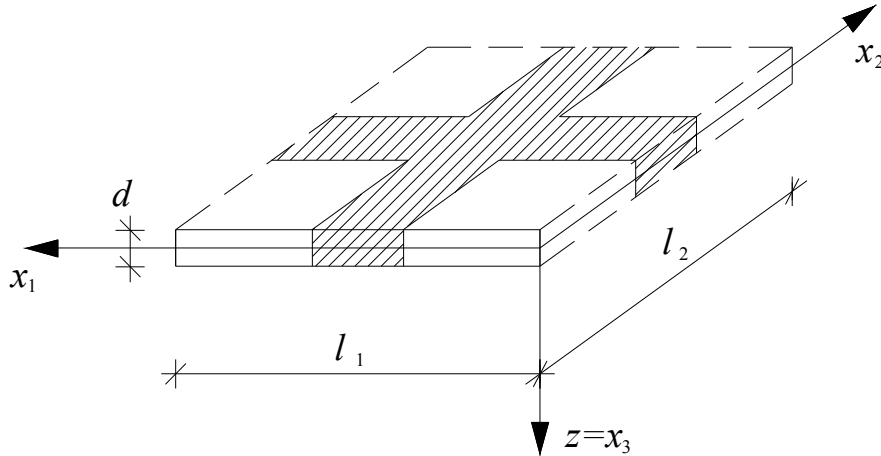


Figure 2. Element of a functionally graded plate

Structures made of functionally graded material are often analysed using averaging approaches for macroscopically homogeneous structures. Models, which are proposed, based on the asymptotic homogenization, where the effect of the microstructure size is neglected in the governing equations.

Using the tolerance averaging technique the effect of the microstructure size can be taken into account in governing equations for structures under consideration, cf. [9,10]. Some applications of this method to the modelling of various periodic structures are shown in a series of papers, [1,5]. The tolerance modelling was adopted to functionally graded structures like transversally tolerance-periodic plates, cf. [2,3,4,5,6] and for longitudinally functionally graded structures [8].

2. Modelling foundations

Denote by $Ox_1x_2x_3$ orthogonal Cartesian coordinate system and by t the time coordinate. Set $\mathbf{x} = (x_1, x_2)$ and $z = x_3$. The region of the undeformed plate is denote by $\Omega \equiv \{(\mathbf{x}, z) : -d(\mathbf{x})/2 \leq z \leq d(\mathbf{x})/2, \mathbf{x} \in \Pi\}$, where Π is the midplane and $d(\cdot)$ is the plate thickness. The “basic cell” on Ox_1x_2 is denoted by $\Omega \equiv [-l_1/2, l_1/2] \times [-l_2/2, l_2/2]$. The diameter of cell Ω , called the *parameter of microstructure*, is defined by $l \equiv [(l_1)^2 + (l_2)^2]^{1/2}$ and satisfies the condition $d_{\max} \ll l \ll (L_1, L_2)$. Thickness $d(\cdot)$ can be a tolerance-periodic function in \mathbf{x} .

Define tolerance-periodic functions in \mathbf{x} : a mass density μ , a rotational inertia ϑ and bending stiffnesses $d_{\alpha\beta\gamma\delta}$ in the form:

$$\begin{aligned}\mu(\mathbf{x}) &\equiv \int_{-d/2}^{d/2} \rho(\mathbf{x}, z) dz, \quad \vartheta(x) \equiv \int_{-d/2}^{d/2} \rho(\mathbf{x}, z) z^2 dz, \\ d_{\alpha\beta\gamma\delta}(\mathbf{x}) &\equiv \int_{-d/2}^{d/2} c_{\alpha\beta\gamma\delta}(\mathbf{x}, z) z^2 dz.\end{aligned}\tag{1}$$

From the Kirchhoff-type plates theory assumptions the equation for deflection $w(\mathbf{x}, t)$ of functionally graded plates with highly oscillating, tolerance-periodic, non-continuous coefficients is described by:

$$\partial_{\alpha\beta}(d_{\alpha\beta\gamma\delta}\partial_{\gamma\delta}w) + \mu\ddot{w} - \partial_\alpha(\vartheta\partial_\alpha\ddot{w}) = p. \quad (2)$$

3. Modelling concepts and assumptions

Averaged equations for functionally graded plates will be obtained using the tolerance averaging technique. The basic concepts of the modelling procedure are defined in books, cf. [9,10].

Let $\Omega(\mathbf{x})=\mathbf{x}+\Omega$, $\Pi_\Omega=\{\mathbf{x}\in\Pi: \Omega(\mathbf{x})\subset\Pi\}$, be a cell at $\mathbf{x}\in\Pi_\Omega$. The averaging operator for an arbitrary integrable function f is defined by

$$\langle f \rangle(\mathbf{x}) = \frac{1}{l_1 l_2} \int_{\Omega(\mathbf{x})} f(y_1, y_2) dy_1 dy_2, \quad \mathbf{x} \in \Pi_\Omega. \quad (3)$$

If a function f is tolerance-periodic in \mathbf{x} , then averaged value by (3) is a slowly-varying function in \mathbf{x} .

Following the aforementioned books let us denote a set of tolerance-periodic functions by $TP_\delta^\alpha(\Pi, \Omega)$, a set of slowly-varying functions by $SV_\delta^\alpha(\Pi, \Omega)$, a set of highly oscillating functions by $HO_\delta^\alpha(\Pi, \Omega)$, where $\alpha \geq 0$, δ is a tolerance parameter. Denote by $h(\cdot)$ a highly oscillating function, $h \in HO_\delta^2(\Pi, \Omega)$, continuous together with gradient $\partial^1 h$ and having a piecewise continuous and bounded gradient $\partial^2 h$. Function $h(\cdot)$ is called *the fluctuation shape function* of the 2-nd kind, if it depend on l as a parameter and satisfies conditions: $\partial^k h \in O(l^{a-k})$ for $k=0,1,\dots,a$, $\partial^k h \equiv h$, and $\langle \mu h \rangle(\mathbf{x}) \approx 0$ for every $\mathbf{x} \in \Pi_\Omega$, $\mu > 0$, $\mu \in TP_\delta^1(\Pi, \Omega)$.

4. Governing equations

In this section will be presented equations for three models: the tolerance model, the asymptotic model and the combined asymptotic-tolerance model.

The tolerance modelling procedure is outlined here following the book [3].

The first assumption of this procedure is *the micro-macro decomposition* plate deflection w :

$$w(\mathbf{x}, t) = U(\mathbf{x}, t) + h^A(\mathbf{x})Q^A(\mathbf{x}, t), \quad A=1,\dots,N, \quad \mathbf{x} \in \Pi. \quad (4)$$

Functions $U(\cdot, t)$ and $Q^A(\cdot, t)$ are kinematic unknowns, called *the macrodeflection* and *the fluctuation amplitudes*, respectively, $h^A(\cdot)$ are the known *fluctuation shape functions*.

The second assumption is *the tolerance averaging approximation*, i.e. terms of an order of $O(\delta)$ are negligibly small.

Using the above assumptions in equation (2), after some manipulations we obtain the system of equations:

$$\begin{aligned} & \partial_{\alpha\beta}(<\!d_{\alpha\beta\gamma\delta}\!>\partial_{\gamma\delta}U + <\!d_{\alpha\beta\gamma\delta}\partial_{\gamma\delta}h^B\!>Q^B) + <\!\mu\!>\ddot{U} - <\!\vartheta\!>\partial_{\alpha\alpha}\ddot{U} = <\!p\!>, \\ & <\!d_{\alpha\beta\gamma\delta}\partial_{\gamma\delta}h^A\!>\partial_{\alpha\beta}U + <\!d_{\alpha\beta\gamma\delta}\partial_{\alpha\beta}h^A\partial_{\gamma\delta}h^B\!>Q^B + \\ & + (<\!\mu h^A h^B\!> + <\!\vartheta\partial_{\alpha}h^A\partial_{\alpha}h^B\!>)Q^B = <\!ph^A\!>, \end{aligned} \quad (5)$$

where all coefficients are slowly-varying functions in \mathbf{x} . Equations (5) together the micro-macro decomposition (4) present the *tolerance model of thin functionally graded plates*. These equations take into account the effect of the microstructure size on dynamic problems of this kind of plates.

The asymptotic modelling procedure is shown in books [3,10].

The starting point of this procedure is equation (2). We introduce a parameter $\varepsilon \in (0,1]$, an interval $\Omega_\varepsilon \equiv [-\varepsilon l_1/2, \varepsilon l_1/2] \times [-\varepsilon l_2/2, \varepsilon l_2/2]$, ε -cell $\Omega_\varepsilon(\mathbf{x}) \equiv \mathbf{x} + \Omega_\varepsilon$, $\mathbf{x} \in \Pi$. For function $\tilde{f}(\mathbf{x}, \cdot) \in H^1(\Omega)$, $\square \mathbf{x} \in \Pi$, we define $\tilde{f}_\varepsilon(\mathbf{x}, \mathbf{y}) \equiv \tilde{f}(\mathbf{x}, \mathbf{y}/\varepsilon)$, $\tilde{f}_\varepsilon(\mathbf{x}, \cdot) \in H^1(\Omega_\varepsilon) \subset H^1(\Omega)$, $\mathbf{y} \in \Omega_\varepsilon(\mathbf{x})$. Functions $h^A(\cdot)$, $h^A(\cdot) \in HO_\delta^2(\Pi, \Omega)$, $A=1, \dots, N$, have their periodic approximations $\tilde{h}^A(\mathbf{x}, \cdot)$, given by $\tilde{h}_\varepsilon^A(\mathbf{x}, \mathbf{y}) \equiv \tilde{h}^A(\mathbf{x}, \mathbf{y}/\varepsilon)$, $\mathbf{y} \in \Omega_\varepsilon(\mathbf{x})$.

The fundamental assumption of the asymptotic modelling in the *asymptotic decomposition* for the deflection $w(\mathbf{x}, t)$,

$$w_\varepsilon(\mathbf{x}, \mathbf{y}, t) = U(\mathbf{y}, t) + \varepsilon^2 \tilde{h}_\varepsilon^A(\mathbf{x}, \mathbf{y}) Q^A(\mathbf{y}, t), \quad (6)$$

where $\mathbf{y} \in \Omega_\varepsilon(\mathbf{x})$, $t \in (t_0, t_1)$, functions w , U , Q^A ($A=1, \dots, N$) are continuous and bounded in Π with their derivatives.

Using the assumption (6) and the limit passage $\varepsilon \rightarrow 0$, after some manipulations we obtain the equations of the *asymptotic model* in the form:

$$\begin{aligned} & \partial_{\alpha\beta}(<\!d_{\alpha\beta\gamma\delta}\!> - \\ & - <\!d_{\alpha\beta\gamma\delta}\partial_{\gamma\delta}h^B\!><\!d_{\alpha\beta\gamma\delta}\partial_{\alpha\beta}h^A\partial_{\gamma\delta}h^B\!>^{-1}<\!d_{\alpha\beta\gamma\delta}\partial_{\alpha\beta}h^A\!>\partial_{\gamma\delta}U) + \\ & + <\!\mu\!>\ddot{U} - <\!\vartheta\!>\partial_{\alpha\alpha}\ddot{U} = <\!p\!>, \\ & Q^B = - <\!d_{\alpha\beta\gamma\delta}\partial_{\alpha\beta}h^A\partial_{\gamma\delta}h^B\!>^{-1}<\!d_{\alpha\beta\gamma\delta}\partial_{\gamma\delta}h^A\!>\partial_{\alpha\beta}U. \end{aligned} \quad (7)$$

These equations have smooth, slowly-varying coefficients in the contrast to equation (2). The effect of the microstructure size is neglected.

The last model presented in this paper is the *combined asymptotic-tolerance model*, cf [10, 6].

At the beginning we apply the asymptotic modelling procedure. Because the macrodeflection U is the solution to equation (7)₁ and the fluctuation amplitudes Q^A are determined by relation (7)₂, we have the known following function

$$w_0(\mathbf{x}, t) = U(\mathbf{x}, t) + h^A(\mathbf{x}) Q^A(\mathbf{x}, t). \quad (8)$$

The next step of this modelling procedure is to apply the tolerance modelling procedure. Using the known function $w_0(\cdot, t)$ and introducing the known fluctuation shape functions $g^K(\cdot) \in FS_\delta^2(\Pi, \Omega)$, $K=1, \dots, N$, we assume the plate deflection as

$$w(\mathbf{x}, t) = w_0(\mathbf{x}, t) + g^K(\mathbf{x}) V^K(\mathbf{x}, t), \quad (8)$$

where V^K are slowly-varying unknown functions in \mathbf{x} .

Finally, after some manipulations, we arrive at the system of equations for *the asymptotic-tolerance model*, which can be written in the following form:

$$\begin{aligned} & \partial_{\alpha\beta} ((< d_{\alpha\beta\gamma\delta} > - \\ & - < d_{\alpha\beta\gamma\delta} \partial_{\gamma\delta} h^B > < d_{\alpha\beta\gamma\delta} \partial_{\alpha\beta} h^A \partial_{\gamma\delta} h^B >^{-1} < d_{\alpha\beta\gamma\delta} \partial_{\alpha\beta} h^A >) \partial_{\gamma\delta} U) + \\ & + < \mu > \ddot{U} - < \theta > \partial_{\alpha\alpha} \ddot{U} = < p >, \\ & < d_{\alpha\beta\gamma\delta} \partial_{\alpha\beta} g^K \partial_{\gamma\delta} g^J > V^J + (< \mu g^K g^J > + < \mu \partial_\alpha g^K \partial_\beta g^J >) \ddot{V}^J = \\ & = < pg^K > - < d_{\alpha\beta\gamma\delta} \partial_{\alpha\beta} g^K \partial_{\gamma\delta} w_0 >. \end{aligned} \quad (9)$$

This model makes it possible to analyse the effect of the microstructure size on vibrations of the plates under consideration.

5. Conclusions

In this paper three modelling procedures are applied to the known differential equation of Kirchhoff-type plates with functionally graded structure. These procedures make it possible to replace the governing equation with non-continuous, tolerance-periodic coefficients by the systems of differential equations with slowly-varying, continuous coefficients for each model.

All three models can be used to analyse various dynamic problems of functionally graded plates.

The tolerance model, which describes the effect of the microstructure size, makes it possible to investigate not only macrovibrations, but also microvibrations, which are related to the microstructure of the functionally graded plates.

Also the governing equations of the combined asymptotic-tolerance model take into account the effect of the microstructure size on vibrations of these plates.

The third presented model, the asymptotic model, neglecting the aforementioned effect, can describe only macrovibrations of the plates.

Acknowledgments

This contribution is supported by the National Science Centre of Poland under grant No. 2011/01/N/ST8/07758.

References

1. Ł. Domagalski, J. Jędrysiak, *On the elastostatics of thin periodic plates with large deflections*, Meccanica, **47** (2012) 1659-1671.
2. J. Jędrysiak, *Higher order vibrations of thin periodic plates*, Thin-Walled Structures, **47** (2009) 890-901.

3. J. Jędrysiak, *Thermomechanics of laminates, plates and shells with functionally graded structure*, Lodz, Publishing House of Lodz University of Technology 2010 [in Polish].
4. J. Jędrysiak, B. Michalak, *On the modelling of stability problems for thin plates with functionally graded structure*, Thin-Walled Structures, **49** (2011) 627-635.
5. M. Kaźmierczak, J. Jędrysiak, *Tolerance modeling of vibrations of thin functionally graded plates*, Thin-Walled Structures, **49** (2011) 1295-1303.
6. M. Kaźmierczak, J. Jędrysiak, *A new combined asymptotic-tolerance model of vibrations of thin transversally graded plates*, Engineering Structures, **46** (2013) 322-331.
7. B. Michalak, *Dynamics and stability of wavy-type plates*, Lodz, Publishing House of Lodz University of Technology 2001 [in Polish].
8. B. Michalak, *Thermomechanics of solids with a certain inhomogeneous microstructure*, Lodz, Publishing House of Lodz University of Technology 2011 [in Polish].
9. Cz. Woźniak, B. Michalak, J. Jędrysiak, *Thermomechanics of heterogeneous solids and structures*, Lodz, Publishing House of Lodz University of Technology 2008.
10. Cz. Woźniak, et al. (eds.), *Mathematical modeling and analysis in continuum mechanics of microstructured media*, Gliwice, Publishing House of Silesian University of Technology 2010.

Fluctuations of Multi-section Aboveground Pipeline Region Under the Influence of Moving Diagnostic Piston

Lidiya KHARCHENKO

Lviv Polytechnic National University

Institute of Computer Science and Information Technology

St. Bandery str., 12, 79013 Lviv, Ukraine

lida.kharchenko@gmail.com

Yevhen KHARCHENKO

University of Warmia and Mazury in Olsztyn, The Faculty of Technical Sciences

Oczapowskiego str., 11, 10-719 Olsztyn, Poland

kharchen@wp.pl

Abstract

A mathematical model of transverse fluctuations of the pipeline straight section is considered in this article. Such fluctuations occur during the movement of diagnostic piston in the pipeline. The analysis is based on the method of generalized displacements. This method provides setting modes of links with distributed parameters according to the boundary conditions. Diagnostic piston is considered as a solid in the calculation model. The equations of mechanical systems motion are derived by the Lagrange scheme equations of the second kind. As the result, we illustrate the influence of the mechanical system parameters and the speed of the piston on the pipeline section deflections, bending moments and stresses in the pipe.

Keywords: mechanical fluctuations, multi-section region of the pipeline, diagnostic piston

1. Introduction

Analysis of oscillatory phenomena in mechanical systems under the action of moving loads is an important problem of modern dynamics of machines and structures [1–8, 10–12]. Its practical value is explained by the need to improve methods of lifting and transport systems calculation, mechanical transmission with flexible links, pipelines, bridges etc. Problem solving of such systems dynamics using continuum computational models is reduced to the integration of partial differential equations with moving boundary conditions [3, 6, 10, 12]. Mathematical models in the form of integral equations are used in studies of fluctuations of rods and filaments of variable length [7].

Building of closed analytical solutions of the equations of motion for these cases is associated with considerable mathematical difficulties. It is only feasible for relatively simple systems. Links of such systems have constant elastic-inertial parameters, and the laws of motion of the boundary conditions are given. Analysis of dynamic processes in real load carrying structures appropriate to perform with the use of mechanical sampling units, which greatly simplifies the problem solving. Method of generalized displacements [9] is quite effective. This method is based on presetting of modes of lengthy items. It allows to describe oscillatory processes by ordinary differential equations through the use of amplitude functions coefficients as generalized coordinates. This approach was successfully tested in the study of the dynamics of continuum-discrete

mechanical systems with lengthy load carrying elements. In this work, it develops on the example of transverse fluctuations of multi-section part of the pipeline under the influence of moving diagnostic piston.

2. Mathematical model of bending fluctuations of multi-section part of the pipeline under the influence of moving diagnostic piston

The mechanical system that includes multi-section part of a pipeline and intelligent moving piston is shown schematically in figure 1, where l – the total length of the part; l_1, l_2, \dots, l_p – distance from the left edge of the area corresponding to the intermediate supports; m_k, J_k, c_k, v_k ($k = 1, 2, \dots, p$) – mass, central moments of inertia, stiffness and viscous friction coefficients of reference sites; m, J – mass and central moment of inertia of the diagnostic piston; v – speed of the piston, which we assume constant; xOy – coordinate system, where we analyse bending fluctuation of the pipeline; x_m – coordinate of the mass center of the diagnostic piston. Density and modulus of elasticity of pipe material are designated as ρ and E ; area and the axial moment of inertia of the cross-section tube as A and I_z .

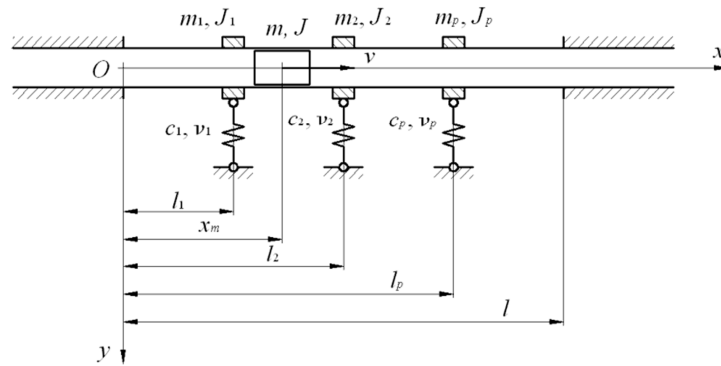


Figure 1. Diagram of the above-ground sections of the pipeline with a moving diagnostic piston

The function, that describes the curved axis of the pipeline section, is presented in the form

$$y(x, t) = \sum_{i=1}^n Y_i(t) \cdot \psi_i(x), \quad (1)$$

where t – time; $y(x, t)$ – deflection of the pipeline; $\psi_i(x)$ – shapes of oscillations, which must be chosen so that the boundary conditions are fulfilled at the ends of sections; $Y_i(t)$ – amplitude coefficients; n – number of degrees of mechanical system freedom, which is equal to the number of discounted modes of pipeline.

We set depending $\psi_i(x)$ as its own form of transverse fluctuation of rod with pinched ends,

$$\psi_i(x) = \psi_{1i}(x) - \frac{\psi_{1i}(l)}{\psi_{2i}(l)} \cdot \psi_{2i}(x) \quad (i=1, 2, \dots, n), \quad (2)$$

where

$$\psi_{1i}(x) = \cos k_i x - \operatorname{ch} k_i x; \quad \psi_{2i}(x) = \sin k_i x - \operatorname{sh} k_i x. \quad (3)$$

Results of $k_i l$, which are calculated for lower ten own forms:

i	1	2	3	4	5	6	7	8	9	10
$k_i l$	4,730	7,853	10,996	14,137	17,279	20,420	23,562	26,704	29,846	32,989

Taking the generalized coordinate values $Y_i(t)$ ($i = 1, 2, \dots, n$), we apply the Lagrange equations of the second kind to describe the motion of a mechanical system,

$$\frac{d}{dt} \left(\frac{\partial T}{\partial \dot{q}_i} \right) - \frac{\partial T}{\partial q_i} + \frac{\partial \Pi}{\partial q_i} + \frac{\partial \Phi}{\partial \dot{q}_i} = Q_i \quad (i = 1, 2, \dots, n), \quad (4)$$

where T and Π – kinetic and potential energies; q_j – generalized coordinate; Φ – Rayleigh function; Q_j – non-conservative generalized force.

The kinetic energy is written in the form of

$$\begin{aligned} T = & \frac{\rho A}{2} \int_0^l \left(\frac{\partial y(x,t)}{\partial t} \right)^2 dx + \frac{\rho I_z}{2} \int_0^l \left(\frac{\partial^2 y(x,t)}{\partial x \partial t} \right)^2 dx + \\ & + \frac{m}{2} \left\{ \left[\frac{dx_m(t)}{dt} \right]^2 + \left[\left(\frac{\partial y(x,t)}{\partial x} \right)_{x=x_m} \cdot \frac{dx_m(t)}{dt} + \frac{\partial y(x_m,t)}{\partial t} \right]^2 \right\} + \\ & + \frac{J}{2} \left[\frac{\partial}{\partial x_m} \left(\left(\frac{\partial y(x,t)}{\partial x} \right)_{x=x_m} \right) \cdot \frac{dx_m(t)}{dt} + \left(\frac{\partial^2 y}{\partial x \partial t} \right)_{x=x_m} \right]^2 + \\ & + \frac{1}{2} \sum_{k=1}^p m_k \left[\frac{\partial y(l_k,t)}{\partial t} \right]^2 + \frac{1}{2} \sum_{k=1}^p J_k \left[\left(\frac{\partial^2 y(x,t)}{\partial x \partial t} \right)_{x=l_k} \right]^2. \end{aligned} \quad (5)$$

The potential energy of pipe section deformation is expressed as

$$\Pi = \frac{EI_z}{2} \int_0^l \left(\frac{\partial^2 y(x,t)}{\partial x^2} \right)^2 dx + \frac{1}{2} \sum_{k=1}^p c_k [y(l_k,t)]^2. \quad (6)$$

Rayleigh function, which is used to calculate the energy dissipation of fluctuations

$$\Phi = \frac{\nu I_z}{2} \int_0^l \left[\frac{\partial^3 y(x,t)}{\partial x^2 \partial t} \right]^2 dx + \frac{1}{2} \sum_{k=1}^p \nu_k \left[\frac{\partial y(l_k,t)}{\partial t} \right]^2, \quad (7)$$

where v – coefficient of hysteresis material deviation from Hooke's law.

Considering the relationships (1), we summarize the expressions (5) – (7) to the following form

$$\begin{aligned}
 T &= \frac{\rho A}{2} \int_0^l \left[\sum_{i=1}^n \dot{Y}_i(t) \cdot \psi_i(x) \right]^2 dx + \frac{\rho I_z}{2} \int_0^l \left[\sum_{i=1}^n \dot{Y}_i(t) \cdot \psi'_i(x) \right]^2 dx + \\
 &+ \frac{m}{2} \left\{ [v(t)]^2 + \left[v(t) \sum_{i=1}^n Y_i(t) \cdot \psi'_i(x_m) + \sum_{i=1}^n \dot{Y}_i(t) \cdot \psi_i(x_m) \right]^2 \right\} + \\
 &+ \frac{J}{2} \left[v(t) \sum_{i=1}^n Y_i(t) \cdot \psi''_i(x_m) + \sum_{i=1}^n \dot{Y}_i(t) \cdot \psi'_i(x_m) \right]^2 + \\
 &\frac{1}{2} \sum_{k=1}^p m_k \left[\sum_{i=1}^n \dot{Y}_i(t) \psi_i(l_k) \right]^2 + \frac{1}{2} \sum_{k=1}^p J_k \left[\sum_{i=1}^n \dot{Y}_i(t) \psi'_i(l_k) \right]^2; \\
 \Pi &= \frac{EI_z}{2} \int_0^l \left[\sum_{i=1}^n Y_i(t) \cdot \psi''_i(x) \right]^2 dx + \frac{1}{2} \sum_{k=1}^p c_k \left[\sum_{i=1}^n Y_i(t) \psi_i(l_k) \right]^2; \\
 \Phi &= \frac{vI_z}{2} \int_0^l \left[\sum_{i=1}^n \dot{Y}_i(t) \cdot \psi''_i(x) \right]^2 dx + \frac{1}{2} \sum_{k=1}^p v_k \left[\sum_{i=1}^n \dot{Y}_i(t) \psi_i(l_k) \right]^2. \tag{8}
 \end{aligned}$$

We transform relationships (8) to a suitable form for the equations of mechanical system motion,

$$\begin{aligned}
 T &= \frac{\rho A}{2} \sum_{i=1}^n \sum_{j=1}^n a_{ij} \dot{Y}_i \dot{Y}_j + \frac{\rho I_z}{2} \sum_{i=1}^n \sum_{j=1}^n b_{ij} \dot{Y}_i \dot{Y}_j + \\
 &+ \frac{1}{2} \sum_{i=1}^n \sum_{j=1}^n (ma_{mij} + Jb_{mij}) \dot{Y}_i \dot{Y}_j + v(t) \sum_{i=1}^n \sum_{j=1}^n (md_{mij} + Je_{mij}) Y_i \dot{Y}_j + \\
 &+ \frac{[v(t)]^2}{2} \sum_{i=1}^n \sum_{j=1}^n (mb_{mij} + Jc_{mij}) Y_i Y_j + \frac{m[v(t)]^2}{2} + \\
 &+ \frac{1}{2} \sum_{k=1}^p \sum_{i=1}^n \sum_{j=1}^n (m_k a_{kij} + J_k b_{kij}) \dot{Y}_i \dot{Y}_j; \\
 \Pi &= \frac{EI_z}{2} \sum_{i=1}^n \sum_{j=1}^n c_{ij} Y_i Y_j + \frac{1}{2} \sum_{k=1}^p \sum_{i=1}^n \sum_{j=1}^n c_k a_{kij} Y_i Y_j; \\
 \Phi &= \frac{vI_z}{2} \sum_{i=1}^n \sum_{j=1}^n c_{ij} \dot{Y}_i \dot{Y}_j + \frac{1}{2} \sum_{k=1}^p \sum_{i=1}^n \sum_{j=1}^n v_k a_{kij} \dot{Y}_i \dot{Y}_j, \tag{9}
 \end{aligned}$$

where

$$\begin{aligned}
 a_{ij} &= \int_0^l \psi_i(x) \psi_j(x) dx ; \quad b_{ij} = \int_0^l \psi_i'(x) \psi_j'(x) dx ; \quad c_{ij} = \int_0^l \psi_i''(x) \psi_j''(x) dx ; \\
 a_{mij} &= \psi_i(x_m) \psi_j(x_m) ; \quad b_{mij} = \psi_i'(x_m) \psi_j'(x_m) ; \quad c_{mij} = \psi_i''(x_m) \psi_j''(x_m) ; \\
 d_{mij} &= \psi_i'(x_m) \psi_j(x_m) ; \quad e_{mij} = \psi_i''(x_m) \psi_j'(x_m) ; \\
 a_{kij} &= \psi_i(l_k) \psi_j(l_k) ; \quad b_{kij} = \psi_i'(l_k) \psi_j'(l_k) . \tag{10}
 \end{aligned}$$

Differentiating the expression (9) and substituting the obtained results to the equality (4)

$$A\ddot{Y} + B\dot{Y} + CY = Q , \tag{11}$$

where \dot{Y} – matrix-column of generalized coordinates,

$$Y = \text{col}[Y_1(t), Y_2(t), \dots, Y_n(t)] ;$$

A, B, C – square matrices,

$$\begin{aligned}
 A_{ij} &= \rho A a_{ij} + \rho I_z b_{ij} + m a_{mij} + Y b_{mij} + \sum_{k=1}^p (m_k a_{kij} + J_k b_{kij}) , \quad B_{ij} = v I_z c_{ij} + \sum_{k=1}^p v_k a_{kij} , \\
 C_{ij} &= \dot{v}(t)(md_{mij} + Ye_{mij}) - [N(t)]^2 (mb_{ij} + Yc_{mij}) + EI_z c_{ij} + \sum_{k=1}^p c_k a_{kij} ;
 \end{aligned}$$

Q – matrix-column of generalized forces,

$$Q = \text{col}[Q_1, Q_2, \dots, Q_n] .$$

To determine the generalized forces of the system, we write the vertical movement of the gravity center of the diagnostic piston as

$$y(x_m, t) = \sum_{i=1}^n Y_i \psi_i(x_m) . \tag{12}$$

Virtual work of weight force of piston follows the relationship

$$\delta A = mg \cdot \delta y(x_m, t) , \tag{13}$$

where $\delta y(x_m, t)$ – virtual displacement, which is found with considering (12),

$$\delta y(x_m, t) = \sum_{i=1}^n \frac{\partial y(x_m, t)}{\partial Y_i} \delta Y_i = \sum_{i=1}^n \psi_i(x_m) \delta Y_i , \tag{14}$$

moreover, δY_i ($i = 1, 2, \dots, n$) – variations of the generalized coordinates.

With taking into account (13), (14) write the virtual work as

$$\delta A = mg \sum_{i=1}^n \psi_i(x_m) \delta Y_i = \sum_{i=1}^n Q_i \delta Y_i . \quad (15)$$

As follows from the relationship (15), generalized forces are defined by the dependencies

$$Q_i = mg\psi_i(x_m) . \quad (16)$$

Thus, the non-stationary bending vibration of the aboveground pipeline section under the moving diagnostic piston are described by the differential equations (11), solution of which perform with consideration the expressions of the generalized forces (16) and the corresponding initial conditions. If at $t = 0$ the mechanical system is at resting state, then the value of the generalized coordinates and their time derivative are equal to zero, i.e.,

$$Y_i(0) = 0 ; \quad V_i(0) = \dot{Y}_i(0) = 0 \quad (i=1, 2, \dots, n) . \quad (17)$$

For the application of the widespread software for solving this task, transform the system of differential equations (11) to the normal form of the Cauchy:

$$\dot{X} = D(t, x) , \quad (18)$$

where $X, D(t, x)$ – matrix-column,

$$\begin{aligned} X &= \text{col}(Y, V); \\ D(t, x) &= \text{col}[V, A^{-1}(-BV - CY + Q)] . \end{aligned}$$

Thus, the analysis of dynamic phenomena in the mechanical system reduces to the solving the Cauchy problem for a system of $2n$ differential equations (18) with taking into account the dependencies for determination the modes of the pipeline section (2), (3), the generalized forces (16) and the initial conditions (17). After finding the generalized coordinates $Y_i(t)$ ($i = 1, 2, \dots, n$) determine pipeline section deflection by the formula (1) and bending moments – by the ratio

$$M(x, t) = EI_z \sum_{i=1}^n Y_i(t) \cdot \psi_i''(x) , \quad (19)$$

which follows directly from the theory of technical bending.

Taking into account dependencies (19), the maximum bending stress in the cross section of the pipeline is calculated as

$$\sigma(x, t) = \frac{M(x, t)}{W_z} = \frac{Ed}{2} \sum_{i=1}^n Y_i(t) \cdot \psi_i''(x) ,$$

where W_z and d – the resistance moment and the outer diameter of tube cross-section.

3. The calculation results of the dynamic processes and their analysis

The dynamic phenomena in the multi-section straight pipeline area with a length of 47 m, an outer diameter of 529 mm and a wall thickness of 10 mm during the passage of the diagnostic piston with mass of 1200 kg at a speed of 5 m/s illustrate the graphical dependencies on the Fig. 2.

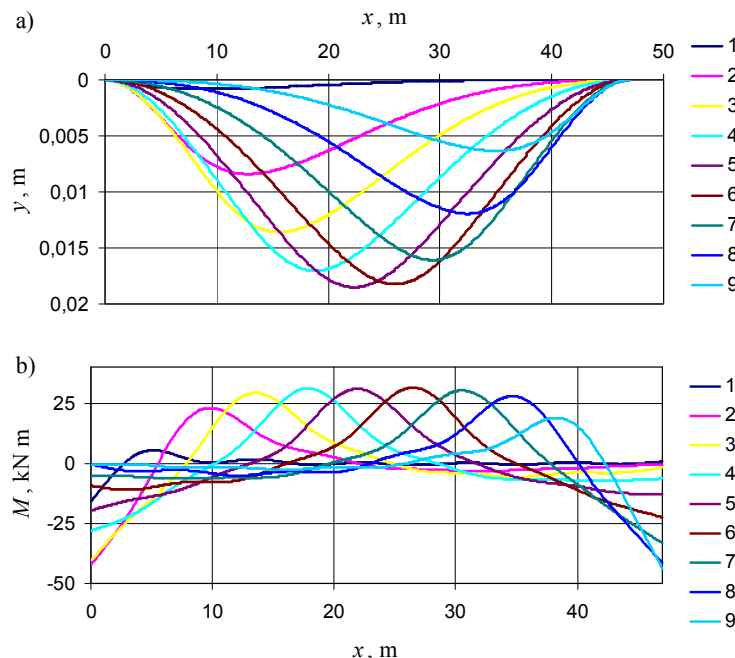


Figure 2. The dependencies of deflections (a) and bending moments (b) from the longitudinal coordinates of the pipeline section. Curves 1–9 correspond to the time points: 0,94 s; 1,88 s; 2,82 s; 3,76 s; 4,7 s; 5,64 s; 6,58 s; 7,52 s; 8,46 s

During the calculation accept that the ends of the pipeline sections are strangulated, in addition, the pipe is based on five intermediate pillars with coordinates $l_1 = 7.833$ m; $l_2 = 15.667$ m; $l_3 = 23.500$ m; $l_4 = 31.333$ m; $l_5 = 39.167$ m. The supporting nodes have equal masses $m_i = 200$ kg, moments of inertia $J_i = 12 \text{ kg}\cdot\text{m}^2$, stiffness $c_i = 2 \cdot 10^5 \text{ N/m}$ and the friction coefficients $v_i = 2 \cdot 10^3 \text{ Ns/m}$, where $i = 1, 2, \dots, 5$. Curves 1, 2, ..., 9 in Fig. 2 correspond to the time points when the diagnostic piston has passed the way 0,1 l ; 0,2 l ; ...; 0,9 l .

The greatest deflection value of 18.613 mm has the point on the axis of the pipe with coordinate $x = 23.400$ m at the time moment $t = 4,675$ s. Significant bending moments that may affect on the strength of the pipeline, arise as in outer cross sections of the area, as well as in cross sections located in the middle of the area. The largest absolute value of the bending moment was 43.814 kN·m and appeared in cross section with coordinate

$x = 47$ m at the time $t = 8,016$ s. The maximum bending stress reached value of 21.102 MPa. Note that in the absence of intermediate pillars maximum deflection is 55.944 mm, the maximum absolute value of the bending moment – 83.343 kN·m, the maximum stress – 40.139 MPa. Thus, the installation of the intermediate pillars contributes significantly on stress and strain reducing of the aboveground sections of the pipelines.

The built mathematical model of the bending vibration of the multi-section constructions makes it possible to choose required number of the intermediate pillars and rational values of their stiffness during the design of the aboveground pipeline sections for ensuring the strength of the pipe and supporting constructions. In the operation of the built pipelines proposed calculation algorithm can be used to determine the permissible speed of the diagnostic piston.

References

1. C.I. Bajer and B. Dyniewicz, *Space-time approach to numerical analysis of a string with a moving mass*. Int. J. Numer. Meth. Engng., 76(10) (2008) 1528-1543.
2. B. Dyniewicz and C.I. Bajer, *New feature of the solution of a Timoshenko beam carrying the moving mass particle*. Arch. Mech., 62(5) (2010) 327-341.
3. L. Fryba, *Vibrations of solids and structures under moving loads*. Thomas Telford House, 1999.
4. Jia Jang Wu, *Study on the inertia effect of helical spring on the absorber on suppressing the dynamic responses of a beam subjected to a moving load*. J. os Sound and Vibration, 297 (2006) 981-999.
5. В.В. Болотин, *Задача о колебаниях мостов под действием подвижной нагрузки*. Механика и машиностроение, № 4 (1961) 109-115.
6. А.И. Весницкий. *Волны в системах с движущимися границами и нагрузками*. М., ФИЗМАТГИЗ, 2001, 320 с.
7. О.А. Горошко, Г.Н. Савин, *Введение в механику деформируемых одномерных тел переменной длины*. К., Наукова думка, 1971, 224 с.
8. И.И. Иванченко, *Метод расчета на подвижную нагрузку стержневых систем, моделирующих мосты*. Изв. АН РФ, Механика твердого тела. №4 (2001) 151-165.
9. Р. Клаф, Дж Пензиен, *Динамика сооружений*. М., Стройиздат, 1979, 320 с.
10. А. Я. Коган, *Динамика пути и его взаимодействие с подвижным составом*. М., Транспорт, 1997, 326 с.
11. С.С. Кохманюк, Е. Г. Янютин, Л. Г. Романенко, *Колебания деформируемых систем при импульсивных и подвижных нагрузках*. К., Наукова думка, 1980, 231 с.
12. С.П. Тимошенко, Д. Х. Янг, У. Уивер, *Колебания в инженерном деле*. М., Машиностроение, 1985, 472 с.
13. А.П. Филиппов, *Колебания деформируемых систем*. М., Машиностроение, 1970, 736 с.

Free Vibration of Structures by Radial Basis Function – Pseudospectral Method

Artur KROWIAK

Cracow University of Technology, Institute of Computing Science
Al. Jana Pawła II 37, 31-864 Kraków, Poland
krowiak@mech.pk.edu.pl

Abstract

The paper deals with the use of the radial basis function-pseudospectral method in vibration analysis of two-dimensional mechanical structures. The method combines meshless features of radial basis function (RBF) with efficiency and simplicity of the pseudospectral method. In present work the main emphasis is laid on appropriate assumption of the interpolant for the sought function due to the number of the boundary conditions in analysed problem. This interpolation function enables to obtain the weighting coefficients for derivative approximation in a governing equation. The method is applied to free vibration analysis of arbitrarily shaped membrane and plate.

Keywords: meshless methods, radial basis function, pseudospectral methods

1. Introduction

Due to some problems encountered during the application of the mesh discretization numerical techniques, in recent years, some methods that discretize the domain with scattered nodes are strongly developed. Many formulations of these so-called meshless techniques have been applied to solve problems from various disciplines of science. An interesting overview can be found in [1,2]. Some formulations of these methods take advantage of radial basis functions (RBF) [3] to approximate the sought solution of the problem analysed. Since the work of Hardy [4], it is well-known that these types of functions are very useful in scattered data approximation.

An interesting example of the mentioned methods is the approach that combines RBF approximation with pseudospectral method [5,6] (RBF-PS). In this approach, derivatives in the governing equation are approximated by a linear weighted sum of unknown function values from all over domain

$$\frac{\partial^r u(\mathbf{x})}{\partial x^p \partial y^q} \Big|_{\mathbf{x}=\mathbf{x}_i} = \sum_{j=1}^N a_{ij}^{(r)} u_j \quad (1)$$

where $a_{ij}^{(r)}$ are the weighting coefficients for the r th order derivative and N denotes the number of nodes $\mathbf{x}=(x, y)$. With these coefficients and by the use of collocation technique, the governing equation and boundary conditions are discretized reducing the problem to the set of algebraic equations. Since the method involves all nodal function values to approximate a derivative at a node, the method leads to relatively fast convergence, what has been proved by the examples [5].

2. RBF-PS for lower order equations

To obtain the weighting coefficients one has to start from the approximation of the unknown function u by the use of RBF

$$u(\mathbf{x}) = \sum_{j=1}^N \alpha_j \varphi(\|\mathbf{x} - \xi_j\|) \quad (2)$$

where α_j are the interpolation coefficients and $\varphi(\|\mathbf{x} - \xi_j\|)$ denote the radial function.

There are different types of RBS [3,5], but their common feature is the dependence on the distance between a collocation point \mathbf{x} and the point ξ_j called as a center $\mathbf{x}, \xi_j \in \mathbb{D}^n$.

In this method, the centers are also considered as the collocation points.

From the interpolation problem one can express the interpolation coefficients in terms of function values, what can be put in the following matrix form

$$\mathbf{a} = \Phi^{-1} \mathbf{u} \quad (3)$$

where \mathbf{a} denotes the vector of interpolation coefficients, \mathbf{u} is the vector that contains the function values at the nodes and the entries of the interpolation matrix has the form:

$$\Phi_{ij} = \varphi(\|\mathbf{x}_i - \xi_j\|) \Big|_{\xi=\mathbf{x}_j}, \quad i, j = 1, \dots, N.$$

Computing appropriate derivative of the interpolant (2) at each node of the domain and introducing the expression (3) one gets the weighting coefficients for the r th order derivative approximation

$$\mathbf{u}^{(r)} = \Phi^{(r)} \Phi^{-1} \mathbf{u} \quad (4)$$

where the entries of matrix $\Phi^{(r)}$ are as follows: $\Phi_{ij}^{(r)} = \frac{\partial^r \varphi(\|\mathbf{x} - \xi\|)}{\partial x^p \partial y^q} \Big|_{\substack{\xi=\mathbf{x}_j \\ \mathbf{x}=\mathbf{x}_i}}$

Once the weighting coefficients $\mathbf{A} = \Phi^{(r)} \Phi^{-1}$ are determined, the differential equation can be discretized.

In the method, the discretization of the mathematical model of a problem is carried out by the collocation technique. Therefore the approach presented can be directly applied to lower order equations that possess one boundary condition at the edge.

In the present work the method is used to solve eigenvalue problem for pre-stretched uniform membrane, for which the governing equation and boundary condition have the form

$$\Delta W = -\Lambda^2 W, \quad W = 0 \text{ for } \mathbf{x} \in \partial\Gamma \quad (5)$$

where Δ is Laplacian operator, W is the mode of vibration and $\Lambda = \omega \sqrt{\rho/T}$ is the wave-number (ω – circular frequency, ρ – mass per unit length, T – uniform tension per unit

length). The membrane of the shape presented in Fig.1 is analysed in the work. Irregularly distributed nodes are applied to discretize the domain – an example of the node distribution is shown in Fig. 1.

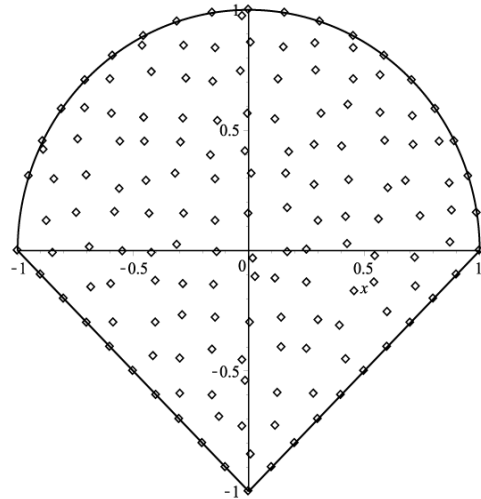


Figure 1. The membrane analysed in the work with an example of the node distribution

Using multiquadratics RBF, the weighting coefficients, described in general way by Eq. (4), for Laplacian operator have been determined. With these coefficients Eq. (5) is reduced to standard eigenvalue problem of the form

$$\mathbf{A}\mathbf{W} = -\Lambda^2 \mathbf{W} \quad (6)$$

where vector \mathbf{W} contains the nodal function values and \mathbf{A} is the matrix reflecting the discrete form of the Laplacian operator.

The wavenumbers obtained from (6) are presented in Tab. 1 and some modes of vibration are shown in Fig. 2.

Table 1. Wavenumbers of the membrane for various numbers of nodes assumed.

	Λ_1	Λ_2	Λ_3	Λ_4	Λ_5
$N = 155$	2.7093	4.2283	4.3580	5.5679	5.9328
$N = 221$	2.7092	4.2263	4.3577	5.5616	5.9340
$N = 314$	2.7099	4.2292	4.3579	5.5676	5.9337
$N = 390$	2.7096	4.2278	4.3579	5.5648	5.9336
Reference results [9]	2.7097	4.2279	4.3579	5.5649	5.9336

The results presented in Tab. 1 are in great agreement with the reference values. The method indicates a proper convergence trend.

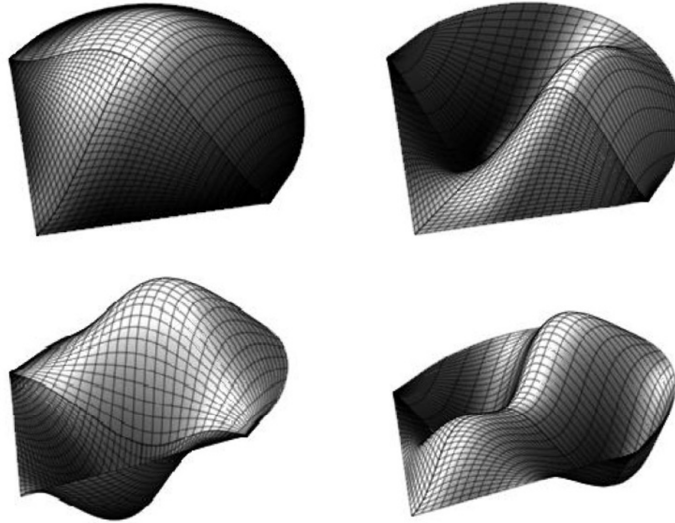


Figure 2. First four modes of vibration of the membrane

3. RBF-PS for higher order equations

For higher order equation, where more than one boundary condition is defined at an edge, one should write more than one discrete equation for each boundary node. It leads to overdetermined system of algebraic equations. Although this system can be solved by least squares technique this approach does not reflect the main idea of the method based on the interpolating function.

To make the method be conveniently applied for higher order equations, one can extend the interpolation formula (2) introducing the additional degrees of freedom. These quantities should correspond to differential operators contained in boundary conditions. The approach can be viewed as a Hermite interpolation problem defined for RBF and in the case of two boundary conditions can be generally written as

$$u(\mathbf{x}) = \sum_{j=1}^{N^I} \alpha_j \varphi(\|\mathbf{x} - \xi\|) \Big|_{\xi=\mathbf{x}_j^I} + \sum_{j=1}^{N^B} \beta_j \left[B_1^\xi \varphi(\|\mathbf{x} - \xi\|) \right]_{\xi=\mathbf{x}_j^B} + \sum_{j=1}^{N^B} \gamma_j \left[B_2^\xi \varphi(\|\mathbf{x} - \xi\|) \right]_{\xi=\mathbf{x}_j^B} \quad (7)$$

where N^I and N^B denote the numbers of interior (\mathbf{x}_i^I) and boundary (\mathbf{x}_i^B) nodes, respectively, B_1^ξ and B_2^ξ are differential operators that act on the radial function treated as a function of ξ variable.

Following the same procedure as previous one can solve interpolation problem (7) and express the interpolation coefficients α_j , β_j , γ_j in terms of function values as well as the values of the derivatives of the function defined at boundaries. Then, by computing

appropriate derivative of the interpolant (7) at each interior node of the domain and introducing the expression for interpolation coefficients one obtains

$$\bar{\mathbf{u}}^{(r)} = \bar{\Phi}^{(r)} \bar{\Phi}^{-1} \bar{\mathbf{u}} \quad (8)$$

where the objects from Eq. (8) have the forms

$$\bar{\Phi}^{(r)} = \begin{bmatrix} \Phi_{L^r} & \Phi_{L^r B_1^x} & \Phi_{L^r B_2^x} \end{bmatrix}, \bar{\Phi} = \begin{bmatrix} \Phi & \Phi_{B_1^x} & \Phi_{B_2^x} \\ \Phi_{B_1^x} & \Phi_{B_1^x B_1^x} & \Phi_{B_1^x B_2^x} \\ \Phi_{B_2^x} & \Phi_{B_2^x B_1^x} & \Phi_{B_2^x B_2^x} \end{bmatrix}, \bar{\mathbf{u}}^{(r)} = \begin{bmatrix} \mathbf{u}_{L^r} \\ \mathbf{u}_{L^r B_1^x} \\ \mathbf{u}_{L^r B_2^x} \end{bmatrix}, \bar{\mathbf{u}} = \begin{bmatrix} \mathbf{u} \\ \mathbf{u}_{B_1^x} \\ \mathbf{u}_{B_2^x} \end{bmatrix}$$

In the above expressions L^r is the differential operator corresponding to the r th order derivative contained in governing equation, B_1^x and B_2^x denote the same differential operators as B_1^{ξ} and B_2^{ξ} , but acting on the radial function viewed as a function of x variable. The details of the approach as well as the entries of the objects presented can be found in [7].

Since vector $\bar{\mathbf{u}}$ in Eq. (8) contains the values of the derivatives defined at boundary nodes, all boundary conditions can be directly involved during discretization process.

The approach presented has been used in the work to solve the free vibration problem for thin, isotropic, plate of the shape presented in Fig. 3. Governing equation for this problem is as follows

$$\Delta^2 w = \Omega^2 w \quad (9)$$

where w denotes the form of vibration and Ω is the free vibration parameter related to free vibration frequency by the formula $\Omega = \omega a^2 \sqrt{\rho h/D}$ (ρ – density of the plate material, D – plate stiffness, h – plate thickness, a – characteristic plate dimension).

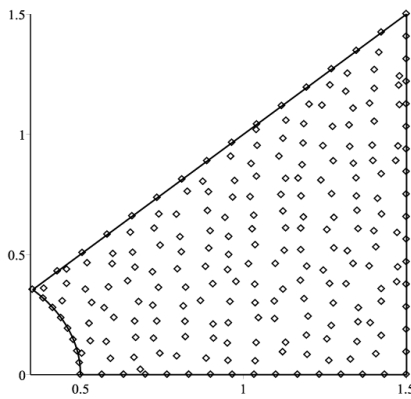


Figure 3. Triangular plate with corner cutout with an example of node distribution

In present paper, the plates with combination of simply supported and clamped boundary conditions are considered

$$w=0, \quad B^x w=0 \text{ for } \partial\Gamma \quad (10)$$

For simply supported edge (S) differential operator B^x has the form

$$B^x = (\cos^2(\theta) + \nu \sin^2(\theta)) \frac{\partial^2}{\partial x^2} + (\sin^2(\theta) + \nu \cos^2(\theta)) \frac{\partial^2}{\partial y^2} + 2(1-\nu) \cos(\theta) \sin(\theta) \frac{\partial^2}{\partial x \partial y}$$

and for the clamped edge (C) B^x is as follows

$$B^x = \cos(\theta) \frac{\partial}{\partial x} + \sin(\theta) \frac{\partial}{\partial y}$$

where θ is the angle between the normal to the plate boundary and the x -axis.

Adapting the approach presented in this section one can reduce Eq. (9) to algebraic problem of the following form

$$\mathbf{A}\mathbf{w}=\Omega^2\mathbf{w} \quad (11)$$

where vector \mathbf{w} contains the nodal function values at the inner nodes and the values of the function as well as the values of derivatives at boundary nodes and \mathbf{A} is the matrix reflecting the discrete form of the biharmonic operator.

Taking into account that only function values at interior nodes can have non zero values, appropriate columns of the matrix \mathbf{A} has to be deleted and then standard, algebraic eigenvalue problem can be solved.

The eigenvalues obtained for various configurations of boundary conditions are presented in the Tab. 2 and some chosen form of vibration are shown in Fig. 4.

Table 2. Results for the triangular plate with corner cutout

	Ω_1	Ω_2	Ω_3	Ω_4	Ω_5
SSSS					
$N=235, N'=175$	22.262	45.692	58.994	77.843	96.239
$N=323, N'=256$	23.198	47.163	60.624	79.699	98.017
Reference results	22.365	47.187	58.968	80.812	97.498
CCCC					
$N=235, N'=175$	41.655	71.250	87.967	110.389	130.327
$N=323, N'=256$	41.786	71.256	87.915	110.685	130.421
Reference results	41.787	71.256	87.896	110.688	130.415
SCSC					
$N=323, N'=256$	28.761	55.707	70.089	89.372	113.577
Reference results	28.869	57.071	69.634	91.974	113.957

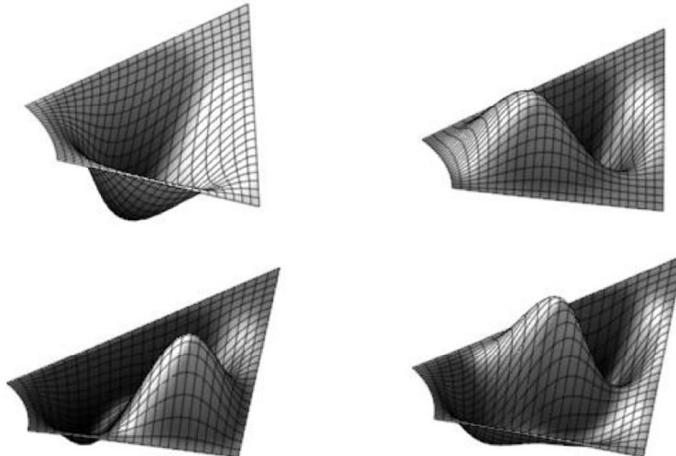


Figure 4. First four modes of vibration of triangular plate with corner cutout

The reference results presented in Tab. 2 have been obtained by the differential quadrature method combined with coordinate transformation. The details of this approach can be found in [8].

The results presented in Tab. 2 show great agreement with reference values. Regardless of the node distribution, the eigenvalues computed are very close to reference results for each configuration of boundary conditions assumed in the work.

4. Conclusions

In the paper the RBF-PS method is applied to free vibration analysis of two-dimensional structures. The basic approach of this method can be easily used for lower order equations, while an extension of this method can be conveniently applied for higher order equations that possess more than one boundary conditions at an edge. Due to the use of RBF, the discretization of the domain can be done by irregularly (randomly) distributed nodes. This feature facilitates the analysis of arbitrarily shaped structures. To show the usefulness of the method, the free vibration analysis for irregularly shaped membrane and plate has been carried out. The results indicate that the method has a potential to become an effective, meshless, numerical technique for wide range of problems.

References

1. T. Belytschko, Y. Krongauz, D. Organ, M. Flrming, P. Krysl, *Meshless methods: an overview and recent developments*, Comp. Meth. Appl. Mech. Eng., **139** (1996) 3-47.
2. G.R. Liu, *Meshlees Methods – Moving beyond the Finite Element Method*, CRC Press, Boca Raton, Florida, 2003.

3. M.D. Buhmann, *Radial Basis Functions: Theory and Implementations*, Cambridge University Press, Cambridge 2003.
4. R.L. Hardy, *Multiquadric equations of topography and other irregular surfaces*, J. Geophysics Res. **176** (1971) 1905-1915
5. G.E. Fasshauer, *Meshfree Approximation Methods with Matlab*, World Scientific Publishing, Singapore, 2007.
6. A.J.M Ferreira, G.E. Fasshauer, *Analysis of natural frequencies of composite plates by an RBF-pseudospectral method*, Compos. Struct., **79** (2007) 202-210.
7. A. Krowiak, *Hermite type RBF-DQ method applied to vibration analysis of plates*, Proceedings of the 12th Conference on Dynamical Systems: Theory and Applications, Łódź 2013, 391-400.
8. M. Malik, C.W. Bert, *Vibration analysis of plates with curvilinear quadrilateral planforms by DQM using blending functions*, J. Sound Vib., **230** (2000) 949-954.
9. S.W. Kang, J.M. Lee, Y.J. Kang, *Vibration analysis of arbitrarily shaped membranes using non-dimensional dynamic influence function*, J. Sound Vib., **221** (1999) 117-132.

Transmission Loss and Pressure Drop of Selected Range of Helicoidal Resonators

Wojciech ŁAPKA

Poznan University of Technology, Institute of Applied Mechanics

Jan Paweł II 24 Street, 61-139 Poznań, POLAND

wojciech.lapka@put.poznan.pl

Abstract

The paper presents the numerical analysis of transmission loss and pressure drop of acoustic helicoidal resonators with constant pitch to cylindrical duct diameter ratio and different number of helicoidal turns n . The ducted system consists of a straight cylindrical duct of constant diameter $d=0.125\text{m}$. The ratio of helicoidal pitch s to cylindrical duct diameter d equals $s/d=1.976$. Other geometrical relationships of helicoidal resonator, as a mandrel diameter d_m to duct diameter ratio $d_m/d=0.024$ and thickness g of helicoidal profile $g/d=0.0024$, were constant as well. The investigated range of numbers of helicoidal turns n was analyzed in the range from 0 to 2.0 for transmission loss parameter and from 0 to 1.0 for pressure drop. The values of normal inflow velocity v [m/s] equals 1, 5, 10, 15 and 20.

Keywords: helicoidal resonator, transmission loss, pressure drop, numerical analysis

1. Introduction

Helicoidal resonator is the newly patented invention [1] in the domain of passive silencers. It is an acoustic filter that attenuates sounds inside cylindrical duct due to its resonant properties. The sound attenuation is realized by the acoustic resonance inside helicoidal profile. The geometrical relationships between helicoidal profile, mandrel and duct diameter determine the acoustic properties of helicoidal resonators. Also its main property is the sound attenuation, and the next are flow properties, as the usually most important pressure drop.

The first predicted acoustic parameter of helicoidal resonators like twisted helicoidal screws with different pitches and turns inside 1m long cylindrical duct was a Noise Reduction (NR) in [2]. This parameter showed the sound pressure level difference between inlet and outlet of duct with screws and the conclusions underlined that the increase of the number of helicoidal turns results in bigger NR in the low- and mid-frequencies. But there were no any informations about band-stop filtering of noise by the helicoid inside duct. Thus, the Transmission Loss (TL) parameter was firstly used for analysis of acoustic attenuation performance of a round silencer with the helicoidal resonator at the inlet in [3]. The increase of TL for the range of helicoid pitch s to cylindrical duct diameter d , ratio s/d , from 0.4 to 8.0 were presented. Also the specific sound pressure levels (SPL) distribution inside the silencing system with selected helicoidal resonator for the highest value of the TL increase was showed. The fully compatible comparison of numerical and experimental SPL distributions for the same type and dimensions of helicoidal resonator was presented in [4].

Already well known Band Stop Filter (BSF) is the Helmholtz Resonator, and it can be substituted by the Helicoidal Resonator, as it was presented in [5]. There was introduced, that for some cases the helicoidal resonator can be much more efficient solution, when considering the sound attenuation inside duct, than the Helmholtz resonator - especially in large diameter cylindrical ducts. The next important step on the recognition of helicoidal resonators properties was the comparison of numerical and experimental acoustic attenuation performances. The simple experimental set-up was prepared to measure Insertion Loss (IL) parameter in [6]. Another time almost full compliance was observed, "almost" due to not so strong resonances in reality. But the range of frequencies of attenuated sounds and so important resonance frequencies were matched. The lack of mathematical descriptions of helicoidal resonators acoustical properties was partially filled by the presented in [7] its substitutional transmittance function. But it is correct for Band Stop Filters with symmetric distribution of attenuation in the frequency domain, also for selected types of helicoidal resonators.

The second important parameter of helicoidal resonators - pressure drop - was raised in the paper [8], about comparison of this parameter obtained in aeroacoustical module and turbulent flow in computational fluid dynamics (CFD) module in the same numerical environment. It showed that the difference between aeroacoustics and CFD turbulent flow is bigger when the mean air volume velocity grew up. The reason is the weak formulation of flow equations for aeroacoustics. But the other way, the aeroacoustic module was used to make some researches on the influence of the air volume velocity on the acoustic attenuation performance of selected helicoidal resonators presented in [9]. The results showed that the greater air volume velocity the lower resonance frequencies of the helicoidal resonators. But, to make the exact conclusions in this field, the experimental researches should be undertaken.

The multi-resonant helicoidal resonators as a passive noise control device in ducted systems was presented in [10]. Conducted research presented helicoidal resonators with different ratio s/d in relation to the existence of a multi resonances. The real industrial application of a large multi-resonant helicoidal resonator was presented in [11].

The other side of scientific considerations under helicoidal resonators was presented in [12], when studying the acoustic-structure interaction of selected helicoidal resonator with flexible helicoidal profile. There were considered properties of metals and non-metals, especially rubber. Final conclusion: applying the elastic material on the helicoidal profile could decrease the acoustic resonance - in the worst case amplify the sound.

The study of pressure drop depending on the air flow rate in duct of selected helicoidal resonators with constant ratio $s/d=1,976$ was presented in [13]. The experimental set-up for testing silencers was used to measure pressure drop of three helicoidal resonators with numbers of turns n that equaled 0.671, 0.695 and 1.0. Also three total pressure drop coefficients ζ were determined for each resonators, that equal 4.3, 4.4 and 4.9, respectively. Thus, the consequent conclusion that the more helicoidal turns the more pressure drop is induced.

This work presents the numerical analysis of transmission loss characteristics and pressure drop for a range of helicoidal resonators with constant s/d ratio that equals 1,976, but for different numbers of helicoidal turns n . As the acoustic attenuation proper-

ties are the most important part of helicoidal resonators considerations, the pressure drop is the consequence and it must be taken into account during the functional analysis of ducted system. Firstly are characterized acoustical and CFD models, and then are presented the results of TL [dB] for the range of n from 0 to 2.0 and pressure drop Δp [Pa] for the range of n from 0 to 1.0. The main objective of this paper is to show the proper way of selection of acoustical and flow properties of helicoidal resonators with ratio $s/d=1,976$, as a continuation of previous research work [4-9, 12, 13].

2. Description of investigated models

In this chapter are characterized investigated acoustic (2.1) and turbulent flow (2.2) models of helicoidal resonators inside a cylindrical duct. In both cases were analyzed three dimensional (3D) models of cylindrical duct with helicoidal resonator in the middle, as presented in Figure 1.

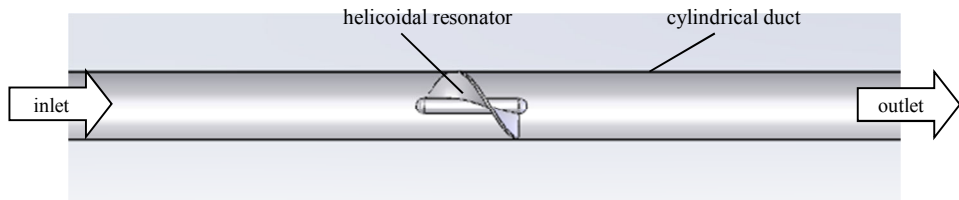


Figure 1. Investigated cylindrical duct with helicoidal resonator

The ducted system consists of a straight cylindrical duct of constant diameter $d=0.125\text{m}$. The ratio of helicoidal pitch s to cylindrical duct diameter d equals $s/d=1,976$. Other geometrical relationships of helicoidal resonator, as a mandrel diameter d_m to duct diameter ratio $d_m/d=0.024$ and thickness g of helicoidal profile $g/d=0.0024$, were constant as well. The length of the cylindrical duct at the inlet and outlet sides of helicoidal resonators equaled 1m.

2.1. Acoustical model

The investigated acoustical model has the same parameters as in previous, well described studies under helicoidal resonators [2-7]. It was used the finite element method in Comsol Multiphysics-Acoustic Module numerical environment [14]. The investigated range of numbers of helicoidal turns n was analyzed in the range from 0 to 2.0. The transmission loss (TL) [15] was computed as the acoustic attenuation performance parameter and the sound propagation in air of temperature 20°C without flow was considered. The following boundary conditions were established:

- hard walls of all elements of helicoidal resonators (perfect reflection) and cylindrical duct,
- plane waves radiation - inlet (incident pressure $p=1\text{Pa}$) and outlet surfaces of the cylindrical duct - that satisfies the anechoic terminations to calculate TL .

The free tetrahedral mesh [14] was created automatically with satisfying the rule of minimum 5 finite elements per sound wave length [16] for maximum frequency- here it

is $f_{max}=2000\text{Hz}$ at 20 Celsius degrees. Also the speed of sound in air $c_s=343\text{m/s}$. Maximum finite element size equals $h_e=0,2(c_s/f_{max})$. Example mesh is presented in Figure 2.

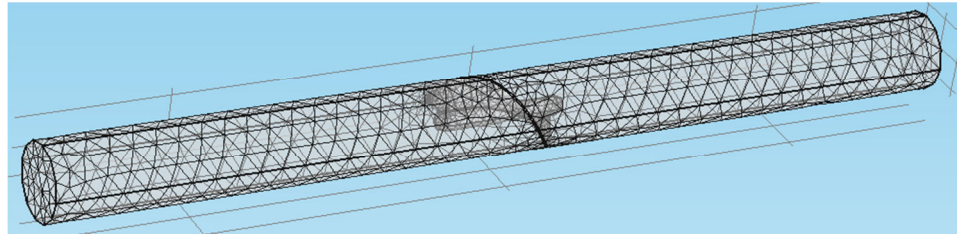


Figure 2. Example view on free tetrahedral mesh of investigated acoustic system

2.2. CFD turbulent flow model

The CFD turbulent flow model was analyzed as the single-phase flow $k-\omega$ turbulence RANS model [14, 17, 18] with compressible flow (Mach number less than 0,3). The main feature is fluid properties, which adds the Navier-Stokes equations and the transport equations for the turbulent kinetic energy k and the specific dissipation ω , and provides an interface for defining the fluid material and its properties [14]. The fluid properties are: temperature $T=20^\circ\text{C}$, reference atmospheric pressure $p_a=1\text{atm}$, density and dynamic viscosity of air were calculated automatically from COMSOL material library [14]. The boundary conditions were described as follows:

- wall slip - there are no viscous effects at the slip wall at all surfaces of cylindrical duct and helicoidal resonators,
- normal inflow velocity at the inlet in the air flow velocities 1m/s, 5m/s, 10m/s ,15 m/s and 20m/s,
- no viscous stress at the outlet, pressure equaled 0Pa.

Finite element mesh was automatically generated as a free tetrahedral and controlled by physics-fluid dynamics. The stationary solver was used. The investigated range of numbers of helicoidal turns n was analyzed in the range from 0 to 1.0 with the step of 0.1.

3. Results

This chapter contains the results of solved 3D pressure acoustics and fluid dynamics problems for investigated models of helicoidal resonators with constant ratio $s/d=1,976$ and different numbers of helicoidal turns n . Due to the acoustic attenuation performance is the most important parameter of helicoidal resonators the TL characteristics as a surface plot are contained in subchapter 3.1. On this basis were performed computations for fluid dynamics of helicoidal resonators with numbers of helicoidal turns n from 0 to 1.0 as it is presented in subchapter 3.2.

3.1. Transmission Loss

The surface plot of TL of helicoidal resonators with ratio $s/d=1,976$ and the range of numbers of helicoidal turns n from 0 to 2.0 for the frequency range from 10Hz to 2000Hz with the calculation step of 10Hz, are presented in Figure 3.

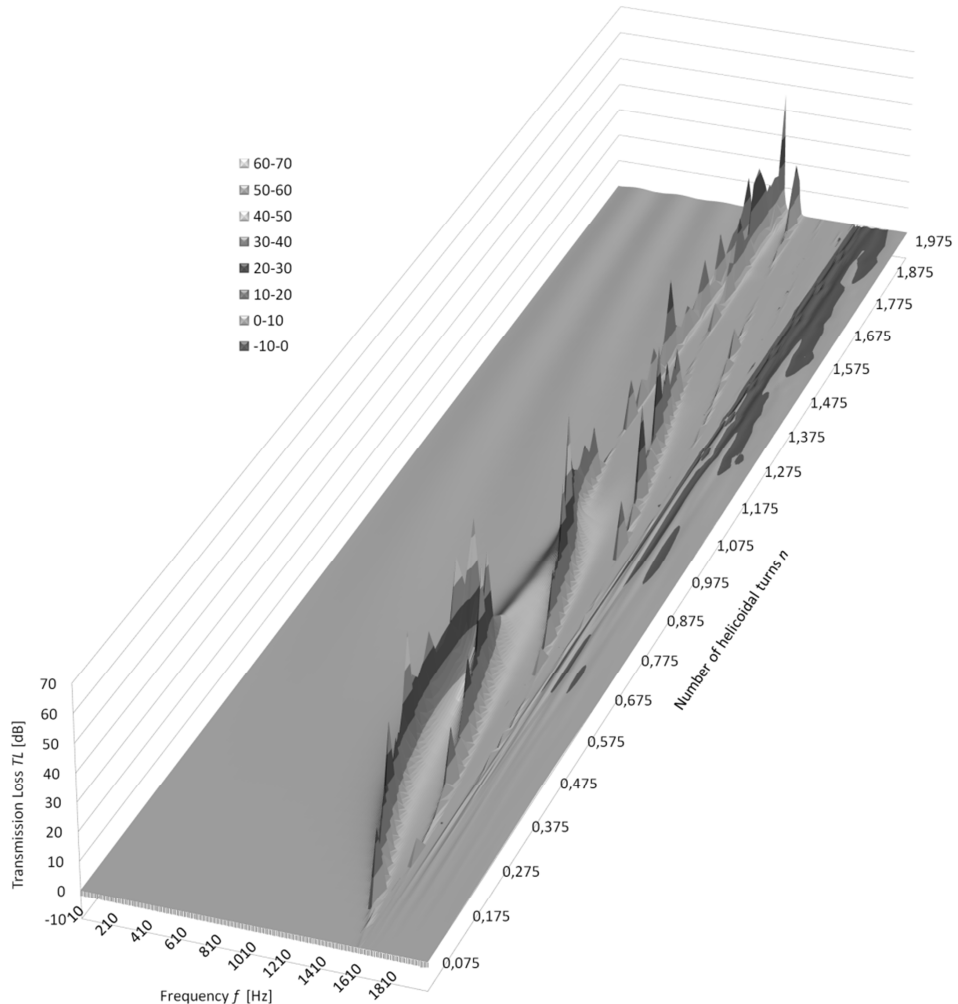


Figure 3. Surface plot of TL [dB] of helicoidal resonators with ratio $s/d=1,976$ and the range of numbers of helicoidal turns n from 0 to 2.0

As it can be observed from Figure 3 the specific band attenuation of sounds of helicoidal resonators with ratio $s/d=1,976$ exist almost for all investigated cases. But the most interesting part of TLs starts from about $n=0.4$ and ends for $n=1.0$. Globally

the attenuation range of $TL=1\text{dB}$ starts from about 1000Hz for $n=0.55$, and it ends on about 1580Hz for few numbers of helicoidal turns n .

3.2. CFD turbulent flow

The pressure drop Δp [Pa], as a difference between pressure at the inlet and outlet of the duct, of helicoidal resonators with ratio $s/d=1,976$ and the range of numbers of helicoidal turns n from 0 to 1.0 with the step of 0.1 are presented in Figure 4.

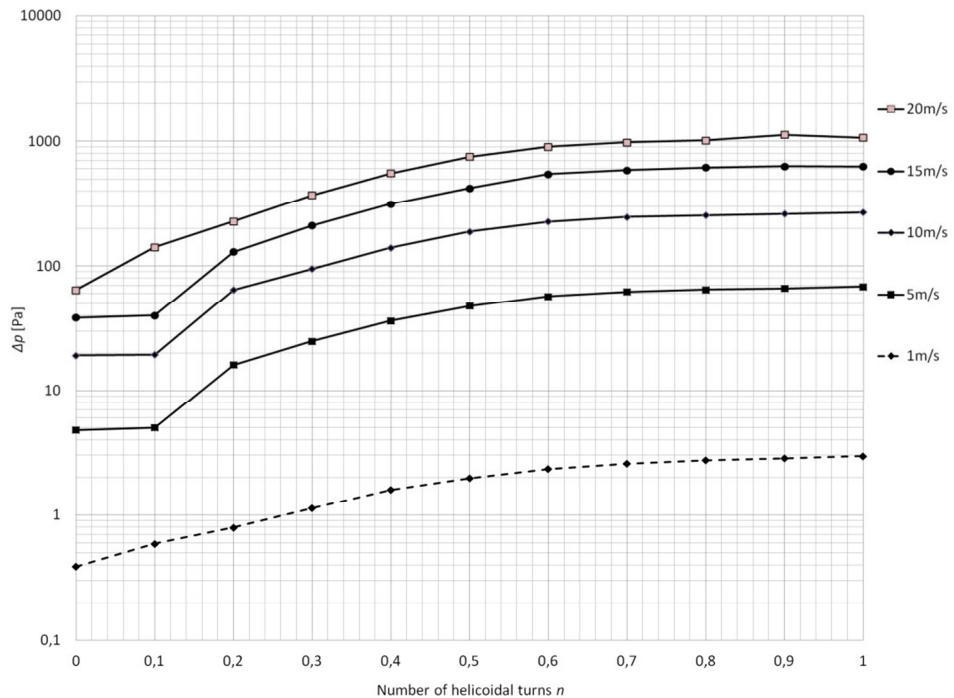


Figure 4. Pressure drop Δp [Pa] of helicoidal resonators with ratio $s/d=1,976$ and the range of numbers of helicoidal turns n from 0 to 1.0

As it can be observed from Figure 4, the pressure drop increases when the mean air volume velocity grows up for all investigated cases. Although the biggest and nearly linear increase of pressure drop takes place for the numbers of helicoidal turns n from about 0.1 to about 0.6. From 0.6 to 1.0 the pressure drop increases nonlinearly.

4. Conclusions

The numerically calculated transmission loss and pressure drops of helicoidal resonators with constant ratio $s/d=1.976$ and different numbers of helicoidal turns n were presented.

The range of helicoidal turns n from 0 to 2.0 was investigated for acoustic modelling. The specific band attenuation of sounds of helicoidal resonators with ratio $s/d=1,976$

exist almost for all investigated cases. But the most interesting part of TLs starts from about $n=0.4$ and ends for about $n=1.0$. Globally the attenuation range of $TL=1\text{dB}$ starts from about 1000Hz for $n=0.55$, and it ends on about 1580Hz for few numbers of helicoidal turns n . Also for investigated models the frequency range of sound attenuation equals nearly 580Hz.

On the basis of most interesting values of acoustic attenuation performance parameter TL , the range of helicoidal turns n from 0 to 1.0 was investigated for computational fluid dynamics with turbulent flow. The pressure drop increases when the mean air volume velocity grows up for all investigated cases. Although the biggest and nearly linear increase of pressure drop takes place for the numbers of helicoidal turns n from about 0.1 to about 0.6. From 0.6 to 1.0 the pressure drop increases nonlinearly.

Acknowledgments

The author gratefully acknowledges that this paper was financially supported in the year 2014 by the research project 02/21/DSPB/337.

References

1. Łapka W., Cempel C., *Acoustic filter for sound attenuation in ducted systems*, Polish Patent Office, PAT.216176, Date of grant 25.07.2013.
2. Łapka W., Cempel C., *Noise reduction of spiral ducts*, International Journal of Occupational Safety and Ergonomics (JOSE), Vol. 13 (4), pp. 419-426, 2007.
3. W. Łapka, *Acoustic attenuation performance of a round silencer with the spiral duct at the inlet*, Archives of Acoustics, Vol. 32 (4) (Supplement), pp. 247-252, 2007.
4. Łapka W., Cempel C., *Computational and experimental investigations of a sound pressure level distribution at the outlet of the spiral duct*, Archives of Acoustics, Vol. 33 (4) (Supplement), pp. 65-70, 2008.
5. Łapka W., Cempel C., *Acoustic attenuation performance of Helmholtz resonator and spiral duct*, Vibrations in Physical Systems, Vol. 23, pp. 247-252, 2008.
6. Łapka W., *Insertion loss of spiral ducts - measurements and computations*, Archives of Acoustics, Vol. 34 (4), pp. 407-415, 2009.
7. Łapka W., *Substitutional transmittance function of helicoidal resonator*, Vibrations in Physical Systems, Vol. 24, pp. 265-270, 2010.
8. Łapka W., *Comparison of numerically calculated pressure drop for selected helicoidal resonators*, Polskie Towarzystwo Akustyczne - Oddział Poznański, tytuł monografii: 59th Open Seminar on Acoustics joint with Workshop on Strategic Management of Noise including Aircraft Noise, pp. 145-148, 2012.
9. Łapka W., *Numerical Aeroacoustic Research of Transmission Loss Characteristics Change of Selected Helicoidal Resonators due to Different Air Flow Velocities*, Vibrations in Physical Systems, Vol. 25, pp. 267-272, 2012.
10. Łapka W., *Multi resonant helicoidal resonator for passive noise control in ducted systems*, Experimental Mechanics - New Trends and Perspectives, Editors J.F. Silva Gomes, Mario A.P. Vaz, Proceedings of the 15th International Conference on Ex-

-
- perimental Mechanics, ICEM15, Porto, Portugalia, 22-27 lipiec 2012, 995-996, 2012.
11. Łapka W., *Helicoidal resonators for passive noise control in ducted systems with practical application*, Proceedings of Internoise 2012, New York, USA, 2012.
 12. Łapka W., *Numerical study of acoustic-structure interaction of selected helicoidal resonator with flexible helicoidal profile*, rozdział w j. ang. w monografii pt. Postępy Akustyki, Polskie Towarzystwo Akustyczne - Oddział w Rzeszowie, Rzeszów, pp. 194-205, 2013.
 13. Łapka W., M. Szymański, R. Górzeński, *Badania oporów przepływu w zależności od strumienia objętości powietrza w kanale dla wybranych rezonatorów helikoidalnych*, rozdział w monografii pt. Postępy Akustyki, Polskie Towarzystwo Akustyczne - Oddział w Rzeszowie, Rzeszów, pp. 168-180, 2013.
 14. COMSOL Multiphysics version 4.2.a, *User's Guide and Model Library Documentation Set*, COMSOL AB, www.comsol.com, Stockholm, Sweden, 2011.
 15. Munjal M. L., *Acoustics of Ducts and Mufflers with Application to Exhaust and Ventilation System Design*, Inc., Calgary, Canada, John Wiley & Sons, 1987.
 16. Marburg S., Nolte B., *Computational Acoustics of Noise Propagation in Fluids – Finite and Boundary Element Methods*, 578, Springer-Verlag, Berlin, Germany, 2008.
 17. Wilcox, D. C., *Turbulence Modeling for CFD*, 3rd edition, DCW Industries, Inc., La Canada CA, 2006.
 18. Wilcox, D. C., *Formulation of the k-omega Turbulence Model Revisited*, AIAA Journal, Vol. 46, No. 11, 2823-2838, 2008.

Design Sensitivity Analysis of Frequency Response Functions and Steady-state Response for Structures with Viscoelastic Dampers

Magdalena ŁASECKA-PLURA

Institute of Structural Engineering, Poznan University of Technology

ul. Piotrowo 5, 60-965 Poznan, Poland

magdalena.lasecka-plura@put.poznan.pl

Roman LEWANDOWSKI

Institute of Structural Engineering, Poznan University of Technology

ul. Piotrowo 5, 60-965 Poznan, Poland

roman.lewandowski@put.poznan.pl

Abstract

In this paper, the design sensitivity of the frequency response function and amplitudes of the steady-state vibration of planar frames with viscoelastic (VE) dampers mounted on them is considered. The dampers are modeled using a five-parameter rheological model with fractional derivatives. The design sensitivity with respect to change of damper parameter is analyzed in detail. The direct method is used to determine the first and the second order sensitivities. Moreover, the results of typical calculations are presented and discussed.

Keywords: Fractional models of VE dampers, Dynamic characteristics, Design sensitivity

1. Introduction

The design sensitivity analysis of structures and mechanical systems is a very important issue, which is helpful in solving many engineering problems, such as: optimization of structures, parametric identification problems, structural health monitoring problems, model updating problems [1], structural reliability problems, damage detection [2] and others. In the recent years, studies on the analysis of sensitivity for systems with viscoelastic dampers have been started e.g., the eigensensitivity analysis of viscoelastic (VE) structures is presented in [3].

The frequency response function is one of the most important tools of evaluation of the dynamic response of structure. Its design sensitivity analysis has been studied by several authors. For example, the direct differentiation method is presented in paper [4] and both the direct differentiation method and the adjoint variable method is described in [5,6].

In this paper, the direct differentiation method for the design sensitivity analysis of structure with viscoelastic dampers modeled by fraction derivatives is presented. This work is an extension of the previous paper [7], which dealt with the sensitivity analysis of eigenvalues and eigenvectors of structure with fractional dampers.

Firstly, in this paper, the model of damper and the equation of motion of a structure with dampers described by fractional derivatives are presented. Then the method of calculation of the frequency response functions (FRF) and amplitudes of steady-state vibration is presented. Next, the design sensitivity analysis is shown. Finally, the two-

storey planar frame is considered. In the example, the sensitivity of FRF with respect to change of parameter of damper is calculated and the correctness of the presented method is proved. At the end, the conclusions are presented.

2. Description of structures with VE dampers

Many rheological models of dampers have been proposed in the literature. The most popular among them are the two classic ones: the Maxwell and the Kelvin models. In order to better describe the damper, so-called fractional models are often used. They describe the rheological properties of dampers more efficiently than the classic ones [8]. A so-called the springpot element, shown as a small diamond in Figure 1, is described by the two constants c and α , where α denotes the order of the fractional derivative.

In this paper, the fractional model of a damper is used (see Figure 1). The damper is described by five parameters: stiffnesses k_0 and k_1 , springpot factors c_0 and c_1 , and the fractional parameter α ($0 < \alpha < 1$). As special cases, it contains a number of specific models, e.g., the three-parameter Maxwell and Kelvin models, the four-parameter fractional Maxwell model.

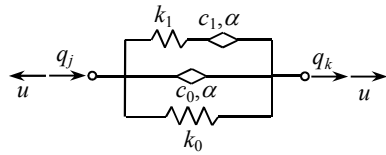


Figure 1. A model of the damper

The force in the considered model of damper is written as:

$$u(t) = u_0(t) + u_1(t) \quad (1)$$

where $u_0(t)$ is the force in the fractional Kelvin element and $u_1(t)$ is the force in the fractional Maxwell element.

Evaluation equations for the Kelvin model can be written as follows:

$$u_0(t) = k_0 \Delta q(t) + c_0 D_t^\alpha \Delta q(t) \quad (2)$$

where: $\Delta q_i(t) = q_k - q_j$, q_k and q_j denote the nodal displacements of the considered model of damper. D_t^α denotes the Riemann-Liouville fractional derivative of the order α with respect to time t [9,10]. For the Kelvin model, the evaluation equations could be described in the following way:

$$u_1(t) + \frac{c_1}{k_1} D_t^\alpha u_1(t) = c_1 D_t^\alpha \Delta q(t) \quad (3)$$

After taking the Laplace transform, Equation (1) can be written in the form:

$$\bar{u}(s) = \bar{u}_0(s) + \bar{u}_1(s), \quad (4)$$

and Equations (2) and (3) take the following form:

$$\bar{u}_0(s) = k_0 \Delta \bar{q}(s) + c_0 s^\alpha \Delta \bar{q}(s) \quad (5)$$

$$\bar{u}_1(s) + \tau_1 s^\alpha \bar{u}_1(s) = c_1 s^\alpha \Delta \bar{q}(s) \quad (6)$$

where the quantities with the bar denote the Laplace transform, i.e.: $\Delta \bar{q}(s) = L[\Delta q(t)]$, $\bar{u}_0(s) = L[u_0(t)]$, $\bar{u}_1(s) = L[u_1(t)]$, $s^\alpha \bar{u}(s) = L[D_t^\alpha u(t)]$, and s is the Laplace variable.

Finally:

$$\bar{u}(s) = G(s) \Delta \bar{q}(s) \quad (7)$$

where:

$$G(s) = k_0 (1 + \tau_0 s^\alpha) + k_1 \frac{\tau_1 s^\alpha}{1 + \tau_1 s^\alpha}, \quad \tau_0 = c_0 / k_0, \quad \tau_1 = c_1 / k_1 \quad (8)$$

The classic Kelvin and Maxwell models are obtained by introducing $\alpha = 1$.

The equation of motion of structures with VE dampers can be written in the following form:

$$\mathbf{M}_s \ddot{\mathbf{q}}(t) + \mathbf{C}_s \dot{\mathbf{q}}(t) + \mathbf{K}_s \mathbf{q}(t) = \mathbf{p}(t) + \mathbf{f}(t) \quad (9)$$

where: \mathbf{M}_s , \mathbf{C}_s and \mathbf{K}_s , denote the mass, the damping and the stiffness matrix of structure, respectively. The structure is modeled as a shear frame with mass lumped at the storey level. Moreover, $\mathbf{q}(t) = [q_1 \dots q_n]^T$ is the vector of displacements of the structure, $\mathbf{p}(t) = [p_1 \dots p_n]^T$ is the vector of excitation forces and $\mathbf{f}(t) = [f_1 \dots f_n]^T$ is the vector of the interaction forces between the frame and the dampers (see Figure 2).

Vector $\mathbf{f}(t)$ is a sum of the vectors $\mathbf{f}_i(t)$. Each of them is formed if only the damper i is located on the frame, i.e.:

$$\mathbf{f}(t) = \sum_{i=1}^m \mathbf{f}_i(t). \quad (10)$$

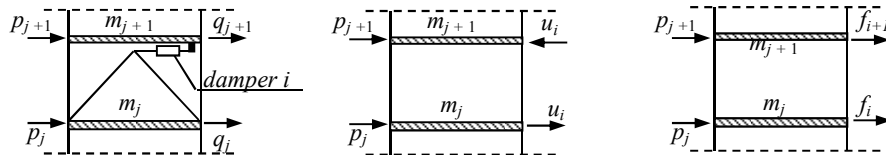


Figure 2. Diagram of frame with VE dampers

For the damper located between the floors j and $j+1$ (see Fig. 2), the following may be written:

$$\mathbf{f}_i(t) = \mathbf{e}_i u_i(t), \quad \mathbf{e}_i = [0 \dots e_j = +1 \quad e_{j+1} = -1 \dots 0]^T. \quad (11)$$

After taking the Laplace transform, the equation of motion could be written as:

$$(s^2 \mathbf{M}_s + s \mathbf{C}_s + \mathbf{K}_s) \bar{\mathbf{q}}(s) = \bar{\mathbf{p}}(s) + \bar{\mathbf{f}}(s) \quad (12)$$

where: $\bar{\mathbf{q}}(s) = L[\mathbf{q}(t)]$, $\bar{\mathbf{p}}(s) = L[\mathbf{p}(t)]$, $\bar{\mathbf{f}}(s) = L[\mathbf{f}(t)]$.

For m dampers, the following equation is obtained:

$$\bar{\mathbf{f}}(s) = \sum_{i=1}^m \mathbf{e}_i \bar{u}_i(s) \quad (13)$$

Substituting Equation (7) written for damper i to Equation (13) leads to:

$$\bar{\mathbf{f}}(s) = -\sum_{i=1}^m G_i(s) \mathbf{L}_i \bar{\mathbf{q}}(s), \quad (14)$$

where: $\mathbf{L}_i = \mathbf{e}_i \mathbf{e}_i^T$. After substituting Equation (14) into (12) the equation of motion of structure with VE dampers could be written as:

$$\mathbf{D}(s) \bar{\mathbf{q}}(s) = \bar{\mathbf{p}}(s) \quad (15)$$

where:

$$\mathbf{D}(s) = s^2 \mathbf{M}_s + s \mathbf{C}_s + \mathbf{K}_s + \sum_{i=1}^m \mathbf{G}_i(s), \quad \mathbf{G}_i(s) = G_i(s) \mathbf{L}_i. \quad (16)$$

3. Frequency response function (FRF)

The dynamic response of structure can be described by using the frequency response functions. In this context, we assume that

$$\mathbf{p}(t) = \mathbf{P} \exp(i\lambda t) \quad (17)$$

where $\mathbf{P} = [P_1, \dots, P_n]^T$ (compare Figure 2), λ is the excitation frequency. The steady-state solution to the motion equation could be assumed in the two equivalent forms:

$$\mathbf{q}(t) = \mathbf{H}(\lambda) \mathbf{P} \exp(i\lambda t) = \mathbf{a} \exp(i\lambda t) \quad (18)$$

where $\mathbf{H}(\lambda)$ is the matrix of frequency response functions and \mathbf{a} is the vector of amplitudes of steady-state vibration. After substituting Formulae (17) and (18) into (9) we obtain:

$$\mathbf{D}(\lambda) \mathbf{H}(\lambda) = \mathbf{I} \quad (19)$$

hence

$$\mathbf{H}(\lambda) = \mathbf{D}(\lambda)^{-1}. \quad (20)$$

We can also obtain the formula describing the matrix $\mathbf{D}(\lambda)$ by substituting relationship $s = i\lambda$ into Equation (16). Hence:

$$\mathbf{D}(\lambda) = \left[-\lambda^2 \mathbf{M} + i\lambda \mathbf{C} + \mathbf{K} + \sum_{i=1}^m \mathbf{G}_i(\lambda) \right], \quad \mathbf{H}(\lambda) = \left[-\lambda^2 \mathbf{M} + i\lambda \mathbf{C} + \mathbf{K} + \sum_{i=1}^m \mathbf{G}_i(\lambda) \right]^{-1}. \quad (21)$$

Based on Relationship (18) we can also write:

$$\mathbf{a} = \mathbf{H}(\lambda)\mathbf{P} \quad (22)$$

4. Design sensitivity

In order to determine the relationship describing the sensitivity of FRF, it is necessary to use the following obvious equation:

$$\mathbf{H}(\lambda)\mathbf{H}(\lambda)^{-1} = \mathbf{I} \quad (23)$$

Differentiating Equation (23) with respect to the design parameter p leads to:

$$\frac{\partial \mathbf{H}(\lambda, p)}{\partial p} = -\mathbf{H}(\lambda, p) \frac{\partial \mathbf{D}(\lambda, p)}{\partial p} \mathbf{H}(\lambda, p) \quad (24)$$

where:

$$\frac{\partial \mathbf{D}(\lambda, p)}{\partial p} = \left[-\lambda^2 \frac{\partial \mathbf{M}(p)}{\partial p} + i\lambda \frac{\partial \mathbf{C}(p)}{\partial \lambda} + \frac{\partial \mathbf{K}(p)}{\partial p} + \sum_{i=1}^m \frac{\partial \mathbf{G}_i(\lambda, p)}{\partial p} \right].$$

Differentiating the Equation (23) the second time, we obtain the second order sensitivity:

$$\frac{\partial^2 \mathbf{H}(\lambda, p)}{\partial p^2} = -\mathbf{H}(\lambda, p) \frac{\partial^2 \mathbf{D}(\lambda, p)}{\partial p^2} \mathbf{H}(\lambda, p) - 2\mathbf{H}(\lambda, p) \frac{\partial \mathbf{D}(\lambda, p)}{\partial p} \frac{\partial \mathbf{H}(\lambda, p)}{\partial p} \quad (25)$$

where:

$$\frac{\partial^2 \mathbf{D}(\lambda, p)}{\partial p^2} = \left[-\lambda^2 \frac{\partial^2 \mathbf{M}(p)}{\partial p^2} + i\lambda \frac{\partial^2 \mathbf{C}(p)}{\partial p^2} + \frac{\partial^2 \mathbf{K}(p)}{\partial p^2} + \sum_{i=1}^m \frac{\partial^2 \mathbf{G}_i(\lambda, p)}{\partial p^2} \right].$$

In the calculation of sensitivity, the first and the second order with respect to the chosen parameter of structure or damper, only the matrices $\partial \mathbf{D}(\lambda, p)/\partial p$ and $\partial^2 \mathbf{D}(\lambda, p)/\partial p^2$ change and can be reduced to a much simpler form.

After calculating the sensitivity of FRF, it is possible to determine the sensitivity of amplitudes of steady-state vibration in a simple way. Differentiating Equation (22) with respect to the design parameter leads to:

$$\frac{\partial \mathbf{a}}{\partial p} = \frac{\partial \mathbf{H}(\lambda, p)}{\partial p} \mathbf{P} \quad (26)$$

where sensitivity of FRF is described by Equation (24).

5. Example

In order to illustrate the presented method, a two-storey building with a three-parameter Maxwell damper situated on the second storey is considered (see Fig. 3). The following data are adopted: the mass of every floor $m = 1000\text{kg}$, the storey stiffness $k_s = 100000\text{N/m}$ and the damper parameters: $k_1 = 50000\text{N/m}$, $c_1 = 8000\text{Ns}^\alpha/\text{m}$ and $\alpha = 0.6$. The damping properties of the structure are neglected.

In this example, the frequency response matrix $\mathbf{H}(\lambda)$ is determined for the excitation frequency taken from the range $\lambda \in (0, 20\text{rad/sec})$. The calculation results are presented in Figure 4, where the real and the imaginary parts of the function $H_{11}(\lambda)$ are shown.

The sensitivity of $H_{11}(\lambda)$ with respect to the change of the stiffness parameter k_1 of the damper is calculated and the frequency taken from the range $\lambda \in (0, 20\text{rad/sec})$. The results are presented in Figure 5.

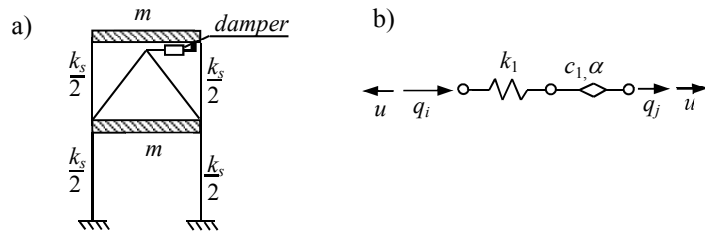


Figure 3. a) Diagram of the considered frame, b) Maxwell model of damper

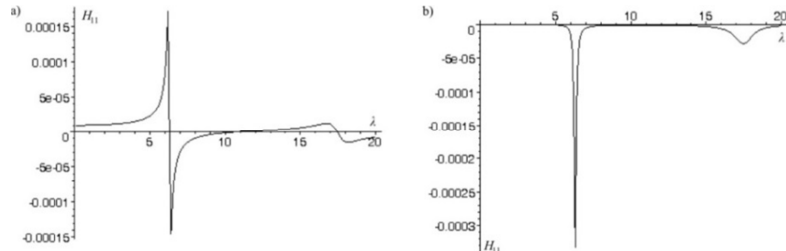


Figure 4. The real and the imaginary parts of the function $H_{11}(\lambda)$: (a) real,
b) imaginary)

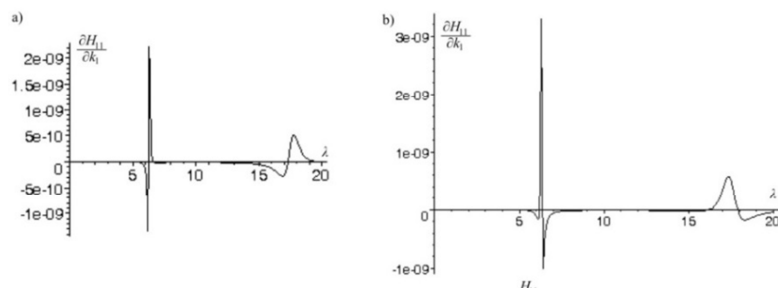


Figure 5. The real and the imaginary parts of sensitivity of $H_{11}(\lambda)$: (a) real,
b) imaginary)

In order to verify the correctness of the calculation, the values of FRF after change of the parameter are determined according to the formula:

$$\mathbf{H}(\lambda, p + \Delta p) \approx \mathbf{H}(\lambda, p) + \frac{\partial \mathbf{H}(\lambda)}{\partial p} \Delta p \quad (27)$$

where Δp denotes a change of the design parameter. The obtained values were compared with the exact solution, when the design parameter changed its own value by 1%. The calculation is carried out for the selected frequencies and the obtained results are presented in Table 1. The results proved the presented method to be correct.

Table 1. A comparison of $H_{11}(\lambda, k_1)$

Frequency λ [rad/sec]	$H_{11}(\lambda, k_1) + \frac{\partial H_{11}(\lambda, k_1)}{\partial k_1} \Delta k_1$	Exact value of $H_{11}(\lambda, k_1 + \Delta k_1)$
4.0	$0.153048 \cdot 10^{-4} - 0.624154 \cdot 10^{-7}i$	$0.153048 \cdot 10^{-4} - 0.624135 \cdot 10^{-7}i$
6.0	$0.824470 \cdot 10^{-4} - 0.158672 \cdot 10^{-4}i$	$0.824476 \cdot 10^{-4} - 0.158668 \cdot 10^{-4}i$
6.5	$-0.983082 \cdot 10^{-4} - 0.418210 \cdot 10^{-4}i$	$-0.983076 \cdot 10^{-4} - 0.418190 \cdot 10^{-4}i$
7.0	$-0.291213 \cdot 10^{-4} - 0.522328 \cdot 10^{-5}i$	$-0.291211 \cdot 10^{-4} - 0.522308 \cdot 10^{-5}i$
7.5	$-0.153077 \cdot 10^{-4} - 0.235479 \cdot 10^{-5}i$	$-0.153076 \cdot 10^{-4} - 0.235470 \cdot 10^{-5}i$

Moreover, a comparison was made by using first-order sensitivity values according to Equation (27) and second-order sensitivity values according to the following equation:

$$\mathbf{H}(\lambda, p + \Delta p) \approx \mathbf{H}(\lambda, p) + \frac{\partial \mathbf{H}(\lambda, p)}{\partial p} \Delta p + \frac{1}{2} \frac{\partial^2 \mathbf{H}(\lambda, p)}{\partial p^2} \Delta p^2. \quad (28)$$

The calculations are carried out for a change of parameter k_1 , taken from the range 1% – 50% and presented in Figure 6. Now, we can conclude that the second order sensitivity gives results which are very close to an exact solution if the change of parameter k_1 is smaller than 20% .

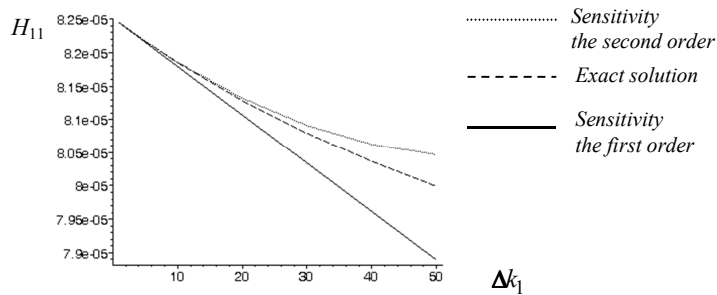


Figure 6. The comparison of $H_{11}(\lambda, k_1 + \Delta k_1)$

6. Conclusions

In this paper the design sensitivity analysis of FRF and amplitudes of the steady-state vibration of structures with VE dampers is presented. The formulae are calculated by

using the direct method. The obtained equations enable determination of the sensitivity of the dynamic characteristics of structures with VE dampers with respect to a chosen design parameter. The considered five-parameter damper model can be used for an analysis of structures with different dampers, described by selected classic and fractional rheological models. In the example, the correctness of the present method is proved.

The method used to calculate the sensitivities of FRF and amplitudes of the steady-state vibration of structures with VE dampers is easy to formulate, systematic to apply, simple to code, and it agrees well with the exact results. Such an analysis has been carried out for the first time.

Acknowledgments

The study was supported by the National Science Centre, Poland, as part of Project No. 2013/09/B/ST8/01733, carried out in the years 2014-2016. The support is gratefully acknowledged.

References

1. J.E. Mottershead, L. Michel, M.J. Friswell, *The sensitivity method in finite element model updating: a tutorial*, Mechanical System and Signal Processing, **25**, (2011), 2275-2296.
2. W.J. Yan, W.X. Ren, *A direct algebraic method to calculate the sensitivity of element modal strain energy*, International Journal for Numerical Methods in Biomedical Engineering, **27**, (2011), 694-710.
3. M. Martinez-Agirre, M.J. Elejabarrieta, *Higher order eigensensitivity-based numerical method for the harmonic analysis of viscoelastically damped structures*, International Journal for Numerical Methods in Engineering, **88**, (2011), 1280-1296.
4. G.J.E. Kramer, D.E. Grierson, *Computer automated design of structures under dynamic loads*, Computers and Structures, **32**, (1989), 313-325.
5. K.K. Choi, J.H. Lee, *Sizing design sensitivity analysis of dynamic frequency response of vibrating structures*, Journal of Mechanical Design, **114**, (1992), 166.
6. K.K. Choi, I. Shim, S. Wang, *Design sensitivity analysis of structure-induced noise and vibration*, Journal of Vibration and Acoustics-ASME, **119**, (1997), 173-179.
7. R. Lewandowski, M. Łasecka-Plura, *Sensitivity analysis of structures with viscoelastic dampers*, Proceedings of CMM-2013, 27–31 August 2013, Poznan, Poland.
8. N. Makris, M.C. Constantinou, *Fractional-derivative Maxwell model for viscous damper*, ASCE Journal of Structural Engineering, **117**, (1991), 2708-2724.
9. I. Podlubny, *Fractional Differential Equations*, Academic Press, 1999.
10. J.S. Leszczyński, *An introduction to fractional mechanics*, Częstochowa University of Technology, 2011.

Distributed Dynamic Vibration Absorber in Beam

Waldemar ŁATAS

*Cracow University of Technology, Institute of Applied Mechanics
31-864 Cracow, Al. Jana Pawła II 37, Poland
latas@mech.pk.edu.pl*

Abstract

The paper deals with forced vibration of Euler-Bernoulli beam with variable cross-section equipped with a distributed dynamic absorber. The beam is subjected to the concentrated and distributed harmonic excitations. The problem is solved using Galerkin's method and Lagrange's equations. Performing time-Laplace transformation the displacement amplitude of arbitrary point of the beam may be written in the frequency domain. The aim of the paper is to find the effectiveness of the distributed vibration absorbers in beams. As an example numerical results of vibration reduction in wind turbine's tower are presented.

Keywords: distributed dynamic vibration absorber, beam vibration, vibration reduction

1. Introduction

As a main application the dynamic vibration absorbers [DVA] (the most common are tuned mass dampers – TMD), correctly attached to vibrating structure and tuned to the frequency of harmonic excitation, can cause to cease the motion at the point of attachment [1-2].

Vibration analysis and the proper choice of the absorbers parameters in beam structures have been very often the subjects of study [3-10]. For continuous structures, such as beams, usually the best location of the vibration absorber is the point of excitation, but it may be difficult due to technical limitations. Depending upon the situation if the local optimization problem (for example minimization of the vibration amplitude at the given point) or global optimization problem (minimization of the kinetic energy of the whole structure) are to be considered, one may obtain different optimal parameters of the single absorber or the system of absorbers and the main issue in optimization is the proper placement of the absorbers.

In many cases there are used systems of tuned mass dampers [MTMD] which may be tuned for several resonant frequencies if broadband excitation is applied or for a single frequency [3,5] [11-14]. To suppress the structural waves in beams there may be used the absorbers distributed continuously along the length of the beam. A special application is the reduction of noise from railway track [15]. Compared with absorber applied at a single point, the distributed absorber is effective in case of arbitrary location of the exciting force and by appropriate tuning may work in a wide frequency band.

In this article a model based on Euler-Bernoulli theory is built for a beam with variable cross-section, subjected to the continuous and concentrated excitation, equipped with a dynamic vibration absorber with distributed parameters. Numerical example presented concerns the problem of passive vibration control in the real-world wind-turbine's tower-nacelle system.

2. Theoretical model

Figure 1 presents a system considered in the paper – a beam with variable cross-section subjected to the distributed and concentrated forces, with a distributed vibration absorber attached. The beam is of length l , the physical and geometrical parameters are functions of the position: mass density $\rho(x)$, cross-section area $A(x)$, area moment of inertia $I(x)$, Young's modulus $E(x)$, viscous damping coefficient $\alpha(x)$ (Voigt-Kelvin rheological model).

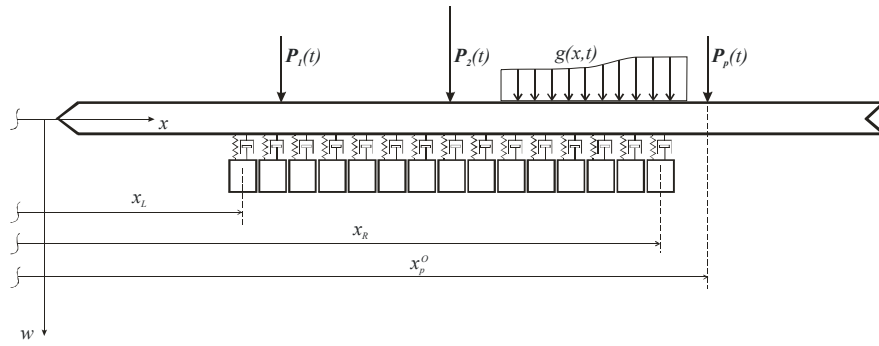


Figure 1. Beam with a distributed dynamic vibration absorber

Assuming Euler-Bernoulli model of the beam deformation and Voigt-Kelvin model of the beam material, the kinetic energy, the elastic potential energy and the dissipative function are given by:

$$T = \frac{1}{2} \int_0^l \rho(x) A(x) \left(\frac{\partial w}{\partial t} \right)^2 dx \quad (1)$$

$$V = \frac{1}{2} \int_0^l E(x) I(x) \left(\frac{\partial^2 w}{\partial x^2} \right)^2 dx \quad (2)$$

$$R = \frac{1}{2} \int_0^l E(x) I(x) \alpha(x) \left(\frac{\partial^3 w}{\partial t \partial x^2} \right)^2 dx \quad (3)$$

The transverse displacement is assumed to have the form of the series:

$$w(x, t) = \sum_{i=1}^n q_i(t) \varphi_i(x) \quad (4)$$

In the above expression $\varphi_i(x)$ are the basic functions, chosen in calculations as the modes of vibration of the beam with constant cross-section area, without absorbers attached. The functions $q_i(t)$ are time-dependent generalized co-ordinate that should be determined.

Substituting the series (4) into discretization (1)–(3) leads to:

$$T = \frac{1}{2} \sum_{i=1}^n \sum_{j=1}^n m_j \dot{q}_i \dot{q}_j \quad (5)$$

$$V = \frac{1}{2} \sum_{i=1}^n \sum_{j=1}^n k_{ij} q_i q_j \quad (6)$$

$$R = \frac{1}{2} \sum_{i=1}^n \sum_{j=1}^n b_{ij} \dot{q}_i \dot{q}_j \quad (7)$$

The terms m_{ij} , k_{ij} , b_{ij} are given by:

$$m_{ij} = \int_0^l \rho(x) A(x) \varphi_i(x) \varphi_j(x) dx \quad (8)$$

$$k_{ij} = \int_0^l E(x) I(x) \varphi_i''(x) \varphi_j''(x) dx \quad (9)$$

$$b_{ij} = \int_0^l E(x) I(x) \alpha(x) \varphi_i''(x) \varphi_j''(x) dx \quad (10)$$

For any given loading of the beam $H(x,t)$ the generalized force is obtained from formula:

$$H_i(t) = \int_0^l H(x,t) \varphi_i(x) dx \quad (11)$$

Using Lagrange's equations leads to a system of ordinary second order differential equations in the time domain with the unknown generalized co-ordinates $q_i(t)$:

$$\sum_{j=1}^n m_{ij} \ddot{q}_j + \sum_{j=1}^n b_{ij} \dot{q}_j + \sum_{j=1}^n k_{ij} q_j = H_i(t), \quad i = 1 \dots n \quad (12)$$

Performing time-Laplace transform (with initial conditions equal to zero) the system of differential equations (12) may be written in the form of the system of linear algebraic equations:

$$\sum_{j=1}^n m_{ij} s^2 Q_j(s) + \sum_{j=1}^n b_{ij} s Q_j(s) + \sum_{j=1}^n k_{ij} Q_j(s) = H_i(s), \quad i = 1 \dots n \quad (13)$$

where $Q_i(s)$, $H_i(s)$ denote Laplace transforms of $q_i(t)$, $H_i(t)$.

Having calculated from the system (13) the transforms $Q_i(s)$ the transforms of the beam deflection may be obtained:

$$W(x, s) = \sum_{i=1}^n Q_i(s) \varphi_i(x) \quad (14)$$

The loading $H(x, t)$ depends on the distributed force $g(x, t)$ and p concentrated forces $P_j(t)$ applied to the beam at the points of coordinate x_j^o , additionally it depends on the distributed force $f(x, t)$ applied to the beam from the distributed vibration absorber:

$$H(x, t) = q(x, t) + \sum_{j=1}^p P_j(t) \delta(x - x_j^o) + f(x, t) \quad (15)$$

Generalized force $H_i(t)$ for the i -th generalized coordinate $q_i(t)$ is obtained from (11):

$$H_i(t) = \sum_{j=1}^p P_j(t) \varphi_i(x_j^o) + \int_0^L g(x, t) \varphi_i(x) dx + \int_{x_L}^{x_R} f(x, t) \varphi_i(x) dx \quad (16)$$

where x_L, x_R are the limits of the distributed dynamic absorber (Figure 1).

The Laplace transform of the i -th generalized force may be expressed as:

$$H_i(s) = \sum_{j=1}^p P_j(s) \varphi_i(x_j^o) + G_i(s) + F_i(s) \quad (17)$$

where it is introduced notations:

$$G_i(s) = \int_0^L g(x, s) \varphi_i(x) dx ; F_i(s) = \int_{x_L}^{x_R} f(x, s) \varphi_i(x) dx \quad (18)$$

In the above expressions $g(x, s), f(x, s)$ are Laplace transforms of the $g(x, t), f(x, t)$.

The Laplace transform of the distributed force applied to the beam from the vibration absorber is given by [10]:

$$f(x, s) = -\frac{(\tilde{c}(x)s + \tilde{k}(x))\tilde{m}(x)s^2}{\tilde{m}(x)s^2 + \tilde{c}(x)s + \tilde{k}(x)} W(x, s) = -\frac{(\tilde{c}(x)s + \tilde{k}(x))\tilde{m}(x)s^2}{\tilde{m}(x)s^2 + \tilde{c}(x)s + \tilde{k}(x)} \sum_{j=1}^n Q_j(s) \varphi_j(x) \quad (19)$$

where: $\tilde{m}(x)$, $\tilde{c}(x)$, $\tilde{k}(x)$ – linear mass density, linear damping and stiffness coefficients densities of the distributed vibration absorber.

Insertion of (19) into (18) gives the system of linear equations (13) written in the form:

$$\begin{aligned} \sum_{j=1}^n \left(m_{ij}s^2 + b_{ij}s + k_{ij} + \int_{x_L}^{x_R} \frac{(\tilde{c}(x)s + \tilde{k}(x))\tilde{m}(x)s^2}{(\tilde{m}(x)s^2 + \tilde{c}(x)s + \tilde{k}(x))} \varphi_i(x) \varphi_j(x) dx \right) Q_j(s) = \\ \sum_{j=1}^p P_j(s) \varphi_i(x_j^o) + G_i(s), \quad i = 1 \dots n \end{aligned} \quad (20)$$

Having solved the system (20) the transform of the beam deflection may be obtained from series (14). Assuming steady state vibration, after substituting $s = j\omega$ ($j = \sqrt{-1}$), it may be obtained the deflection of the beam in the frequency domain.

3. Numerical results: tuned distributed vibration absorber – wind-turbine's tower-nacelle system

It has been built a numerical algorithm which determines in s -domain the transform of the deflection of the beam for any set of functions describing its physical and geometrical characteristics: $A(x)$, $I(x)$, $E(x)$, $\alpha(x)$, $\rho(x)$, and for arbitrary boundary conditions at the ends of the beam. When harmonic excitation is considered the algorithm allows to obtain the amplitude-frequency characteristics of the beam deflection and allows for further calculations of the similar frequency characteristics of the slope, bending moment, transverse force and the time-averaged kinetic energy.

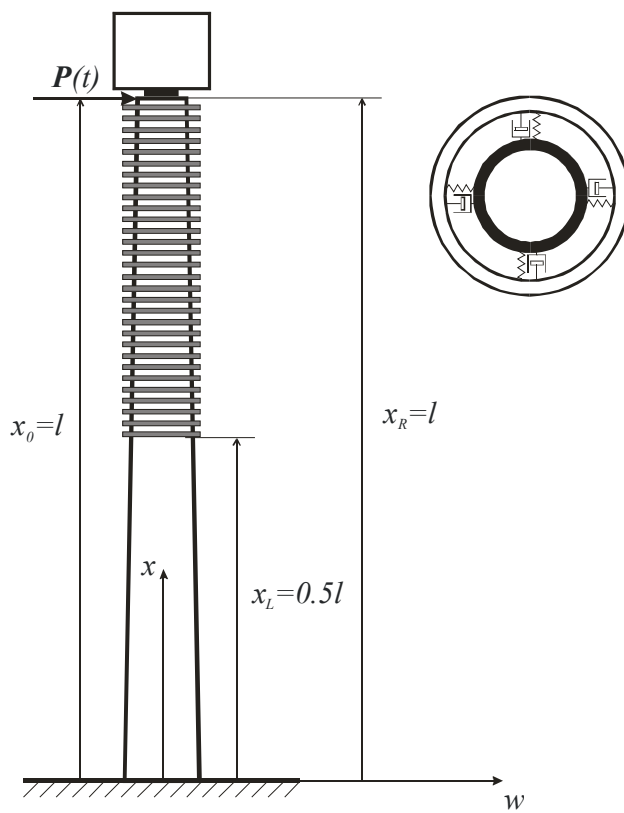


Figure 2. Model of the wind-turbine's tower-nacelle system with a distributed vibration absorber attached

Wind turbine towers are slender structures built usually as steel pipes with a diameter decreasing with altitude. Because of the simplicity of the tower geometry it is modeled as a vertically oriented beam, fixed to the ground at the bottom and with a solid mass, modeling a nacelle, attached to the upper end of the beam. Due to the low intrinsic damping, steel slender structures are prone to low frequency vibration (caused by wind flow, seismic motions) and for this reason are provided with damping devices, such as pitch actuators and vibration absorbers, tuned usually to the very first natural frequencies. The Figure 2 presents a model of the wind-turbine's tower-nacelle system with a distributed vibration absorber attached along half the length of the tower. The following parameters of the real-world full-scale Vensys 82 wind tower are taken in calculations [16–17]:

- length of the tower: 85.0 m;
- mass of the tower: 169000 kg;
- mass of the nacelle: 90000 kg;
- mass density $\rho = 7800 \text{ kg/m}^3$;
- Young's modulus $E = 2.1 \cdot 10^{11} \text{ N/m}^2$.

The functions approximating cross-section area $A(x)$ and area moment of inertia $I(x)$ are determined based on the actual dimensions of the tower cross-section, where maximal values are as follows: $A_{MAX} = 0.2949 \text{ m}^2$, $I_{MAX} = 0.746 \text{ m}^4$. The internal damping of the tower is neglected.

The basic functions in formula (4) are chosen as the modes of vibration of the beam with constant cross-section area and moment of inertia, equal the average values for the tower, with the bottom end fixed and with a solid mass, equal the mass of a nacelle, attached to the upper end.

The proposed distributed vibration absorber may be an alternative to the absorber applied at a single point near the nacelle, because it can be easier attachment of a number of smaller masses along the tower instead of one large mass at the top.

The total weight of the absorber is 4225 kg, 2.5 percent of the weight of the turbine's tower. Parameters of the distributed absorber are taken to be constant along the length of the beam: $\tilde{m}(x) = \text{const}$, $\tilde{c}(x) = \text{const}$, $\tilde{k}(x) = \text{const}$. The first three natural frequencies of the presented tower-nacelle system are: $f_1 = 0.352 \text{ Hz}$, $f_2 = 2.721 \text{ Hz}$, $f_3 = 8.132 \text{ Hz}$. In numerical calculations presented it is assumed that the tower is excited by a concentrated harmonic force applied at the top (Figure 2).

As the first mode of vibration is the most important, as the easiest excited, it will be presented the results of tuning of the distributed absorber to the first natural frequency $f_1 = 0.352 \text{ Hz}$. The calculated dimensionless displacement amplitude of the top of the beam, referenced to the static deflection, is shown in Figure 2 for a few sets of the distributed absorber physical parameters.

The graphs show the amplitude as a function of frequency for the case without the absorber attached, for the absorber with optimal values of stiffness $\tilde{k}(x)$ and damping $\tilde{c}(x)$ coefficients densities (calculated for a given absorber mass distribution along the length of the beam) and additionally for other values of parameters.

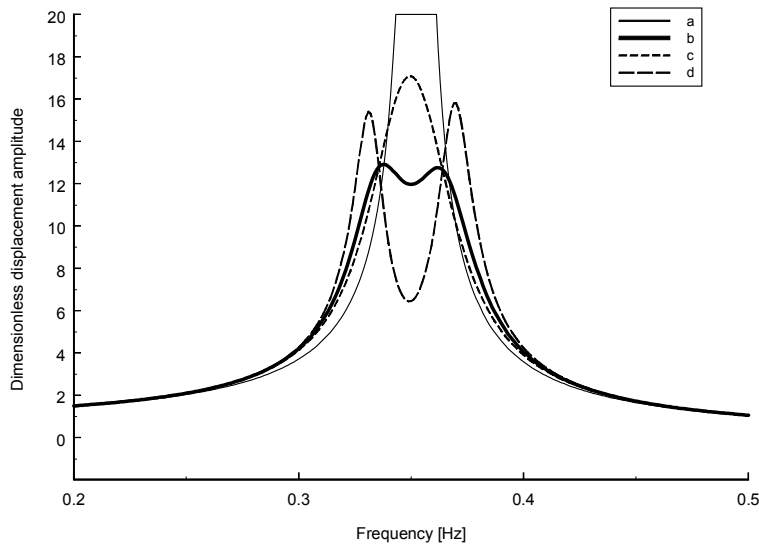


Figure 3. Dimensionless displacement amplitude of the top of the beam:
a) without absorber attached;

- b) $\tilde{c}(x) \cdot l = 40370 \text{ N/m}$, $\tilde{k}(x) \cdot l = 2800 \text{ Ns/m}$;
- c) $\tilde{c}(x) \cdot l = 40370 \text{ N/m}$, $\tilde{k}(x) \cdot l = 4000 \text{ Ns/m}$;
- d) $\tilde{c}(x) \cdot l = 40370 \text{ N/m}$, $\tilde{k}(x) \cdot l = 1500 \text{ Ns/m}$

4. Conclusions

The computational model presented can be used in local and global problems of optimal choice of the distributed vibration absorber parameters in Euler-Bernoulli beam with variable cross-section. Theoretical calculations are illustrated by an example of the possible use of the distributed vibration absorber in wind turbine's tower vibration passive control. Distributed absorbers can be effective in those cases when it is not precisely defined a position of the concentrated force applied and in a case of the distributed load.

The model presented in the paper can be further used in investigation of the optimal location of the absorber band on the beam and various tuning methods, in particular studying of the tunable absorber and with variable parameters along its length.

References

1. J.P. Den Hartog, *Mechanical Vibrations*, Dover Publications, Mineola, NY, 1985.
2. C.M. Harris, A.G. Piersol, *Harris' Shock and Vibration Handbook*, McGraw-Hill, 2002.

-
3. M. Luu, V. Zabel, C. Könke, *An optimization method of multi-resonant response of high-speed train bridges using TMDs*, Finite Elements in Analysis and Design **53** (2012) 13–23.
 4. Quan. Li, J. Fan, J. Nie, Quanwang. Li, Y. Chen, *Crowd-induced random vibration of footbridge and vibration control using multiple tuned mass dampers*, Journal of Sound and Vibration, **329** (2010) 4068–4092.
 5. E. Caetano, Á. Cunha, F. Magalhães, C. Moutinho, *Studies for controlling human-induced vibration of the Pedro e Inês footbridge, Portugal. Part 2: Implementation of tuned mass dampers*, Engineering Structures, **32** (2010) 1082–1091.
 6. E. Esmailzadeh, N. Jalili, *Optimal design of vibration absorbers for structurally damped Timoshenko beams*, ASME Journal of Vibration and Acoustics, **120** (1998) 833–841.
 7. M.J. Brennan, J. Dayou, *Global control of vibration using a tunable vibration neutralizer*, Journal of Sound and Vibration, **232**(3) (2000) 585–600.
 8. D. Younesian, E. Esmailzadeh, R. Sedaghati, *Passive vibration control of beams subjected to random excitations with peaked PSD*, Journal of Vibration and Control, **12**(9) (2006) 941–953.
 9. F. Yang, R. Sedaghati, *Vibration suppression of non-uniform curved beams under random loading using optimal tuned mass damper*, Journal of Vibration and Control, **15**(2) (2009) 233–261.
 10. Y.L. Cheung, W.O. Wong, *Isolation of bending vibration in a beam structure with a translational vibration absorber and a rotational vibration absorber*, Journal of Vibration and Control, **14**(8) (2008) 1231–1246.
 11. J.D. Yau, Y.B. Yang, *A wideband MTMD system for reducing the dynamic response of continuous truss bridges to moving train loads*, Journal of Structural Engineering, **26** (2004) 1795–1807.
 12. J.D. Yau, Y.B. Yang, *Vibration reduction for cable-stayed bridges traveled by high-speed trains*, Finite Elements in Analysis and Design, **40** (2004) 341–359.
 13. J. Li, M. Su, L. Fan, *Vibration control of railway bridges under high-speed trains using multiple tuned mass dampers*, ASCE Journal of Bridge Engineering, **10**(3) (2005) 312–320.
 14. H.N. Li, X.L. Ni, *Optimization of non-uniformly distributed multiple tuned mass damper*, Journal of Sound and Vibration, **308** (2007) 80–97.
 15. D.J. Thompson, *A continuous damped vibration absorber to reduce broad-band wave propagation in beams*, Journal of Sound and Vibration, **311** (2008) 824–842.
 16. W. Łatas, P. Martynowicz, *Modeling of vibration of wind turbine tower-nacelle system with dynamic absorber (in Polish)*, Modelowanie Inżynierskie, **44**(13) (2012) 187–198.
 17. W. Łatas, P. Martynowicz, J. Snamina, *Dynamic similarity of wind turbine's tower-nacelle system and its scaled model*, Solid State Phenomena, **208** (2014) 29–39.

Multiple Tuned Tunable Translational-rotational Vibration Absorbers in Beam

Waldemar LATAS

*Cracow University of Technology, Institute of Applied Mechanics
31-864 Cracow, Al. Jana Pawła II 37, Poland
latas@mech.pk.edu.pl*

Abstract

The paper deals with vibration of the beam with a system of the translational-rotational dynamic vibration absorbers attached. The beam is subjected to the distributed and concentrated harmonic excitation forces. Assuming small and linear vibration, an analytical Euler-Bernoulli model is applied and the solution to the problem is found with the use of Fourier method. Performing time-Laplace transformation the displacement amplitude of arbitrary point of the beam may be written in the frequency domain. The aim of the paper is to investigate the improvement of the efficiency of the translational-rotational absorbers compared with the translational ones in global vibration control problems. As an example reduction of the kinetic energy of the host structure is considered. Numerical simulations shows a considerable improvement of vibration reduction when the translational-rotational absorbers are utilized.

Keywords: dynamic vibration absorber, beam vibration, vibration reduction

1. Introduction

The primary task of dynamic vibration absorbers [DVA] – mainly the most common passive tuned mass dampers [TMD] – attached to the vibrating structure subjected to harmonic loading is to cease the steady-state oscillations at the point of attachment [1–4]. They are used both for damping of longitudinal and torsional vibration. Many theoretical studies have been devoted to methods of optimal choice of tuned mass dampers parameters for both linear and nonlinear problems [5–17].

Due to the number of possible applications in a wide variety of structures a lot of attention has been directed to the proper selection of TMD parameters in beam structures [20–26]. For continuous systems such as beams, usually the best location of a mass damper is a point of application of the load, but it might be technically impossible. In such situation and in the case of distributed loading, improperly chosen localization may increase the amplitude of vibration in certain areas of the system.

Depending on whether there is considered a local optimization problem – for example, minimization of the amplitude of the structure at a fixed point, or a global optimization problem – for example, minimization of the kinetic energy of the vibrating system, there may be obtained different optimal parameters of the damper and a key issue in global optimization problems is the right location of the damper [24,27].

To improve the efficiency of damping there are used systems of tuned mass dampers, tuned in the most general case for a single or several resonant frequencies for broadband excitation [17–19, 28] [20,22].

In this article a model based on Euler-Bernoulli theory is built for a beam subjected to the distributed and concentrated harmonic excitation forces, equipped with a system

of the translational-rotational dynamic vibration absorbers. It is shown that the rotational vibration absorbers used together with the translational ones can significantly improve the effectiveness of vibration isolation.

2. Theoretical model

Figure 1 presents a system considered in the paper – a beam subjected to the distributed loading and p concentrated forces, with r translational-rotational vibration absorbers. The beam is of: length L , mass density ρ , cross-section area A , geometrical moment of inertia I , Young's modulus E .

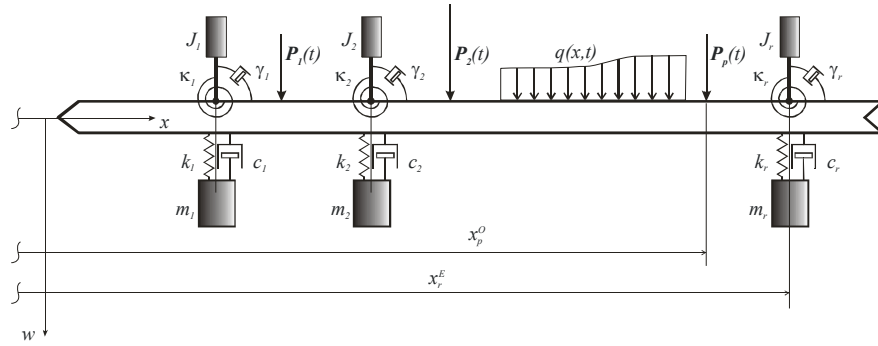


Figure 1. Beam with a system of translational-rotational vibration absorbers

Assuming small, linear vibrations of the Euler-Bernoulli beam with internal damping described by parameter α (Voigt-Kelvin model) the equation of motion takes the form [27]:

$$\rho A \frac{\partial^2 w}{\partial t^2} + EI \alpha \frac{\partial^5 w}{\partial x^4 \partial t} + EI \frac{\partial^4 w}{\partial x^4} = q(x,t) + \sum_{j=1}^p P_j(t) \delta(x - x_j^o) + \sum_{j=1}^r F_j(t) \delta(x - x_j^E) + \sum_{j=1}^r \frac{\partial M_j(t)}{\partial x} \delta(x - x_j^E) \quad (1)$$

where:

$q(x,t)$ –distributed loading;

$P_j(t)$ – j -th concentrated force applied at the point of coordinate x_j^o ;

$F_j(t)$ – j -th concentrated force applied from the translational vibration absorber at the location of coordinate x_j^E ;

$M_j(t)$ – j -th concentrated torque applied from the rotational vibration absorber at the location of coordinate x_j^E ;

m_j, c_j, k_j – mass, damping and stiffness coefficients of the j -th translational vibration absorber;

J_j, γ_j, κ_j – moment of inertia, damping and stiffness coefficients of the j -th rotational vibration absorber;

p – number of concentrated forces; r – number of translational-rotational vibration absorbers.

To solve the equation of motion (1) the method of separation of variables is utilized:

$$w(x, t) = \sum_{i=1}^{\infty} q_i(t) \varphi_i(x) \quad (2)$$

In the above expression $\varphi_i(x)$ are the eigenfunctions of the beam without absorbers attached, which depend on the boundary conditions. The functions of time $q_i(t)$ need to be determined. It is assumed the following form of the distributed loading: $q(x, t) = h(t)g(x)$.

After substitution of the series (2) into equation (1) the time Laplace transformation is performed (with initial conditions equal to zero) and it is obtained:

$$\begin{aligned} \sum_{i=1}^{\infty} [\rho A s^2 Q_i(s) + EI \alpha \beta_i^4 s Q_i(s) + EI \beta_i^4 Q_i(s) - a_i H(s) - \sum_{j=1}^p d_{ji} P_j(s) - \\ \sum_{j=1}^r b_{ji} F_j(s) - \sum_{j=1}^r e_{ji} M_j(s)] \varphi_i(x) = 0 \end{aligned} \quad (3)$$

Assuming that the eigenfunctions $\varphi_i(x)$ are orthogonal with the weight function $\eta(x)$, the numerical values of the coefficients in equation (3) can be expressed as:

$$a_i = \frac{\int_0^L g(x) \varphi_i(x) dx}{K_i^2}, \quad d_{ji} = \frac{\varphi_i(x_j^o)}{K_i^2}, \quad b_{ji} = \frac{\varphi_i(x_j^E)}{K_i^2}, \quad e_{ji} = \frac{-\varphi'_i(x_j^E)}{K_i^2} \quad (4)$$

where: $K_i^2 = \int_0^L \eta(x) \varphi_i^2(x) dx$, and additionally $\beta_i^4 = \frac{\rho A}{EI} \omega_i^2$; ω_i is the i -th resonance frequency of the beam without vibration absorbers attached and with the internal damping neglected ($\alpha = 0$). In equation (3) the symbols: $Q_i(s)$, $H(s)$, $P_j(s)$, $F_j(s)$, $M_j(s)$ denote the Laplace transforms of the: $q_i(t)$, $h(t)$, $P_j(t)$, $F_j(t)$, $M_j(t)$ respectively.

Taking into account the linear independence of the eigenfunctions $\varphi_i(x)$ it can be obtained from equation (3) an expression for the Laplace transform $W(x, s)$ of the beam deflection $w(x, t)$:

$$W(x, s) = \sum_{i=1}^{\infty} \frac{a_i H(s) + \sum_{j=1}^p d_{ji} P_j(s) + \sum_{j=1}^r b_{ji} F_j(s) + \sum_{j=1}^r e_{ji} M_j(s)}{\rho A s^2 + EI(1 + \alpha s) \beta_i^4} \varphi_i(x) \quad (5)$$

and the Laplace transform of the beam slope

$$\frac{\partial W(x, s)}{\partial x} = \sum_{i=1}^{\infty} \frac{a_i H(s) + \sum_{j=1}^p d_{ji} P_j(s) + \sum_{j=1}^r b_{ji} F_j(s) + \sum_{j=1}^r e_{ji} M_j(s)}{\rho A s^2 + EI(1 + \alpha s) \beta_i^4} \varphi'_i(x) \quad (6)$$

Transforms of the force $F_j(s)$ and torque $M_j(s)$, transmitted on the beam from the j -th translational-rotational vibration absorber, mounted at the point of coordinate x_j^E , are given by the expressions [27]:

$$F_j(s) = -W(x_j^E, s) \frac{(c_j s + k_j) m_j s^2}{m_j s^2 + c_j s + k_j} \quad (7)$$

$$M_j(s) = -\Theta(x_j^E, s) \frac{(\gamma_j s + \kappa_j) J_j s^2}{J_j s^2 + \gamma_j s + \kappa_j} \quad (8)$$

where it is introduced the symbol: $\Theta(x, s) = -\frac{\partial W(x, s)}{\partial x}$.

The transforms given by formulas (7) and (8) should be substituted into expressions (5) and (6). The resulting transforms of the line deflection and slope of the beam should be satisfied at the points where the translational-rotational absorbers are attached to the beam. These conditions furnish with the system of linear equations to determine $W(x_k^E, s)$ and $\Theta(x_k^E, s)$ ($k = 1, 2, \dots, r$).

In order to simplify the notation, the following symbols are introduced:

$$\begin{aligned} W(x_j^E, s) &= W_j, \quad \Theta(x_j^E, s) = \Theta_j, \quad \varphi_i(x_j^E) = \varphi_{ij}, \quad \varphi'_i(x_j^E) = \varepsilon_{ij}, \quad a_i H(s) + \sum_{j=1}^p d_{ji} P_j(s) = A_i \\ \rho A s^2 + EI(1 + \alpha s) \beta_i^4 &= B_i, \quad \frac{(c_j s + k_j) m_j s^2}{m_j s^2 + c_j s + k_j} b_{ji} = D_{ji}, \quad \frac{(\gamma_j s + \kappa_j) J_j s^2}{J_j s^2 + \gamma_j s + \kappa_j} e_{ji} = E_{ji} \end{aligned} \quad (9)$$

System of $2r$ linear equations for the unknown W_k, Θ_k ($k = 1, 2, \dots, r$) takes the form:

$$\begin{aligned} W_k \left[1 + \sum_{i=1}^{\infty} D_{ki} \frac{\varphi_{ik}}{B_i} \right] + \sum_{j=1, j \neq k}^r \sum_{i=1}^{\infty} W_j D_{ji} \frac{\varphi_{ik}}{B_i} + \sum_{j=1}^r \sum_{i=1}^{\infty} \Theta_j E_{ji} \frac{\varphi_{ik}}{B_i} &= \sum_{i=1}^{\infty} A_i \frac{\varphi_{ik}}{B_i} \\ \Theta_k \left[\sum_{i=1}^{\infty} D_{ki} \frac{\varepsilon_{ik}}{B_i} - 1 \right] + \sum_{j=1, j \neq k}^r \sum_{i=1}^{\infty} \Theta_j E_{ji} \frac{\varepsilon_{ik}}{B_i} + \sum_{j=1}^r \sum_{i=1}^{\infty} W_j D_{ji} \frac{\varepsilon_{ik}}{B_i} &= \sum_{i=1}^{\infty} A_i \frac{\varepsilon_{ik}}{B_i} \end{aligned} \quad (10)$$

Having solved the system (10) the transforms of the forces $F_j(s)$ and torques $M_j(s)$ may be obtained from expressions (7–8) and utilized then to calculate from formulas (5) and (6) the transforms of the deflection and slope of the beam. Assuming steady state vibration, after substituting $s = j\omega$ ($j = \sqrt{-1}$), it may be obtained the expressions for the deflection and slope of the beam in the frequency domain.

3. Numerical results: tunable translational-rotational vibration absorber – global control problem

It has been built a numerical algorithm which determines in s -domain the transforms of the deflection and slope for arbitrary boundary conditions at the ends of the beam. When harmonic excitation is considered the algorithm allows to obtain the amplitude-frequency characteristics at any cross-section of the beam for the deflection and slope respectively, for the bending moment and transverse force, the time-averaged kinetic energy of the system or its part can also be determined.

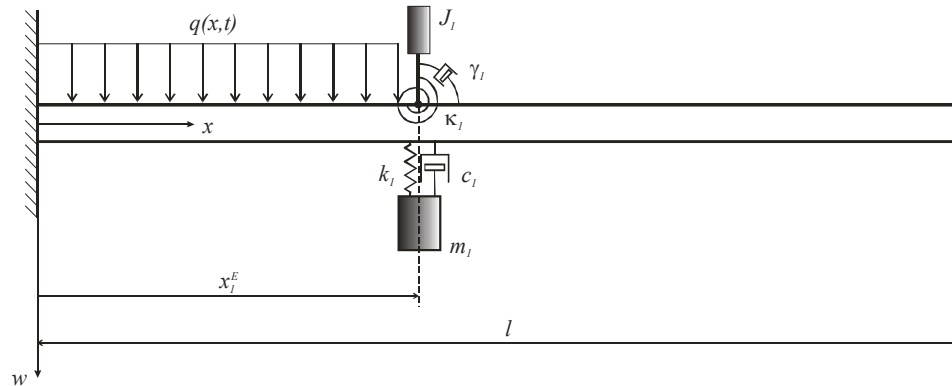


Figure 2. Cantilever beam of length l excited by a uniform distributed harmonic loading with a tunable translational-rotational absorber attached

A cantilever steel beam is considered excited by a uniform distributed harmonic loading in the region: $0 < x < x_1^E$ (Figure 2), with parameters: $l = 1.0 \text{ m}$, $x_1^E = 0.3l$, $E = 2.1 \cdot 10^{11} \text{ N/m}^2$, $\rho = 7800 \text{ kg/m}^3$. The internal damping of the beam is neglected. The beam has a rectangular cross-section with a width of $b = 0.05 \text{ m}$ and a height of $h = 0.005 \text{ m}$. There is only one translational-rotational absorber of mass $m_1 = 0.1 \text{ kg}$ and moment of inertia $J_1 = 0.0001 \text{ kgm}^2$ attached at $x_1^E = 0.3l$ – the right border of the loading. The aim of the absorber is isolation of vibration transferred from the loaded to the unloaded area of the beam. As a global measure of vibration is used the time-averaged kinetic energy in the unloaded region: $x_1^E < x < l$.

Because a simple control algorithm can be used, from the practical point of view it is preferable to use the tunable dampers [24]. The first four natural frequencies of the presented beam are: $f_1 = 4.191$ Hz, $f_2 = 26.264$ Hz, $f_3 = 73.541$ Hz, $f_4 = 144.110$ Hz.

The calculated time-averaged kinetic energy of the unloaded region of the beam is shown in Figure 2, for comparison, for three cases:

- only the translational vibration absorber attached to the beam;
- the translational-rotational vibration absorber attached to the beam;
- the beam alone, without any vibration absorber attached.

It is assumed in further calculations that the absorbers attached are tuned so that they are resonant at each single frequency and do not have energy dissipating appliances ($c_1 = 0$, $\gamma_1 = 0$).

It can be seen from the graph in Figure 2 that there is a much improvement in the efficiency of the translational-rotational absorber compared to the translational one – a reduction of the kinetic energy in the range of frequency $\langle 1.0$ Hz, 8.0 Hz \rangle is almost of two orders of magnitude (around eighty times for the frequency equal 8.0 Hz).

The drawback of the tunable absorbers is that they cause an increase in global vibration at the new natural frequencies of the resulting structure which coincide with the excitation frequency. In this case the better performance may be obtained by detuning the absorber [24].

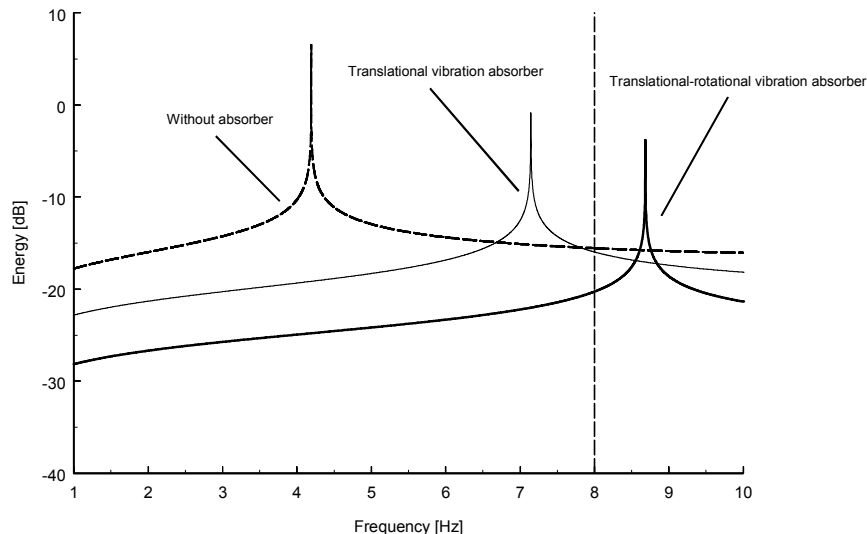


Figure 3. Kinetic energy of the unloaded region of the cantilever beam: without any absorber; with the translational absorber; with the translational-rotational absorber – the absorbers attached are tuned to be resonant at each frequency

4. Conclusions

The computational model presented can be used in local and global problems of optimal choice of position and parameters of the system of translational-rotational vibration absorbers in beams. Theoretical calculations are illustrated by an example of the use of tunable translational-rotational absorber in global control of vibration. The numerical results obtained demonstrate the possible significantly improved effectiveness of the translational-rotational absorber compared to the translational one, due it can absorb and isolate both the translational and rotational motion of the beam.

References

1. J.P. Den Hartog, *Mechanical Vibrations*, Dover Publications, Mineola, NY, 1985.
2. B.G. Korenev, L.M. Reznikov, *Dynamic Vibration Absorbers, Theory and Technical Applications*, Wiley, New York, 1993.
3. C.M. Harris, A.G. Piersol, *Harris' Shock and Vibration Handbook*, McGraw-Hill, 2002.
4. D.J. Mead, *Passive Vibration Control*, Wiley, New York ,1999.
5. C.L. Lee, Y.T. Chen, L.L. Chung, Y.P. Wangd, *Optimal design theories and applications of tuned mass dampers*, Engineering Structures, **28** (2006) 43-53.
6. F. Rüdinger, *Tuned mass damper with fractional derivative damping*, Engineering Structures **28** (2006) 1774-1779.
7. C. Li, B. Zhu, *Estimating double tuned mass dampers for structures under ground acceleration using a novel optimum criterion*, Journal of Sound and Vibration, **298** (2006) 280-297.
8. S. Krenk, J. Høgsberg, *Tuned mass absorbers on damped structures under random load*, Probabilistic Engineering Mechanics, **23** (2008) 408-415.
9. A. Mohtat, E. Dehghan-Niri, *Generalized framework for robust design of tuned mass damper systems*, Journal of Sound and Vibration, **330** (2011) 902-922.
10. A.Y.T. Leung, H. Zhang, *Particle swarm optimization of tuned mass dampers*, Engineering Structures, **31** (2009) 715-728.
11. S. Sgobba, G.C. Marano, *Optimum design of linear tuned mass dampers for structures with nonlinear behaviour*, Mechanical Systems and Signal Processing, **24** (2010) 1739-1755.
12. G.C. Marano, R. Greco, S. Sgobba, *A comparison between different robust optimum design approaches: Application to tuned mass dampers*, Probabilistic Engineering Mechanics, **25** (2010) 108-118.
13. S. Chakraborty, B.K. Roy, *Reliability based optimum design of tuned mass damper in seismic vibration control of structures with bounded uncertain parameters*, Probabilistic Engineering Mechanics, **26** (2011) 215-221.
14. B. Farshi, A. Assadi, *Development of a chaotic nonlinear tuned mass damper for optimal vibration response*, Communication in Nonlinear Science and Numerical Simulation, **16** (2011) 4514-4523.

-
15. M. Jokic, M. Stegic, M. Butkovic, *Reduced-order multiple tuned mass damper optimization: A bounded real lemma for descriptor systems approach*, Journal of Sound and Vibration, **330** (2011) 5259-5268.
16. O.F. Tigli, *Optimum vibration absorber (tuned mass damper) design for linear damped systems subjected to random loads*, Journal of Sound and Vibration, **331** (2012) 3035-3049.
17. J.D. Yau, Y.B. Yang, *A wideband MTMD system for reducing the dynamic response of continuous truss bridges to moving train loads*, Journal of Structural Engineering, **26** (2004) 1795-1807.
18. J.D. Yau, Y.B. Yang, *Vibration reduction for cable-stayed bridges traveled by high-speed trains*, Finite Elements in Analysis and Design, **40** (2004) 341-359.
19. J. Li, M. Su, L. Fan, *Vibration control of railway bridges under high-speed trains using multiple tuned mass dampers*, ASCE Journal of Bridge Engineering, **10**(3) (2005) 312–320.
20. M. Luu, V. Zabel, C. Könke, *An optimization method of multi-resonant response of high-speed train bridges using TMDs*, Finite Elements in Analysis and Design, **53** (2012) 13-23
21. Quan. Li, J. Fan, J. Nie, Quanwang. Li, Y. Chen, *Crowd-induced random vibration of footbridge and vibration control using multiple tuned mass dampers*, Journal of Sound and Vibration, **329** (2010) 4068-4092.
22. E. Caetano, Á. Cunha, F. Magalhães, C. Moutinho, *Studies for controlling human-induced vibration of the Pedro e Inês footbridge, Portugal. Part 2: Implementation of tuned mass dampers*, Engineering Structures, **32** (2010) 1082-1091.
23. E. Esmailzadeh, N. Jalili, *Optimal design of vibration absorbers for structurally damped Timoshenko beams*, ASME Journal of Vibration and Acoustics, **120** (1998) 833-841.
24. M.J. Brennan, J. Dayou, *Global control of vibration using a tunable vibration neutralizer*, Journal of Sound and Vibration, **232**(3) (2000) 585-600.
25. D. Younesian, E. Esmailzadeh, R. Sedaghati, *Passive vibration control of beams subjected to random excitations with peaked PSD*, Journal of Vibration and Control, **12**(9) (2006) 941-953.
26. F. Yang, R. Sedaghati, *Vibration suppression of non-uniform curved beams under random loading using optimal tuned mass damper*, Journal of Vibration and Control, **15**(2) (2009) 233-261.
27. Y.L. Cheung, W.O. Wong, *Isolation of bending vibration in a beam structure with a translational vibration absorber and a rotational vibration absorber*, Journal of Vibration and Control, **14**(8) (2008) 1231-1246.
28. H.N. Li, X.L. Ni, *Optimization of non-uniformly distributed multiple tuned mass damper*, Journal of Sound and Vibration, **308** (2007) 80-97.

Geometrically Nonlinear Free Transversal Vibrations of Thin-Walled Elongated Panels with Arbitrary Generatrix

Mykhailo MARCHUK

Pidstryhach Institute for Applied Problems of Mechanics and Mathematics, NASU

3 b Naukova Str., L'viv, 79053, Ukraine

and National University "L'viv Polytechnic

12 Bandera Str., L'viv, 79013, Ukraine

mv_marchuk@ukr.net; marchuk@iapmm.lviv.ua

Taras GORIACHKO

Pidstryhach Institute for Applied Problems of Mechanics and Mathematics, NASU

3 b Naukova Str., L'viv, 79053, Ukraine

taras.horyachko@gmail.com

Vira PAKOSH

Pidstryhach Institute for Applied Problems of Mechanics and Mathematics, NASU

3 b Naukova Str., L'viv, 79053, Ukraine

v.pakosh@ukr.net

Abstract

The algorithm for finding a finite number of the first values of natural frequencies and forms of geometrically nonlinear free transverse vibrations of thin-walled elongated panels with arbitrary generatrix is proposed and verified. Under normal coordinate quadratic the approximation of displacements is used. Along the tangential coordinates used one-dimensional finite elements. The discrete variation problem is built. For its solving the perturbation method is applied. The numerical results are compared with previously obtained by other authors.

Keywords: elongated panels, vibrations, nonlinearity, perturbations method

1. Introduction

Thin elongated panels with various curves as generatrix medial surfaces are widely used in the construction and hardware for various purpose. In the operating conditions they are subjected to intense dynamic loading, in particular, cyclic. These loads are causing in panels the normal displacement commensurate with their thickness. The last are causing to their geometrically nonlinear dynamic stress-strain state.

To avoid resonance phenomena for the actions of cyclic loading is necessary at the design stage to determine the spectrum of frequencies of said structural elements. Issues of geometrically nonlinear vibrations of plate and shell elements of the constructions on the basis classical and shear theories thoroughly examined in [11] for the definition of the fundamental frequency. Significant progress in this field together with experimental approaches is done in [1, 2] and some analytical results are given in [8]. However, for nonlinear oscillations in many cases it is necessary to define a number of first frequencies and forms to detect the phenomena of internal, subharmonic and combina-

tion resonances [4]. A numerical method for determining the first several frequencies and forms at geometrically nonlinear vibrations of shells is proposed in the work [5].

In this paper is developed and verified algorithm for determining a finite number of natural frequencies and forms elongated thin panels for geometrically nonlinear vibrations. For the primary relations is taken spatial equation geometrically nonlinear dynamic theory of elasticity. Used quadratic approximation of displacements by the normal coordinate and finite-element by tangential. The discrete variation problem is built. For its solving the method of perturbations is applied.

2. Problem statement

Curved anisotropic elastic layer with thickness h we take to natural mixed system of coordinate $\alpha_1, \alpha_2, \alpha_3$ on the median surface. This surface is formed by the motion of the line $\alpha_1 = 0; \alpha_3 = 0$ on the segment of arbitrary generatrix. We consider that layer is significantly larger along the axis α_2 to the length of the section arc $\alpha_2 = 0$ of the middle surface $\alpha_3 = 0$. So we have an elongated panel. If the conditions of fixing the ends of the panel $\alpha_1 = \pm\alpha_1^0$ and the initial conditions are independent of the coordinate α_2 , then through little influence of conditions fixing the edges $\alpha_2 = \pm\alpha_2^0$, the functions, that determine the characteristics of geometrically nonlinear vibration processes in the plane of the middle section, are dependent from α_1, α_3 . To find these functions are [9]:

- motion equations

$$\operatorname{div} \hat{S} = \rho \frac{\partial^2 U}{\partial t^2}; \quad (1)$$

- elasticity relations

$$\hat{\Sigma} = \tilde{A} \otimes \hat{\varepsilon}; \quad (2)$$

- deformation relation between the strain tensor components $\hat{\varepsilon}$ and the components of the elastic displacement vector $\vec{U} = u_i \vec{e}_i \vec{e}_j$

$$\varepsilon_{ij} = \frac{1}{2} (\nabla_i u_j + \nabla_j u_i + \nabla_i u^k \nabla_j u_k); \quad (3)$$

- relation between the components S^{ij} of the nonsymmetrical Kirchhoff stress tensor \hat{S} and the components σ^{ik} of the symmetric Piola stress tensor $\hat{\Sigma}$

$$S^{ij} = \sum_k \sigma^{ik} (\delta_k^j + \nabla_k u^j). \quad (4)$$

In equations (1) and (2) \tilde{A} – tensor of elastic properties of anisotropic layer, and ρ – its density.

Boundary conditions on the front surface of the panel $\alpha_3 = \pm h/2$ for the free vibrations has the form

$$S^{31}(\alpha_1, \pm h/2, t) = S^{33}(\alpha_1, \pm h/2, t) = 0, \quad |\alpha_1| \leq \alpha_1^0. \quad (5)$$

At the elongated ends of the panel $\alpha_1 = \pm \alpha_1^0$ under the conditions of the fixing the hinge on the lower surface of the front $\alpha_2 = -h/2$ boundary conditions has the form

$$S^{1i}(a, \alpha_3, t) = 0, \quad (6)$$

$$u_i(a, \pm h/2, t) = 0, \quad |\alpha_3| \leq h/2, \quad i = 1, 3, \quad a = 0, l. \quad (7)$$

The motion equations (1) together with relations (2)–(4) and boundary conditions (5)–(7) describe geometrically nonlinear transverse vibrations of the middle section of the panel, if the initial conditions specify as follows:

$$u_i(\alpha_1, \alpha_3, t)|_{t=t_0} = v_i^0(\alpha_1, \alpha_3), \quad \frac{\partial u_i(\alpha_1, \alpha_3, t)}{\partial t}|_{t=t_0} = v_i^1(\alpha_1, \alpha_3), \quad i = 1, 3, \quad (8)$$

$$|v_3^0(\alpha_1, \alpha_3)| > |v_1^0(\alpha_1, \alpha_3)|, \quad (\alpha_1, \alpha_3) \in \Omega = [-\alpha_1^0, \alpha_1^0] \times [-h/2, h/2]. \quad (9)$$

3. Discretized problem

Considered above differential formulation of the problem of geometrically nonlinear free vibrations is equivalent to the problem of minimizing the functional L [10]:

$$\begin{aligned} L = & - \int_{\Omega} \sum_i \sum_j u_i \frac{\partial S^{ij}}{\partial x_j} d\Omega - \int_{\Omega} \rho \frac{\partial^2 U^T}{\partial t^2} \cdot U d\Omega = \\ & = - \int_{\Omega} \sum_i \sum_j S^{ij} \frac{\partial u_i}{\partial x_j} d\Omega - \int_{\Omega} \rho \frac{\partial^2 U^T}{\partial t^2} \cdot U d\Omega \rightarrow \min. \end{aligned} \quad (10)$$

Boundary conditions (5) and (6) for the variation formulation of the problem is a natural [10], and condition (7) must take into account during its solution.

Assuming that the considering panel is thin-walled, approximate the unknown displacement at transverse coordinate [7]:

$$u_i(\alpha_1, \alpha_2) = \sum_{k=1}^2 u_{ik}(\alpha_1) p_k(\alpha_3), \quad i = 1, 3, \quad (11)$$

where

$$p_0(\alpha_3) = \frac{1}{2} - \frac{\alpha_3}{h}, \quad p_1(\alpha_3) = \frac{1}{2} + \frac{\alpha_3}{h}, \quad p_2(\alpha_3) = 1 - \left(\frac{2\alpha_3}{h} \right)^2.$$

For finding unknown coefficients $u_{ik}(\alpha_1)$ in (11) we use approximation by the tangential coordinate α_1 on one-dimensional izoparametrical linear finite elements [10]:

$$u_{ik}^{(e)} = \sum_{k,m}^2 u_{ikm}^{(e)}(\alpha_1) \varphi_m^{(e)}(\xi), \quad \xi = \frac{2\alpha_1}{\alpha_{12}^{(e)} - \alpha_{11}^{(e)}} - 1, \quad (12)$$

where e – element number; $u_{ikm}^{(e)} = u_{ik}(\alpha_{1m}^{(e)})$; $\alpha_{1m}^{(e)}(\alpha_1)$, $m=1,2$ – coordinates of the element nodes; $\varphi_1^{(e)}(\xi) = \frac{1}{2}(1-\xi)$; $\varphi_2^{(e)}(\xi) = \frac{1}{2}(1+\xi)$.

After substituting (11) into (4) and the result together with (11) into (10) we obtain:

$$L^\Delta = \{\mathbf{u}\}^T K_L \{\mathbf{u}\} + \{\mathbf{u}\}^T K_{NL}(\mathbf{u}) \{\mathbf{u}\} + \{\mathbf{u}\}^T M \{\ddot{\mathbf{u}}\} \rightarrow \min, \quad (13)$$

where $\{\mathbf{u}\} = \{\mathbf{u}\}(t)$ – vector of values of the coefficients $u_{ikm}^{(e)}$ at points in the finite-element partition of the section $[-\alpha_1^0, \alpha_1^0]$; K_L – linear, and K_{NL} – nonlinear components of stiffness matrix; M – matrix of mass [10].

Non-linear component of stiffness matrix K_{NL} presented in the form

$$K_{NL}(\{\mathbf{u}\}(t)) = B(\{\mathbf{u}\}(t)) \cdot \{\mathbf{u}\}^T(t) \cdot B^T(\{\mathbf{u}\}(t)). \quad (14)$$

Matrix $B(\{\mathbf{u}\}(t))$ we obtain by integrating in (10) members, who are the product of partial derivatives, the displacement u_i [10].

Minimum of discrete functional (13) is achieved at the point $\{\mathbf{u}\}(t)$, where the equation is satisfied

$$K_L(\{\mathbf{u}\}(t)) + K_{NL}(\{\mathbf{u}\}(t)) \{\mathbf{u}\}(t) + M(\{\ddot{\mathbf{u}}\}(t)) = 0. \quad (15)$$

4. The method of perturbations

The system of nonlinear equations (15) is written as

$$K_L(\{\mathbf{u}\}(t)) + \mu K_{NL}(\{\mathbf{u}\}(t)) \{\mathbf{u}\}(t) + M(\{\ddot{\mathbf{u}}\}(t)) = 0, \quad (16)$$

where $\mu (0 \leq \mu \leq 1)$ – the parameter perturbation. At $\mu = 0$ have a system of linear algebraic equations for the vector $\{\mathbf{u}\}$, while $\mu = 1$ the nonlinearity is taken into account fully. The method of perturbations the desired vector of functions $\{\mathbf{u}\}(t)$ and matrix K_L presented in the form

$$\begin{aligned} \{\mathbf{u}\}(t) &= \{\mathbf{u}\}_0(t) + \mu \{\mathbf{u}\}_1(t) + \dots, \\ K_L &= K - \mu K_{L1} - \dots. \end{aligned} \quad (17)$$

The result of substituting (17) into (16) and grouping expressions under the same powers of μ are the equations

$$M \{\ddot{\mathbf{u}}\}_0(t) + K \{\mathbf{u}\}_0(t) = 0, \quad (18)$$

$$M \{\ddot{\mathbf{u}}\}_1(t) + K \{\mathbf{u}\}_1(t) - K_{L1}(\{\mathbf{u}\}_0(t)) + K_{NL}(\{\mathbf{u}\}_0(t)) \{\mathbf{u}\}_0(t) = 0. \quad (19)$$

Solution of equation (18) is written as

$$\{u\}_0(t) = \tilde{u} \cos \omega t, \quad (20)$$

and the solution of (19) can be written as follows. Consider equation (17), which seeks a solution in the form

$$\{u\}_1(t) = \{u\}_1^*(t) + \{u\}_1^\times(t), \quad (21)$$

where $\{u\}_1^*(t)$ i $\{u\}_1^\times(t)$ – solutions of homogeneous and inhomogeneous equations (19).

According to [6] matrix K_{L1} can be represented as

$$K_{L1} = \frac{3}{4} B \{\tilde{u}\} \{\tilde{u}\}^T B^T. \quad (22)$$

After substituting (20) and (22) into (19) and taking into account formula [3]

$$4 \cos^3 \omega t = 3 \cos \omega t + \cos 3\omega t, \quad (23)$$

for finding $\{u\}_1^\times(t)$ we obtain the equation

$$M \{\ddot{u}\}_1^\times(t) + K \{u\}_1^\times(t) = -\frac{1}{4} B \{\tilde{u}\} \{\tilde{u}\}^T B^T \{\tilde{u}\} \cos 3\omega t, \quad (24)$$

solution of which we take as

$$\{\tilde{u}\}_1^\times(t) = \tilde{c} \cos 3\omega t. \quad (25)$$

After substituting (25) into equation (24) we arrive at a relations for determination of parameter \tilde{c} :

$$(K - 9\omega^2 M) \tilde{c} = -\frac{1}{4} B \{\tilde{u}\} \{\tilde{u}\}^T B^T \{\tilde{u}\}. \quad (26)$$

If the initial moment the panel is deformed on a certain law, which describes the first formula in (8) and is stationary, then the initial conditions for the functions $\{u\}_0(t)$ and $\{u\}_1(t)$ can be represented as

$$\{u\}_0(0) = \bar{A}, \quad \{\dot{u}\}_0(0) = 0, \quad (27)$$

$$\{u\}_1(0) = 0, \quad \{\dot{u}\}_1(0) = 0. \quad (28)$$

In view of (21), we write:

$$\{u\}(t) = (\bar{A} - \tilde{c}) \cos \omega t + \tilde{c} \cos 3\omega t. \quad (29)$$

This allows you to build an algorithm for partial finding a finite number of the first natural frequencies and amplitudes geometrically nonlinear vibrations of the panel:

1. Set $r = 1$ and $a_{(0)} = 0$.

2. Compute $K_{(r-1)} = K + \frac{3}{4} Ba_{(r-1)} a_{(r-1)}^T B^T$.
3. Find the eigenvalues $\omega_{(r)}$ and eigenvectors $a_{(r)}$ from the system $(K_{(r-1)} - \omega_{(r)} M)a_{(r)} = 0$.
4. If the conditions are satisfied $\|a_{(r)} - a_{(r-1)}\|/\|a_{(r)}\| \leq \varepsilon_1$, $\|\omega_{(r)} - \omega_{(r-1)}\|/\|\omega_{(r)}\| \leq \varepsilon_2$, where ε_1 and ε_2 – specified accuracy, then go to step 5, otherwise $r := r + 1$, and go to step 2.
5. As the solution we accept $a := a_{(r)}$, $\omega := \omega_{(r)}$ and find a vector \tilde{c} having solved the a system of algebraic equations $(K_{(r)} - 9\omega^2 M)\tilde{c} = -\frac{1}{4} B a a^T B^T a$.

5. Analysis of results and conclusions

To verify the proposed algorithm practicing it for problem, where are known analytical and numerical solutions [6]. We consider an isotropic plate-strip elongated edges which are fixed by with stationary hinges on the lower front of the plane (see Fig. 1), with characteristics: geometric $l = 1$ m; $h = 0.1$ m and mechanical $E = 40000$ N/m²; $\nu = 0.3$.

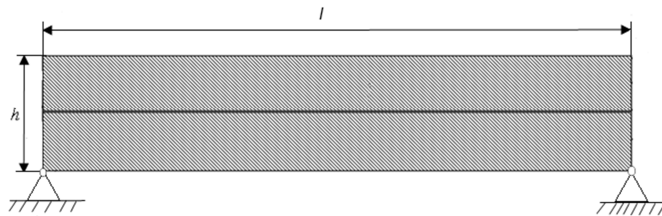


Figure 1. The plate-strip with stationary hinges on the elongated edges

In Figure 2 shows graphs of free vibrations of the point that has coordinates $(l/2; 0)$ for linear (●), analytical (▲) and obtained using the proposed algorithm (■). Sufficiently good correlation with the analytical solution is marked.

In Figure 3 shows the first four own forms (modes) for geometrically nonlinear vibrations the considered plate-strip.

In Figure 4 shows the skeletal curves [11], constructed using the proposed method (dashed line) and the results presented in the work [5] (solid line). The maximum relative error does not exceed 9%, indicating a sufficiently good approximation property of the proposed method. Subsequently, it is advisable to perform a similar study for a wider class of thin-walled elements of constructions and anisotropy of mechanical properties.

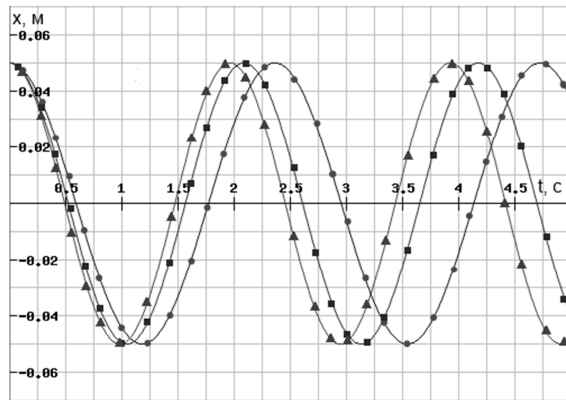
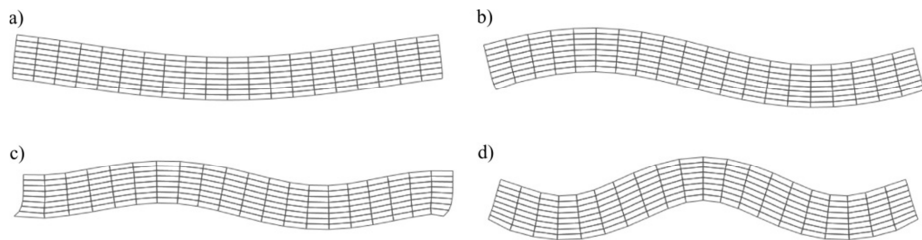
Figure 2. Free vibrations of point $(l/2; 0)$ 

Figure 3. View panels in different modes: a) – the first mode; b) – second; c) – third; d) – the fourth

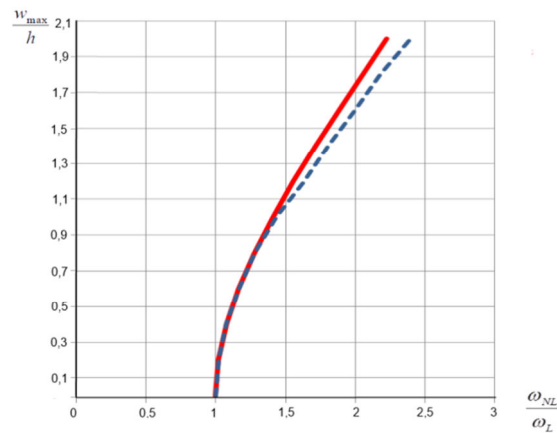


Figure 4. Comparison of amplitude-frequency characteristics obtained from the use of perturbation method and the results of the work [5]

Acknowledgments

This research is conducted with a partial support of the Ukrainian State Fund for Fundamental Researches (project code: F 53.1/028).

References

1. M. Amabili, *Nonlinear vibrations and stability of shells and plates*, Cambridge: Cambridge Univ. Press, 2008.
2. M. Amabili, *Nonlinear vibrations of rectangular plates with different boundary conditions: theory and experiments*, Comput. Struct., **82**(2004) 2587 – 2605.
3. G. Korn, T. Korn, *Handbook of high society mathematics*, M.: Nauka, 1974.
4. V. D. Kubenko, P. S. Kovalchuk, N. P. Podchasov, *Nonlinear vibrations of cylindrical shells*, K.: Vyshcha Shkola, 1989.
5. L. V. Kurpa, N. A. Budnikov, *Investigation of forced nonlinear vibrations of laminated shallow shells using a multimode approximation*, Bulletin of Donetsk Univ. Series A. Natural Sciences, **1**(2013) 55 – 60.
6. R. Lewandowski, *Analysis of strongly nonlinear free vibration of beams using perturbation method*, Civil and Env. Eng. Reports, **1**(2005) 153–168.
7. M. Marchuk, I. Mukha, T. Goriachko, *A comparative analysis of the characteristics of geometrically nonlinear stress-strain state of composite plates and cylindrical panels on the basis refined model and elasticity theory*, Modelling and Stability: Abstracts of Conference Reports, K: Taras Shevchenko National Univ. of Kyiv, 2011.
8. M. Marchuk, V. Pakosh, O. Lesyk, I. Hurayewska, *Influence of Pliability to Transversal Deformations of Shear and Compression on Correlation Frequency from Amplitude for Nonlinear Oscillations of Composite Plates*, Vibrations in Physical Systems, **22**(2006) 251–256.
9. N. F. Morozov, *Selected two-dimensional problem of elasticity theory*, Leningrad: Publishing House of Leningrad. University Press, 1978.
10. J. N. Reddy, *An introduction to nonlinear finite element analysis*, Oxford Univ. Press, 2004.
11. A. S. Volmir, *Nonlinear dynamics of plates and shells*, M.: Nauka, 1972.

Analysis of Vibrations of Plate Strip with Concentrated Masses Using Tolerance Averaging Technique

Jakub MARCZAK

Department of Structural Mechanics, Łódź University of Technology

Al. Politechniki 6, 90-924 Łódź, Poland

jakub.marczak@p.lodz.pl

Jarosław JĘDRYSIAK

Department of Structural Mechanics, Łódź University of Technology

Al. Politechniki 6, 90-924 Łódź, Poland

jarek@p.lodz.pl

Abstract

In this note vibrations of thin periodic plate strips with periodically distributed system of two concentrated masses are analysed. Moreover, it is assumed that every concentrated mass is connected to a string, which cause the effect of damping in vibrations. Governing equation for such structure is defined as a differential equation with highly oscillating, periodic and non-continuous coefficients. In order to solve the equation, tolerance averaging technique is applied. As a result, governing equations with constant coefficients are obtained. In an example, derived model is used to calculate lower and higher frequencies of the travelling wave related to the internal periodic structure.

Keywords: periodic plate strip, vibrations, tolerance averaging technique

1. Introduction

In this paper thin plate strips with span L are considered. It is assumed, that these plate strips have certain internal periodic microstructure related to a system of two concentrated masses, distributed periodically along the x_1 -axis. Additionally, there are strings attached to concentrated masses, which make it possible to observe the effect of damping on plate's strips vibrations. Given system of concentrated masses and strings makes it possible to distinguish a small, repeatable element, called the *periodicity cell*. The span of every *cell* is equal to l , which is called the *microstructure parameter* and is small compared to the plate span L .

Vibrations of these structures are described by the governing equation with highly oscillating, periodic, non-continuous coefficients, which is not a good tool to analyse special problems. Hence, investigations of such structures can be performed using different models. The most popular one is based on the homogenization method, which uses e.g. effective plate stiffness (cf. [3]). However, equations of these models neglect the effect of the microstructure size on the plate strip behaviour. Thus, to take into account this effect the tolerance averaging technique is used to average the differential equation of this plate strip. As a result, governing equations with constant coefficients are obtained.

The main aim of this paper is to derive exact formulas for frequencies of the travelling wave for the plate strip using the tolerance averaging technique, which was pro-

posed and explained by Woźniak and Wierzbicki [5], Woźniak, Michalak and Jędrysiak (eds.) [4]. Afterwards, some numerical examples of the plate strips behaviour are presented.

2. Modelling foundations

Let $Ox_1x_2x_3$ be an orthogonal Cartesian coordinate system and define t as the time coordinate. It is also assumed, that our considerations are treated as independent of x_2 -coordinate. Let us introduce the following denotations: $x \equiv x_1$, $z \equiv x_3$, $x \in [0, L]$, $z \in [-h/2, h/2]$, where h is the constant thickness of the plate. Hence, it can be assumed that the plate strip is described in the interval $\Lambda = (0, L)$, with the basic cell $\Omega \equiv [-l/2, l/2]$ in the interval $\bar{\Lambda}$, where l is the length of the basic cell, called a *microstructure parameter*. For further transformations, it is crucial, that the *microstructure parameter* l satisfies conditions: $l \ll L$ and $h \ll l$. Deflections of the plate strip are denoted as $w(x, t)$ ($x \in \bar{\Lambda}$, $t \in (t_0, t_1)$).

Let us assume, that the material properties of the plate strip $E(x)$, $\rho(x)$, $x \in \Lambda$, are periodic functions in x . Hence, functions describing the mass density per unit area of midplane μ and the bending stiffness B can be stated as follows:

$$\mu(x) \equiv h\rho(x), \quad B \equiv \frac{h^3}{12(1-\nu^2)} E(x). \quad (1)$$

Moreover, the plate strip is connected to a system of periodically distributed strings, which are described by the damping parameter $c(x)$. In order to apply the tolerance averaging technique, the parameter $c(x)$ must satisfy all conditions of a periodic function.

It is assumed, that the plate strip fulfils prerequisites of the Kirchhoff-type thin plate theory. Denoting the derivative of x by ∂ , and the time derivative by dots, the partial differential equation of the fourth order for deflection $w(x, t)$ takes the following form:

$$\partial\partial[B(x)\partial\partial w(x, t)] + c(x)\dot{w}(x, t) + \mu(x)\ddot{w}(x, t) = 0, \quad (2)$$

with coefficients being highly oscillating, non-continuous, periodic functions in x . Equation (2) describes free vibrations of the plate strip with the effect of damping on its vibrations and stands a starting point for further investigations in the framework of the tolerance averaging technique.

In the tolerance modelling procedure some introductory concepts, like: an *averaging operator*, a *slowly varying function*, a *tolerance-periodic function* and a *highly oscillating function*, are used. These concepts were presented in a various literature, for example: by Woźniak and Wierzbicki [5].

3. Modelling assumptions

There are two main assumptions in the tolerance averaging technique. The first of them is the *micro-macro decomposition* of the plate strip deflection w , which can be formulated as follows:

$$w(x, t) = W(x, t) + g^A(x)Q^A(x, t), \quad A = 1, \dots, N, \quad x \in \Lambda, \quad (3)$$

where $W(\cdot, t)$ is the *macrodeflection* of the plate strip, $Q^A(\cdot, t)$ are the *fluctuation amplitudes* and $g^A(\cdot)$ are the known *fluctuation shape functions*. Functions $W(\cdot, t)$ and $Q^A(\cdot, t)$ are the new basic kinematic unknowns, which are for every t slowly varying functions.

The *tolerance averaging approximation* is the second modelling assumption. Assuming that the terms $O(\delta)$ are negligibly small, the following relations can be proved in the course of modelling:

$$\begin{aligned} <\Phi>(x) &= <\bar{\Phi}>(x) + O(\delta), & <\Phi F>(x) &= <\Phi>(x)F(x) + O(\delta), \\ <\Phi \partial_\alpha(g^A F)>(x) &= <\Phi \partial_\alpha g^A>(x)F(x) + O(\delta), \\ x \in \Lambda; \quad \alpha = 1,2; \quad A = 1, \dots, N; \quad 0 < \delta \ll 1; \end{aligned} \quad (4)$$

where δ is a tolerance parameter, Φ is tolerance periodic function, $\bar{\Phi}$ is a periodic approximation of Φ , F is a slowly varying function and $g^A(\cdot)$ is a fluctuation shape function.

4. Modelling procedure

Basing on the introductory concepts presented in [4] nad [5] and the calculations developed by Jędrysiak in [1] and Jędrysiak and Michalak [2], the modelling procedure can be outlined as follows.

As mentioned before, the starting point is the Kirchhoff-type thin plate free vibrations differential equation (2). In order to obtain equations with constant coefficients, some transformations must be performed. These transformations are: substituting the micro-macro decomposition (3) to equation (2), applying the averaging operator and using the tolerance averaging approximations (4). As a result, we arrive at a system of equations for $W(\cdot, t)$ and $Q^A(\cdot, t)$ in the form:

$$\begin{aligned} < B > \partial \partial \partial W + < B \partial \partial g^A > \partial \partial Q^A + < c > \dot{W} + \underline{< c g^A > \dot{Q}^A} + < \mu > \ddot{W} &= 0, \\ < B \partial \partial g^A > \partial \partial W + < B \partial \partial g^A \partial \partial g^B > Q^A + & \\ + \underline{< c g^A > \dot{W}} + \underline{< c g^A g^B > \dot{Q}^A} + & \underline{< \mu g^A g^B > \ddot{Q}^A} = 0. \end{aligned} \quad (5)$$

In the system of equations (5) the first equation describes vibrations of the plate strip in the macro scale, while the second stands for the system of N equations, which refers to microvibrations. It can be observed, that only the underlined terms are dependent on the microstructure parameter l . Keeping in mind the fact, that coefficients in the system of equations above are constant, it is possible to obtain a convenient solution describing free vibrations of the plate strip, including both the effect of the microstructure and damping.

5. Frequencies of plate strip free vibrations with the influence of damping

In this section a homogenous weightless and unbounded plate strip along the x -axis is considered. Periodicity of the structure is related to a system of two periodically distributed concentrated masses M_1 and M_2 and strings attached to those masses. Strings are described by their damping parameters, c_1 and c_2 respectively, cf. Figure 1.

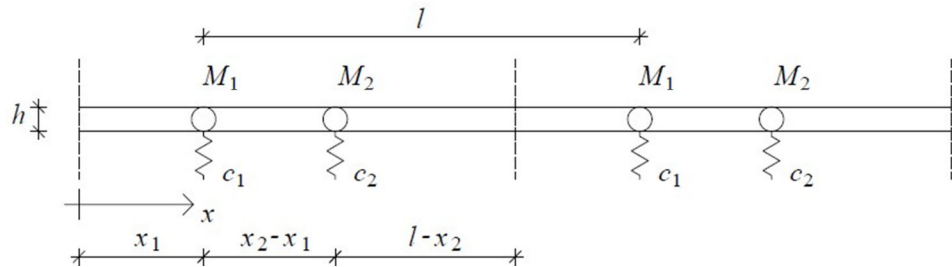


Figure 1. The plate strip with a system of two periodically distributed concentrated masses and strings

In the further investigations Young's modulus E , Poisson's ratio ν and thickness h of the plate are assumed to be constant. Moreover, the plate mass is negligibly small when compared to concentrated masses M_1 and M_2 .

According to a structure of the periodicity cell of plate strips and bearing in mind the normalizing condition $\langle \mu g \rangle = 0$, only one fluctuation shape functions g^A , $A=1$, is assumed. Denoting as follows:

$$\begin{aligned} g &\equiv g^1 \\ \tilde{D} &\equiv \langle B \partial \partial g \partial \partial g \rangle, & \hat{D} &\equiv \langle B \partial \partial g \partial \partial g \rangle, \\ \tilde{m} &\equiv \langle \mu \rangle, & \hat{m} &\equiv l^{-4} \langle \mu g g \rangle, \\ \tilde{c} &\equiv \langle c \rangle, & \bar{c} &\equiv l^{-2} \langle c g \rangle, & \hat{c} &\equiv l^{-4} \langle c g g \rangle, \end{aligned} \quad (6)$$

equations (5) take the form:

$$\begin{aligned} \tilde{D} \partial \partial \partial \partial W + \tilde{c} \dot{W} + \tilde{m} \ddot{W} + l^2 \bar{c} \dot{Q} &= 0, \\ l^2 \bar{c} \dot{W} + \hat{D} Q + l^4 \hat{c} \dot{Q} + l^4 \hat{m} \ddot{Q} &= 0. \end{aligned} \quad (7)$$

Equations (7) stand for a system of equations for the macrodeflection W and the fluctuation amplitude Q . The first equation describes fundamental vibrations of the plate strip (e.g. lower frequencies of the travelling wave), while the second refers to micro-structural vibrations (related to higher frequencies of the travelling wave). Solutions to those equations can be assumed in the form:

$$\begin{aligned} W(x,t) &= A_W \exp[i(kx - \omega t)], \\ Q(x,t) &= A_Q \exp[i(kx - \omega t)], \end{aligned} \quad (8)$$

where A_W , A_Q are amplitudes, k is a wave number, t is a time coordinate and ω is a frequency. After some transformations formulas for the lower (ω_-) and higher (ω_{+1}) frequencies can be obtained as roots of the characteristic equation in the form:

$$\begin{aligned} l^4 \tilde{m} \hat{m} \omega^4 + l^4 (\tilde{m} \hat{c} + \tilde{c} \hat{m}) i \omega^3 - (k^4 l^4 \tilde{D} \hat{m} + l^4 \tilde{c} \hat{c} - l^4 \bar{c} \bar{c} + \tilde{m} \hat{D}) \omega^2 + \\ - (k^4 l^4 \tilde{D} \hat{c} + \tilde{c} \hat{D}) i \omega + k^4 \tilde{D} \hat{D} = 0. \end{aligned} \quad (9)$$

By solving the equation above, it is possible to obtain four different roots of the characteristic equation: a pair of numbers, which refers to lower frequencies of the plate strip's free vibrations (macrovibrations) and a pair of complex conjugate numbers, which describes higher frequencies of the structure (vibrations related to microstructure).

6. Eigenvalue problem

Coefficients in equations (7) are strongly dependent on the type of assumed fluctuation shape function g^4 . In the following calculations, the exact fluctuation shape function is derived as a solution to an eigenvalue problem on the periodicity cell. In the case under consideration, eigenvalue problem takes the following form:

$$B \partial \partial \partial \partial g(x) - \mu(x) \lambda^2 g(x) = 0, \quad (10)$$

where B is the stiffness defined by (1)₂ and $g(x)$ is a periodic function related to eigenvalue $\lambda = \alpha l$ (α is the wave number). Assuming that the plate mass is negligibly small when compared to the concentrated masses and applying proper periodic boundary conditions and the normalizing condition $\langle \mu g \rangle = 0$, it is possible to obtain only one eigenfunction $g(x)$, which describe a shape of free vibrations of the cell.

In order to obtain the exact fluctuation shape function $g(x)$, methods known from the structural mechanics can be used. For each point, in which the concentrated mass is posed to the plate, equilibrium equations for transversal forces and moments can be written. By applying certain boundary conditions in the form:

$$\begin{aligned} g(0) &= g(l), & \partial g(0) &= \partial g(l), \\ \partial \partial g(0) &= \partial \partial g(l), & \partial \partial \partial g(0) &= \partial \partial \partial g(l), \end{aligned} \quad (11)$$

we arrive at the characteristic equation in the form of determinant equal to zero:

$$\det L_{pr} = 0, \quad p, r = 1..4. \quad (12)$$

As a result, the second order equation for ω is obtained. Hence, it is possible to derive one eigenvalue ω^2 . Basing on the obtained eigenvalue, the exact values of deflections along the periodicity cell can be calculated similarly to deflections of beams.

7. Results of calculations

Using the tolerance averaging technique is a convenient way of investigating plate strips behaviour in the micro-scale. In this section, several numerical examples are presented in order to verify obtained formulas.

Let us assume, that the concentrated mass M_2 is a mass of reference, to which the mass M_1 is compared. Similarly, let the damping coefficient c_2 be a reference value for the coefficient c_1 . As a result, the following denotations can be made:

$$M_1 \equiv \zeta M_2, \quad c_1 \equiv \xi c_2, \quad (13)$$

where ζ is a mass ratio and ξ is a damping coefficient ratio.

Calculation examples has been performed for several different calculation cases. In every case, it has been assumed that the plate strip thickness h is equal to $0.1l$. Additionally, in order to obtain the exact dimensionless parameters of free vibrations frequencies, the ratio between reference mass M_2 and stiffness coefficient B are defined as follows:

$$B \equiv \frac{h^3}{12} M_2 \quad (14)$$

The calculation cases differ from each other with mass distributions (coordinates x_1 and x_2), mass proportion and values (M_1 and M_2), and dispersion coefficients (c_1 and c_2). For details, cf. Table 1.

Results are shown in Table 1 and Table 2 and in the form of charts describing the microvibrations amplitude versus time coordinate, cf. Figure 2. Additionally, all the calculations are performed for different values of dimensionless wave number $q \equiv kl \in [-\pi; \pi]$, cf. Table 2.

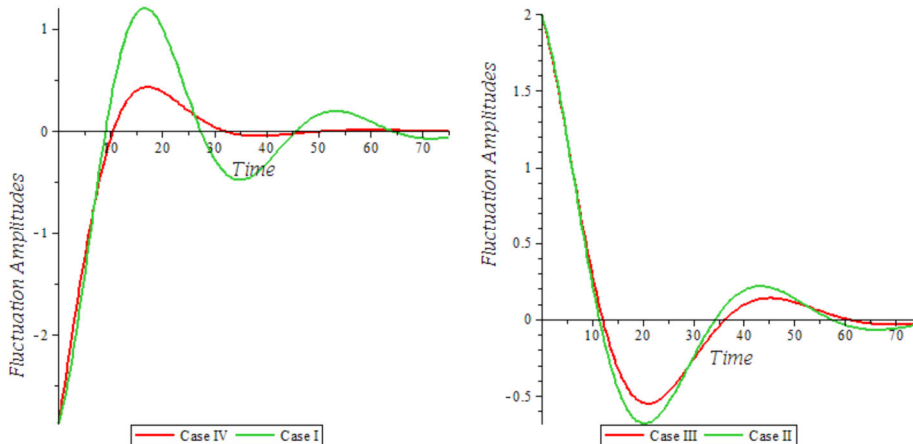


Figure 2. Damping of fluctuation amplitudes in chosen cases
Table 1. Lower and higher frequencies of travelling wave in calculation cases

and for dimensionless wave number $q=1.0$

Case	Mass coordinates		Mass proportions		Dispersion coefficients		Lower frequencies	Higher frequencies
	x_1	x_2	M_1	M_2	c_1	c_2		
I	$0,25l$	$0,75l$	1	1	10^{-1}	10^{-1}	-0,00042 -0,09958	-0,05±0,1718i
II	$0,25l$	$0,75l$	3	1	10^{-1}	10^{-1}	-0,00021 -0,09979	-0,05±0,1372i
III	$0,25l$	$0,75l$	3	1	$2 \cdot 10^{-1}$	10^{-1}	-0,00012 -0,18557	-0,057±0,1297i
IV	$0,25l$	$0,75l$	1	1	$2 \cdot 10^{-1}$	$2 \cdot 10^{-1}$	-0,00021 -0,19979	-0,10±0,1483i
V	$0,4l$	$0,7l$	1	1	10^{-1}	10^{-1}	-0,00042 -0,09958	-0,05±0,2070i
VI	$0,4l$	$0,7l$	3	1	10^{-1}	10^{-1}	-0,00021 -0,09979	-0,05±0,1665i
VII	$0,4l$	$0,7l$	3	1	$2 \cdot 10^{-1}$	10^{-1}	-0,00012 -0,18328	-0,058±0,1595i
VIII	$0,4l$	$0,7l$	1	1	$2 \cdot 10^{-1}$	$2 \cdot 10^{-1}$	-0,00021 -0,19979	-0,10±0,1880i

Table 2. Comparison of lower and higher frequencies of travelling wave in different calculation cases depending on different dimensionless wave number q

Case	Lower frequencies			Higher frequencies		
	$q=0.1$	$q=1.0$	$q=2.0$	$q=0.1$	$q=1.0$	$q=2.0$
I	$-4,2 \cdot 10^{-8}$	-0,00042	-0,00718	-0,05±0,1718i	-0,05±0,1718i	-0,05±0,1718i
	-0,10000	-0,09958	-0,09282			
II	$-2,1 \cdot 10^{-8}$	-0,00021	-0,00345	-0,05±0,1372i	-0,05±0,1372i	-0,05±0,1372i
	-0,10000	-0,09979	-0,09655			
III	$-1,2 \cdot 10^{-8}$	-0,00012	-0,00192	-0,057±0,1297i	-0,057±0,1297i	-0,057±0,1297i
	-0,18568	-0,18557	-0,18391			
IV	$-2,1 \cdot 10^{-8}$	-0,00021	-0,00339	-0,10±0,1483i	-0,10±0,1483i	-0,10±0,1483i
	-0,20000	-0,19979	-0,19661			
V	$-4,2 \cdot 10^{-8}$	-0,00042	-0,00718	-0,05±0,2070i	-0,05±0,2070i	-0,05±0,2070i
	-0,10000	-0,09958	-0,09282			
VI	$-2,1 \cdot 10^{-8}$	-0,00021	-0,00345	-0,05±0,1665i	-0,05±0,1665i	-0,05±0,1665i
	-0,10000	-0,09979	-0,09655			
VII	$-1,2 \cdot 10^{-8}$	-0,00012	-0,00192	-0,058±0,1595i	-0,058±0,1595i	-0,058±0,1595i
	-0,18340	-0,18328	-0,18157			
VIII	$-2,1 \cdot 10^{-8}$	-0,00021	-0,00339	-0,10±0,1880i	-0,10±0,1880i	-0,10±0,1880i
	-0,20000	-0,19979	-0,19661			

8. Final remarks

In this paper *the tolerance averaging technique* has been used to obtain the governing equations with constant coefficients for thin plate strips with internal periodic structure. By analyzing results shown in Tables 1 and 2 and Figure 2, it can be observed that:

- the tolerance model is a convenient tool for the analysis of micro- and macro vibrations in case, in which the effect of damping has to be taken into account;
- the lower frequencies of the travelling wave are dependent on the dimensionless wave number q ;
- as long as the mass proportions ζ and the dimensionless wave number q are constant and $\xi = 1$, the lower frequencies do not depend on the mass distribution;
- the obtained values of the higher frequencies are complex numbers, which real part describes the damping of vibrations while the imaginary part describes the period of vibrations;
- the mass proportions and coordinates of the concentrated masses have an influence on the imaginary part of the higher frequency, but it seems that they have no effect on its real part;
- the damping coefficients affect both real and imaginary part of the higher frequencies;
- the higher frequencies are not dependent on the dimensionless wave number q ;
- higher damping coefficients make vibration amplitudes decrease faster.

References

1. J. Jędrysiak, *Dispersion models of thin periodic plates. Theory and applications, Habilitation Thesis*, Sci. Cull. of Łódź Techn Univ., No 872, series: Transactions, 289, Łódź 2001 (in Polish).
2. J. Jędrysiak, B. Michalak, *Some remarks on dynamic results for averaged and exact models of thin periodic plates*, J. Theor. Appl. Mech., Vol. **43**, 2, 2005, p.405-425.
3. R.V. Kohn, M. Vogelius, *A new model of thin plates with rapidly varying thickness*, Int. J. Solids Struct., Vol. **20**, 1984, p.333-350.
4. Cz. Woźniak, B. Michalak, J. Jędrysiak, (eds.), *Thermomechanics of microheterogeneous solids and structures*, Wyd. PL, Łódź, 2008.
5. Cz. Woźniak, E. Wierzbicki, *Averaging techniques in thermomechanics of composite solids*, Wyd. PCz, Częstochowa, 2000.

Model Based Local Fault Detection in Helical Gears

Jędrzej MĄCZAK

Institute of Vehicles, Warsaw University of Technology

Narbutta 84, 02-524 Warszawa

jma@mechatronika.net.pl

Abstract

In the paper the possibility of model based detection of local faults in helical gears is analysed. Presented methods allow early detection of anomalies in the time vibration signal that could be linked to the fatigue tooth damages like pitting and tooth fracture. They relies on calculation of different signal parameters for the consecutive meshes and allows for acquiring information about the disturbances of the meshing process for particular tooth pairs. They permit the observation of the energy density changes for the consecutive teeth (or tooth pairs) during the normal exploitation of the gearbox. All the described methods are based on analysis of the time signals. Contrary to the methods based on spectral analysis these methods allow for precise localisation of gear defects and linking them to the particular pinion or gear teeth. Additionally they could be used in the procedure of gear manufacturing quality assessment.

Keywords: local meshing plane tooth fault detection, helical gear diagnostics, gear meshing model

1. Introduction

Local damage to the gear teeth causes short-term, local impulses in gear vibration signal repeated every rotation of the shaft and resulting in the phenomenon of amplitude and phase modulation [1–3]. It could be proved [4], that in the initial stage of failures development, when the energy of signal changes is particularly small, the signal is dominated by the phenomenon of phase modulation. This type of disturbances, manifested in the formation and evolution of the phenomena of amplitude, frequency, and multi-parametric modulation are referred to as low-energy [5]. Low-energy means that the power increase of the vibroacoustic signal as a result of the development of nonlinear effects is small compared to the changes in the power structure of the individual meshing harmonic.

The main difficulty with studying these phenomena stems from the fact that in the signal spectrum the difference between the frequency and amplitude modulation, particularly in the initial period characterized by a small modulation index, are difficult to distinguish. The main differences are apparent in the phase dependencies of the frequencies modulating the carrier frequency [6]. Phase relationships between these spectrum components are at the same disturbed by the difficult to be determined signal transfer function from the signal source to the sensor.

In recent years, the time-frequency and wavelet methods are used more frequently for the diagnosis of fatigue damage of gears [7–11]. These methods allow locating of the disturbed portion of the signal that could be linked to the fatigue local damages like pitting and tooth fracture. One of them is the method of spectral Kurtosis developed by Antoni [12,13]. This method allows finding the local nonstationarities occurring in the signal and determining the signal frequency for which the nonstationarity occur.

The method was adapted by Gelman [14] to detect pitting in its early stage. An example of its use in the diagnosis of tooth break in the planetary gear of a wind turbine can be found in [15].

As could be seen from the above short preview of the diagnostic methods of gears, current trends in their development are aimed at searching for the detection of individual defects. More and more methods are focused not only on the assessment of the technical state of a gear, but also on precise determining the location, type and size of the damage.

The main imperfection of most of these methods is that in the search for diagnostic information they use integration methods that are by default averaging analyzed signals. In this way, small changes in the signals appropriate for the initial phases of development failures are further minimized by the use of signal analysis algorithms.

The aim of this study was to present diagnostic methods enabling the identification of local damage of gears, allowing at the same time precise locations of the damage. The objective of these methods was the direct use of time signal processing algorithms. Their advantage is the simplicity and speed of action that is of great significance for the implementation in the autonomous transmission diagnostic systems and diagnostic systems working online. These methods were first tested on a simulation model of the gear assembly and later tested during the experiments on a back-to-back test stand.

2. Simulation model used for testing of the methods

Possibility of testing new diagnostic methods on a well identified simulation model that behaves similarly to the mechanical system simplifies their development allowing generation of signal frequently impossible to obtain in real experiments. Additionally it opens the unique chance to analyse the signal in connection with the known gear behaviour.

All the developed diagnostic methods were tested on a simulation model which uses the method of apparent interference for modelling tooth mesh [16, 17]. The simplified diagram of the model is presented on Figure 1. In the model the mating of teeth is realized by means of a complex flexible element representing meshing. It is assumed that both the gear and the pinion have the possibility of making an additional rotation in relation to the motion resulting from the revolution of their base circles. Thus the principle of the constant transmission ratio is not maintained enabling analysis of the modulation effects which occur during the toothed gear's operation. This requires modelling of the forces working between the mating teeth to define the relationship between the angular velocities of both toothed wheels. The result of such a wheels motion is the apparent interference, i.e. mutual penetration of meshing teeth which should be interpreted as their deflection. This interference can be determined by taking into account the meshing geometry and is being compensated by the flexible deformation of teeth.

While calculating the interference of the teeth and the meshing force, a series of factors which influence the geometry of meshing were taken into account:

- variable distance between gear axes (shaft runout or flexible shaft deformation),
- instantaneous error of standard contact angle,
- pitch errors, variable meshing stiffness along the path of contact etc.

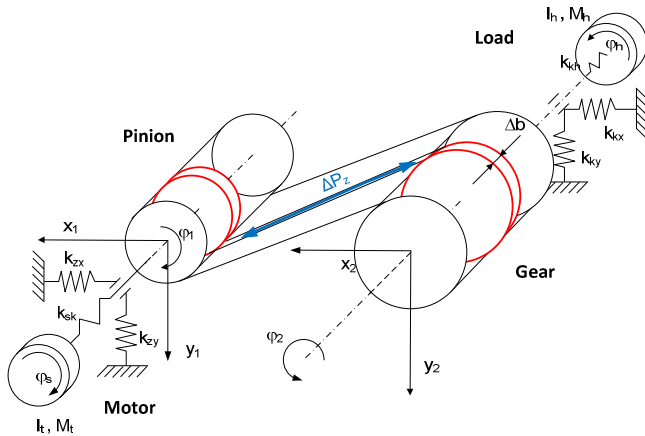


Figure 1. Simplified scheme of the simulation model of helical gear [18]

The meshing stiffness and the changes of its value for the entire path of contact were defined by way of a three-dimensional model of a toothed wheel developed with the use of FEM. More information about the model with comparison of the digital results with results obtained on the test stand could be found in [17].

3. Simulation of local gear faults

Possibility of modelling of the teeth stiffness along the path of contact makes possible simulation of tooth fatigue cracks as changes of stiffness for the particular tooth pair and pitting as a lack of contact on a part of the tooth profile. As for now the model does not allow for the similar changes of friction coefficient that would make pitting simulation more realistic.

In order to show the possibilities offered by the analysis of the signals recorded on the test bench supported with simulation model, gear acceleration measurement signals are listed together with the simulated meshing force waveforms (continuous and dashed lines on upper diagrams of Figure 2). For easiest comparison all the signals were rescaled to obtain the same maximum amplitudes. In addition, these waveforms were compared with waveforms of the simulated meshing stiffness (bottom diagram). Presented signal fragments waveforms correspond to about half rotation of the pinion shaft.

Figure 2 corresponds to the 68 minutes of the tooth fatigue experiment [17], lasting a total of about 72 minutes, when the local signal amplitude change caused by the change of the pinion tooth stiffness caused by emerging crack at its base is evident. The corresponding simulated signal of the total meshing force that matched this was obtained for a case of reducing the stiffness of one of the teeth of the pinion by about 6%. It is worth noting that despite of various manufacturing and mounting deviations of the transmission, the amplitude of the signal transmissions in the damaged spot does not still exceed the peak amplitude of the entire signal.

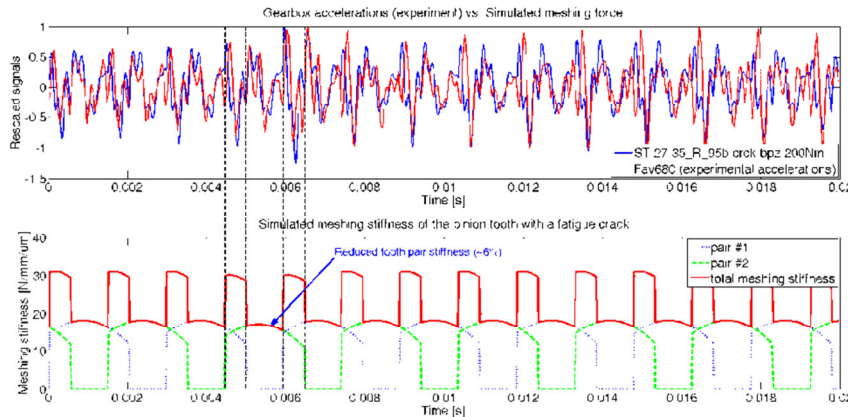


Figure 2. Comparison of gearbox acceleration recorded during the experiment and simulated meshing force for 6% reduction of stiffness on one tooth pair

On the diagrams on Figure 2, using simulated stiffness waveforms, the vertical cursors were used to mark the changes in mesh conditions. Successively: entering of the damaged tooth into two-pair contact, beginning of the one-pair contact, second beginning of the two-pair contact and exiting from the contact of the damaged tooth. It should be noted similarity of the total meshing force waveforms obtained through simulation (with a fatigue crack at the base of the tooth) to the actual measurement results of the gear. Please note that the pitch errors in the simulation were chosen at random, not mapping actual deviations of the test drive. Additionally, used a model is not completely consistent with a kinematics of the back-to-back test stand.

Closer look at Figure 2 point out slightly increased amplitude and disturbed time waveform during the second two-pair contact phase of the pair with a damaged tooth. Detailed analysis of these waveforms allows drawing conclusions according to the quality of meshing in case of emerging tooth crack. Entering into contact of the damaged tooth causes only slight disturbances in the signal. This is due to its higher stiffness during the contact around the tooth base and the fact that the contact is two-pair. Working properly previous pair of teeth then carries most of the load torque and reduce of the stiffness of the damaged pair is of minor importance.

Significant changes in the signal occur at the time of the transition to one-pair contact, since the occurrence of increased susceptibility of the tooth gap caused by fatigue causes the increased deflection, resulting in a greater impulse of force at the time of entering into contact of the next pair of teeth [19]. Additional impulse is visible in the moment of exiting from the contact of the damaged pair.

4. Methods of detection of local disturbances in the gear signal

Local disturbances of the vibroacoustic signal caused by fatigue defects discussed in the previous chapter could be detected with the use of envelope analysis. Signal envelope is usually calculated as the absolute value of the analytic signal [20-22].

$$A(t) = |\tilde{x}(t)| = \sqrt{x^2(t) + \mathcal{H}[x(t)]^2} \quad (1)$$

As calculating Hilbert Transform is time and resource consuming in the digital systems requiring performing FFT and inverse FFT alternatively Teager Kaiser Operator (TKEO) could be used to obtain similar results. TKEO energy operator was first proposed by Teager [23], but the method of its calculation for digital signals and analyzes its properties for the first time gave Kaiser [24].

TKEO operator is the operator of a non-linear, for continuous signals it has the following form:

$$\Psi[x(t)] \triangleq \dot{x}^2(t) - x(t)\ddot{x}(t) \quad (2)$$

This operator allows the estimation of the instantaneous signal energy, so-called. Teager energy, and is often used in the process of demodulating signals instead of the traditional approach of using a Hilbert transform [25-26].

For digitally sampled signals Teager Kaiser Energy Operator takes the form:

$$\Psi[x_n] = x_n^2 - x_{n-1}x_{n+1} \quad (3)$$

where x_{n-1}, x_n, x_{n+1} are consecutive signal samples.

Let us note the simplicity of calculation resulting in multiplying the signal by itself and multiplication of the signal by the time shifted signal, which is very easy to obtain in digital systems. Trouble-free is also its online calculation since it requires simultaneous access to only the last three samples of the signal. Note also the similarity of the operator (3) to the square of the amplitude of the signal (see also Figure 3).

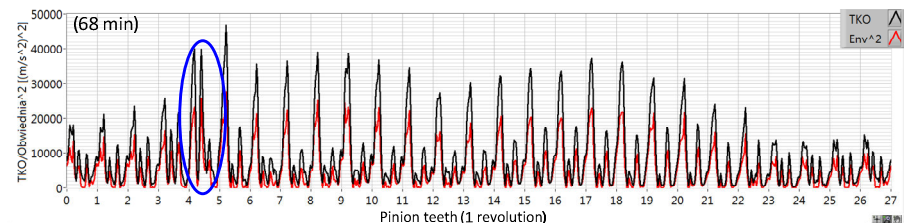


Figure 3. Comparison of squared envelope and TKEO for the acceleration signal from the 68 min. of the experiment (see Figure 2)

As it was proved above pure signal envelope is not sensitive to the detection early stages of defect resulting in subtle changes of the structure of time signals. In the work [27] author proposes a methodology to diagnose such lesions based on the segmentation of instantaneous signal power. It was later developed in the works [28-29].

The method involves comparing each of successive segments of the envelope of the averaged signal synchronously related to the lengths of the transverse radial pitch. A contractual beginning of segments are determined by the geometry of the gears and shaft speed marker, and therefore shifts of the beginning of contacts resulting from teeth inaccuracies, deflection of teeth etc. are reflected in the resulting parameter. The envelope of the signal, as opposed to the measured signal is less sensitive to the slow-changing phase shift, which allows obtaining accurate results for the comparison of

the respective segments. The inclusion of a square envelope further enhances the sensitivity of the method to small changes in the signal. Developed diagnostic parameter, called Envelope Contact Factor (ECF) is a new time signal calculated as the difference between the squares of the envelope waveform of the signal for the related segments of adjacent teeth contacts at subsequent times.

$$ECF(t) = |A^2(i, t) - A^2(i-1, t)| \quad (4)$$

where $i-1$ and i are numbers of consecutive signal segments. Time symbol t existing in equation (4) should be treated conventionally. It means further samples of the signal in the respective segments.

ECF is the energy parameter emphasizing changes in cooperating teeth, due to differences in meshing forces in neighbouring contacts, as a result of pitch errors, differences in the stiffness of the teeth and any inaccuracies of manufacturing of shafts and gears. Differences in tooth contacts result in a growth of the teeth dynamic loading and resulting stress growth. The higher the volatility index, the more loaded is appropriate pair of teeth and the greater the probability that damage will occur at this place. Parameter ECF due to the fact that it is a differential parameter is insensitive to slow the changes in the signal, and is very well suited for the detection of signals containing pulse-type changes that often occur in the case of pitting and breaking gear teeth. Its calculation is very fast, because it can be obtained by moving the cyclic data buffer corresponding to the entire rotation of the shaft of one segment of the signal (i.e. the first segment becomes final), and subtracting the two buffers from each other.

$$ECF(t) = |A^2(t-\tau) - A^2(t)| \quad (5)$$

where τ is the time shift corresponding to the transverse radial pitch.

While calculating the ECF index in this way one does not have to divide the signal into segments. What is important is that the length of the sample corresponding to the averaged rotation of the shaft was divisible by the number of teeth on a gear mounted on this shaft. This means adopting the same length for each segment corresponding to transverse radial pitch.

Figure 4 shows changes of the ECF index for the last 40 minutes of the experiment lasting 72 minutes calculated for the envelope of the signal. Exactly the same results were obtained substituting envelope with TKEO operator.

5. Conclusions

The proposed methods, in part relate to the differential transforms (e.g. Teager-Kaiser Energy Operator), show that it is possible to trace the source of diagnostic information without the use of commonly used integral transforms. These methods allow the identification of the type of defects and their location, both in terms of damage of the individual shafts (e.g., the appearance of eccentricities, or damage of the coupling), as well as damage to the individual teeth of the pinion or wheel. They refer directly to the time signals bypassing the most complicated procedures of integration. Their advantage is the simplicity and speed of action of great significance for their implementation in autonomous diagnostic systems of gears [30] and diagnostic systems working online.

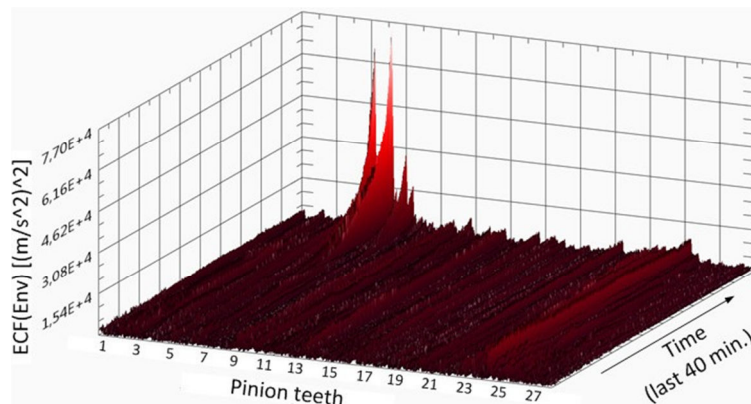


Figure 4. ECF signal for the last 40 min. of the experiment (total of 72 min.)

References

1. R.B. Randall, *A new method of modelling gear faults*, J. Mech. Des., **104** (1982) 259-267.
2. P.D. McFadden, *Detecting fatigue cracks in gears by amplitude and phase demodulation of the meshing vibration*, J. Vib. Acoust. Stress Reliab. Des., **108** (1986) 165-170.
3. P.D. McFadden, *Determining the location of a fatigue crack in a gear from the phase of the change in the meshing vibration*, Mech. Syst. Signal Process., **2**(4) (1988) 403-409.
4. J. Mączak, S. Radkowski, *Low-energy spectrum components as a symptom of failure*, Mach. Dyn. Probl., **8** (1994) 4564.
5. S. Radkowski, *Vibroacoustic diagnostics of low energy failures*, Institute for Sustainable Technologies, Radom 2002.
6. R.B. Randall, *Vibration-based condition monitoring: industrial, aerospace, and automotive applications*, Wiley, Hoboken, NJ 2011.
7. A. Pryor, D.G. Lewicki, D.G., M. Mosher, *The Application of Time-Frequency Methods to HUMS*, American Helicopter Society's 57th Annual Forum, Washington D.C. 2001.
8. B. Łazarz, H. Madej, A. Wilk, T. Figlus, G. Wojnar, *Diagnozowanie złożonych przypadków uszkodzeń przekładni zębatych*, Institute for Sustainable Technologies, Radom 2006.
9. E.B. Halim, S. Shah, M.J. Zuo, *Fault detection of gearbox from vibration signals using time-frequency domain averaging*. Proc. of the 2006 American Control Conference, Minneapolis, Minnesota, USA, (2006) 4430-4435.
10. W. Bartelmuś, R. Zimroz, *A new feature for monitoring the condition of gearboxes in non-stationary operating conditions*, Mech. Syst. Signal Process., **23**(5) (2009) 1528-1534.
11. N. Baydar, A. Ball, *Detection of gear failures in helical gears by using wavelet transforms*, Proceedings of the 33rd International MATADOR Conference (2000) 171-176.
12. J. Antoni, *The spectral kurtosis: a useful tool for characterising non-stationary signals*, Mech. Syst. Signal Process., **20**(2) (2006) 282-307.

-
13. J. Antoni, R.B. Randall, *The spectral kurtosis: application to the vibratory surveillance and diagnostics of rotating machines*, Mech. Syst. Signal Process., **20**(2) (2006) 308-331.
 14. F. Combet, L. Gelman, *Optimal filtering of gear signals for early damage detection based on the spectral kurtosis*, Mech. Syst. Signal Process., **23**,(3) (2009) 652-668.
 15. T. Barszcz, R.B. Randall, *Application of spectral kurtosis for detection of a tooth crack in the planetary gear of a wind turbine*, Mech. Syst. Signal Process., **23**(4) (2009) 1352-1365.
 16. R. Filonik, J. Mączak, S. Radkowski, *Simulation and modelling of low - energy tooth failure in a helical gearbox*, Mach. Dyn. Probl., **26**(2/3) 2002 89-104.
 17. J. Mączak, *Diagnostyka lokalnych uszkodzeń w przekładniach zębatych*, Institute for Sustainable Technologies, Radom 2013.
 18. R. Filonik, J. Mączak, S. Radkowski, *Apparent interference method as a way of modeling the meshing process disturbances*, Mach. Dyn. Probl., **19** (1998) 95-108.
 19. J. Mączak, S. Radkowski, *Modeling and tooth crack growth simulation as a vibroacoustic signal disturbances in gears*, Proceedings of the VII Polish-French Seminar of Mechanics, Warszawa 2001.
 20. R.B. Randall, *Frequency analysis*, Brüel & Kjaer, Copenhagen 1987.
 21. J. Mączak, *Wykorzystanie zjawiska modulacji sygnału vibroakustycznego w diagnozowaniu przekładni o zębach śrubowych*, PhD Dissertation, Warsaw University of Technology, 1988.
 22. M. Feldman, *Hilbert transform in vibration analysis*, Mech. Syst. Signal Process., **25**(3) (2011) 735-802.
 23. H. M. Teager, *Some observations on oral flow during phonation*, IEEE Trans Acoust. Speech Signal Process., **28**(5) (1980) 599-601.
 24. J. F. Kaiser, *On a simple algorithm to calculate the energy of a Signac*, International Conference on Acoustics, Speech, and Signal Processing, ICASSP-90, (1990) 381-384.
 25. E. Kvedalen, *Signal processing using the Teager energy operator and other nonlinear operators*, Master Univ. Oslo Dep. Inform. 2003.
 26. D. Dimitriadis, A. Potamianos, P. Maragos, *A Comparison of the Squared Energy and Teager-Kaiser Operators for Short-Term Energy Estimation in Additive Noise*, IEEE Trans. Signal Process., **57**(7) (2009) 2569-2581.
 27. J. Mączak, S. Radkowski, *Use of envelope contact factor in fatigue crack diagnosis of helical gears*, Mach. Dyn. Probl., **26**(2/3) (2002) 115-122.
 28. J. Mączak, *A method of detection of local disturbances in dynamic response of diagnosed machine element*, in Proceedings of the International Conference on Condition Monitoring 2005, King's College Cambridge (2005) 219-228.
 29. J. Mączak, *Local meshing plane as a source of diagnostic information for monitoring the evolution of gear faults*, Proceedings of the 4rd World Congress on Engineering Asset Management (WCEAM 2009), Athens (2009) 661-670.
 30. J. Mączak, A. Roszczewski, *Autonomous diagnostic unit for threat identification and risk minimization in technical systems*, Diagnostyka, **36** (2005) 45-52.

Dynamics of cellular rotor of asynchronous motor with deformable stator

Waldemar MORZUCH

Wrocław University of Technology

50-370 Wrocław, Wybrzeże Wyspiańskiego 27

waldemar.morzuch@pwr.wroc.pl

Abstract

The analysis of the dynamic stability of cellular rotor in asynchronous motor with deformable stator has been determined. The values of magnetic tension and angular velocities of the rotor under which the loss of stability is observed has been determined. A model of rotor with continuous mass distribution and changeable rigidity has been applied in the analysis. In order to estimate the stability of the rotor the equations of its transverse vibration has been formulated. This equations connecting the dynamic deflection of rotor with space and time. Then the differential equations has been solved. On the basis of the mentioned equations the values of magnetic tension and angular velocities of the rotor under which the loss stability is observed, have been determined.

Keywords: rotor, dynamic stability.

1. Introduction

Among in electric machines, the squirrel-cage asynchronous motors occupy a particular space. These motors have small value of the magnetic gap. For this reason, the basic problem encountered in the phase of construction of such machines is to estimate the stability of the rotors. The problem of stability rotors is in relation to the problem of vibration. On certain values of some quantities, such as rotational speed, magnetic tension, rigidity etc., the effect of instability can take place. The assessment of the stability is of particular importance in the case of long rotors loaded by axial force, for example rotors of motors of deep-well pumps. Such pumps works in deep waters. Problem of estimation of stability of transverse motion of rotors collaborations in non-deformable stator are presented in the works [3, 4, 5, 6]. In this paper the influence of deformability of the stator on the dynamic stability of rotor has been determined.

2. Dynamic stability of rotor

The model of rotor accepted for calculations shown in Fig. 1.

In order to simplify the considerations a vertical position of the rotor has been assumed. The basis for describing the dynamic stability of the rotor is the differential equation of the centre line of the beam. The equation can be written as:

$$S \frac{\partial^4 y}{\partial x^4} = q_x \quad (1)$$

where:

S – flexural rigidity of the section 2,
 y – deflection of the rotor,
 q_x – load intensity.

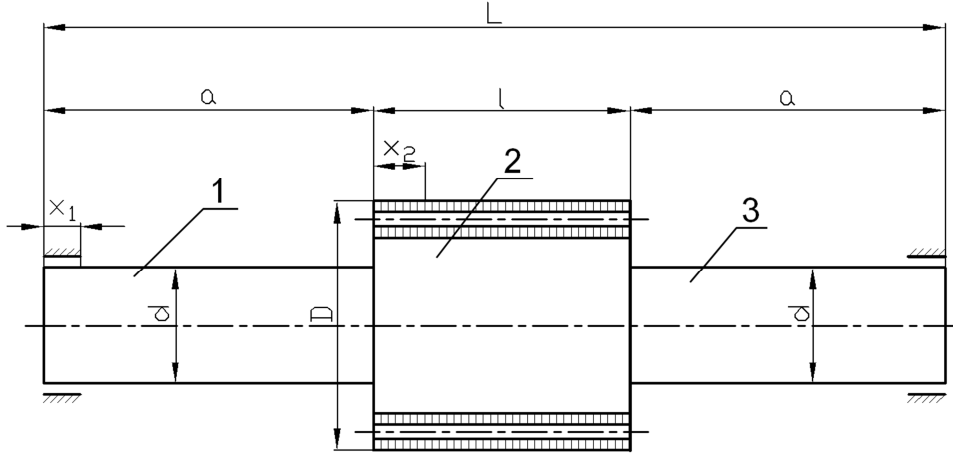


Figure 1. The model of rotor accepted for calculations; 1, 2, 3 – sections of the rotor

The load intensity q_x can be introduced in the form:

$$q_x = q_{1x} + q_{2x} \quad (2)$$

where:

q_{1x} – load intensity related to the influence of the forces of inertia,
 q_{2x} – load intensity related to the influence of the magnetic tension.

Deflection of the rotor $y(x)$ can be introduced in the form:

$$y(x) = y_1(x) + y_2(x) \quad (3)$$

where:

$y_1(x)$ – deflection of the rotor,
 $y_2(x)$ – deflection of the stator.

The load intensity q_{1x} can be expressed as:

$$q_{1x} = -\mu \frac{\partial^2 y}{\partial t^2} \quad (4)$$

where:

μ – unit mass (per unit length) of the section 2 for rotor,
 t – time.

The load intensity q_{2x} can be expressed as [1, 2, 3]:

$$q_{2x} = C \cdot y(x) \quad (5)$$

where:

C – coefficient of magnetic tension [1, 2, 3].

Based on equations (1) and (3) differential equations described vibrations of the rotor and of the stator has been introduced:

$$\beta_1^2 \frac{\partial^4 y_1}{\partial x_1^4} + \frac{\partial^2 y_1}{\partial t^2} - \gamma_1(y_1 + y_2) = 0 \quad (6)$$

where:

$$\beta_1^2 = \frac{S_1}{\mu_1}, \quad \gamma_1 = \frac{C}{\mu_1} \quad (7)$$

S_1 – flexural rigidity of the rotor (of the section 2),

μ_1 – unit mass (per unit length) of the section 2 for rotor.

$$\beta_2^2 \frac{\partial^4 y_2}{\partial x_2^4} + \frac{\partial^2 y_2}{\partial t^2} - \gamma_2(y_1 + y_2) = 0 \quad (8)$$

where:

$$\beta_2^2 = \frac{S_2}{\mu_2}, \quad \gamma_2 = \frac{C}{\mu_2} \quad (9)$$

S_2 – flexural rigidity of the stator (of the section 2),

μ_2 – unit mass (per unit length) of the section 2 for stator,

x – spatial variable.

The solutions of the equation (6) and (8) can be presented in the form an infinite series:

$$y_1(x, t) = \sum_{n=1}^{\infty} X_{n1}(x) T_{n1}(t), \quad y_2(x, t) = \sum_{n=1}^{\infty} X_{n2}(x) T_{n2}(t) \quad (10)$$

After a separation of variables the following equation has been obtained:

$$\frac{d^4 T_{n1}}{dt^4} + a_n \frac{d^2 T_{n1}}{dt^2} + b_n T_{n1} = 0 \quad (11)$$

where:

$$a_n = \omega_{n1}^2 + \omega_{n2}^2 = \omega_{n1}^2(0) + \omega_{n2}^2(0) - (\gamma_1 + \gamma_2) \quad (12)$$

$$b_n = \omega_{n1}^2 \omega_{n2}^2 - \gamma_1 \gamma_2 = \omega_{n1}^2(0) \omega_{n2}^2(0) - \omega_{n1}^2(0) \gamma_2 - \omega_{n2}^2(0) \gamma_1 \quad (13)$$

ω_{n1} denotes the n-order frequency of free vibrations of rotor (with non-deformable stator),

ω_{n2} denotes the n-order frequency of free vibrations of stator (with non-deformable rotor),

$\omega_{n1}(0)$ and $\omega_{n2}(0)$ denotes n-order frequency of free vibrations of rotor and stator in which $\gamma_1 = \gamma_2 = 0$.

Based on the equation (11) the characteristic equation has been obtained:

$$\lambda_n^4 + a_n \lambda_n^2 + b_n = 0 \quad (14)$$

The solutions of the above equation can be presented in the following form:

$$\lambda_{1,2} = \pm \sqrt{\frac{-a_n - \sqrt{a_n^2 - 4b_n}}{2}} \quad (15)$$

$$\lambda_{3,4} = \pm \sqrt{\frac{-a_n + \sqrt{a_n^2 - 4b_n}}{2}} \quad (16)$$

Based on the equation (11) the following condition of instability has been obtained:

$$\omega_{n1}^2(0)\omega_{n2}^2(0) - \omega_{n1}^2(0)\gamma_2 - \omega_{n2}^2(0)\gamma_1 \leq 0 \quad (17)$$

The above condition has been obtained:

$$C \geq \frac{\mu_1 \mu_2 \omega_{n1}^2(0)}{p \mu_1 + \mu_2} \quad \text{or} \quad C \geq \frac{C_\infty}{pr+1} \quad (18)$$

where:

$$p = \frac{\omega_{n1}^2(0)}{\omega_{n2}^2(0)} \quad (19)$$

$$C_\infty = \mu_1 \omega_{n1}^2(0) \quad (20)$$

$$r = \frac{\mu_1}{\mu_2} \quad (21)$$

C_∞ – coefficient of magnetic tension of the rotor with non-deformable stator.

Based on inequality (18) the values of magnetic tension under which the loss of stability is observed has been determined:

$$C_{kr} = \frac{C_\infty}{pr+1} \quad (22)$$

C_{kr} – coefficient of magnetic tension of rotor with deformable stator.

The following angular velocities of the rotor in which the loss of stability is observed has been determined:

$$\omega = \sqrt{\frac{1}{2}(a_n + \sqrt{a_n^2 - 4b_n})} \quad \text{or} \quad \omega = \sqrt{\frac{1}{2}(a_n - \sqrt{a_n^2 - 4b_n})} \quad (23)$$

3. Example of calculations

This chapter presents calculations of a rotor for following data: $L = 0,7 \text{ m}$, $l = 0,375 \text{ m}$, $d = 0,05 \text{ m}$, $D = 0,08 \text{ m}$. Dimensions of the stator:

$$D_z = 0,11 \text{ m}, \quad D_w = 0,1 \text{ m}$$

has been accepted. D_z and D_w the outside and inside diameters has been signified. The unit mass of the rotor:

$$\mu_1 = 39,2 \frac{\text{kg}}{\text{m}}$$

and unit mass of the stator:

$$\mu_2 = 16,72 \frac{\text{kg}}{\text{m}}$$

has been accepted.

$$\omega_{n1}(0) = 873,33 \text{ s}^{-1}, \quad \omega_{n2}(0) = 3370,8 \text{ s}^{-1}$$

$$C_\infty = 29,9 \text{ MPa}, \quad C_{kr} = 25,83 \text{ MPa}.$$

Then angular velocities of the rotor in which the loss of stability occurs has been obtained.

In which $C = 19,62 \text{ MPa}$, $\omega = 451,7 \text{ s}^{-1}$ (with deformable stator).

In which $C = 19,62 \text{ MPa}$, $\omega = 512,12 \text{ s}^{-1}$ (with non-deformable stator).

In which $C = 24,525 \text{ MPa}$, $\omega = 370,37 \text{ s}^{-1}$ (with non-deformable stator).

4. Conclusions

1. The deformability of the stator of asynchronous motor decrease of the values of the magnetic tension at which the loss of stability occurs.
2. The deformability of the stator of asynchronous motor decrease of the values angular velocity at which the loss of stability occurs. The first velocity is less than natural frequency of free vibrations rotors in case of non-deformable stator. The second velocity is less than natural frequency of free vibrations stator in case of non-deformable rotor.

References

1. A.E. Aleksiejew, *Konstrukcja maszyn elektrycznych*, Warszawa, PWT 1953.
2. M. Dąbrowski, *Konstrukcja maszyn elektrycznych*, Warszawa WNT 1977.
3. Z. Gabryszewski, W. Morzuch, *Analiza dynamiczna wirników silników asynchronicznych klatkowych*, Archiwum elektrotechniki, Vol. XXX, No. 1, 1981.
4. W. Morzuch, *Krytyczna prędkość obrotowa wirnika silnika elektrycznego*, Przegląd Mechaniczny, Nr 5, 2003.

5. W. Morzuch, *Dynamika wirnika silnika elektrycznego obciążonego siłą osiową*, Przegląd Elektrotechniczny, Nr 6, 2006.
6. W. Morzuch, *Dynamic stability of rotor of electric motor loaded by axial compression and magnetic tension*, Przegląd Elektrotechniczny, Nr 7, 2010.

Influence of the Damping in the Sandwich Bar on the Dynamic Stability

Waldemar MORZUCH

Wrocław University of Technology

50-370 Wrocław, Wybrzeże Wyspińskiego 27

waldemar.morzuch@pwr.wroc.pl

Abstract

In the paper influence of the damping in the sandwich bar on its dynamic stability is studied using analytical methods. This paper presents an analysis of dynamic buckling of a sandwich bar compressed by a periodically variable force. In order to determine the dynamic stability of the bar equations of its transverse vibration were formulated. From the equations of motion, differential equations interrelating of the dynamic deflection with space and time were derived. The partial differential equations were solved using the method of separation of variables (Fourier's method). Then the ordinary differential equation describing the bar vibrations was solved. An analysis of the solution became the basis for determining the regions of sandwich bar motion instability. Finally, the value of the compressive force at which dynamic stability occurs have been calculated.

Keywords: sandwich bars, stability.

1. Introduction

Sandwich constructions are characterized by light weight and high strength. Such features are highly valuable in aviation, building engineering and automotive applications. The primary aim of using sandwich constructions is to obtain properly strong and rigid structures with vibration damping capacity and good insulating properties. Figure 1 shows a scheme of a sandwich construction which is composed of two thin faces and relatively thick core [4, 5, 6, 7, 8]. The core, made of plastic and metal sheet or foil, transfers transverse forces and maintains a constant distance between the faces. Sandwich constructions are classified into bars, plates and beams. A major problem in the design of sandwich constructions is the assessment of their stability under axial loads causing their buckling or folding. The existing methods of calculating such structures are limited to the assessment of their stability under loads constant in time [7, 8]. There are no studies dealing with the analysis of parametric vibration and dynamic stability.

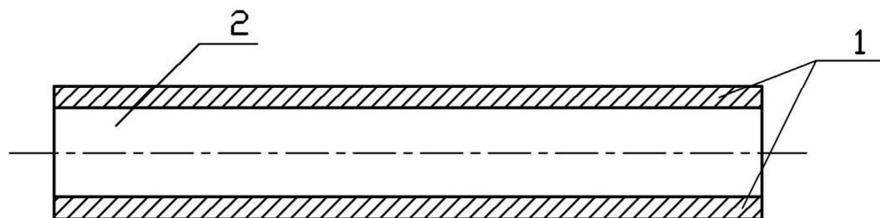


Figure 1. Scheme of sandwich construction: 1 – faces, 2 – core

This paper presents a dynamic analysis of a sandwich bar compressed by a periodically variable force, assuming that the core is linearly viscoelastic. Differential equations describing the dynamic flexural buckling of bars are derived and regions of instability are identified. The dynamic analysis of sandwich constructions is of great importance for vehicles and aeroplanes, since most of the loads which occur in them have the form of time-dependent forces.

2. Equation of sandwich bar motion

The basis for describing the dynamic buckling of a sandwich bar is the differential equation of sandwich beam centre line.

The equation can be written as

$$E_t I \frac{\partial^4 y}{\partial x^4} = q - k \frac{E_t I}{S} \cdot \frac{\partial^2 q}{\partial x^2} \quad (1)$$

where:

- E_t – Young's modulus of the plate,
- I – moment of inertia of the plates,
- y – deflection of the bar,
- q – load intensity,
- k – a coefficient representing the influence of the transverse force on the deflection of the bar,
- S – transverse rigidity of the bar,
- x – coordinate signifying position of the cross section of the sandwich bar.

The cross section of the sandwich bar is shown in Fig. 2.

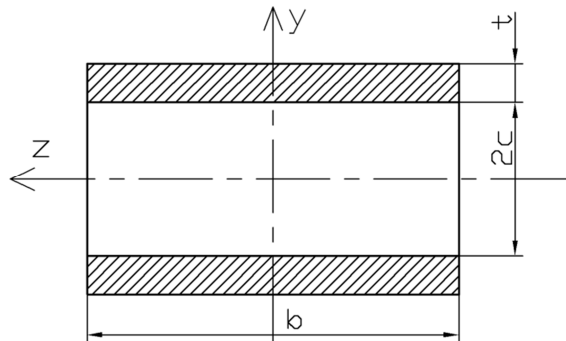


Figure 2. Cross section of sandwich bar

In sandwich constructions a coefficient $k = 1$.

$$S = 2bcG_c \quad (2)$$

where:

- b, c – dimensions of the core (Fig. 2),

G_c – modulus of the rigidity of the core material.

Load intensity q can be written in the form:

$$q = q_1 + q_2 + q_3 \quad (3)$$

$$q_1 = -F \frac{\partial^2 y}{\partial x^2}, \quad q_2 = -\mu \frac{\partial^2 y}{\partial t^2}, \quad q_3 = -\eta_r \frac{\partial y}{\partial t} \quad (4)$$

where:

F – compressive force

μ – unit mass of the sandwich bar

η_r – damping coefficient of the core material.

Force F can be expressed as follows:

$$F = F_1 + F_2 \cdot \cos pt \quad (5)$$

where:

F_1 – constant component of the compressive force,

F_2 – amplitude of the variable component of the compressive force,

p – frequency of the variable component F_2 ,

t – time.

After substituting equations (3) into differential equation (1) the following differential equation is obtained:

$$E_t I \left(1 - \frac{F}{S} \right) \frac{\partial^4 y}{\partial x^4} + F \frac{\partial^2 q}{\partial x^2} - \frac{E_t I}{S} \mu \frac{\partial^4 y}{\partial x^2 \partial t^2} + \mu \frac{\partial^2 y}{\partial t^2} + \eta_r \frac{\partial y}{\partial t} - \frac{E_t I}{S} \eta_r \frac{\partial^3 y}{\partial x^2 \partial t} = 0 \quad (6)$$

The above equation is a fourth-order homogenous equation with time-dependent coefficients. It was solved by the method of separation of variables (Fourier's method). The solution can be presented in the form of an infinite series:

$$y = \sum_{n=1}^{\infty} X_n(x) T_n(t) \quad (7)$$

where:

$X_n(x)$ – eigenfunctions,

$T_n(t)$ – functions dependent on the time t .

The eigenfunctions $X_n(x)$, satisfying the boundary conditions at the supports of the bar at its ends, have the following form:

$$X_n(x) = A_n \sin \frac{\pi n x}{l} \quad (8)$$

where:

l – length of the bar.

Having substituted equations (7) and (8) into equation (6), one gets the following ordinary differential equation describing functions $T_n(t)$.

$$\ddot{T}_n + 2h\dot{T}_n + \omega_{0n}^2 (1 - 2\psi_n \cos pt) T_n = 0 \quad (9)$$

where:

$$2h = \frac{\eta_r}{\mu}, \quad 2\psi_n = \frac{F_2 \left(\frac{\pi n}{l} \right)^2}{\mu \omega_{0n}^2} \quad (10)$$

The square of frequency ω_{0n} can be expressed as follows:

$$\omega_{0n}^2 = \omega_0^2 - \frac{F_1 \left(\frac{\pi n}{l} \right)^2}{\mu} \quad (11)$$

where:

ω_0 – the natural frequency of vibration of the bar when $F_1 = 0, F_2 = 0, \eta_r = 0$.

The square of frequency ω_0 can be expressed as follows:

$$\omega_0^2 = \frac{E_t I \left(\frac{\pi n}{l} \right)^4}{\mu \left[1 + \frac{E_t I}{S} \left(\frac{\pi n}{l} \right)^2 \right]} \quad (12)$$

Differential equation (9) is Hill's equation in the form [1, 2, 3, 4, 5, 6]:

$$\ddot{T}_n + 2h\dot{T}_n + \Omega_n^2 [1 - f(t)] T_n = 0 \quad (13)$$

where h and Ω_n are coefficients.

By solving of equation (13) the boundary lines of the first region of instability has been obtained (Fig. 3).

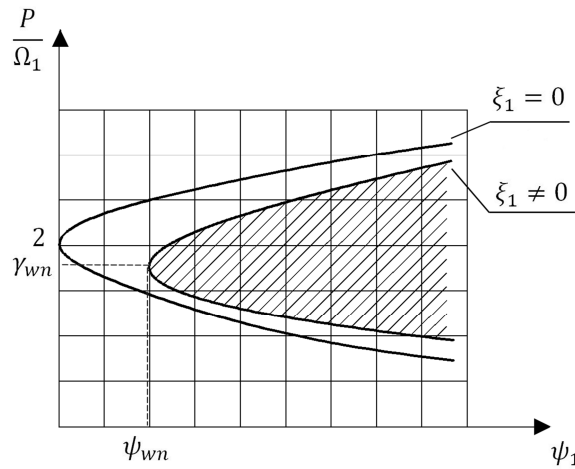


Figure 3. First region of instability ($\xi_1=0$ – without damping, $\xi_1 \neq 0$ – with damping)

Hence the “wedge” of the first region instability has the coordinates:

$$\psi_{w1} = 2\sqrt{\xi_1 - 2\xi_1^2}, \quad \gamma_{w1} = 2\sqrt{1 - 3\xi_1} \quad (14)$$

where:

$$\xi_1 = \left(\frac{h}{\Omega_1}\right)^2 \quad (15)$$

From formula (14) the boundary value of coefficient ψ_{w1} at which parametric resonance occurs has been obtained. If $\psi_1 < \psi_{w1}$, no parametric resonance arises. It follows from the above that there exists compressive force F_1 and F_2 at which the bar does not lose stability. Then the component F_2 satisfies a condition:

$$F_2 < \frac{2\sqrt{\xi_1 - 2\xi_1^2} \cdot \mu \omega_{0n}^2}{\left(\frac{\pi n}{l}\right)^2} \quad (16)$$

3. Example of calculations

Calculations of the sandwich bar has been performed for the following data assumed:

$$b = 25 \text{ mm}, c = 7,5 \text{ mm}, t = 0,5 \text{ mm}, l = 50 \text{ cm}, E_t = 7 \cdot 10^4 \text{ MPa}, G_c = 70 \text{ MPa}$$

$$\mu = 7 \cdot 10^{-2} \text{ kg} \cdot \text{m}^{-1},$$

$$\xi_1 = 0,01:$$

If $F_1 = 800 \text{ N}$, then $F_2 < 78,87 \text{ N}$

If $F_1 = 1000 \text{ N}$, then $F_2 < 39,6 \text{ N}$

If $F_1 = 1100 \text{ N}$, then $F_2 < 20,6 \text{ N}$.

$$\xi_1 = 0,1:$$

If $F_1 = 800 \text{ N}$, then $F_2 < 225,34 \text{ N}$

If $F_1 = 1000 \text{ N}$, then $F_2 < 113,14 \text{ N}$

If $F_1 = 1100 \text{ N}$, then $F_2 < 58,86 \text{ N}$.

4. Conclusions

Stability of sandwich bar depends on damping in the core. Damping reduces the areas of instability sandwich bar compressed by periodically variable force. Exist values of damping in which motion of sandwich bar is stability. It follows from the above that there exist compressive force components F_1 and F_2 at which the sandwich bar does not lose stability.

References

1. Z. Dżygadło, S. Kaliski, L. Solarz, E. Włodarczyk, *Vibrations and waves*, WAT, Warsaw 1965.
2. N.W. McLachlan, *Theory and application of Mathieu functions*, Oxford 1947.
3. W. Morzuch, *Stateczność dynamiczna pręta przekładkowego ściskanego siłą określowo-zmienną*, Rozprawy Inżynierskie, 37, 2, 1989.
4. W. Morzuch, *Wyboczenie dynamiczne pręta przekładkowego ściskanego siłą określowo-zmienną*, Przegląd Mechaniczny, 7-8, 2006

5. W. Morzuch, *Dynamic buckling of a sandwich bar compressed by periodically variable force*, Engineering Transations, 55,3,217-227,2007
6. W. Morzuch, *Dynamic Stability of Sandwich Rod and of Rotor in Bipolar Electric Drive Motor with Damping*, Mechanics and Mechanical Engineering, Vol 14, Number 2, Łódź 2010.
7. J.F. Plantema, *Sandwich construction*, Stanford University, London 1966.
8. F. Romanów, L. Sticker, J. Teisseyre, *Stability of sandwich structures [in Polish]*, Skrypt Politechniki Wrocławskiej, Wrocław 1972.

Novel Method of Physical Modes Generation for Reduced Order Flow Control-Oriented Models

Marek MORZYŃSKI

Poznan University of Technology, Piotrowo 3, 60-965 Poznan, Poland

Marek.Morzynski@put.poznan.pl

Michał NOWAK

Poznan University of Technology, Piotrowo 3, 60-965 Poznan, Poland

Michal.Nowak@put.poznan.pl

Witold STANKIEWICZ

Poznan University of Technology, Piotrowo 3, 60-965 Poznan, Poland

Witold.Stankiewicz@put.poznan.pl

Abstract

Physical flow modes are of particular interest for Reduced Order Flow Control-Oriented Models. Computation of physical modes as the eigensolution of linearized Navier-Stokes equations is a cumbersome and difficult task, especially for large, 3D problems. Instead we propose the solution of Navier-Stokes equation in the frequency domain and investigation of the system response to local or global perturbation. The flow variables are perturbed around steady basic state and the system response is used to construct mode basis suitable for ROMs.

Keywords: Navier-Stokes equation, eigenmodes, Reduced Order Modelling, flow control.

1. Introduction

The Reduced Order Models (ROMs) of flow are often based on Galerkin Method [1]. This method strongly depends on flow mode basis. In flow modelling we can employ mathematical modes, empirical ones or eigenmodes of linearised system. The use of mathematical modes is rather a hypothetical solution as the mode basis can be hardly defined for general flow conditions. It has been proven that adequate use of both, empirical and physical modes assures high dynamical quality of the flow model [2].

There are many well established methods to generate the empirical modes basis. Traditionally, Proper Orthogonal Decomposition (POD) [3,4] and its modifications are used for this purpose. Recently Dynamic Mode Decomposition (DMD) [5,6] being the dynamical system identification method is widely used. In the same time there is a substantial progress in eigensolution of linearized Navier-Stokes equations [7,8,9] but eigensolution of generalized, non-hermitian, complex eigenvalue problem remains a cumbersome and difficult task. It is particularly pronounced for discretized 3D flow problems, described by systems of $(0)10^6$ Degrees of Freedom and requiring the eigensolution of such large eigenvalue problems.

We present here an alternative, novel method of physical modes generation. It is based on solution of linearized disturbance equation in frequency domain. Flow variables are perturbed around steady basic state. Flow responses to random or localized volume forces characterized by assumed frequencies closely resemble eigenmodes.

2. Governing equations

The incompressible fluid motion is described by the unsteady Navier-Stokes equation in the form:

$$\dot{V}_i + V_{i,j}V_j + P_{,i} - \frac{1}{Re}V_{i,jj} = 0 \quad (1)$$

The incompressibility condition is expressed by the continuity equation:

$$V_{i,i} = 0 \quad (2)$$

The Reynolds number is defined as:

$$Re = \frac{UL}{\mu} \quad (3)$$

where U is characteristic velocity, L characteristic length and μ kinematic viscosity of the fluid.

We assume that the unsteady solution of the Navier-Stokes equation (1) can be expressed as the sum of its steady solution and the disturbance:

$$\begin{aligned} V_i &= \bar{V}_i + \dot{V}_i \\ P &= \bar{P} + \dot{P} \end{aligned} \quad (4)$$

This assumption leads us to the disturbance equation, in the form:

$$\dot{\bar{V}}_i + \dot{V}_j \bar{V}_{i,j} + \bar{V}_j \dot{V}_{i,j} + \dot{V}_j \dot{V}_{i,j} + \dot{P}_{,i} - \frac{1}{Re} \dot{V}_{i,jj} = 0 \quad (5)$$

Further we assume small value of the disturbance and linearize equation (5). In the disturbance equation we separate the time and space dependence

$$\begin{aligned} \dot{\bar{V}}_i(x, y, z, t) &= \tilde{V}_i(x, y, z) e^{\lambda t} \\ \dot{P}(x, y, z, t) &= \tilde{P}(x, y, z) e^{\lambda t} \end{aligned} \quad (6)$$

With introduction of equation (6) to the linearized disturbance equation (5) we obtain a differential eigenvalue problem having form:

$$\begin{aligned} \lambda \tilde{V}_i + \tilde{V}_j \bar{V}_{i,j} + \bar{V}_j \tilde{V}_{i,j} + \tilde{P}_{,i} - \frac{1}{Re} \tilde{V}_{i,jj} &= 0 \\ \tilde{V}_{i,i} &= 0 \end{aligned} \quad (7)$$

Discretization of (7) gives:

$$\lambda Bx + Ax = 0 \quad (8)$$

This equation represents the generalized complex, non-hermitian eigenvalue problem. The number of DOFs for (8) is usually very large, of order of $(0)10^5$ for two-dimensional problem and $(0)10^6$ for three-dimensional one.

Particularly three-dimensional eigensystem is a challenging numerical problem to be solved. Eigenvalues are often complex conjugate pairs what causes additional problems for solution algorithms.

Instead of direct solution of (9) we investigate frequency response function having form:

$$\begin{aligned} Ax_{Re} + \lambda_{Re}Bx_{Re} + \lambda_{Im}Bx_{Im} &= F_{Re} \\ Ax_{Im} + \lambda_{Re}Bx_{Im} - \lambda_{Im}Bx_{Re} &= F_{Im} \end{aligned} \quad (9)$$

to localized or random forcing. In equation (9) we split real and imaginary part of the equation to use real value computer algebra.

3. Flow solver for 2D and 3D computations

Solution of disturbance equation in frequency domain required development of adequate numerical solver. It is based on our earlier UNS3 system (MF3 for structural problems) widely used in flow stability, control and Reduced Order Modelling [1]. UNS3 is based on unstructured FEM in penalty formulation and employs second and third order triangular (2D) or tetrahedral elements (3D).

The three-dimensional version of the program is parallelized and based on METIS [10] domain partitioning. UNS3 scales linearly up to hundreds of CPUs enabling computation on grids having several millions of grid points. Two-dimensional solver uses scalar, single processor code.

For purpose of frequency domain computation the Finite Element has doubled (for real and imaginary part) number of DOFs in comparison to our regular Navier-Stokes computations. In Figure 1 example grid partitioning to 16 domains, used later for the computations of a flow around sphere is shown.

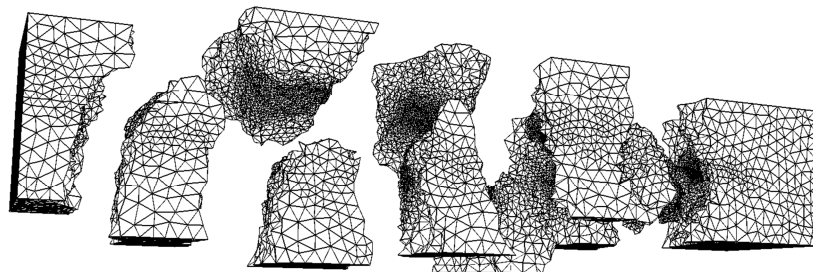


Figure 1. Finite Element (FEM) grid, domain partitioning and grid refinement for flow around a sphere

4. Numerical results

Solution of disturbance equation requires firstly steady basic solution of the Navier-Stokes equations. It has been obtained with classical version of UNS3 code. In Figure 3 the example steady solution for flow around the sphere at $Re=250$ is shown.

In Figure 2 we present real and imaginary parts of the modes. It is relatively easy to obtain von Karman mode as depicted in the first row. It is the response of the flow for random forcing and the complex value of $(0.1 + i 0.87)$ yields neutral stability corrobor-

rating the results of flow stability analysis based on eigensolutions of the equation (8). In the second row the response to point volume force at different frequencies and locations is shown.

With the 2D results, closely following earlier stability analysis we apply the method to three-dimensional flows. For 3D flow the stability investigations are much more rare [8].

The results for the flow around a sphere at $Re=250$ are depicted in Figure 3. The solution is obtained for random perturbation of the flow and develops around steady solution shown in the left part of the figure. Dominating mode is shown with the use of Lambda2 criterion. It shows characteristic periodicity of the flow and spreading angle of the shedding vortices.

It should be noted that dominating mode can be relatively easily retrieved also with DMD or POD method. In the case of POD physical modes can be found by analysis of time history of slightly perturbed steady solution.

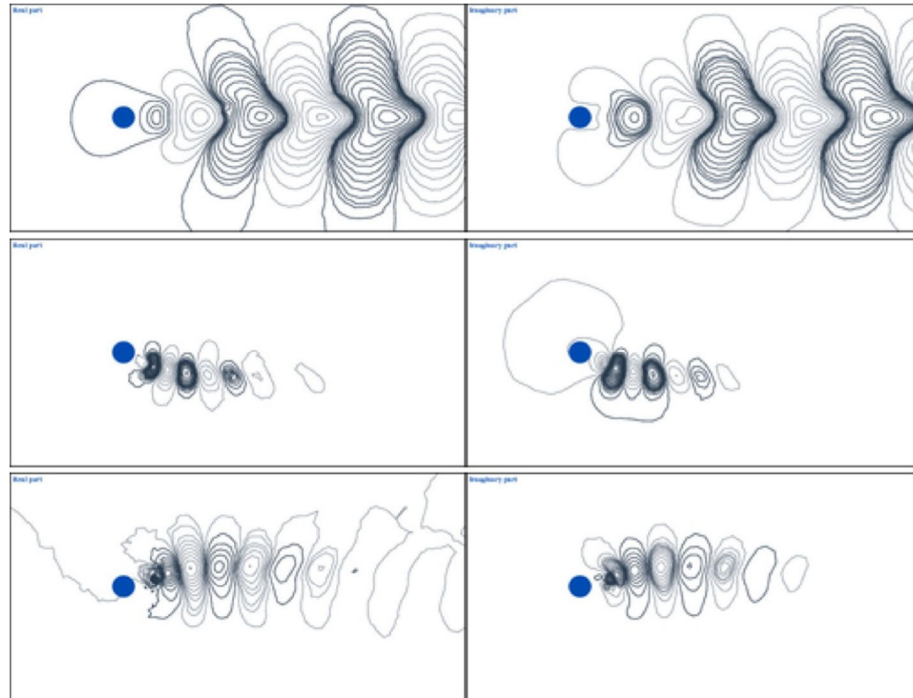


Figure 2. Real (left) and imaginary (right) part of the mode for different forcing of the flow around two-dimensional circular cylinder at $Re = 100$

While for finding the dominating mode any of the mentioned methods can be used, physical modes characterized by higher frequencies are difficult to determine. DMD method shows Fourier modes, doubling the mode frequency and POD determines energetically optimal modes for the limit cycle being, however, not physical ones.

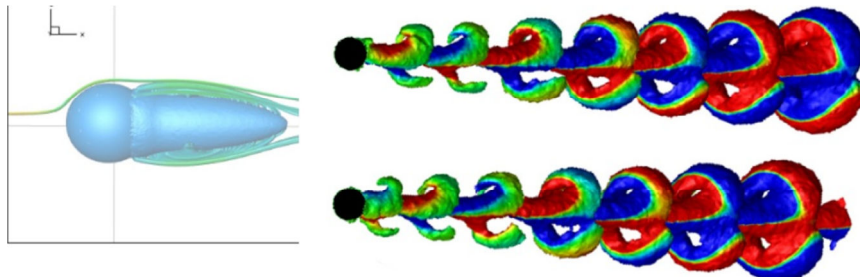


Figure 3. Steady flow around a sphere at $Re=250$ (left). Streamlines and wake contour is shown (isosurface of $V_x = 0$). Right: real (top) and imaginary (bottom) part of the dominating shedding mode visualized with the Lambda2 criterion

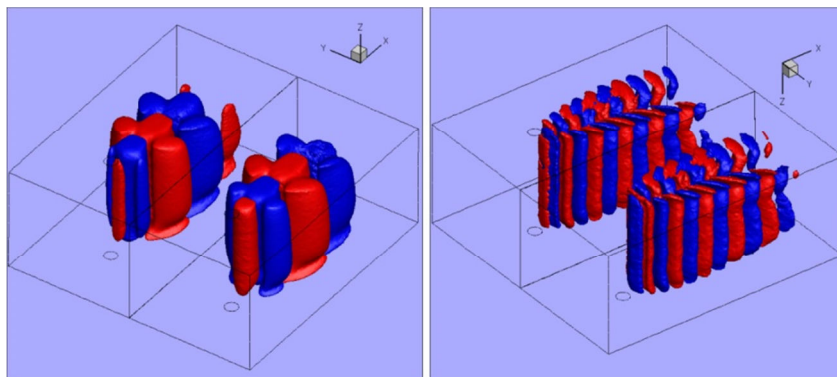


Figure 4. Real and imaginary part of modes for the flow around the wall-mounted cylinder. Left: von Karman mode, right: higher, shear-layer mode

In the next Figure 4 we show both, dominating Karman mode and higher one, determined with the presented here method. Flow develops around a wall-mounted cylinder.

In Figure 5 the Lambda2 visualization (top view) of unsteady flow is also shown as the reference.

5. Conclusions

We presented a novel method of finding physical modes for complex, two- and three-dimensional flows with the use of frequency domain solutions of linearized Navier-Stokes equations. It has been shown that the method enables computation of dominant modes as well as higher frequency ones. The modes determined with this method will serve as the basis for Reduced Order Models of the flow. The method can be also applied for investigation of effect of flow actuators. Both placement and actuation character can be modelled with the presented method. In this way flow control can be more effectively planned.

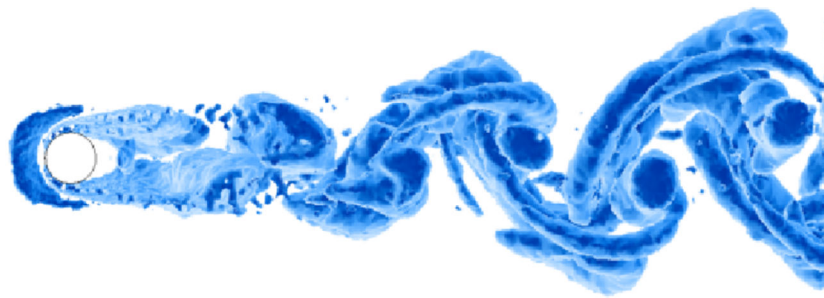


Figure 5. Unsteady flow around wall-mounted cylinder (top view) visualized with the Lambda2 criterion

Acknowledgments

This work has been funded by National Centre of Science under research grant no. DEC-2011/01/B/ST8/07264.

References

1. B.R. Noack, M. Morzyński, G. Tadmor. *Reduced-Order Modelling for Flow Control*. Number 528. Springer, 2011.
2. B.R. Noack, K. Afanasiev, M. Morzyński, G. Tadmor, F. Thiele, *A hierarchy of low-dimensional models for the transient and post-transient cylinder wake*, J. Fluid Mech., **497** (2003), 335-36
3. P. Holmes, J. Lumley, G. Berkooz, *Turbulence, Coherent Structures, Dynamical Systems and Symmetry*, Cambridge University Press, Cambridge, 1998.
4. L. Sirovich, *Turbulence and the dynamics of coherent structures*. Quart. Appl. Math., **45** (1987), 561-590.
5. P.J. Schmid, J. Sesterhenn, *Dynamic Mode Decomposition of Numerical and Experimental Data*, J. Fluid Mech., **656** (1) (2010), 5-28.
6. Ch.J. Mack, P.J. Schmid. *Global stability of swept flow around a parabolic body: features of the global spectrum*. J. Fluid Mech., **669**, (2011) 375-396.
7. M. Morzyński, K. Afanasiev, F. Thiele, *Solution of the eigenvalue problems resulting from global non-parallel flow stability analysis*, Comput. Meth. Appl. Mech. Engrng., **169** (1999), 161-176.
8. V. Theofilis. *Global linear instability* Annual Review of Fluid Mechanics, **43**, (2011), 319-352.
9. W. Stankiewicz, M. Morzyński, B.R. Noack, F. Thiele, *Stability Properties Of 2D Flow Around Ahmed Body*, Math. Model. Analysis (2005), 129-134.
10. G. Karypis, V. Kumar, *A Fast and Highly Quality Multilevel Scheme for Partitioning Irregular Graphs*, SIAM Journal on Scientific Computing, Vol. **20**, (1), (1999), 359-392.

3D Dynamic Model of the Unicycle – Unicyclist System

Michał NIEŁACZNY

Division of Dynamics, Technical University of Łódź

Stefanowskiego 1/15, 90-924 Łódź, Poland

nielaczek@gmail.com

Juliusz GRABSKI

Division of Dynamics, Technical University of Łódź

Stefanowskiego 1/15, 90-924 Łódź, Poland

julgrabs@p.lodz.pl

Jarosław STRZAŁKO

Division of Dynamics, Technical University of Łódź

Stefanowskiego 1/15, 90-924 Łódź, Poland

jstrzalk@poczta.onet.pl

Abstract

The problem of motion of a unicycle – unicyclist system in 3D is studied. The equations of motion of the system were derived using the Boltzmann-Hamel equations. Automatic generation of the Hamel coefficients eliminates all the difficulties associated with the determination of these equations. Description of the unicycle – unicyclist system dynamical model and simulation results are presented in the paper.

Keywords: unicycle, unicyclist, 3D dynamic model, Boltzmann-Hamel equations

1. Introduction

1.1. Unicycle – one wheel vehicle

Unicycle – one wheel vehicle is a specific type of single track vehicle commonly named a bicycle. It has only one road wheel. Unicycle is a "descendant" of Penny-farthing which is a bicycle with a large front driving wheel and a small rear rolling wheel. Penny-farthing and unicycle are shown in Fig. 1.

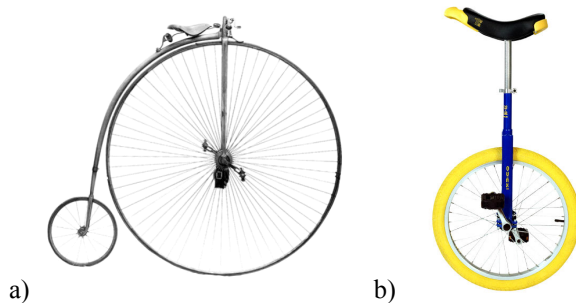


Figure 1. a) Penny-farthing [1]; b) unicycle [2]

Unicycle was created in the late nineteenth century, after removing from penny-farthing rear wheel with frame [3]. Unicycle has considerably fewer parts than a regular bicycle. Its parts resemble counterparts for bicycles only visually.

The main feature of unicycle is fixed gear. It means that the cranks are connected rigidly to the wheels. Therefore, the rotation of the cranks directly controls the rotation of the wheel. Riding is impossible without pedalling. This gives the option to ride backwards or to stand up. Furthermore, the fixed gear imposes that the bicycle has only one ratio.

The average person standing in upright position has a centre of gravity around the belly button, as shown in Fig. 2. The unicyclist can easily maintain upright position. However, to ride comfortably, the distance between the saddle and the pedal in its lowest position must be slightly shorter than the length of the unicyclist's leg. Thus, the centre of gravity is higher than the distance from the ground to the pedal at its lowest position. Undoubtedly, it makes riding more difficult.

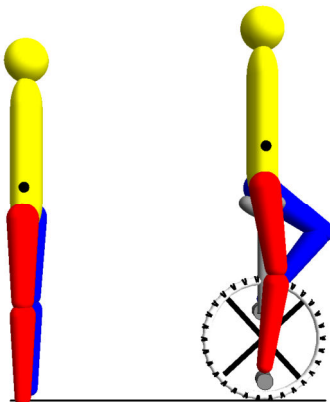


Figure 2. Average person's centre of gravity and the unicyclist's centre of gravity position

Riding a unicycle is more difficult than a regular bicycle, also due to the fact that there is only one point of support. For this reason, balance must be maintained in two planes simultaneously. Maintaining the balance in the plane transversal to the direction of riding (lateral) involves balancing with hips to maintain the centre of gravity above the fulcrum of the wheel. In contrast, maintaining balance in the plane parallel to the direction of travel ("forward - backward"), consists of accelerating or slowing down the drive wheel so that the centre of gravity oscillates above the fulcrum of the wheel.

1.2. Unicycle in technical aspect

In mechanical aspect unicycle with unicyclist, can be considered as a moving double inverted spherical pendulum. The first part is the unicyclist's body, while the second, unicycle's frame with unicyclist's legs. If we assume that the wheel is also one of

the links of the pendulum the model has the form of triple spherical pendulum. Such approach to the unicycle – unicyclist system fully corresponds to reality. It is impossible to stand in place without balancing.

During riding a unicycle the initial set value is the vertical position. Theoretically, unicyclist begins to lose balance. By measuring element, which is the membranous labyrinth feels that swings from a position of unstable equilibrium. This deflection is treated as a control error. Then, the control unit, in this case the unicyclist's brain, sends signals to appropriate parts of the body, or actuators. As the result the unicyclist balances with the whole body and returns to the upright position.

Summarizing, the unicycle with a ride-on unicyclist, in control aspect can be treated as a follow-up control system.

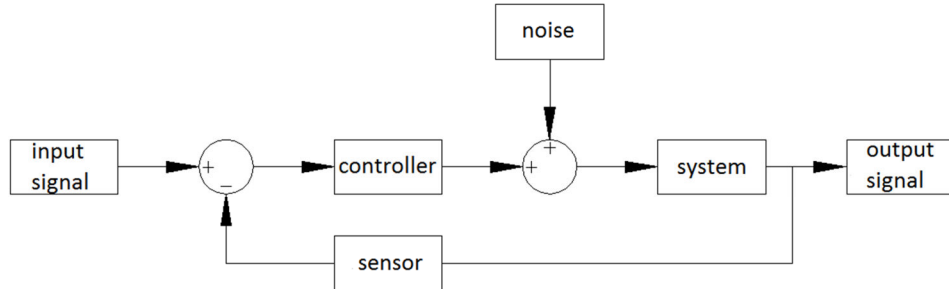


Figure 3. Follow-up control system

1.3. Boltzmann-Hamel equations

Quasi-velocities are convenient in description of motion of variable configuration systems. The introduction of quasi-velocities into the description of motion of a system is convenient when their use allows compact notation of kinetic energy and equations of motion, e.g. when investigating systems containing elements undergoing relative motion.

The Boltzmann-Hamel equations are rarely used because of complicated formulae containing Hamel coefficients (γ_{nj}^i) and complex relationships for the determination of these coefficients [4-8].

The classic form of the Boltzmann-Hamel equations for a system with the number of coordinates equal to k is as follows (see [4, 5])

$$\frac{d}{dt} \left(\frac{\partial T^*}{\partial w_n} \right) - \frac{\partial T^*}{\partial \pi_n} + \sum_{m=1}^{m=k} \sum_{l=1}^{l=k} \sum_{i=1}^{j=k} \sum_{j=1}^{j=k} b_{li} b_{mj} \left(\frac{\partial a_{im}}{\partial q_l} - \frac{\partial a_{il}}{\partial q_m} \right) \frac{\partial T^*}{\partial w_i} w_j = \Pi_n, \quad (n=1,\dots,k) \quad (1)$$

where w_j ($j=1,\dots,k$) denotes quasi-velocities defined by generalized velocities \dot{q}_n

$$\dot{q}_n = \sum_{j=1}^{j=k} b_{nj} w_n, \quad (n=1,\dots,k). \quad (2)$$

Introducing Hamel coefficients (γ_{nj}^i) defined as

$$\gamma_{nj}^i = \sum_{m=1}^{m=k} \sum_{l=1}^{l=k} b_{ln} b_{mj} \left(\frac{\partial a_{im}}{\partial q_l} - \frac{\partial a_{il}}{\partial q_m} \right), \quad (3)$$

we obtain simple form of Boltzmann-Hamel equations

$$\frac{d}{dt} \left(\frac{\partial T^*}{\partial w_n} \right) - \frac{\partial T^*}{\partial \pi_n} + \sum_{i=1}^{i=k} \sum_{j=1}^{j=k} \gamma_{nj}^i \frac{\partial T^*}{\partial w_i} w_j = \Pi_n, \quad (n = 1, \dots, k). \quad (4)$$

Matrix form [9] of Boltzmann-Hamel equations

$$\frac{d}{dt} \left(\frac{\partial T^*}{\partial \mathbf{w}} \right) + \mathbf{B}^T (\dot{\mathbf{A}}^T - \mathbf{D}^T \mathbf{B} \mathbf{w}) \frac{\partial T^*}{\partial \mathbf{w}} - \mathbf{B}^T \frac{\partial T^*}{\partial \mathbf{q}} = \mathbf{B}^T \left(\mathbf{f} - \frac{\partial \mathbf{V}}{\partial \mathbf{q}} \right) \quad (5)$$

allows to automate generation of Hamel coefficients and eliminates all the difficulties associated with the determination of these quantities [9].

Analysis of dynamics of unicycle based on Boltzmann-Hamel formalism is presented in the next section.

2. Description of the analysed model

For the unicycle-unicyclist model description we use fixed inertial frame $Oxyz$ (Fig. 4) as well as moving frame $Bx'y'z'$ – parallel to $Oxyz$. Third frame $Bx_Iy_Iz_I$ is the wheel plane embedded no inertial frame.

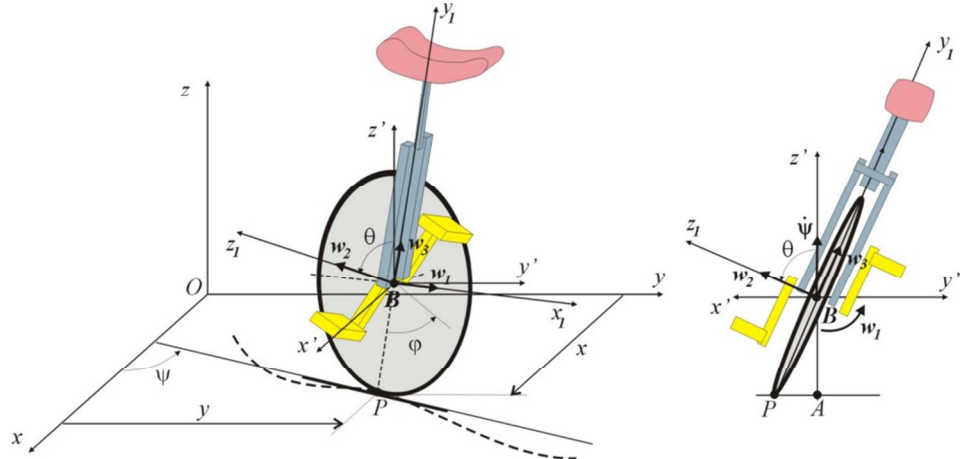


Figure 4. Model of the unicycle – without unicyclist

To consider the motion of the unicycle wheel model, we introduce the following generalized coordinates

$$\mathbf{q}_w = [\theta, \varphi, \psi, x, y]^T, \quad (6)$$

where θ, φ, ψ are Euler angles describing wheel spatial orientation and x, y are coordinates of the contact point P . The unicycle frame orientation with respect to the wheel (frame $Bx_1y_1z_1$) is described by angle β_1 whereas the unicyclist upper torso orientation by angles α_2, β_2 and γ_2 . The frame-unicyclist model generalized coordinates are

$$\mathbf{q}_f = [\beta_1, \alpha_2, \beta_2, \gamma_2]^T. \quad (7)$$

Unicyclist legs orientation depends on coordinates $\theta, \varphi, \psi, \beta_1$.

Quasi-velocities (Fig. 4) defining the wheel model velocities are assumed in the following form:

$$\begin{aligned} w_1 &= \omega_1 = \dot{\theta}, & w_2 &= \omega_2 = \dot{\varphi} + \psi \cos \theta, & w_3 &= \omega_3 = \dot{\psi} \sin \theta, \\ w_4 &= -\dot{x} + a \dot{\varphi} \cos \psi, & w_5 &= -\dot{y} + a \dot{\varphi} \sin \psi, \end{aligned} \quad (8)$$

(a is the radius of the wheel). Equations (8) are valid under assumption that the wheel is a rigid disc making point contact with the road and rolls without longitudinal slip on a flat surface. It means that the constraint equations for the wheel are: $w_4=0, w_5=0$.

Matrix form of (8) defines matrices \mathbf{B} and \mathbf{A} used in equation (5):

$$\mathbf{w} = \begin{bmatrix} w_1 \\ w_2 \\ w_3 \\ w_4 \\ w_5 \end{bmatrix} = \begin{bmatrix} 1 & 0 & 0 & 0 & 0 \\ 0 & 1 & \cos \theta & \cos \theta & 0 \\ 0 & 0 & \sin \theta & 0 & 0 \\ 0 & a \cos \psi & 0 & -1 & 0 \\ 0 & a \sin \psi & 0 & 0 & -1 \end{bmatrix} \begin{bmatrix} \dot{\theta} \\ \dot{\varphi} \\ \dot{\psi} \\ \dot{x} \\ \dot{y} \end{bmatrix} = \mathbf{A} \dot{\mathbf{q}}_w, \quad \mathbf{B} = \mathbf{A}^{-1}. \quad (9)$$

Kinetic energy of the wheel is obtained by formula

$$T_w = \frac{1}{2} m_w a (w_1^2 + w_2^2) + \frac{1}{2} (J_1 w_1^2 + J_2 w_2^2 + J_3 w_3^2). \quad (10)$$

Kinetic energy for the other parts of unicycle-unicyclist model are expressed similarly (however, these relations are more complicated).

Equations of model dynamics based on Boltzmann-Hamel equation (5) were generated automatically and solved using *Mathematica*.

3. Simulation results

Some results of numerical simulation for the unicycle-unicyclist model motion are shown in Figures 5-8.

Wheel – floor contact point trajectory and wheel centre trajectory for particular data ($a = 0.3$ m; $m_w = 5$ kg; $J_1 = 0.25$ kgm 2 ; $J_2 = 0.25$ kgm 2 ; $J_3 = 0.5$ kgm 2) are depicted in Fig. 5. The comparison of trajectories for different initial velocity ($\dot{\varphi}$) and roll angle (θ) are shown in Figures 6-7.

Accuracy of simulation results is shown in the Figure 8 where changes in quasi-velocities values w_4 and w_5 during simulation process are presented. Constraints equation errors have values 10^{-11} [m] (for exact solution $w_4=0$, $w_5=0$).

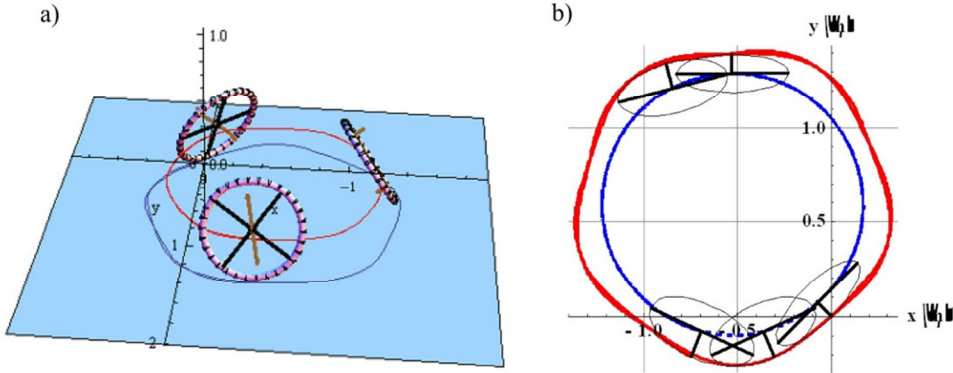


Figure 5. Unicycle wheel simulation results: a) 3D view, b) wheel – floor contact point trajectory (dashed line) and wheel centre trajectory (solid line)

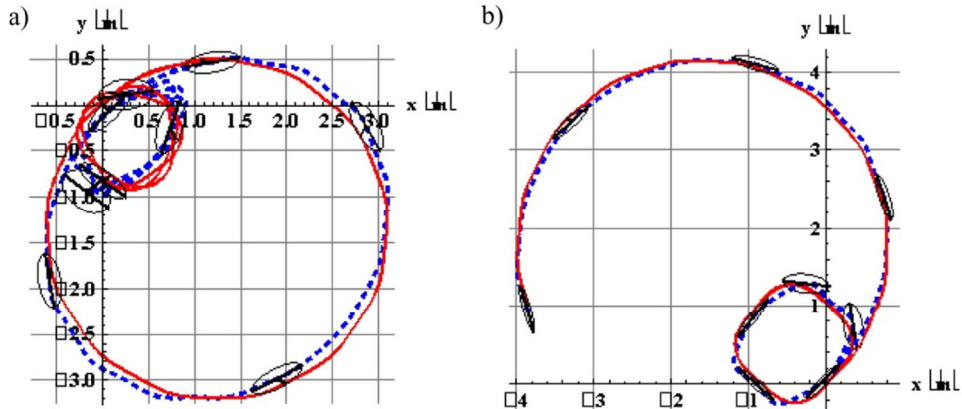


Figure 6. Comparison of contact point trajectories and wheel centre trajectory for different initial velocity ($\dot{\phi}$) and roll angle (θ):

- a) $\dot{\phi}(0) = -3 \text{ rad/s}$ and $\dot{\phi}(0) = -6 \text{ rad/s}$ (for $\theta(0) = 110^\circ$),
- b) $\dot{\phi}(0) = -3 \text{ rad/s}$ and $\dot{\phi}(0) = -5 \text{ rad/s}$ (for $\theta(0) = 90^\circ$)

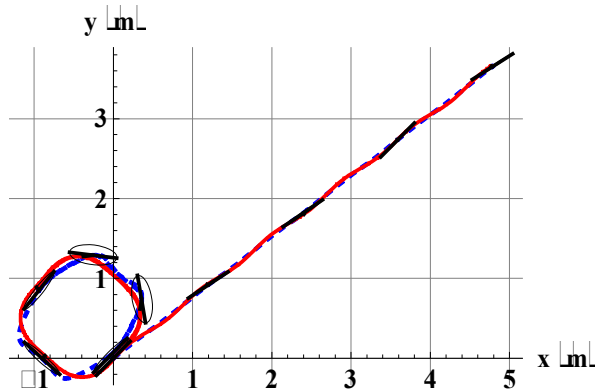


Figure 7. Comparison of contact point trajectories and wheel centre trajectory for $\dot{\phi}(0) = -3 \text{ rad/s}$ and $\ddot{\phi}(0) = -5 \text{ rad/s}$ ($\theta(0) = 80^\circ$)

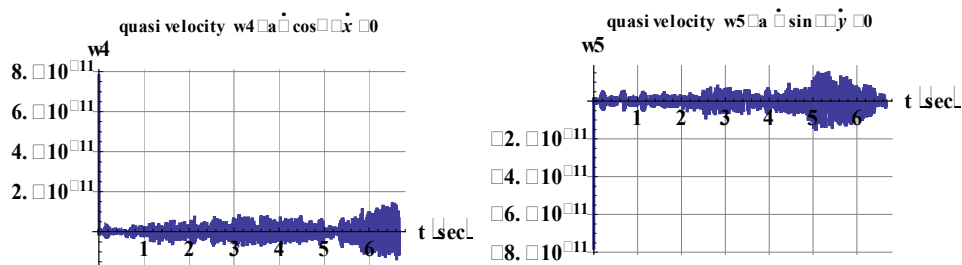


Figure 8. Constraints equations error (quasi-velocities values w_4 and w_5)

4. Conclusions

The matrix notation of Boltzmann-Hamel equations eliminates drawbacks occurring with the classical formulation of these equations. Its use allows the automation of the process of generating equations of motion. To obtain equations of motion in the form of quasi-coordinates and quasi-velocities it is sufficient to set the matrix transforming the generalized velocities into quasi-velocities, the kinetic energy and the vector of generalized forces. This procedure is general and can be used for solving many problems.

Motion analysis of a unicycle – unicyclist 3D model presented in the paper is the first step of larger work. In the future, the model will be extended and the system control method will be proposed in order to design a prototype of the unicycle, which can keep balance for unicyclist. Dynamic stability of unicycle will be also analysed.

References

1. <http://www.weranda.pl/galeria-zdjec/bicykl/1/?id=23758> [dostęp: 18-12-2011]
2. <http://qu-ax.com/en/products> [dostęp: 18-12-2011]

3. Pawełczak K.: Poradnik monocyklisty. Wydanie I, Warszawa 2009.
4. R. Gutowski R, *Mechanika analityczna*, PWN Warszawa 1971.
5. J.I. Nejmark, N.A. Fufajew, *Dynamika układów nieholonomicznych*, PWN Warszawa 1971.
6. W. Blajer, *Metoda projekcyjna - teoria i zastosowania w badaniu nieswobodnych układów mechanicznych*. WSI Radom, 13/1994.
7. W. Blajer, Projective formulation of Lagrange's and Boltzmann-Hamel equations for multibody systems. ZAMM, **75** (1995). 107 – 108.
8. J.M. Maruskin, A.M. Bloch, *The Boltzmann's Hamel equations for the optimal control of mechanical systems with nonholonomic constraints*, Int. J. Robust. Nonlinear Control **21** (2011).
9. J. Grabski, J. Strzałko, *Automatic Generation of Boltzmann-Hamel Coefficients for Mechanical Problems*. Mechanics and Mechanical Engineering International Journal, 1 (1997) 61 – 77.

Paper presented on XXVI Symposium on Vibrations in Physical Systems, Poznan – Bedlewo, May 4-8, 2014.

Finite Element Analysis of Dynamic Properties of Thermally Optimal Two-phase Composite Structure

Maria NIENARTOWICZ

*Institute of Applied Mechanics, Poznan University of Technology
ul. Jana Pawla II 24, 60-965 Poznan, Poland
maria.nienartowicz@doctorate.put.poznan.pl*

Tomasz STREK

*Institute of Applied Mechanics, Poznan University of Technology
ul. Jana Pawla II 24, 60-965 Poznan, Poland
tomasz.strek@put.poznan.pl*

Abstract

This paper presents modelling and a FEM analysis of dynamic properties of a thermally optimal two-phase composite structure. Simulations were provided for 2D models. At the first step, topology optimization was performed, where an internal energy was minimized. At the second step, analysis of dynamic properties was executed. Calculations allowed to determine eigenfrequencies and the mode shape of the structure. Solid isotropic material with penalization (SIMP) model was used to find the optimal solution. The optimization algorithm was based on SNOPT method and Finite Element Method.

Keywords: topology optimization, SIMP model, SNOPT, internal energy

1. Introduction

Determination of natural frequencies and mode shapes of the structure are usual first steps in performing a dynamic analysis. It is caused by the fact that these factors show how the structure will respond to dynamic load.

Natural frequencies of a structure are the frequencies at which system tends to oscillate without the absence of damping or driving force, whereas the mode shape (normal mode of vibration) is a deformed shape of the structure which appears at a specific natural frequency of vibration. Natural frequencies and mode shapes are functions of boundary conditions and structural properties.

There are many reasons why the analysis of dynamic properties is executed. One of them is to determine the dynamic interaction between a component and a structure to which it is attached, like for example, an air conditioner installed on the roof of a building. In this case, it is essential to check if the operating frequency of the rotating fan is not too close to the eigenfrequency of the building. Another example is comparing the results of the analysis with results obtained in real tests. Thereby, the results of the analysis can support the experiment, e.g. showing areas where accelerometers should be placed. Determination of eigenfrequencies and mode shapes is also used in the design process. It is necessary to check the influence of particular design changes of the structure on the dynamic parameters.

There are many examples of analysis of dynamic properties in literature. Paper [1] presents an investigation into the frequency dependant viscoelastic dynamics of a multi-functional composite structure from a finite element analysis and experimental validation. After model parameter identification, a numerical simulations were carried out. Thereby, the damping behaviour of first two vibrations modes was predicted. At the next step, the numerical results were validated by the experimental tests on the layered composite beam.

The dynamic problem of reinforced concrete slabs stiffened by steel beams with deformable connection including creep and shrinkage effect is considered in [2]. In the papers, authors took into consideration the in-plane forces and deformations of the plate in the adopted models and also the axial forces and deformations of the beam. The mode shapes and eigenfrequencies of the stiffened concrete slab were determined.

In papers [3], a four types of integral finite elements were developed and used to estimate the dynamical characteristics of elastic-viscoelastic composite structures. The composite structures were sandwich beam, plate and shell structures with viscoelastic materials as core layers. The results from the direct frequency response method and experiment were compared to the results of the integral finite element prediction, which revealed that integral finite elements are passable regarding to engineering applications.

An analysis of the dynamic properties of multiple damping layer, laminated composite beams with anisotropic stiffness layers was investigated in [4]. For this purpose the finite-element-based modal strain energy method was used. In this study the variation of resonance frequencies and modal loss factors of various beam samples with temperature were analyzed.

The dynamic behaviour of fibre reinforced plastic sandwich plates with PCV foam core was considered in [5]. The equations of motion, which were obtained by authors, are used to perform steady state analysis and to determine the natural frequencies and modal loss factors of specific composite sandwich plates.

Study [6] is intended to analyze the damping of PVC foams under flexural vibrations of clamped free beams. A finite element analysis based on the sandwich theory was used to model the natural frequencies and the damping of the beams. Authors took into account the numerical and experimental results to derive the shear modulus and the damping of PVC foams as functions of the frequency.

Papers [7] were devoted to examination of the viscoelastic damping model of the cylindrical hybrid panels with co-cured, free and constrained layers. For this purpose, the refined finite element method based on the layerwise shell theory was used. In this study, the damped natural frequencies, modal loss factors and frequency response functions of cylindrical viscoelastic hybrid panels were determined and compared with those of the base composite panel without a viscoelastic layer.

In [13] authors present computational analysis of sandwich-structured composites with an auxetic phase. The total energy strain is analyzed. In papers the application of SIMP model was used to find the optimal distribution of a given amount of materials in sandwich-structured composite. Authors also propose a multilayered composite structure in which internal layers surfaces are wavy.

2. Optimization of the average internal energy

The first step in presented effort was to optimize the average internal energy in considered two-phase structure. The average internal energy Ei_{avg} is calculated using equation 1:

$$Ei_{avg} = \frac{1}{A} \int_{\Omega} Ei \, d\Omega \quad (1)$$

Here Ω refers to the design domain, Ei is the internal energy and A is the area of the domain.

The objective function of the considered design optimization problem depends on the design variable $r = r(x)$ as follows:

$$Ei_{avg}(r) = \frac{1}{A} \int_{\Omega} Ei(r) \, d\Omega \quad (2)$$

The internal energy of the solid was calculated by the following equation:

$$Ei_{avg}(r) = c_p T(r) \quad (3)$$

where c_p is the heat capacity and $T(r)$ is the temperature.

The temperature is calculated using Fourier's equation 4 (Fourier's law of steady state pure conduction) [12]:

$$-\nabla \cdot (k(r) \nabla T) = Q, \quad (4)$$

where $k(r)$ is the thermal conductivity and Q is the heat source.

Using the Solid Isotropic Material with Penalization (SIMP) model in topology optimization in a two-phase structure [8], one can write the generalized thermal conductivity in the form of:

$$k(r) = k_1 + (k_2 - k_1) \cdot r^p, \quad p > 1, \quad k_1 < k_2 \quad (5)$$

Here r is a control variable (design variable), p is a penalty parameter, k_1 and k_2 are thermal conductivity values of the first and the second material respectively.

In the considered case, the control variable is related to thermal conductivity parameter of the isotropic material and is interpolated from 0 to 1, which corresponds to the first and the second material respectively, using penalty scheme which affects the material distribution. The value of the penalty parameter above 1 ensures that density values of 0 (first material) or 1 (second material) are favoured ahead of the intermediate values.

One can interpret a control (design) variable $r = r(x)$ as a generalized material density which satisfies the following constraints:

$$0 \leq \int_{\Omega} r(x) \, d\Omega \leq V, \quad 0 \leq r(x) \leq 1, \quad (6)$$

where V is the second material's volume available for distribution.

In the considered structure, the optimal material distribution is found for a given objective and constraints by assigning each element an individual control variable value. For the purposes of this research, Sparse Nonlinear Optimizer (SNOPT) code was used. This gradient optimization algorithm was developed by P. E. Gill, W. Murray and M. A. Saunders [9]. In this method, the objective function can have any form and any constraints can be applied. SNOPT is suitable for large-scale linear and quadratic program-

ming and for linearly constrained optimization, as well as for general nonlinear programs. This algorithm minimizes a linear or nonlinear function subject to bounds on the variables and sparse linear or nonlinear constraints.

3. Equation of motion of the solid

For the purpose of calculation the Navier's equation of motion was used which takes a form of [10]:

$$\rho \frac{\partial^2 \mathbf{u}}{\partial t^2} - \nabla \cdot \boldsymbol{\sigma} = 0 \quad (7)$$

where the force has been omitted, \mathbf{u} is the displacement vector, ρ is the density, $\boldsymbol{\sigma}$ is the stress tensor and can be written as [11]:

$$\boldsymbol{\sigma} = \mathbf{D}\boldsymbol{\varepsilon} = \lambda(\nabla \cdot \mathbf{u})\mathbf{I} + 2\mu\boldsymbol{\varepsilon}. \quad (8)$$

Here \mathbf{I} is the identity matrix, $\boldsymbol{\varepsilon} = \frac{1}{2}(\nabla \cdot \mathbf{u} + (\nabla \cdot \mathbf{u})^T)$ is the strain tensor, λ i μ are Lame parameters presented in the equation:

$$\mu = G = \frac{E}{2(1+\nu)}, \lambda = \frac{E \cdot \nu}{(1-2\nu)(1+\nu)} \quad (9)$$

where E – Young's modulus, G – shear modulus, ν – Poisson's ratio.

Using the aforementioned equation one can write Navier's equation of motion for isotropic solid for the linear constitutive relation between stresses and deformations [10] as:

$$\rho \frac{\partial^2 \mathbf{u}}{\partial t^2} - (\mu \nabla^2 \mathbf{u} + (\lambda + \mu) \nabla \nabla \cdot \mathbf{u}) = \mathbf{0}. \quad (10)$$

A real harmonic displacement satisfies the equation:

$$\frac{\partial^2 \mathbf{u}}{\partial t^2} = -\omega^2 \mathbf{u}. \quad (11)$$

where ω is the circular frequency with period $2\pi/\omega$.

The displacement vector can be written in the complex form of:

$$\mathbf{u}(x) = \mathbf{u}_1(x) + i\mathbf{u}_2(x). \quad (12)$$

Here the harmonic displacement became a real part of complex field:

$$\mathbf{u}(x, t) = \mathcal{R}e[\mathbf{u}(x)e^{-i\omega t}]. \quad (13)$$

Pursuant to the above equations the harmonic equation of motion satisfies formula:

$$-\rho\omega^2 \mathbf{u} - (\mu \nabla^2 \mathbf{u} + (\lambda + \mu) \nabla \nabla \cdot \mathbf{u}) = \mathbf{0}. \quad (14)$$

The foregoing equation can be viewed as an eigenvalue equation for the operator $\mu \delta_{ij} \nabla^2 + (\lambda + \mu) \nabla_i \nabla_j$ with eigenfunction $\mathbf{u}(x)$ and eigenvalue in the form of $-\rho\omega^2$ [10].

4. Numerical results

This section presents an analysis of dynamic properties for a two-phase structure whose topology was optimized. The considered model consists of steel and polyurethane foam. The thermal and mechanical properties are presented in Table 1.

As it was mentioned above, the first step was to minimize the average internal energy. For this purpose, a 2D model, with applied boundary conditions, was prepared (see

Figure 1). A fraction of the domain to use for the distribution of the second material is equal to A_{frac} and took the value of 0.4.

Table 1. Thermal and mechanical properties of the model

Property	Material 1 – Polyurethane foam	Material 2 – Steel
E [Pa]	4e9	2e11
ν	0.4	0.25
ρ [kg/m ³]	50	8000
k [W/mK]	0.03	58

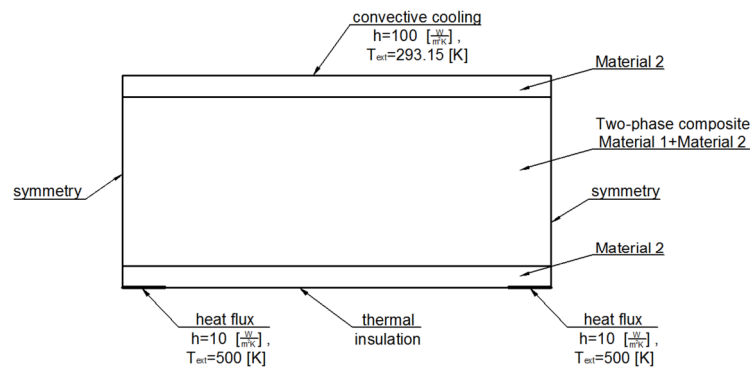


Figure 1. Boundary conditions for topology optimization

During the optimization process, a distribution of the control variable was obtained, as it is presented in Figure 2. In the figure below, value 1 is assigned to material 2 (white colour) with higher thermal conductivity, and value 0 is assigned to material 1 (black colour) [14].

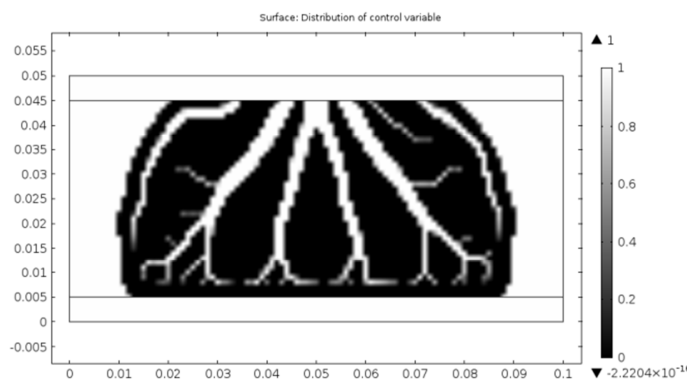


Figure 2. Distribution of control variable for $A_{frac}=0.4$

In Figure 3, boundary conditions for analysis of dynamic properties are presented. At the top of the model, boundary load $F(t)$ was applied, additionally the model was fixed on two sections at the bottom boundary.

At the second step of calculations, six eigenfrequencies were determined. The values of the eigenfrequencies are presented in Table 2. In Figures 4–9, the amplitude of the forced vibration and mode shapes are presented for each eigenfrequency.

Table 2. Determined eigenfrequencies

No.	1	2	3	4	5	6
Value of eigenfrequency [Hz]	5502.93	7712.40	14618.93	15047.05	17713.10	19548.60

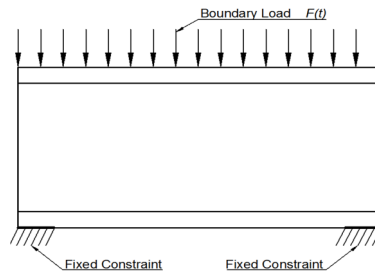


Figure 3. Boundary conditions for analysis of dynamic properties

The boundary load can be written as:

$$F(t) = F_{load} \sin(\omega t), \quad (15)$$

where $F_{load} = 10000 [N/m^2]$.

For the purpose of the analysis of dynamic properties Young modulus, Poisson's ratio and material density were written in the form of interpolation scheme SIMP for isotropic materials, as it is presented in formulas (16), (17) and (18).

$$E(r) = E_1 + (E_2 - E_1) \cdot r^p, \quad p > 1, \quad E_1 < E_2 \quad (16)$$

$$\nu(r) = \nu_1 + (\nu_2 - \nu_1) \cdot r^p, \quad p > 1, \quad \nu_1 > \nu_2 \quad (17)$$

$$\rho(r) = \rho_1 + (\rho_2 - \rho_1) \cdot r^p, \quad p > 1, \quad \rho_1 < \rho_2 \quad (18)$$

where: E_1 and E_2 are Young's moduli, ν_1 and ν_2 are Poisson's ratios, ρ_1 and ρ_2 are densities for the first and the second material respectively.

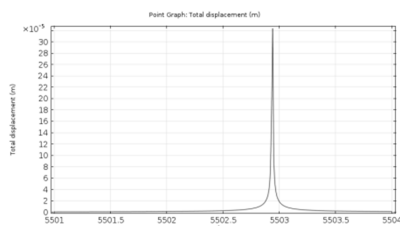


Figure 4. a)The amplitude of the forced vibration

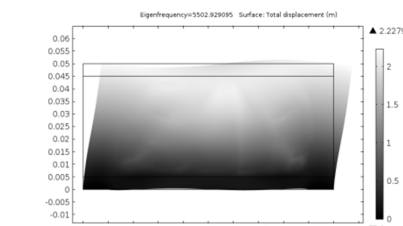


Figure 4. b) Mode shape for the first eigenvalue

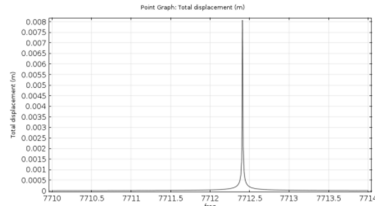


Figure 5. a) The amplitude of the forced vibration

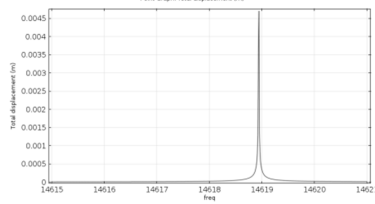


Figure 6. a) The amplitude of the forced vibration

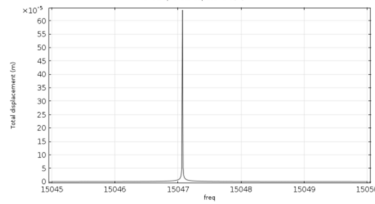


Figure 7. a) The amplitude of the forced vibration

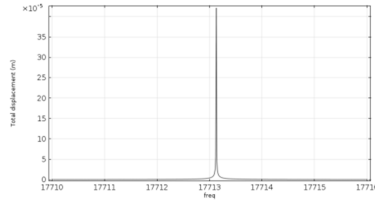


Figure 8. a) The amplitude of the forced vibration

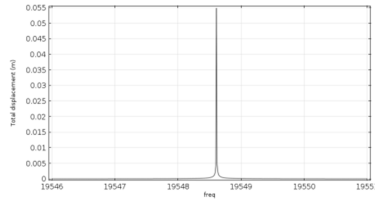


Figure 9. a) The amplitude of the forced vibration

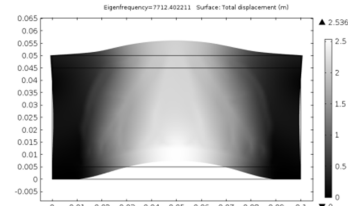


Figure 5. b) Mode shape for the second eigenvalue

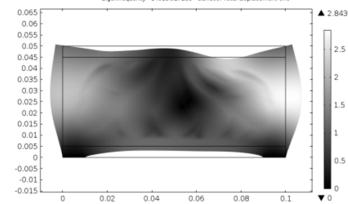


Figure 6. b) Mode shape for the third eigenvalue

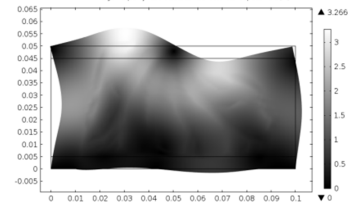


Figure 7. b) Mode shape for the fourth eigenvalue

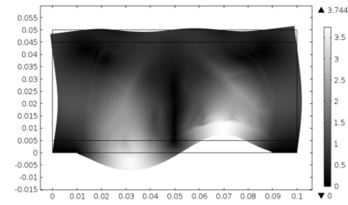


Figure 8. b) Mode shape for the fifth eigenvalue

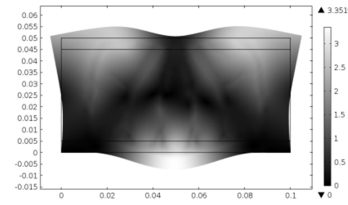


Figure 9. b) mode shape for the sixth eigenvalue

5. Conclusions

The paper presents an analysis of the dynamic properties of a thermally optimal two-phase structure. In the first stage of the calculations, a 2D model of a two-phase structure was optimized. Thereby, the minimum average internal energy was achieved. At

the second step, six eigenfrequencies were determined for the model with the optimal topology. Subsequently, the amplitude of the forced vibration and mode shapes are presented for each eigenfrequency.

References

1. Y. Wang, D. J. Inman, *Finite element analysis and experimental study on dynamic properties of a composite beam with viscoelastic damping*, Journal of Sound and Vibration, **332** (2013) 6177-6191.
2. E.J. Sapountzakis, *Dynamic analysis of composite steel-concrete structures with deformable connection*, Computers and Structures, **82** (2004) 717-729.
3. Q. Chen, Y.W. Chan, *Integral finite element method for dynamical analysis of elastic-viscoelastic composite structures*, Computers and Structures, **74** (2000) 51-64.
4. M. D. Rao, R. Echempati, S. Nadella, *Dynamic analysis and damping of composite structures embedded with viscoelastic layers*, Composites Part B, **28B** (1997) 547-554.
5. M. Meunier, R. A. Shenoi, *Dynamic analysis of composite sandwich plates with damping modelled using high-order shear deformation theory*, Composite Structures, **54** (2001) 243-254.
6. M. Assrar, A. E. Mah, J. M. Berthelot, *Evaluation of the dynamic properties of PVC foams under flexural vibrations*, Composite Structures, **94** (2012) 1919-1931.
7. I. K. Oh, *Dynamic characteristics of cylindrical hybrid panels containing viscoelastic layer based on layerwise mechanics*, Composites: Part B, **38** (2007) 159-171.
8. M.P. Bendsøe, O. Sigmund, *Topology Optimization Theory, Methods, and Applications*, Springer 2003.
9. P.E. Gill, W. Murray, M.A. Saunders, *SNOPT: An SQP Algorithm for Large-Scale Constrained Optimization*, SIAM REVIEW, **47**(1) (2005) 99-131.
10. B. Lautrup, *Physics of Continuous Matter, Exotic and Everyday Phenomena in the Macroscopic World*, IOP 2005.
11. O. C. Zienkiewicz, R. L. Taylor, *The Finite Element Method, Volume 2, Solid Mechanics*, Butterworth-Heinemann 2000.
12. S. Wiśniewski, T. S. Wiśniewski, *Heat Transfer (in Polish: Wymiana ciepła)*, WNT 2000.
13. Strek T., Jopek H., Maruszewski B. T., Nienartowicz M., *Computational analysis of sandwich-structured composites with an auxetic phase*, Phys. Status Solidi (b)., Vol. 251, Issue 2, DOI: 10.1002/pssb.201384250, (2014) 354-366,
14. M. Nienartowicz, T. Strek, Topology optimization of the effective thermal properties of two-phase composites, *Recent Advances in Computational Mechanics*, T. Łodygowski, J. Rakowski, P. Litewka (Red.), CRC Press (2014) 223-236

Transverse Vibration Analysis of a Compound Plate with Using Cyclic Symmetry Modeling

Stanisław NOGA

Faculty of Mechanical Engineering and Aeronautics, Rzeszów University of Technology
al. Powstańców Warszawy 12, 35–959 Rzeszów, Poland
noga@prz.edu.pl

Abstract

In the paper the transversal vibration of a representative annular plate with complex geometry is studied on the basis of the numerical method and simulation. The research is focused on preparing the numerical model by using the cyclic symmetry modeling approach. The obtained results are discussed and compared with the experimental data. FE models are formulated by using ANSYS code.

Keywords: transversal vibration, cyclic model, annular plate

1. Introduction

Problems of transverse vibration of annular plates have been the subject of many recent investigations [1, 4]. This is due to the fact that some rotating systems can be treated as annular plates, where both their shape and dimensions are affected by the design of these systems. In papers [1, 4] the authors analyse free transverse vibration of toothed gears by using the finite element (FE) technique. In papers [3, 4] the cyclic symmetry modeling is included in the solving process of the vibration problems of compound systems. In the above presented article free transverse vibration of a compound annular plate is analysed by using the FE technique and experimental investigation.

2. Formulation of the problem

The objective of this paper is to present the methods of FE modeling of the compound annular plates transverse vibration and analyse their usefulness in the representation of the vibration process. For that purpose, a set of two compound circular plates has been analysed. The analysed systems have the geometry as it is displayed in Figure 1. Primary geometrical dimensions of the systems (diameters: d_z , d_w , d_l ; thickness: l_r , l_w) are shown in Table 1.

Table 1. Parameters characterizing the analysed plates

No of models	d_z [m]	d_w [m]	d_l [m]	l_r [m]	l_w [m]	E [Pa]	ρ [kg/m ³]	ν
1	0.191	0.159	0.02	0.008	0.002	$2.1 \cdot 10^{11}$	$7.85 \cdot 10^3$	0.28
2	0.203	0.147						

In these Table, E is Young's modulus of elasticity, ρ is the mass density and ν is the Poisson ratio, respectively.

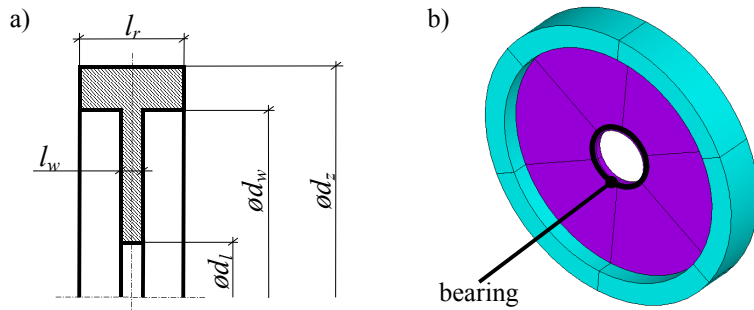


Figure 1. Geometrical models of the systems

For each case the problem of free vibration is solved by the finite element method. After elaboration of discrete models of the structures to be analysed, the differential equations of motion of the each analysed system can be written in the form [2]

$$\mathbf{M}\ddot{\mathbf{u}} + \mathbf{K}\mathbf{u} = 0 \quad (1)$$

where \mathbf{M} is the global mass matrix, \mathbf{K} is the global stiffness matrix, and \mathbf{u} is the nodal displacement vector. Both global mass and stiffness matrices are obtained from the element matrices that are given by [2]

$$\mathbf{M}^{(e)} = \int_{V^{(e)}} \rho^{(e)} \mathbf{N}^T \mathbf{N} dV^{(e)}, \quad \mathbf{K}^{(e)} = \int_{V^{(e)}} \mathbf{B}^T \mathbf{E} \mathbf{B} dV^{(e)} \quad (2)$$

where $\rho^{(e)}$ is density of the element, \mathbf{N} is the matrix of the element shape functions, \mathbf{B} is the element shape function derivatives matrix, \mathbf{E} is the material stiffness matrix, and $V^{(e)}$ is volume of the element. The natural frequencies of the system are obtained by solving the eigenvalue problem

$$(\mathbf{K} - \omega^2 \mathbf{M}) \bar{\mathbf{u}} = 0 \quad (3)$$

where ω is natural frequency and $\bar{\mathbf{u}}$ is corresponding mode shape vector, which is determined by the relation (3). The number of eigenpairs $(\omega_i, \bar{\mathbf{u}}_i)$ corresponds to the number of degrees of freedom of the system. The block Lanczos method is applied to solve the eigenvalue problem (3). Because of the discretization process, the FE models of the considered systems are treated as approximations of the exact systems. The error between the objects and the FE models is defined by

$$\varepsilon = (\omega^f - \omega^e) / \omega^e \times 100 [\%] \quad (4)$$

where ω^f is the natural frequency from the FE solution, while ω^e is the natural frequency of the exact system. Equation (4) is the so-called frequency error [2]. For the investigation presented in this paper the needed accurate values of the natural frequencies are achieved by the realization of experimental investigation.

3. Numerical analysis

In this section, the FE models of the systems under consideration are prepared and natural frequencies of the transverse vibration are determined. In accordance with the circular and annular plate vibration theory [2] the particular natural frequencies of vibration are denoted as ω_{mn} where m refers to the number of nodal circles and n is the number of nodal diameters. For each system, three FE models are realized. The first FE model is prepared as follows. Each geometrical model of these systems is meshed by using standard procedures of the ANSYS software. The 3-D solid mesh is prepared and the ten node tetrahedral element (solid187) with three degrees of freedom in each node is employed to realize each model. During the mesh generation process, it is assumed that the maximum length of each element's side needs to be no more than 2 [mm]. The bigger FE model refers to the second object and includes 143760 solid elements. The smaller FE model includes 97404 solid elements. For all models discussed here, calculations were continued until the natural frequency ω_{16} was determined. Tables 2 and 5 display the natural frequencies obtained by using the discussed FE models.

Table 2. Natural frequencies of the first FE model related to the object no 1 ω_{mn} [Hz]

	<i>n</i>							
	0	1	2	3	4	5	6	
<i>m</i>	1	236.5	149.4	643.6	1770	3340	5292	7523
	2	1932	2240	2899	3931	5327	7009	
	3	4531	5167	6580				

The second FE model of each system is prepared by using cyclic symmetry feature of the analysed systems. Geometrical model of each system consists of six sectors (see Fig. 1b) which have the cyclic symmetry feature. One of these segments is meshed by using standard procedures of the ANSYS software and the cyclic symmetry boundary conditions are included. The mesh generation and the computation process are conducted under the same conditions as for the previously discussed FE model cases (the full model cases). The bigger cyclic FE model refers to the second object and includes 23960 solid elements. The smaller cyclic FE model includes 16234 solid elements. Thus, the solution of free vibration is obtained on the basis of these single symmetric sectors. Tables 3 and 6 display the natural frequencies obtained by using the discussed cyclic symmetry FE models (the first cyclic model cases).

Table 3. Natural frequencies of the second FE model related to the object no 1 ω_{mn} [Hz]

	<i>n</i>							
	0	1	2	3	4	5	6	
<i>m</i>	1	236.4	149.4	643.6	1770	3340	5292	7523
	2	1935	2240	2898	3930	5327	7009	
	3	4530	5166	6579				

The third FE model of each system is prepared in the same manner as the second FE model cases, but the maximum length of each element's side is different. For these cases

the maximum length of each element's side is no more than 1.5 [mm]. So, the bigger cyclic FE model, which refers to the second object, includes 57834 solid elements and the smaller cyclic FE model includes 38131 solid elements, respectively. Tables 4 and 7 show the natural frequencies obtained by using the above cyclic symmetry FE models (the second cyclic model cases).

Table 4. Natural frequencies of the third FE model related to the object no 1 ω_{mn} [Hz]

	<i>n</i>						
	0	1	2	3	4	5	6
<i>m</i>	1	235.8	148.9	643.4	1770	3340	5291
	2	1928	2233	2890	3922	5317	6997
	3	4520	5157	6566			

Table 5. Natural frequencies of the first FE model related to the object no 2 ω_{mn} [Hz]

	<i>n</i>						
	0	1	2	3	4	5	6
<i>m</i>	1	213.5	123.4	658.9	1804	3398	5403
	2	1916	2458	3337	4507	6059	
	3	4109	4680	6321			

Table 6. Natural frequencies of the second FE model related to the object no 2 ω_{mn} [Hz]

	<i>n</i>						
	0	1	2	3	4	5	6
<i>m</i>	1	213.5	123.3	658.9	1804	3398	5403
	2	1916	2457	3336	4507	6059	
	3	4108	4679	6321			

Table 7. Natural frequencies of the third FE model related to the object no 2 ω_{mn} [Hz]

	<i>n</i>						
	0	1	2	3	4	5	6
<i>m</i>	1	212.8	122.9	658.8	1804	3398	5403
	2	1913	2452	3326	4496	6046	
	3	4092	4666	6312			

4. Experimental studies

In this section the results related to the experimental verification of the considered numerical models are discussed. LMS measurement environment is used in the experimental study. The measuring set contained the PCB model 086C03 type modal hammer, accelerometer PCB model 353B18, LMS SCADA data acquisition system, and SCM-V4E type measuring module supported by LMS Test.Lab software. The experimental study is conducted to identify natural frequencies and corresponding mode shapes related to the transverse vibration of the considered objects. The values of the excited natural

frequencies are shown in Table 8 (for the first object) and in Table 12 (for the second object), respectively.

Table 8. Natural frequencies of the first object ω_{mn} [Hz] (experimental investigation)

	<i>n</i>						
	0	1	2	3	4	5	6
<i>m</i>	1	263.8	141.9	575.6	1697	3272	5233
	2	1847	2247	2948	3976	5318	6941
	3	4397	5001	6453			

In Tables 9–11 the values of the frequency error related to the FE models of the first object are displayed. In each FE model case, only for two natural frequencies (ω_{l0} and ω_{l2}) the frequency error is above 10 [%]. In Tables 13–15 the values of the frequency error related to the FE models of the second object are displayed. In this object, only nine natural frequencies were excited. In each FE model case, for two natural frequencies the frequency error is above 10 [%].

Table 9. Frequency error related to the first FE model of the first object ε_{mn} [%]

	<i>n</i>						
	0	1	2	3	4	5	6
<i>m</i>	1	-10.35	5.29	11.81	4.3	2.08	1.13
	2	4.6	-0.31	-1.66	-1.13	0.17	0.98
	3	3.05	3.32	1.97			

Table 10. Frequency error related to the second FE model of the first object ε_{mn} [%]

	<i>n</i>						
	0	1	2	3	4	5	6
<i>m</i>	1	-10.39	5.29	11.81	4.3	2.08	1.13
	2	4.76	-0.31	-1.7	-1.16	0.17	0.98
	3	3.02	3.3	1.95			

Table 11. Frequency error related to the third FE model of the first object ε_{mn} [%]

	<i>n</i>						
	0	1	2	3	4	5	6
<i>m</i>	1	-10.61	4.93	11.78	4.3	2.08	1.11
	2	4.39	-0.62	-1.97	-1.36	-0.02	0.81
	3	2.8	3.12	1.75			

Table 12. Natural frequencies of the object no 2 ω_{mn} [Hz] (experimental investigation)

	<i>n</i>						
	0	1	2	3	4	5	6
<i>m</i>	1	221.3	106.3	596.3	1740		5330
	2		2444	3254	4389		7709
	3						

Table 13. Frequency error related to the first FE model of the second object ε_{mn} [%]

		<i>n</i>						
		0	1	2	3	4	5	6
<i>m</i>	1	-3.53	16.09	10.5	3.68		1.37	0.93
	2		0.57	2.55	2.69			
	3							

Table 14. Frequency error related to the second FE model of the second object ε_{mn} [%]

		<i>n</i>						
		0	1	2	3	4	5	6
<i>m</i>	1	-3.53	16	10.5	3.68		1.37	0.93
	2		0.53	2.52	2.69			
	3							

Table 15. Frequency error related to the third FE model of the second object ε_{mn} [%]

		<i>n</i>						
		0	1	2	3	4	5	6
<i>m</i>	1	-3.84	15.62	10.48	3.68		1.37	0.93
	2		0.33	2.21	2.44			
	3							

5. Conclusions

The present paper deals with free transverse vibration of a compound annular plate. Three FE models are proposed. For all the FE model cases discussed, comparable results have been obtained. The most attractive is the second FE model case, which includes cyclic symmetry features. Moreover, this model includes a substantially lower number of finite elements compared to the remainder of models. It is worth pointing out that in the preferred FE model case the maximum length of each element's side equal to the lesser plate thickness was assumed. At this stage of the research, it seems that further investigation needs to be continued.

References

1. R. Bogacz, S. Noga, *Free transverse vibration analysis of a toothed gear*, Arch. Appl. Mech., **82** (2012) 1159–1168 DOI: 10.1007/s00419–012–0608–6.
2. C. de Silva, *Vibration and Shock Handbook*, Taylor & Francis, Boca Raton 2005.
3. A. Grolet, F. Thouverez, *Free and forced vibration analysis of a nonlinear system with cyclic symmetry: Application to a simplified model*, J. Sound Vib., **331** (2012) 2911–2928.
4. S. Noga, R. Bogacz, K. Frischmuth, *Vibration analysis of toothed gear with cyclic symmetry modelling*, Vibration in Physical System, vol. XXV (2012) 299–304.

Vibration Analysis of a Thick Ring Interacting with the Disk Treated as an Elastic Foundation

Stanisław NOGA

*Faculty of Mechanical Engineering and Aeronautics, Rzeszów University of Technology
al. Powstańców Warszawy 12, 35–959 Rzeszów, Poland
noga@prz.edu.pl*

Tadeusz MARKOWSKI

*Faculty of Mechanical Engineering and Aeronautics, Rzeszów University of Technology
al. Powstańców Warszawy 12, 35–959 Rzeszów, Poland
tmarkow@prz.edu.pl*

Abstract

In this study the in plane flexural vibration of a thick ring interacting with Winkler foundation is analysed on the basis of the analytical and numerical method. The effect of rotary inertia and shear deformation is included. The normal frequencies and natural mode shapes of the system vibration are determined. Achieved results are discussed and compared with an experimental data. FE models are formulated by using ANSYS code.

Keywords: in-plane vibration, Timoshenko's theory, thick ring with foundation

1. Introduction

The problems of in-plane flexural vibration of circular rings with wheel-plate as an elastic foundation find application in several practical problems [6]. The fundamental circular rings vibration theory is presented in [5]. In the article [6] authors analyse free vibration of a ring gear by using thin ring theory. Free vibration of Timoshenko beam attached to linear elastic foundation are investigated in the paper [1]. The introductory studies related to the systems of the rings with wheel-plate as the elastic foundation are conducted in [3, 4]. In paper [2] the special three-parameter elastic foundation is proposed. In above paper the free in-plane flexural vibration of a circular ring with wheel-plate as a special three-parameter elastic foundation is analyzed using the classical thick ring theory, and the finite element (FE) technique. The procedure of determining the substitute mass density of a ring with massless foundation is presented. Obtained results of calculation are discussed and compared with experimental data. Experimental investigation are conducted by using two objects with the arbitrary chosen geometry.

2. Theoretical formulation

The mechanical model of the system under study consists of circular ring with wheel-plate as a special three-parameter, linear, elastic foundation. It is assumed that ring is homogeneous, perfectly elastic and it has rectangular, and constant cross-sectional area. It is additionally assumed that the centerline of the ring has radius R and an element of the ring, fixed by angle θ , displaces in the radial and circumferential direction, respec-

tively (see Fig. 1). The small displacements in these directions are denoted as $u(\theta, t)$ and $w(\theta, t)$, respectively, and t is time. According with the theory, discussed in [2], the foundation is represented by the special three-parameter Winkler model. The coefficients k_f , k_p and k_s represent the radial and the tangential stiffness per length unit, and the ring cross-section angle rotation stiffness modulus, respectively.

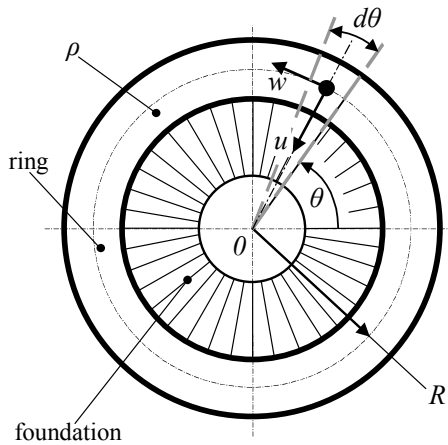


Figure 1. Vibrating system under study

Making use of the classical theory of vibrating thick rings [5], the partial differential equations of motion for the free in-plane flexural vibration can be combined into an only one equation in terms of the radial deflection $u(\theta, t)$ as

$$\begin{aligned} \frac{\partial^6 u}{\partial \theta^6} + & \left(2 - k_f \frac{R^2}{kAG} - k_s \frac{R^2}{EI_1} \right) \frac{\partial^4 u}{\partial \theta^4} + \left(1 + k_p \frac{R^2}{kAG} - 2k_s \frac{R^2}{EI_1} + k_f k_s \frac{R^4}{kAGEI_1} + \right. \\ & \left. + k_f \frac{R^4}{EI_1} \right) \frac{\partial^2 u}{\partial \theta^2} - \left(k_s \frac{R^2}{EI_1} + k_p k_s \frac{R^4}{kAGEI_1} + k_p \frac{R^4}{EI_1} \right) u - \left(\frac{\rho R^2}{E} + \frac{\rho R^2}{kG} \right) \frac{\partial^6 u}{\partial \theta^4 \partial t^2} + \\ & + \frac{\rho^2 R^4}{kGE} \frac{\partial^6 u}{\partial \theta^2 \partial t^4} + \left(-2 \frac{\rho R^2}{E} + k_f \frac{\rho R^4}{kAGE} + \frac{\rho R^2}{kG} + k_s \frac{\rho R^4}{kGEI_1} + \frac{\rho A R^4}{EI_1} \right) \frac{\partial^4 u}{\partial \theta^2 \partial t^2} + \\ & - \frac{\rho^2 R^4}{kGE} \frac{\partial^4 u}{\partial t^4} - \left(\frac{\rho R^2}{E} + k_p \frac{\rho R^4}{kAGE} + k_s \frac{\rho R^4}{kGEI_1} + \frac{\rho A R^4}{EI_1} \right) \frac{\partial^2 u}{\partial t^2} = 0 \end{aligned} \quad (1)$$

where E denotes Young's modulus of elasticity, G is the Kirhoff modulus, I_1 is the area moment of inertia of the rim cross section, ρ is the mass density, A is the cross section area, k is the shear correction factor. The general solution of equation (1) is assumed to be harmonic, i.e.

$$u(\theta, t) = U(\theta) e^{i\omega t} \quad (2)$$

where ω is the natural frequency and $i = \sqrt{-1}$ is the imaginary unit. Substituting solution (2) into equation (1) gives the following expression

$$\begin{aligned} & \frac{d^6U}{d\theta^6} + \left(2 - b_0 k_f - k_s \frac{a_0}{R^2} \right) \frac{d^4U}{d\theta^4} + \left(1 + b_0 k_p - 2k_s \frac{a_0}{R^2} + k_f k_s \frac{h_0}{\rho I_1} + k_f a_0 \right) \frac{d^2U}{d\theta^2} + \\ & - \left(k_s \frac{a_0}{R^2} + k_p k_s \frac{h_0}{\rho I_1} + k_p a_0 \right) U + (c_0 + d_0) \omega^2 \frac{d^4U}{d\theta^4} + c_0 d_0 \omega^4 \frac{d^2U}{d\theta^2} - c_0 d_0 \omega^4 U + \\ & - \left(-2c_0 + k_f h_0 + d_0 + k_s \frac{h_0 A}{I_1} + \rho A a_0 \right) \omega^2 \frac{d^2U}{d\theta^2} + \left(c_0 + k_p h_0 + k_s \frac{h_0 A}{I_1} + \rho A a_0 \right) \omega^2 U = 0 \end{aligned} \quad (3)$$

where

$$a_0 = \frac{R^4}{EI_1}, \quad b_0 = \frac{R^2}{kAG}, \quad c_0 = \frac{\rho R^2}{E}, \quad d_0 = \frac{\rho R^2}{kG}, \quad h_0 = \frac{\rho R^4}{kEAG} \quad (4)$$

The solution of equation (3) is assumed in the form

$$U(\theta) = \sum_{j=1}^3 C_{jn} \sin(n\theta + \varphi_{jn}), \quad n = 2, 3, \dots \quad (5)$$

where C_{jn} and φ_{jn} are constants. When equation (5) is substituted into equation (3), it yields the following frequency equation.

$$\begin{aligned} & -c_0 d_0 (n^2 + 1) \omega_n^4 + \left[(c_0 + d_0) n^4 + \left(-2c_0 + k_f h_0 + d_0 + k_s \frac{h_0 A}{I_1} + \rho A a_0 \right) n^2 + \right. \\ & \left. + \left(c_0 + k_p h_0 + k_s \frac{h_0 A}{I_1} + \rho A a_0 \right) \right] \omega_n^2 - n^6 + \left(2 - b_0 k_f - k_s \frac{a_0}{R^2} \right) n^4 + \\ & - \left(1 + b_0 k_p - 2k_s \frac{a_0}{R^2} + k_f k_s \frac{h_0}{\rho I_1} + k_f a_0 \right) n^2 - \left(k_s \frac{a_0}{R^2} + k_p k_s \frac{h_0}{\rho I_1} + k_p a_0 \right) = 0 \end{aligned} \quad (6)$$

Equation (6) is a quadratic equation in ω_n^2 and hence two frequency values are associated with each value of n . The smaller value of ω_n^2 corresponds to the flexural mode, and the higher value corresponds to the thickness-shear mode. In equation (6) n must be an integer with a value greater than 1.

3. The finite element models

In this section the FE models of the system under consideration are formulated to discretize the continuous model given by the equation (1). To find the eigenpairs (eigenvalue, eigenvector) related to the natural frequencies and natural mode shapes of the ring with elastic foundation, the block Lanczos method is employed [5]. The essential problem of

this section is prepared the FE model of the system with proper value of the ring substitute mass density ρ_z and massless elastic foundation, respectively. Two objects are considered. Analysed systems have the geometry as it is shown in Figure 2. For each object, the FE model is realized as follows. The ring part is modeled as the solid body and the foundation part is modeled as the masses solid body. The ten node tetrahedral element (solid187) with three degrees of freedom in each node is used to solve the problem. For each case, the proper value of the ring substitute mass density ρ_z is selected during calculations to minimise the frequency error defined by [2, 3]

$$\varepsilon_n = (\omega_n^f - \omega_n^c) / \omega_n^c \cdot 100 \% \quad (7)$$

where ω_n^f is the natural frequencies of the model and ω_n^c is the the natural frequencies of the object, respectively.

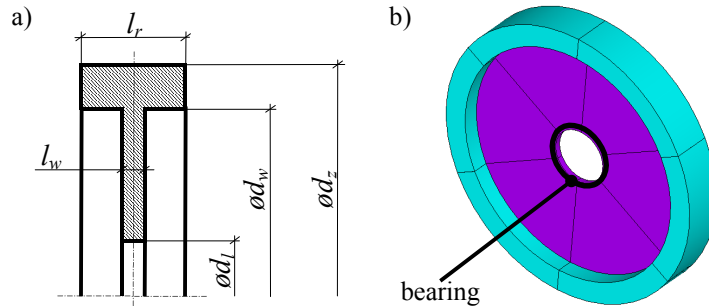


Figure 2. (a) geometrical dimensions, (b) model of the system

The prepared models include 97404 (for the first object) and 143760 (for the second object) solid elements, respectively.

4. Numerical analysis

Numerical analysis results of the circular ring with wheel–plate free vibration are obtained using the models suggested earlier. For all results presented here, the first seven natural frequencies and mode shapes are discussed.

Table 1. Parameters characterizing the systems of rings with foundation

No. of object	d_z [m]	d_w [m]	h [m]	ρ [kg/m ³]	R [m]	d_I [m]	l_r [m]	l_w [m]	E [Pa]	ν
1	0.191	0.159	0.016	$7.85 \cdot 10^3$	0.0875	0.02	0.008	0.002	$2.1 \cdot 10^{11}$	0.28
2	0.203	0.147	0.028	$7.85 \cdot 10^3$						

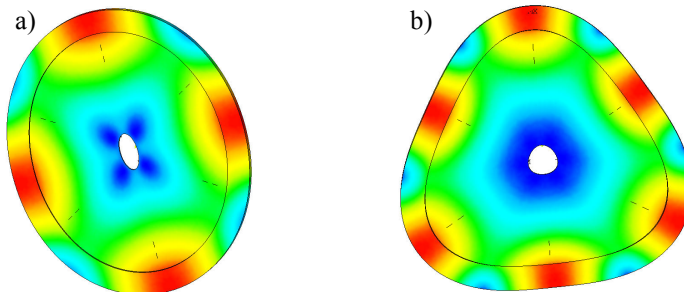
Table 1 displays the parameters characterizing the objects under investigation. In this table, h is the depth of the ring; ν is the Poisson ratio and the rest of geometrical dimensions are defined as shown in Figure 2. At first the computations are conducted to evaluate the ring substitute mass density ρ_z of the FE models related to the corresponding

objects. Satisfactory results are obtained for the following values of ρ_z . So, for the FE model related to the first object $\rho_z = 9.8 \cdot 10^3$ [kg/m³] and for the FE model referred to the second object $\rho_z = 9.17 \cdot 10^3$ [kg/m³]. For both cases, the same values of ρ_z are included in the analytical solutions. Moreover the proper values of stiffness modulus k_f , k_p and k_s in the corresponding analytical models are selected during numerical simulations. The results of calculation of the natural frequencies are shown in Table 2.

Table 2. Results of computation related to the systems

No.	k_f [N/m ²]	n	k_p [N/m ²]	k_s [N/m]	2	3	4	5	6	7	8
natural frequencies of the considered models ω_n [Hz] (analytical solutions)											
1	$2.65 \cdot 10^9$	$6 \cdot 10^7$	$3.6 \cdot 10^7$		8747	12939	17243	21582	25944	30328	34734
2	$1.2 \cdot 10^9$	$6 \cdot 10^7$	$8.85 \cdot 10^7$		7065	12189	17158	22033	26865	31682	36500
natural frequencies of the considered models ω_n [Hz] (FE solutions)											
1	—	—	—		8903	13296	16796	20277	23931	27806	31898
2	—	—	—		7363.4	11786	15980	20439	25142	30012	34982

In the Figure 3 two mode shapes comes from the FE model of the first object are displayed.

Figure 3. Mode shapes related to the following frequencies:(a) ω_2 , (b) ω_3 (FE solution)

5. Experimental verification

In this section the results related to the experimental verification of the considered analytical and numerical models are discussed. LMS measurement environment is used in the experimental investigation. The measuring set consisted of the PCB model 086C03 type modal hammer equipped with a gauging point made of steel, accelerometer PCB model 353B18, LMS SCADA data acquisition system, and SCM-V4E type measuring module supported by LMS Test.Lab software. The experimental investigation is conducted to identify natural frequencies and corresponding mode shapes related to the in-plane flexural vibration of the considered objects. As mentioned earlier, for the measurement experiment, two objects with the geometry shown in Figure 2 and Table 1 are made. The values of the excited natural frequencies are shown in Table 3. These values

are compared with the values of natural frequencies from the FE and analytical models, respectively. In the same Table the values of the frequency error related to the discussed models are presented. Achieved results are satisfactory albeit, the best fit is obtained for the analytical model related to the first object.

Table 3. Results of verifications of the systems

n No. of models	2	3	4	5	6	7	8
natural frequencies of the considered objects ω_n [Hz] (experimental data)							
1	8660	12943.8	16802.5	20618.1	25211.9	29550.6	34155.6
2	7207.5	11537.5	16058.8	20933.8	26278.8	31647.5	37106.3
frequency error ε_n [%] (comparison of the analytical solutions with the experimental data)							
1	1.01	-0.04	2.62	4.68	2.9	2.63	1.69
2	-1.98	5.65	6.84	5.25	2.23	0.11	-1.63
frequency error ε_n [%] (comparison of the FE solutions with the experimental data)							
1	2.81	2.72	-0.04	-1.65	-5.08	-5.9	-6.61
2	2.16	2.15	-0.49	-2.36	-4.33	-5.17	-5.73

6. Conclusions

Based on the classical theory of vibrating rings, a comprehensive study of the free in-plane flexural vibration analysis of thick rings with wheel–plate as a three–parameter Winkler elastic foundation is investigated. The separation of variables method is applied to solve the eigenvalue problem. Obtained analytical solutions are compared with the corresponding FE solution results. Presented in the paper theoretical and numerical investigation, are verified successfully during experimental studies.

References

1. S. Noga, R. Bogacz, *Free vibration of the Timoshenko beam interacting with the Winkler foundation*, Symulacja w Badaniach i Rozwoju, **2** (2011) 209-223.
2. S. Noga, R. Bogacz, T. Markowski, *Vibration analysis of wheels composed of a ring and wheel–plate modeled as the three–parameters elastic foundation*, during reviews in J. Sound Vib., (2014).
3. S. Noga, T. Markowski, R. Bogacz, *Natural frequencies of flexural vibration of a ring with wheel–plate as the Winkler elastic foundation*, Symulacja w Badaniach i Rozwoju, **3** (2012) 39-46.
4. S. Noga, T. Markowski, *In plane flexural vibration of a ring interacting with the Winkler foundation*, Vibration in Physical System, vol. XXV (2012) 305-310.
5. S. Rao, *Vibration of Continuous Systems*, Wiley, Hoboken, 2007.
6. X. Wu, R. Parker, *Vibration of rings on a general elastic foundation*, J. Sound Vib., **295** (2006) 194-213.

Modal Analysis of Viscous Flow and Reduced Order Models

Michał NOWAK

*Poznan University of Technology, Division of Virtual Engineering
ul. Piotrowo 3, Poznań, Poland
michal.nowak@put.poznan.pl*

Witold STANKIEWICZ

*Poznan University of Technology, Division of Virtual Engineering
ul. Piotrowo 3, Poznań, Poland
witold.stankiewicz@put.poznan.pl*

Marek MORZYŃSKI

*Poznan University of Technology, Division of Virtual Engineering
ul. Piotrowo 3, Poznań, Poland
marek.morzynski@put.poznan.pl*

Abstract

Phenomena occurring in the flows are very complex. Their interpretation, as well as an effective impact on them in the flow control is often only possible with the use of modal analysis and low-dimensional models. In this paper, the selected modal decomposition techniques, namely Proper Orthogonal Decomposition (POD), Dynamic Mode Decomposition (DMD) and global stability analysis, are briefly introduced. The design of Reduced Order models basing on Galerkin projection is presented on the example of the flow past a bluff body. Finally, the issues of widening of the application of the models are addressed.

Keywords: Reduced Order Models, ROM, Galerkin method, modal analysis, POD, DMD, stability

1. Introduction

The progress in the aerospace and automotive industry is possible by improvement of newly-designed vehicles. The reduction of aerodynamic drag, generated noise and exhaust fumes emission, as well as the increase of lift and the growth of performance might be achieved by the change in the flow phenomena, that might be obtained by the means of flow control. Such control is expected to be the most effective when the operation of the actuators is in accordance with the state/phase of the flow, measured by the sensors and processed by the controller with proper model of the flow.

The high-fidelity solution based on Navier-Stokes, LES/DES, RANS or even Euler equations, is very time-consuming. Real-life problems consisting of millions of degrees of freedom are possible to be solved only on parallel machines like computer clusters. Due to the high computational complexity of the high-fidelity flow models, an essential element of the closed-loop controller is low dimensional model of the flow. Such a model strongly depends on the proper choice of modal basis used in the approximation and projection stages.

In this paper, a short overview of the methods of modal analysis of viscous flows, described by incompressible Navier-Stokes equations (1) is presented, and a design of Reduced Order Models of the flow basing on the modal decomposition is described.

$$\dot{V} + \nabla(V \otimes V) + \nabla P - \frac{1}{Re} \Delta V = 0 \quad (1)$$

Finally, the methods of the design of broadband Galerkin models, capable to cover wide range of operating and boundary conditions, are briefly discussed.

2. Modal decomposition techniques

The most popular method of modal analysis is Proper Orthogonal Decomposition (POD) [1,2]. In this method, the M flow vectors (snapshots), resulting from experiment or numerical analysis, are centred using time-averaged solution U_0 :

$$V'_i = V_i - U_0, \quad \text{where} \quad U_0 = \frac{1}{M} \sum_{i=1}^M V_i \quad (2)$$

Next, the auto-correlation matrix for the matrix containing fluctuation vectors is calculated:

$$C = \frac{1}{M} SS^T, \quad \text{where} \quad S = [V'_1, V'_2, \dots, V'_M] \quad (3)$$

The eigenvectors of the auto-correlation matrix (POD modes, fig. 1), related to the eigenvalues of the largest module, might be used in Reduced Order Modelling of the flow.

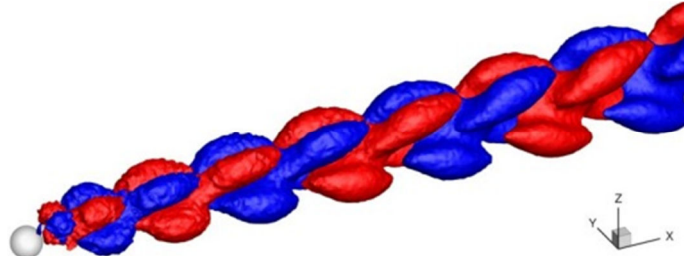


Figure 1. The most dominant POD mode for a flow past a sphere. Iso-surfaces of transverse velocity V_y are depicted

Another, physical mode basis results from global, linear stability analysis of the flow [3,4]. The decomposition of the instantaneous flow field onto base (steady or time-averaged) solution \bar{V} and small, oscillatory disturbance:

$$V' = \tilde{V} e^{-\lambda t} \quad (4)$$

and the linearization of the resulting equation leads to the generalized eigenvalue problem:

$$\lambda \tilde{V} + \nabla(\tilde{V} \otimes \bar{V}) + \nabla(\bar{V} \otimes \tilde{V}) + \nabla \tilde{P} - \frac{1}{Re} \Delta \tilde{V} = 0 \quad (5)$$

Complex eigenvectors of such problem (global stability eigenmodes, Fig. 2) represent the behaviour of the dynamical system close to fixed point, describing, for example,

the transition between symmetrical wake and von Karman street of vortices in the case of bluff body wakes.

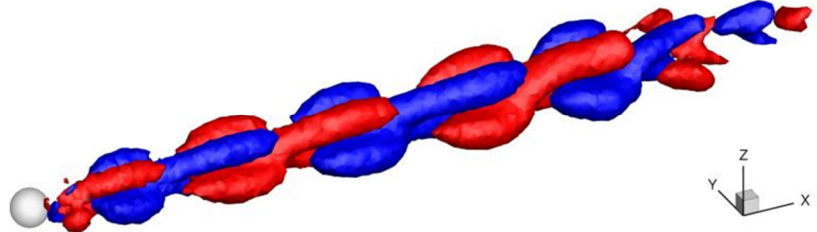


Figure 2. Real part of the most dominant eigenmode for a flow past a sphere. Iso-surfaces of transverse velocity V_y are depicted

The two aforementioned methods for modal basis design have very important drawbacks. For example, as will be discussed in further section of this paper, POD modes represent very narrow range of the conditions of the flow. Additionally, there might be problems to obtain correct modes outside the limit cycle, when the oscillation is amplified or suppressed. On the other hand, eigenmodes of global stability analysis are very difficult to obtain, particularly for 3D flows.

To overcome these problems, the idea of Dynamic Mode Decomposition [5,6] has been proposed. In DMD, it is assumed that any instantaneous solution might be obtained from a linear combination of previous solutions:

$$q(t + \Delta t) \approx e^{\Delta t A} q(t) \quad (6)$$

The product of previous state vectors and a linear operator $\tilde{A} \approx e^{\Delta t A}$ might be approximated using the product:

$$\tilde{A} V_{0..n} \approx V_{0..n} S, \quad (7)$$

where $V_{0..n}$ is the sequence of known solutions and S is the companion matrix as defined below:

$$S = \begin{pmatrix} 0 & 0 & \dots & 0 & c_0 \\ 1 & 0 & \dots & 0 & c_1 \\ 0 & 1 & \dots & 0 & c_2 \\ \dots & \dots & \dots & \dots & \dots \\ 0 & 0 & \dots & 1 & c_n \end{pmatrix} \quad (8)$$

The coefficients $c_0..c_n$ are obtained from the solution of the over-determined system of equations (1). The eigenvectors of matrix S are used to obtain the DMD modes (Fig. 3), while the eigenvalues determine modal growth ratios (real part) and frequencies (imaginary parts).

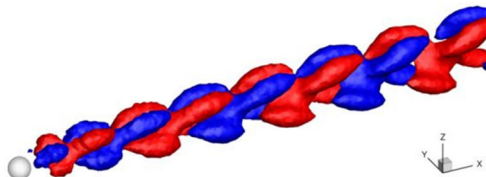


Figure 3. Real part of the most dominant DMD mode for a flow past a sphere.
Iso-surfaces of transverse velocity V_y are depicted

3. Reduced Order Models

Reduction of dimension of the flow model is based on the assumption that the velocity field might be decomposed onto the sum of the base flow U_0 and n products of spatial modes U_j and temporal coefficients a_j (9):

$$V(t_i) \approx U_0 + \sum_{j=1}^n a_j(t_i) U_j = V^{[n]}(t_i) \quad (9)$$

Such decomposition leads to approximated governing equation. Truncation of mode basis to a limited (preferably small) number of modes results in the residuum:

$$\dot{V}^{[n]} + \nabla(V^{[n]} \otimes V^{[n]}) + \nabla P^{[n]} - \frac{1}{Re} \Delta V^{[n]} = R^{[n]} \quad (10)$$

Projection of the residuum onto the space spanned by the modes, called Galerkin projection [7], is equivalent in Hilbert space to the zeroing of the integrals of the products of modes and the residuum:

$$\left(U_i, R^{[n]} \right)_\Omega = \int_\Omega U_i R^{[n]} d\Omega = 0 \quad (11)$$

The result of this projection is a system of ODEs, called Galerkin system:

$$\dot{a}_i = \frac{1}{Re} \sum_{j=0}^N l_{ij} a_j + \sum_{j=0}^N \sum_{k=0}^N q_{ijk} a_j a_k, \quad (12)$$

where linear and quadratic terms are derived as follows:

$$l_{ij} = \left(U_i, \Delta U_j \right)_\Omega \quad \text{and} \quad q_{ijk} = - \left(U_i, \nabla \cdot (U_j \otimes U_k) \right)_\Omega. \quad (13)$$

The proper choice of mode basis makes the resulting model comparable to the high-fidelity data from Direct Numerical Simulation (DNS) of Navier-Stokes equations.

4. Enhanced Galerkin models

Reduction of fluid model by projection of governing equations onto orthonormal mode basis (Galerkin Projection) results in approximate flow solution. Truncation of mode basis, as well as differences between low-dimensional model formulation and high-dimensional data used in mode expansion (like the neglection of pressure term, assumption of incompressibility, etc.), result in the deterioration of model quality.

To improve the quality of the Reduced Order Models of fluid flow, corrections to the linear and quadratic terms might be added, as computed in Genetic Algorithm-based calibration [8]:

$$\dot{a}_i = \frac{1}{\text{Re}} \sum_{j=0}^N (l_{ij} + l_{ij}^+) a_j + \sum_{j=0}^N \sum_{k=0}^N (q_{ijk} + q_{ijk}^+) a_j a_k \quad (14)$$

Mode basis used in Galerkin expansion allows reconstruction of the flow for a given set boundary and operating conditions. In the case of changing flow conditions, used mode basis has to be adjusted, for example using hybrid models [7] designed with the basis consisting of both empirical and physical modes, or mode parameterization, for example with some kind of look-up table [9] or Double-POD [10] approach. Another choice is Continuous Mode Interpolation [11], where the mode bases for two or more operating/boundary conditions are interpolated by referring to the Fredholm eigen-problem in space domain:

$$\int_{\Omega} A(x, y) U_i(y) dy = \lambda U_i(x), \quad (15)$$

with autocorrelation function (kernel) A :

$$A^{\kappa}(x, y) = U_1^{\kappa}(x) \otimes U_1^{\kappa}(y) + U_2^{\kappa}(x) \otimes U_2^{\kappa}(y) \quad (16)$$

In the case of interpolation between two states, the Fredholm kernel is linearly interpolated in $\kappa \in [0;1]$:

$$A^{\kappa} = A^0 + \kappa(A^1 - A^0) \quad (17)$$

The approach presented above allows smooth and continuous interpolation between corresponding structures (modes) for different operating conditions, enabling e.g. the modelling of the transition from fixed point dynamics to limit-cycle oscillations (Fig. 4).

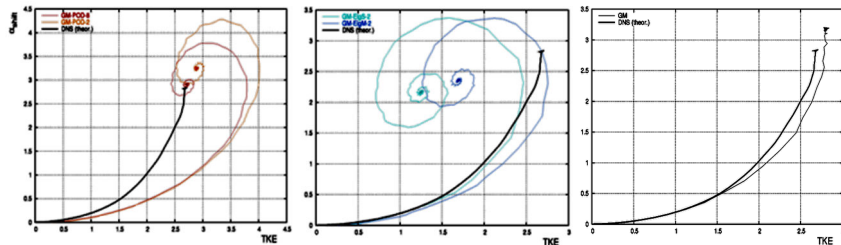


Figure 4. Phase portraits of Galerkin models, compared to reference data (thick black line): empirical POD-based (left), stability-based models (center) and the model using Continuous Mode Interpolation (right) for a flow past a NACA-0012 airfoil [12]

5. Conclusions

Modal analysis of the flow and its Reduced Order Models are key enablers for feedback flow control. In this paper basic issues related to the model order reduction and Galerkin

projection are presented and the most popular methods for obtaining the mode basis, such as POD, global stability analysis and DMD, are described. Modelling of the flow in changing boundary and operating conditions is possible with the use of parameterization methods such as Continuous Mode Interpolation.

Acknowledgments

This work has been funded by National Centre of Science under research grant no. DEC-2011/01/B/ST8/07264.

References

1. P. Holmes, J. Lumley, G. Berkooz, *Turbulence, Coherent Structures, Dynamical Systems and Symmetry*, Cambridge University Press, Cambridge, 1998.
2. L. Sirovich, *Turbulence and the dynamics of coherent structures*. Quart. Appl. Math., **45** (1987), 561–590.
3. M. Morzyński, K. Afanasiev, F. Thiele, *Solution of the eigenvalue problems resulting from global non-parallel flow stability analysis*, Comput. Meth. Appl. Mech. Engrng., **169** (1999), 161-176.
4. W. Stankiewicz, M. Morzyński, B.R. Noack, F. Thiele, *Stability Properties Of 2D Flow Around Ahmed Body*, Math. Model. Analysis (2005), 129-134.
5. P.J. Schmid, J. Sesterhenn, *Dynamic Mode Decomposition of Numerical and Experimental Data*, J. Fluid Mech., **656** (1) (2010), 5-28.
6. O. Frederich, D.M. Luchtenburg, *Modal analysis of complex turbulent flow*, 7th International Symposium on Turbulence and Shear Flow Phenomena (2011).
7. B.R. Noack, K. Afanasiev, M. Morzyński, G. Tadmor, F. Thiele, *A hierarchy of low-dimensional models for the transient and post-transient cylinder wake*, J. Fluid Mech., **497** (2003), 335-363.
8. W. Stankiewicz, R. Roszak, M. Morzyński, *Genetic Algorithm-based Calibration of Reduced Order Galerkin Models*, Math. Model. Anal., **16** (2) (2011), 233 – 247.
9. O. Lehmann, M. Luchtenburg, B. Noack, R. King, M. Morzyński, G. Tadmor, *Wake stabilization using POD Galerkin models with interpolated modes*, 44th IEEE Conference on Decision and Control and European Control Conference ECC 2005, Seville, Spain, 12.-15.12.2005, 500–505.
10. S. Siegel, J. Seidel, C. Fagley, D.M. Luchtenburg, K. Cohen, T. McLaughlin, *Low-dimensional modelling of a transient cylinder wake using double proper orthogonal decomposition*, J. Fluid Mech., **610** (1) (2008), 1-42.
11. M. Morzyński, W. Stankiewicz, B. Noack, F. Thiele, G. Tadmor, *Generalized mean-field model with continuous mode interpolation for flow control*, 3rd AIAA Flow Control Conference, San Francisco, 5-8.06.2006, AIAA-Paper 2006-3488.
12. W. Stankiewicz, M. Morzyński, B.R. Noack, G. Tadmor, *Reduced Order Galerkin Models of Flow around NACA-0012 Airfoil*, Math. Model. Analysis, **13** (1) (2008), 113-122

On-board vibration diagnostics of shaft damage of the aviation engine

Oleksii PAVLOVSKYI

National Technical University of Ukraine "Kiev Polytechnic Institute"

37 Peremogy Pr., Kyiv, Ukraine

a_pav@ukr.net

Nadiia BOURAOU

National Technical University of Ukraine "Kiev Polytechnic Institute"

37 Peremogy Pr., Kyiv, Ukraine

bureau@pson.ntu-kpi.kiev.ua

Abstract

This work is devoted to the further researches and development a new on-board multilevel vibration control system of aviation gas-turbine engines (GTE). We propose to introduce new diagnosis level (subsystem) into development multilevel vibration control system for detection of the initial crack-like damage of rotor shaft. The proposed subsystem works at the non-steady-state modes of GTE, for example during startup at the acceleration to operating speed. The basis of this approach is the fact of the occurrence of sub harmonic resonances of accelerating cracked shaft response. It is necessary to extract the main rotor harmonic vibration at the non-steady-state mode for crack diagnosis in practice. The narrow-band digital tracking filter is carried out for this aim, the central frequency of pass band is changing according the rotor rotation frequency. The efficiency of the proposed subsystem is demonstrated by the results of computer simulation.

Keywords: gas-turbine engine, cracked shaft, vibration diagnosis, digital tracking narrow-band filter.

1. Introduction

Available on-board vibration control systems of aviation gas-turbine engines (GTE) are destined for current control and awareness about actual levels of vibration at the harmonics of the rotor rotation. However, many initial defects of rotor elements (microcracks of shafts, blades, disks) cannot be detected at early stages of the crack development in this case. We proposed to expand the functional capabilities of the above mentioned systems by using the auxiliary level for diagnostics of initial crack-like damages of engine blades. The new multilevel vibration control system of aviation GTE has been presented in the previous work [1]. The developed system contains complementary dedicated microcontroller for analysis of the “normal vibration” in order to predict or detect small damages of engine blades. In addition, another diagnostic level can be carried out for diagnostics of dangerous damages rotor elements such as crack-like damages of rotor shaft.

The theoretical bases of the vibration method were presented in [2] for diagnosis of the cracks of rotating shafts during acceleration through resonance. The model of the transverse crack is a function of “breathing”, the changing of the rotor rigidity ΔK depends on cross location of crack section and stress-strain area of shaft. The accelerated rotation of the shaft with crack is investigated. It has been shown, the responses of

cracked shaft have sub-critical peaks (1/2 order and 1/3 order sub-harmonics resonance of the main harmonic of rotor rotation). For example, the absence and the presence of 1/2 order sub-critical peak are illustrated in Fig. 1 at the absence ($\Delta K=0$) and the presence of initial crack ($\Delta K=0,05$), accordingly. The time plots are represented in the relative scale on the ordinate axis (non-dimensional vibration amplitude z) and on the abscissa (non-dimensional time τ). Value $\tau=1000$ corresponds to transition through critical frequency of rotation.

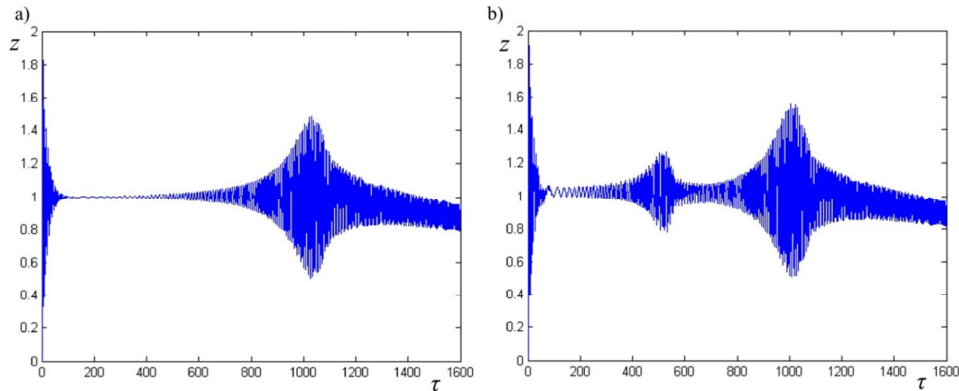


Figure 1. Vibration amplitude of accelerated rotor at the $\Delta K=0$ (a) and $\Delta K=0,05$ (b)

Researches have shown, that sensitivity of sub-critical peaks to crack presence many times over surpasses sensitivity of nature frequencies and shapes of oscillations. However it is necessary to estimate vibration levels on the rotor rotation harmonics at the essential changing of frequency of rotation for the usage of sub-critical peaks values as the features of crack-like damages of rotor shaft.

The purpose of this work is the development a new diagnostics subsystem of above mentioned multilevel vibration control system for diagnostics of crack-like damages of rotor shaft at the non-steady-state mode of GTE.

2. Subsystem development

The generalized block scheme of the developed diagnostics subsystem is shown in Fig. 2. Signals arrive from vibration sensors to the digital tracking narrow-band filter after preliminary processing and conversion. The central frequency f_0 of a pass-band of the filter is time-dependent and changes synchronously with change of frequency of rotation of a rotor shaft. Sensors of frequency of rotation are used for this purpose. Instantaneous value $\omega_r(t)$ of the frequency of main rotor harmonic is defined, then coefficients of the tracking narrow-band filter are calculated for the given value of mentioned frequency. Recalculation of coefficients is carried out for each new value of the central frequency of a pass-band of the filter which is equal to the calculated value of instantaneous frequency of shaft rotation. Peak values of vibration amplitudes are determined after a filtration in the field of sub-harmonic resonances. The received values are com-

pared with threshold and the decision is made on crack presence or absence of a shaft. The algorithm of the synthesis of digital tracking narrow-band filter and a filtration of a non-stationary vibrating signal is shown in Fig. 3.

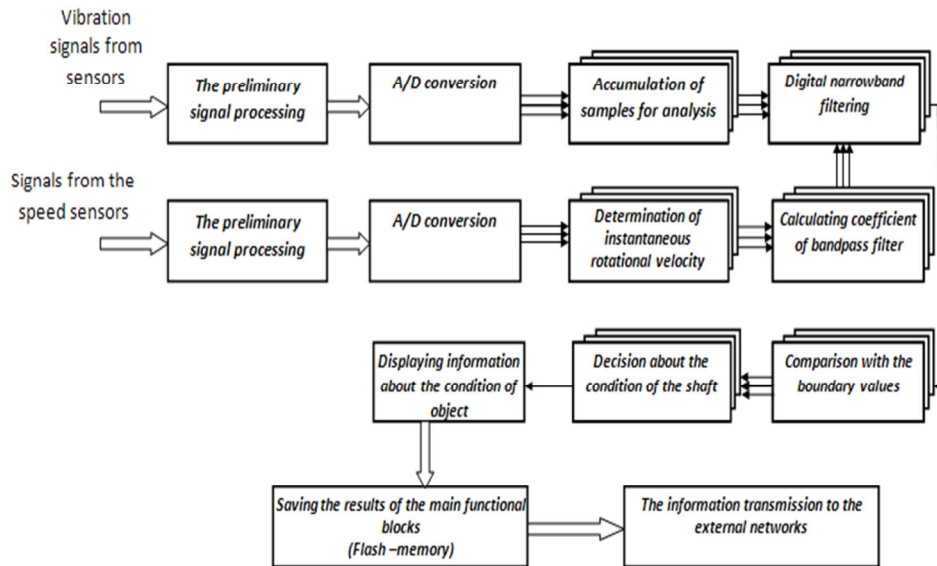


Figure 2. Generalized block scheme of the subsystem for diagnostics of crack-like damages of rotor shaft at the non-steady-state mode of GTE

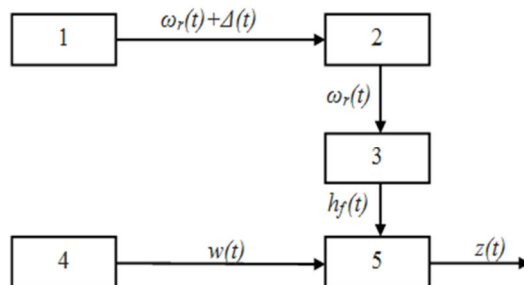


Figure 3. Algorithm of the synthesis of digital tracking narrow-band filter and the filtration of the non-stationary vibrating signal

The following symbols are indicated on Fig. 3: 1 - speed sensor; 2 - unit of determination of instantaneous rotation frequency; 3 - unit of calculating coefficient of digital filter; 4 - vibration sensor; 5 - filtration unit; $\Delta(t)$ - noise of measurement of the time-dependent rotation frequency; $h_f(t)$ - filter impulse response; $w(t)$ – input vibration signal; $z(t)$ - selected component of vibration.

Recalculation of coefficients of the digital tracking narrow-band filter is carried out at change of the central frequency of a pass-band according to change of frequency of rotor rotation. It is necessary to provide recalculation of coefficients with the period of definition of current frequency of rotor rotation in this case. As a rule, regular means of registration of parameters of the engine provide the period of registration 0,25 second at flight tests. Therefore, it is necessary to consider the restrictions connected with change of frequency rotation and the period of registration. We propose to use filters with the infinite pulse characteristic [3] and the least optimum order for a delay exception in calculations of filter coefficients. The Butterworth adaptive (tracking) filter is designed, minimal order is equal to 10 at the change of central frequency f_0 of a pass-band in the range of 10....100 Hz, the pass-band of filter is constant and it is equal $\Delta f_p=3$ Hz. The time of calculation of coefficients of the mentioned filter is equal to 0,122 second.

Computer simulation is carried out for the validation of efficiency of the designed filter. Vibration signals are simulated at the accelerated rotation of a shaft without damage ($\Delta K=0$) and with damage ($\Delta K=0,05; 0,1; 0,15; 0,2$) by using the mathematical model of rotary shaft, presented in [2]. Various corners of crack orientation relative to vector of vibration and various corners of unbalanced weight orientation relative to a middle line of a crack are considered. The mentioned vibration signals together with the white noise and high-frequency interferences are used as the input signals to the filtration unit (Fig. 3). Difference values Δz of amplitudes of signals after filtering at the presence ($\Delta K \neq 0$) and at the absence ($\Delta K=0$) shaft damages and their approximations are used for an estimation of quality of tracking filtration [4]. The non-dimension time set of values Δz and approximation are represented in Fig. 4.

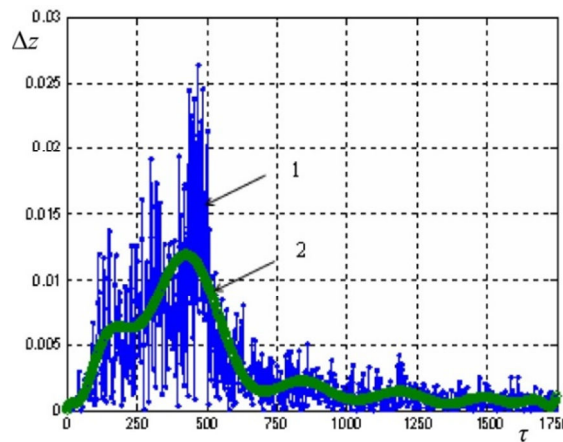


Figure 4. Set of difference values Δz (1) and approximation (2) of amplitudes of signals after filtering by using Butterworth adaptive (tracking) filter

Maxima of difference values Δz are located in a range of 1/2 order and 1/3 order sub-harmonics resonances of the main harmonic of rotor rotation. The presence of crack do not influence on resonance of main harmonic of rotor rotation, therefore difference val-

ues Δz are small. The presented results confirm the efficiency of the adaptive (tracking) filtering of non-steady vibration signals.

The subsystem for diagnostics of crack-like damages of rotor shaft at the non-steady-state mode of GTE is developed as virtual device by using LabVIEW (NI, USA). The front panel of virtual device is represented in Fig. 5.

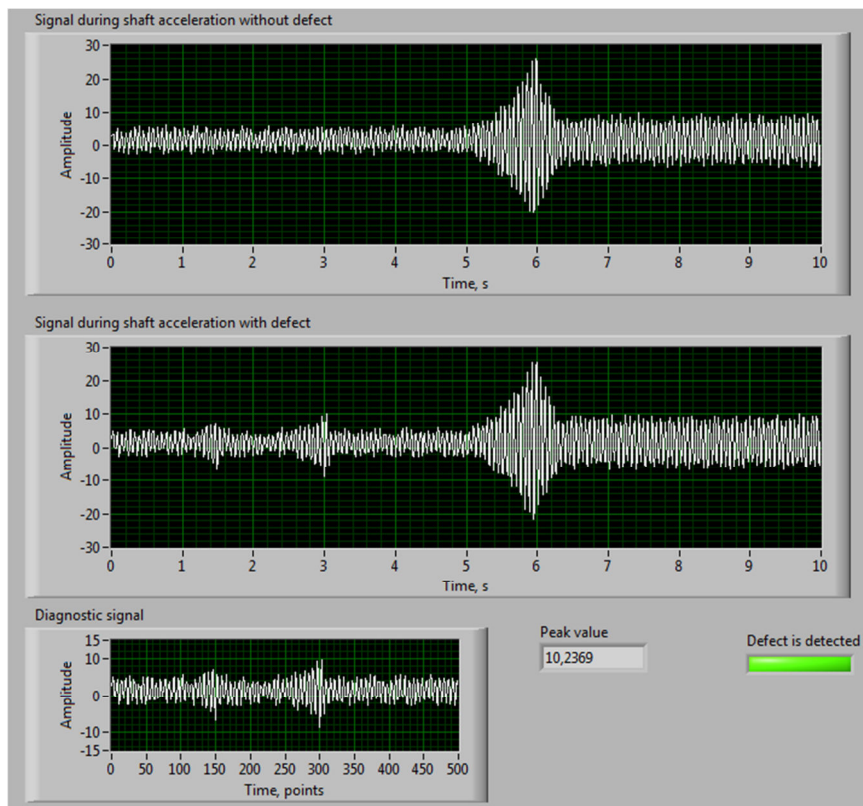


Figure 5. The front panel of virtual device - subsystem for diagnostics of crack-like damages of rotor shaft at the non-steady-state mode of GTE

The window “Diagnostic signal” contain the informative part of vibration signal to resonance of main harmonic of rotor rotation. Peak values z_p are estimated in this range and compared with the installed threshold (vibration amplitude is equal to 10 m/s). The alarm indicator “Defect is detected” lights up at excess of threshold value.

The carried out researches of virtual device have shown, that the increase of a crack parameter ΔK calls increase in peak values of vibration amplitude in the range of a sub-harmonic resonances at the same values of corners of crack orientation relative to vector of vibration and corners of unbalanced weight orientation relative to a middle line of a crack. The functional relation is similar to linear function (Fig. 6).

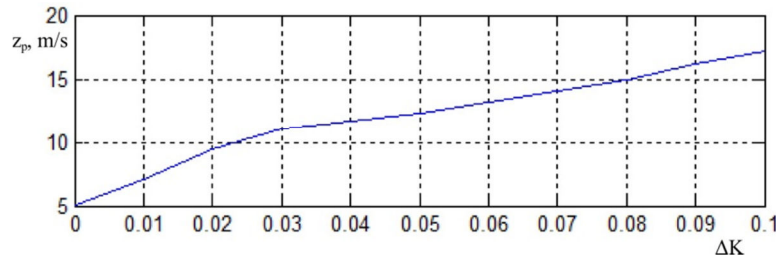


Figure 6. Relation between peak values of vibration amplitude and the crack parameter

3. Conclusions

The new diagnostics subsystem of multilevel vibration control system is developed for diagnostics of crack-like damages of rotor shaft at the non-steady-state mode of GTE.

The generalized block scheme of the subsystem is designed and principle of its operation is substantiated. The digital tracking narrow-band filter is designed in order to extract of vibration signal on the time-depended frequency of rotor rotation. The central frequency of a pass-band of filter is changing according to change of frequency of rotor rotation. Sub-critical peaks values (1/2 order and 1/3 order sub-harmonics resonances) of extracted vibration signal are used as the features of crack-like damages of rotor shaft. The diagnostics subsystem as a virtual device is developed and investigated.

The developed subsystem of multilevel vibration control system will allow to detect initial crack-like damages of rotor shaft and to ensure awareness of GTE.

References

1. O. Pavlovskyi, N. Bouraou, L. Iatsko, *Multilevel vibration control system of aviation gas-turbine engines*, Vibrations in Physical Systems **25** (2012) 323-328.
2. J. Sawicki, X. Wu, G. Baaklini, A. Gyekenyesi, *Vibration-based crack diagnosis in rotating shafts during acceleration through resonance*, Proc. of SPIE, **5046** (2003)1-10.
3. A. Sergienko, *Digital signal processing*, Piter, Snt. Petersburg 2006.
4. N. Bouraou, O. Pavlovskyi, L.Iatsko, A.Ivanchenko, *Development and investigation of the digital tracking filters for the vibration control system of aviation engine at the non-steady-state modes*, Aerospace technique and technology, **10** (2013) 171-176.

Signals Representation on Energetic Plane Based on Teager-Kaiser Energy Operator

Stanisław RADKOWSKI

*Institute of Vehicles, Warsaw University of Technology
Street 84, 02-524 Warsaw, Poland
ras@simr.pw.edu.pl*

Adam GAŁEZIA

*Institute of Vehicles, Warsaw University of Technology
Street 84, 02-524 Warsaw, Poland
agalezia@simr.pw.edu.pl*

Abstract

Development of complicated machines and need for maintaining high efficiency and safety of their work is main reason for development of new and more reliable monitoring techniques. One of the main aims of condition monitoring is detection of early stage of failure and monitoring of its development [1]. Such techniques should be sensitive for change in diagnostic signal due to arise of failure.

Paper presents exemplary representations of signals types on energetic plane calculated using Teager-Kaiser energy operator (TKEO). First basic information on TKEO is presented. Next energetic plane is introduced and models of signals are showed. In final section of the paper example of model of signal containing disturbance related with meshing is presented. Teager-Kaiser energy operator, due to its properties, can be used for detection of transient events such as impulses resulting from disturbances of mating of teeth in gearboxes. Such a disturbance of mating is related with decrease of stiffness of given tooth due to crack or development of pitting [2]. Sensitivity of Teager-Kaiser energy operator allow for earlier detection of transient disturbances than use of raw data methods such as Hilbert transform demodulation.

Keywords: Teager-Kaiser energy operator, energetic plane, vibration signal, gearbox

1. Introduction

Constant development of machines, use of new, lighter materials, care for environment and socio-economical costs of machine failures are main reasons of making every effort to develop new and reliable techniques of determination of technical condition of machines and structures. Among these techniques one can list new techniques of signal processing [3, 4], application of sensors embedded in structure [5], use of different physical phenomena for detection of early stages of failures [6, 7]. Teager-Kaiser energy operator (TKEO) is signal processing technique which allow for calculation of energy waveform of diagnostic signal.

Change of technical condition of machine, or its component, due to arise and development of failure, is related with change of amplitude and frequency structure, or in general energetic structure, of vibration signal generated by working machine [1]. This change of technical state of machine is related with change of energy dissipated in form of noise, vibrations or heat [8]. Early detection of change of energy can allow determining early phase of failure and monitoring its development. This can lead to choose of optimal maintenance strategy and allow for measurable savings.

At present number of signal processing techniques are used for detection of symptoms of change of technical state. However still new techniques are developed and applied in task of condition monitoring. Such technique is Teager-Kaiser energy operator. One might find publications presenting successful application of TKEO in different tasks of condition monitoring, such as: bearing fault diagnosis [9, 10] or detection faults of gears [11].

2. Teager-Kaiser energy operator

Teager-Kaiser energy operator is non-linear operator which applied to time signal calculates measure which can be interpreted as energy of this signal [12]. Publications [13-16] contain description and analysis of properties of TKEO. For continuous signals this operator has following form:

$$\Psi(x(t)) = \dot{x}^2(t) - x(t)\ddot{x}(t) \quad (1)$$

However for implementation of TKEO in numeric environments following discrete version is most common:

$$\Psi_d(x_n) = x_n^2 - x_{n-1}x_{n+1} \quad (2)$$

In publication authors will constantly refer to discrete signals and energy operator of discrete signals so for simplicity $\Psi(x)$ will be used as denotation of result of TKEO acting on analyzed signal x and will be called measure of energy of signal.

Teager-Kaiser energy operator acting on time signal x calculates waveform of measure of energy of analyzed signal. As a result one obtains new signal $\Psi(x)$ which is also a function of time. Number of publications presents results of implementation of TKEO as useful tool for bearing [9, 10] and gearbox failure detection [11].

An important issue, one should remember using Teager-Kaiser energy operator, is that $\Psi(x)$ is not energy in classical meaning but its measure. As pointed out in [12] $\Psi(x)$ can have negative values and its result can differ depending on parameters of analyzed signal.

For discrete single harmonic signal $x_n = A\cos(\Omega n)$, Teager-Kaiser energy operator calculates result (3) which for low values of $\Omega = 2\pi f/f_s$ estimates product of square of amplitude multiplied by square of frequency.

$$\Psi(x) = A^2 \sin^2(\Omega) \approx A^2 \Omega^2 \quad (3)$$

This result depend both from amplitude and frequency structure of signal. Change of amplitude or frequency in signal will influence measure of energy of signal indicating change in monitored machine. Interesting property of Teager-Kaiser energy operator (2) is its sensitivity to sudden changes in analyzed signal due to transient disturbances such as impulses.

3. Energetic plane – examples of signals

Concept of energetic plane assumes observation of diagnostic signal represented in coordinates of measure of energy, expressed by equation 3, and velocity of change of measure of energy. Nomenclature of Lie brackets allows for calculation of higher order energetic operators as it is presented in [15]. From point of view of concept of energetic plane most interesting is energetic operator of order 3:

$$Y_3(x) = [x, x^{(2)}] = \dot{x}\ddot{x} - x\ddot{x} = d(\Psi(x))/dt \quad (4)$$

which can be treated as velocity of change of measure of energy of signal x .

To present representation of few types of signals on energetic plane following abscis models were created:

- single harmonic signal:

$$x(t) = A \cos(2\pi f t + \phi) \quad (5)$$

- signal with amplitude modulation

$$x_{AM}(t) = A * (1 + M * \cos(2\pi f_{AM} t)) * \cos(2\pi f t + \phi) \quad (6)$$

- signal with frequency modulation

$$x_{FM}(t) = A \cos(2\pi f t + m * \cos(2\pi f_{FM} t)) + \phi \quad (7)$$

- signal with amplitude and frequency modulation

$$x_{AMFM}(t) = x_{AM}(t) * \cos(2\pi f t + x_{FM}(t) + \phi) \quad (8)$$

where: A – amplitude of carrier signal, f – frequency of carrier signal, M – modulation depth, f_{AM} – frequency of amplitude modulation, m – modulation index, f_{FM} – frequency of frequency modulation, ϕ – initial phase.

Figures 1 to 4 present representation of mentioned above signals on energetic plane. All presented have same parameters of carrier signal, i.e. amplitude A , frequency f , phase ϕ , and differ only with values of modulation depth and index. As one may see, for single harmonic signal representation on energetic plane is constant and has form of a point. It is due to unchangeable amplitude and frequency of signal. Change of amplitude or frequency value would cause shifting of point along energy axis. Appearance of amplitude or frequency modulation change signal's representation significantly. Increase of modulation depth M or index m causes increase of size of curve being representation of the signal. It is worth to point out that however size of curve changes its general character is similar for given type of modulation: in case of AM – elliptic-like curve, in case of FM – curve creates characteristic loops. Occurrence of amplitude and frequency modulation creates complicated shape. This representation will depend most importantly from values of modulation parameters (M, f_{AM}, m, f_{FM}). However, also in this case, it can be seen that increase of parameters M and m will result in increase of size and centre of gravity of curve. Change of modulation frequencies will also change location and size of signal's representation on energetic plane.

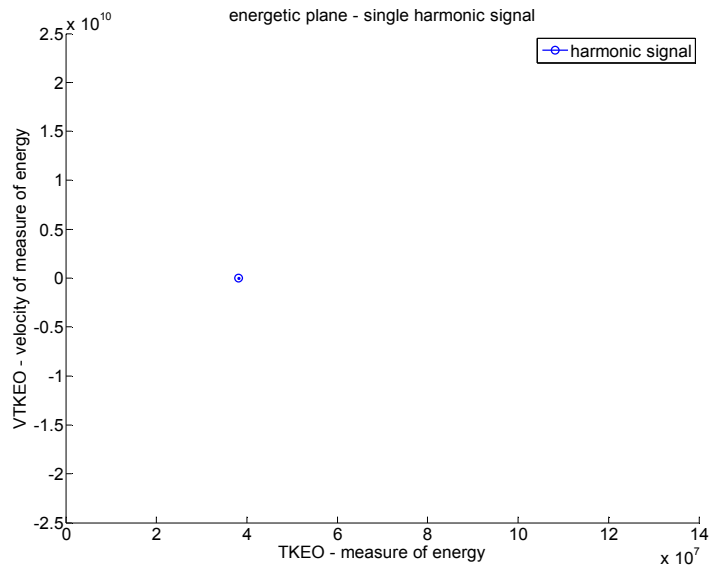


Figure 1. Single harmonic signal on energetic plane

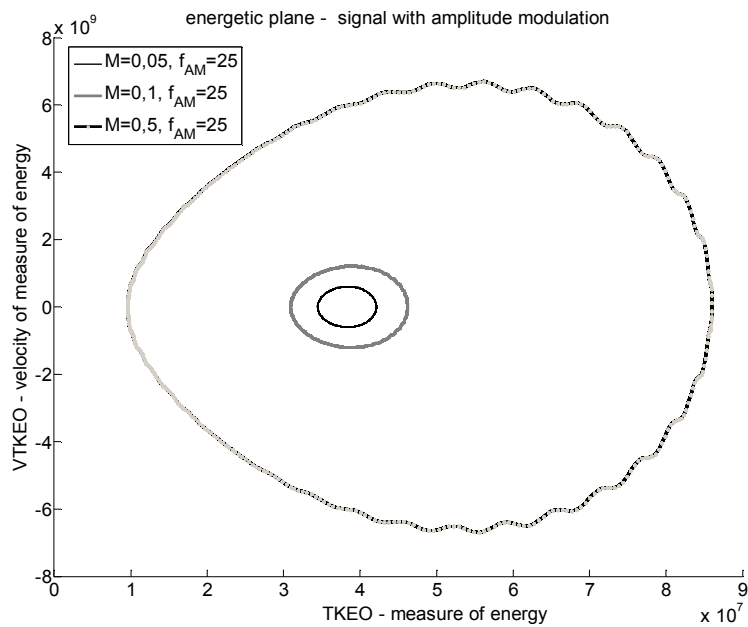


Figure 2. Signals with amplitude modulation with different depth of modulation on energetic plane

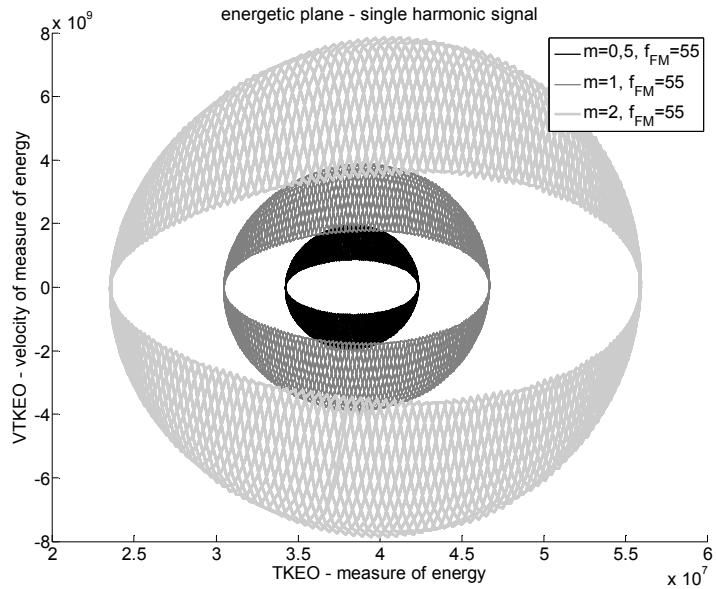


Figure 3. Signals with frequency modulation with different index of modulation on energetic plane

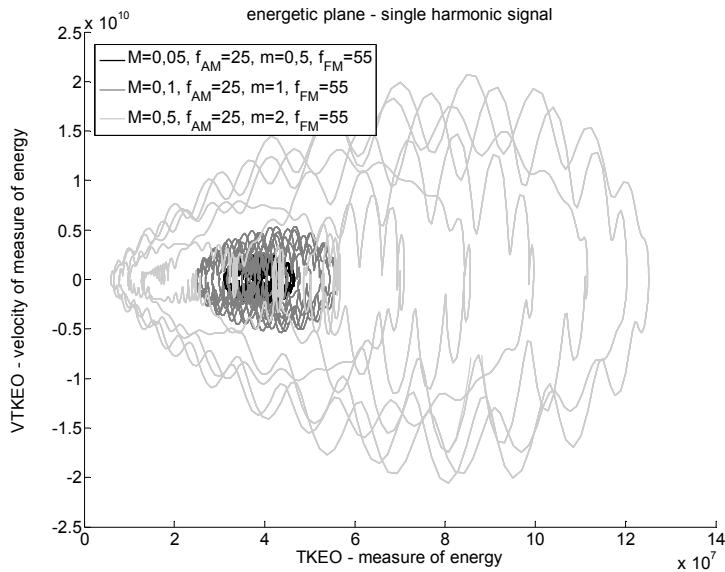


Figure 4. Signals with AM and FM modulation with different parameters of modulation on energetic plane

During operation of gearbox, progressing degradation process causes appearance of local disturbances in signal. This can be caused by coming in to contact of tooth with lower stiffness. Such disturbance can have form of transient change of depth of modulation [17, 2]. To analyze usability of energetic plane based on calculation of Teager-Kaiser energy operator for detection of transient events in signal, model was created allowing occurrence of transient disturbance of depth of amplitude modulation. The purpose of the model is to model local and transient change of meshing of tooth in gearbox. For purpose of test, AM signal was generated with bell-shape disturbance of depth of modulation M. Such shape of disturbance was chosen in order to perform change of parameter as smooth as possible. Duration of disturbance was chosen in such way it would correspond to time of mesh of pair of teeth. Parameters of signal were constant except modulation depth which for one tooth increased 20% from its nominal value. Figure 5 presents comparison of representation of signal with and without disturbance. Change is easily observable.

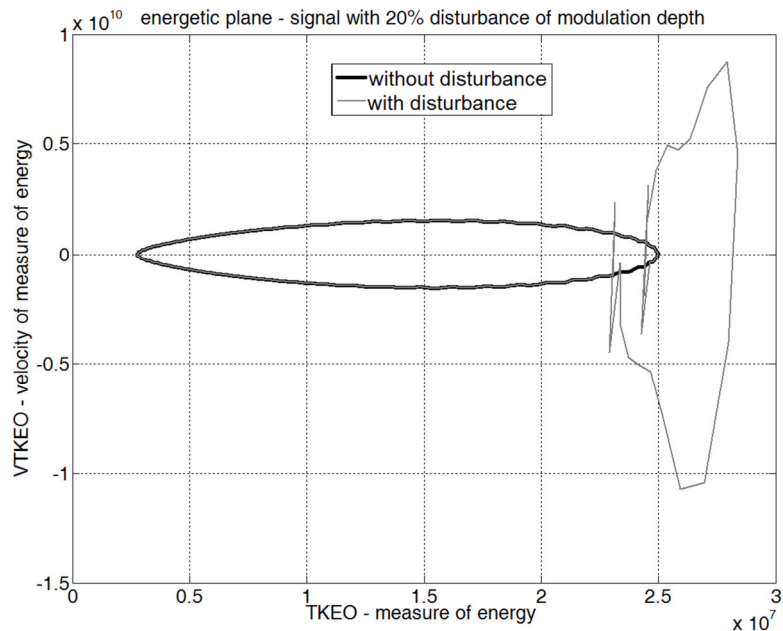


Figure 5. Signal with and without distribution of depth of AM, disturbance 20%

Change of size of signal representation due to disturbance of modulation parameter might be used as a diagnostic information testifying about change in meshing of gearbox. During modelling process other values of disturbance were also tested to analyse sensitivity of energetic plane to size of disturbance. According to observations it can be concluded that lowest realistic value of change of modulation depth which can be detected is between 2 and 5% of its nominal value.

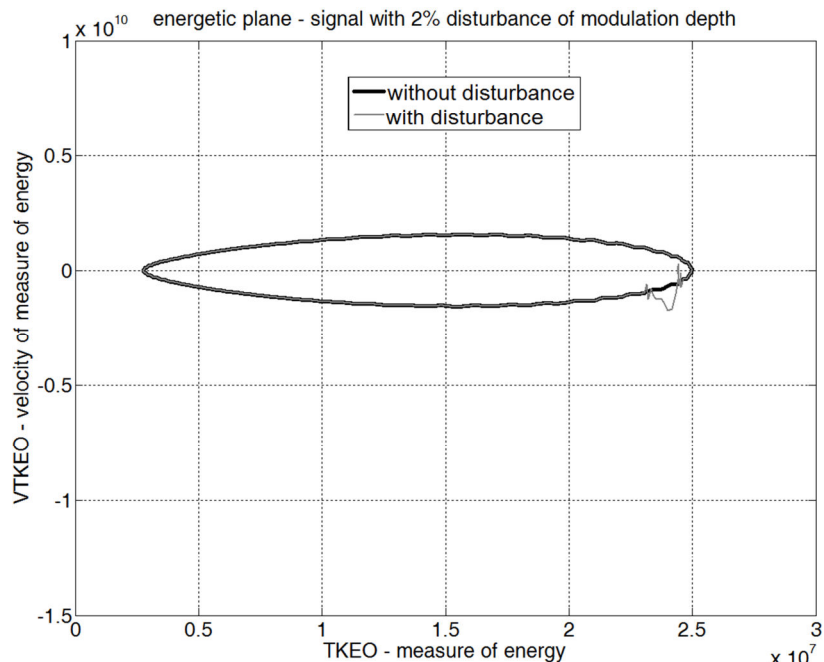


Figure 5. Signal with and without distribution of depth of AM, disturbance 2%

4. Conclusions

Paper presented concept of energetic plane which presents representation of signal in coordinates of measure of energy and value of velocity of change of measure of energy calculated using Teager-Kaiser energy operator. On this plane, given types of signals have similar representations which size depends from modulation parameters. Presented results shows usability of energetic plane in detection of transient events and disturbances of modulation parameters. Further research will be carried out in order to analyse usability of energetic plane in condition monitoring based on vibration signals from real gearbox.

References

1. S. Radkowski, *Diagnostyka wibroakustyczna uszkodzeń niskoenergetycznych*, ITE, Radom 2002.
2. J. Maćzak, *Local meshing plane analysis as a source of information about the gear quality*, Mech. Syst. Signal Process. (2012). <http://dx.doi.org/10.1016/j.ymssp.2012.09.012>
3. J. Dybała, *Vibrodiagnostics of gearboxes using NBV-based classifier: A pattern recognition approach*, Mech. Syst. Signal Process. (2012). <http://dx.doi.org/10.1016/j.ymssp.2012.08.021>

4. S. Delvecchio, *On the Use of Wavelet Transform for Practical Condition Monitoring Issues*, (Baleanu D. (Ed.), Advances in Wavelet Theory and Their Applications in Engineering. Physics and Technology, InTech), (2012). DOI: 10.5772/35964
5. A. Orlowska, P. Kolakowski, J. Holnicki-Szulc, *Detecting delamination zones in composites by embedded electrical grid and thermographic methods*, Smart Materials and Structures, vol. **20**, no. 10. (2011), DOI: 10.1088/0964-1726/20/10/105009
6. S. Gontarz, S. Radkowski, *Impact of different factors on relationship between stress and eigenmagnetic field in steel specimen*. IEEE Transactions on Magnetics Vol. **B**, no. **3** (2012), pp. 1143-1154. DOI: 10.1109/TMAG.2011.2170845
7. S. Radkowski, R. Gumiński, *Impact of vibroacoustic diagnostics on certainty of reliability assessment*, Engineering Asset Lifecycle Management, Part 16, (2010), pp. 574-582. DOI: 10.1007/978-0-85729-320-6_66
8. C. Cempel, B. Żółtowski, *Inżynieria Diagnostyki Maszyn*, PTDT/ITE, 2004.
9. P. Henriquez, P. R. White, J. B. Alonso, M. A. Ferrer, C. M. Travieso, *Application of Teager-Kaiser Energy Operator to the Analysis of Degradation of a Helicopter Input Pinion Bearing*, available at: http://jean.fabri.perso.sfr.fr/sfm/papiers_surveillance/8_Henriquez.pdf (access: 2012-11-28).
10. H. Li, L. Fu, Y. Zhang, *Bearing Faults Diagnosis Based on Teager Energy Operator Demodulation Technique*, Measuring Technology and Mechatronics Automation, 2009. ICMTMA '09. International Conference on, Volume: 1, (2009) DOI:10.1109/ICMTMA.2009.421
11. H. Li, H. Zheng, L. Tang, *Gear Fault Detection Based on Teager-Huang Transform*, International Journal of Rotating Machinery, vol. 2010, (2010). doi:10.1155/2010/502064
12. J. F. Kaiser, *On a simple algorithm to calculate the 'energy' of a signal*, Proc IEEE ICASSP-90, Albuquerque, NM, April 1990, (1990), pp. 381-384.
13. J. F. Kaiser, *On Teager's Energy Algorithm and its generalization to continuous signals - a simple algorithm to calculate the 'energy' of a signal*, Proc IEEE Digital Signal Processing Workshop, New Paltz, NY, Septemer 1990, (1990).
14. P. Maragos P., J. F. Kaiser, T. F. Quatieri, *On amplitude and Frequency Demodulation Using Energy Operators*, IEEE Transactions on Signal Processing, vol. **41**, (1992), pp. 1532-1550.
15. P. Maragos, A. Potamianos, *Higher order differential energy operators*, IEEE Signal Processing Letters, Vol. **2**, Issue: **8**, (1995), pp. 152 – 154.
16. A. Gałęzia, *Averaged signal measures of TKEO energy waveform in detection of tooth break in gearbox*, Measurement Automation and Monitoring, vol. **60**, no **1/2014**, (2014) pp. 31 – 34.
17. J. Dybała, *Wykrywanie wczesnych faz uszkodzeń metodami sztucznej inteligencji*, Wydawnictwo Naukowe Instytutu Technologii Eksplotacji, Warszawa–Radom, 2008.

Extended Models of Sedimentation in Coastal Zone

Igor SELEZOV

*Dr. Prof. Department of Wave Processes, Institute of Hydromechanics NASU
Sheliabov Str. 8/4, Kiev, Ukraine; 03680
selezov@yandex.ru*

Abstract

Construction of a generalized hyperbolic model of sediment dynamics predicting a sediment evolution on the bottom surface with a finite velocity is presented. The transport equation is extended with introducing a generalized operator of flux change and a generalized operator of gradient. Passing to the convenient model is a singular degeneration of extended model. In this case the results are obtained in the class of generalization solutions. Some expressive examples of constructions of hyperbolic models predicting a finite velocity of disturbance propagation are presented. This problem is developed starting from Maxwell (1861). His approach in the theory of electromagnetism and the kinetic theory of gases is commented. A brief review on propagation of heat and diffusive waves is presented. The similar problems in the theory of probability and diffusion waves are considered. In particular, it was shown on the microscopic level for metals that the conservation law can be violated.

Keywords: sediment dynamics, hyperbolic equation, finite velocity, disturbance propagation

1. Introduction

The problem of sediment reformation under the effect of water waves is referred directly to ocean lithodynamics [1, 2]. Thus interconnected processes of hydro- and lithomass transport occur under the wave action. Mathematical modeling of such processes in the shoreline zone on the basis of the classical approach is presented in [3].

We consider the generalized hyperbolic model of sediment evolution which predicts a finite velocity of sediment transport [3] unlike the convenient model of parabolic type predicting an infinite velocity of propagation of small perturbations.

It is known that a real process of sediment transport occurs with a finite speed [4]. As it is shown in the natural observations, a velocity of transport of the energy and substance mass in the coastal zone is a finite magnitude. It can be noted that some investigations have been conducted for aggraded channels in [5] and for the channel degradation which fits to the observed degradation in [6].

The question, which is of great interest, is a comparison of possibilities and a physical content of “parabolic” and “hyperbolic” models of sediment dynamics in a coastal zone. A generalized hyperbolic model was firstly proposed in [7].

Some examples are presented in this paper but the problems of thermoelasticity are not considered.

2. Mathematical model

Wave motion of the inviscid incompressible fluid of the variable depth in the rectangular Cartesian co-ordinate system (x, y, z) is considered. A plane $z = 0$ coincides with the

undisturbed free surface and an axis Oz is directed upwards. The ground surface can be deformed and it is described by the equation

$$z = -H_d(x, y, t).$$

So the depth $H(x, y, z, t)$ varies in time due to the sediment transport. Hereinafter a plane problem is considered corresponding to frontal incoming waves.

The mathematical problem is formulated as follows: to determine the fluid depth $H(x, z, t)$ and the energy flux vector $\vec{Q} = \vec{Q}(x, z, t)$ in the area $\Omega = \Sigma \times T$, where $\Sigma \subset R^3$, $T = \{t | \in [0, t_1]\}$, as solutions of equations (1) and (2), which satisfy corresponding boundary and initial conditions.

The conservation law is written in the form

$$\frac{\partial H}{\partial t} + \vec{\nabla} \cdot \vec{Q} = 0. \quad (1)$$

The transport equation for the closure of the system, unlike the previous researches, is postulated in the generalized form [7]

$$L\vec{Q} = -\vec{M}H, \quad (2)$$

where the scalar operator L characterizes a flux change in time:

$$L \equiv \gamma_0 + \gamma_1 \partial_t + \gamma_3 \partial_{ttt} + \dots + \gamma_{2n+1} \underbrace{\partial \partial_{tt\dots t}}_{(2n+1) \text{ times}}, \quad (3)$$

with coefficients $\gamma_0, \gamma_1, \gamma_3, \dots$, and a vector operator \vec{M} is represented by the operator of gradient type:

$$\vec{M} \equiv \vec{k}_0 + k_1 \vec{\nabla} + k_3 \vec{\nabla} \nabla^2 + \dots + k_{2n+1} \vec{\nabla} \nabla^{2n} \quad (4)$$

with coefficients $\vec{k}_0, k_1, k_3, \dots$.

Keeping operators to a certain order generates a set of the generalized hyperbolic models [8].

In the case when all the terms in (3) are equal to zero except γ_1 , i.e. $\gamma_0 = 0, \gamma_1 \neq 0, \gamma_3 = 0, \dots, \gamma_{2n+1} = 0$, and all the terms in (4) are equal to zero except k_1 , i.e. $\vec{k}_0 = 0, k_1 \neq 0, k_3 = 0, \dots, k_{2n+1} = 0$ ($n = 1, 2, \dots$), we obtain the known parabolic model of sediment evolution. However if all the operators remain to a certain order s , in (3), (4), in that case we obtain a set of the generalized hyperbolic models [7].

For the case $n = 1$ from relations (3), (4) the elementary hyperbolic model can be derived in the form

$$\nabla^2 H - \frac{1}{c_1^2} \frac{\partial^2 H}{\partial t^2} - \frac{1}{k_1} \frac{\partial H}{\partial t} = 0, \quad (5)$$

where c_1 is the speed of propagation of disturbance, which is defined as $c_1 = \sqrt{k_1 / \eta}$, η is the relaxation parameter, k_1 is the kinematic viscosity.

In the classical case, when relaxation parameter η tends to zero, equation (5) is degenerates into (6) and for the depth $H(x, y, t)$ we obtain the equation of parabolic type

$$\nabla^2 H - \frac{1}{k_1} \frac{\partial H}{\partial t} = 0, \quad (6)$$

which satisfies the conservation law and is used in all traditional studies [3]. In what follows consider the case of frontal approach waves (plane problem).

3. Singular degeneration

Statement of the initial boundary value (IBV) problem for the equation (5) has the form

$$\varepsilon H_{tt} + H_t = k_1 H_{xx}, \quad (7)$$

$$H|_{t=0} = u_0(x), \quad H_t|_{t=0} = H_1(x), \quad H|_{x=0} = H|_{x=1} = 0, \quad (8)$$

where ε is the small parameter, $\varepsilon = \eta$.

We investigate the singular degeneracy problem (7), (8) with $\varepsilon \rightarrow 0$. Called a generalized solution of problem (7), (8) the function H из $W_{20}^{11}(Q_T)$ of satisfying to integral identity

$$\begin{aligned} & -\varepsilon \int_0^T (H_t, \Phi_t)_\Omega dt + k_1 \int_0^T (H_x, \Phi_x)_\Omega dt + \\ & + \int_0^T (H_t, \Phi)_\Omega dt + \varepsilon \int_0^T (H_1(x), \Phi(0))_\Omega dt = 0, \\ & \forall \Phi \in W_2^{1,1}(Q_T), \quad \Phi(T) = 0, \quad (H, \Phi)_\Omega = \int_\Omega H \Phi dx, \end{aligned} \quad (9)$$

where $\Omega = (0, 1)$, $Q_T = [0, T] \times \Omega$.

For the generalized solution of the problem (7), (8) the theorem is true: if $H_1(x) \in L_2(\Omega)$, $u_0(x) \in W_2^1(\Omega)$, then for the problem (7), (8) there exists a unique generalized solution. The proof of solvability is given in [9].

Passing in (7) to the limit at $\varepsilon \rightarrow 0$, we can obtain the identity that is a solution of the problem

$$\begin{aligned} & H_t = k_1 H_{xx}, \\ & H|_{t=0} = u_0(x), \quad H|_{x=0} = H|_{x=1} = 0. \end{aligned} \quad (10)$$

Thus, we arrive to the following theorem: a Generalized solution of the problem (7), (8) passes at $\varepsilon \rightarrow 0$ to the generalized solution of the problem (6).

4. Some examples

A finite propagation velocity of electromagnetic waves. A development of the generalized models originates from the works of Maxwell. He was the first who realized the

FV-principle (the principle of the propagation velocity finiteness of perturbation) at the development of the electromagnetic field model (1861-1864), and then he has generalized this principle to the theory of gases [10].

We consider Maxwell's equations for the nonconducting homogeneous isotropic medium. Before the Maxwell work the following system of equations described a perturbation propagation with the infinite velocity

$$\begin{aligned}\vec{\nabla} \times \vec{H} &= \boxed{0}, \quad \vec{\nabla} \times \vec{E} = -\frac{\partial \vec{B}}{\partial t}, \\ \vec{\nabla} \times \vec{B} &= 0, \quad \vec{\nabla} \times \vec{D} = 0, \\ \vec{B} &= \mu \vec{H}, \quad \vec{D} = \varepsilon \vec{E}.\end{aligned}\tag{11}$$

After the Maxwell work the system of equations describes a perturbation propagation with the finite velocity, which equals to the speed of light

$$\begin{aligned}\vec{\nabla} \times \vec{H} &= \boxed{\frac{\partial \vec{D}}{\partial t}}, \quad \vec{\nabla} \times \vec{E} = -\frac{\partial \vec{B}}{\partial t}, \\ \vec{\nabla} \times \vec{B} &= 0, \quad \vec{\nabla} \times \vec{D} = 0, \\ \vec{B} &= \mu \vec{H}, \quad \vec{D} = \varepsilon \vec{E}.\end{aligned}\tag{12}$$

The system (12) can be reduced to the hyperbolic equation (wave equation)

$$\left(\nabla^2 - \frac{1}{c_e^2} \frac{\partial^2}{\partial t^2} \right) \begin{cases} \vec{H} \\ \vec{E} \end{cases} = 0,\tag{13}$$

where $c_e = \sqrt{1/\mu\varepsilon}$ is the speed of light.

A comparison of (11) and (12) shows that (12) differs from (11) by a symmetry. From the mathematical point of view this procedure is an expansion of the nonhyperbolic differential operator to the hyperbolic one [11].

Heat propagation [10]. The transport equation following from the kinetic theory of gases is represented as

$$\left(1 + \xi \frac{\partial}{\partial t} \right) \vec{q} = -k \vec{\nabla} \theta,\tag{14}$$

and the conservation equation can be taken in the form

$$\gamma m \frac{\partial \theta}{\partial t} = -\vec{\nabla} \cdot \vec{q}.\tag{15}$$

The resolving equations for the flux \vec{q} and heat θ , following from (14) and (15), take the form

$$\left[(\vec{\nabla} \times \vec{\nabla} \times \nabla^2) - \xi \gamma \frac{m}{k} \frac{\partial^2}{\partial t^2} \right] q - \gamma \frac{m}{k} \frac{\partial}{\partial t} \vec{q} = 0,\tag{16}$$

$$\left(\nabla^2 - \xi\gamma \frac{m}{k} \frac{\partial^2}{\partial t^2} \right) \theta - \gamma \frac{m}{k} \theta = 0, \quad (17)$$

where the propagation speed is equal to $c_m = \sqrt{\xi\gamma m/k}$, for example, $c_m = 150$ m/s for nitrogen.

Fock (1926) [12] considers probabilities $u(x,t)$ of light particles to be at time t in the point x and to move upwards, and probabilities $v(x,t)$ of light particles to be at the same place, but to move downwards. As a result functions u and v satisfy to the hyperbolic equation

$$\frac{\partial^2 U}{\partial x^2} = \frac{1}{c^2} \frac{\partial^2 U}{\partial t^2} + \frac{1}{D} \frac{\partial U}{\partial t}. \quad (18)$$

Presence of the term $\frac{1}{c^2} \frac{\partial^2 U}{\partial t^2}$ in (18) shows, that any perturbation and concentration inhomogeneities are spread with a finite velocity c . But after these inhomogeneities have smoothed out (that happens quickly, if a velocity c is large), the further process differs a little from the process, which is described by the usual diffusion equation

$$\frac{\partial^2 U}{\partial x^2} = \frac{1}{D} \frac{\partial U}{\partial t}. \quad (19)$$

Later on for more extended discussion this result considered by Kac (1956) [13] and announced again in [14].

It is well known that the classical theory of the thermoconductivity is based on the Fick law. According to this law the heat flux q is directly proportional to the gradient of temperature T :

$$q = -k \frac{\partial T}{\partial x}, \quad (20)$$

where k is the heat conductivity coefficient. This law leads to the heat conduction equation of parabolic type

$$\frac{\partial T}{\partial t} = k \frac{\partial^2 T}{\partial x^2}. \quad (21)$$

It follows from (20) and (21) that the heat flux is directed from areas with a high temperature to areas with a low temperature. Thus, the infinite large propagation speed of temperature perturbations is postulated.

The hyperbolic heat conduction equation is investigated in [15] according to [16]. On the basis of the works [17] and [18] it is shown that a time of the mean free part of an electron with a velocity 10^6 m/s in metals is on 2-4 order less than the electron - photon relaxation time $t_p \sim 10^{-11}$ s [19]. This value coincides well with a magnitude t_p for aluminum [16] and the velocity

$$c_t = \sqrt{a/t_p} \quad (22)$$

has a value of some kilometers per second, i.e. in the order of magnitude it is equal to the sound velocity (22). It leads to the hyperbolic heat conduction equation

$$\frac{\partial T}{\partial t} + \frac{a}{c_t^2} \cdot \frac{\partial^2 T}{\partial t^2} = a\Delta T. \quad (23)$$

In the work of [20] the estimation of the geometrical area has been carried out, when a thermal process is described by the hyperbolic equation (23) at the given initial and boundary conditions. It was shown that for a copper $l = 0.0002$ mm, for a cork $l < 2$ mm. This effect can be important for the armor penetration or for explosion.

At the same time it should be noted that the analysis of propagation of thermal waves in metals at the microscopic level was conducted in the work [21]. It has been shown that generalization of the transport equation (Fourier's law) by taking into account the relaxation time is inadmissible, as it leads to a violation of the fundamental law of energy conservation.

For the case of the heat propagation within very short time intervals the classical equation should be substituted by the more general equation of hyperbolic type [22]

$$\tau \frac{\partial^2 T}{\partial t^2} + \frac{\partial T}{\partial t} = k \frac{\partial^2 T}{\partial x^2}. \quad (24)$$

The calculations on the basis of the equation (24) and comparisons with the data of experiments [22] have shown that in many cases, which are important for modern applications, the diffusion equation (21) leads to the rather underestimated values of temperature at the wave front. The qualitative effect consisting in the strong concentration of energy in a peak zone, which appears at the wave front, according to the hyperbolic equation, is also has been discovered. In the diffusion theory the energy is always "spread" on the whole area. Mc Nelly (1970) [23] obtained experimental results for dielectric crystals of sodium fluoride NaF. Distribution of thermal impulse (pulse height) as a function of arrival time (μs) shows clearly the presence of two front zones.

There are some considerations about diffusion waves which lack wave fronts and don't travel very far [24]. These considerations are based on revolutionary measurement technologies.

Useful contribution to the study of wave propagation with a finite speed is presented in the works [25-32]. Recently, a numerical simulation of hyperbolic heat equation has been presented in [33]. It is remarkable that the similar situation also takes place in the classical mechanics. As it is known, the classical Galilei-Newton mechanics is a special case of the Einstein mechanics when the speed of light is considered as an infinite big magnitude. Such an analogy gives the grounds to pay much attention to the problem of the group transformations of dependent and independent variables [34], which considers diffusion and hyperbolic heat conduction equations as invariants. Similarly it could be expected, that the equations of "diffusion" and "hyperbolic" heat conduction could assume various groups of transformations.

5. Conclusions

A new generalized hyperbolic model for the evolution of sediment is presented. It predicts a finite speed of formation of bottom sediments unlike the traditional model of parabolic type , predicting infinite speed of propagation of small disturbances . This is consistent with field observations from which it follows that the rate of transport of energy and mass of the substance in the coastal zone is a finite quantity [4]. On the basis of the corresponding initial-boundary value problem, a singular degeneration of the generalized hyperbolic model into traditional parabolic ones is carried out. The existence of generalized solutions is demonstrated. Some examples of generalization of parabolic models into hyperbolic ones starting from Maxwell (1867) are considered.

References

1. B. A. Shulyak, *Physics of waves on a surface of loose medium and a liquid*, M.: Nauka 1971.
2. V. V. Longinov, *Outlines of ocean lithodynamics*, M.: Nauka 1973.
3. I. Selezov, R. Volynski, *Wave refraction and sediment dynamics modeling in coastal zone*, Kiev: SMP “AVERS” 2013.
4. E. I. Ignatov, V. A. Robsman,, *Problems of mathematical modeling of coastal morphosystem*, In Issue 149. Sea Coast. Geography Problems. M.: Mysl, (1982) 40-54.
5. H. Zang, R. Kahawita,, *Nonlinear hyperbolic system and its solution for aggrated channels*, J. Hydraulic Reseach, **26**, N 3 (1988) 323-342.
6. A. T. Hjelmfelt,, *River bed degradation in the Missouri river loess hills*, The 23rd Congress of Int. Association for Hydraulic Research (IAHR), Theme: Hydraulics and Environment. Proc. Technical Session B: Fluvial Hydraulics, Canada, Ottawa, (21–25 August 1989) B-233 – B-239.
7. I. T. Selezov,, *Wave hydraulic models as mathematical approximations*, Proc. 22th Congress, Int. Association for Hydraulic Research (IAHR), Lausanne, 1987. Techn. Session B., (1987) 301–306.
8. I. T. Selezov, *The concept of hyperbolicity in the theory of controlled dynamical systems*, Issue 1. Cybernetics and Computation Engineering. Kiev: Nauk. Dumka, (1969) 131–137.
9. O.A. Ladyzhenskaya, *Boundary value problems of mathematical physics*, M.: Nauka 1973.
10. I. C. Maxwell,, *On the dynamical theory of gases*, Phil. Trans. Roy. Soc., **157** (1867) 49-88.
11. I. T. Selezov,, *Some degenerate and generalized wave models in elasto- and hydrodynamics*, J. Applied Mathematics and Mechanics, **67**, N 6 (2003) 871–877.
12. V. A. Fock,, *Solution of one problem of the diffusion theory by finite difference method and its application to a light diffusion*, Leningrad: Publ. State Optical Institute. (1926). § 13. Connection with differential equations and the expression for a diffusivity, 29-31.
13. M. Kac, *Some stochastic problems in physics and mathematics*, Collected Lectures in Pure and Applied Science, N 2, 1956.

-
14. A. D. Kolesnik, A. F. Turbin,, *The equation of symmetric Markovian random evolutions in a plane*, Stoch. Proc. Appl., **75** (1998) 67-87.
15. V. G. Andreev, P. I. Ulyakov,, *Thermoelastic wave taking into account a velocity of heat propagation*, Inzh.-Fiz. J, **21**, № 1 (1971) 176-180.
16. A. V. Lykov, *The theory of thermal conduction*, M.: Higher School 1967.
17. Ch. Kittel, *Introduction to solid state physics*, John Wiley&Sons, 8th Editions 2005.
18. M. I. Kaganov, I. M. Lifshits, L. V. Tanatarov,, *The relaxation between electrons and a lattice*, J. Exper. Theor. Phys., **31** (1956) 232-237.
19. J. Z. M. Ziman, *Electrons and phonons*, Oxford: Clarendon Press 1960.
20. K. V. Lakusta, Yu. A. Timopheev,, *Some estimations of boundaries of applicability of a hyperbolic heat conduction equation*, Inzh.-Fiz. J., № 2 (1979) 366-370.
21. C. Körner, H. W. Bergmann,, *The physical defects of the hyperbolic heat conduction equation*, Appl. Phys. A: Mater. Sci. Process, **67** (1998) 397-401.
22. B. Vick, M. N. Ozisik,, *Growth and decay of a thermal pulse predicted by the hyperbolic heat conduction equation*, ASME J. Heat Transfer, **105** (1983) 902-907.
23. T. F. Mc Nelly,, *Second sound in NaF: Onset of second sound*, Phys. Reviews, **24(3)** (1970) 100-102.
24. A. Mandelis,, *Diffusion waves and their uses*, Physics Today,(August 2000) 29-34.
25. V. S. L'vov, S. Nazarenko,, *Discrete and mesoscopic regimes of finite-size wave turbulence*, Physical Review, **E82** (2010) 05322.
26. J. L. Maistrenko, A. N. Sharkovsky,, *Turbulence and simple hyperbolic systems*, Preprint. Institute of Mathematics, Acad. Sci. Ukr. SSR, № 2 (1984).
27. A. S. Monin,, *On diffusion with a final velocity*, Izv. Acad. Sci. USSR. Ser. Geophys., № 3 (1955) 234-248.
28. A. S. Monin,, *On turbulent diffusion in a surface air*, Izv. Acad. Sci. USSR. Ser. Geophys., № 12 (1956) 1461-1473.
29. F. S. Monin, F. M. Yaglom, *Statistical hydromechanics. Part 1*. M.: Science 1965, (10.6. Diffusion with a finite velocity).
30. I.T. Selezov, *Construction of hyperbolic approximations of hydrodynamic equations*, Hydromechanics, Issue 29 (1974) 3-7.
31. I. T. Selezov, *Modeling of wave and diffraction processes in continuous media*, Kiev: Nauk. Dumka 1989.
32. I. Selezov,, *Some hyperbolic models for wave propagation*, Hyperbolic Problems: Theory, Numerics, Applications. 7th Int. Conf. in Zurich, 1998, Vol. 2. Int. Ser. of Numerical Mathematics. Vol. 130 / Ed. by M. Fey and R. Jeltsch. – Basel / Switzerland: Birkhauser Verlag, Vol. 2 (1999) 833–842.
33. P. N. Vabishchevich,, *Splitting schemes for hyperbolic heat conduction equation*, BIT Number Math., (2013) DOI 10.1007/s10543-013-0423-7.
34. G. Birkhoff, *Hydrodynamics. A study in logic, fact and similitude*, Princeton University Press 1960.

Damped Vibration of a Non-prismatic Beam with a Rotational Spring

Wojciech SOCHACKI

*Institute of Mechanics and Fundamentals of Machinery Design
University of Technology, Czestochowa, Poland
sochacki@imipkm.pcz.pl*

Marta BOLD

*Institute of Mechanics and Fundamentals of Machinery Design
University of Technology, Czestochowa, Poland
bold@imipkm.pcz.pl*

Abstract

In this paper a problem pertaining to the damped lateral vibrations of a beam with different boundary conditions and with a rotational spring is formulated and solved. In the adopted model the vibration energy dissipation derives from the internal damping of the viscoelastic material (Kelvin–Voigt rheological model) of the beam and from the resistance motion in the supports. The rotational spring can be mounted at any chosen position along the beam length. The influence of step changes in the cross-section of the beam on its damped lateral vibrations is also investigated in the paper. The damped vibration frequency and the vibration amplitude decay level are calculated. Changes in the eigenvalues of the beam vibrations along with the changes in the damping ratio and the change in the model geometry observed on it are also presented. The considered beam was treated as Euler- Bernoulli beam.

Keywords: Vibration damping, non-prismatic beam, rotational spring.

1. Introduction

The transverse vibration of prismatic and non-prismatic beams with additional discrete elements has been investigated in a number of studies. Study [1] presents the transverse vibration of a beam with a stepped cross-section together with the phenomenon of damped vibration in the body where the system is present. The problem of the vibration and dynamic stability of beams with different boundary conditions with additional discrete elements was presented in study [2]. Study [3] concerned the modal analysis of a semi-infinite Euler-Bernoulli beam with discrete elements in the form of a rotational and a translational spring. Investigations concerning damped vibration were discussed in [4-7]. Study [4] discussed the effect of small internal and external damping on the stability of non-conservative beam systems. The authors of study [5] demonstrated the effect of internal damping on the vibrations of a supported beam with a mass attached to the free end of the beam. Study [6] examined the vibration of an axially-loaded Timoshenko beam with local internal damping. The effect of constructional damping of the fixations on free vibration of the Bernoulli-Euler beam was presented in study [7].

This study formulates and solves the problems of transverse damped vibration in a C-P (clamped-pinned) beam with a stepped cross-section and with a rotational spring. Dissipation of the vibration energy occurs as a result of the simultaneous internal damping

of the viscoelastic material of the beam and structural damping in the support. The constructional damping was modelled using a rotational viscous damper. The study analyses the simultaneous effect of the structural damping and internal damping, the spring rigidity and its location and the effect of the location of the stepped cross-section of the beam on the properties of the considered system. The results obtained in the study are presented as 2D figures and spatial presentations.

2. Mathematical model

A scheme of the considered C-P beam is presented in Fig. 1.

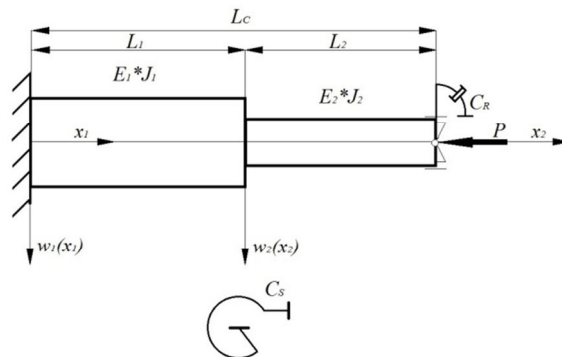


Figure 1. Model of the C-P beam with step changes in the cross-section with a rotational spring C_s and rotational viscous damper C_r

Viscoelastic material was characterized by the Young's modulus E_n and the viscosity coefficient E_n^* of the beam material. The coefficient of constructional damping in the rotational viscous damper was denoted as C_r .

The vibration equation for the two parts of a beam is known and has the following form:

$$\begin{aligned} & E_n J_n \frac{\partial^4 W_n(x,t)}{\partial x^4} + E_n^* J_n \frac{\partial^5 W_n(x,t)}{\partial x^4 \partial t} + \\ & + P_n \frac{\partial^2 W_n(x,t)}{\partial x^2} + \rho_n A_n \frac{\partial^2 W_n(x,t)}{\partial t^2} = 0 \end{aligned} \quad (1)$$

where:

- $W_n(x,t)$ – the lateral displacement of beam,
- A_n – the cross-section area of the beam,
- J_n – the moment of inertia for the beam section,
- ρ_n – the density of the beam material,
- P_n – longitudinal forces in beam,
- $n = 1, 2$
- x – space coordinate,
- t – time,

Solutions to equations (1) take the form:

$$W_n(x,t) = w_n(x)e^{i\omega^* t} \quad (2)$$

where: ω^* – the complex eigenvalue of the system, $i = \sqrt{-1}$

Substitution of (2) into (1) leads to:

$$w_n^{IV}(x) + \beta_n^2 w_n^{II}(x) - \gamma_n w_n(x) = 0 \quad (3)$$

where:

$$\gamma_n = \frac{\rho_n A_n \omega^{*2}}{(E_n + iE_n^* \omega^*) J_n}, \quad \beta_n = \sqrt{\frac{P_n}{(E_n + iE_n^* \omega^*) J_n}} \quad (4)$$

Boundary conditions:

$$\begin{aligned} w_1(0) &= 0, \quad w_1(l_1) = w_2(0), \quad w_1^I(0) = 0, \quad w_2(l_2) = 0, \\ w_1^I(l_1) &= w_2^I(0), \quad (E_2 + iE_2^* \omega^*) J_2 w_2^{II}(l_2) = -C_R i \omega^* w_2^I(l_2), \\ (E_1 + iE_1^* \omega^*) J_1 w_1^{III}(l_1) + (E_2 + iE_2^* \omega^*) J_2 w_2^{III}(0) &= 0, \\ (E_1 + iE_1^* \omega^*) J_1 w_1^{II}(0) + C_S w_1^I(l_1) &= (E_2 + iE_2^* \omega^*) J_2 w_2^{II}(0) \end{aligned} \quad (5)$$

The solution to equations (3) is expressed in the form of functions:

$$w_n(x) = D_{1n} e^{\lambda_n x} + D_{2n} e^{-\lambda_n x} + D_{3n} e^{i\bar{\lambda}_n x} + D_{4n} e^{-i\bar{\lambda}_n x} \quad (6)$$

where:

$$\lambda_n = \sqrt{-\frac{\beta_n^2}{2} + \sqrt{\frac{\beta_n^4}{4} + \gamma_n}}, \quad \bar{\lambda}_n = \sqrt{\frac{\beta_n^2}{2} + \sqrt{\frac{\beta_n^4}{4} + \gamma_n}} \quad (7)$$

By substituting (6) into (5) a homogeneous system of equations was obtained with respect to unknown constants D_{kn} , and can be written in the matrix form as:

$$[A](\omega^*) D = 0 \quad (8)$$

where:

$$A(\omega^*) = [a_{pq}], \quad (p, q = 1, 2..8), \quad D = [D_{kn}]^T, \quad k = 1, 2 - 4 \quad (9)$$

The system has a nontrivial solution when the matrix determinant of coefficients is equal to zero with constants D_{kn} .

$$\det A(\omega^*) = 0 \quad (10)$$

Finding the complex eigenvalues of matrix $A(\omega^*)$ leads to the determination of damped vibration frequency $Re(\omega^*)$ and the vibration amplitude decay level $Im(\omega^*)$ of the considered system.

3. Numerical calculation results

Computations were carried out assuming the following dimensionless quantities:

$$\eta = \frac{E_n^*}{aE_n}, \quad a^2 = L_C^4 \frac{\sum_n \rho_n A_n}{\sum_n E_n J_n}, \quad \mu = \frac{C_R}{L_C \sqrt{\rho_2 A_2 (E_2 + iE_2^* \omega^*) J_2}}, \quad (11)$$

$$c = \frac{C_S L_C}{(E_1 + iE_1^* \omega^*) J_1}, \quad J = \frac{J_2}{J_1}, \quad l = \frac{L_1}{L_C}, \quad p = \frac{P}{P_C} \quad (12)$$

where: P_C – the critical load of the tested beam with a constant cross-section.

The results of the calculations are presented in Figs. 2 to 6. Investigations were carried out for different ratios of the moments of inertia for the two parts of the beam ($J=0.5$, $J=5$) and for a beam with a constant cross-section ($J=1$). The system was loaded with longitudinal force P ($p=0.05$). The dependency of the eigenvalues (real parts $Re(\omega^*)$ and imaginary parts $Im(\omega^*)$) on the coefficients of constructional damping μ , spring rigidity c and location of the change in the beam cross-section l was also determined.

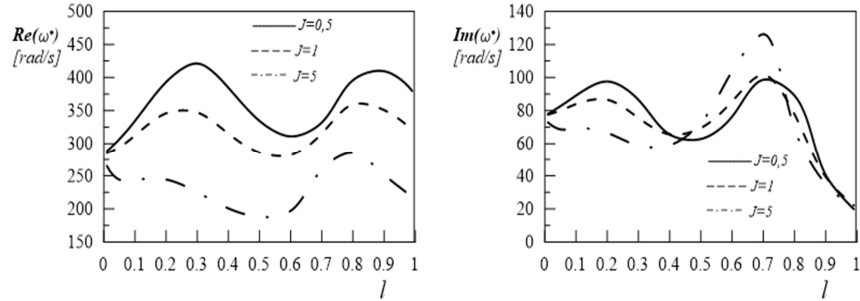


Figure 2. The dependency of real parts ($Re(\omega^*)$) and imaginary parts ($Im(\omega^*)$) of the first beam eigenvalue on the coefficient l at $\eta=0.002$, $\mu=0.3$, $c=10$

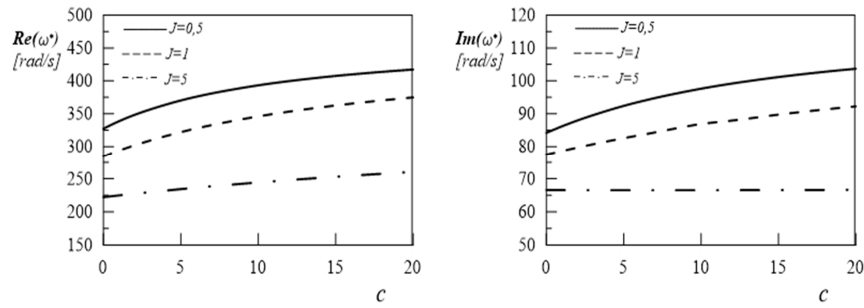


Figure 3. The dependency of real parts ($Re(\omega^*)$) and imaginary parts ($Im(\omega^*)$) of the first beam eigenvalue on the spring rigidity coefficient c at $\eta=0.002$, $\mu=0.3$ and $l=0.2$

Figures 5 and 6 present collective diagrams of the dependency of eigenvalues ($Re(\omega^*)$ and $Im(\omega^*)$) in the studied system on the change in the rigidity of elastic support c and constructional damping μ . The calculations were carried out for selected values of internal damping and for a central location of the rotational spring and two values of the relation of the moments of inertia ($J=5$ and $J=0.5$). The results are presented as spatial diagrams.

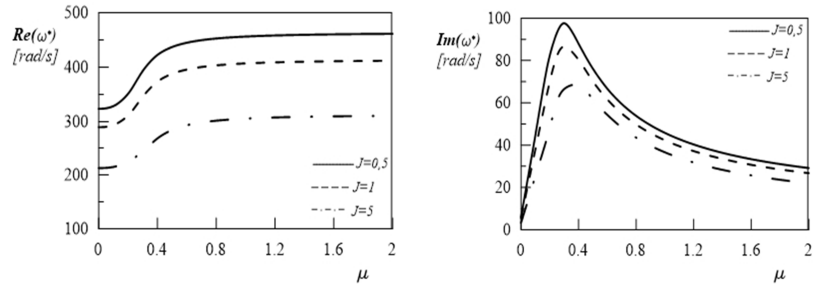


Figure 4. The dependency of real parts ($Re(\omega^*)$) and imaginary parts ($Im(\omega^*)$) of the first beam on structural damping μ at $\eta=0.002$, $c=10$ and $l=0.2$

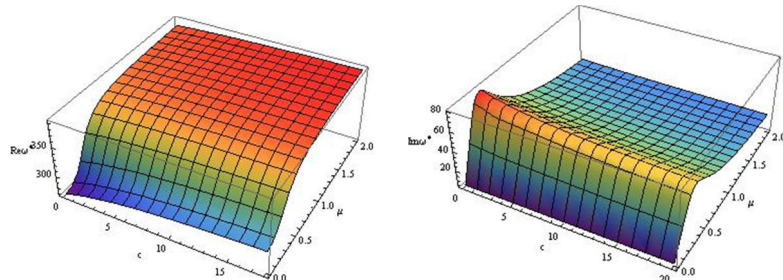


Figure 5. The dependency of real parts ($Re(\omega^*)$) and imaginary parts ($Im(\omega^*)$) of the first eigenvalue of the beam on the coefficient of structural damping μ and spring rigidity coefficient c for $l=0.5$ and $J=0.5$, $\eta=0.002$

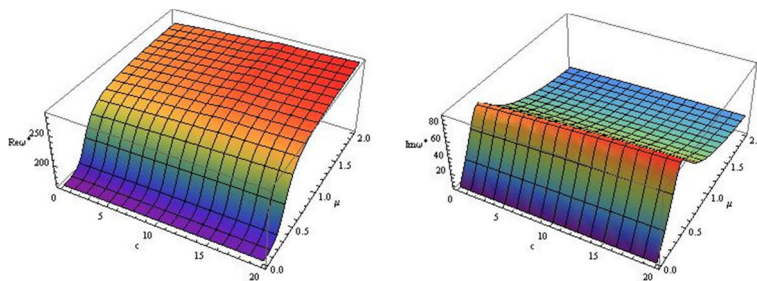


Figure 6. The dependency of real parts ($Re(\omega^*)$) and imaginary parts ($Im(\omega^*)$) of the first eigenvalue of the beam on the coefficient of structural damping μ and spring rigidity coefficient c for $l=0.5$ and $J=5$, $\eta=0.002$

4. Conclusions

The damped frequencies of system $Re(\omega^*)$ and the degree of amplitude decay $Im(\omega^*)$ in the system depend on the location of the rotational spring along the beam. No uniform tendency for changes was observed in the case studied (Fig. 2). Improved spring rigidity causes a constant increase in the damped frequencies of the first eigenvalue of the system (for selected values of coefficients η , μ and l). The degree of amplitude decay in this case depends on the ratio of rigidity J for the two beam parts. For the central location of the change in the cross-section ($l=0.5$), an increase in c causes a decrease in the coefficient of the amplitude decay for $J=0.5$, and an increase for $J=5$ (Fig. 5 and 6). The constructional damping of the fixation points with selected values of spring rigidity causes much more substantial changes in the eigenvalues of the system than in the reverse case (the change in coefficient c for selected value μ). The results presented in the study help determine the geometric parameters and values of the coefficients that characterize the damping and elasticity of the system for which the maximum degree of amplitude decay is maintained.

Acknowledgments

This research was supported in 2014 by the Ministry of Science and Higher Education, Warsaw, Poland.

References

1. M. I. Friswell, A. W. Lees, *The modes of non-homogeneous damped beams*, Journal of Sound and Vibration **242**(2) (2001) 355-361.
2. W. Sochacki, *Dynamic stability of discrete-continuous mechanical systems as working machine models*, Monographic series **147**, Czestochowa University of Technology, Czestochowa 2008.
3. A. Pau, F. Vestroni, *Modal Analysis of a Beam with Radiation Damping: Numerical and Experimental Results*, Journal of Vibration and Control **13**(8) (2007), 1109-1125.
4. O. N. Kirillov, A. O. Seyranian, *The effect of small internal and external damping on the stability of distributed non-conservative systems*, Journal of Applied Mathematics and Mechanics **69** (2005), 529-552.
5. M. Gürgöze, A. N. Doğruoğlu, S. Aeren, *On the eigencharacteristics of a cantilevered visco-elastic beam carrying a tip mass and its representation by a spring-damper-mass system*, Journal of Sound and Vibration **301** (2007), 420-426.
6. Wei-Ren Chen, *Bending vibration of axially loaded Timoshenko beams with locally distributed Kelvin-Voigt damping*, Journal of Sound and Vibration **330** (2011), 3040–3056.
7. G. Oliveto, A. Santini, E. Tripodi, *Complex modal analysis of flexural vibrating beam with viscous end conditions*, Journal of Sound and Vibration **200** (1997), 327-345.

The Influence of Internal and Constructional Supports Damping on the Γ -type Frame Vibrations

Wojciech SOCHACKI

*Institute of Mechanics and Fundamentals of Machinery Design
University of Technology, Częstochowa, Poland
sochacki@imipkm.pcz.pl*

Piotr ROSIKÓŃ

*Institute of Mechanics and Fundamentals of Machinery Design
University of Technology, Częstochowa, Poland
p.rosikon@imipkm.pcz.pl*

Sandra TOPCZEWSKA

*Institute of Mechanics and Fundamentals of Machinery Design
University of Technology, Częstochowa, Poland
s.topczewska@imipkm.pcz.pl*

Abstract

The paper presents the formulation and solution of Γ -type frame damping vibration. The physical system model takes into account the energy dissipation of the vibrating frame due to the internal vibration damping of the viscoelastic frame material and the constructional damping in the place of frame bolt support. As the results of the problem solution, the damping and system geometry effects on the first frame eigenvalue (damped frequencies and coefficients of amplitude decay factor) were presented.

Keywords: vibration damping, Γ -type frame, eigenvalue, amplitude decay factor.

1. Introduction

The constructional damping vibration problems of frames are extremely significant from the point of view of mechanical structural designs. Also the structures of frames in a square Γ -type [1], T-type [2, 3, 4] or other two or three bar frames [5] form have been described in many scientific publications. Experimental, theoretical and numerical study associated with Γ type frame with reference to stability and free vibrations, have been carried out in the monograph [1].

The type of instability of a T-type frame with joint mass M subjected to a compressive follower force P applied at the joint was researched in the work [2]. In paper [3] a formulation and solution for the problem of damped vibration in T-type frame was presented. The energy dissipation in a vibrating frame as a result of constructional damping in the points of the frame mounting and the supports in physical model was also took into account. T-type frame theoretical, numerical and experimental research on the stability and free vibrations was also described in [4]. The author investigated frame loaded by longitudinal force in relation to its bolt.

Importance of two-bar frames research was emphasized by describing the variational method for investigation of the stability of a rectangular two-bar frame in the work [5].

Also interesting studies in the field of numerical procedure for the complex frequencies and vibration modes evaluation were carried out in the article [6]. Interesting research results related to the effects of small both internal and external damping on the stability of disturbed non-conservative systems could be found in the paper [7].

In this paper the formulation and solution of Γ -type frame damped vibration was presented. In the vibration model, internal damping of viscoelastic material in frame (rheological model by Kelvin-Voigt) and constructional damping in the place of frame bolt support was taken into account. As the results of the problem solution, the damping and system geometry effects on the first frame eigenvalue were presented. The results obtained in the study were presented in 2D figures and spatial presentations.

2. Physical and mathematical model

Physical model of the considered system is shown in Fig. 1. Considered frame consists of a column with an l_1 length and l_2 long bolt. Constructional damping of the bolt support vibrations was modelled by viscous rotary damper with a damping factor denoted as C_R . Viscoelastic material has been characterized by the Young's modulus E_i and the viscosity coefficient E_i^* of frame material.

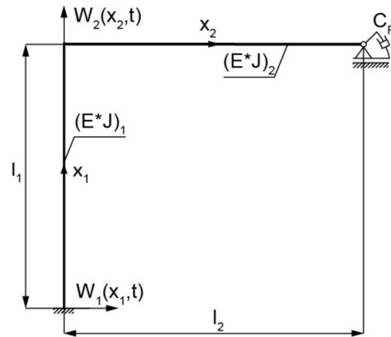


Figure 1. Physical model of the Γ -type frame

The equations of motion of the individual frame beams can be written as:

$$E_i J_i \frac{\partial^4 W_i(x, t)}{\partial x^4} + E_i^* J_i \frac{\partial^5 W_i(x, t)}{\partial x^4 \partial t} + \rho_i A_i \frac{\partial^2 W_i(x, t)}{\partial t^2} = 0 \quad (1)$$

where:

- $W_i(x, t)$ – the lateral displacement for individual beams of frame, $i = 1, 2$,
- A_i – the cross-section area of the beams,
- J_i – the moment of inertia for beam section,
- E_i – Young's modulus,
- E_i^* – material viscosity coefficient,
- ρ_i – the density of the beam material,
- x – space coordinate,
- t – time.

Geometric boundary conditions and continuities are as follows:

$$\begin{aligned} W_1(0, t) &= W_2(l_2, t) = 0, \\ \frac{\partial W_1(x_1, t)}{\partial x_1} \Big|_{x_1=0}^{x_1=l_1} &= \frac{\partial W_2(x_2, t)}{\partial x_2} \Big|_{x_2=0}, \\ \frac{\partial W_1(x_1, t)}{\partial x_1} \Big|_{x_1=0} &= 0 \end{aligned} \quad (2)$$

The boundary issues are complemented by the natural boundary conditions of the form:

$$\begin{aligned} (E_2 + jE_2^* \omega^*) J_2 \frac{\partial^2 W_2(x_2, t)}{\partial x_2^2} \Big|_{x_2=0}^{x_2=l_2} &= -C_R \frac{\partial^2 W_2(x_2, t)}{\partial x_2 \partial t} \Big|_{x_2=0}^{x_2=l_2} \\ (E_1 + jE_1^* \omega^*) J_1 \frac{\partial^3 W_1(x_1, t)}{\partial x_1^3} \Big|_{x_1=0}^{x_1=l_1} &= 0, \\ (E_1 + jE_1^* \omega^*) J_1 \frac{\partial^3 W_1(x_1, t)}{\partial x_1^3} \Big|_{x_1=0}^{x_1=l_1} - (E_2 + jE_2^* \omega^*) J_2 \frac{\partial^2 W_2(x_2, t)}{\partial x_2^2} \Big|_{x_2=0}^{x_2=l_2} &= 0, \\ (E_2 + jE_2^* \omega^*) J_2 \frac{\partial^3 W_2(x_2, t)}{\partial x_2^3} \Big|_{x_2=0} &= 0 \end{aligned} \quad (3)$$

The last boundary condition for $x_2=0$ in many publications is assumed to be $W_2(0, t) = 0$ (cf. [8]). Adoption of such condition requires the assumption that during the vibration the vertical rod (pole) of the frame at the end of $x_1=l_1$ performs so small vibrations (displacement) that they could be identified as negligible. However, assuming that displacement is $W_1(l_1, t) \neq 0$ and taking into account the restoring force of the bending frame (slender system) in $x_2=0$, then one of the variances of the potential energy element

is $(E_2 + jE_2^* \omega^*) J_2 \frac{\partial^3 W_2(x_2, t)}{\partial x_2^3} \delta W_2(x_2, t) \Big|_{x_2=0}$. Assuming that the variation

$\delta W_2(x_2, t) \Big|_{x_2=0} \neq 0$ the natural boundary condition becomes

$$(E_2 + jE_2^* \omega^*) J_2 \frac{\partial^3 W_2(x_2, t)}{\partial x_2^3} \Big|_{x_2=0} = 0 \quad [1, 5].$$

3. The solution to the problem

The solutions of the equation (1) are as follows:

$$W_i(x,t) = w_i(x)e^{j\omega^* t} \quad (4)$$

where: ω^* – the complex eigenvalue of the system, $j = \sqrt{-1}$.

By substituting (4) to (1-3) we obtain:

$$w_i^{IV}(x) - \gamma_i w_i(x) = 0, i = 1, 2 \quad (5)$$

where:

$$\gamma_i = \frac{\rho_i A_i \omega^{*2}}{(E_i + j E_i^* \omega^*) J_i}. \quad (6)$$

The boundary conditions (after the separation of variables) of considered system, are as the following:

$$\begin{aligned} w_1(0) &= w_2(l_2) = 0, \\ w_1^I(l_1) &= w_2^I(0), \\ w_1^I(0) &= 0, \\ (E_2 + j E_2^* \omega^*) J_2 w_2^{II}(l_2) &= -C_R j \omega^* w_2^I(l_2), \\ (E_1 + j E_1^* \omega^*) J_1 w_1^{III}(l_1) &= 0, \\ (E_1 + j E_1^* \omega^*) J_1 w_1^{II}(0) - (E_2 + j E_2^* \omega^*) J_2 w_2^{II}(0) &= 0, \\ (E_2 + j E_2^* \omega^*) J_2 w_2^{III}(0) &= 0 \end{aligned} \quad (7)$$

The solution of equations (5) is expressed in the form of functions:

$$w_i(x) = D_{1i} e^{\lambda_i x} + D_{2i} e^{-\lambda_i x} + D_{3i} e^{j\bar{\lambda}_i x} + D_{4i} e^{-j\bar{\lambda}_i x} \quad (8)$$

The substitution of the solution (8) into equation (7) leads to a system of equations because of the constant D_{ki} ($k=1,2,4$). The solution of such a system is the solution of boundary problem and it leads determine the eigenvalues of studied system, in the form of damped frequencies $Re(\omega^*)$ and the amplitude decay factor $Im(\omega^*)$.

4. The results of numerical computations

The study of the analyzed frame damping vibrations were performed for the following geometrical and material data: $(EJ)_i = 6.443$ [Nm²], $(\rho A)_i = 15.433$ [kg/m] and for the beam lengths: $l_1 = 2$ and $l_2 = 0.5$. Calculations were made after the adoption of the dimensionless damping coefficients and the relationship of moments of inertia of the column sections and bolt frame J in the form of:

$$\eta = \frac{E_i^*}{aE_i}, \quad a^2 = (l_1 + l_2)^4 \sum_i \frac{(\rho A)_i}{(EJ)_i}, \quad \mu = \frac{C_R}{l_2 \sqrt{(\rho A)_i (EJ)_i}}, \quad J = \frac{J_2}{J_1}. \quad (9)$$

In Figures 2-5 results of the calculation are shown. In Fig. 2 the results of research of dependency between the frame eigenvalues and constructional damping in the place of bolt support.

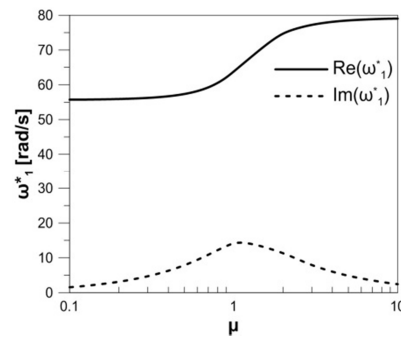


Figure 2. The dependence between the real parts ($Re(\omega_1^*)$) and imaginary parts ($Im(\omega_1^*)$) of the first beam eigenvalue and the constructional damping μ

In the next figure (Fig. 3) the results of frame eigenvalues (with the selected constructional damping value $\mu = 0.2$) changes along with the bolt length (l_2) changes were presented.

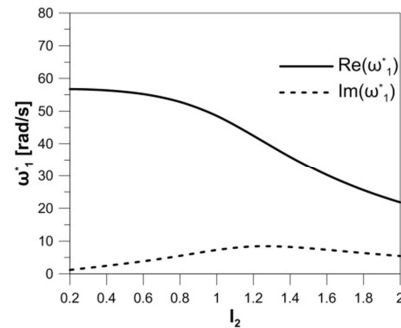


Figure 3. The dependence between the real parts ($Re(\omega_1^*)$) and imaginary parts ($Im(\omega_1^*)$) of the first beam eigenvalue and the horizontal beam l_2

The results of studies on the impact of changes in stiffness of the bolt and the column of the frame on the eigenvalues of the system are shown in Fig. 4. The constructional damping factor in this case also was $\mu = 0.2$. By changing the relation between the moments of cross-section inertia J , in each case constant inertia moment J_2 was taken.

In Figure 5 the results of research on the frame's viscoelastic material internal damping influence on its eigenvalues were presented.

In Figure 6 the summary graphs of the dependence of the real ($Re(\omega_1^*)$) and imaginary parts ($Im(\omega_1^*)$) of the first beam eigenvalue in analyzed system, relative to the constructional damping μ parameter and internal damping coefficient η , were presented.

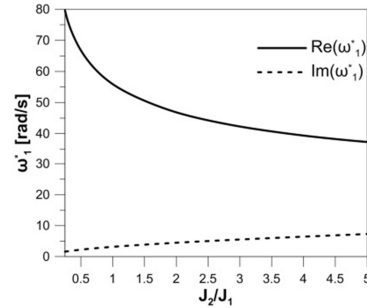


Figure 4. The dependence between the real parts ($Re(\omega_1^*)$) and imaginary parts ($Im(\omega_1^*)$) of the first beam eigenvalue and the beam cross-section J moment of inertia

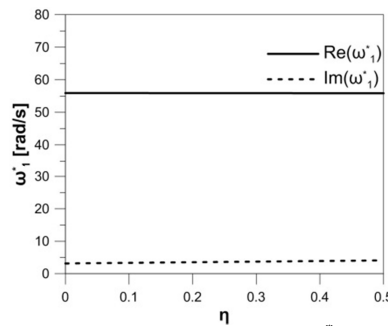


Figure 5. The dependence between the real parts ($Re(\omega_1^*)$) and imaginary parts ($Im(\omega_1^*)$) of the first beam eigenvalue and internal damping coefficient η

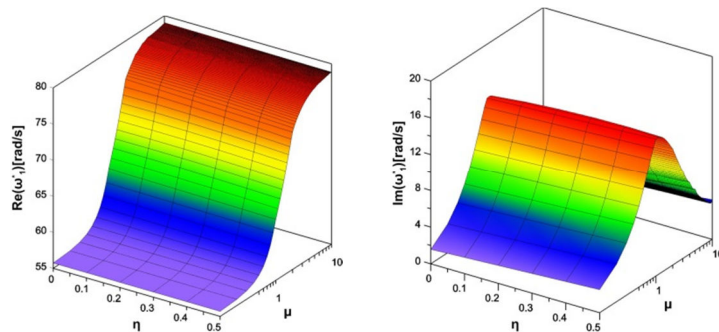


Figure 6. The dependence between the real parts ($Re(\omega_1^*)$) and imaginary parts ($Im(\omega_1^*)$) of the first beam eigenvalue and the constructional damping parameter μ and internal damping coefficient η

4. Conclusions

The paper presents a model of damped vibrations of Γ -type frame. Based on the obtained results it could be concluded that including constructional damping mounting, causes significant changes in the frame eigenvalues. The change of the damping coefficient μ , significantly affects on the first eigenvalue (both on the damped frequency $Re(\omega_1^*)$ and the amplitude decay factor $Im(\omega_1^*)$). The damped frequency $Re(\omega_1^*)$ is increasing to a value corresponding to the two-sided rigid frame mounting. It can be seen that with the increase of the rotary damper damping coefficient, the amplitude decay coefficient rises to a maximum value and then tends to 0 when $\mu \rightarrow \infty$.

Analyzing the impact of the frame bolt length on its eigenvalues, it could be concluded that that suitable damped vibrations $Re(\omega_1^*)$ decrease with the elongation of the bolt (l_2), which was to be expected. However, the amplitude decay factor increases to a maximum value, and then decreases.

Significant changes in the eigenvalues of research system could be seen when changing relations of cross-section inertia moments of the two parts of frame. The increase in the ratio of J moments causes stronger vibration damping in the system (growth of coefficient $Im(\omega_1^*)$). The inclusion of internal damping in the frame vibration model, causes a slight change in the first eigenvalue (damped vibrations $Re(\omega_1^*)$ as well as the amplitude decay factor $Im(\omega_1^*)$).

Based on the research it could be determined such geometric parameters of the frame, for which the amplitude decay factors are greatest, and hence it is possible to design systems providing minimum vibration amplitudes.

Acknowledgments

This research was supported by the Ministry of Science and Higher Education in 2014, Warsaw, Poland.

References

1. J. Szmidla, *Free vibrations and the stability of slender systems subjected to a specific load*, Monographic series **165**, Czestochowa University of Technology, Czestochowa 2009.
2. A. N. Kounadis, A. P. Ecomonou, *The effects of the joint stiffness and of the constraints on the type of instability of a frame under follower force*, Acta Mech, **Vol. 36** (1980), 157–168.
3. W. Sochacki, P. Rosikoń, S. Topczewska, *Constructional damping mounting influence on T type frame vibrations*, Vibroengineering. Journal of Vibroengineering **Vol. 15(4)** (2013), 1866-1872.
4. J. Szmidla, *Vibrations and stability of T-type frame loaded by longitudinal force in relation to its bolt*, Thin-Walled Structures **45** (2007), 931–935.
5. L. Tomski, J. Przybylski, J. Szmidla, *Stability and vibrations of a two-bar frame under a follower force*, Zeit Ang Math Mech, **S5(76)** (1996), 521–522.

7. G. Oliveto, A. Santini, E. Tripodi, *Complex modal analysis of flexural vibrating beam with viscous end conditions*, Journal of Sound and Vibration **200** (1997), 327-345.
8. O. N. Kirrllov, A. O. Seyranin, *The effect of small internal and external damping on the stability of distributed non-conservative systems*, Journal of Applied Mathematics and Mechanics **69** (2005), 529-552.
9. G. I. Ioannidis, I. G. Raftoyiannis, A. N. Kounadis, *A method for the direct of buckling loads of an imperfect two-bar frame*, Archive of Applied Mechanics, **74** (2005), 299–308.

Nonlinear Vibrations of Rotating System Near Resonance

Roman STAROSTA

*Poznan University of Technology, Institute of Applied Mechanics
ul. Piotrowo 3, 60-965 Poznań, Poland
roman.starosta@put.poznan.pl*

Grażyna SYPNIEWSKA-KAMIŃSKA

*Poznan University of Technology, Institute of Applied Mechanics
ul. Piotrowo 3, 60-965 Poznań, Poland
grazyna.sypniewska-kaminska@put.poznan.pl*

Abstract

The paper concerns analysis of nonlinear vibration of the rotating system consisted of two disks and shaft. The analytical multiple time scale method is applied to the analysis dynamics of the system near main resonance. The transition phenomenon depending on the value of the nonlinearity parameter is discussed. All the analytical results have been confirmed numerically.

Keywords: nonlinear vibrations, asymptotic methods, resonance

1. Introduction

Torsional vibrations are one of main problem in design of the power transmission systems [2]. Dynamic stresses caused by torsional vibrations, especially when their amplitudes grow significantly near resonance, may be very large and lead to failure of the whole system.

Both discrete and continuous models are commonly used in order to investigate the torsional vibrations of the power transmission systems [1,4,6]. We have attempted to apply the Limiting Phase Trajectories (LPT) method in order to investigate nonlinear torsional vibrations. LPT is an analytical approximate method, developed recently by Manevitch and used to analyse of discrete systems [3]. The discrete model was chosen as the most convenient to use this method. Similar approach was applied in [5].

2. Mathematical model

Let us consider a rotating system, consisting of two disks mounted on a shaft. The system studied is shown in Fig. 1. The disks are considered as rigid. Their moments of inertia around the axis of rotation are denoted by I_1 and I_2 , respectively. The shaft is relatively thin and light, so its mass may be neglected. The shaft provides torsional stiffness only. The nonlinear relationship between the angle of twist and the torque was assumed. Two coefficients of stiffness, marked by k and k_n , are introduced. Moreover viscous damping, of which the damping coefficient equal to c , is taken into account. The whole system is mounted on frictionless bearings which are also ideal in the geometric sense. One of the disks is under the action of the harmonically changing torque

$M(t) = M_0 \cos(p_0 t)$. The system has two degree of freedom. The angles of rotation of both wheels are chosen as the generalized coordinate.

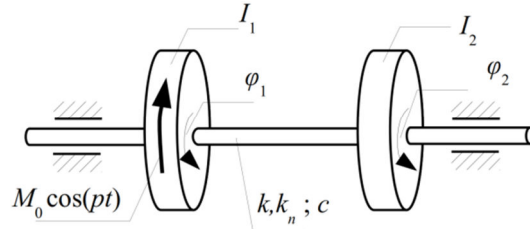


Figure 1. Model of rotating system

The Lagrangian of the system is as follows:

$$L = \frac{1}{2} I_1 \dot{\phi}_1^2 + \frac{1}{2} I_2 \dot{\phi}_2^2 - \frac{1}{2} k(\phi_1 - \phi_2)^2 - \frac{1}{4} k_n (\phi_2 - \phi_1)^4, \quad (1)$$

where I_1 and I_2 are the moments of inertia, k and k_n are the stiffness coefficients.

The equations of motion are as follows

$$I_1 \ddot{\phi}_1 - k(\phi_2 - \phi_1) - k_n(\phi_2 - \phi_1)^3 - c(\dot{\phi}_2 - \dot{\phi}_1) = M_0 \cos(p_0 t), \quad (2)$$

$$I_2 \ddot{\phi}_2 - k(\phi_2 - \phi_1) - k_n(\phi_2 - \phi_1)^3 - c(\dot{\phi}_2 - \dot{\phi}_1) = 0. \quad (3)$$

Dividing eqs. (2) and (3) respectively by I_1 and I_2 and subtracting then eq (2) from eq (3) we obtain the equation, in which only the differences of the unknown functions and their derivatives are present. Hence let us introduce the new function

$$\Phi(t) = \phi_1(t) - \phi_2(t). \quad (4)$$

The function $\Phi(t)$ is simply the angle of twist of the shaft between the discs. The substitution (4) leads to the equation

$$\ddot{\Phi}(t) + K^2 \Phi(t) + K_n \Phi(t)^3 + C \dot{\Phi}(t) = \frac{M_0}{I_1} \cos p_0 t, \quad (5)$$

where $K = \sqrt{k/I_1 + k/I_2}$, $\eta_e = k_n/I_1 + k_n/I_2$, $C = c/I_1 + c/I_2$.

The eq. (5) describes the internal motion which is especially important with respect of vibrational process.

Introducing dimensionless time $\tau = Kt$, the more convenient form of the equation of motion can be written:

$$\ddot{\phi}(\tau) + \phi(\tau) + \eta_e \phi(\tau)^3 + \gamma_e \dot{\phi}(\tau) = \mu \cos p\tau, \quad (6)$$

where $\mu = M_0/I_1 K^2$, $p = p_0/K$, $\gamma_e = C/K$ and ϕ is the angle of twist with respect to τ .

3. Asymptotic solution

Further analysis concerns the eq. (6). Let us assume that the system is weakly nonlinear and moreover the damping coefficient and the amplitude of the external torque are of the order of small parameter. The above assumptions allow to write the governing equation in the form:

$$\ddot{\phi} + 2\varepsilon\gamma\dot{\phi} + \phi + 8\varepsilon\eta\phi^3 = 2\varepsilon f \cos(p\tau), \quad (7)$$

where $2\varepsilon\gamma = \gamma_e$, $8\varepsilon\eta = \eta_e$, $2\varepsilon f = \mu$.

The initial conditions are assuming to be homogeneous $\phi(0) = 0$, $\dot{\phi}(0) = 0$.

Let us introduce the function $v(\tau) = \dot{\phi}(\tau)$. Then the eq. (7) can be written as the set of equations of the first order:

$$\begin{aligned} v - \dot{\phi} &= 0, \\ \dot{v} + 2\varepsilon\gamma\dot{\phi} + \phi + 8\varepsilon\eta\phi^3 &= 2\varepsilon f \cos(p\tau). \end{aligned} \quad (8)$$

The key point for the next analysis is the introduction complex functions

$$\psi = v + i\phi \text{ and } \bar{\psi} = v - i\phi. \quad (9)$$

Substituting the definitions (9) into eq. (8) we obtain the equation

$$\frac{d\psi}{d\tau} - i\psi + \gamma\varepsilon(\psi + \bar{\psi}) + i\eta\varepsilon^2(\psi - \bar{\psi})^3 = 2\varepsilon f \cos(p\tau), \quad (10)$$

with the initial conditions $\psi(0) = 0$, which is equivalent to the system (8).

After introducing once more substitution

$$\psi = \Psi e^{i\tau} \text{ and } \bar{\psi} = \bar{\Psi} e^{-i\tau}, \quad (11)$$

\we get the following equation with unknown complex function $\Psi(\tau)$.

$$\begin{aligned} \frac{d\Psi}{d\tau} + \gamma\varepsilon(\Psi + \bar{\Psi}e^{-2i\tau}) + i\eta\varepsilon\left(\Psi^3 e^{2i\tau} - \bar{\Psi}^3 e^{-4i\tau} - 3|\Psi|^2\Psi + 3|\Psi|^2\bar{\Psi}e^{-2i\tau}\right) &= \\ = 2\varepsilon e^{-i\tau} f \cos(p\tau), \end{aligned} \quad (12)$$

with the initial condition $\Psi(0) = 0$. The appropriate complex conjugate formulation could be written as well.

Let us focus attention on the case of the main resonance, that occurs when $p \approx 1$. In order to consider this case, the small detuning parameter σ is introduced in the form $p = 1 + \sigma = 1 + \varepsilon\tilde{\sigma}$.

The initial value problem (12) is solved with the help of the Multiple Scale Method. Let us introduce two time scales $\tau_0 = \tau$ and $\tau_1 = \varepsilon\tau$. The assumed form of the solution is as follows:

$$\Psi(\tau) = \Psi_0(\tau_0, \tau_1) + \varepsilon \Psi_1(\tau_0, \tau_1). \quad (13)$$

After substituting (13) into eq. (12) and arranging it with respect to powers of small parameter ε we obtain

- the equation of order ε^0

$$\frac{\partial \Psi_0}{\partial \tau_0} = 0, \quad (14)$$

- the equation of order ε^1

$$\begin{aligned} & \frac{\partial \Psi_1}{\partial \tau_0} + \frac{\partial \Psi_0}{\partial \tau_1} + \gamma (\Psi_0 + \bar{\Psi}_0 e^{-2i\tau_0}) + \\ & + i\eta \left(\Psi_0^3 e^{2i\tau_0} - 3|\Psi_0|^2 \Psi_0 + 3\Psi_0^2 \bar{\Psi}_0 e^{-2i\tau_0} - \bar{\Psi}_0^3 e^{-4i\tau_0} \right) = \\ & = f \left(e^{i(\tilde{\sigma}\tau_1)} + e^{-i(2\tau_0 + \tilde{\sigma}\tau_1)} \right) \end{aligned} \quad (15)$$

From eq. (14) appears that $\Psi_0 = \Psi_0(\tau_1)$.

The solution of eq. (15) should be limited. In that reason, the secular terms in (15) should be eliminated. That leads to the solvability condition

$$\frac{\partial \Psi_0}{\partial \tau_1} + \gamma \Psi_0 - 3i\eta |\Psi_0|^2 \Psi_0 = f e^{i(\tilde{\sigma}\tau_1)}. \quad (16)$$

Introducing polar representation

$$\Psi_0(\tau_1) = a(\tau_1) e^{i\delta(\tau_1)}, \quad (17)$$

where $a, \delta \in \Re$, we obtain the new form of the solvability condition

$$\frac{da}{d\tau_1} + ia \frac{d\delta}{d\tau_1} + \gamma a - 3i\eta a^3 = f e^{i(\tilde{\sigma}\tau_1)} e^{-i\delta}. \quad (18)$$

Taking advantage of the fact that $a(\tau_1)$ and $\delta(\tau_1)$, then multiplying the eq. (18) by ε and returning to the original denotations occurring in (6), one can obtain

$$\frac{da}{d\tau} + ia \frac{d\delta}{d\tau} + \frac{1}{2} \gamma_e a - \frac{3}{8} i \eta_e a^3 = \frac{\mu}{2} e^{i(\sigma\tau)} e^{-i\delta}. \quad (19)$$

Writing the exponential functions in the trigonometric form, and then separating real and imaginary parts in the equation, we have

$$\begin{aligned} & \frac{da}{d\tau} + \frac{1}{2} \gamma_e a = \frac{\mu}{2} \cos \theta, \\ & -a \frac{d\theta}{d\tau} + a\sigma - \frac{3}{8} \eta_e a^3 = \frac{\mu}{2} \sin \theta, \end{aligned} \quad (20)$$

where $\theta = \sigma\tau - \delta$ is modified phase. The eqs. (20) describe the modulation of the amplitude a and the modified phase θ .

4. Non-steady vibrations

In order to apply the LPT method, let us consider the non-damped vibrations ($\gamma_e = 0$). In that case the set of equations (20) has the first integral

$$H = -a \frac{\mu}{2} \sin \theta + \sigma \frac{a^2}{2} - \frac{3}{32} \eta_e a^4 = \text{const}, \quad (21)$$

where the constant of the right side depends on the initial conditions. The eq. (21) represents one-parameter family of the curves on the plane (a, θ) .

We are especially interested in the case, when maximal energy exchange between the system and the external loading appears. This situation takes place for $H=0$. In that case the first integral (21) has the form:

$$-16\mu \sin \theta + 16\sigma a - 3\eta_e a^3 = 0. \quad (22)$$

It is easy to show that the curve given by eq. (22) has extrema for $\theta = -\pi/2$ and $\theta = \pi/2$. The qualitative change in the behaviour of the system is observable for the critical value of nonlinearity parameter

$$\eta_e = \eta_c = \frac{64\sigma^3}{81\mu^2}. \quad (23)$$

In Figure 2 the trajectory curves on the plane (a, θ) for three values of η_e obtained from (22) are presented. All the graphs presented in the Figs. 2-6 are made assuming $\sigma = 0.01, \mu = 0.002$.

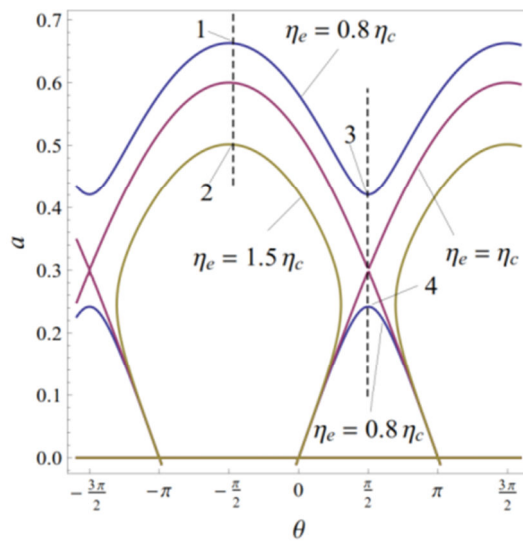


Figure 2. Phase trajectories for three values of η_e . Points 1, 2, 3, 4 identify roots of the eq. (22) for $\theta = -\pi/2$ and $\theta = \pi/2$

The maximum values of the amplitude $a_{max}(\eta_e)$ of vibrations are presented in Fig. 3. Points 1,2,3 and 4 in this figure identify the same solutions as in Fig. 2.

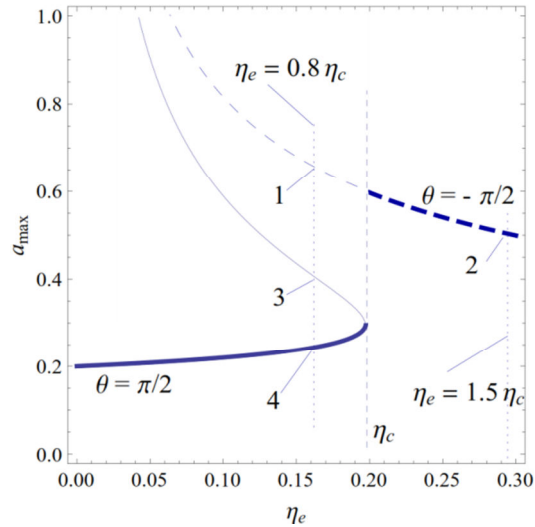


Figure 3. Graphs of $a_{max}(\eta_e)$ according to (22); thick line identifies a_{max} ; thin line reflect the open trajectories in the plane (a, θ) and do not describe vibrations

There is one more qualitative change in the phase portrait of vibrations on the plane (a, θ) for $\eta_e = 2\eta_c$. The metamorphoses of behavior of the system is clearly visible in time history of general co-ordinate. When η_e exceeds the critical value η_c or $2\eta_c$, the shape of modulation of amplitude rapidly changes. Amplitude modulation in time τ , obtained from the eqs. (20), are presented in Figs. 4-6.

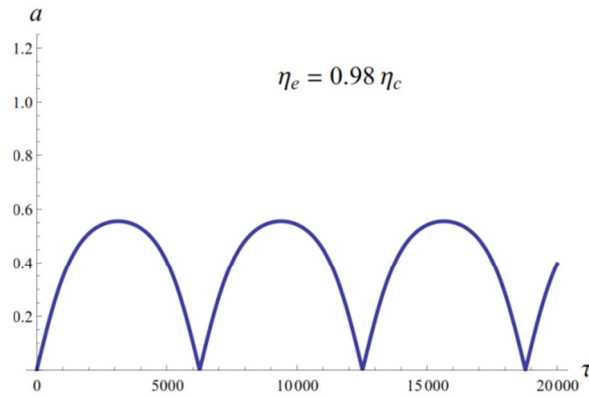


Figure 4. Amplitude modulation for η_e just below η_c ($\sigma = 0.01, \mu = 0.002$)

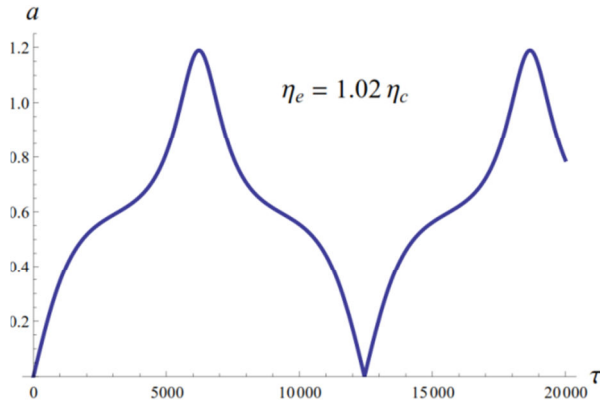


Figure 5. Amplitude modulation for η_e just above η_c ($\sigma = 0.01, \mu = 0.002$)

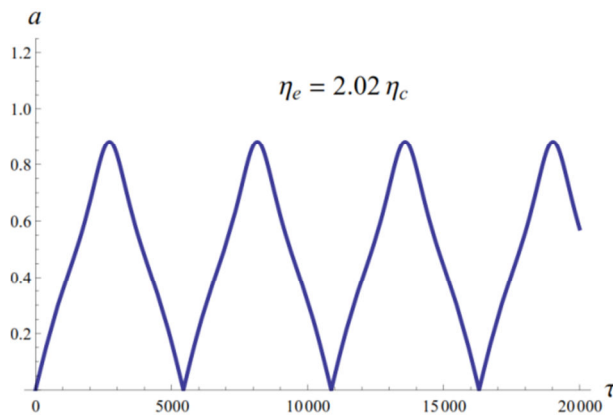


Figure 6. Amplitude modulation for η_e just above $2\eta_c$ ($\sigma = 0.01, \mu = 0.002$)

There are no other transformations of the phase-plane portraits and qualitative changes in behavior of a and θ for $\eta_e > 2\eta_c$.

5. Conclusions

Analysis of the nonlinear disks-shaft system has been done. The asymptotical Multiple Time Scale method has been adopted to solve the problem. It allowed us to exhibit an important dynamical transition in the non-steady state vibrations, leading to the drastic change of amplitude with increasing nonlinearity parameter (see Figs. 4- 6). The maximal amplitudes and trajectories on the plane (a, θ) have been presented (see Figs. 2,3). The graphs presented in the paper indicate the intensive energy exchange between the system and external excitation. All presented results have been obtained analytically and confirmed numerically.

Acknowledgments

The paper is supported by grant DS 21-418/2014 DS-PB.

References

1. Y.Huang Ying, S.Yang, F.Zhang, C.Zhao, Q.Ling, H.Wang, *Non-linear Torsional Vibration Characteristics of an Internal Combustion Engine Crankshaft Assembly*, Chinese J. Mech. Eng., **25**(4) (2012) 797- 808.
2. J. Kożešnik, Dynamika maszyn, WNT 1963.
3. L.I. Manevitch, A.I. Musienko, *Limiting Phase Trajectories and Energy Exchange Between Anharmonic Oscillator and External Force*, Nonlinear Dynamics **58** (2009) 633- 642.
4. B. Porter, *Non-Linear Torsional Vibration Of A Two-Degree of-Freedom System Having Variable Inertia*, J. Mech. Eng. Sci., **7**(1) (1965), 101- 113.
5. R. Starosta, *Nieliniowa dynamika układów dyskretnych w obszarach rezonansów w ujęciu asymptotycznym*, Nr 457 Rozprawy, Wydawnictwo PP, Poznań 2011.
6. Z. Wenming, W. Bohua, Z. Shuangshuang, L. Shuang, *Study on Bifurcation and Chaotic Motion of a Strongly Nonlinear Torsional Vibration System under Combination Harmonic Excitations*, Int. J. Com. Sci. **10**(3) (2013) 293- 299.

Effect of Pad Offset on the Stability of Jeffcott Rotor Operating in Tilting 4-Pad Journal Bearings

Stanisław STRZELECKI, Zdzisław SOCHA

Research Development Institute of Textile Machinery "POLMATEX-CENARO"

Wolczańska 55/591/15, 90-924 Łódź, Poland

stanislaw.strzelecki@p.lodz.pl, mariusz_krajewski@wp.pl

Zygmunt TOWAREK, Sergiusz ZAKRZEWSKI

Lodz University of Technology, Stefanowskiego 1/15, 90-924 Łódź, Poland

zygtow@p.lodz.pl, sergiusz.zakrzewski@p.lodz.pl

Abstract

Tilting-pad journal bearings are applied in high-speed rotor systems. Excellent stability properties allow obtaining the reliable, vibration free, operation of bearings and rotor. There is still need for better knowledge of such bearings static and dynamic characteristics. In case of tilting-pad journal bearings the stability can be evaluated by the system damping. The system damping gives the damping reserve of the bearings-rotor system and can be obtained by the solution of basic hydrodynamic and rotor motion equations. In this paper the hydrodynamic equations were solved by means of finite difference method. As result, the dynamic characteristics of bearings in form of stiffness and damping coefficients were obtained. These coefficients were the basis for the determination of the system damping.

Keywords: tilting-pad journal bearings, stability of rotor

1. Introduction

The journal bearing systems of modern high speed rotating machinery apply widely the radial tilting-pad journal bearings [1-6]. For such bearings the determination of both static and dynamic characteristics of system rotor-bearings, critical speeds, response of system on the dynamic load, stability of rotor and system damping, are very essential.

Tilting-pad pivot (pad support) can be positioned centrally or shifted from the centre of pad angular length. Angular position of pad pivot has an effect on the bearing static and dynamic characteristics. At assumed load applied to the bearing there are different bearing characteristics for the case of centrally pivoted pad or for the pivot offset, e.g. 0.6 to 0.7. The shifting of pivot from the central position to at least 55 percent position leads to a decrease of the maximum temperature of about 15°C [1]. Klumpp [3] obtained an increase in the values of oil film pressure at the increase of pivot-offset to 0.7.

The representative of tilting-pad journal bearings is the bearing with 4-pads. Some performances and applications of this bearing are showed in Table 1.

In case of tilting-pad journal bearings there is no stability limit [3-5]. It means that the stability properties of these bearings cannot be evaluated by method used for the multilobe or cylindrical bearings [1]. In case of tilting pad bearing the magnitude of stability reserve for the point of bearing operation in the range of stability is important. The value of damping determines how fast the vibrations decline after the disturbance of static position of operation [1-5].

Table 1 Performances of centrally pivoted, tilting 4-pad (4-PT) journal bearing

Type of bearing	Peripheral speed m/s	Unit load MPa	Sommerfeld number	Stiffness, Damping	Costs	Application
	30...100	0...2,5 (3,0)	0...1,0	oooo, oooo	oooo	Gear trains Steam turbines One shaft compressors

oooo – very high

(.) maximum values

Calculation of system damping consists in the application of the characteristic equation of the system rotor-bearings. But quite different as in case of the calculation of limiting speed, the damping is determined from characteristic equation at different angular speeds [1].

The paper presents the results of the theoretical investigation into the stability of Jeffcott rotor (symmetrically supported one mass rotor) operating in tilting 4-pad journal bearings at adiabatic, laminar oil film. The Reynolds', energy, viscosity and geometry equations determine the oil film pressure, temperature distributions, oil film resultant force that are the starting point for the calculations of dynamic characteristics of bearings and stability of rotor. Perturbation method was applied for the calculation of stiffness and damping coefficients of oil film. Stability limit was determined on the basis of system damping [5-8].

2. Oil film pressure and temperature distributions

The oil film pressure, temperature and viscosity distributions have been determined by means geometry, Reynolds, energy and viscosity equations [9-11]. The geometry of tilting 4-pad journal bearings and the system of coordinates show Fig. 1; the pads can be arranged in such a way that the applied load goes between the bottom pads (Fig. 1a) or is directed on the bottom pad (Fig. 1b).

The geometry of lubrication gap besides of the pad relative clearance ψ_s and the angle τ_0 of lobe centre line at stationary state is decided by angular orientation τ_1 centre point of pad. During determination of static equilibrium position of pad, the angle τ_1 should be varied as long as the magnitude of lubricating gap allows obtaining the oil film pressure distribution, which gives the resultant force to go through the support point of pad [3,9].

Geometry of lubricating gap of tilting pad journal bearing determines Eqn. (1).

$$\bar{H}(\varphi) = \psi_s + \frac{\psi_s - 1}{\cos(\tau_1 - \tau_o)} \cdot \cos(\varphi - \tau_1) - \varepsilon \cdot \cos(\varphi - \alpha) \quad (1)$$

where: ψ_s - pad relative clearance, φ - peripheral coordinate, α - attitude angle, ε - relative eccentricity of journal.

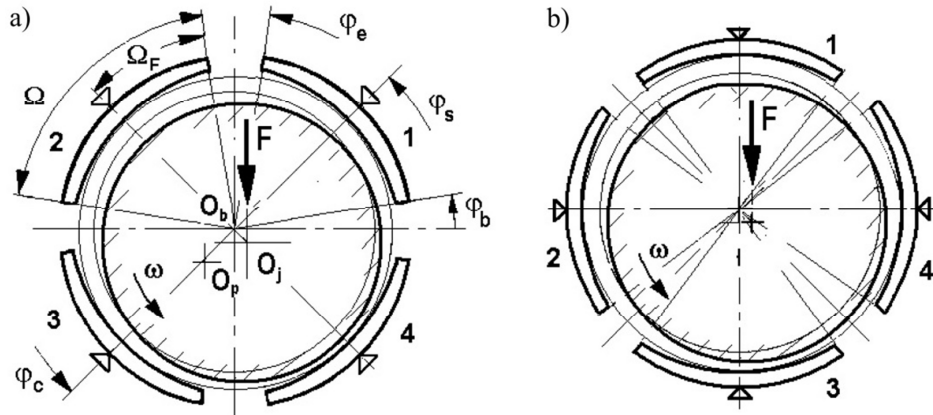


Figure 1. Geometry of tilting 4-pad journal bearings with centrally pivoted pads; a) – load between pads, b) – load on pad; φ_b , φ_c , φ_e , φ_s - angle of pad: begin, centre, end and support, respectively, Ω_F / Ω - pivot offset, $\Omega_F / \Omega = (\varphi_{s1} - \varphi_{b1}) / (\varphi_{e1} - \varphi_{b1})$

Reynold's equation applied in this paper has the form:

$$\frac{\partial}{\partial \varphi} \left(\frac{\bar{H}^3}{\bar{\eta}} \frac{\partial \bar{p}}{\partial \varphi} \right) + \frac{\partial}{\partial \bar{z}} \left(\frac{\bar{H}^3}{\bar{\eta}} \frac{\partial \bar{p}}{\partial \bar{z}} \right) = 6 \frac{\partial \bar{H}}{\partial \varphi} + 12 \frac{\partial \bar{H}}{\partial \phi} \quad (2)$$

where: $\bar{H} = h/(R-r)$ - dimensionless oil film thickness, h - oil film thickness (m), \bar{p} - dimensionless oil film pressure, $\bar{p} = p \psi^2 / (\eta \omega)$, p - oil film pressure (MPa), L - bearing length (m), D -sleeve diameter (m), R , r - sleeve and journal radius (m), \bar{z} - dimensionless axial co-ordinate, $\bar{\eta}$ - dimensionless viscosity, ΔR - radial clearance, $\Delta R = R-r$ (m), $\phi = \omega t$ - dimensionless time, t - time, ψ - bearing relative clearance, $\psi = \Delta R/r$ (%), ω - angular velocity (sec^{-1}).

It has been assumed for the pressure region that on the bearing edges the oil film pressure $\bar{p}(\varphi, \bar{z}) = 0$ and in the regions of negative pressure, $\bar{p}(\varphi, \bar{z}) = 0$. The oil film pressure distribution computed from Eqn. (2) was introduced in the transformed energy equation [9]. Temperature and viscosity distribution were found by the iterative solution of equations (1), (2) and energy one [9-11].

3. Stability of Jeffcot rotor

The equations of motion for the journal and the centre of elastic shaft are given in matrix form by Eqn. (3). All the stiffness and damping coefficients were calculated by means of perturbation method [1,6].

The motion of simple symmetric rotor can be described by the following equation [2]:

$$M \cdot \ddot{x} + B \cdot \dot{x} + C \cdot x = \hat{a} \cos \omega t + \hat{b} \sin \omega t \quad (3)$$

where: M, B, C –matrices of mass, damping and stiffness, \hat{a}, \hat{b} - coefficients of dynamic constraints.

After transformations of equation (3) the real and imaginary part was obtained [2,3]. The stability of elastic rotor-bearing system is analysed based on the following characteristic frequency equation of 6-th order with regard to (λ/ω) [2-6].

$$c_6(\lambda/\omega)^6 + c_5(\lambda/\omega)^5 + c_4(\lambda/\omega)^4 + c_3(\lambda/\omega)^3 + c_2(\lambda/\omega)^2 + c_1(\lambda/\omega) + c_0 = 0 \quad (4)$$

Solution assumption for Eqn. (4) is: $\lambda = -u + iv$, where: $u=1/(\omega T_z)$ and $v=\omega_e/\omega_{cr}$ with ω_e as self-frequency. The coefficients c_0 through c_6 in Eqn. (4) give the set of equations (5):

$$\begin{aligned} c_0 &= A_0; & c_1 &= A_1; & c_2 &= A_2 + a_0(2A_0 + b_0A_4); & c_3 &= a_0(2A_1 + b_0A_3) \\ c_4 &= 2a_0A_2 + a_0^2(b_0^2 + A_0 + b_0 \cdot A_4); & c_5 &= a_0^2(A_1 + b_0 \cdot A_3); & c_6 &= a_0^2A_2 \end{aligned} \quad (5)$$

where: a_0 – ratio of angular velocity to the angular self-frequency of stiff shaft, $a_0 = \omega^2 / \omega_{cr}^2$, b_0 – ratio of Sommerfeld number to the relative elasticity of shaft, $b_0 = So/c_s$, c^* – shaft stiffness, (Nm^{-1}), c_s – relative elasticity of shaft, $c_s = f/\Delta R = g/(\omega_{cr}^2 \cdot \Delta R)$, f – static deflection of shaft, (m), F – resultant force of oil film (N), F_{stat} – static load of bearing, (N), g – acceleration of gravity, (ms^{-2}), m – mass of the rotor, (kg), So – Sommerfeld number, $So = F \cdot \psi^2 / (L \cdot D \cdot \eta \cdot \omega)$, S_{ok} – critical Sommerfeld number, $S_{ok} = So \omega / \omega_{cr}$, ω_{cr} – angular self frequency of stiff rotor, $\omega_{cr} = \sqrt{c^* / m}$.

The terms A_0, A_1, A_2, A_3, A_4 , consist the stiffness g_{ik} ($i=1,2$ and $k=1,2$) and damping b_{ik} ($i=1,2$ and $k=1,2$) coefficients and they have the following meaning:

$$\begin{aligned} A_0 &= g_{11} \cdot b_{22} - g_{12} \cdot b_{21}; & A_1 &= g_{11} \cdot b_{22} + g_{22} \cdot b_{11} - g_{12} \cdot b_{21} - g_{21} \cdot b_{12} \\ A_2 &= b_{11} \cdot b_{22} - b_{12} \cdot b_{21}; & A_3 &= b_{11} + b_{22}; & A_4 &= g_{11} + g_{22} \end{aligned} \quad (6)$$

where: g_{ik} – dimensionless stiffness coefficients, $g_{ik} = So(\Delta R/F_{stat})$, g'_{ik} – stiffness coefficients, (N/m), b_{ik} – dimensionless damping coefficients, $b_{ik} = So(\Delta R/F_{stat})\omega \cdot b'_{ik}$, b'_{ik} – damping coefficients, ($N sec / m$)).

In case of bearing with the tilting pads interesting is not the absolute stability limiting speed but the magnitude of stability reserve (Fig. 2) for the point of bearing operation in the range of stability. Gienicke [1] investigated into the reserve of stability based on the damping of free vibration and introduced the term “System-damping”. The physical meaning of this term is shown in Fig. 2. The value of damping u determines how fast the vibrations decline after the disturbance of the static position of operation. It gives the magnitude of the stabilizing action of oil film with regard to the destabilizing effect of outside effects.

The damping is determined from characteristic equation (4) at different angular speeds ω . The explanation according to Fig. 2 has such advantage that the system damping u can be obtained as the function of revolutions or as the limiting speed ($u = 0$).

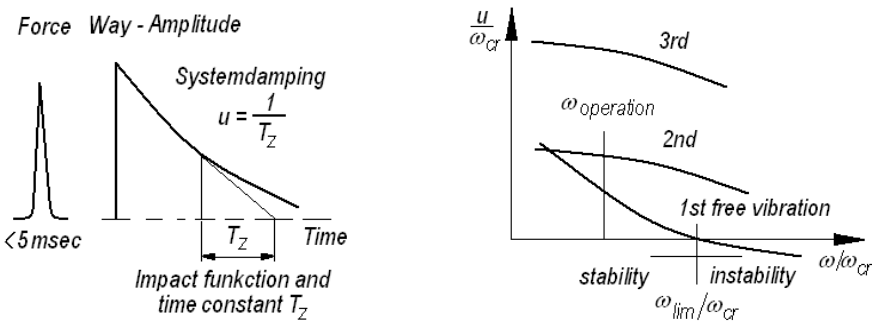


Figure 2. Damping of system according to Glienicke [1]; T_z – time constant

4. Results of calculations

The tilting 4-pad journal bearings of the length to diameter ratio $L/D=0.5$, the bearing relative clearance $\psi=2.0\%$ and $\psi=1.16\%$, relative clearance of the pad $\psi_s=2$ and the pivot offset $\Omega_F/\Omega=0.5$ and $\Omega_F/\Omega=0.6$ (Fig. 1) were taken into consideration. Calculations of dynamic characteristics were carried out for the bearings with the laminar oil film for the range of relative eccentricities $\varepsilon=0.1$ to $\varepsilon=0.8$. Vertical direction of load was assumed. The values of thermal coefficients were assumed as $K_T=0.114$ and $K_T=0.712$ at the oil feeding temperature $T_0=30^\circ\text{C}$ and $T_0=50^\circ\text{C}$, respectively and rotational speed 30000 rpm.

Some results of calculations of journal displacements ε versus Sommerfeld number S_0 , the stiffness g_{ik} and damping b_{ik} coefficients as well as the system-damping are shown in Fig. 3 through Fig. 7.

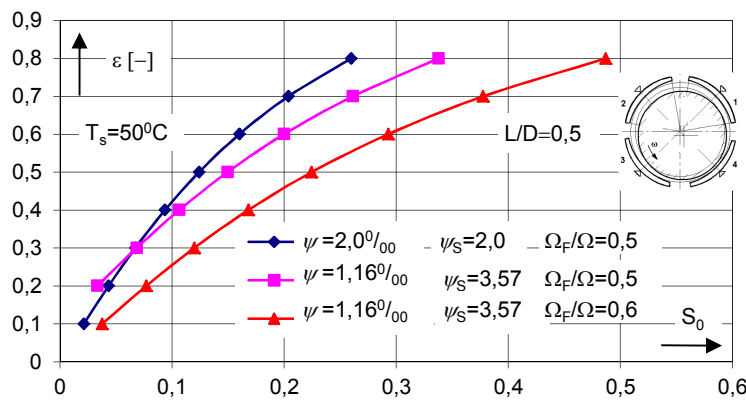


Figure 3. Journal displacement ε versus Sommerfeld number S_0 at different bearing parameters of tilting 4-pad journal bearing

The displacements of journal ε versus the load capacity S_0 (Sommerfeld number) at the length to diameter ratio $L/D=0.5$, different values of bearing relative clearance ψ , pad relative clearance ψ_s , pad offset Ω_F/Ω and the feeding oil temperature $T_s=50^\circ\text{C}$ is shown in Fig. 3. At assumed Sommerfeld number S_0 and pad offset Ω_F/Ω , and increase in the bearing relative clearance ψ at decreasing pad relative clearance ψ_s causes the increase in the journal displacement ε . However, at assumed bearing relative clearance ψ and pad relative clearance ψ_s the pad offset decreases the journal displacements (e.g. Fig. 3, at $S_0=0.2$ and $\Omega_F/\Omega=0.5$ the displacement $\varepsilon=0.6$ but at $\Omega_F/\Omega=0.6$ the displacement is $\varepsilon=0.45$).

Exemplary dynamic characteristics in form of stiffness g_{ik} and damping b_{ik} coefficients determined for the pad pivot offset $\Omega_F/\Omega=0.6$ are shown in Fig. 4 and Fig. 5. Stiffness g_{11} and g_{22} as well as damping b_{11}, b_{22} coefficients show the increase at the increase in Sommerfeld number S_0 . Among these coefficients the largest values have the stiffness g_{22} and damping b_{22} coefficients particularly at larger values of Sommerfeld numbers (e.g. Figure 4 and Figure 5). The coupled stiffness coefficients $g_{12} = g_{21}$ (Figure 4) and damping ones $b_{11} = b_{22}$ (Figure 5) are equal, respectively. However, the coupled stiffness g_{12}, g_{21} and damping coefficients b_{11}, b_{22} decrease at the increase in Sommerfeld numbers (Figure 4 and Figure 5); this is in agreement with the results of another authors, e.g. Klumpp [3].

The Systemdamping u/ω_{cr} was calculated with the use of the program Mathematica 5.0.

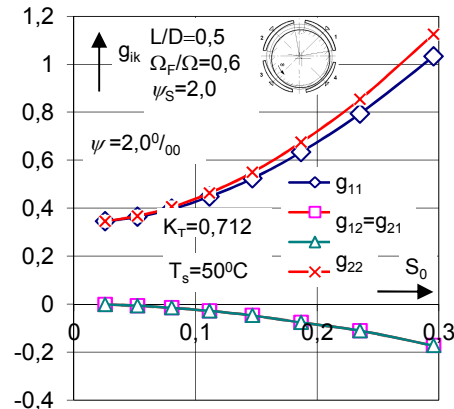


Figure 4 Stiffness coefficients of tilting 4-pad journal bearing

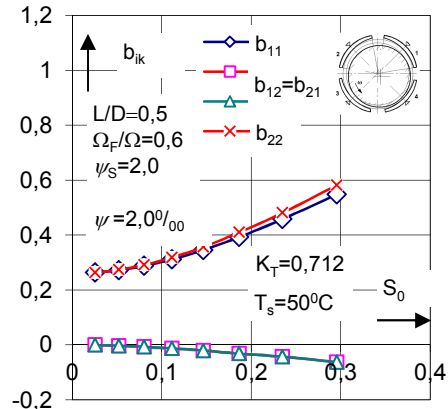


Figure 5 Damping coefficients of tilting 4-pad journal bearing

The system-damping u/ω_{cr} obtained by Klumpp [3] and Walle [4] is presented in Fig. 6. Author's results that were obtained for two values of pad offset, i.e. $\Omega_F/\Omega=0.6$ and $\Omega_F/\Omega=0.6$ are showed in Fig. 7; the run of all curves is similar to the runs that were obtained by Klumpp [3] and Walle [4] but different in the values of system-damping.

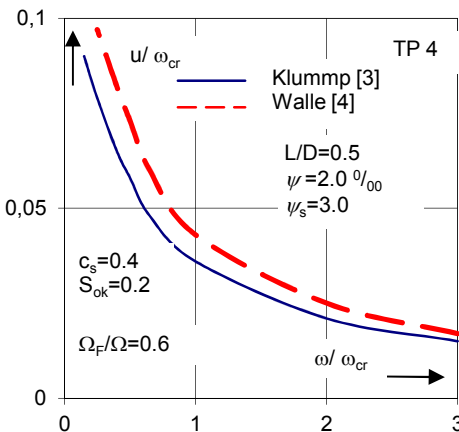


Figure 6. System-damping of tilting 4-pad journal bearing [3,17]

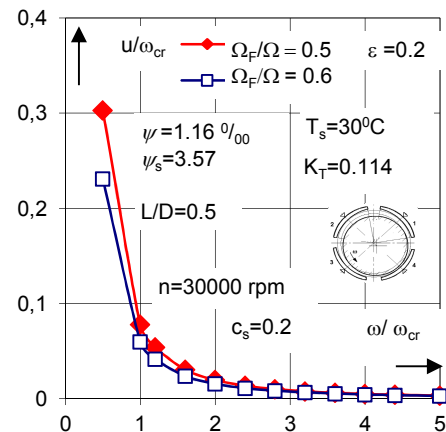


Figure 7. System-damping of tilting 4-pad journal bearing at different pad offset

5. Conclusions

The calculations and analysis of results has allowed drawing the conclusions given below.

1. An increase in pad offset Ω_F/Ω causes the variations in the journal displacements at assumed Sommerfeld number.
2. The stiffness and damping coefficients show changes at the variations of pad offset
3. An increase in pad offset generates the decrease in the system damping.

References

1. J. Glienick, *Theoretische und experimentelle Ermittlung des Systemdämpfung gleitgelagerter Rotoren und ihre Erhöhung durch eine äußere Lagerdämpfung*. Fortschritt Berichte. VDI, Reihe 11 Nr 13. 1972.
2. R. Gasch, H. Pfützner, *Rotordynamik*. Springer -Verlag. 1975
3. R. Klumpp, *Ein Beitrag zur Theorie von Kippsegmentlagern*. Dissertation, Technische Universität Karlsruhe. 1975.
4. F. Walle, *Unwuchtschwingungen und Systemdämpfung gleitgelagerter Rotoren unter praxisnahen Bedingungen*. Ph. D. Thesis. University Karlsruhe. Karlsruhe. 1975
5. D.C. Han, *Statische und dynamische Eigenschaften von Gleitlagern bei hohen Umgangsgeschwindigkeiten und bei Verkantung*. Dissertation. Karlsruhe. 1979.
6. S. Strzelecki, G.C.Jr. Brito, *Dynamics of Tilting Pad Journal Bearings of Large Overall Dimensions Applied in Hydro Generating Units*. Encontro Nacional de

- Monitoramento. Proceedings of the III ENAM. 29.10 – 03.11.2006. Foz de Iguasu. PR - Brasil. 1-12.
- 7. S. Strzelecki, S.M. Ghoneam, Z. Tawarek, *Stability of Tilting 5-Pad Journal Bearing*. Proceedings of the ISCORMA-4. Calgary 27-31.08. Canada. 2007.
 - 8. S. Strzelecki, Z. Tawarek, *Stability of rotor operating in multilobe or tilting-pad journal bearings*. 10th Conference on DYNAMICAL SYSTEMS. THEORY AND APPLICATIONS. December 7-10, 2009, Łódź, Poland. Proceedings Vol. 1. 473-480.
 - 9. S. Strzelecki, S.M. Ghoneam, *Static characteristics of tilting 3-pad journal bearing*. INTERTRIBO 2009 (October 21-23.2009, Slovak Republik). Proc. of the Conference. 52-55.
 - 10. S. Strzelecki, H. Kapusta, *Effect of Pivot Offset on the Oil Film Temperature Distribution in the Tilting 5-Pad Journal Bearing*. 14th International Colloquium Tribology, January 13-15, 2004. Germany. 971-976
 - 11. S. Strzelecki, *Effect of pivot location on the maximum oil film temperature of tilting 5-pad journal bearing*. IX International Symposium INTERTRIBO 2006. October 11-13, Vysoke Tatry Stara Lesna. 2006.

Acoustic Investigations of the Contemporary Churches in Poznań

Anna SYGULSKA

Poznan University of Technology, Faculty of Architecture

ul. Nieszawska 13 C, 61-021 Poznań

anna.sygulska@put.poznan.pl

Abstract

The paper discusses acoustic issues of contemporary churches. Church interiors should be designed so as to obtain intelligibility of speech and simultaneously take organ music into account. It is a tough task as acoustic parameters required for speech and organ music are entirely different. Analysis of the issue was carried out on the basis of investigations in five contemporary churches in Poznań. In total, seven interiors were investigated as two of the churches were two-storeyed. The acoustic investigations were conducted by means of an omnidirectional sound source, a SVAN 945A Sound Level Meter and the DIRAC programme. RT , Ts , $C80$ and $C50$ were measured. The acoustic parameters were compared with values recommended for churches. The investigations allowed to draw clear conclusions concerning the influence of architecture of the interior on acoustic parameters.

Keywords: church acoustics, acoustic investigation in church.

1. Introduction

Acoustics of the interior are tightly connected with the architecture of the building. Architecture of many churches promotes the occurrence of excessive reverberation, which limits intelligibility of speech. In result, the main function of the sacral interior, i.e. the conduct of liturgy, is considerably hindered. In addition, it is crucial to realize that acoustics in church interiors is a complex issue as it is difficult to combine entirely different acoustic requirements in one interior. The basis of a Roman Catholic liturgy is intelligibility of speech; however, liturgy involves organ music. Acoustic requirements for speech differ diametrically from those for organ music. Depending on the main function designed for a sacral interior, the recommended reverberation time takes different values, contingent on the cubature (Fig. 1).

In literature dealing with the issues of church acoustics, there are books like “*Czynnik akustyki w architektonicznym projektowaniu kościołów*” by Dominika Wróblewska and Andrzej Kulowski [10] and “*Podstawy akustyki obiektów sakralnych*” by Zbigniew Engel, Jacek Engel, Krzysztof Kosała and Jerzy Sadowski [4]. *Worship Space Acoustics* by Mendel Kleiner, David Lloyd Klepper and Rendell R. Torres [8] discusses issues of religious buildings of different faiths.

The issue of reverberance was described, among others, in the papers mentioned below. “*Akustyka wielofunkcyjna wnętrz sakralnych*” by Kosała K., Kamisiński T. [9] discusses the issue of excessive reverberance on the example of the St. Paul's Church in Bochnia. On the basis of measurements and acoustic simulations, acoustic treatment was suggested. *Acoustic properties of the selected churches in Poland* by Z. Engel, K. Kosała [5] presents a new method of acoustic assessment of religious buildings by means of the global index of the acoustic quality. The paper describes the application of the indexing

method for five Roman Catholic churches. *Acoustical characterization of the underground chapels of the new Holy Trinity church in the Fatima shrine* by Carvalho A. P. O., Nascimento B. F. O. [3] discusses acoustics of chapels of the Church of the Holy Trinity in Fatima. Acoustic measurements were taken and acoustic properties of the chapels were compared with typical religious buildings in Portugal. *Acoustic rehabilitation of middle twentieth century Portuguese churches* by Carvalho A. P. O., Cruz M. T., Pereira G. C. G. [2] describes the issue of too long reverberation time and poor intelligibility of speech in two churches from the first half of the 20th century. After investigations, acoustic treatment was suggested. *The improvement of acoustic situation in two modern churches* by Horvat M., Domitrovic H., Jambrosic K. [7] describes acoustic treatment of two newly built churches in Croatia. Results of the investigations were presented for each stage of the applied acoustic treatment.

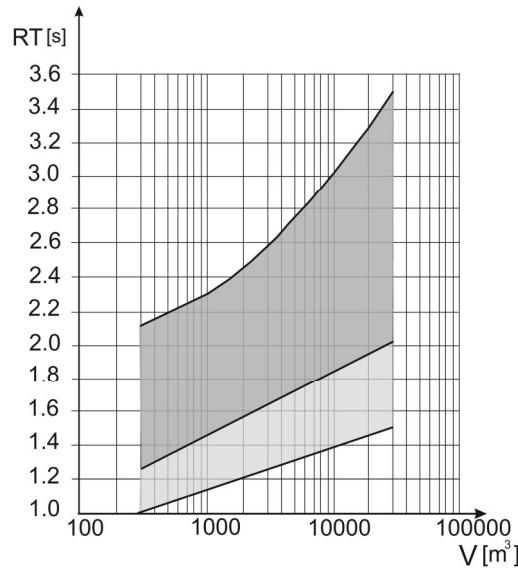


Figure 1. Range of optimum reverberation time for churches [6]

2. Description of the investigations

Acoustic problems of interiors were presented on chosen examples of contemporary churches in Poznań. The acoustic investigations were conducted by means of an omnidirectional sound source, a SVAN 945 A Sound Level Meter and the DIRAC programme. The Brüel & Kjær ZE-0948 USB Audio Interface was used. The e-sweep signal was generated and RT , Ts , $C80$ and $C50$ were measured. The measured acoustic parameters were compared with values recommended for churches. In total, seven interiors were investigated as two of the buildings were two-storeyed. The churches under investigation were compared in Table 1.

Table 1 Investigated churches

	<p>1 and 1a. Visitation of Blessed Virgin Mary Church (two-storey church)</p> <p>1. Upper church - cubature = 19000 m³ 1a. Lower church – cubature = 4800 m³</p>
	<p>2. Church of the Blessed Virgin Mary Mother of the Church</p> <p>Cubature = 6700 m³</p>
	<p>3 and 3a. Christ the King church (two-storey church)</p> <p>3. Upper church - cubature = 4600 m³ 3a. Lower church – cubature = 315 m³</p>
	<p>4. Church of the Nativity</p> <p>Cubature = 4800 m³</p>
	<p>5. Church of the Ascension</p> <p>Cubature = 4800 m³</p>

Table 2 shows the comparison of reverberation time RT and centre time Ts . Fig 2. shows the comparison of reverberation time RT in the frequency characteristics. The recommended values in all tables were taken from the book [10].

Table 2 Comparison of reverberation time and centre time

Name of the church	RT [s]			Ts [ms]	
	mean	500-1000 [Hz]	recommended mean	mean	recommended
1. Visitation of Blessed Virgin Mary Church – upper church	5.9	7.1	1.5-3.3	410	120 - 180
1a. Visitation of Blessed Virgin Mary Church – lower church	3.8	4.1	1.3 -2.7	298	60-100 organ music to 180
2. Church of the Blessed Virgin Mary Mother of the Church	2.7	3.2	1.3-2.8	196	70 – 120 organ music 120 -180
3. Christ the King church – upper church	3.3	3.8	1.3 -2.7	248	60-100 organ music to 180
3a. Christ the King church – lower church	1.6	1.6	1.3 -2.7	135	60-100 organ music to 180
4. Church of the Nativity	5.0	5.4	1.3 -2.7	367	60-100 organ music to 180
5. Church of the Ascension	2.9	3.2	1.3 -2.7	194	60-100 organ music to 180

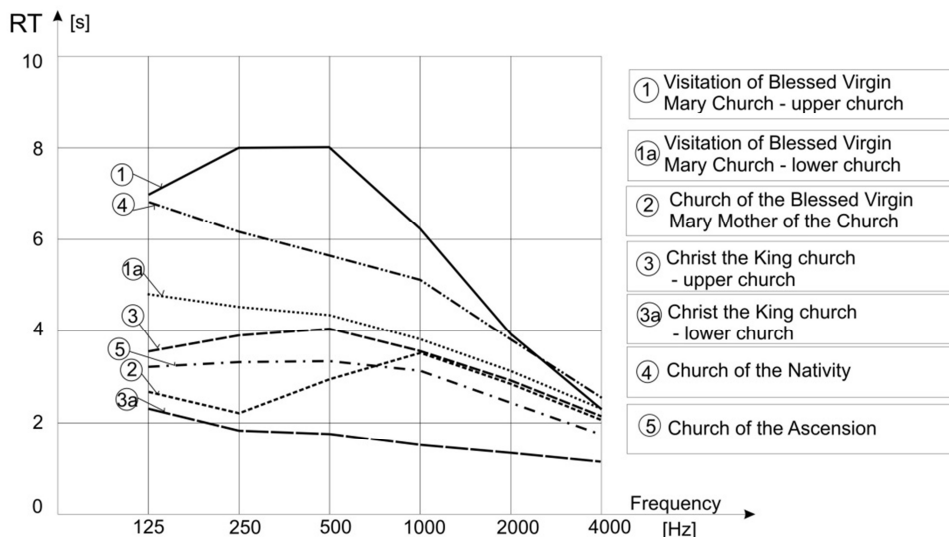


Figure 2. Frequency characteristics of averaged reverberation time in the investigated churches

In most of the investigated cases, reverberation time was too long. Most notably, church No 1 (of cubature equal to 19000 m^3) had a considerably exceeded reverberation time. The measured reverberation time was $RT = 5.9 \text{ s}$, whereas the recommended reverberation time for a church of this cubature equals $RT = 1.5 - 3.3 \text{ s}$. Reverberation time close to the recommended value occurred in churches No 2, 3a and 5. To assess the clarity of music sound, centre time T_s is applied; T_s is the center of gravity along the time axis of the squared impulse response [1]. T_s close to the recommended value occurred in churches No 2 and 5.

Table 3 shows results of measurements of clarity index $C80$. This parameter is applied to determine quality of the music sound. In the logarithmic scale, it describes the ratio of the energy of the sound reaching the measuring point within first 80 ms to the energy of the sound reaching it after 80 ms [6]. According to recommendations given in literature [10], $C80$ was averaged for 0.5, 1, 2 kHz. Apart from the rear part of church No 1a, the investigated churches had conditions suitable for organ music.

Table 4 presents results of measurements of clarity index $C50$. By analogy, the index is defined like $C80$. The measurements allow to calculate the weighted value of clarity index $C50$. Octave bands 0.5, 1, 2, 4 kHz are multiplied by the weighting factor equal to 0.15, 0.25, 0.35 and 0.25 for each band respectively; thus obtained results are added. In all examined churches, index $C50$ did not reach recommended values. It was at its closest to the recommended value in church No 3a, while it was particularly unfavourable in the rear part of church No 1a.

Table 3 Comparison of clarity index C80

Name of the church	C80 [dB]				
	first row	recommended	last row	recommended	general recommendations
1. Visitation of Blessed Virgin Mary Church – upper church	-2.6 -4.5 -8.2	>0	-5.9 -7.3 -8	-1 to 1	organ music -8 to -3 oratorio music -3 to 6
1a. Visitation of Blessed Virgin Mary Church – lower church	-1.8 -2.3 -3.3	>0	-17.3 -18.6 -17.9	>2	symphonic and oratorio music -3 to 6 organ music < -3
2. Church of the Blessed Virgin Mary Mother of the Church	-2.5 -1.4 -0.4	>0	-3.5 -5.1 -5.3	>2	symphonic and oratorio music -3 to 6 organ music < -3
3. Christ the King church – upper church	-2.0 -4.8 -6.2	>0	-5.3 -6.0 -5.3	>2	symphonic and oratorio music -3 to 6 organ music < -3
3a. Christ the King church – lower church	-0.7 0.3	3 to 8	-1.7 -1.6	-	> 6 electronic organ
4. Church of the Nativity	-4.5 -5.0 -5.6	>0	-8.4 -8.2 -8.0	>2	symphonic and oratorio music -3 to 6 organ music < -3
5. Church of the Ascension	-1.3 -3.3 -0.4 -3.6	>0	-4.6 -4.0 -4.1 -3.6	>2	symphonic and oratorio music -3 to 6 organ music < -3

Table 4 Comparison of clarity index $C50$

Name of the church	$C50$ [dB]		
	mean	range of variation	recommended
1. Visitation of Blessed Virgin Mary Church – upper church	- 8.6	-2 to -13	> -2
1a. Visitation of Blessed Virgin Mary Church – lower church	- 15.4	-3.8 to -41	> -2
2. Church of the Blessed Virgin Mary Mother of the Church	-8.1	-4.3 to -17	> -2
3. Christ the King church – upper church	-7.9	-2.9 to -12	> -2
3a. Christ the King church – lower church	-3.7	-2.7 to -5.5	> -2
4. Church of the Nativity	-8.6	-5.8 to -10.5	> -2
5. Church of the Ascension	-5.4	-0.6 to -8.0	> -2

3. Conclusions

The interiors of the examined churches show prominent lack of acoustic adaptation. Acoustic conditions in the churches result from the applied building materials with low sound absorptive coefficient. They are materials typical of the Polish religious buildings, i.e. brick, concrete, plaster, stone and glass. If the acoustic conditions are close to the recommended values, it is owing to either a small cubature of the building or the application of truss roof construction with a suspended ceiling. Church 3a with a small cubature is actually used as a chapel, while churches 2, 3 and 5 have suspended ceilings mounted on bottom chord of the truss. In church No 2, thin aluminium plates tiles were applied; the way of mounting ensures penetration of the sound to the spaces between the bars of the trusses. In church No 5, a construction of plaster-cardboard tiles was attached to the truss; among the tiles, there are several centimetres spaces. This way of mounting ensures penetration of the sound to the space between the ceiling and the roof. In both churches, such ceiling constructions boost sound absorption in contrast with a monolithic reinforced concrete ceiling in church No 4. Church No 3 also has a suspended ceiling mounted on trusses, but the church's timber construction tightly cuts off the interior from the space between the bars of the trusses, which results in the decrease of sound absor-

tion. It is recommended that churches with considerably exceeded reverberation time (1, 1a and 5) undergo acoustic treatment.

References

1. M. Barron, *Auditorium acoustics and architectural design*, Taylor & Francis, London; New York 2005.
2. A. P. O. Carvalho, M. T. Cruz, G. C. G.Pereira, *Acoustic rehabilitation of middle twentieth century Portuguese churches*, ICSV, Vilnius, Lithuania, July 08-12, 2012.
3. A. P. O. Carvalho, B. F. O. Nascimento, *Acoustical characterization of the underground chapels of the new Holy Trinity church in the Fatima shrine*, Portugal, Dania, Aalborg, Proceedings of Forum Acusticum (2011), 1429-1434.
4. Z. Engel, J. Engel, K. Kosała, J. Sadowski, „*Podstawy akustyki obiektów sakralnych*”, ITE, Kraków, 2007.
5. Z. Engel, K. Kosała, *Acoustic properties of the selected churches in Poland*, MECHANICS Vol. 24 No. 3. (2005), 173-181
6. F. A. Everest, K. C. Pohlmann, *Master handbook of acoustics*, Fifth edition, Mc Graw Hill, USA, 2009.
7. M. Horvat, H. Domitrovic, K. Jambrosic, *The improvement of acoustic situation in two modern churches*, Dania, Aalborg, Proceedings of Forum Acusticum (2011), 1439-1444.
8. M. Kleiner, D. L.Klepper , R. R. Torres, *Worship Space Acoustics* J. Ross Publishing, 2010.
9. K. Kosała, T. Kamisiński, „*Akustyka wielofunkcyjna wnętrz sakralnych*”, Czasopismo Techniczne / Politechnika Krakowska ; Seria: Architektura. Zeszyt 11, (2011), 115 -122.
10. D. Wróblewska, A. Kulowski, „*Czynniki akustyki w architektonicznym projektowaniu kościołów*”, Wydawnictwo Politechniki Gdańskiej, Gdańsk, 2007.

Impact of Pre-Stress on Stability and Vibration of Geometric Nonlinear Column at a Load Force Directed to the Positive Pole

Janusz SZMIDLA

Institute of Mechanics and Fundamentals of Machinery Design

University of Technology, Czestochowa, Poland

szmidla@imipkm.pcz.czest.pl

Ilona CIEŚLIŃSKA-GĄSIOR

Institute of Mechanics and Fundamentals of Machinery Design

University of Technology, Czestochowa, Poland

cieslinska@wp.pl

Abstract

The subject of the results of theoretical and numerical studies measures to designate the effect of pre-stress on the vibration of geometrically non-linear column exposed to the load force directed to the positive pole. Considering the total mechanical energy of the system the equation of motion and the boundary conditions necessary to solve the boundary problem were determined. Based on the kinetic stability criterion the range of values of internal compression forces was determined in which the growth of critical load of the column above the local loss of stability was achieved. In the research the geometrically non-linear system was analysed with variable asymmetry of bending stiffness and at selected values of geometrical parameters of the head realizing the load.

Keywords: free vibrations, geometrically non-linear system, pre-stressing

1. Introduction

The geometrically non-linear slender systems are the subjects of many scientific papers in which considered the issue of their stability and free vibrations at different ways of load and setup. In terms of stability testing of slender systems different load cases were investigated including conservative load (Euler's – [1]) and specific ([2]) and non-conservative load (generalized of Beck - 3). For columns which are geometrically non-linear critical load was determined using linear ([4]) and curvilinear ([5]) form of static balance. The course of changes in frequency of free vibrations as a function of the external load ([4,5]).

Another issue are the study of local and global instability geometrically non-linear systems ([4]). In this case, comparative analyses on the value of bifurcation load of geometrically non-linear columns and critical load of the respective linear columns. Under consideration of this system load cases the value of the external load at which loss of linear static balance was obtained, a function of the asymmetry factor bending stiffness between the rods geometrically non-linear column was determined. The local loss of stability occurs with much lower coefficients of bending stiffness asymmetry of models geometrically non-linear systems. In this case, the value bifurcation load of these models is less than the critical force of suitable linear model.

2. The physical model of the system

Figure 1 shows the physical model of geometrically non-linear column (**KN**) realizing the load force directed to the positive pole ([6]). The column consists of two pairs of rods (1,2) with symmetrical distribution of bending stiffness $(EJ)_1$, $(EJ)_2$, compressive stiffness $(EA)_1$, $(EA)_2$ and mass per unit length $(\rho A)_1$, $(\rho A)_2$. Linear system (**KL**) ([7]) was built with two rods with a total bending stiffness $(EJ)_1$ (without internal rods). The column is loaded by a Q -force by redundancy beam (5) and tension member (3) with a length l_B , whose angle with respect to the undeformed column axis x has a value of β . The rods of column are rigidly constrained ($x = 0$). At the free end ($x = l$) are hingedly connected to tie rod (3) by means of redundancy cubes (4) having a mass m . The direction of the external load P passes through a fixed point P , lying on the undeformed axis of the column. Variable position of the pole O was achieved by mechanical system (6).

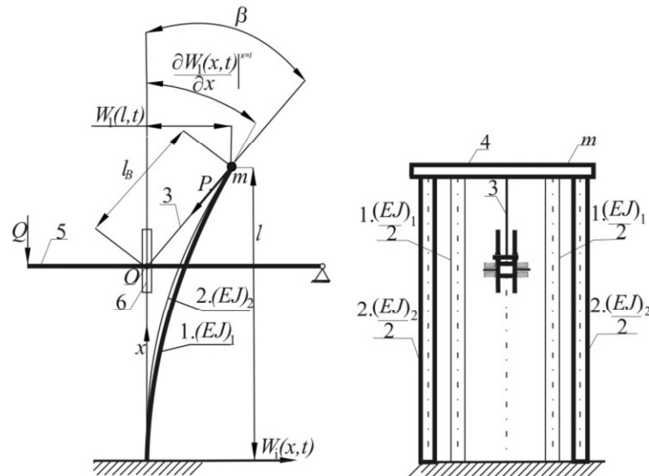


Figure 1. Physical model of geometrically non-linear column (**KN**) loaded with force tracking directed to the positive pole ([6])

In the description of the column (**KN**) is defined asymmetry value of bending stiffness μ :

$$\mu = \frac{(EJ)_2}{(EJ)_1}, \quad (1)$$

assuming that the sum of the bending stiffness geometrically non-linear system (**KN**) is constant:

$$T = \sum_{i=1}^2 \frac{(\rho A)_i}{2} \int_0^{l_i} \left[\frac{\partial W_i(x_i, t)}{\partial t} \right]^2 dx_i \quad (2)$$

$$\sum_{i=1}^2 (EJ)_i = idem \quad (3)$$

The rigidity in bending of the column rods (**KL**) is the same as the stiffness of rods the column index 1 (**KN**) with accepted asymmetry of bending stiffness of the model of geometrically nonlinear column described by coefficient μ .

Taking into account the physical model of the column shall be determined according with Bernoulli - Euler's theory of bending components of kinetic and potential energy. Kinetic energy T is the sum of kinetic energy of the individual column rods and body with a concentrated mass m :

$$T = T_1 + T_2 = \frac{1}{2} \sum_{i=1}^2 (\rho A)_i \int_0^l \left[\frac{\partial W_i(x, t)}{\partial t} \right]^2 dx + \frac{1}{2} m \left[\frac{\partial W_1(l, t)}{\partial t} \right]^2. \quad (4)$$

The total potential energy of the system is composed of energy: internal forces, elasticity in bending and components of external load.

$$V = \frac{1}{2} \sum_{i=1}^2 (EJ)_i \int_0^l \left[\frac{\partial^2 W_i(x, t)}{\partial x^2} \right]^2 dx + PU_1(l, t) + \frac{P}{2l_B} (W_1(l, t))^2 + \\ + \frac{1}{2} \sum_{i=1}^2 (EA)_i \int_0^l \left[\frac{\partial U_i(x, t)}{\partial x} + \frac{1}{2} \left(\frac{\partial W_i(x, t)}{\partial x} \right)^2 \right] dx. \quad (5)$$

where in: $W_i(x, t)$, $U_i(x, t)$ are appropriately transverse and longitudinal movement, and - the pair of rods of the geometrically non-linear system.

3 The wording of problems, the equations of motion, the boundary conditions

The issue of stability and vibration of geometrically nonlinear column solved using Hamilton's principle ([8]):

$$\delta \int_{t_1}^{t_2} (T - V) dt = 0 \quad (6)$$

where: δ means the operator of variations

Taking into account dependences (3) and (4) in equation (5) the prior use property of the commutative integration operation (with respect to x and t) and calculating the variation of mechanical energy, the equation of motion were obtained ([9]):

$$(EJ)_i \frac{\partial^4 W_i(x, t)}{\partial x^4} + S_i(t) \frac{\partial^2 W_i(x, t)}{\partial x^2} + (\rho A)_i \frac{\partial^2 W_i(x, t)}{\partial t^2} = 0 \quad i=1, 2, \quad (7a,b)$$

and the equation of longitudinal displacements of the individual rods of system:

$$U_i(x,t) = -\frac{S_i(t)}{(EA)_i}x - \frac{1}{2} \int_0^x \left[\frac{\partial W_i(x,t)}{\partial x} \right]^2 dx \quad i=1, 2, \quad (8a,b)$$

where in dependencies (6a,b) and (7a, b) included the definition of the longitudinal force

$$S_i(t) = -(EA)_i \left(\frac{\partial U_i(x,t)}{\partial x} + \frac{1}{2} \left(\frac{\partial W_i(x,t)}{\partial x} \right)^2 \right). \quad (9)$$

Geometrical boundary conditions considered system:

$$W_1(0,t) = W_2(0,t) = U_1(0,t) = U_2(0,t) = 0, \quad (10a-d)$$

$$U_1(l,t) = U_2(l,t), \quad W_1(l,t) = W_2(l,t), \quad (10e,h)$$

$$\left. \frac{\partial W_1(x,t)}{\partial x} \right|_{x=0} = \left. \frac{\partial W_2(x,t)}{\partial x} \right|_{x=0} = 0 \quad \left. \frac{\partial W_1(x,t)}{\partial x} \right|^{x=l} = \left. \frac{\partial W_2(x,t)}{\partial x} \right|^{x=l}, \quad (10i,j)$$

substituted into the equation (5) to give the other boundary conditions necessary to solve the boundary problem:

$$\sum_{i=1}^2 (EJ)_i \left. \frac{\partial^3 W_i(x,t)}{\partial x^3} \right|^{x=l} + P \left[\left. \frac{\partial W_i(x,t)}{\partial x} \right|^{x=l} - \frac{W_i(l,t)}{l_B} \right] - m \frac{\partial^2 W_i(l,t)}{\partial t^2} = 0, \quad (10k)$$

$$\sum_{i=1}^2 (EJ)_i \left. \frac{\partial^2 W_i(x,t)}{\partial x^2} \right|^{x=l} = 0 \quad (10l)$$

4. The results of calculations

Considering the solution of boundary value problem obtained on the basis of equations (6a, b), (7a, b) and the boundary conditions (9a-j) numerical studies on stability and free vibration on considered system was obtained.

In the figure 2a presented change of the force values of geometrically nonlinear bifurcation column (**KN**) and the critical load of the linear column (**KL**) as a function of the asymmetry bending stiffness factor μ . Critical load parameter λ_{cr}^* system (**KN**) and (**KL**) refers to the total bending stiffness of the system (**KN**) (Formula 10). It has been shown that this geometrically nonlinear system is characterized by a local and a global loss of stability. In terms of changes in values $\mu \in (0, \mu_{gr})$ bifurcation load (loss of linear static balance) is less than the critical load of the column (**KL**). For the local loss of stability corresponds instability of pair of rods with a smaller bending stiffness. Removal of geometrically nonlinear column of said bars causes a rapid increase in the critical force (transition from point A_1 to point A_2). Consequently in terms of the variation of

asymmetric distribution coefficient to bending stiffness of the rods $\mu \in (0, \mu_{gr})$ there is local instability of the system. For $\mu > \mu_{gr}$ there is a global loss of stability.

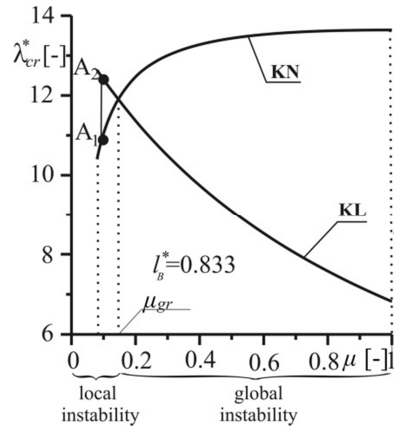


Figure 2a. Change of the critical parameter of load λ_{cr}^* in function of asymmetry factor bending stiffness distribution μ

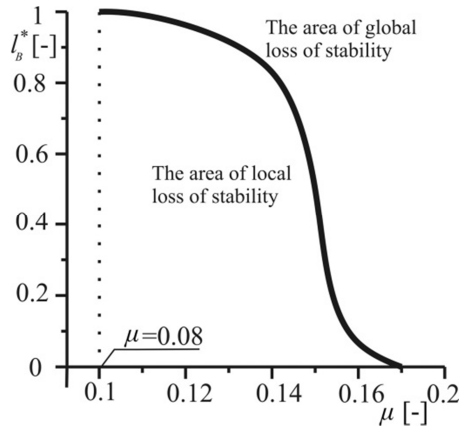


Figure 2b. Change the factor of length of the tendon l_B^* as a function of the limit distribution of the asymmetry factor u to the bending stiffness of the column

$$\lambda_{cr}^* = \frac{P_{cr}l^2}{\sum_{i=1}^2 (EJ)_i} \quad (11)$$

Characteristic of curve describing the range of variation values of the distance to the pole l_B^* (implementing head load parameter) based on the limit value of the asymmetry factor μ_{gr} bending is shown in Figure 2b. Discussed curve describes the value of the parameters (l_B^*, μ_{gr}) , and where there is equality of bifurcation load column (KN) and the critical load corresponding column (KL). On the basis of the presented curve range of local and global stability loss rectilinear form of static equilibrium system has been designated (KN).

In a paper considered the problem of the impact of pre-stress on the stability of the geometrically non-linear (KN). Figure 3 presents value range of critical load of geometrically non-linear column at initial pressurization (KNW) as a function of pre-stress (solid line). Calculations were performed at the selected asymmetry bending stiffness μ and given l_B^* parameter of implementing load head. Pre-stressing was achieved by introducing an additional force which initially stretched rods of smaller bending stiffness $(EJ)_2$. In this case the pair of rods - index (1) is subjected to a compression by force S_0 . Taking into account the description of the phenomenon of pre-stress, equal longitudinal displacement at the free end of the system (cf. formula (9e)) and Hooke's law, distribution of internal forces in each pair of rods of the geometrically non-linear system was defined (KNW).

$$S_1 = S_0 + \frac{P(EA)_1}{\sum_{i=1}^2 (EA)_i}, \quad S_2 = -S_0 + \frac{P(EA)_2}{\sum_{i=1}^2 (EA)_i}, \quad (12a,b)$$

where in $S_i > 0$ - strut, $S_i < 0$ – tension rebar

The lines number 3 and 4 mean the distribution parameter of internal forces S_1^* (curve 3), S_2^* (curve 4) corresponding to the critical load. S_0^* , S_1^* , S_2^* are defined as follows:

$$S_j^* = \frac{S_j l^2}{\sum_{i=1}^2 (EJ)_i} \quad j = 0, 1, 2. \quad (13)$$

If $S_0^* > 1.45$ hat the loss of stability occurs only as a result of the instability of rods bending stiffness $(EJ)_1$. In this case, the parameter S_2^* internal force in the rods of the bending stiffness $(EJ)_2$ is negative (tensile). It has been shown that in the range of pre-stress $S_0 \in (S_0^*, S_0^{**})$ to an increase of the critical load $(\lambda_{cr}^*)_{KNW}$ of the column (KNW) above the critical force contribution $(\lambda_{cr}^*)_{KL}$ line (line 2) - "out" from the scope of the local loss of stability. At point C, the column loses the stability as a result of the exclusive action of pre-stress.

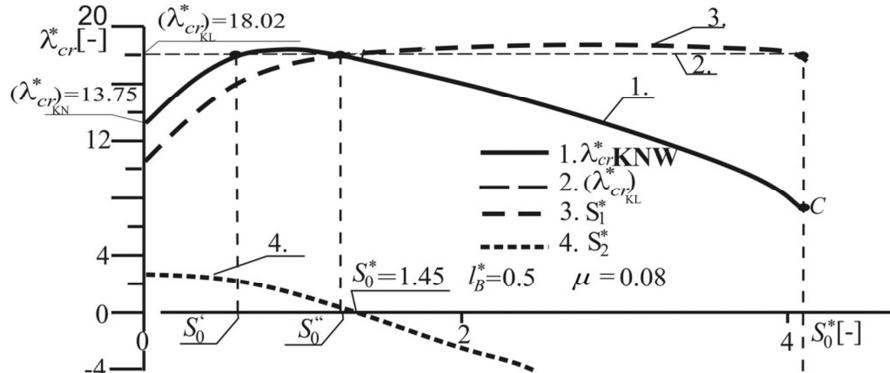


Figure 3. Critical force parameter λ_{cr}^* as a function of the internal forces S_0^*

Comparing the values of the bifurcation load of system (KN) and the column load (KNW) at selected values of the parameter S_0^* (Fig. 4a) showed that pre-stressing should be used in a limited range of changes in the asymmetry factor of flexural rigidity μ such $\mu \in (0, \mu_2)$ for $S_0^* = 3.434$ $\mu \in (0, \mu_3)$ for $S_0^* = 1.717$. The positive effects of pre-stress are obtained when the critical load parameter λ_{cr}^* column (KNW) is larger than the column parameter (KN) (curve 2, 3). In the case of $S_0^* = 4.85$ (curve 1), the -pre-stressing should not be used.

Figure 4b shows an example of the course of the frequency of free vibrations the system under consideration. In terms of parameter changes the internal force of the rods S_1^*

the bending stiffness $(EJ)_1$ in the range of $S_1^* \in (0, S_0^*)$ is pre-compressed system. Then the rod is exposed to external load λ^* where in:

$$\lambda^* = \frac{Pl^2}{\sum_{i=1}^2 (EJ)_i}, \quad \Omega^* = \frac{\sum_{i=1}^2 (\rho A)_i l^4 \omega^2}{\sum_{i=1}^2 (EJ)_i}. \quad (14a,b)$$

The value of the critical load were obtained for $\Omega=0$ parameters.

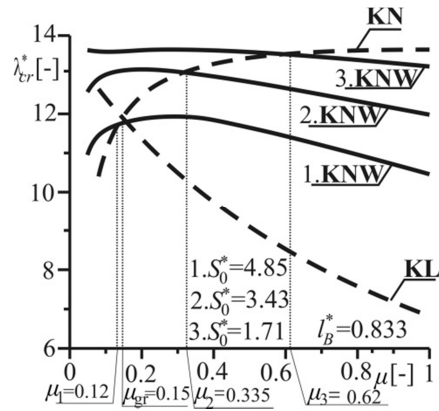


Figure 4a. Critical force parameter λ_{cr}^* as a function of variables internal forces S_0^*

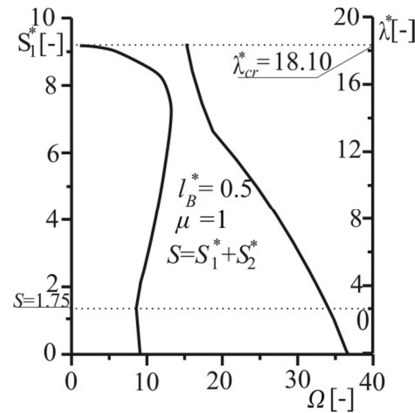


Figure 4b Mileage frequency of free vibrations of the system studied pre-compressed and loaded a dimensionless value of the external force λ^*

5. Conclusion

The subject of the paper was an analysis of vibration and stability of geometrical nonlinear column loaded with a force directed to the positive pole. The analysis of numerical results shows that the system under consideration depending on the value of the asymmetry factor decomposition bending stiffness is characterized by local or global loss of stability. Asymmetry parameter bending stiffness affects the value of the critical force of the geometrically nonlinear column. In terms of the influence of pre-stress on the vibration and stability of geometrically nonlinear column loaded with a force directed to the positive pole defines the scope of the pre-stressing for which it receives an increase in the critical load of the column above the limit of local loss of stability. It was found that the initial compression of the column in whole possible extent from the viewpoint of the value of bifurcation force is undesirable.

This applies especially to high pre-stress force values for which the results are opposite to expected (a significant reduction of the critical load). Pre-compression should be used for the columns characterized by local loss of stability.

Acknowledgments

The study has been carried out within the framework of project BS/PB-1-101-3020/11/P realized at Czestochowa University of Technology.

References

1. Z. P. Bazant, L. Cedolin, *Stability of Structures*. Oxford University Press, New York 1991.
2. L. Tomski, J. Szmidla, *Drgania i stateczność układów smukłych*, rozdział III. *Drgania swobodne i stateczność kolumn poddanych działaniu swoistemu – sztywne węzły konstrukcyjne układu wymuszającego i przyjmującego obciążenie*, Praca zbiorowa wykonana pod kierownictwem naukowym i redakcją L. TOMSKIEGO, Wydawnictwo Naukowo- Techniczne Fundacja Książki Naukowo-Techniczna Warszawa 2004.
3. M. Beck, *Die knicklast des einseitig eingespannten tangential gedruckten stabs*, ZAMP 4, 1953, 225-228, 476-477.
4. L. Tomski, J. Szmidla, *Local and global instability and vibration of overbraced Euler's column*, Journal of Theoretical and Applied Mechanics 41(1), 2003, 137-154.
5. L. Tomski, S. Uzny, *Free vibration and the stability of a geometrically non-linear column loaded by a follower force directed towards the positive pole*, International Journal of Solids and Structures, 45 (1), 2008, 87-112.
6. L. Tomski, J. Szmidla, *Drgania swobodne i stateczność obiektów smukłych, jako układów liniowych lub nieliniiowych*, rozdział IV, *Drgania swobodne i stateczność układów podanych działaniu obciążenia swoistego*, Praca zbiorowa wykonana pod kierownictwem naukowym i redakcją L. Tomskiego, Wydawnictwo Naukowo- Techniczne Fundacja Książki Naukowo-Techniczna Warszawa 2007.
7. A. Gajewski, M. Życzkowski, *Optymalne kształtowanie pręta ściskanego silą skierowaną do bieguna*, Rozprawa Inżynierska 1969, 2, 17, 299-329.
8. H. Goldstein, *Classical Mechanics*. Addison –Wesley Publishing Company, Inc., Cambridge, Mass 1950, 38-40.
9. M. Życzkowski, *Stateczność prętów i ustrojów prętowych część III, Wytrzymałość elementów konstrukcyjnych*, Mechanika Techniczna T.IX, Państwowe Wydawnictwo Techniczne, Warszawa 1988.

The Vibrations and the Stability of a Flat Frame Type Γ Realizing the Euler's Load Taking Into Account the Vulnerability of the Structural Node Connecting the Pole and the Bolt of the System

Janusz SZMIDLA

*Institute of Mechanics and Fundamentals of Machinery Design
University of Technology, Czestochowa, Poland
szmidla@imipkm.pcz.pl*

Justyna WIKTOROWICZ

*Institute of Mechanics and Fundamentals of Machinery Design
University of Technology, Czestochowa, Poland
wiktowicz@imipkm.pcz.pl*

Abstract

The paper presents the results of theoretical research and numerical calculations of the vibration and the stability of a twin rod flat frame subjected to the Euler's load. Considering the total mechanical energy of the system and using the kinematic stability criterion (Hamilton's principle) is determined by the equations of motion and boundary conditions considered system. The results of numerical calculations are presented at selected geometrical and physical parameters in the system for selected values of the rotary spring stiffness modeling the structural rigidity of the node connecting bolt with the column of frame.

Keywords: flat frame, free vibrations, Euler's load

1. Introduction

In the scientific literature concerning the stability of slender elastic systems stands out conservative and non-conservative load. Euler load and a force directed to the pole are classified as a conservative load type [1]. However Beck's generalized load [2] and Reut's load [3] are the cases of non-conservative load. Euler's load is a load by the longitudinal force and have a fixed anchor point and the direction who does not change during buckling.

In the case the conservative load there are also the system realizing a specific load [4]. The cases of this load formulated by L. Tomski [4, 5] combine the features of generalized load [6] or tracking load [2] and the load with force directed to the pole [7].

The flat frames are classified as open or closed. At the ends of closed frame system [11, 12] has been installed the support or heads which are carrying the load. In case when one of the ends of the system is free this system is called an open frame [8]. Most of scientific publications are considered a simple frames type Γ who have got the form of angle [8], three-rod type T [10, 15] and portal systems which is built of several simple framework [14]. In many scientific papers many of the theoretical and numerical research of framework due to the type of system load and the criteria of loss of stability had been drawned. In paper were presented the range of variation of the natural frequencies of system as a function of the external force [9] and the changes in the value of the

critical load [17] for the selected parameters of carrying load heads. In the studied issues of stability of flat frame also had been considered the initial inaccuracies of systems in the form of an eccentric load application [15] the elasticity of structural components (translational and rotational springs) for the method of connection the pole and bolt frame [16] or fixing these elements in the supports [8,12]. Shows the results of analysis of the influence of geometric imperfections in the form of right angle to the stability of the flat frames.

In this paper had been studied the impact of structural node connecting the bolt and the column to its own vibration and stability of twin rod closed flat frame type Γ treated Euler's load. Based on the kinetic stability criterion determined the equation of motion and the boundary conditions necessary to solve the boundary value problem. Taking into account the adopted geometric and physical parameters of the system the results theoretical and numerical calculations had been showed.

2. The physical model

Figure 1 shows the diagram of a flat frame type Γ subjected to the Euler's load.

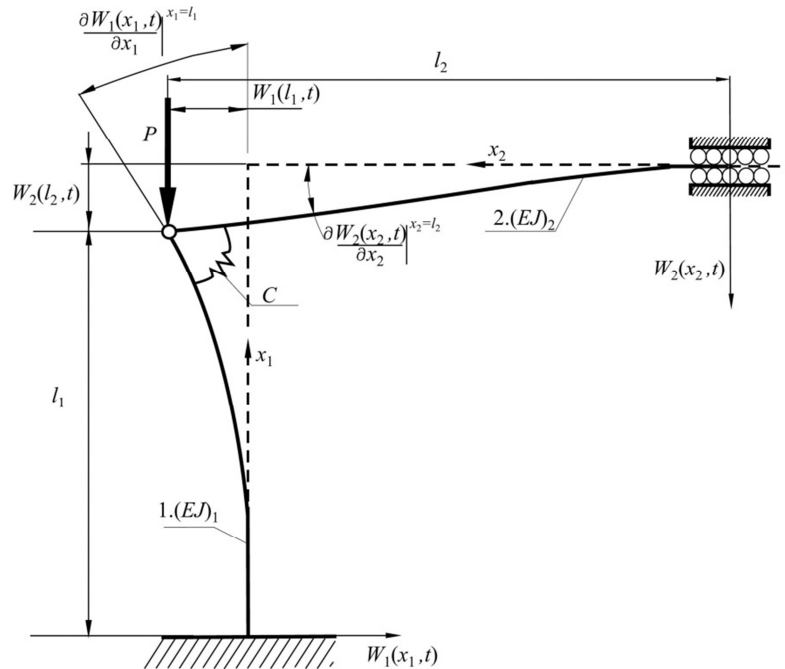


Figure 1. The physical model of frame type Γ subjected to Euler's load

The frame bolt of flexural rigidity $(EJ)_2$ was fixed rigidly but there is a possibility to longitudinal displacement however the pole of flexural rigidity $(EJ)_1$ was fixed rigidly without a possibility to longitudinal displacement. Both of them are connected by using

C - rigid spring. In the considered load case the pole of frame was charged by conservative force P which the direction of action passes through the pole and bolt connection.

3. Mechanical energy of systems, the equations of motion, boundary conditions

The kinetic energy T of contemplated flat frame is the sum of the kinetic energy of its individual bars:

$$T = \sum_{i=1}^2 \frac{(\rho A)_i}{2} \int_0^{l_i} \left[\frac{\partial W_i(x_i, t)}{\partial t} \right]^2 dx_i \quad (1)$$

The V - potential energy recording takes into account the elasticity of bending of the individual rods the direction of the external load and susceptibility structural node of flatframe (C -spring stiffness):

$$\begin{aligned} V = & \sum_{i=1}^2 \frac{(EJ)_i}{2} \int_0^{l_i} \left[\frac{\partial^2 W_i(x_i, t)}{\partial x_i^2} \right]^2 dx_i - \frac{P}{2} \int_0^{l_1} \left[\frac{\partial W_1(x_1, t)}{\partial x_1} \right]^2 dx \\ & + \frac{1}{2} C \left[\left. \frac{\partial W_1(x_1, t)}{\partial x_1} \right|_{x_1=l_1} - \left. \frac{\partial W_2(x_2, t)}{\partial x_2} \right|_{x_2=l_2} \right]^2 \end{aligned} \quad (2)$$

Considering the total mechanical energy of the system defined by (1), (2), the equation of motion and the boundary conditions of a frame were determined using principle of Hamilton [14]:

$$\delta \int_{t_1}^{t_2} (T - V) dt = 0 \quad (3)$$

The equation of motion:

$$\begin{aligned} (EJ)_1 \frac{\partial^4 W_1(x_1, t)}{\partial x_1^4} + P \frac{\partial^2 W_1(x_1, t)}{\partial x_1^2} + (\rho A)_1 \frac{\partial^2 W_1(x_1, t)}{\partial t^2} &= 0 \\ (EJ)_2 \frac{\partial^4 W_2(x_2, t)}{\partial x_2^4} + (\rho A)_2 \frac{\partial^2 W_1(x_1, t)}{\partial t^2} &= 0 \end{aligned} \quad (4a,b)$$

Geometrical boundary conditions:

$$\begin{aligned} W_1(0, t) = W_2(0, t) &= 0 \\ \left. \frac{\partial W_1(x_1, t)}{\partial x_1} \right|^{x_1=0} &= \left. \frac{\partial W_2(x_2, t)}{\partial x_2} \right|^{x_2=0} = 0 \end{aligned} \quad (5a-d)$$

Natural boundary conditions:

$$\begin{aligned} \frac{\partial^3 W_1(x_1, t)}{\partial x_1^3} \Big|_{x_1=0} + \frac{P}{(EJ)_1} \frac{\partial W_1(x_1, t)}{\partial x_1} \Big|_{x_1=l_1} &= 0 \\ \frac{\partial^3 W_2(x_2, t)}{\partial x_2^3} \Big|_{x_2=0} &= 0 \end{aligned} \quad (6a-d)$$

$$\begin{aligned} \frac{\partial^2 W_1(x_1, t)}{\partial x_1^2} \Big|_{x_1=0} + C_r \left[\frac{\partial W_1(x_1, t)}{\partial x_1} \Big|_{x_1=l_1} - \frac{\partial W_2(x_2, t)}{\partial x_2} \Big|_{x_2=l_2} \right] &= 0 \\ \frac{\partial^2 W_2(x_2, t)}{\partial x_2^2} \Big|_{x_2=0} + \frac{C_r}{\mu} \left[\frac{\partial W_2(x_2, t)}{\partial x_2} \Big|_{x_2=l_2} - \frac{\partial W_1(x_1, t)}{\partial x_1} \Big|_{x_1=l_1} \right] &= 0 \end{aligned}$$

in which:

$$\mu = \frac{(EJ)_2}{(EJ)_1}, \quad C_r = \frac{C}{(EJ)_1} \quad 7(a,b)$$

4. The results of numerical calculations

In this part of the paper the results of numerical calculations was presented. They were made on the basis of the solution of boundary value problem, while taking a constant flexural rigidity of the frame $(EJ)_1 + (EJ)_2 = const$ and a fixed sum of lengths of the bars of the $l_1 + l_2 = const$. The results were presented using the following dimensionless size:

$$\begin{aligned} \lambda^* &= \frac{P_{kr} (l_1 + l_2)^2}{(EJ)_1 + (EJ)_2}, \quad \mu = \frac{(EJ)_2}{(EJ)_1}, \quad \phi = \frac{l_2}{l_1}, \\ c_{lr}^* &= \frac{C(l_1 + l_2)}{(EJ)_1 + (EJ)_2}, \quad \Omega^* = \frac{[(\rho A)_1 + (\rho A)_2] \omega^2 (l_1 + l_2)^4}{(EJ)_1 + (EJ)_2} \end{aligned} \quad (8a-e)$$

The results of numerical simulations concerning the course of changes in the critical load parameter λ^* as a function of the parameter μ was presented in relation to the parameter of elasticity of the structural node c^* (Fig. 2). Taking into account a variable value of the parameter μ and maximum value of critical parameter of load λ^* obtained with the rigid connection of the column and the bolt of frame ($1/c^* = 0$). The nature of the presented curves mainly due to the assumed condition of constant bending stiffness of the system.

Figure 3 shows the sequence of changes in the critical load parameter λ^* as a function of the parameter of elasticity of the structural node c^* . The results are shown for various asymmetry value of the bending stiffness of the column and the bolt of frame μ . In any

case, you can determine the value of c^* above which the value of the critical load is only slightly modified. The graph curves 1.a - 4.a presents the stabilization of critical load λ^* with increasing rigidity of structural node. This occurs irrespective of the value of the asymmetry factor bending stiffness of the column and the bolt frame μ .

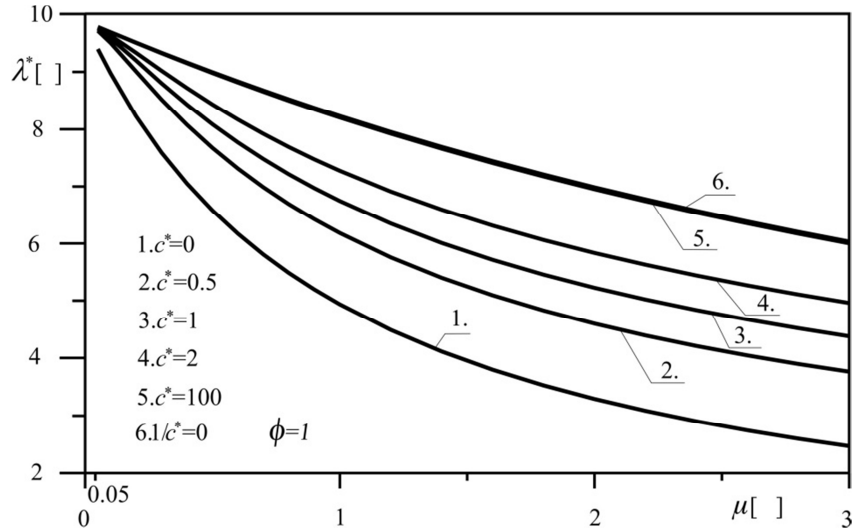


Figure 2. change the critical load parameter λ^* as a function of the parameter μ

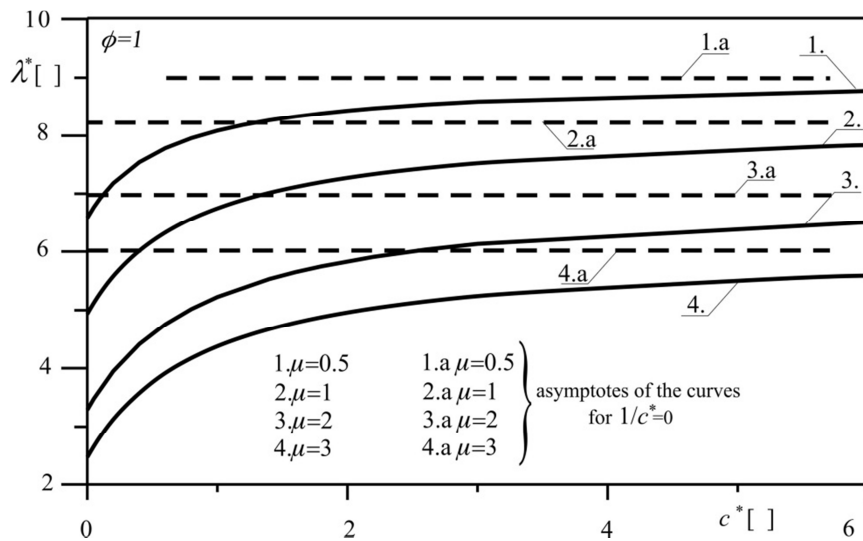


Figure 3. Change of the critical parameter of load λ^* as a function of c^* parameter

Figure 4 presents the results of numerical calculations for the free vibration of the frame. Illustrated are the relationship of the dimensionless external load parameter λ^* as a function of the dimensionless parameter frequency of free vibrations Ω^* . In terms of numerical calculations the nature of changes in the value of the first two fundamental natural frequencies Ω_1^* , Ω_2^* was determined. Constant asymmetry value of the bending stiffness of the column and lock the frame and the constant μ asymmetry value of the length of the bolt to the length of the pole frame ϕ was assumed. In the case of presented the course of changes in frequency of free vibrations, the value of the critical load λ^* obtained with the parameter frequency of free vibrations $\Omega_1^* = 0$. The results obtained parameter values of the critical load obtained on the basis of the kinetic stability criterion are the same as when using the static stability criterion.

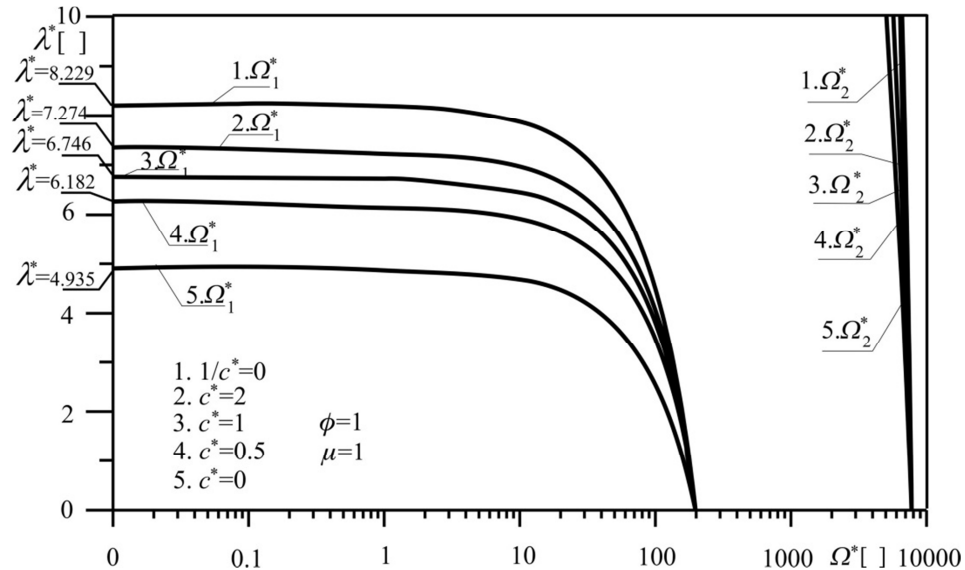


Figure 4. The curves in the plane: load parameter λ^* , the parameter resonance frequency Ω^* for a variable elasticity of connecting the pole with bolt of frame c^*

5. Conclusions

This paper presents the results of theoretical studies and numerical calculations on the twin rod flat frame type Γ vibration subjected to Euler's load. Taken into account the total mechanical energy of the system and based on kinematic stability criterion determined the equations of motion and boundary conditions considered system. Numerical calculations were performed at different values of the parameters under consideration, which include the asymmetry coefficient μ bending stiffness and rigidity of the structural node c^* connecting the pole with bolt frame. Taking into account the structural rigidity of the node connecting bolt to the column increases the critical load. The diagram

changes in frequency of free vibrations corresponds to systems with a load of slender conservative (divergent type system).

Acknowledgments

The study has been carried out within the framework of project BS/PB-1-101-3020/11/P realized at Częstochowa University of Technology.

References

1. H.H.E. Leipholz, *On Conservative Elastic Systems of the First and Second Kind*, Ingenieur-Archiv **43** (1974) 255-271.
2. M. Beck, *Die kniclast des einseitig eingespannten tangential gedruckten Stabes*. ZAMP **4** (1953) 225-228, 476-477.
3. S. Nemat-Nasser, G. Herrmann, *Adjoint Systems in Nonconservative Problems of Elastic Stability*, AIAA Journal **4**(12) (1966) 2221-2222.
4. L. Tomski, *Obciążenia układów oraz układy swoiste, rozdział 1, Drgania swobodne i stateczność obiektów smukłych jako układów liniowych lub nieliniowych*, Praca zbiorowa wykonana pod kierunkiem naukowym i redakcją L. TOMSKIEGO, Wydawnictwa Naukowo Techniczne, Fundacja „Książka Naukowo-Techniczna”, Warszawa 2007, 17-46.
5. L. Tomski, J. Szmidla, *Drgania swobodne i stateczność kolumn poddanych obciążeniu swoistemu - sztywne węzły konstrukcyjne układu wymuszającego i przejmującego obciążenie*, rozdział 3, *Drgania i stateczność układów smukłych*, Praca zbiorowa wykonana pod kierunkiem naukowym i redakcją L. TOMSKIEGO, Wydawnictwa Naukowo-Techniczne, Fundacja „Książka Naukowo-Techniczna”, Warszawa, 2004, 68-133.
6. Z. Kordas, *Stability of the Elastically Clamped Compressed Bar in the General Case of Behaviour of the Loading*, Bulletin de L'Academie Polonaise des Sciences **XI** (1963) 419-427.
7. A. Gajewski, M. Życzkowski, *Optimal shaping of an elastic homogeneous bar compressed by polar force*, Biulletyn de L'Academie Polonaise des Sciences, **17** (10) (1969) 479-488.
8. J. Szmidla, *Drgania swobodne i stateczność układów smukłych poddanych obciążeniu swoistemu*, Wydawnictwo Politechniki Częstochowskiej, Częstochowa 2009, 106-131.
9. J. Szmidla, *Stateczność i drgania ramy typu Γ obciążonej siłą skierowaną do biegu na*, Stability of Structures XIIth Symposium, Zakopane 2009, 395-402.
10. J. Szmidla, *Vibrations and stability of T – type frame loaded by longitudinal force in relation to its bolt*, Thin Walled Structures **45**(10-11) (2007) 931- 935.
11. M.H.R. Godley, A.H. Chilver, *Elastic buckling of overbraced frames*, Journal Mechanical Engineering Science **12**(4) (1970) 238-247.
12. L. Tomski, J. Szmidla, A. Kasprzycki, *Wybrane rozwiązania konstrukcyjne ram płaskich poddanych obciążeniu konserwatywnemu*, XXIII Sympozjum Podstaw Konstrukcji Maszyn, Rzeszów – Przemyśl 2007, 527-536.

13. A.N. Kounadis, G.I. Ioannidis, *The primary bending effect and buckling boundary-value problem in elastic framed structures*, Engineering Structures **19**(6) (1997) 432-438.
14. E. Mesquita Neto, S.F.A. Barretto, Pavanellor, *Dynamic behaviour of frame structures by boundary integral procedures*, Engineering Analysis with Boundary Elements **24** (2000) 399-06.
15. J. Przybylski, L. Tomski, *Postbuckling Behaviour of T-frame with Reinforced Vertical Bar*, Stability of Steel Structures, Edited by M. Ivanyi, Vol.1, Akademiai Kaido, Publishing House of Hungarian Academy of Science, Budapest 1995, 173-180.
16. D.S. Sophianopoulos, The effect of joint flexibility on the free elastic vibration characteristic of steel plane frames, Journal of Construction Steel Research **59** (2003) 995-1008.
17. L. Tomski, M. Gołebiowska – Rozanow, J. Przybylski, J. Szmidla, *Stability and vibration of two-member frame under generalised load*, Stability of Steel Structures, Edited by M. Ivanyi, Vol.1, Akademiai Kaido, Publishing House of Hungarian Academy of Science, Budapest 1995, 493- 500.
18. L. Meirovitch, *Analytical methods in vibration*, Macmillan Company, New York, 1967, 42- 45.

An Application of Longitudinal Elastic Waves for Investigation of Materials Under High Strain Rates Using the Hopkinson Bar

Tomasz SZOLC

Institute of Fundamental Technological Research of the Polish Academy of Sciences
ul.A. Pawińskiego 5B, 02-106 Warszawa
tszolc@ippt.pan.pl

Zbigniew L. KOWALEWSKI

Institute of Fundamental Technological Research of the Polish Academy of Sciences
ul.A. Pawińskiego 5B, 02-106 Warszawa
zkowalew@ippt.pan.pl

Abstract

In the paper there is presented a discrete-continuous model of the Split Hopkinson Pressure Bar (SHPB) for numerical simulations of a dynamic behaviour of material specimens under high strain-rates. For this purpose several material theories describing visco-elasto-plastic properties of the tested specimens can be applied. Using this model impact-type dynamic responses are sought by means of the longitudinal elastic wave analytical solution of the d'Alembert type. The proposed model enables us theoretical strength investigations for various elasto-plastic materials under great deformation velocities as well as structural parameter determination of the real SHPB designed to play a role of the laboratory test-rig.

Keywords: Hopkinson bar, elastic wave propagation, d'Alembert solution, numerical simulation

1. Introduction

High strain rate experimental tests are important in mechanical property analysis of materials under strongly dynamic conditions. The Split Hopkinson Pressure Bar (SHPB) has been widely used to investigate dynamic behaviour of various materials within the strain rate range of 10^2 to 10^4 s^{-1} [1-4]. In 1872 John Hopkinson investigated a stress wave propagation in a wire [1] which was the starting point for his son Bertram, who developed a measurement method for the movement recording of a cylinder during strongly dynamic conditions [2]. In 1948, Kolsky used two elastic bars instead of one with the specimen placed between them [3]. Since that date, this device has been known as the SHPB. Such experimental technique can be applied in many configurations, for example in compression, tension, torsion and shear. According to the one-dimensional elastic wave propagation theory, the "safe" maximum impact velocity is directly related to the elastic limit of the incident bar. Such condition limits the maximum strain rate in the test. As it was mentioned above, many problems appear using the SHPB technique. In order to provide better understanding of this technique, in this paper a discrete-continuous, semi-analytical model of the SHPB with an elasto-plastic material specimen has been developed as an alternative to the commonly applied, time-consuming, non-linear finite element models with huge numbers of degrees of freedom.

2. Continuous modelling and wave solution for the Split Hopkinson Pressure Bar

Since the longitudinal elastic wave propagation process is going to be investigated as a measurement tool for material specimens under high strain rates, in the proposed model the incident and transmitting bar of the SHPB are represented by continuous and homogeneous elastic cylindrical elements of mutually identical circular cross-sections and lengths l_1 and l_2 , respectively. The transmitting bar is visco-elastically fixed to a rigid wall by the use of the mass-less spring of stiffness k_0 and damping coefficient c_0 . The material specimen of mass $2m$, the length of which is much smaller than these of the incident and transmitting bar, can be substituted by two rigid bodies of identical masses m connected with each other by means of the mass-less, non-linear spring with response dependent visco-elastic characteristics $c(\Delta\ddot{u}(t))$ and $k(\Delta u(t))$ describing visco-elasto-plastic properties of the investigated material. The wafer has usually a cylindrical shape with length $l_0 \ll l_1, l_2$ and cross-sectional stiffness EA equal to these of the incident and transmitting bar. Despite of its natural continuous structure, in order to simulate the impact process, the wafer can be regarded as a rigid body of mass m_0 impacting the incident bar with initial velocity v_0 using an intervention of the mass-less spring. Stiffness k_e of this spring has been determined assuming that the incident wave excited due to the impact has a length corresponding to the double-period of the longitudinal elastic wave propagation in the wafer. Thus, $k_e = EA\pi^2/l_0$. According to the above assumptions, the proposed discrete-continuous model of the SHPB has a structure demonstrated in Fig. 1.

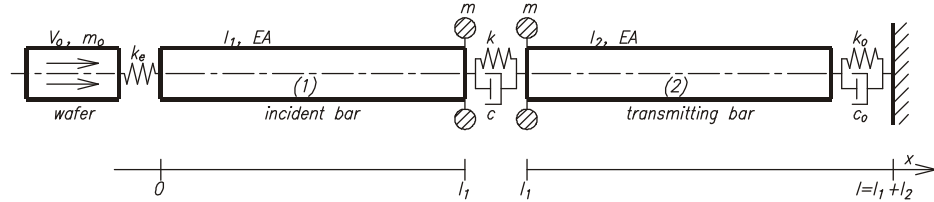


Figure 1. Discrete-continuous model of the SHPB

Motion of cross-sections of the continuous elements representing the incident and transmitting bar is governed by the following homogeneous partial differential equations

$$a^2 \frac{\partial^2 u_i(x,t)}{\partial x^2} - \frac{\partial^2 u_i(x,t)}{\partial t^2} = 0, \quad a = \sqrt{E/\rho}, \quad i = 1, 2, \quad (1)$$

where E is Young's modulus, ρ denotes the material density and $u_i(x,t)$ are the longitudinal displacements of bar cross-sections, x is the spatial co-ordinate and t denotes time. Equations of motion (1) are solved with the following boundary conditions describing the support of the SHPB by the rigid wall, dynamic interaction of the elasto-plastic material specimen as well as an impact-type excitation by the wafer:

$$m_0 \frac{du_0(t)}{dt^2} - k_e [u_0(t) - u_1(x,t)] = 0, \quad EA \frac{\partial u_1(x,t)}{\partial x} - k_e [u_0(t) - u_1(x,t)] = 0 \text{ for } x = 0,$$

$$\begin{aligned}
m \frac{\partial u_1(x,t)}{\partial t^2} + c(\Delta u) \left[\frac{\partial u_1(x,t)}{\partial t} - \frac{\partial u_2(x,t)}{\partial t} \right] + EA \frac{\partial u_1(x,t)}{\partial x} + k(\Delta u) [u_1(x,t) - u_2(x,t)] &= 0, \\
m \frac{\partial u_2(x,t)}{\partial t^2} + c(\Delta u) \left[\frac{\partial u_2(x,t)}{\partial t} - \frac{\partial u_1(x,t)}{\partial t} \right] - EA \frac{\partial u_2(x,t)}{\partial x} + k(\Delta u) [u_2(x,t) - u_1(x,t)] &= 0 \\
&\quad \text{for } x = l_1, \\
EA \frac{\partial u_2(x,t)}{\partial x} + d_0 \frac{\partial u_2(x,t)}{\partial t} + k_0 u_2(x,t) &= 0 \quad \text{for } x = l_1 + l_2, \quad (2)
\end{aligned}$$

where A denotes the area of the bar cross-section and $u_0(t)$ is the generalized co-ordinate describing motion of the wafer mass center.

A dynamic response of the SHPB model excited by a wafer impact is sought using the d'Alembert wave solutions of motion equations (1) in the similar form, as in [5]:

$$u_i(x,t) = f_i(a(t-t_{0i}) - x + x_{0i}) + g_i(a(t-t_{0i}) + x - x_{0i}), \quad i = 1, 2. \quad (3)$$

The functions f_i and g_i represent longitudinal waves induced by the excitation impulse due to the wafer impact, where the function f_i represents a longitudinal wave propagating in the i -th continuous macro-element along the x -axis positive sense, Fig. 1; however, the function g_i represents a longitudinal wave propagating along the x -axis negative sense and a denotes the wave propagation velocity. According to the one-dimensional wave propagation theory, it is taken into account in (3) that the first perturbation in the i -th macro-element occurs in the cross-section of the co-ordinate x_{0i} after the finite time delay t_{0i} . Furthermore, it is assumed that the functions f_i and g_i are continuous and are null for negative arguments, i.e. before arriving the first perturbation.

Since solutions (3) identically satisfy motion equation (1), actual values of the wave functions, f_i and g_i , are determined by the boundary conditions of the problem. Thus, by substituting the wave solutions (3) into the boundary conditions (2), denoting the largest argument in each equation by z , and by rearranging these equations in such a way that their right-hand sides are always known, in the considered case of the bars with a constant cross-sections we obtain the following system of ordinary differential equations of the second order with a "retarded" argument for the functions f_i and g_i , $i=1,2$:

$$\begin{aligned}
(R + D_0)g''_2(z) + K_0g'_2(z) &= (R - D_0)f''_2(z - 2\lambda_2) - K_0f'_2(z - 2\lambda_2), \\
\begin{bmatrix} M & 0 \\ 0 & M \end{bmatrix} \begin{bmatrix} g''_1(z + \lambda_1) \\ f''_2(z) \end{bmatrix} + \begin{bmatrix} p & -C \\ -C & p \end{bmatrix} \begin{bmatrix} g'_1(z + \lambda_1) \\ f'_2(z) \end{bmatrix} + \begin{bmatrix} K & -K \\ -K & K \end{bmatrix} \cdot \begin{bmatrix} g_1(z + \lambda_1) \\ f_2(z) \end{bmatrix} &= \\
= \begin{bmatrix} -Mf''_1(z - \lambda_1) + rf'_1(z - \lambda_1) + Cg'_2(z) + K[g_2(z) - f_1(z - \lambda_1)] \\ -Mg''_2(z) + rg'_2(z) + Cf'_1(z - \lambda_1) - K[g_2(z) - f_1(z - \lambda_1)] \end{bmatrix}, \quad (4)
\end{aligned}$$

$$\begin{bmatrix} M_0 & 0 \\ 0 & 0 \end{bmatrix} \begin{bmatrix} u''_0(z) \\ f''_1(z) \end{bmatrix} + \begin{bmatrix} 0 & 0 \\ 0 & R \end{bmatrix} \begin{bmatrix} u'_0(z) \\ f'_1(z) \end{bmatrix} + \begin{bmatrix} K_e & -K_e \\ -K_e & K_e \end{bmatrix} \begin{bmatrix} u_0(z) \\ f_1(z) \end{bmatrix} = \begin{bmatrix} K_e g_1(z) \\ R g'_1(z) - K_e g_1(z) \end{bmatrix},$$

where:

$$R = \frac{EAl_s}{a^2 m_s}, K_0 = \frac{k_0 l_s^2}{a^2 m_s}, D_0 = \frac{d_0 l_s}{am_s}, C(\Delta\dot{u}(z)) = \frac{c(\Delta\dot{u}(t))l_s}{am_s}, \lambda_i = \frac{l_i}{l_s}, i = 1, 2,$$

$$K(\Delta u(z)) = \frac{k(\Delta u(t))l_s^2}{a^2 m_s}, K_e = \frac{k_e l_s^2}{a^2 m_s}, M_0 = \frac{m_0}{m_s}, M = \frac{m}{m_s}, u_0(z) \equiv u_0(t),$$

$p=R+C$, $r=R-C$ and l_s [m], m_s [kg] are the reference distance and mass, respectively.

The above equations have been solved numerically by means of the Newmark method using the appropriately small direct integration step in order to obtain a sufficient accuracy of results of simulation of the impact-type dynamic process. The right-hand sides of the equations with a shifted argument, which are known after each integration step, similarly as in [5], enable us their very efficient solving one after another, i.e. in the sequence defined here by (4). In the considered case, it has been assumed that when the impact process is over, i.e. when the elastic strain in the incident bar cross-section $x=0$ goes back to zero value, the quantities m_0 and k_e in (2) and (4) will become null during simulation.

3. Computational example

An object of consideration is the discrete-continuous model of the real laboratory test rig in the form of a classical SHPB. Here, the diameters of the incident and transmitting steel bar as well as of the wafer are equal to 0.02 m. The incident bar length l_1 is equal to 1.05 m and the length of the transmitting bar $l_2=1.07$ m. By means of the presented SHPB model three cylindrical specimens of diameter 0.01 m and length 0.01 m each and made of 34GS steel, M1E copper and 7075 aluminium alloy have been tested. In all cases the SHPB was impacted by the wafer of mass $m_0=0.61$ kg with an initial velocity 50 m/s. The characteristics $c(\Delta\dot{u}(t))$ and $k(\Delta u(t))$ for all specimens mentioned above have been properly identified using the simplified Burgers material model, [6], which for the force equilibrium formulation in (2) can be reduced to the Voigt material model. This approach seems to be very convenient at the introductory stage of this problem investigation, where a demonstration of system dynamic responses in the form of longitudinal elastic wave propagation due to wafer impact is the main goal of the presented considerations. Nevertheless, the functions $c(\Delta\dot{u}(t))$ and $k(\Delta u(t))$ in (2), (4) can be regarded here as properly identified constants or response dependent variables, [7].

In Fig. 2 there are shown plots of the system dynamic response in the form of time-histories of the incident bar impacted free end velocity (Fig. 2a), specimen dynamic strain (Fig. 2b) and of the specimen strain rate (Fig. 2c). In all figures the grey lines

correspond to the steel specimen, the solid black lines to the copper specimen and the dashed black lines correspond to the aluminium alloy specimen. As a reference, by the dotted line in Fig. 2a there is denoted the time history of the wafer velocity which naturally tends to zero, when the impact process is over. Here, according to [4], the specimen strain and strain rate are respectively defined as:

$$\varepsilon_s(t) = -\ln(\psi(t)), \quad \dot{\varepsilon}_s(t) = \dot{\varepsilon}_p(t)/\psi(t), \quad \psi(t) = 1 - \varepsilon_p(t),$$

where $\varepsilon_p = (f_1(at-l_1) + g_1(at+l_1) - f_2(at) - g_2(at))/l_p$ and l_p denotes the initial specimen length.

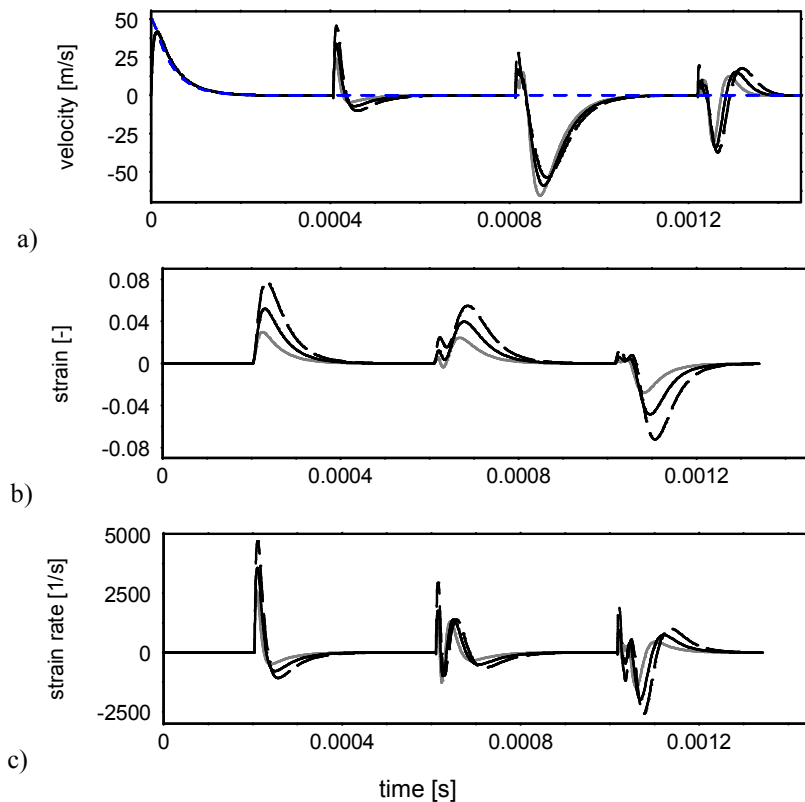


Figure 2. Dynamic response of the SHPB due to the wafer impact

In Fig. 2a there is shown a rapid increase followed by the gradual decrease of the incident bar free end velocity and then there are observed three subsequent velocity perturbations caused by successive longitudinal wave reflections upon each time interval $(l_1 + l_2)/a \approx 0.0004$ s. However, the plots in Figs. 2b and 2c are characterized by three significant perturbations, where the first ones are excited by the incident waves transmitted by the specimen after $l_1/a \approx 0.0002$ s and the two next perturbations are induced by the successive reflected waves of the strain and strain rate, respectively. It is to remark

that the greatest perturbations resulting from the dynamic response of the assumed SHPB model have been obtained for the aluminium specimen which is characterized by the smallest values of functions k and c in (2) and (4). Here, the maximum strain reaches 0.08 and the greatest strain rate is close to 5000 1/s. The steel specimen, however, is the hardest one and thus, it experiences the smallest extreme values of velocity, strain and strain rate in comparison to the analogous extremes obtained for the copper specimen, see Fig. 2.

4. Conclusions

In the paper there was investigated a longitudinal elastic wave propagation process in the cylindrical homogeneous rods representing the incident and transmitting bar in the discrete-continuous model of the SHPB. For this purpose, an analytical wave solution of the d'Alembert type has been applied in order to simulate system dynamic responses obtained for various metallic specimens. Although the specimen material models assumed here require essential improvements in the next steps of research in this field, the obtained results of computations have indicated reasonable values of the commonly expected maximal strains and strain rates observed during analogous experimental measurements. According to the above, the proposed model of the SHPB, apart of theoretical investigations of material elasto-plastic properties, can be successfully used for designing of test rigs in the form of Hopkinson bars.

Acknowledgments

These investigations have been supported by the National Science Center: Research Project UMO-2012/07/D/ST-8/02668.

References

1. J. Hopkinson, *On the rupture of iron wire by a blow*, Proc. Literary and Philosophical Society of Manchester, (1872) 40 – 45.
2. B. Hopkinson, *A method of measuring the pressure produced in the detonation of high explosives or by the impact of bullets*, Philosophical Transactions of the Royal Society of London 213, (1914) 437 – 456.
3. H. Kolsky, *An investigation of the mechanical properties of materials at very high rates of loading*, Proc. of the Physical Society 62, (1949) 676 – 700.
4. J. Janiszewski, *Investigations of the engineering materials under dynamic loadings*, Military Academy of Technology (WAT) Eds., Warsaw 2012. (in Polish)
5. T. Szolc, *Continuous one-dimensional macro-elements as a natural alternative crack detection tool to the spectral fin. el. meth.*, Arch. Mech., 59, 6 (2007) 473-499.
6. Z. L. Kowalewski, *A creep phenomenon in metals. Experiments and modeling*, Institute of Fundamental Technological Research Eds., Warsaw 2005. (in Polish)
7. L. Dietrich, T. Lekszycki, K. Turski, *Problems of identification of mechanical characteristics of viscoelastic composites*, Acta Mechanica 126, (1998), 153-167.

Free Vibrations of Column Built Out Pipe and Rod with Two-Parametric Elastic Connector

Sebastian UZNY

Częstochowa University of Technology

Institute of Mechanics and Machine Design Foundations

ul. Dąbrowskiego 73, 42-200 Częstochowa

uzny@imipkm.pcz.czest.pl

Abstract

In this paper the geometrically nonlinear system subjected to compressive external Euler's load has been investigated. The column is composed of pipe and rod. The rod is concentrically installed in the pipe. Between pipe and rod at given distance from the end of the column the two-parametric elastic connector has been placed. The numerical calculations were performed for different parameters of the system on the basis of free vibration boundary problem. The parameters are as follows: spring stiffness (translational and rotational) which models elastic connector, coefficient of asymmetry flexural rigidity, location of the connector.

Keywords: column, free vibrations, elastic connector

1. Introduction

In the investigations on slender supporting systems the discrete elements (rotational and translational springs, dumpers) are being considered. These elements have an influence on critical or bifurcation load magnitude and natural vibration frequency of the systems. When the non-conservative load is taken into account the discrete elements have an effect on type of instability (see [3-10]). By means of these elements an influence of real life elements on instability and free vibrations can be modeled. In the literature the papers devoted to instability and free vibrations with consideration of elastic and viscoelastic supports can be found (see [1,2]).

In [12] the investigations of one-parametric elastic connector on vibration and instability of a system built out pipe and rod have been presented. Elastic connector has been placed between pipe and rod. It has been shown that the translational stiffness of elastic connector at specific magnitude of coefficient of asymmetry flexural rigidity causes the increase of bifurcation load. This element of elastic connector has an influence on vibration frequency and change of buckling mode. In the case when the system is characterized by the local instability the presence of the elastic connector becomes more significant. The viscoelastic connector has been taken into account in [11]. In this paper an influence of the connector on first vibration frequency in the range of external load from zero up to bifurcation force has been investigated. In the mathematical model the Kelvin - Voigt model of viscoelastic connector was considered. An increase of connector damping factor causes an increase of the first vibration frequency magnitude.

The main scope to this paper is to study an influence of two-parametric elastic connector on natural vibrations of the system built out pipe and rod. Particularly the parameter of rotational elasticity has been investigated.

2. Boundary problem formulation on the basis of Hamilton's principle

The column composed of pipe and rod is presented in the Figure 1. The system is subjected to Euler's compressive load. Between pipe and rod the two-parametric elastic connector has been modeled. This connector consists of two springs: translational (C_R stiffness) and rotational (C_T stiffness). The length l_{11} describes connector location. The column is hinged on both ends. The model of the system is created by means of four elements. Elements marked as 11 and 22 corresponds to pipe while 21 and 22 stands for rod.

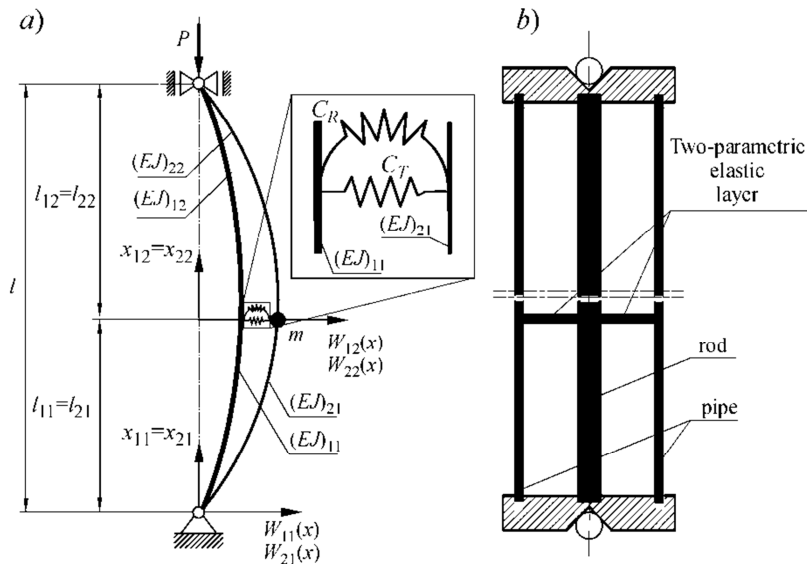


Figure 1. Considered column loaded by Euler's load: a) mathematical model,
b) column consists of pipe and rod

The differential equations of motion in the transversal direction of the investigated system are as follows: (comp. [11]):

$$(EJ)_{ij} \frac{\partial^4 W_{ij}(x,t)}{\partial x^4} + S_{ij}(t) \frac{\partial^2 W_{ij}(x,t)}{\partial x^2} + (\rho A)_{ij} \frac{\partial^2 W_{ij}(x,t)}{\partial t^2} = 0 \quad (1)$$

Moreover the differential equations of motion in the transversal direction (1) there exists the differential equation of longitudinal displacements. Performing mathematical operations on it allows one to obtain (see [12]):

$$U_{ij}(x_{ij}, t) - U_{ij}(0, t) = -\frac{S_{ij}(t)}{(EA)_{ij}} x_{ij} - \frac{1}{2} \int_0^{x_{ij}} \left(\frac{\partial W_{ij}(x_{ij}, t)}{\partial x_{ij}} \right)^2 dx_{ij} \quad (2)$$

In equations (1) and (2) the following designations were made: $W_{ij}(x_{ij}, t)$, $U_{ij}(x_{ij}, t)$ – transversal and longitudinal displacements respectively, $(EJ)_{ij}$, $(EA)_{ij}$, $(\rho A)_{ij}$ – bending, compression stiffness, mass attributable to length unit of each member, S_{ij} – longitudinal force in element of the system. The investigated column is characterized by:

- geometrical boundary conditions:

$$W_{11}(0, t) = W_{11}(l_{i1}, t) = W_{12}(l_{i2}, t) = W_{12}(l_{i2}, t) = U_{11}(0, t) = U_{21}(0, t) = 0 \quad (3a-f)$$

$$\frac{\partial W_{11}(x_{11}, t)}{\partial x_{11}} \Big|_{x_{11}=0} = \frac{\partial W_{21}(x_{21}, t)}{\partial x_{21}} \Big|_{x_{21}=0} \quad (3g)$$

$$\frac{\partial W_{12}(x_{12}, t)}{\partial x_{12}} \Big|_{x_{12}=l_{i2}} = \frac{\partial W_{22}(x_{22}, t)}{\partial x_{22}} \Big|_{x_{22}=l_{i2}} \quad (3h)$$

$$\frac{\partial W_{i1}(x_{i1}, t)}{\partial x_{i1}} \Big|_{x_{i1}=l_{i1}} = \frac{\partial W_{i2}(x_{i2}, t)}{\partial x_{i2}} \Big|_{x_{i2}=0}, \quad W_{i1}(l_{i1}, t) = W_{i2}(0, t) \quad (3i,j)$$

$$U_{12}(l_{i2}, t) = U_{22}(l_{i2}, t), \quad U_{i1}(l_{i1}, t) = U_{i2}(0, t) \quad (3k,l)$$

- natural boundary conditions:

$$\sum_i (EJ)_{i1} \frac{\partial^2 W_{i1}(x_{i1}, t)}{\partial x_{i1}^2} \Big|_{x_{i1}=0} = 0, \quad \sum_i (EJ)_{i2} \frac{\partial^2 W_{i2}(x_{i2}, t)}{\partial x_{i2}^2} \Big|_{x_{i2}=l_{i2}} = 0 \quad (4a,b)$$

$$(EJ)_{11} \frac{\partial^3 W_{11}(x_{11}, t)}{\partial x_{11}^3} \Big|_{x_{11}=l_{i1}} - (EJ)_{12} W_{12}^{III}(x_{12}, t) \frac{\partial^3 W_{12}(x_{12}, t)}{\partial x_{12}^3} \Big|_{x_{12}=0} + \quad (4c)$$

$$- C_T (W_{11}(l_{i1}, t) - W_{21}(l_{i2}, t)) = 0$$

$$(EJ)_{21} \frac{\partial^3 W_{21}(x_{21}, t)}{\partial x_{21}^3} \Big|_{x_{21}=l_{i2}} - (EJ)_{22} \frac{\partial^3 W_{22}(x_{22}, t)}{\partial x_{22}^3} \Big|_{x_{22}=0} + \quad (4d)$$

$$+ C_T (W_{11}(l_{i1}, t) - W_{21}(l_{i2}, t)) - m \frac{\partial^2 W_{21}(x_{21}, t)}{\partial t^2} \Big|_{x_{21}=l_{i2}} = 0$$

$$- (EJ)_{11} \frac{\partial^2 W_{11}(x_{11}, t)}{\partial x_{11}^2} \Big|_{x_{11}=l_{i1}} + (EJ)_{12} \frac{\partial^2 W_{12}(x_{12}, t)}{\partial x_{12}^2} \Big|_{x_{12}=0} + \quad (4e)$$

$$- C_R \left(\frac{\partial W_{11}(x_{11}, t)}{\partial x_{11}} \Big|_{x_{11}=l_{i1}} - \frac{\partial W_{21}(x_{21}, t)}{\partial x_{21}} \Big|_{x_{21}=l_{i2}} \right) = 0$$

$$\begin{aligned}
& - (EJ)_{21} \frac{\partial^2 W_{21}(x_{21}, t)}{\partial x_{21}^2} \Big|_{x_{21}=l_{21}} + (EJ)_{22} \frac{\partial^2 W_{22}(x_{22}, t)}{\partial x_{22}^2} \Big|_{x_{22}=0} + \\
& + C_R \left(\frac{\partial W_{11}(x_{11}, t)}{\partial x_{11}} \Big|_{x_{11}=l_{11}} - \frac{\partial W_{21}(x_{21}, t)}{\partial x_{21}} \Big|_{x_{21}=l_{21}} \right) = 0
\end{aligned} \tag{4f}$$

$$S_{11}(t) = S_{12}(t), \quad S_{21}(t) = S_{22}(t), \quad S_{11}(t) - S_{22}(t) - P = 0 \tag{4g-i}$$

The equation of longitudinal displacements is a non-linear one. Due to geometrical nonlinearities the small parameter method has been used to solve the boundary problem (see [12]). The non-linear equations are being written in a power series of small parameter. Rectilinear and curvilinear forms of static equilibrium are present in the investigated system. The power series for each form are different. In this paper the rectilinear form of static equilibrium has been considered. The power series are as follows:

$$W_{ij}(x, t) = \sum_{k=1}^N \varepsilon^{2k-1} W_{ij(2k-1)}(x, t) + O(\varepsilon^{2(N+1)}) \tag{5}$$

$$U_{ij}(x, t) = U_{ij(0)}(x) + \sum_{k=1}^N \varepsilon^{2k} U_{ij(2k)}(x, t) + O(\varepsilon^{2(N+1)}) \tag{6}$$

$$S_{ij}(t) = S_{ij(0)} + \sum_{k=1}^N \varepsilon^{2k} S_{ij(2k)}(t) + O(\varepsilon^{2(N+1)}) \tag{7}$$

$$\omega^2 = \omega_0^2 + \sum_{k=1}^N \varepsilon^{2k} \omega_{(2k)}^2 + O(\varepsilon^{2(N+1)}) \tag{8}$$

where: ω – natural vibration frequency.

The power series (5-8) are being introduced into equations (1-2) and boundary conditions. The coefficients at the same power of small parameter are being collected what leads to sequences of equations with corresponding boundary conditions. In this paper the basic vibration frequency ω_0 has been presented (obtained on the basis of equations at zero and first power of the small parameter). The first components of expansions ($W_{ij(1)}(x_{ij}, t)$, $U_{ij(0)}(x_{ij})$, $S_{ij(0)}$) are only considered in computations of basic vibration frequency. Separating space and time variables in the form:

$$W_{ij(1)}(x_{ij}, t) = Y_{ij(1)}(x_{ij}) \cos(\omega t) \tag{9}$$

allows one to write the differential equation of transversal displacements:

$$(EJ)_{ij} \frac{d^4 Y_{ij(1)}(x_{ij})}{dx_{ij}^4} + S_{ij(0)} \frac{d^2 Y_{ij(1)}(x_{ij})}{dx_{ij}^2} - (\rho A)_{ij} \omega_0^2 Y_{ij(1)}(x_{ij}) = 0 \tag{10}$$

The distribution of internal forces $S_{11(0)}$ i $S_{21(0)}$ can be calculated from equation (2). The relation between forces is as follows:

$$S_{12(0)} = S_{22(0)} \frac{(EA)_{12}}{(EA)_{22}} \quad (11)$$

The solution of equations (10) can be presented as a function:

$$Y_{ij(1)} = B1_{ij(1)} \cosh(\alpha_{ij(1)}x_{ij}) + B2_{ij(1)} \sinh(\alpha_{ij(1)}x_{ij}) + \\ + B3_{ij(1)} \cos(\beta_{ij(1)}x_{ij}) + B4_{ij(1)} \sin(\beta_{ij(1)}x_{ij}) \quad (12)$$

where: $B1_{ij(1)}$, $B2_{ij(1)}$, $B3_{ij(1)}$, $B4_{ij(1)}$ are constants of integration and $\alpha_{ij(1)}$, $\beta_{ij(1)}$ are quantities obtained from the characteristic differential equations (10). Introducing solution (12) into boundary condition allows on to write system of equations. The determinant of the matrix of coefficients equated to zero leads to transcendental equation on the basis of which the vibration frequency $\omega_{(0)}$ can be calculated.

3. Results of numerical calculations

In Figures 2 and 3 the characteristic curves on the plane external load - natural vibration frequency have been plotted. Numerical calculations were performed at different magnitude of the rotational spring. Graphs presented in Figures 2 and 3 have been created for different magnitudes of coefficient of asymmetry flexural rigidity $\mu = 0.004$ and $\mu = 0.5$. Parameters at which the numerical calculations were performed are as follows:

$$\lambda = \frac{Pj^2}{(EJ)}, \Omega = \frac{\omega_{(0)}^2 \left(\sum_i (\rho A)_{ii} \right) l^2}{(EJ)}, \kappa = \frac{E_{21}}{E_{11}}, \mu = \frac{(EJ)_{21}}{(EJ)_{11}}, \quad (13a-d)$$

$$c_R = \frac{C_R l}{(EJ)}, c_T = \frac{C_T l^3}{(EJ)}, \zeta = \frac{l_{11}}{l} \quad (13e-g)$$

The total flexural stiffness of the system (EJ) is constant. It has been shown that with lower magnitude of coefficient of asymmetry flexural rigidity the mode of free vibration is changing. The mode of free vibration depends on rotational spring stiffness c_R . At smaller stiffness of c_R the investigated system is characterized by buckling mode M3. At greater rotational spring stiffness the mode M1 is present. The characteristic curve corresponding to mode M3 may cross the ones related to modes M2 and M1. At greater magnitude of coefficient of asymmetry flexural rigidity the mode of free vibrations does not change. The modes of free vibrations were plotted in the Figure 4. An influence of the rotational spring stiffness on investigated parameters is greater at lower magnitude of coefficient μ . The characteristic curves related to modes M1 and M2 do not depend on rotational spring stiffness.

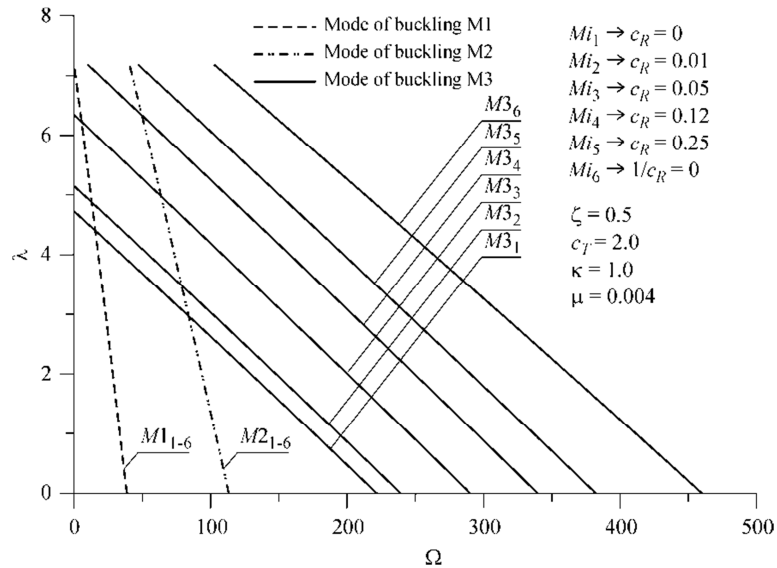


Figure 2. Parameter of loading force λ in relation to parameter of free vibration frequency Ω at $\mu = 0.004$

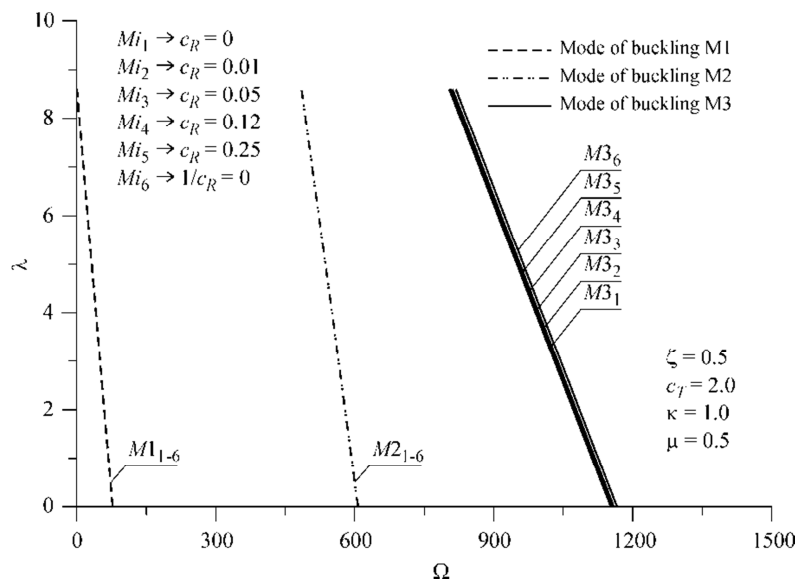


Figure 3. Parameter of loading force λ in relation to parameter of free vibration frequency Ω at $\mu = 0.5$

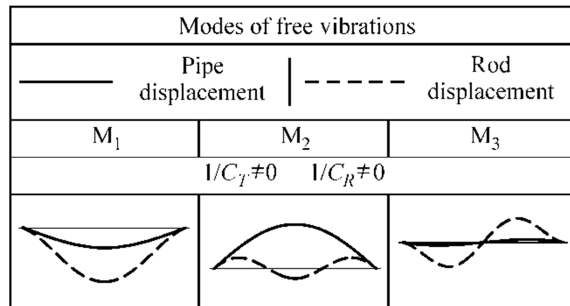


Figure 4. Modes of free vibrations

4. Conclusions

In this paper the result of theoretical study and numerical calculations of slender system built out pipe and rod have been presented. Between pipe and rod the two-parametric elastic connector is placed. The main purpose of numerical studies was to describe an influence of rotational stiffness of elastic connector on vibration frequency. It can be concluded that at smaller magnitude of coefficient of asymmetry flexural rigidity an influence of rotational stiffness of elastic connector on vibration frequency becomes intensified than at greater magnitudes of μ coefficient. There exist modes of vibrations irrespective of considered stiffness.

Acknowledgments

The study has been carried out within the statutory funds of the Czestochowa University of Technology (BS/PB-1-101/3020/11/P).

References

1. T.M. Atanackovic, B. Stankovic, *Stability of an elastic rod on a fractional derivative type of foundation*, Journal of Sound and Vibration, **277** (2004) 149-161
2. A.N. Kounadis, J. Mallis, A. Sbarounis, *Postbuckling analysis of columns resting on an elastic foundation*, Archive of Applied Mechanics, **75** (2006) 395-404
3. A.N. Kounadis, *Divergence and flutter instability of elastically restrained structures under follower forces*, International Journal of Engineering Science, **19**(4) (1981) 553-562.
4. H. Leipholz, R. Piche, *Stability of follower-force rods with weight*, Journal of Engineering Mechanics-ASCE, **110**(3) (1984) 367-379.
5. J.B. Ryu, Y. Sugiyama, K.B. Yim, G.S. Lee, *Dynamic stability of an elastically restrained column subjected to triangularly distributed subtangential forces*, Computers & Structures, **76** (2000) 611-619.
6. K. Sato, *Instability of a clamped-elastically restrained Timoshenko column carrying a tip load, subjected to a follower force*, Journal of Sound and Vibration **194**(4) (1996) 623-630.

7. C. Sundararajan, *Influence of an elastic end support on the vibration and stability of Beck's column*, International Journal of Mechanical Sciences, **18**(5) (1976) 239-241.
8. L. Tomski, S. Uzny, *Free vibrations and stability of a new slender system subjected to a conservative or non-conservative Load*, Journal of Engineering Mechanics-ASCE, **139**(8) (2013) 1133-1148
9. L. Tomski, S. Uzny, *The regions of flutter and divergence instability of a column subjected to Beck's generalized load, taking into account the torsional flexibility of the loaded end of the column*, Research Mechanics Communications, **38** (2011) 95-100
10. L. Tomski, J. Szmidla, S. Uzny, *Divergence and flatter instability of a column subjected to Reut's generalized load with regard to rotational elasticity*, Vibrations in Physical Systems, **24** (2010) 423-428.
11. S. Uzny, *Vibrations of a column consisting of a pipe and rod with a viscoelastic layer subjected to Euler's load*, Vibrations in Physical Systems, **25** (2012) 435-440.
12. S. Uzny, *Local and global instability and vibrations of a slender system consisting of two coaxial elements*, Thin-Walled Structures, **49** (2011) 618-626

Free Vibrations of Column Subjected to Euler's Load with Consideration of Timoshenko's Theory

Sebastian UZNY

Częstochowa University of Technology

Institute of Mechanics and Machine Design Foundations

ul. Dąbrowskiego 73, 42-200 Częstochowa

uzny@imipkm.pcz.pl

Krzysztof SOKÓŁ

Częstochowa University of Technology

Institute of Mechanics and Machine Design Foundations

ul. Dąbrowskiego 73, 42-200 Częstochowa

sokol@imipkm.pcz.czest.pl

Abstract

In this paper the single-rod cantilever column subjected to compressive Euler's load is investigated. The boundary problem has been formulated on the basis of Hamilton's principle and Timoshenko's theory. Numerical simulations of characteristic curves have been plotted on the plane external load-vibration frequency for different magnitudes of slenderness factor of the system. The results of numerical calculations of Timoshenko's beam are compared to the ones obtained from mathematical Bernoulli-Euler's model. The comparison of the results of characteristic curves calculated by means of Timoshenko's theory and Bernoulli-Euler's model are done for first three vibration frequencies.

Keywords: column, Timoshenko's theory, Bernoulli-Euler's theory, free vibrations, kinetic criterion of stability, divergence instability, characteristic curves

1. Introduction

The results of numerical calculations of supporting systems subjected to external loads of various types are often presented in the form of characteristic curves (see [5-8]). By means of these curves the relation between vibration frequency and external load which changes from zero up to the critical load can be observed. In the case when the system is subjected to a non-conservative load (it is destroyed by the vibrations of increasing amplitude - flutter type of instability) the critical force can be only determined on the basis of the characteristic curves (kinetic stability criterion) (see [5, 7, 8]). The supporting systems (columns) are generally characterized by great slenderness factor. For systems with great slenderness in order to formulate the boundary problem it is sufficient to apply the theory of Bernoulli - Euler. With the decrease of slenderness factor magnitude the noticeable effect of shear potential energy and cross-section rotational kinetic energy on the characteristic curves can be observed (see [1-4]). An influence of these two components is taken into account in the theory of Timoshenko's beam.

The study on the influence of non-dilatational strain and rotational inertia on the critical flutter loading have been performed by Kounadis and Katsikadelis (comp. [3]). They have studied the different types of supports and column shapes by means of variable

slenderness magnitude of the considered system. Stability of columns subjected to the follower force with consideration of Timoshenko's theory has been presented by Nemat-Nasser in [4]. It has been concluded that, at lower magnitudes of slenderness factor associated with shear force and rotational inertia of the cross-section a significant effect of these parameters on the critical load can be observed (destabilizing effect). In considerations of Nemat-Nasser the material of the rod was Kelvin's type.

In the paper [1] Glabisz solved the vibrations problem of the column with consideration of Timoshenko's theory. The areas of instability of the cantilever column loaded by independently of one another conservative and non-conservative force have been presented.

The main purpose of this paper is to study an influence of non-dilatational strain (shear effect) and rotational inertia of cross-section on characteristic curves (curves plotted on the plane external load - vibration frequency).

2. Boundary problem formulation on the basis of Hamilton's principle

The investigated system has been presented in the figure 1. The cantilever column is subjected to compressive load (force P) with constant line of action (Euler's load). The investigated system is considered as a single-rod column.

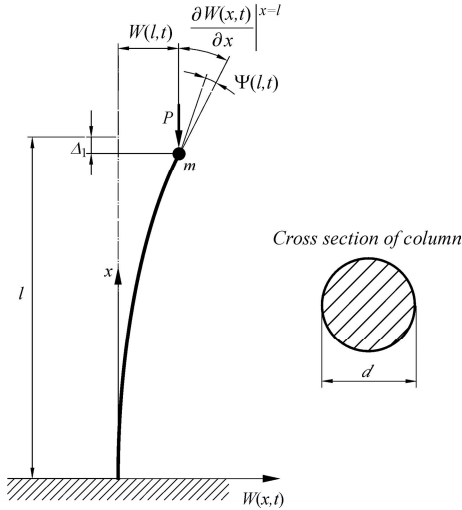


Figure 1. Considered column subjected to Euler's load

In this paper the boundary problem of natural vibrations has been formulated on the basis of Hamilton's principle:

$$\delta \int_{t_1}^{t_2} (T - V) = 0 \quad (1)$$

The kinetic energy of the column is expressed as follows:

$$T = \frac{1}{2}(\rho A) \int_0^l \left[\frac{\partial W(x,t)}{\partial t} \right]^2 dx + \frac{1}{2}(\rho J) \int_0^l \left[\frac{\partial \Psi(x,t)}{\partial t} \right]^2 dx + \frac{1}{2}m \left[\frac{\partial W(x,t)}{\partial t} \Big|_{x=l} \right]^2 \quad (2)$$

The potential energy is equal to potential energy of bending and shear and compression caused by external load:

$$\begin{aligned} V = & \frac{1}{2}(EJ) \int_0^l \left[\frac{\partial^2 \Psi(x,t)}{\partial x^2} \right]^2 dx + \frac{1}{2}(AG\kappa) \int_0^l \left[\frac{\partial W(x,t)}{\partial x} - \Psi(x,t) \right]^2 dx + \\ & - \frac{1}{2}P \int_0^l \left[\frac{\partial W(x,t)}{\partial x} \right]^2 dx \end{aligned} \quad (3)$$

where: $W(x,t)$ – deflection of the section, $\Psi(x,t)$ – rotation angle of the section, E – Young modulus, G – Kirchhoff modulus, A – cross-section area, J – axial geometrical moment of inertia of the column's section, κ - the shear coefficient which depends on section's shape (for circular cross-section $\kappa=0.91$), ρ - density of the material.

Introducing the kinetic and potential energies (2 and 3) into Hamilton's principle allows one to obtain the two differential equations:

$$(EJ) \frac{\partial^2 \Psi(x,t)}{\partial x^2} + AG\kappa \left[\frac{\partial W(x,t)}{\partial x} - \Psi(x,t) \right] - (\rho J) \frac{\partial^2 \Psi(x,t)}{\partial t^2} = 0 \quad (4)$$

$$AG\kappa \left[\frac{\partial^2 W(x,t)}{\partial x^2} - \frac{\partial \Psi(x,t)}{\partial x} \right] - P \frac{\partial^2 W(x,t)}{\partial x^2} - (\rho A) \frac{\partial^2 W(x,t)}{\partial t^2} = 0 \quad (5)$$

Performing mathematical operation and separating space and time variables $W(x,t) = Y(x)\cos(\omega t)$; $\Psi(x,t) = \psi(x)\cos(\omega t)$ (where: ω – natural vibration frequency) leads to differential equations in the form:

$$y''''(\xi) + \Gamma y''(\xi) - \Phi y(\xi) = 0 \quad (6)$$

$$\psi''''(\xi) + \Gamma \psi''(\xi) - \Phi \psi(\xi) = 0 \quad (7)$$

where:

$$\Gamma = \frac{\Theta^2(-\Omega^2[\phi+1]-\Theta^2\phi\lambda)+\Omega^2\lambda}{\Theta^2(\lambda-\Theta^2\phi)}; \Phi = -\frac{\Omega^2(\Theta^4\phi-\Omega^2)}{\Theta^2(\lambda-\Theta^2\phi)} \quad (8)$$

The non-dimensional parameters ξ , $y(\xi)$, λ , Θ , ϕ and Ω are expressed as follows:

$$\xi = \frac{x}{l}, \quad y(\xi) = \frac{Y(x)}{l}, \quad \lambda = \frac{Pl^2}{(EJ)}, \quad \Theta^2 = \frac{Al^2}{J}, \quad (9a-d)$$

$$\phi = \frac{\kappa G}{E}, \quad \Omega^2 = \frac{(\rho A)\Gamma^4\omega^2}{(EJ)}, \quad \zeta_m = \frac{m}{\rho Al} \quad (10a-c)$$

The introduction of geometrical boundary conditions into Hamilton's principle

$$y(0) = \psi(0) = 0 \quad (11a,b)$$

allows one to obtain the natural ones:

$$\Theta^2 \phi \left[\psi(1) - y^I(\xi) \right]_{\xi=1} + \lambda y^I(\xi)_{\xi=1} + \zeta_m \Omega^2 y(1) = 0, \quad \psi^I(\xi)_{\xi=1} = 0 \quad (12a,b)$$

2. Solution of the boundary problem

The solution of differential equations (6) and (7) depends on relation between Γ and Φ . The three different types of solutions are presented in the form:

- solution A - if ($\Gamma > 0$ and $\Gamma/2 < (\Gamma^2/4 + \Phi)^{0.5}$) or ($\Gamma < 0$ and $(\Gamma/2 + (\Gamma^2/4 + \Phi)^{0.5}) > 0$):

$$y(\xi) = B_{A1} \cosh(\alpha_A \xi) + B_{A2} \sinh(\alpha_A \xi) + B_{A3} \cos(\beta_A \xi) + B_{A4} \sin(\beta_A \xi) \quad (13)$$

$$\psi(\xi) = C_{A1} \cosh(\alpha_A \xi) + C_{A2} \sinh(\alpha_A \xi) + C_{A3} \cos(\beta_A \xi) + C_{A4} \sin(\beta_A \xi) \quad (14)$$

where:

$$\alpha_A = \sqrt{-\frac{\Gamma}{2} + \sqrt{\frac{\Gamma^2}{4} + \Phi}}, \quad \beta_A = \sqrt{\frac{\Gamma}{2} + \sqrt{\frac{\Gamma^2}{4} + \Phi}} \quad (15a,b)$$

- solution B - if ($\Gamma > 0$ and $\Gamma/2 > (\Gamma^2/4 + \Phi)^{0.5}$):

$$y(\xi) = B_{B1} \cos(\beta_B \xi) + B_{B2} \sin(\beta_B \xi) + B_{B3} \cos(\beta_B \xi) + B_{B4} \sin(\beta_B \xi) \quad (16)$$

$$\psi(\xi) = C_{B1} \cos(\beta_B \xi) + C_{B2} \sin(\beta_B \xi) + C_{B3} \cos(\beta_B \xi) + C_{B4} \sin(\beta_B \xi) \quad (17)$$

where:

$$\beta_{B1} = \sqrt{\frac{\Gamma}{2} + \sqrt{\frac{\Gamma^2}{4} + \Phi}}, \quad \beta_{B2} = \sqrt{\frac{\Gamma}{2} - \sqrt{\frac{\Gamma^2}{4} + \Phi}} \quad (18a,b)$$

- solution C - if ($\Gamma < 0$ and $(\Gamma/2 + (\Gamma^2/4 + \Phi)^{0.5}) < 0$):

$$y(\xi) = B_{C1} \cosh(\alpha_C \xi) + B_{C2} \sinh(\alpha_C \xi) + B_{C3} \cosh(\alpha_C \xi) + B_{C4} \sinh(\alpha_C \xi) \quad (19)$$

$$\psi(\xi) = C_{C1} \cosh(\alpha_C \xi) + C_{C2} \sinh(\alpha_C \xi) + C_{C3} \cosh(\alpha_C \xi) + C_{C4} \sinh(\alpha_C \xi) \quad (20)$$

where:

$$\alpha_{C1} = \sqrt{-\frac{\Gamma}{2} - \sqrt{\frac{\Gamma^2}{4} + \Phi}}, \quad \alpha_{C2} = \sqrt{-\frac{\Gamma}{2} + \sqrt{\frac{\Gamma^2}{4} + \Phi}} \quad (21a,b)$$

The constants of integration of solutions $\psi(\xi)$ depend on constants of integration of solutions $y(\xi)$. Constants of integration C_{Ai} , C_{Bi} , C_{Ci} are expressed as follows:

- solution A:

$$C_{A1} = B_{A2} \frac{\alpha_A^2 (\phi\Theta^2 - \lambda) + \Omega^2}{\alpha_A \phi\Theta^2}, \quad C_{A2} = B_{A1} \frac{\alpha_A^2 (\phi\Theta^2 - \lambda) + \Omega^2}{\alpha_A \phi\Theta^2} \quad (22a,b)$$

$$C_{A3} = B_{A4} \frac{\beta_A^2 (\phi\Theta^2 - \lambda) - \Omega^2}{\beta_A \phi\Theta^2}, \quad C_{A4} = B_{A3} \frac{-\beta_A^2 (\phi\Theta^2 - \lambda) + \Omega^2}{\beta_A \phi\Theta^2} \quad (22c,d)$$

- solution B:

$$C_{B1} = B_{B2} \frac{\beta_{B1}^2 (\phi\Theta^2 - \lambda) - \Omega^2}{\beta_{B1} \phi\Theta^2}, \quad C_{B2} = B_{B1} \frac{-\beta_{B1}^2 (\phi\Theta^2 - \lambda) + \Omega^2}{\beta_{B1} \phi\Theta^2} \quad (23a,b)$$

$$C_{B3} = B_{B4} \frac{\beta_{B2}^2 (\phi\Theta^2 - \lambda) - \Omega^2}{\beta_{B2} \phi\Theta^2}, \quad C_{B4} = B_{B3} \frac{-\beta_{B2}^2 (\phi\Theta^2 - \lambda) + \Omega^2}{\beta_{B2} \phi\Theta^2} \quad (23c,d)$$

- solution C:

$$C_{C1} = B_{C2} \frac{\alpha_{C1}^2 (\phi\Theta^2 - \lambda) + \Omega^2}{\alpha_{C1} \phi\Theta^2}, \quad C_{C2} = B_{C1} \frac{\alpha_{C1}^2 (\phi\Theta^2 - \lambda) + \Omega^2}{\alpha_{C1} \phi\Theta^2} \quad (24a,b)$$

$$C_{C3} = B_{C4} \frac{\alpha_{C2}^2 (\phi\Theta^2 - \lambda) + \Omega^2}{\alpha_{C2} \phi\Theta^2}, \quad C_{C4} = B_{C3} \frac{\alpha_{C2}^2 (\phi\Theta^2 - \lambda) + \Omega^2}{\alpha_{C2} \phi\Theta^2} \quad (24c,d)$$

Introducing solutions $y(\xi)$ and $\psi(\xi)$ into boundary conditions one obtains:

$$[a_{ij}] \text{col}\{B_{i1}, B_{i2}, B_{i3}, B_{i4}\} = 0, \quad i \equiv A \text{ or } B \text{ or } C \quad (25)$$

The determinant of the matrix of coefficients equated to zero is a equation from which the natural vibration frequency can be computed for given system's parameters:

$$|a_{ij}| = 0 \quad (26)$$

3. Results of numerical calculations

In the Figures 2-4 the change of $\Lambda_{\omega i}$ parameter have been presented (where i stands for natural vibration frequencies, $i = 1, 2, 3$) in relation to external load of the system λ . By means of $\Lambda_{\omega i}$ parameter the comparison of natural vibration frequencies computed on the basis of Bernoulli - Euler's model ω_{B-E} and Timoshenko's theory ω_T are presented. The $\Lambda_{\omega i}$ parameter is expressed as follows:

$$\Lambda_{\omega i} = \frac{\omega_{Ti} - \omega_{B-Ei}}{\omega_{B-Ei}} 100\% \quad (27)$$

The investigated system with circular cross-section is made of duraluminium. The numerical calculations were performed for different slenderness parameter λ_s magnitude ($\lambda_s = 300, 250, 200, 150, 100, 50$). The slenderness parameter λ_s is expressed as follows:

$$\lambda_s = \frac{\mu_b l}{\sqrt{J/A}} \quad (28)$$

where: buckling factor for investigated system is $\mu_b = 2$.

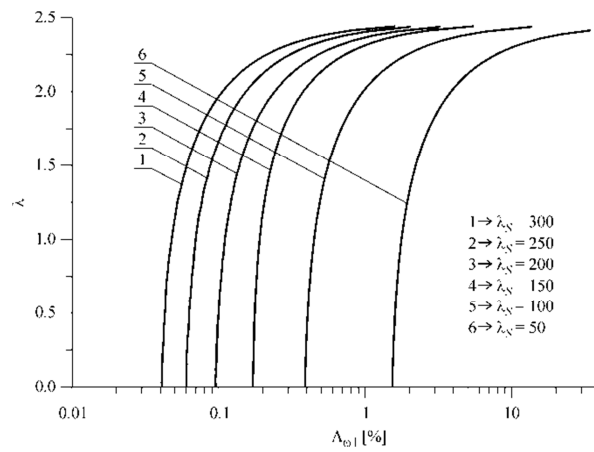


Figure 2. External load parameter λ in relation to parameter of free vibration frequency $\Lambda_{\omega 1}$

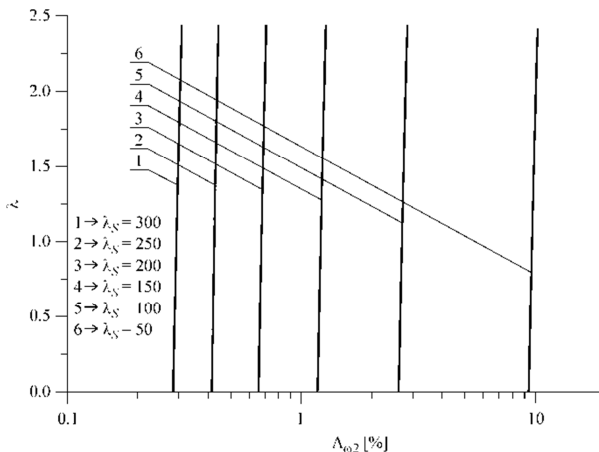


Figure 3. External load parameter λ in relation to parameter of free vibration frequency $\Lambda_{\omega 2}$

On the basis of the performed numerical simulations it can be concluded that the greatest change in Λ_ω parameter in relation to external load λ appears for first natural vibration frequency. In this case an increase of external load magnitude results in increase of difference in magnitudes of natural vibration frequencies calculated with Bernoulli - Euler's model and Timoshenko's theory. The slenderness factor has also an influence on Λ_ω parameter. While taking into account second and third natural vibration frequencies the change in Λ_ω parameter is inconsiderable with the increasing magnitude of external load.

At smaller magnitudes of external load the slenderness factor has greater influence on difference between frequencies (second and third) computed with Bernoulli - Euler's model and Timoshenko's theory.

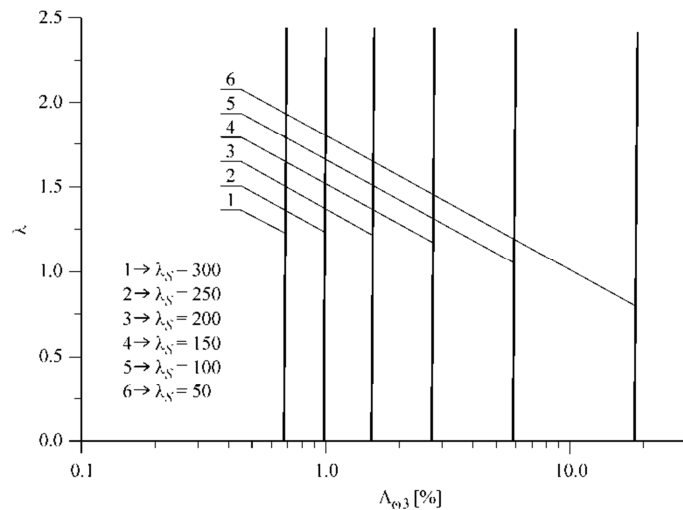


Figure 4. External load parameter λ in relation to parameter of free vibration frequency $\Lambda_{\omega3}$

At the greatest slenderness $\lambda_s = 300$ and external force $\lambda = 0$ parameters $\Lambda_{\omega i}$ are as follows: $\Lambda_{\omega 1} \approx 0.04\%$, $\Lambda_{\omega 2} \approx 0.27\%$, $\Lambda_{\omega 3} \approx 0.67\%$. While $\lambda_s = 50$ (the lowest considered slenderness) and external force $\lambda = 0$ parameters $\Lambda_{\omega i}$ are: $\Lambda_{\omega 1} \approx 1.4\%$, $\Lambda_{\omega 2} \approx 9.4\%$, $\Lambda_{\omega 3} \approx 18\%$.

4. Conclusion

In this paper column subjected to a compressive Euler's load has been investigated. Comparison of results of numerical calculations of natural vibration frequencies obtained on the basis of two theories: Bernoulli - Euler (ω_{B-E}) and the Timoshenko (ω_T) have been performed. In order to demonstrate the differences in the frequencies of vibrations ω_{B-E} and ω_T the new parameter has been defined on the basis of which the percentage change

in the first three natural frequencies can be presented for different magnitudes of the external load. The calculations are also concern on different values of slenderness parameter. The greatest differences in the two mathematical models (Euler - Bernoulli and Timoshenko) occurs at the third vibration frequency. The differences between the theories of Bernoulli - Euler and Timoshenko are increasing with greater magnitude of external load. In the case of the first characteristic curve corresponding to the first vibration frequency the differences are the greatest. For the second and third curves the change in magnitude of external load results in small difference between ω_{B-E} and ω_I frequencies.

Acknowledgments

The study has been carried out within the statutory funds of the Czestochowa University of Technology (BS/PB-1-101/3020/11/P).

References

1. W. Grabisz, *O granicach obszarów stateczności pręta pod dwuparametrowym obciążeniem niepotencjalnym*, Mechanika Teoretyczna i stosowana, **1(29)** (1991) 173-188
2. L.Y. Jiang, Z. Yan, *Timoshenko beam model for static bending of nanowires with surface effects*, Physica E, **42** (2010) 2274-2279
3. A.N. Kounadis, J.T. Katsikadelis, *Shear and rotary inertia effect on Beck's columns*, J. Sound and Vib., **49(2)** (1976) 171-178
4. S. Nemat-Nasser, *Instability of a cantilever under a follower force according to Timoshenko beam theory*, J. Appl. Mech., **34** (1967) 484-485
5. C. Sundararajan, *Influence of an elastic end support on the vibration and stability of Beck's column*, Int. J. Mech. Sci., **18** (1976) 239-241.
6. L. Tomski, S. Uzny, *Free vibration and the stability of a geometrically non-linear column loaded by a follower force directed towards the positive pole*, International Journal of Solids and Structures, **45(1)** (2008) 87-112.
7. L. Tomski, S. Uzny, *The regions of flutter and divergence instability of a column subjected to Beck's generalized load, taking into account the torsional flexibility of the loaded end of the column*, Research Mechanics Communications, **38** (2011) 95-100.
8. L. Tomski, S. Uzny, *Free Vibrations and Stability of a New Slender System Subjected to a Conservative or Non-Conservative Load*, Journal of Engineering Mechanics-ASCE, **139(8)** (2013) 1133-1148

Infrasound and Low Frequency Noise of a Wind Turbine

Malgorzata WOJSZNIS

Institute of Applied Mechanics, Poznań University of Technology

3 Piotrowo Street, 60-965 Poznań

Malgorzata.Wojsznis@put.poznan.pl

Jacek SZULCZYK

Environmental Acoustics Laboratory EKO – POMIAR

4 Słoneczna Street, 64-600 Oborniki

Jacek.Szulczyk@eko-pomiar.com.pl

Abstract

The paper presents noise evaluation for a 2 MW wind turbine. The obtained results have been analyzed with regard to infrasound and low frequency noise generated during work of the wind turbine. The evaluation was based on standards and decrees binding in Poland. The paper presents also current literature data on the influence of the infrasound and low frequency noise on a human being. It has been concluded, that the permissible levels of infrasound for the investigated wind turbine were not exceeded.

Keywords: low frequency noise, infrasound, wind turbine

1. Introduction

Research that has been conducted in the world for many years shows that noise can be described as sound below and above so called *hearing threshold*. It can be assumed that the *infrasound*, which cannot be heard by a human being, concerns frequencies below 20 Hz, and the *ultrasound* concerns frequencies above 20 kHz [1]. We receive it as mechanical vibrations of the medium it passes through, transferring energy from the source in the form of acoustic waves. Puzyna in [1] describes infrasound as *infraacoustic vibrations*. Some investigations show that for some people the hearing level begins already at 16Hz, and sometimes even at 4Hz. Such a phenomenon occurs at appropriate conditions and at a high level of sound pressure [2]. According to standards PN-ISO 7196:2002P, ISO 9612:1997 and PN-Z-01338:2010 [3, 4, 5] the infrasound noise concerns frequencies between 1 and 20 Hz.

The term *low frequency noise* is more and more commonly used to describe the frequency range from 10 Hz to 250 Hz (e.g. according to Polish instruction ITB 358/98) [6]. In other countries this range is defined differently and it is closely related to medical research concerning the influence of infrasound noise on the hearing organ [6, 7].

2. Influence of infrasound and low frequency noise on a human being

The influence of infrasound on a human being is closely related to conduction of the middle ear and internal ear, i.e. its effect on the hearing organ (*hearing effects*) and on the whole body, and particularly on the nervous system and internal organs (*non-hearing*

effects). Infrasound is annoying and its effects appear already when the hearing threshold is slightly exceeded [8].

Figure 1 shows hearing thresholds for infrasound and low frequency noise obtained by Watanabe and Møller [9, 10] set against the values from the ISO:226 2003 standard and compared with the respective levels in other countries [11,12].

Based on Watanabe and Møller's results, Leventhal determined the hearing threshold for infrasound and low frequency sound [10] – Table 1.

Figure 2 shows so called equal annoyance contours for infrasound obtained by Whittle (1972) set against Møller's and Andresen's results (1984) [12] and equal loudness contours from ISO 226: 2003 standard [11].

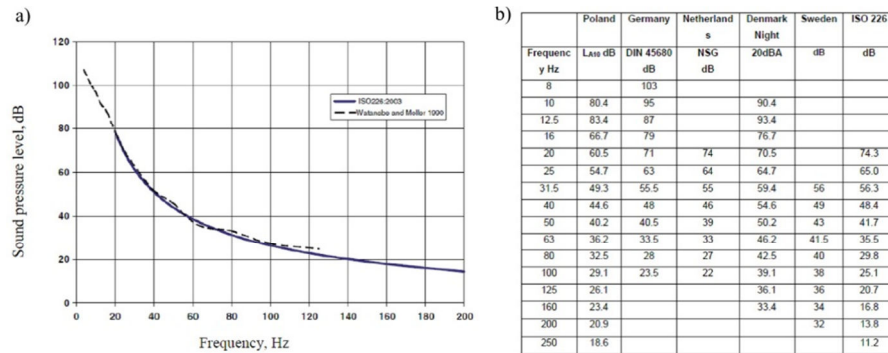


Figure 1. Hearing thresholds in the infrasound and low frequency ranges
a) acc. to ISO 226:2003, Watanabe and Møller b) in selected countries [9, 10, 11, 12]

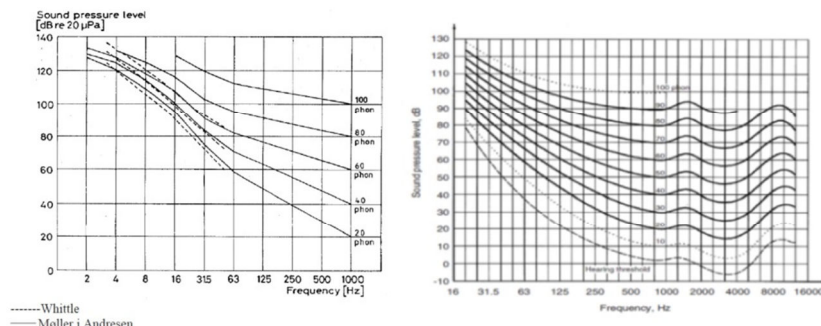


Figure 2. Equal annoyance contours for infrasound and equal loudness contours from the ISO 226: 2003 standard for audible sound [11, 12]

Table 1. Hearing threshold according to Leventhall[10]

Frequency (Hz)	4	8	10	12,5	16	20	25	31,5	40	50	63	80	100	125	160	200
Sound pressure level (dB)	107	100	97	92	88	79	69	60	51	44	38	32	27	22	18	14

Like in case of equal loudness contours for audible sound, the equal annoyance contours for infrasound were obtained using the expressed in phons loudness level based on subjective sensing of sound by the hearing organ. A frequency drop causes sudden increase in audio perception, which means that even at small change the annoyance of infrasound increases. In the range of 127-132 dB a painless constriction is observed in the middle ear. Earache and so called temporary shift of the hearing threshold appear most often at the level of 140 dB for frequency 40 Hz and 160 dB for 3 Hz [13]. At higher frequencies the internal ear can be damaged.

At the levels above 100 dB the perception of vibrations generated by infrasound is similar to the perception of vibrations generated mechanically [14]. Infrasound may be sensed by telereceptors of vibrations located, for example, in muscles, joints and tendons, and so called sensory receptors (mechanoreceptors). In this case the threshold of vibration sensing is higher than the hearing threshold by about 20-40 dB. Landström in [15] claims, that the vibrational perception of infrasound occurs at the level of 124 dB for frequency 4 Hz, for which the hearing threshold equals 107 dB.

The most typical symptom of influence of infrasound and low frequency sound on a human being is the pressure in ears together with the sensation of internal vibration. At the levels of 140-150 dB vibrations of the rib cage cause voice modulation and suffocation in the throat leading to coughing. It can be said that infrasound may cause arrhythmia, fatigue and increase in heart rate [13, 16]. All these symptoms may appear after the hearing threshold has been exceeded, which has been confirmed by the research conducted on the deaf [13].

3. Evaluation of infrasound noise under the current regulations

The evaluation of exposure to infrasound noise is made based on spectral analysis in third octave or octave bands using G-weighting [3] developed based on the analysis of hearing perception threshold. Its peak lies at the frequency of 20 Hz, and the average value of the hearing threshold equals 102 dB [17]. It has been observed, that to evaluate low frequency noise the A-weighting cannot be used because it gives too low values [18].

The PN-Z-01338:2010P standard, which defines permissible values of infrasound noise at work-places, being a criterion for annoyance, and a regulation of the Ministry of Labour and Social Policy, where additionally the peak, unweighted acoustic pressure level is determined [4,19] are in force in Poland – Table 2.

Table 2. Permissible values of infrasound noise – annoyance criterion [4]

Evaluated quantity	Permissible value, dB
Equivalent, G-weighted sound pressure level normalized to an 8-hour working day, $L_{Geq,Te}=L_{Geq,8h}$	102
Equivalent, G-weighted sound pressure level related to a nominal working week, $L_{Geq,Te}=L_{Geq,w}$	102
Equivalent, G-weighted sound pressure level during the occupation of a workstation by an employee (at work places for conceptual work requiring particular concentration)	86

4. Noise evaluation for a 2 MW wind turbine

A wind farm consisting of several 2.0 MW wind turbines Gamesa G90 with tower height of 100 m and blade length of 45 m was analyzed (Figure 3). The measurements of noise was performed by a research laboratory accredited by Polish Centre for Accreditation.



Figure 3. A 2 MW wind turbine with a total height of 145 m

The obtained results were analyzed paying special attention to evaluation of infrasound and low frequency noise generated by a working wind turbine, located at the edge of the wind farm [23, 24]. The evaluation was made based on standards and regulations being in force in Poland.

Figure 4 shows the equivalent, G-weighted sound pressure levels for the turbine for various distances of measuring points from the turbine and at the wind velocities of 3-4 m/s and 4-5 m/s measured at the height of 10 m above the ground in frequency bands of 1-20 Hz and 0,8–250 Hz. The measuring points were selected at places without any buildings and natural obstacles.

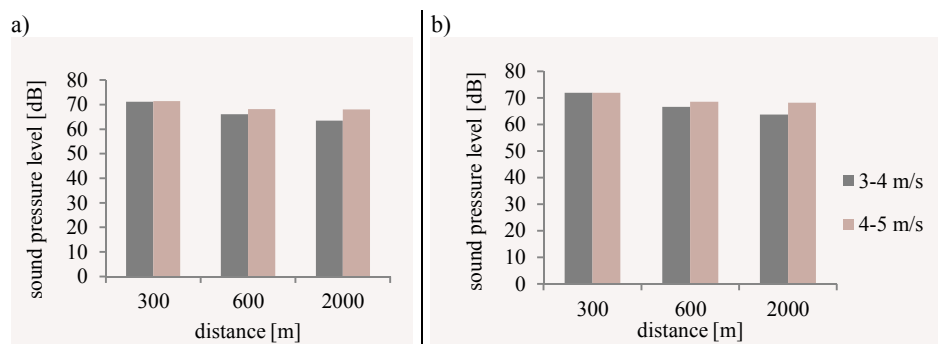


Figure 4. Equivalent, G-weighted sound pressure level for a 2 MW turbine determined based on the standard [3] in the range of a) infrasound and b) low frequency noise

As it can be seen from Figure 4 the annoyance criterion of 102 dB has not been exceeded.

At a distance of 600 m from the turbine, where the closest residential property was located, additional measurements at variable wind velocity were performed. The wind velocity measured at 10 m height can be converted into the velocity at the tower height by means of a coefficient, which equals about 1.45. It means that acoustic measurements were performed for the wind velocity between 4.3 m/s and 13 m/s at the tower height (Figure 5).

Tower height [m]	H = 67m	H = 78m	H = 100m
W _S / W ₁₀ [m/s]	1.36	1.39	1.45

Ratio between W_S and W₁₀ in accordance with IEC 61400-11 standard.

W ₁₀ [m/s]	H = 100m	
	dB(A)	W _S [m/s]
3	91.4	4.3
4	96.7	5.8
5	101.6	7.2
6	105	8.7
7	105	10.1
8	105	11.6
9	105	13.0
10	105	14.5

Figure 5. Method of conversion of wind velocity measured at 10 meters above the ground W₁₀ into the velocity at any tower height W_S [25]

As it can be seen from the tables shown above, the G90 turbine reaches the maximum level of acoustic power for the wind velocity of 6 m/s at 10 m height, i.e. 8.7 m/s at the tower height. The infrasound levels during measurements were generated by the wind turbines for maximum acoustic power (determined according to PN-EN 61400-11) and maximum rotational speed of the turbine [22].

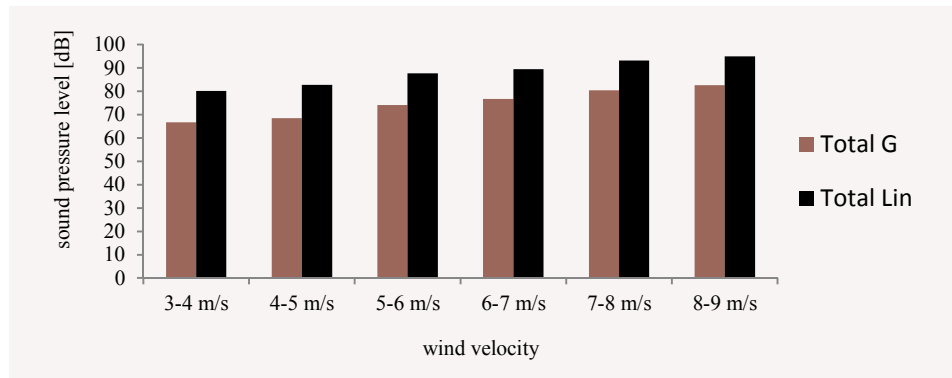


Figure 6. Equivalent sound pressure level for a 2 MW turbine in the infrasonic range for the distance of 600 m

The equivalent sound pressure level for the 600 m distance which can be seen in Figure 6 increases significantly with the increase of the wind velocity. It does not exceed, however, the permissible values specified in Polish regulations.

The obtained results for the low frequency range and the 600 m distance, at different wind velocities has been set against the data from Table 1 (Leventhal), the current hearing threshold in Germany and the 40 phon equal loudness contour from the ISO 226: 2003 standard [10, 11, 12, 21] – Figure 7.

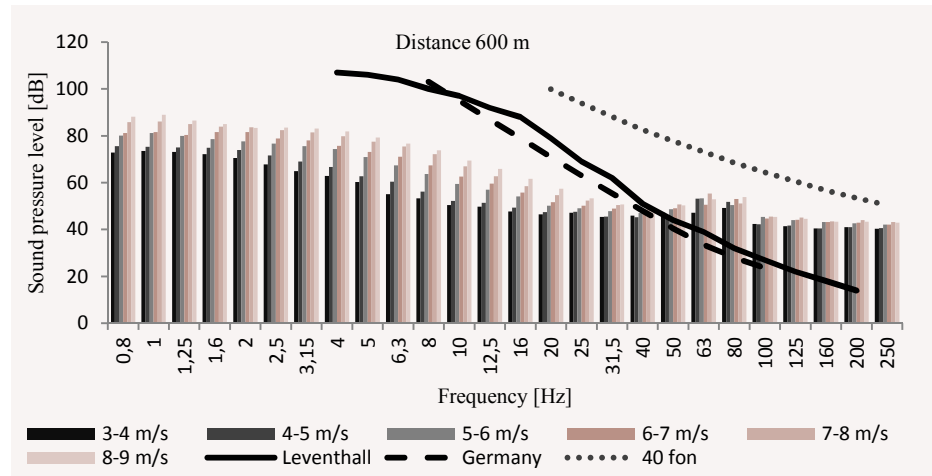


Figure 7. Sound pressure level of a 2 MW turbine for the 600 m distance, set against hearing thresholds

Analyzing the data from Figure 7 it can be clearly seen that in the infrasonic range the levels generated by the turbine working at maximum electrical power and maximum rotational speed are safe. We have different situation at frequencies above 40 Hz, i.e. already in the audible range, where the hearing threshold was exceeded at some places even by 50 %. If, however, we take into account the equal loudness contours [11] for the audible range, and particularly the most frequently used 40 phon one, the values obtained for the turbine in this range are below the threshold.

5. Conclusions

Based on the conducted analyses it can be said, that the investigated wind turbine does not pose any danger to people staying in its vicinity. Such a conclusion can be drawn based on the current regulations related to infrasound and low frequency sound. One should remember, however, that the regulations concern the 8-hour-exposition, and people stay in the area of the turbine continuously, even at night.

The permissible levels in the infrasonic range have not been exceeded. In the low frequency range above 40 Hz it would be necessary to conduct an in depth analysis, because the results are equivocal.

Referring to the report of the American Wind Energy Association and the Canadian Wind Energy Association from 2009 [20] it can be said, that at present there is no scientific evidence, that modern wind turbines generate vibrations perceptible by people and pose any danger related thereto.

Acknowledgments

The work was partially financed by dB-Projekt Sp. z o.o.

References

1. Cz. Puzyna, *Ochrona środowiska pracy przed hałasem, tom I*, Wydawnictwa Naukowo-Techniczne, Warszawa 1981;
2. F. Duck, S. Darby, G. Haar, M. Hanson, G. Leventhall, D. Noble, J. Sienkiewicz, I. Zequir, *Health Effects of Exposure to Ultrasound and Infrasound, Report of the Independent Advisory Group on Non-ionising Radiation*, Documents of the Health Protection Agency, Radiation, Chemical and Environmental Hazards, February 2010;
3. PN-ISO 7196:2002P *Akustyka – charakterystyka częstotliwościowa filtra do pomiarów infradźwięków*;
4. ISO 9612:1997, *Akustyka – wytyczne do pomiarów i oceny ekspozycji na hałas w środowisku pracy*;
5. PN-N-01338:2010P *Akustyka – Pomiar i ocena hałasu infradźwiękowego na stanoiwiskach pracy*.
6. M. Stopa, *Hałas niskoczęstotliwościowy w górnictwie skalnym*, Prace Naukowe Instytutu Górnictwa Politechniki Wrocławskiej, Nr 134, Studia I Materiały Nr 41, Wrocław 2012;
7. M. Alves-Pereira, N. Castelo-Branco, E. Kotlicka, J. Motylewski, *Low frequency noise legislation*, Inter-noise, Istanbul 2007;
8. K. Marek, *Choroby zawodowe*, Wydawnictwo Lekarskie PZWL, Warszawa 2003;
9. T. Watanabe, H. Moller, *Low frequency hearing thresholds in pressure field and free field*, Journal Low Frequency Noise Vibration 9, pp 106-115, 1990;
10. H.G. Leventhall, *What is infrasound?*, Progress in Biophysics and Molecular Biology 93, pp 130-137, 2007;
11. ISO 226:2003 *Acoustics – normal equal – loudness contours*;
12. H.G. Leventhall, S. Benton, P. Pelmeir, *A Review of Published Research on Low Frequency Noise and its Effects*, Report for DEFRA, Department for Environment, Food and Rural Affairs, 2003;
13. A. J. Indulski, *Higiena pracy*, Oficyna Wydawnicza Inst. Med. Pracy, tom II, Łódź 1999;
14. S.D. Smith, *Characterizing the effect of airborne vibration on human body vibration response*, Aviation, Space and Environmental Medicine 73, pp 36-45, 2002.
15. U. Landström, *Laboratory and field studies on infrasound and its effects on humans*, Journal of Low Frequency Noise, Vibration and Active Control 6, 1, pp 29-33, 1987;
16. Z. Damijan, *Zmiany wybranych parametrów biochemicznych i fizjologicznych organizmu po ekspozycji drganiami niskoczęstotliwościowymi*, Diagnostyka, vol. 33, 2005, pp 29 – 34;
17. D. Augustyńska, *Wartości graniczne ekspozycji na infradźwięki – przegląd piśmiennictwa*, Podstawy i Metody Oceny Środowiska Pracy, nr 2(60), s. 5-15, 2009;

18. H. Seungki, K. Jaehwan, K. Kyutae, L. Soogab, *Laboratory study on low-frequency noise weighting curve based on the acceptability limit*, Istanbul, Turkey, Inter-Noise 2007;
19. Rozporządzenie MPiPS z 29 listopada 2002 r., *w sprawie najwyższych dopuszczalnych stężeń i natężeń czynników szkodliwych dla zdrowia w środowisku pracy*;
20. D.W. Colby, R. Dobie, G. Leventhall, G. Lipscomb, R.J. Mccunney, M.T. Seilo, B. Søndergaard, *Wind Turbine Sound and Health Effects An Expert Panel Review*, American Wind Energy Association and Canadian Wind Energy Association, December 2009;
21. A. Rogers, J. Manwell, S. Wright, *Wind Turbine Acoustics Noise*, Renewable Energy Research Laboratory, University of Massachusetts at Amherst, 2006;
22. PN-EN 61400-11:2004+ A1 *Turbozespoły wiatrowe – Część 11: Procedury pomiaru hałasu*;
23. J. Szulczyk, C. Cempel, *Hałas turbin wiatrowych w zakresie infradźwięków*, Monitoring Środowiska 2010, Kraków Maj 2010.
24. J. Szulczyk, C. Cempel, *Analizy symulacyjne propagacji dźwięku farm wiatrowych*, Monitoring Środowiska 2010, Kraków Maj 2010.
25. IEC 61400-11 2002-12 *Wind Turbine Generator Systems – Part 11: Acoustic Noise Measurement Techniques*

Deployment of Long-measured Flexible Structure in Orbit

Alexandr E. ZAKRZHEVSKY

S. P. Timoshenko Institute of Mechanics NAS of Ukraine

3, Petra Nesterova Street, Kiev, Ukraine, 03057

alex.zakr@mail.ru

Abstract

Dynamics of the spacecraft with giro-gravitational system of stabilisation, in which the pantograph design deployed in an orbit and containing on the end the concentrated mass is used as the gravitational stabilizer and the carrier of solar batteries, is investigated. The analysis of the obtained information is carried out and graphs that illustrate behaviour of characteristic variables are discussed.

Keywords: Spacecraft, pantograph structure, deployment

1. Introduction

The deployment of spacecraft delivered into orbit in a compact form perturbs their attitude. The study of such transformed configurations is required for minimization of deployment duration, mass, and power resources, for analysis of the effect of such structures on the spacecraft attitude motion. There exist a large number of studies in the literature dedicated to the deployment of elastic appendages of different shape from the fixed basis as well as from a rotating SC. A short review of these publications is contained in [1].

Works, except for work [2], which would investigate the dynamics of deployment in orbit of pantograph designs, are unknown to the author. This research generalises the work [2] by the additional account of transversal displacements of the deployed pantograph design with objective to study their effect on the dynamics of the SC and its elements.

2. Physical model of system

Here the SC that includes the gyro-gravitational system of stabilization is studied during the deployment of the flexible pantograph structure according to the program motion into the elongated flexible gravitational stabilizer (GS). It serves also as the carrier of solar batteries and tip mass. The SC includes two gyro-dampers (GD) which are installed for attitude stabilization. The SC is injected in a circular earth orbit with altitude 400 km. Basic elements of the SC are shown in Fig. (1). Here, element 1 is the SC main module, element 2 is the spatial structure that consists of two plain coupled pantographs, elements 3 and 4 represent the GD.

The deployment is initiated when the points joining each plain pantograph to the main module start to approach synchronously. The distance between these points in each pantograph is $b(t)$. The dynamics of the deployment actuating drive are not taken into

consideration here since this mechanism is very simple and may be realized as a device that has no effect on the SC dynamics.

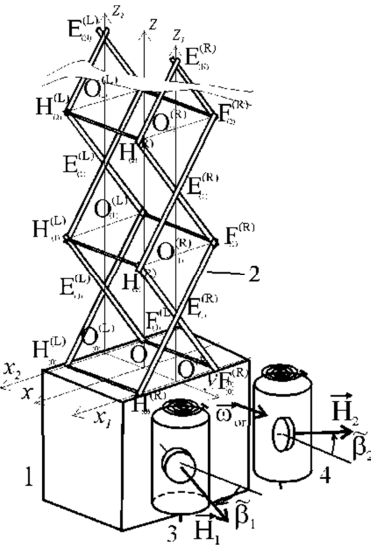


Figure 1. Basic elements of the spacecraft

The deployable structures possess considerable flexibility. Because of requirements to maintain the shape of the gravitational stabilizer, some restrictions must be imposed on the deployment and design parameters. They can be determined via the process of numerical simulations. The GD role in the process of deployment and after its completion is also studied further.

3. Mechanical model of system

The generalized mechanical model of the system under consideration may be represented as a main rigid body S_1 and body S_2 of variable configuration attached to it. The body S_1 is the gyro-static part and includes the GD, which do not change the rotational body inertia. The motion of the body S_1 is defined by the velocity vector \mathbf{v}_O of the point O and vector of absolute angular velocity ω .

The following frames of reference will be useful for the problem statement: $\bar{C}\bar{X}\bar{Y}\bar{Z}$ is an earth-centered inertial reference frame; $Oxyz$ is the body S_1 fixed reference frame (Figure 1) with Oz along the design position of the GS axis; the orbital frame of reference $Cx^or y^or z^or$ is fixed in the SC mass centre. These frames are introduced in such a way as in Ref. [3].

The position vector \mathbf{r} defines the location of the arbitrary point P with respect to the reference frame $\bar{C}\bar{X}\bar{Y}\bar{Z}$, and the position vector \mathbf{r}' – with respect to the reference frame $Oxyz$. In contrast to the problem of the relative motion of attached bodies described by

Lurie [5], here one has the more general case when the expression for \mathbf{r}' depends on time t explicitly, and not only through the generalized coordinates:

$$\mathbf{r}' = \mathbf{r}'(q_1, \dots, q_n, t) \quad (1)$$

As a result, \mathbf{r}' varies during deployment even in the absence of the relative elastic motion of the design.

Each of two pantographs is made of elastic rods in length $2a$ and mass $2m_a(i)$, where index i is used for the numbering of tiers that form full rhombuses. These rods are connected at the joints $E_{(i)}^{(R)}, E_{(i)}^{(L)}$, ($i = \overline{0, N}$), where N is the number of the tiers, and at points $H_{(i)}^{(R)}, H_{(i)}^{(L)}, F_{(i)}^{(R)}, F_{(i)}^{(L)}$, ($i = \overline{1, N}$), where the superscripts identify the pantograph as per Figure 1.

The pantograph structure has a compact form in the beginning (a transport condition). The inclination angles of the rods of all pantograph tiers with respect to axis Ox are equal to 5° . After deployment of the design, values of the specified angles reach 75° .

Elastic rods of the physical model have been replaced in the mechanical model by equivalent constructions of two rigid rods connected by the spring-bias cylindrical hinges with damping. Damping is used in order to approach the dynamics to reality at least in a qualitative sense. Stiffness of the springs in the hinges is defined from the condition of equal deflections of two constructions (Figure 2) under equal loads. The equivalent construction (in Figure 2 below) has the same deflection when spring resistance c_{joint} in the hinge is equal to $3EJ/(2a)$. Such a replacement is completely justified, as the configuration of the design is defined by mutual positions of the middle and end points of the rods. Besides, all dynamic values for the real design and its mechanical model at identical positions and velocities of mentioned above points with the same name are almost identical. It is applicable to the expressions for their tensor of inertia, moment of momentum, kinetic energy, and potential energy.

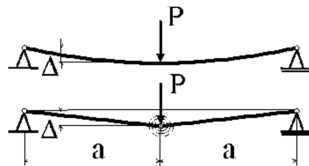


Figure 2. Beams with equivalent bending stiffness

4. Mathematical model of system

The equations of motion of the system under consideration become the most compact and convenient for numerical integration, if one chooses the instantaneous position of the mass centre C as an origin. Then one can obtain the following Lagrange's equations of the second kind for the generalized co-ordinates q_s :

$$E_s(T_r^O) - M \mathbf{r}_C^{**} \cdot \frac{\partial \mathbf{r}_C'}{\partial q_s} - \frac{1}{2} \boldsymbol{\omega} \cdot \frac{\partial \Theta^C}{\partial q_s} \cdot \boldsymbol{\omega} + \dot{\boldsymbol{\omega}} \cdot \frac{\partial \mathbf{K}_r^C}{\partial \dot{q}_s} + \boldsymbol{\omega} \cdot E_s^*(\mathbf{K}_r^C) = Q_s \quad (2)$$

The equation of the attitude motion may be obtained as the Euler-Lagrange equation [4]

$$\Theta^C \cdot \dot{\omega} + \Theta^C \cdot \dot{\omega} + \omega \times (\Theta^C \cdot \omega) + \omega \times \mathbf{K}_r^C = \mathbf{m}^C \quad (3)$$

The following notations are used here: Θ^C is the inertia tensor of the whole system with respect to point C , $\mathbf{K}_r^C = \int_m^* \mathbf{r}' \times \mathbf{r}' dm - M \mathbf{r}_c' \times \mathbf{r}_c'$ is the relative moment of momentum of the deployed part with respect to point C ; \mathbf{r}_c' is position vector of the instant position of the mass centre C in the frame of reference $Oxyz$; the symbol * denotes time differentiation in the reference frame $Oxyz$; M is the total mass of the system; T_r^o is the kinetic energy of the relative motion of the carried bodies calculated under condition of definition of relative velocities of their points with respect to O ; Q_s are generalized forces that take into account the elastic and dissipative characteristics of the construction;

$E_j(\cdot) = \frac{d}{dt} \frac{\partial(\cdot)}{\partial \dot{q}_j} - \frac{\partial(\cdot)}{\partial q_j}$ is the Euler's operator; $E_j^*(\cdot) = \frac{\partial}{\partial t} \frac{\partial(\cdot)}{\partial \dot{q}_j} - \frac{\partial(\cdot)}{\partial q_j}$ is also the Euler's operator, but the time differentiation is performed in the reference frame $Oxyz$; \mathbf{m}^C is the gravitational torque; symbols \times and \cdot in Eqs. (2), (3) denote vector and scalar product respectively.

If to supplement Eqs. (2), (3) with the kinematical equations, one obtains a closed system of equations of motion. The parameters of Rodrigues-Hamilton were chosen as the attitude parameters [4]. Further, it is necessary to choose proper generalized coordinates q_s and determine expressions for \mathbf{r}_c' , Θ^C , T_r^C , \mathbf{K}_r^C , Π and all their derivatives with respect to time and generalized co-ordinates, which appear into expressions for factors of the equations (2), (3).

During deployment, Coriolis forces act on the material points because of the rotational-translational motion. These forces can produce deformations of an elastic structure in the transverse direction. At the same time, transverse forces are absent in the direction of the orbit binormal. Hence, the displacements of the design along the axis Oy can be neglected.

In this study, values of co-ordinates x_i, z_i ($i=1, N$) of points E_i of each tier, lying on axis Oz on the straight lines connecting points $E_{(i)}^{(L)}, E_{(i)}^{(R)}$, and angles $\tilde{\beta}_k$ ($k=1, 2$) (Figure 1) have been chosen as the generalized co-ordinates. (Note that $z_i = z_{i,p}(t) + z_{i,e}$, where $z_{i,p}(t)$ are prescribed functions of time and $z_{i,e}$ are independent variables). The pantograph structures having 20 tiers were studied.

The original computation package is developed for the numerical integration of the obtained ordinary differential equations in the frame of the Cauchy problem. The majority of operators of the program is obtained as Fortran-expressions in Mathematica⁵ in the codes written specifically for the system studied.

It is obvious that the dynamics of a complex flexible structure depend on the time history of the deployment. Two such time histories were used here. The deployment of space designs often used such a law $b(t)$ that the velocity time history of an actuating motor $\dot{b}(t)$ looks like the line 1 in Figure 3. Such a function $\dot{b}(t)$ has two angular points, and a function $\ddot{b}(t)$ (so and a function of an actuating force or torque) has four points of discontinuities. Action of such a force on an oscillating system brings additional perturbations in its dynamics.

Therefore, the alternative law of deployment of the design was considered. For this law $\ddot{b}(t)$ does not contain points of discontinuities. Such a law can be constructed using the solution of the optimal control problem (see [6], Special Case II). It brings essentially less perturbation in the dynamics of the system than the first one as the numerical simulations had shown.

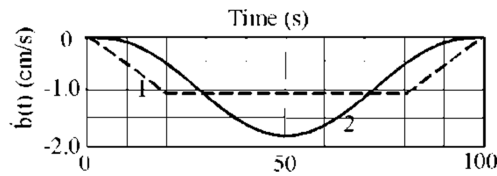


Figure 3. Laws of deployment

5. Numerical simulation

The torque of the central Newtonian field, corresponding to a circular orbit of 600 km altitude was considered as the external perturbing torque. Though the SC movement along an orbit is not considered here, the orbit parameters are used to calculate the gravitational torque and projections of the total SC moment of momentum to the inertial frame of reference. It is necessary for the monitoring of errors of the numerical integration of the initial value problem. Expressions governing the change of the total moment of momentum of the system are derived and numerically integrated along with the equations of motion for the system dynamics in order to identify mistakes in the code. The results agree within eight significant figures for each projection during monitoring.

Key system parameter values are: mass of main body $m_1 = 350$ kg, rods mass $m_1 = 1$ kg, bending stiffness $EJ = 20-80$ N m², decrement of oscillations $\vartheta = 0.001$, components of the main body inertia tensor $J_{xx}=4000$ kg m², $J_{yy}=5000$ kg m², $J_{zz}=2000$ kg m², angular momentum of one GD rotor $h_{rot}=20$ kg m²/s, GD damping coefficient $k_{3\beta_1\beta_2}=40$ N m / s², duration of deployment $T_f=100-1000$ s.

The pantograph deployment essentially increases the components of the inertia tensor $\Theta_{1,1}^C$ and $\Theta_{2,2}^C$ and decreases slightly the component $\Theta_{3,3}^C$. Generally speaking, the inertia tensor is not a diagonal one in the presence of transverse design deviations along Ox axis. Because of transverse deviations, there is a nonzero component $\Theta_{1,3}$, but it is neg-

ligible small also as compared to the diagonal components of the inertia tensor and has no essential effect on the SC dynamics.

The increase in the inertia tensor components leads to the sharp decrease in the ω_2 magnitude (Figure 4) and to the SC orientation violation. Figure 5 shows how amplitude of ω_2 attenuate in the long-term consideration because of the GD operation.

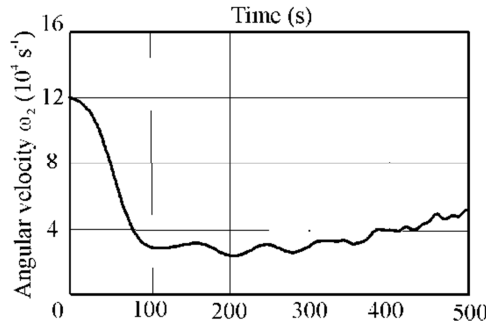


Figure 4. Time histories of absolute angular velocity projection ω_2

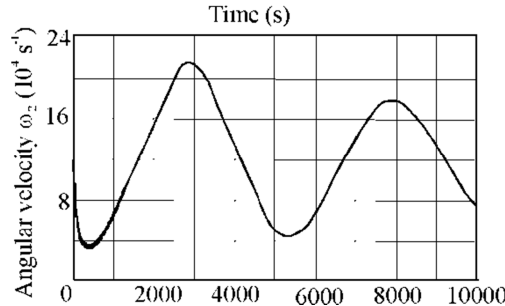


Figure 5. Time history of absolute angular velocity projection ω_2 in long-term consideration

At the same time, generalized co-ordinates $z_i (i=1,20)$ behave as it is shown in Figure 0. (Note that $z_i = z_{i,p}(t) + z_{i,e}$, where $z_{i,p}(t)$ are functions of time and $z_{i,e}$ are independent variables that determine elastic oscillations.) The dash lines correspond here to the usual deployment law, the solid lines – to the optimal law (Figure 0). This behaviour shows the appreciable longitudinal oscillations of the design at the deployment stage. Optimization of the deployment law reduces the vibration amplitudes considerably. The oscillating motions are induced by excitation of elastic oscillations of the design rods with the spring hinges. Their amplitudes grow with increase of the number of the tiers. Longitudinal oscillations have noticeable influence upon the components of the inertia tensor (Figure 4). In Figure 6 one may see that amplitude of oscillatory component of $z_{20,e}$ (opt) is half of the same value for $z_{20,e}$ (nonopt).

The transverse relative deviations of the design longitudinal axis that are defined by the generalized co-ordinates x_{20} are shown in Figure 7. Practically all these deviations are directed opposite to the vector of the SC velocity under the effect of the Coriolis forces.

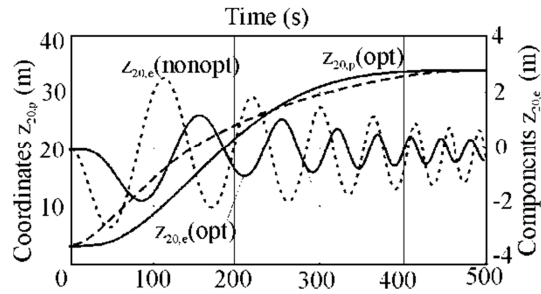


Figure 6. General coordinates z_{20} vs time

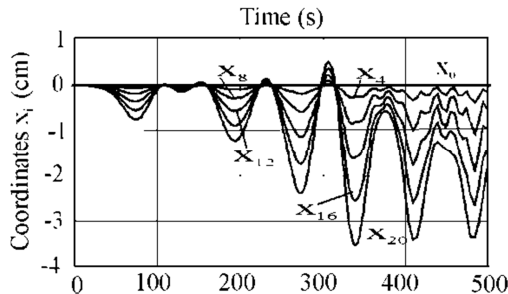


Figure 7. General coordinates x_i vs time

SC with switched off GD enters into a condition of simple harmonic pitch oscillations under the influence of the gravitational torque. Taking into account the Coulomb friction in design hinges practically has no influence on damping of these oscillations since elastic longitudinal oscillations of the design damp quickly enough. Transverse vibrations, on the contrary, damp very slowly as compared to deployment duration even under the influence of forces of structural damping since their amplitudes and velocities are very small as one can see in Fig. 7.

At twice as long deployment, the behaviour of the generalized co-ordinates becomes smooth enough; the oscillation amplitudes of overall design length do not exceed 0.15 m. The transversal deviations have a smooth mode. The design replicates the behaviour of a cantilever beam. The oscillating components are superimposed on these deviations. These deviations lead to a reduction of the amplitudes of vibration because of their strong connectedness with the pitch oscillations, which damp through the GD effect, even if the structural damping is not taken into consideration. At deployment of this design during 500 s from very heavy ideally stabilized space station, the amplitudes and frequencies of longitudinal and transversal oscillations visibly decrease.

The deviations of the GD angles $\tilde{\beta}_i$ during the stabilization process do not exceed 0.1 rad.

6. Conclusions

The present study deals with the exploration of the dynamics of the gyro-gravitational stabilized spacecraft in the mode of the deployment of the flexible pantograph structure. A novel mathematical model, computer simulations, new control profile for design deployment is presented. Novelty of the approach consists in the taking into account additional internal degrees of freedom of the pantograph design in comparison with known earlier settings of the problem; in using the developed by author method of derivation of the dynamic equations of mechanical systems with internal degrees of freedom and non-stationary connections; in using optimum with respect to damping of elastic oscillations control profile for deployment of flexible designs. A detailed simulation study has allowed to analyze the dynamic behaviour of the design at various values of parameters both the spacecraft with flexible pantograph structure and the laws of deployment. Data obtained permit the designer to select the most appropriate deployment, structure and gyro-dampers parameters. The results obtained from using the optimum control profile have been compared with those of the standard control profile. The comparison demonstrates that the proposed profile can significantly reduce the vibration of the flexible structure during deployment operations.

The developed computational FORTRAN code may be easily adopted for other deployed systems.

Acknowledgement

The author wishes to express his gratitude to Prof. V. S. Khoroshilov for his technical contributions in the work reported here.

References

1. V. Dranovskii, V. Khoroshylov, A. Zakrzhevskii, *Spacecraft dynamics with regard to elastic gravitational stabilizer deployment*, Acta Astronautica, **64** (2009) 501-513.
2. V. Khoroshilov, A. Kovalenko, A. Zakrzhevsky, *Dynamics of deployment of elastic pantograph designs on space vehicle*. XXII Symposium - Vibrations in physical systems – Poznań-Będlewo, (2006) 167- 172.
3. <http://www.vibsys.strefa.pl/journal/2006-22/167.pdf>
4. V. V. Beletsky, *Motion of an Artificial Satellite about its Center of Mass*, Israel Program for Scientific Translations, Jerusalem, 1966.
5. J. Awrejcewicz, *Classical Mechanics. Dynamics*, Springer-Verlag, New York, 2012.
6. A. I. Lurie, *Analytical mechanics*, Springer, 2002.
7. A. E. Zakrzhevskii, *Slewing of Flexible Spacecraft with Minimal Relative Flexible Acceleration*, J. of Guidance, Control, and Dynamics, **31** (2008) 563- 570.

Research of Work of a Rotor Crush Machine on Elastic Foundation with the Use of Graphs

Roman ZINKO

*Department of Mechanical Engineering
Institute of Engineering Mechanics and Transport
National University "Lvivska polytechnika"
apt.8 Bandera Street, 79013, Lviv, Ukraine
rzinko@gmail.com*

Abstract

The use of graphs for the research of a rotor crush machine work on elastic foundation is offered. For machines the structure graph of its design is being written. The graph of levels structure of the generalized coordinates of mathematical model is being formed on the basis of structure graph of machine design. It allows building of the mathematical model, which describe the physical processes of the machine work quickly and qualitatively.

Keywords: mathematical model, rotor crush machine, elastic foundation.

1. Introduction

The process of solid bodies crushing is used in many industries in which this or that material has to be crushed. The costs of crushing within of total costs can reach 70% [1-2].

2. The analysis of recent studies

Analyzing the state of the crushing theory and practice [3-7], it is necessary to conclude that the efficiency of modern crushing machines is rather low. The existent types of these machines do not contain elements, the improvement of which would radically increase the effectiveness of crushing process. One of the possible ways of the crushing process improvement can be the realization of the idea of combining several methods of crushing, for example, the impact with vibration [8-10]. In such circumstances, the study of mechanisms of crushing machines, in which several methods of crushing are used simultaneously, is particularly expedient. Thus, the body vibration of crushing machine of percussion action would help to destroy the established layer of material, which is crushed. In addition, the elastically fixed rotor crusher beaters would have a greater amplitudes of relative fluctuations, that would facilitate better offtaking of the crushing products. Accordingly, it is expedient to elaborate new machine schemes, in which two physical phenomena: impact and vibration, would be used simultaneously, in order to increase the efficiency of the rotor crushing machine.

In the process of new machine models of creation, it is expedient to use computer experiments that allows developers to use efficiently their resources and time. At the same time, to carry out the computer experiments it is necessary to have the designed

machines mathematical model of the sufficient quality level. The elaboration of the construction methods of such mathematical models is an urgent problem.

3. General regulations

As an example of the graphs usage in the study of crushing machines work, let's consider the rotor crushing machine work with the crusher on the elastic foundation and rigidly fixed gear and beaters.

Subsequently, generally accepted assumptions in studies of the machines dynamics will be used [11,12]: – the body of crusher, which is in the plane-parallel movement in the vertical plane, the rotor with imbalances and beaters which are in a compound motion in the vertical plane, are considered to be hard inert bodies; – elastic elements of the body crusher bearer – inertialess bodies with tensile stiffness and shearing rigidity; – ignoring elasticity of rotor crushing machines drive components it is considered to be rigid inertial body, the rotation of which is caused by the driving torque of the drive engine; it is changed according to the external static mechanical characteristic.

Accepted third assumption leads to a change of graphs structures of constructive schemes of rotor crushing machine [13]. In this case it takes the form (Fig. 1). Based on the constructive scheme graph structure (Fig. 1), the design diagram of the rotor crushing machine was formed (Fig. 2) with discretely distributed elastic inertialess and rigid inertial elements. This design diagram allows to investigate the crusher body dynamics of plane-parallel motion, compound motion of its rotor with imbalance and beaters, rotational motion of the crush machine drive members, operation of crushing and, consequently, to study the impact of crusher vibration on the crushing process, to find out the peculiarities of the interaction of elements of the "energy source – vibration exciter – working body – technological loading" in various operation modes of the machine with stable or variable masses of technological loading.

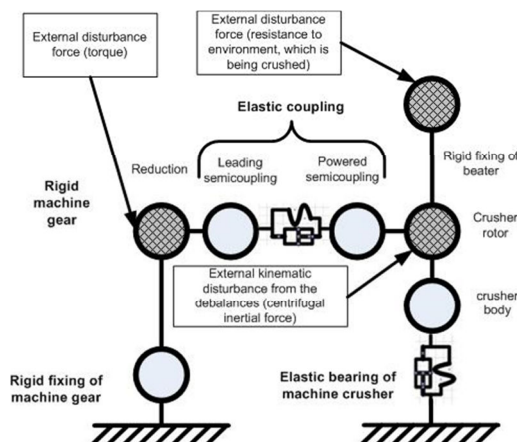


Figure 1. Graph of constructive scheme structure of rotor crushing machine with the crusher on the elastic foundation and rigidly fixed positive drive

Based on the first assumption was adopted the plane coordinate system XOY , which is rigidly joined with the land and is located in the vertical plane. In addition, $X_1O_1Y_1$, system was rigidly joined with the crusher body of the rotor crushing machines, the axes of which form a plane parallel to the coordinate plane XOY . Subsequently, it is more convenient to use the term " free state of the mechanical system". In the case of rotor crushing machine – it is a condition of state of rest of its inertial elements that are beyond the gravitational and electromagnetic forces (machine engine drive is disconnected from electric energy sources).

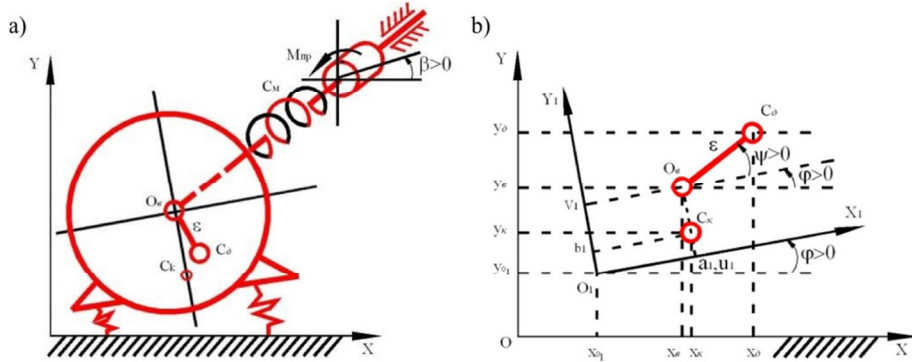


Figure 2. Desigh diagram of rotor crushing machine with the crusher on the elastic foundation and rigidly fixed positive drive and beaters a); accepted coordinate system and generalized coordinates b)

Taking into consideration the research tasks, based on constructive scheme structure graph (Fig. 3) and designed diagram (Fig. 4) through the modernization of the graph 2 a, which is represented in the table 1, the graph structure of generalized coordinates level couplings (Fig. 3) of rotor crush machine work mathematical model on elastic foundation and rigidly fixed positive drive, was recorded, where as the generalized coordinates were taken:

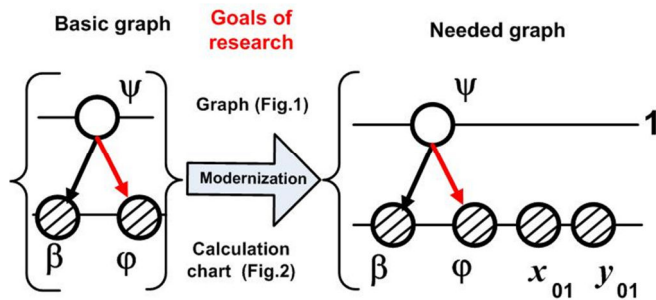


Figure 3. The graph structure of generalized coordinates level couplings (Fig. 3) of rotor crush machine work mathematical model on elastic foundation and rigidly fixed positive drive

q_1, q_2, q_3 – coordinates of point O_1 (Fig. 4) of the coordinate system $X_1O_1Y_1$ beginning, in a fixed coordinate system XOY and the angle of its rotation relatively to the fixed system, that is: $q_1 = x_{01}$; $q_2 = y_{01}$; $q_3 = \varphi$; $q_4 = \psi$ – angle of the rotor crusher rotation with imbalance and beaters relatively to the variable coordinate system $X_1O_1Y_1$; $q_5 = \beta$ – angle of shaft rotation of the leading semicoupling of machine gear; the angles of bodies rotation counterclockwise were considered as additional.

Using the general equation of dynamics [14] of a discrete mechanical systems in generalized coordinates (1), based on the graph of level relations strucuture of generalized coordinates (Fig. 3) futher, a mathematical model of rotor crush machine work on elastic foundation and rigidly fixed positive drive was being built.

$$\frac{d}{dt} \left(\frac{\partial T}{\partial \dot{q}_s} \right) - \frac{\partial T}{\partial q_s} = Q_s, \quad s = 1, \dots, n; \quad (1)$$

where T – the total kinetic energy of the movable inertial elements of rotor crush machine; \dot{q}_s – the time derivative of the generalized coordinates; n – the number of freedom degrees of rotary crush machine elements; Q_s – generalized force, which corresponds to the generalized coordinate q_s .

The total kinetic energy T of the entire mechanical system equals:

$$T = T_K + T_\theta + T_\delta + T_{\partial\theta},$$

where $T_K = \frac{1}{2} [m_k \cdot (\dot{x}_k^2 + \dot{y}_k^2) + I_k \cdot \dot{\varphi}_1^2]$ – kinetic energy of the crusher body; m_k, I_k – mass of the body and its central moment of inertia; x_k, y_k – coordinates of the center of the body weight in a coordinate system XOY ; $T_\theta = \frac{1}{2} [m_\theta (\dot{x}_\theta^2 + \dot{y}_\theta^2) + I_\theta (\dot{\varphi} + \dot{\psi})^2]$ – kinetic energy of the clusher rotor shaft with the beaters and semicoupling; m_θ, I_θ – correspondingly, the mass and moment of inertia of the shaft with the beaters and semicoupling of elastical joining coupling relatively to the axis of their rotation in the crusher body; x_θ, y_θ – coordinates of the rotation axis of the shaft with beaters in a coordinate system XOY ; $T_\delta = \frac{1}{2} [m_\delta (\dot{x}_\delta^2 + \dot{y}_\delta^2) + I_\delta (\dot{\varphi} + \dot{\psi})^2]$ – kinetic energy of the imbalances; m_δ, I_δ – the mass and moment of inertia of the imbalances relatively to the axis of shaft rotation in the crusher body; x_δ, y_δ – coordinates of the imbalances center of gravity in a coordinate system XOY ; $T_{\partial\theta} = \frac{1}{2} I_{\partial\theta} \cdot \dot{\beta}^2$ – kinetic energy of the machine drive elements that are in rotational motion; $I_{\partial\theta}$ – total moment of inertia of these elements is brought to the axis of the leading semicoupling shaft of the drive gear; $\dot{\beta}$ – the angular velocity of the leading semicoupling shaft.

$$\left\{ \begin{array}{l} q_1 = x_{01}; \\ \frac{d}{dt} \left(\frac{\partial T}{\partial \dot{x}_{01}} \right) - \frac{\partial T}{\partial x_{01}} = m_k [\ddot{x}_{01} - \ddot{\varphi} \cdot L_1(\varphi) - (\dot{\varphi})^2 \cdot L_2(\varphi)] + m_e [\ddot{x}_{01} - \ddot{\varphi} \cdot l_1(\varphi) - (\dot{\varphi})^2 \cdot l_2(\varphi)] + \\ + m_o [\ddot{x}_{01} - \ddot{\varphi} \cdot l_1(\varphi) - (\dot{\varphi} + \ddot{\psi}) \cdot l_3(\varphi, \psi) - (\dot{\varphi})^2 \cdot l_2(\varphi) - (\dot{\varphi} + \dot{\psi})^2 \cdot l_4(\varphi, \psi)]; \\ q_2 = x_{01}; \\ \frac{d}{dt} \left(\frac{\partial T}{\partial \dot{y}_{01}} \right) - \frac{\partial T}{\partial y_{01}} = m_k [\ddot{y}_{01} + \ddot{\varphi} \cdot L_2(\varphi) - (\dot{\varphi})^2 \cdot L_1(\varphi)] + m_e [\ddot{y}_{01} + \ddot{\varphi} \cdot l_2(\varphi) - (\dot{\varphi})^2 \cdot l_1(\varphi)] + \\ + m_o [\ddot{y}_{01} + \ddot{\varphi} \cdot l_2(\varphi) + (\dot{\varphi} + \ddot{\psi}) \cdot l_4(\varphi, \psi) - (\dot{\varphi})^2 \cdot l_1(\varphi) - (\dot{\varphi} + \dot{\psi})^2 \cdot l_3(\varphi, \psi)]; \\ q_3 = \varphi; \\ \frac{d}{dt} \left(\frac{\partial T}{\partial \dot{\varphi}} \right) - \frac{\partial T}{\partial \varphi} = m_\kappa \cdot \left\{ \ddot{x}_{01} \cdot L_1(\varphi) + \ddot{\varphi} \cdot (a_1^2 + b_1^2) + \ddot{y}_{01} \cdot L_2(\varphi) \right\} + I_\kappa \cdot \ddot{\varphi} + \\ + m_e \cdot \left\{ -\ddot{x}_{01} \cdot l_1(\varphi) + \ddot{\varphi} \cdot (u_1^2 + v_1^2) + \ddot{y}_{01} \cdot l_2(\varphi) \right\} + I_e \cdot (\dot{\varphi} + \ddot{\psi}) + \\ + m_o \cdot \left\{ -\ddot{x}_{01} \cdot [l_1(\varphi) + l_3(\varphi, \psi)] + \ddot{y}_{01} \cdot [l_2(\varphi) + l_4(\varphi, \psi)] + \ddot{\varphi} \cdot [u_1^2 + v_1^2] + \right. \\ \left. + 2 \cdot \ddot{\varphi} \cdot \varepsilon \cdot l_5(\psi) + \ddot{\psi} \cdot \varepsilon \cdot l_5(\psi) + 2 \cdot \dot{\varphi} \cdot \dot{\psi} \cdot \varepsilon \cdot l_6(\psi) + (\dot{\psi})^2 \cdot l_6(\psi) \right\} + \\ + I_o \cdot (\dot{\varphi} + \ddot{\psi}); \\ q_4 = \psi; \\ \frac{d}{dt} \left(\frac{\partial T}{\partial \dot{\psi}} \right) - \frac{\partial T}{\partial \psi} = m_o \cdot \left\{ -\ddot{x}_{01} \cdot l_3(\varphi, \psi) + \ddot{\varphi} \cdot \varepsilon \cdot l_5(\psi) + \ddot{y}_{01} \cdot l_4(\varphi, \psi) - (\dot{\varphi})^2 \cdot \varepsilon \cdot l_6(\psi) \right\} + \\ + (\dot{\varphi} + \ddot{\psi}) \cdot [I_e + (m_o \cdot \varepsilon^2 + I_o)]; \\ q_4 = \beta; \\ \frac{d}{dt} \left(\frac{\partial T}{\partial \dot{\beta}} \right) - \frac{\partial T}{\partial \beta} = I_{np} \cdot \ddot{\beta}. \end{array} \right. \quad (2)$$

$$\left\{ \begin{array}{l} q_1 = x_{01}; Q_{x_{01}} = -(F_{II}^x + F_{II}^x); \\ q_2 = y_{01}; Q_{y_{01}} = -[F_{II}^y + F_{II}^y + G_K + G_B + G_M + G_{II}]; \\ q_3 = \varphi; Q_\varphi = +M(F_{II}^x) + M(F_{II}^x) - M(F_{II}^y) - M(F_{II}^y) - M_{GK} - M_{GB} - M_{GII} \end{array} \right. \quad (3)$$

$$q_4 = \psi; Q_\psi = c_m \cdot (\beta - \psi - \varphi) - \left[m_\beta \cdot g \cdot \varepsilon \cdot \cos(\varphi + \psi) + \int_{R_\beta - h_w}^{R_\beta} \alpha_{uu} \cdot L_3 \cdot \Delta v^2(r) \cdot \rho(r) \cdot dr \right].$$

$$q_5 = \beta; Q_\beta = M_{PP}(\dot{\beta}) - c_m \cdot (\beta - \psi - \varphi).$$

The left parts of the equation (1) have the form of (2). The right parts of equation (1) have the form of (3).

Dependencies(2) and (3) are the sets of left and right parts of the equations of the rotor crush machine work mathematical model on elastic foundation and rigidly fixed

positive drive, which is based on the graph of level relations structure of generalized coordinates (Fig. 5). The comparison of the results of the study of the machine obtained by means of physical and mathematical model experiment shows its good matches.

As a result of the research the following conclusions can be made:

1. The character of engine's drive machine operation does not change by the presence of vibrating crusher body. The reaction of the engine on the change of the necessary productivity values, type of crushed grain and its moisture content is similar to the machines with rigidly fixed crusher body.
2. Movement of the crusher body doesn't alternate with a change of the material quantity in it within a wide range of changes in the estimated productivity, before the reduction of the drive motor rotation. Amplitude of drum vibration decreases at the moment of initial loading at the sudden gate opening.
3. The drum installation on the elastic foundation leads to the appearance of three additional frequencies, the values of which are determined by the ratio between the mass and moment of the drum inertia, rigidity in the horizontal and vertical directions of its elastic bearing, place of its fixation to the drum.

Amplitude of the drum body vibration, the form of its values field in a vertical plane considerably depends on the ratio between the values of the vibration exciter mass imbalance, distance from the point of suspension to the center of mass, angular velocity of the rotor rotation, drum machines mass and rigidity of elastic bearings.

Value of the amplitudes of the drum forced vibrations along the coordinate axes x , y by the dependency:

$$A = \frac{m_d \epsilon (\dot{\psi}_{ycm})^2}{(m_k + m_e + m_d) \cdot \left[\frac{C_n^x + C_x^x}{m_k + m_e + m_d} - (\dot{\psi}_{ycm})^2 \right]}.$$

where $\sum m_i$ – the total mass of all drum elements; $\dot{\psi}_{hom}$ – the nominal angular velocity of the machine rotor. It is necessary to replace " C_x " by " C_y " in order to estimate the amplitude along the axis " y_m " to the dependency (8).

The values, obtained theoretically and experimentally at different intervals of adjustable parameters varying are presented on the diagrams (Fig. 4).

Studying the relationship of crusher productivity with its structural and dynamic parameters one cleared out the following:

1. Oscillograms of beaters acceleration in the crushing mode have non-sinusoidal shape (Fig. 4, a) with amplitude factor $kA = 4,1$. Boundary frequency of the signal spectrum on the 10% amplitude criterion is $fhr = 300$ Hz, harmonic factor $kh = 0,58$, the distortion factor $ky = 0,87$. Considering the allocation of the normalized power of the spectrum harmonics (Fig. 6, b) it appears that more than 80% of power is transferred by the first harmonic.
2. The crusher productivity Q_{TEOP} at the constant access rate n and width of discharge gap δ with increasing bias of imbalance h is decreased.

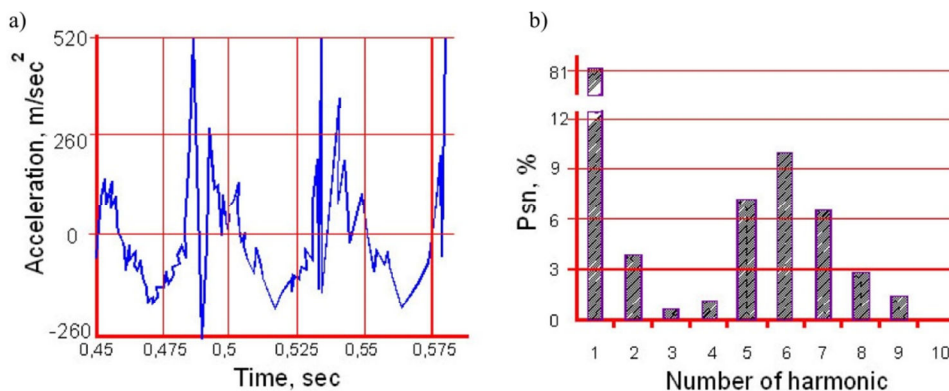


Figure 4. Oscillogram of acceleration (a) and the allocation of the normalized power of the spectrum harmonics (b)

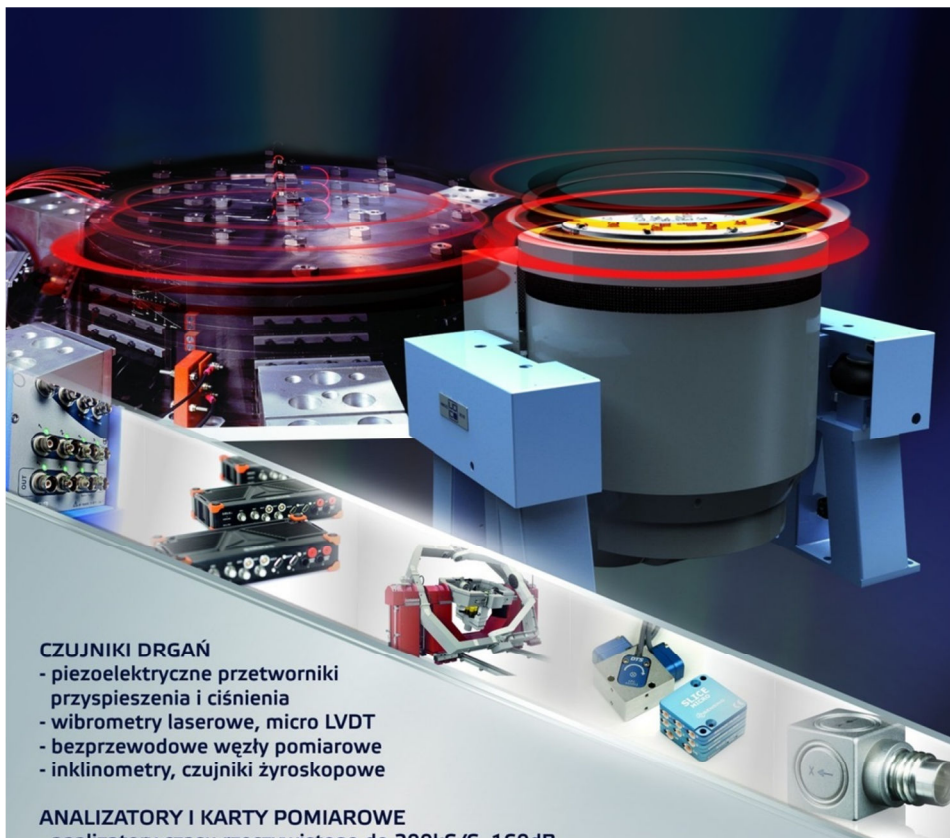
4. Conclusions

The proposed methodology of the creation of mathematical models using graphs of necessary complexity allows to describe the physical processes of the machine work quickly and qualitatively.

References

1. V.I. Akulov, *On the coefficient of efficiency of grinding processes and specific expenditures of energy*, Chemical Industry, **10** (1996) 7-10.
2. A.R. Demidov, S.E. Chirkov, *Grinding methods and methods for its efficiency estimation*, M: Goskomzaga USSR, 1969.
3. A.I. Boyko, A.V. Nowicki, *Reliability analysis of feed mill by the method of fault tree*, Design, manufacture and operation of agricultural machinery, Kirovograd: KSTU. **28** (1999) 46-54.
4. V.T. Diodriev, S.V. Chausov, *Methods of the energy performance improvement of small feed mill plants*, Problems of energy supply and energy saving in agriculture of Ukraine: Bulletin of Kharkiv state technical Univ. of agriculture, Kharkiv: HSTUA. **10** (2002) 136-141.
5. M.V. Hurtovoy, O.V. Gavrilov, *Justification of the mode of apricots grinding with rotor crusher*, Science. Labour HSTUA. Kharkiv HSTUA. **1** (2005) 230-236.
6. Y.I. Revenko, O.M. Pylypenko, S.M. Chybs, *Estimation of quality joint grinding and mixing of components of mixed fodder with hammer crusher*, Collected works NAU: Mech. of agricultural production. Kyiv: educ. Dep. of NAU. **9** (2000) 172-176.
7. V.I. Kirichenko, *Selection of parameters and work mode of forced grinding mills*, Coal of Ukraine, **5** (1998) 45-46.

8. Pat. 22533 Ukraine, V02S13/00. Impact crusher. O.D. Semkovych, P.S. Korunyak, I.O. Nishchenko, G.M. Rayvych (Ukraine) - № 97020459; appl. 02.04.97, Pub. 17/03/98.
9. F. Semerak, P. Korunyak, I. Lozovyy, V. Borovets, *Mathematical model of work of vibroimpact crushing machine of hammer type*, Bulletin of the Lviv State Agrarian Univ: Agroengineering study. Lviv: educ. Dep. of LSAU. **2** (1998) 99-102.
10. P.S Korunyak, *A mathematical model of rotary crusher work for bulk materials crushing*, Agricultural machines: Science works. Lutsk:educ. Dep. of LSTU. **5** (1999) 367-374.
11. I.F. Goncharevich, K.V. Frolov, *Theory of vibrating technics and technology*, Moscow: Nauka, 1981.
12. V.I. Syrovatka, K.V. Frolov, *Main regularities of grain crushing process in hammer crushing machine*, Moscow: Agroprom publicaton, 1985.
13. R.V. Zinko, I.C. Lozovyy, *Graphs of level relations structure of generalized coordinates for autotracking and transporting machines and method of constructing mathematical models*, Bulletin of the Podillya University of Technology. Hmelnitskyj: educ. Dep. of PUT. **1** (2001) 29-33.
14. A.I. Lurie, *Analytical Mechanics*, Moscow: Fizmatgiz, 1961.



CZUJNIKI DRGAŃ

- piezoelektryczne przetworniki przyspieszenia i ciśnienia
- wibrometry laserowe, micro LVDT
- bezprzewodowe węzły pomiarowe
- inklinometry, czujniki żyroskopowe

ANALIZATORY I KARTY POMIAROWE

- analizatory czasu rzeczywistego do 200kS/S, 160dB
- rejestratory pokładowe, stacjonarne ultra-mobilne (1.5cm^3 / kanał)
- wzmacniacze sygnałów, karty pomiarowe
- wynajem, serwis, szkolenia, kalibracja

WZBUDNIKI DRGAŃ I SYMULATORY RUCHU

- elektrodynamiczne
- elektrohydrauliczne
- pneumatyczne
- stoły ślimakowe, akcesoria, serwis
- układy od 1 do 5 osi ruchu
- systemy naprowadzania i śledzenia
- wirówki oraz systemy łączone z komorą klimatyczną
- wsparcie techniczne, integracja, akcesoria, serwis

WIBROAKUSTYKA, DYNAMIKA UKŁADÓW I DIAGNOSTYKA



Envibra Sp. z o.o.
Ul. Koperkowa 35a/2
62-064 Plewiska k/ Poznania
Tel. +48 61 86 00 660 / Fax. +48 61 6100 357
www.envibra.pl

EN VIBRA